Cranfield University

School of Industrial and Manufacturing Science
Advanced Materials Department

PhD Thesis
Academic years 1994 / 1997

Panagiotis I. Karkanas

Cure Modelling and Monitoring of Epoxy / Amine Resin Systems

Supervisor: Dr Ivana K. Partridge

March 1998

ABSTRACT

Thermoanalytical techniques and dielectric analysis were used in this study to describe and characterise the cure processes occurring during the isothermal and dynamic cures of four epoxy/amine resin systems.

The complexity of the cure reactions was illustrated by results from DSC and FTIR experiments and was attributed to the variety of chemical reactions between the epoxy and the amine groups. Several phenomenological and mechanistic cure kinetics models were constructed, based on the cure reaction mechanisms, in order to simulate the degree of conversion during the cure. A one-to-one relationship was established between the degree of cure and the glass transition temperature of the curing resin, which was further used in the construction of chemoviscosity models and in a simulation of the viscosity advancement during the cure.

A number of mathematical techniques were utilised to evaluate the parameters involved in all the models, varying from simple linear regression methods to complex non-linear least squared estimation procedures.

An in-situ dielectric monitoring technique was used in combination with the above mentioned chemorheological models, to investigate the feasibility of a quantitative correlation between the changes in the dielectric signal, the cure advancement and the major physical transformations, namely gelation and vitrification. The imaginary impedance response of the curing resin, as measured by the dielectric technique, showed good agreement with the degree of conversion, depicting all the crucial characteristics of the curing mechanism, such as autocatalysis and diffusion. The endset of the cure reaction was also identified from the endset of the conductivity changes and correlated to the vitrification time.

The analytical chemorheological models developed in this study to describe the cure processes for some epoxy/amine resin systems, along with the dielectric monitoring technique used, suggest that a real-time link between the above mentioned models and the cure monitoring technique can be achieved. This would greatly enhance the predictive capability of the technique and form the basis of a future feedback-loop control system.

ACKNOWLEDGEMENTS

The author would like to express his gratitude to his supervisor, Dr. Ivana K. Partridge for her supportive advice and the very useful discussion on various subjects of this project. Also acknowledged, is the useful comments of Professor Harry Block in the interpretation of a major part of the experimental results of the present study.

The support of all the partners of the DTI/EPSRC LINK Structural Composites programme "Process Optimisation and the Relationship of Performance to Process Conditions" (PORPPC), as a part of which this study was undertaken, is equally acknowledged. In particular, the author would like to express his gratitude to Dr. Gordon Cracknell and Mr. Andrew Milburn from Short Brother's plc, Belfast, for the chemical information supplied from HPLC experiments on the resin systems used in this study. The support of Dr. David Attwood from Sowerby Research Centre, British Aerospace (Operations) Ltd., Filton, is also acknowledged for his support on this work and the useful discussions and exchange of information throughout the time scale of this PhD thesis. His hospitality at the Sowerby Research Centre at Filton and the use of the Thermal Analysis Laboratory facilities are also acknowledged.

The contribution of the Chemistry Department of Surrey University, Guildford is also acknowledged, for allowing us to use their facilities and especially the use of the FTIR spectrometer, on which all the experiments presented in this study were carried out.

The author is also thankful to his colleagues in the Polymers Group for the useful co-operation during this project and especially to Dr. George Maistros for his support and help to carry out the dielectric experiments and to interpret the results.

CONTENTS

List of Figures

List of Tables

NOTATION

A) Symbols (by order of appearance)

f	functionality of reactive species
p_c	critical point of epoxy conversion for gelation
f_e	functionality of epoxy resin
f_α	functionality of amine
r	ratio of amine hydrogens to epoxy groups
T_g	glass transition temperature
T_{g0}	glass transition temperature of monomer
$T_{g\infty}$	glass transition temperature of fully cured resin
${}_{gel}T_g$	glass transition temperature at gel point
T_c	cure temperature
T	absolute temperature
f	fractional free volume
f_g	free volume fraction at T_g
α	expansion coefficient of the free volume
E_x	lattice energy for crosslinked polymer
E_m	lattice energy for uncrosslinked polymer
F_x	segmental mobility for crosslinked polymer
F_m	segmental mobility for uncrosslinked polymer
X_g	extent of conversion
K_i	reaction rate constant
$[C_i]$	concentration of species C_i
X_E	concentration of epoxy groups
x_E	fractional degree of epoxy conversion
ξ_α	conversion of amine hydrogens
ξ_b	conversion of epoxy groups

e_b	ratio between epoxy groups and diamines
$F_0(z)$	probability generation function of the number of bonds issuing from an f-functional monomer in the root of a molecular tree
$F(z)$	probability generation function of the number of bonds issuing from an f-functional monomer placed in a generation $g > 0$ in a molecular tree
M_n	number average molecular weight
M_A	molecular weight of amine
M_E	molecular weight of epoxy
η	viscosity
P	pressure
$\dot{\gamma}$	shear rate
t	time
α	degree of conversion
η_∞	viscosity of fully cured resin
ΔE_η	Arrhenius activation energy for viscosity
R	universal gas constant
k_∞	kinetic analog of the viscosity of the fully cured resin
ΔE_∞	kinetic analog of the Arrhenius activation energy for viscosity
α_{gel}	degree of cure at gel point
η_0	initial viscosity at temperature T
T_s	reference temperature in WLF equation
C_1, C_2	parameters in WLF equation
A	absorbance in the Beer-Lambert law
E	extinction coefficient in the Beer-Lambert law
p	dipole moment
P_V	macroscopic dipole moment in a volume V
P	polarisation
D_m	displacement field resulting from a dielectric
E_m	electric field resulting from a dielectric
ε_0	permittivity of the free space

χ_r	relative dielectric susceptibility
ε_r	relative dielectric permittivity
ε	absolute permittivity
E_L	local electric field in a dielectric
E_{dip}	electric field resulting from the presence of dipoles
α	polarisabillity
α_e	electronic polarisation
α_a	ionic polarisation
α_o	orientation polarisation
α_{in}	interfacial polarisation
ω	angular frequency
ε_r'	real part of complex permittivity
ε_r''	imaginary part of complex permittivity
$tan\delta$	loss angle or dissipation factor
k	Boltzmann's constant
ε_{rs}	relaxed permittivity
ε_∞	unrelaxed permittivity
τ	relaxation time
σ	ionic conductivity
u	ion mobility
t_b	electrode blocking layer thickness
ε'	relative permittivity or dielectric constant
ε''	dielectric loss
ε'_x	measured permittivity with electrode polarisation effects
ε''_x	measured dielectric loss with electrode polarisation effects
Z	complex impedance
Z'	real part of imaginary complex impedance
Z''	imaginary part of complex impedance
R_p	ionic resistance

ρ	resistivity
ρ_0	initial resistivity
ρ_m	maximum resistivity
H	enthalpy
ΔH_T	total heat of reaction
ΔH_{res}	residual heat of reaction of a partially cured resin
C_s	sample capacitance
C_0	air capacitance
G_s	sample conductance
f	test frequency
E_i	epoxy ring absorption in Eq. 4.1
R_i	reference band absorption in Eq. 4.1
A_i	pre-exponential factor of Arrhenius dependent reaction rate constant
E_i	activation energy of Arrhenius dependent reaction rate constant
α_{iso}	isoconversion
β	heating rate
T_m	temperature at maximum reaction rate
W_i	relative weight of reaction i in the dynamic cure of 934 resin (Eq. 4.19)
λ	parameter in Di Benedetto's equation (Eq. 5.3)
k_d	reaction rate constant of a diffusion controlled reaction
E_d	activation energy for diffusion
T_r	reference temperature of the modified WLF equation (Eq. 7.5)
f_c	critical frequency at the maximum of the imaginary impedance in the frequency domain
Y	admittance
Y'	real part of the complex admittance
Y''	imaginary part of the complex admittance
R	resistance
C	capacitance
K	cell constant

S	effective surface measured by the dielectric sensors
L	effective inter-electrode spacing
d_i	inter-electrode spacing
n	number of electrodes in the comb-electrode
Y_s	admittance of the Kapton substrate of the dielectric sensors
Y_a	admittance of the free air
Y_r	admittance of the curing resin
$Y_{t,\,air}$	total admittance measured in the free air
$Y_{t,\,resin}$	total admittance measured in the resin
$Z''_{r,\,peak}$	imaginary impedance of the curing resin at the characteristic peak in the frequency domain
ε''_{cond}	conductivity component of the measured dielectric loss

B) Abbreviations (by order of appearance)

RTM	Resin Transfer Moulding
DGEBA	DiGlycidylEther of Bisphenol A
TGDDM	N,N' - tetraglycidyl - 4,4' - diaminodiphenylmethane
TGPAP	TriGlycidylParaAminoPhenol
EDA	EthyleneDiAmine
DETA	DiEthyleneTriAmine
TETA	TriEthyleneTetrAmine
PACM	bisParaAminoCyclohexylMethane
DACH	1,2-DiAminoCycloHexane
IPDA	IsoPhoroneDiAmine
DDM	Diamino-DiphenylMethane
DDS	Diamino-DiphenylSulphone
DETDA	DiEthylToluneneDiAmine
TGIC	Tri-GlycidylIsoCyanurate
HHPA	Hexa-HydroPhthalic Anhydride

TMA	Tri-Mellitic Anhydride
DGA	DiGlycidylAniline
TTT	Time-Temperature-Transformation
CHT	Continuous-Heating-Transformation
T_gTP	T_g-Temperature-Property
pgf	probability generation function
WLF	Williams-Landel-Ferry
SEC	Size Exclusion Chromatography
DSC	Differential Scanning Calorimetry
DTA	Differential Thermal Analysis
TGA	Thermogravimetric Analysis
TMA	Thermomechanical Analysis
DMTA	Dynamic Mechanical Thermal Analysis
TBA	Torsion Braid Analysis
IR	Infrared
FTIR	Fourier Transform Infrared
HPLC	High Performance Liquid Chromatography
FRA	Frequency Response Analyser

Chapter One

1. Introduction

The curing of thermosetting composites is a complex process, which can be illustrated by the flow-chart in Figure 1.1. The effective process control of the manufacture of these materials depends on the existence of valid mathematical models (heat transfer, resin cure kinetics, chemoviscosity, glass transition temperature advancement), and on the implementation of a real-time cure monitoring technique. It is necessary to have a link in real-time between the above mentioned models and the cure monitoring signal, in order to have the basis for feedback-loop control. Irrespective of the experimental route selected for the monitoring of the cure, the predictive capability required to achieve a feedback-loop can only come from a valid set of models, as illustrated in Figure 1.1.

The present study aims to explore the potential in developing accurate models for the cure kinetics and the chemoviscosity of the curing resins (see shaded area in Figure 1.1). During the cure of a thermosetting resin a number of complex chemical and physical changes occur as the material turns from a viscous liquid to a highly crosslinked solid. All these changes, which are reflected in the cure kinetics and the chemoviscosity characteristics of each individual resin system, determine the optimum set of process parameters for the production of a material that will have the best morphological and structural properties for a given application.

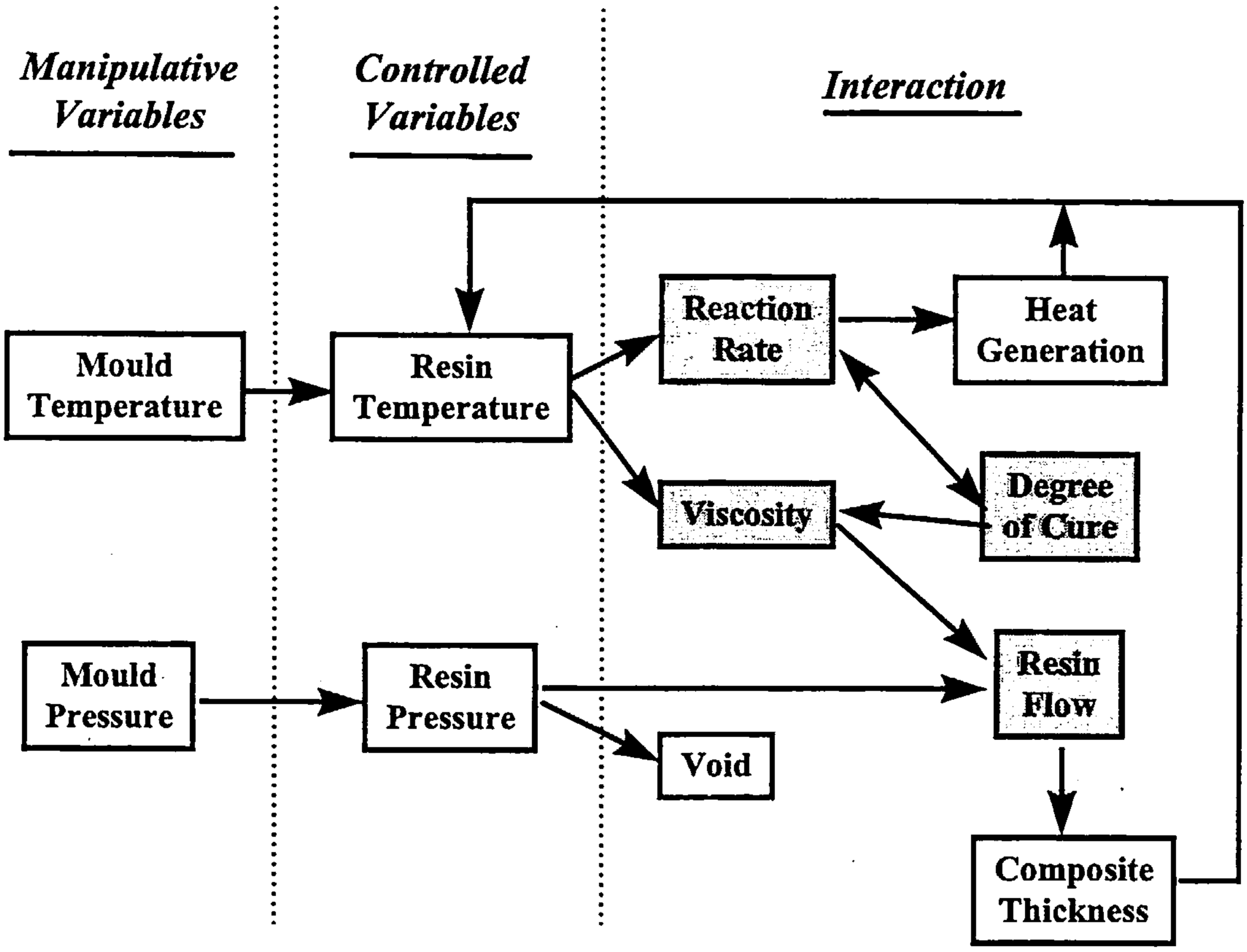

Figure 1.1 *Parameters in composites cure*

To date, an extensive effort has been applied to the study of the nature of the chemical reactions that occur during the cure of thermosets and in particular of epoxy resins [1-3], as these form the majority of the resin matrices used in the aerospace composite industry. Apart from the qualitative evaluation of the chemical processes involved in epoxy cure, a range of mathematical models has also been produced, in order to simulate the conversion advancement during the cure. They range from purely phenomenological models to models based on the actual cure mechanism and on the evolution of the concentration profiles of all the reactive species involved [4, 5]. Despite the effort that has been expended in the exploitation of the cure kinetics of the epoxy resins, there is still no general model that can apply to the cure of all epoxy resins. The fact is that, for each epoxy resin system or at least for a family of epoxy resins, the cure kinetics of the system have to be reevaluated.

Such a situation represents a severe limitation to an industrial application of any monitoring or control system that requires a quantitative knowledge of the resin cure kinetics.

The present study was undertaken in the context of a large, collaborative, industrial programme. It has the aim of exploring the feasibility of constructing a set of mathematical and numerical models that can be applied to the majority of epoxy resins. Reasons for any failure of applicability will be analysed.

The major physical transformation that occur during the epoxy cure, gelation and vitrification, are important parameters in the processing of fibre reinforced composites. Whether or not a particular thermoset resin system is suitable for a given fibre-reinforced composite processing technique, depends critically on its viscosity evolution during the processing cycle. For fabrication of composite parts from prepreg, knowledge of the viscosity profile gives guidance on when the pressure should be applied during the cure cycle (prior to gelation), in order to achieve part consolidation without excessive resin flow. For resin transfer moulding (RTM), the viscosity of the resin at the early stages of the cure is an additional concern. The requirements for successful mould filling are low resin viscosity for satisfactory impregnation of the preform and long pot-life. Therefore, knowledge of the evolution of rheological properties of curing thermosets is essential for their successful processing [6 - 8]. Determination of the end of the cure is also a key issue in the composite industry. Vitrification times indicate the completion of the cure at the cure cycle of interest and the end of the processing run.

The ideal cure monitoring technique would be capable of following, in a direct way, the parameters involved within the shaded boxes of Figure 1.1. An extensive report from the US Department of Commerce [9] assesses the "State-of-the-art for Process Monitoring Sensors for Polymer Composites". Dielectric techniques were at that stage significantly ahead of the alternatives, in terms of practical development. Recent years have witnessed a great rise in interest in real-time cure monitoring techniques.

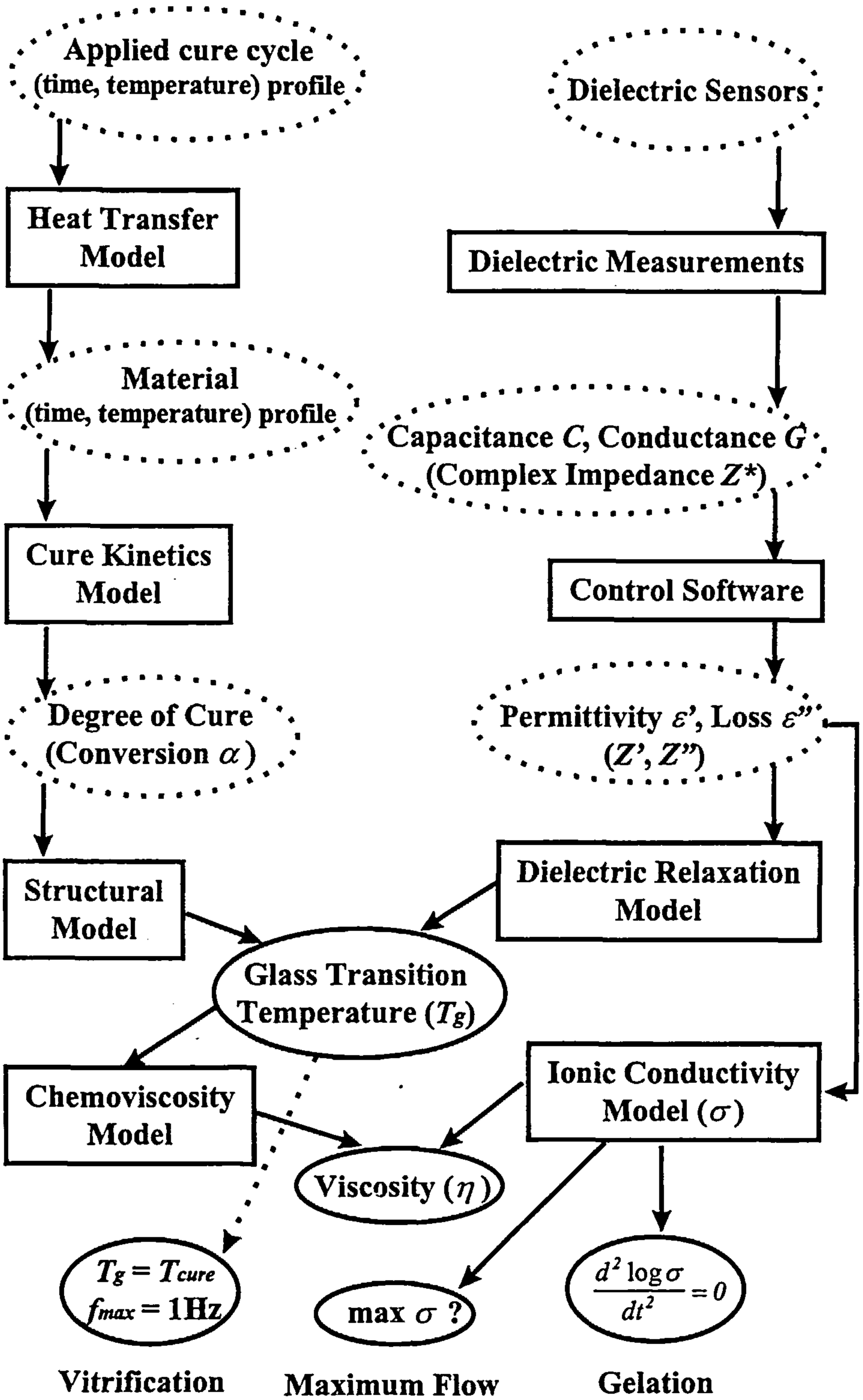

Figure 1.2 *Flow diagram depicting the essential elements of an overall control model of thermoset cure.*

The debate on the "pros and cons" of the two most advanced methods, in particular, the microdielectrometry based on following the dielectric changes in a curing resin via embedded dielectric sensors [10] and the fiber optics, which follow the changes in the IR spectrum of a curing resin via embedded optical fibers [11], has demonstrated that, in reality, neither offers a complete solution.

Previous work on the implementation of microdielectrometry in epoxy cure monitoring has demonstrated the effectiveness of this method to establish the points of maximum flow and the onset of gelation and to identify the completion of the cure in most of the commonly utilised aerospace composites [12]. The ability of the technique to follow the cure advancement continuously during a thermal cure cycle, makes this technique even more competitive [13]. Microdielectrometry has been used in this study as a means of detecting the characteristic points in the epoxy cure (gelation and vitrification) and to simulate the cure advancement from the changes in the dielectric signal. The feasibility of correlating the changes in the dielectric signal with the changes in the cure will be exploited and comprehensive relationships will be constructed as a means of representing these changes in a mathematical form. The generic nature of this approach will be tested and considerations will be made for its application for the eventual design of a feedback loop control system for composites processing (see Figure 1.2).

Chapter Two

2. Theoretical Background

2.1 Epoxy resins

The term "epoxy resin" is applicable to both the prepolymer and to the cured resin, with the former containing reactive epoxy groups (also called oxiranes or ethoxyline rings), hence their name (see Figure 2.1). In the cured resin, the epoxy groups may have all reacted, forming a crosslinked three-dimensional network, so that although there are not any groups left, the cured resin is still called epoxy resin. Epoxy resins are important industrial polymers, but their relatively high cost restricts their use to applications where there is a need for their high technical advantages.

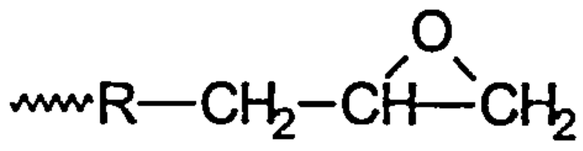

Figure 2.1 *Epoxy ring*

Commercial epoxy resins were marketed for the first time in the 1940s, although similar products had been patented in the 1930s. The reaction product of bisphenol A and epichlorohydrin was the first marketed epoxy resin, a route that is still followed today for the major production of these resins (see Figure 2.2). For a more detailed analysis of the epoxy resins manufacture, the reader is invited to look at Bryan Ellis' discussion on the subject [14].

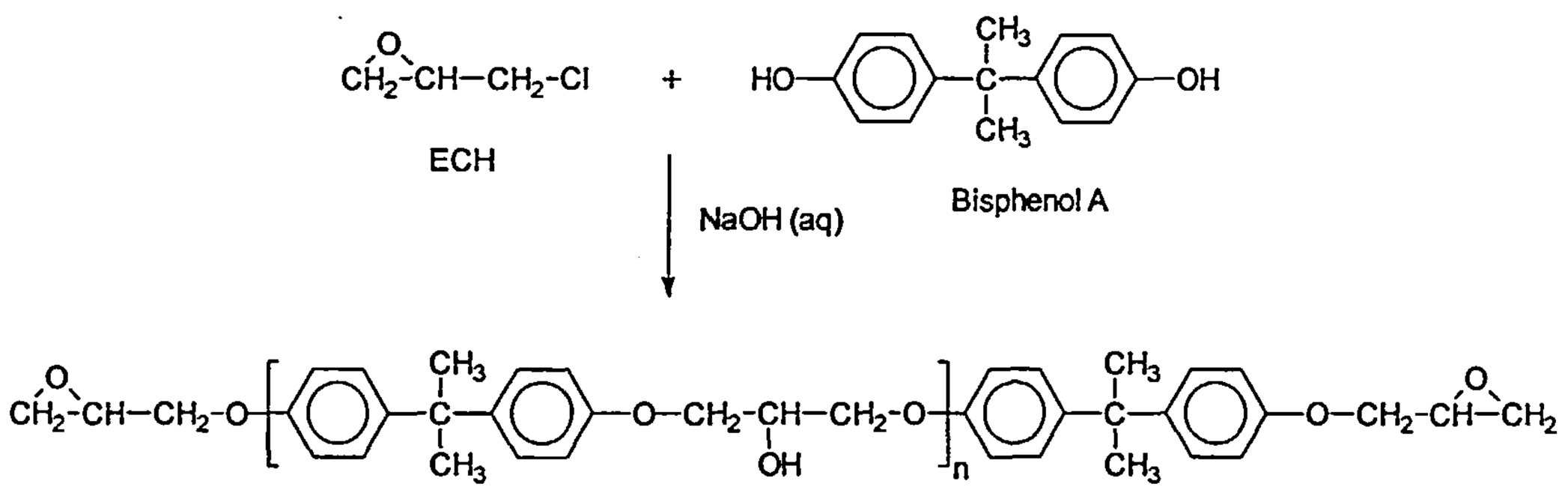

Figure 2.2 *Production of DGEBA resin from bisphenol A and epichlorohydrin*

The continuous demand for materials for specialised applications has given rise to innovations in epoxy resin technology that have involved the synthesis of epoxy resins with specific characteristics and properties. For the aerospace industry, these innovations have led to the manufacture of epoxy resins which have become the main matrix components for the production of continuous fibre reinforced composites (see Figure 2.3).

The cure of epoxy resins involves the formation of a three-dimensional network as a result of the reaction with an appropriate hardener (effective functionality $f > 2$). These tightly crosslinked networks provide the properties that are highly demanded from the advanced materials industry, such as very high glass transition temperatures (T_g), low shrinkage, high adhesive strength, good chemical resistance, and good heat resistance.

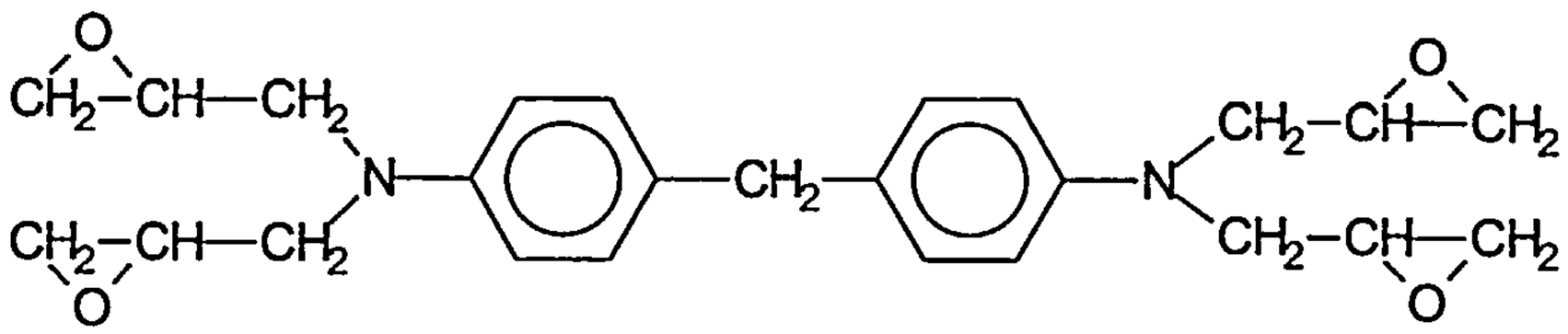

N, N' - tetraglycidyl - 4, 4' - diaminodiphenylmethane (TGDDM)

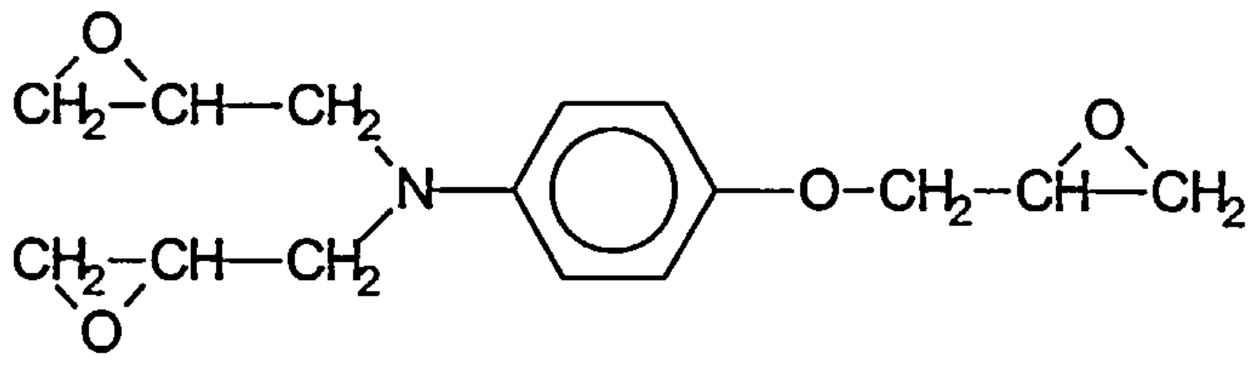

Triglycidyl para - aminophenol (TGPAP)

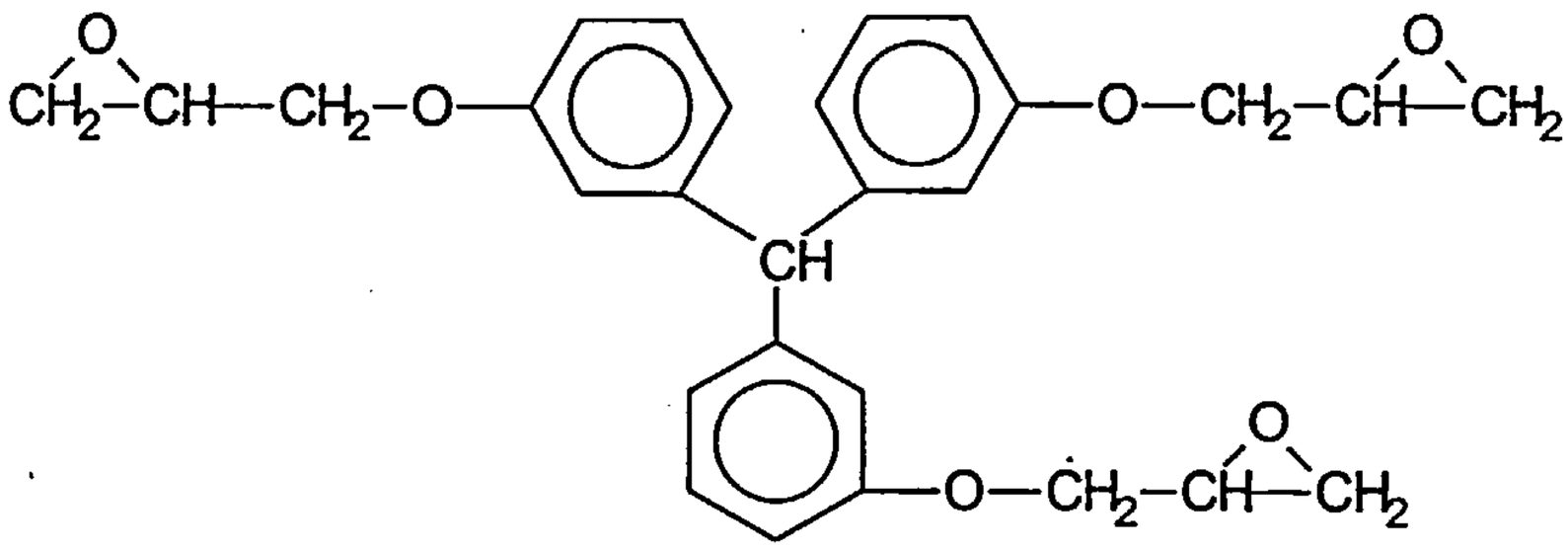

Triglycidyl ether of tris(hydroxyphenyl)methane

Figure 2.3 *Some of the main epoxy resins used in composite manufacture*

2.2 Curing of Epoxy Resins

The conversion of epoxy resins to hard, rigid thermosets with a three-dimensional network is directly related to the use of crosslinking agents, that provide the appropriate linkages for the epoxy molecules to connect with each other. Cure reaction mainly involves homopolymerisation of the epoxy groups initiated by a catalytic

curing agent and a polyaddition/copolymerisation reaction with a multifunctional curing agent.

2.2.1 Curing Agents

The rapid development of highly technological end products has increased the demand for specialised curing agents that meet the specifications of the product.

The most common curing agents for the epoxy resin cure are:

I. Curing agents containing nitrogen.
   - A. aliphatic amines and derivatives (EDA, DETA, TETA), cycloaliphatic amines and derivatives (PACM, DACH, IPDA), aromatic amines and derivatives (DDM, DDS, DETDA). They act as curing agents for the polyaddition reaction.
   - B. Catalysts and co-curing agents (tertiary amines, imidazoles, ureas). They act either as catalysts for the crosslinking by homopolymerisation or as accelerators and co-curing agents for polyamines, polyamides and anhydrides, or as activators.

II. Curing agents containing oxygen.
   - A. Carboxylic acids and anhydrides (TGIC, HHPA, TMA), phenol formaldehyde resins (P-F resins) and amino formaldehyde resins (M-F resins).

III. Curing agents containing sulphur (polysulphides, polymercaptons).

2.2.2 Cure Reaction Path

In general, epoxy resin curing reactions involve opening of the epoxide ring followed either by a homopolymerisation reaction with further epoxide, or reaction with other curing agents to form additional products. Amongst the curing agents of greatest technological importance are the polyamines and anionic or cationic catalysts.

General Reaction Scheme

The most common procedure in curing epoxy resins is the reaction with polyfunctional amines. A great variety of aliphatic di- and poly-amines and aromatic diamines are

used as epoxy resin curing agents.

The basic reaction of epoxides based on diglycidyl ether of bisphenol A (DGEBA) with primary and secondary amines, in the absence of catalyst, involves the addition of the primary and secondary amino groups of the polyamine to the epoxy group, with the simultaneous evolution of one hydroxyl group due to opening of the epoxy ring. This reaction scheme can be represented by the following reactions [15, 16] :

- Primary amine addition:

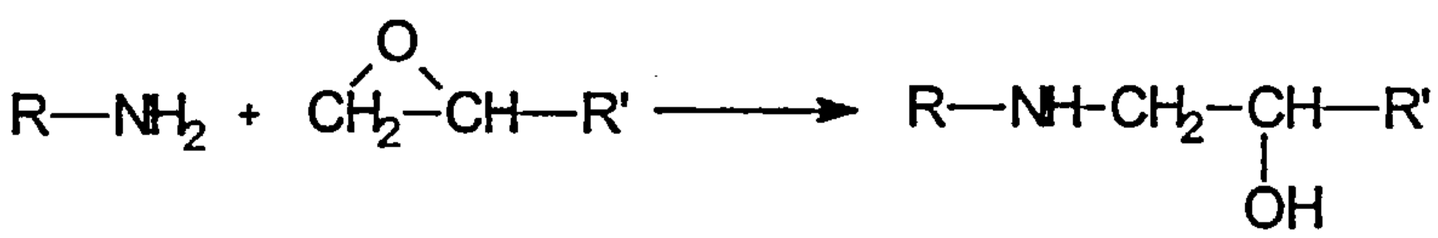

- Secondary amine addition:

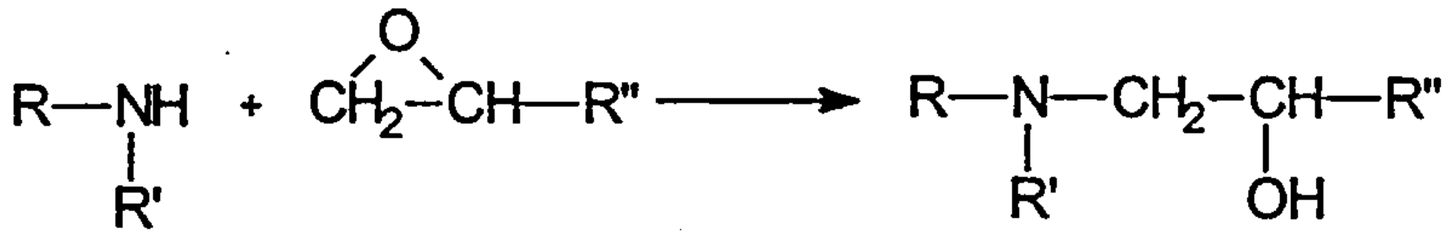

Experimental evidence shows that the two epoxy groups of this type of resins have the same reactivity, hence these reactions proceed with the -NH amino group attacking the epoxy ring randomly.

These reactions are catalysed by acids such as Lewis acids, phenols and alcohols. The hydroxyl groups formed by the amine/epoxide addition reaction can act as catalysts, accelerating the reaction at the early stages and showing the typical performance of an auto-catalysed reaction.

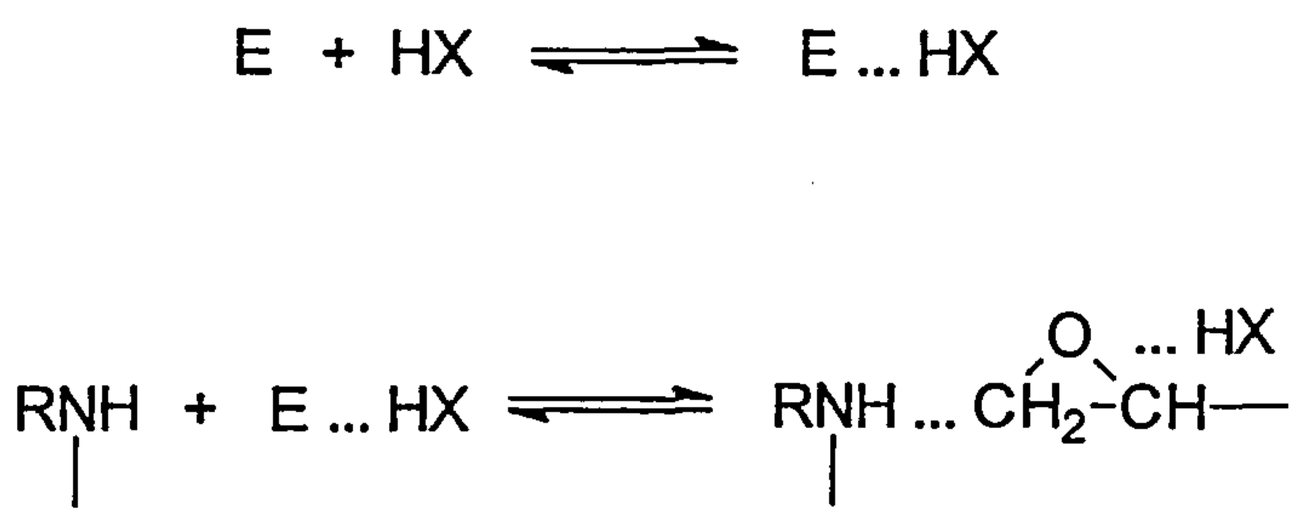

Figure 2.4 *Catalytic effect of hydroxyl groups on the epoxy - amine reaction by the formation of an activated complex in the combined reaction of amine, epoxide and hydroxyl*

The catalytic effect of hydroxyl groups on the epoxide/amine addition reaction involves an activated complex formed in the combined reaction of amine, epoxide and hydroxyl. Smith [16] suggests that an activated complex is formed in a bimolecular reaction between an adduct formed from the epoxy group and the proton donor (HX), and the amine (see Figure 2.4), with the reaction of the activated complex being the rate-determining step.

Barton, in his paper on the application of Differential Scanning Calorimetry to the study of the epoxy resin curing reaction[15], has summarised the catalytic effects of the hydroxyl groups on the amine addition reaction. The proposed reaction scheme is the formation of either an epoxy-proton donor adduct or more likely an amine - proton donor adduct because of the higher basicity of the amine in respect to the epoxy group.

In cases where the amine is present in less than stoichiometric concentrations, further reaction of the epoxy groups with the hydroxyl groups may occur, producing an ether group according to the general reaction:

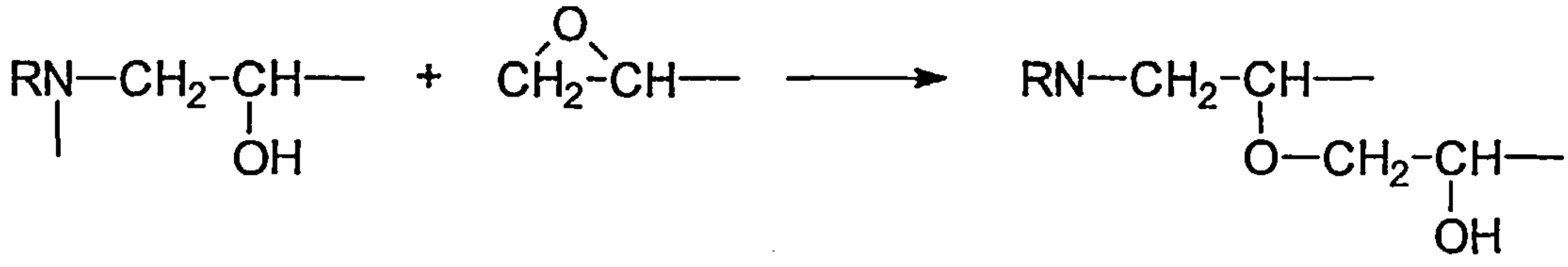

According to the type of the epoxy/amine system, some other reactions can also become operative to various extents, i.e. anionic or cationic polymerisation reaction of the epoxy groups, initiated by an interaction of the epoxy group with tertiary amine or a Lewis acid, occasionally also in the presence of a proton donor.

Polyfunctional Epoxy/Amine Systems

The preparation of high-performance composites involves polyfunctional epoxy resins (functionality $f > 2$) in mixture with diamines and catalysts for the acceleration of the overall reaction. Typical epoxy resins used in such applications are those based on the tetrafunctional epoxy resin tetraglycidyl-diaminodiphenyl-methane (TGDDM).

The general reaction scheme of such epoxy/amine systems follows the same path as the systems based on diglycidyl ether of bisphenol A (DGEBA) resin. This involves the primary and secondary amine additions as the major steps for the curing reaction, followed by side reactions such as etherification and homopolymerisation, where the type of the reacting system and the conditions under which these reactions occur are favorable.

The most significant difference of the reaction of TGDDM with amines from that of epoxides based on diglycidyl ether of bisphenol A is the strong tendency of TGDDM and its derivatives to cyclisation, in contrast to DGEBA where no cyclisation occurs. Direct recognition of such structural elements has been attempted recently using various spectroscopic techniques. Cyclic structures within a polymer network have been identified using model compounds of polyfunctional epoxy/amine systems. In the reaction of N-diglycidyl systems with amines, intramolecular cyclisation occurs under the general reaction shown in Figure 2.5[17], to give morpholine (II), perhydro-1,4-oxazepine (III), perhydro-1,5-diazocine (IV) and perhydro-1,4-diazepine (V) ring

systems, in addition to the intermolecular reaction giving chain products (VI).

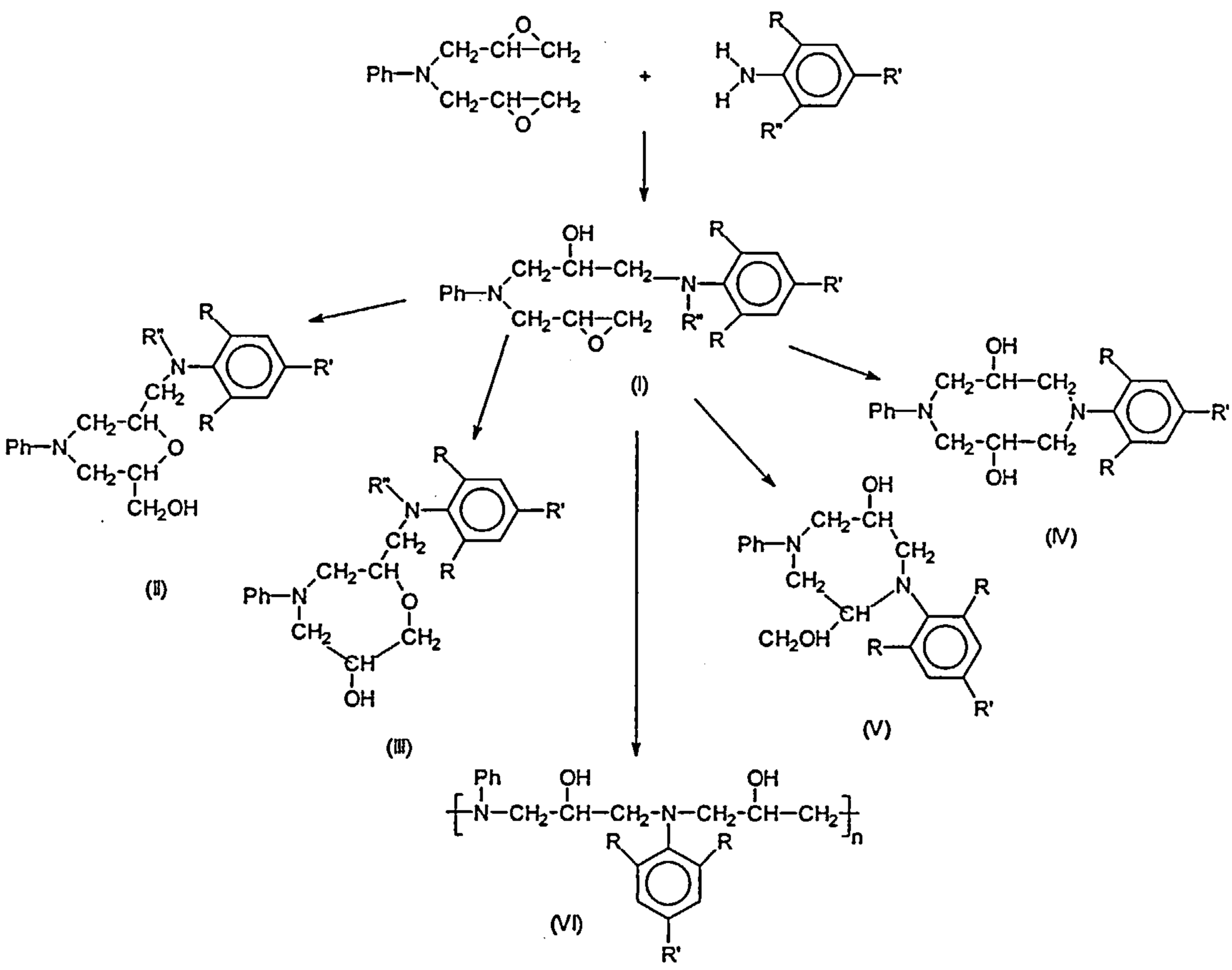

Figure 2.5 *Products of cyclisation reactions during the cure of a polyfunctional epoxy/amine system (from Ref. 17)*

Although nucleophilic attack of amines on epoxides usually occurs at the least hindered carbon atom, Baldwin's rules for ring closure [18], which are based on stereochemical considerations, predict that in a six versus seven membered ring formation (ring compound II versus ring compound III), the former is favoured. Although Baldwin does not consider a competitive ring forming situation of seven versus eight membered ring formation (ring compound V versus ring compound IV), he does predict the formation of seven membered rings, whereas experimental evidence so far only supports the formation of eight membered rings.

Matejka and co-workers [19, 20] have studied cyclisation during the reaction between diglycidylaniline (DGA) and amines. Cyclisation was proved to occur in a model bifunctional system of DGA and aniline (A). Several types of rings were isolated from the reaction mixture and identified. The eight membered ring (ring compound IV), was found to be formed at the very beginning of the reaction by intramolecular addition, whereas six- and seven-membered rings (ring compounds II and III) were found to arise in a later stage of the reaction, mainly when epoxide was used in excess. It was estimated that some 60-70% of the etherification reactions take place through the intramolecular ring formation reactions.

Catalyst Accelerated Reactions and Homopolymerisation

The extensive application of thermosetting resins in polymer matrix composites has given rise to areas of work related to the decrease of total energy consumption without accompanying loss of properties. In practice, this has led to formulations incorporating catalysts to accelerate the thermal curing reaction. Such formulations, because of the low reactivity that is provided by the catalyst at ambient and sub-ambient temperatures, allow a degree of storage that offers good stability of the uncured resin, an issue of great importance to the composite manufacturing industry. The borontrifluoride ethylamine (BFE) complexes are found to be particularly well suited in this context.

The two most common catalysts of this type, used commercially to cure epoxy resins, are boron trifluoride monoethylamine, $BF_3{:}NH_2C_2H_5$, and boron trifluoride piperidine, $BF_3{:}NHC_5H_{10}$, complexes. Such complexes are latent catalysts at room temperature but enhance epoxide group reactivity at higher temperatures. The catalytic effects of such compounds give rise to a rather complicated reaction mechanism[21], which depends on the chemical composition of the catalyst itself and on the complexes that are formed during the reaction. Commercial compositions of BF_3-amine catalysts are variable and contain BF_4^- and $BF_3(OH)$ salts together with other highly reactive species. At 85°C and above, solid $BF_3{:}NH_2C_2H_5$ slowly converts to the $BF_4^-NH_3^+C_2H_5$ salt with associated fluorine loss. This salt formation is accelerated in the presence of TGDDM

resin but not in the presence of DDS curing agent. In the presence of H_2O, $BF_3{:}NH_2C_2H_5$ hydrolyses to $BF_3(OH)^-NH_3^+C_2H_5$ at 85°C, whereas at ambient temperature this hydrolysis is slow. The chemically stable and mobile $BF_4^-NH_3^+C_2H_5$ salt is identified as the predominant catalytic species and acts as a cationic catalyst for the cure reaction. The general scheme for the catalytic mechanism of the catalyst $BF_3{:}NH_2C_2H_5$ was given by Happe et al [22] and mainly involves the following steps:

- $BF_3{:}NH_2C_2H_5$ disproportionation to:

$$2BF_3{:}NH_2C_2H_5 \Leftrightarrow BF_4^-NH_3^+C_2H_5 + BF_2NHC_2H_5 \quad \text{or} \quad [BF_4]^-[BF_2(NH_2C_2H_5)_2]^+$$

- Monoboroester formation:

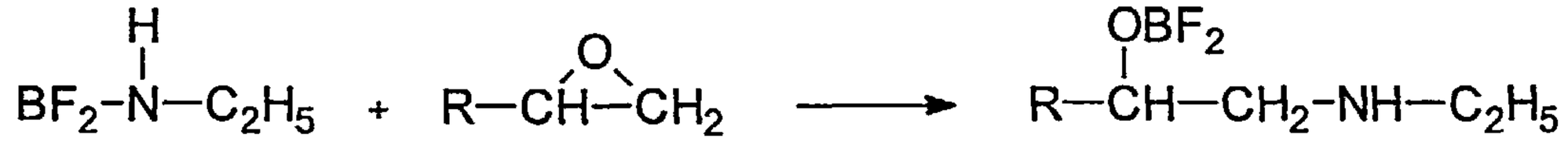

- Monoborester catalysis for epoxy-epoxy reaction:

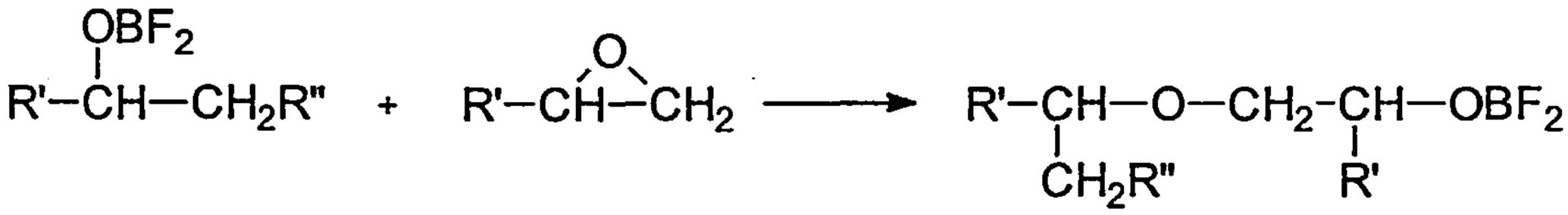

Evidence exists for catalyst deactivation, especially due to hydrolysis of the monoboroester, although the presence of impurities in the reactive mixture such as mica, asbestos and alkaline could also lead to deactivation.

Miscellaneous Aspects of the Reaction Mechanism

In general, cured epoxy resins are brittle because of their highly crosslinked structures. In the adhesive field the usual route to improve the toughness of epoxies is to incorporate a reactive liquid rubber in the epoxy network as a secondary phase. However, this can lead to the rubber partly dissolving in the epoxy matrix, and produce unacceptable decreases in both modulus and glass transition temperature. Another possible way of toughening is to alter the structure of the prepolymers. For this purpose, a variety of curing agents have been tried, differing in their backbone stiffness, to maintain a high value of glass transition temperature of the matrix. Grillet et al[23] have studied the effects of the structure of the aromatic curing agent on the epoxy network using formulations based on a DGEBA prepolymer. Their results show that curing agents containing SO_2 groups are less reactive, because these are highly electron-attracting groups which decrease the basicity of the amine. The group $-CH_2-$, as an electron donor, increases the reactivity of the amine, whereas the -O- group decreases the reactivity of the amine.

Other aspects that can alter the normal reaction path for the epoxy/amine cure are the interfaces between the fibres and the epoxy matrix in a composite material. The fibres may induce morphological modifications near the surface, which are not present in the bulk, thus, the chemical composition of the surface zone might be totally different from the bulk composition. Surface treatments of the fibres are often carried out (oxidation, irradiation, coating deposition), producing reactive groups that may act as catalysts when the network is being formed. Grenier-Loustalot and Grenier[24] have studied the influence of the reinforcement on the mechanism of epoxy/amine curing for both glass and carbon fibre composites. The results show differences in the reactivity of the matrix (decrease in the autocatalytic part of the reaction, variation of the overall reaction rate), which means in principles, that the heating cycle in the production of the composites should be adapted depending on the reinforcement that is used.

Wang and Garton[25] have studied the interface interactions between a carbon fibre and a boron trifluoride catalysed epoxy matrix, based on TGDDM, and have demonstrated the complex fashion by which the presence of an oxidised carbon fiber surface can

affect the reaction path. If the fibre is aged in a humid environment, the affinity of the oxidised fibre for water leads to destruction of the catalyst and retardation of the cure. For oxidised fibres that are stored under ambient conditions, the catalytic effect of the acidic fibre surface become operative, with an overall increase of the epoxy consumption and the proportion of the epoxy-epoxy reaction relative to the epoxy-amine reaction. This leads to retardation of vitrification, implying less crosslinking and more epoxy-epoxy sequences in the network.

2.3 Major Transitions During Epoxy - Amine Cure

The presence of polyfunctional units in a reactive system results in the formation of structures of macroscopic dimensions, depending on the degree of crosslinking during the reaction. An epoxy - amine system, which is a polyfunctional system, will therefore produce infinite networks during the cure reaction. It has been observed that during cure a number of high molecular weight particles are formed, which are dispersed in a low molecular weight phase that constitutes the continuous phase. The number and molecular weight of these microgel particles increase as the cure reaction proceeds, and crosslinking becomes operative. Finally, a stage is reached where phase transition occurs, with microgels conforming the continuous phase and the original phase of low molecular weight particles being entrapped in the matrix of the new phase (see Figure 2.6). The point where the growth and branching of polymer chains, caused by intramolecular reactions, causes phase transition from the liquid state to the rubbery state, is called "gelation". This transformation is a critical point in resin cure. It occurs at a specific point of chemical conversion, and depends on the curing system itself and the environment in which the reaction takes place.

Many attempts have been made to model the critical phenomenon of gelation and produce a mathematical theory that can describe it accurately. Flory[26] was the first to model this process, and his gelation theory (branching theory) gave the mathematical background to other researchers for further investigation.

Some basic assumptions have been made in the development of this theory, such as

that all the functional groups have identical reactivity and that no intramolecular reactions take place. The results give satisfactory agreement with experimental data for systems that follow the assumptions of the theory, like the bifunctional epoxy DGEBA, where it has been found experimentally that the reactivities of the epoxy groups are independent of each other.

Thus, for a bifunctional epoxy-amine system, with the only reaction occurring being the epoxy/amine addition, the mathematical formula that gives the critical point of epoxy conversion for gelation is given by:

$$p_c = \left(\frac{1}{(f_e - 1) \cdot (f_a - 1) \cdot r} \right)^{\frac{1}{2}} \qquad \text{(Eq. 2.1)}$$

where p_c is the critical degree of epoxy conversion, f_e and f_a are the functionalities of epoxy resin and amine respectively, and r is the ratio of amine hydrogens to epoxy groups initially present in the resin system.

At epoxy conversions below p_c, all the molecules have finite size, whereas at higher conversions, some are infinite. Eventually, a network will be formed, with one single molecule in the total mass.

Many researchers have tried to expand Flory's original theory of gelation following the rules of the so-called branching or cascade theory, with Gordon[27] being the best representative of all. A more detailed analysis of this theory will be given in following sections (see section 2.4.3).

Another theory that has been used to describe and predict gelation, is the Avrami theory of phase change. This can be described as a nuclei generation - growth theory, in which impingement of grown nuclei is assumed to lead to cessation of growth of the new phase. Pollard and Kardos[28] employed this theory in a TGDDM - DDS system and the results were found in good agreement with the experimental data.

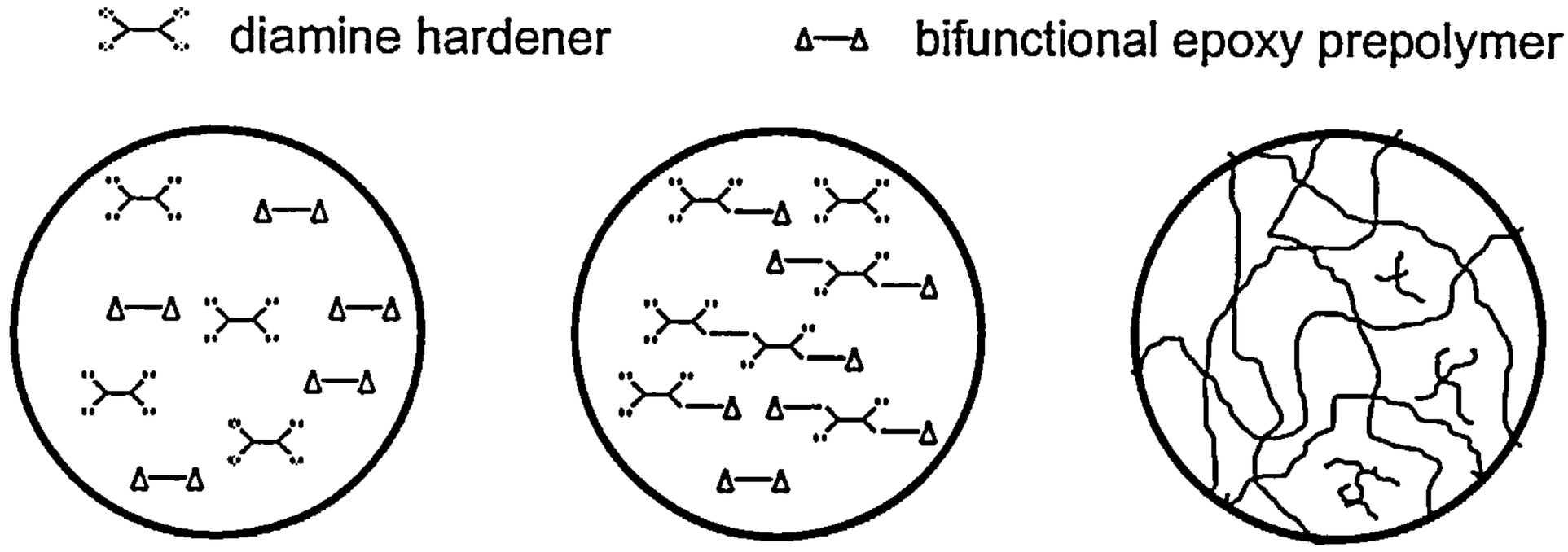

Figure 2.6 *The cure of epoxy resin.* ***Stage A:*** *Uncured resin,* ***Stage B:*** *Partially cured resin (small branched molecules are present),* ***Stage C:*** *Gelation (critical point where branched structures extend throughout the whole sample)*

Many other changes in the physical state of the epoxy - amine system take place during the cure reaction as a consequence of the changes in the free volume and in the glass transition temperature of the reactive system.

During cure to full conversion at isothermal conditions, the glass transition temperature (T_g) increases from the value representative of the uncured monomer mixture (T_{g0}) to the fully cured value ($T_{g\infty}$). Molecular gelation, the formation of infinite molecules at a fixed conversion, is a transition that occurs at an intermediate T_g value between T_{g0} and $T_{g\infty}$, that of ${}_{gel}T_g$. When the isothermal cure temperature, T_c, is much lower than the $T_{g\infty}$, the reaction generally becomes diffusion controlled as T_g increases through T_c and a limiting value of T_g, which depends on T_c, is obtained. This gradual cessation of the reaction marks the transition from the rubbery to the glassy state of the curing material. The resin eventually solidifies, and no further reaction will take place unless it is triggered by a further increase in the curing temperature. This transition, which will occur when T_g reaches T_c, is defined as "vitrification" and be considered as the identification of the end of the cure. Graphical representation of the above phenomena

on the well known Time - Temperature - Transformation (TTT) diagram, which was first adopted for the epoxy resin cure by Gillham[29], provides an intellectual framework for the understanding of the curing process and the optimisation of the processing and the final material properties. A similar diagram to the TTT cure diagram is the Continuous - Heating - Transformation (CHT) cure diagram[30], which illustrates the time for transformations that occur during the course of continuous heating of the resin at different heating rates. Other isothermal physical properties of epoxy glasses, such as density, modulus, water absorption and creep, which change with the extent of cure, can also be represented in a similar manner, producing the T_g - Temperature - Property (T_gTP) diagram[31] (see Figure 2.7).

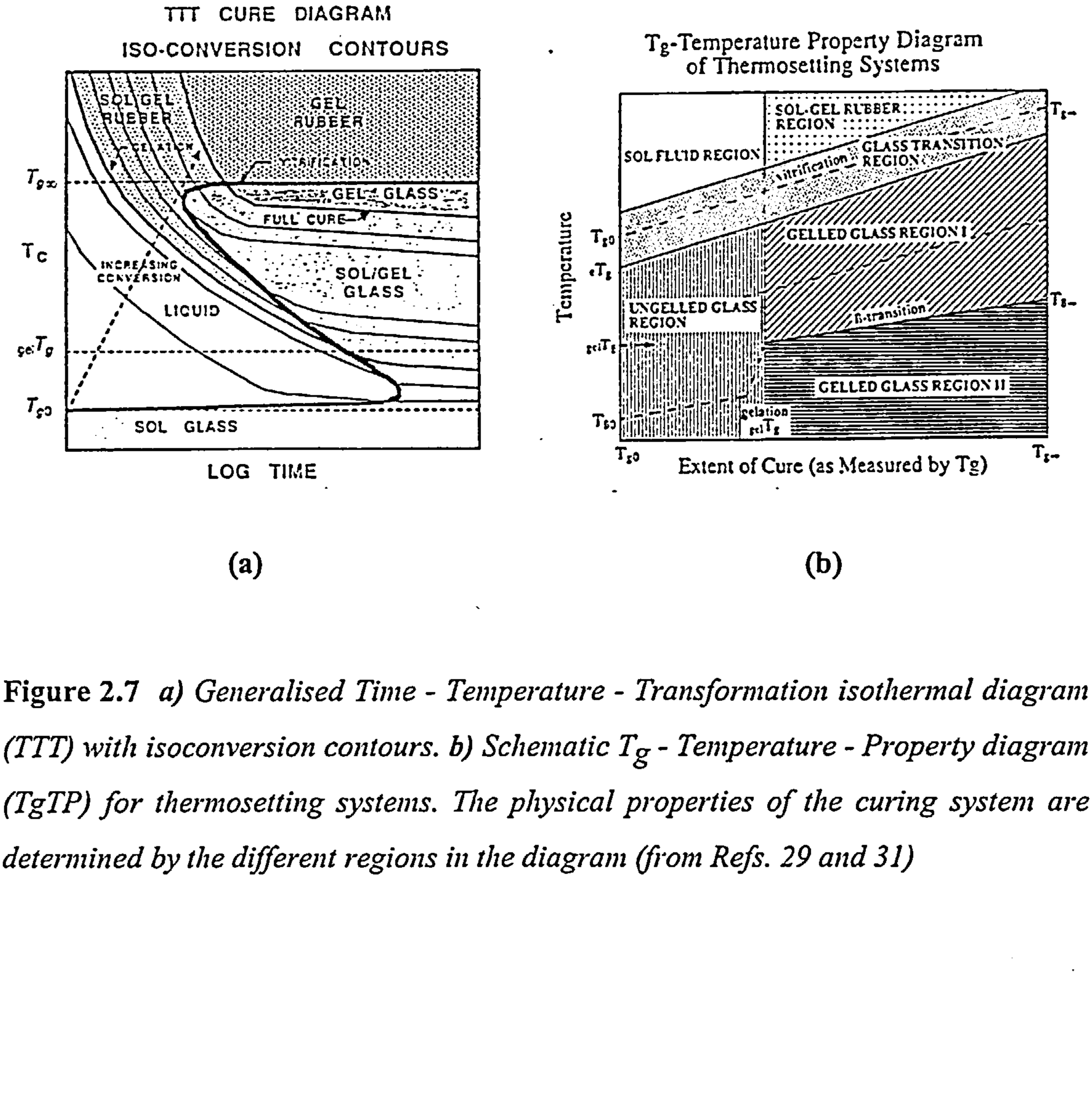

Figure 2.7 *a) Generalised Time - Temperature - Transformation isothermal diagram (TTT) with isoconversion contours. b) Schematic T_g - Temperature - Property diagram (TgTP) for thermosetting systems. The physical properties of the curing system are determined by the different regions in the diagram (from Refs. 29 and 31)*

The concept of the free volume considered as unoccupied space between molecules, resulting from their thermal motions and steric hindrance effects, can be very helpful in explaining many phenomena and properties of various polymer systems, in different physical states [32]. The expression that correlates the free volume with a structural dependent property of the polymer network, such as T_g, may be expressed as a linear function of the difference between the resin temperature, T, and its glass transition temperature, T_g [33] :

$$f = f_g + \alpha \cdot \left(T - T_g\right) \qquad \text{(Eq. 2.2)}$$

where f is the fractional free volume, f_g is the free volume fraction at T_g and α is the thermal expansion coefficient of the free volume.

A more comprehensive expression that correlates segmental mobility and conversion along with T_g, is the expression derived by Adabbo and Williams[34] using Di Benedetto's equation[35], and has the form of:

$$\frac{T_g - T_{g0}}{T_{g0}} = \frac{\left(\frac{E_x}{E_m} - \frac{F_x}{F_m}\right) \cdot X_g}{1 - \left(1 - \frac{F_x}{F_m}\right) \cdot X_g} \qquad \text{(Eq. 2.3)}$$

where E_x and E_m are the lattice energies for crosslinked and uncrosslinked polymer respectively, F_x and F_m are the corresponding segmental mobilities and X_g is the extent of conversion at T_g.

In the presentation of the experimental results, adequate expressions will be developed to describe the relationship between T_g and conversion, based on Eqs. 2.2 and 2.3

2.4 Cure Kinetics

The processing of thermosetting polymers involves the exposure of these materials to various levels of heat treatment. During such treatment, the control of temperature distribution and the rate of temperature rise is very important in determining the quality and ultimate properties of the cured resin. The temperature variation in these materials depends to a large extent on the heat of reaction, the specific heat capacity and the thermal conductivity of the material at different stages of the cure cycle. Therefore, in the analysis, control and design of thermoset processing operations, the knowledge of the above properties and their variation with temperature and degree of cure is important. Knowledge of the stage of network formation during cure becomes an important issue in thermoset processing since it provides the basis for further understanding of the overall cure process and of the end product. Determinations of the exothermic heats of reaction and of the kinetics of cure provide the tools for the understanding and prediction of network formation.

In section 2.2.2, the complexity of the reaction mechanism of a thermosetting system under cure, such as a polyfunctional epoxy - amine system, was shown, involving a number of inter- and intra-molecular reactions that finally produce a rigid three-dimensional network.

The determination of the kinetics of cure of epoxy resins involves more than just measurement of the rates of reaction of epoxy groups with the hardener. The determination of the gel point and of the onset of diffusion control as vitrification is reached, are among other important issues of the cure process. A complete evaluation of the reaction kinetics would involve elucidation of the mechanisms of the chemical reactions occurring during cure and construction of a system of a number of coupled differential kinetic equations that describe the mechanism and a comprehensive way to resolve the above system as accurately as possible. For a general reaction of the form of:

$$A + B + \cdots \xrightarrow{K} C + D + \cdots$$

the differential equation that describes the kinetics of the reaction in respect to reactant *A*, is of the form:

$$\frac{d[A]}{dt} = -K \cdot [A] \cdot [B] \cdots = K \cdot [C] \cdot [D] \cdots \qquad \text{(Eq. 2.4)}$$

where the brackets indicate the concentration of the involved species, the differential $\frac{d[A]}{dt}$ the reaction rate and K the reaction rate constant with an Arrhenius temperature dependence.

The solution of a system of equations of the above form would give the evolution of concentrations of all the involved species with time and temperature. Knowledge of initial concentrations and reaction rate constants, or initial concentrations and concentrations of some of the species with time and temperature would be needed, in order that this solution be attainable. A priori knowledge of reaction rate constants is not possible for obvious reasons while evolution of concentrations with time and temperature is difficult to obtain, especially in a complex system such as the epoxy - amine system. Therefore, in most of the cases, an exact solution of the above system is impossible. Assumptions have to be made, either about the actual reaction mechanism or about some of the parameters involved.

Generally, a kinetic analysis of the cure mechanism can be made by the following approaches:

- Generalised empirical rate equations [15, 36]
- Rate equations derived from proposed "true" chemical mechanisms [37, 38]
- Statistical kinetics (branching or cascade theory) [39, 40]

All of these approaches, one way or another, are mathematical representations of reaction mechanisms that are believed to be true or that apply for a predetermined temperature range which is usually the temperature range of the experiment.

2.4.1 Generalised Empirical Rate Equations

Amine addition, as it was established in section 2.2.2, has the most important role in the reaction mechanism of an epoxy - amine system. It has thus been the main study for many research groups over the last four decades. The pioneer work of Horie and co-workers[36] has been the basis for many subsequent treatments of the kinetics of epoxy - amine cure. The reaction mechanism that they proposed was the primary amine addition given by:

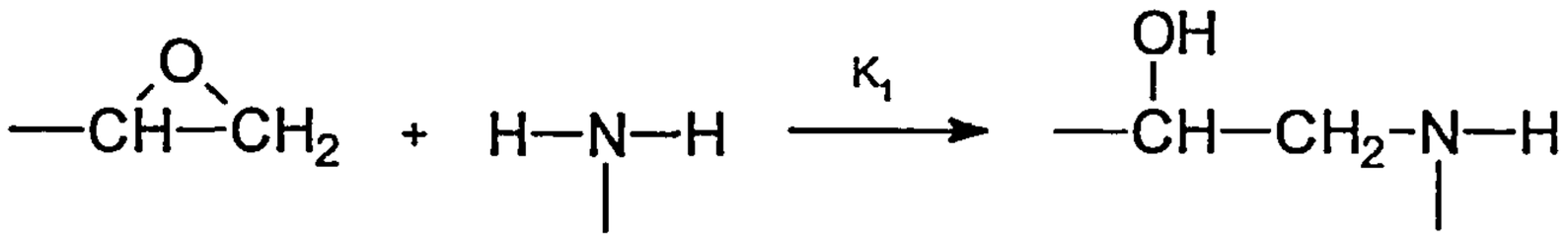

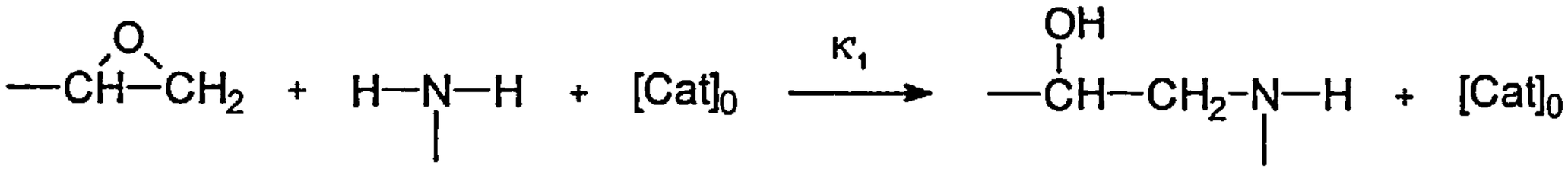

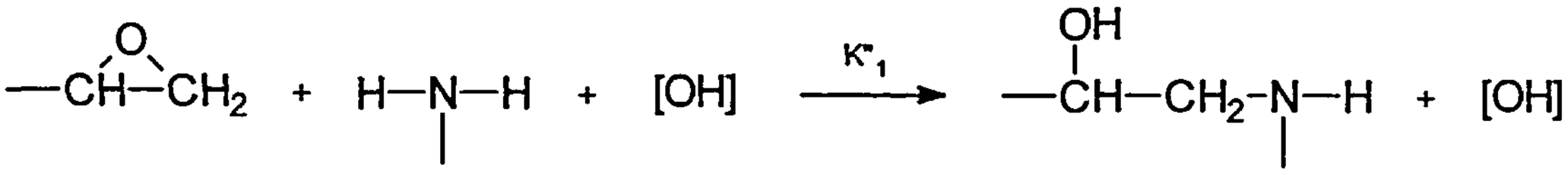

where K_1 is the reaction constant for the uncatalysed reaction, K'_1 is the reaction constant for the reaction catalysed by any impurities, with concentration $[Cat]_0$ present in the reactive system initially, and k''_1 the reaction rate constant for the hydroxyl catalysed reaction. A similar set of reactions for the secondary amine addition can also be written, with reaction rate constants K_2, K'_2 and K''_3 respectively. Similarly with the etherification reaction, reaction between hydroxyl and epoxy groups, with a reaction rate constant K_{OH} and the homopolymerisation reaction with reaction rate constant K_E. Thus the rate equation for the consumption of epoxy groups, according to the above described mechanism, is:

$$-\frac{dE}{dt} = K_1 EA_1 + K'_1 C_0 EA_1 + K''_1 EA_1(OH) + \\ + K_2 EA_2 + K'_2 C_0 EA_2 + K''_2 EA_2(OH) + \\ + K_{OH} E(OH) + K_E E^2(Cat) \qquad \text{(Eq. 2.5)}$$

where E, A_1, A_2, etc. represent concentrations and K_i are rate constants. The first term represents the reaction of the primary amine with concentration A_1, the second term the reaction of the secondary amine with concentration A_2 and the third and fourth term the etherification and homopolymerisation reactions respectively. (Cat) is the catalyst concentration for the homopolymerisation reaction.

Horrie and co-workers considered that only the catalysed reactions of epoxy groups were important, which means that in the mathematical representation of the reaction rate of Eq. 2.5 one should set $K_1 = K_2 = K_{OH} = K_E = 0$. The following assumptions were also made:

- The reactivities of the epoxy groups are independent of each other.
- The reactivities of the amine-hydrogens in the primary and secondary amine are independent of each other.

Using the above assumptions, the expression that connects the reaction rate constants for the primary and secondary amine addition is, $K_1^i = 2 \cdot K_2^i$, as primary amines have two reactive hydrogens in the amino group instead of one in the secondary amines. It is useful to define the relative reaction rate constant, K, as $K = K_2^i / K_1^i$, which is the rate constant of secondary to primary amine hydrogen addition reaction, independent of the reaction having been catalysed or not, that is $K = 0.5$ for all the reactions. With the assumption that the rate constants can depend on the extent of reaction but their ratio must not, and using $X_E = E_0 - E$ where E_0 is the initial concentration of the epoxy groups, the reaction rate for the epoxy group consumption of Eq. 2.5, after some algebraic manipulation, is given by:

$$\frac{dX_E}{dt} = \left(E_0 - X_E\right)\cdot\left(K''_1 X_E + K'_1 C_0\right)\cdot\left(A_1 + KA_2\right) \qquad \text{(Eq. 2.6)}$$

When there is a substitution effect operative, that is the reactivity of the hydrogens of the amine groups in primary and secondary amines are not equal, the relative reaction rate can be expressed as $K = 0.5 + \Delta K$. If the initial concentration of primary amines in the reactive system is A_0, and there are not any secondary amines initially present, then the stoichiometric relation for reacted epoxy groups and active hydrogens is: $A_1 + A_2 / 2 = A_0 - X_E / 2$. Incorporation of the above relations into Eq. 2.6 will give:

$$\frac{1}{\left(E_0 - X_E\right)\cdot\left(A_0 - \frac{X_E}{2}\right)}\cdot\frac{dX_E}{dt} = \left(K'_1 C_0 + K''_1 X_E\right)\cdot\left[1 + \frac{2A_2\cdot\Delta K}{2A_1 + A_2}\right] \qquad \text{(Eq. 2.7)}$$

The last term of the right hand side of the above equation will be initially zero and small up to maybe 50% conversion compared to unity, so a plot of the left hand side against X_E will be initially linear and will start to deviate from linearity as the curing reaction rate decreases because of diffusion.

By using a normalised conversion term $x_E = (E_0 - E) / E_0$ and assuming exact initial stoichiometry and exact initial concentrations of active hydrogen atoms and epoxy groups, Eq. 2.7 becomes:

$$\frac{dx_E}{dt} = \left(1 - x_E\right)^2\cdot\left(K_1 + K_2 x_E\right)\cdot H_c \qquad \text{(Eq. 2.8)}$$

where $K_1 = K'_1 C_0 E_0 / 2$, $K_2 = K''_1 E_0^2 / 2$ and $H_c = 1 + \left(2A_2\cdot\Delta K / \left(2A_1 + A_2\right)\right)$.

A generalised form of the above equation has been the most commonly used expression to describe the reaction kinetics in an epoxy - amine system, that is:

$$\frac{dx_E}{dt} = \left(K_1 + K_2 x_E^m\right) \cdot \left(1 - x_E\right)^n \qquad \text{(Eq. 2.9)}$$

where m and n are reaction orders. Several researchers have used parts of Eq. 2.9 to fit conversion data. Prime[41] used the *nth* order reaction part, which is the term:

$$\frac{dx_E}{dt} = K_1 \left(1 - x_E\right)^n \qquad \text{(Eq. 2.10)}$$

whereas Keenan[42] and Kamal and Sourour[43] used the autocatalytic reaction part, which is the term:

$$\frac{dx_E}{dt} = K_2 x_E^m \cdot \left(1 - x_E\right)^n \qquad \text{(Eq. 2.11)}$$

It must be emphasised that the generalised expression of reaction kinetics of Eq. 2.9 cannot be related to any reaction steps actually occurring during an epoxy - amine cure and can only be used as a fitting expression to the experimentally obtained conversion data.

2.4.2 True Chemical Kinetics

A more comprehensive way to follow the kinetics of the curing reaction is to monitor the changes in concentration of the various reactive species during the cure. This will indicate the possible reactions that may occur which in turn will make the construction of the reaction mechanism easier and more accurate. Infrared spectroscopy has been established as the most accurate technique for such an investigation, giving information of the true chemical kinetics even for complex systems such as epoxy resins.

An extensive work has been done on the study of chemical kinetics for various epoxy - amine systems. George and co-workers[37] have followed the cure of a TGDDM/DDS

system using near-infrared spectroscopic data for the concentrations of epoxy, hydroxyl, ether groups and primary, secondary and tertiary amines. The epoxide reaction with both primary and secondary amines was found to be autocatalytic, being catalysed by the hydroxyl groups produced in the epoxy - amine reaction. A substitution effect was observed in the amine hydrogens, greatly affected by the mobility of these species during the reaction. The epoxy - hydroxyl reaction was found to follow two reaction mechanisms: a direct second order reaction and a reaction catalysed by the tertiary amines produced during the epoxy - secondary amine reaction. Experimental results obtained from a combined calorimetric/infrared instrumental method from the same author[44] in a similar epoxy - amine system, yielded the reaction enthalpies for the reactions of epoxide with primary amine, -83 kJ/mol, secondary amine, -131 kJ/mol and hydroxyl, -65 kJ/mol. The lower reaction enthalpy for the primary amine - epoxy reaction was found to be consistent, as the preceding reaction is the formation of a stable unit, the donor - acceptor complex.

Near-infrared spectroscopic data were also used by Kozielski et al[45] to follow the kinetics of the crosslinking reactions of DDS with stoichiometric quantities of polyfunctional epoxy resins. Domination of the reaction mechanism by the primary amine addition, along with the catalytic effects of the hydroxyl groups, was observed. The substitution effect in the amine hydrogens was also found to be operative, attributed to steric hindrance, while the etherification reaction was insignificant, as with most stoichiometric epoxy - amine systems. The reported values for the activation energies of the various reactions are:

- 69 - 73 kJ/mol for the uncatalysed primary amine - epoxy reaction;
- 59 - 68 kJ/mol for the hydroxyl catalysed primary amine - epoxy reaction;
- 68 - 76 kJ/mol for the hydroxyl catalysed secondary amine - epoxy reaction.

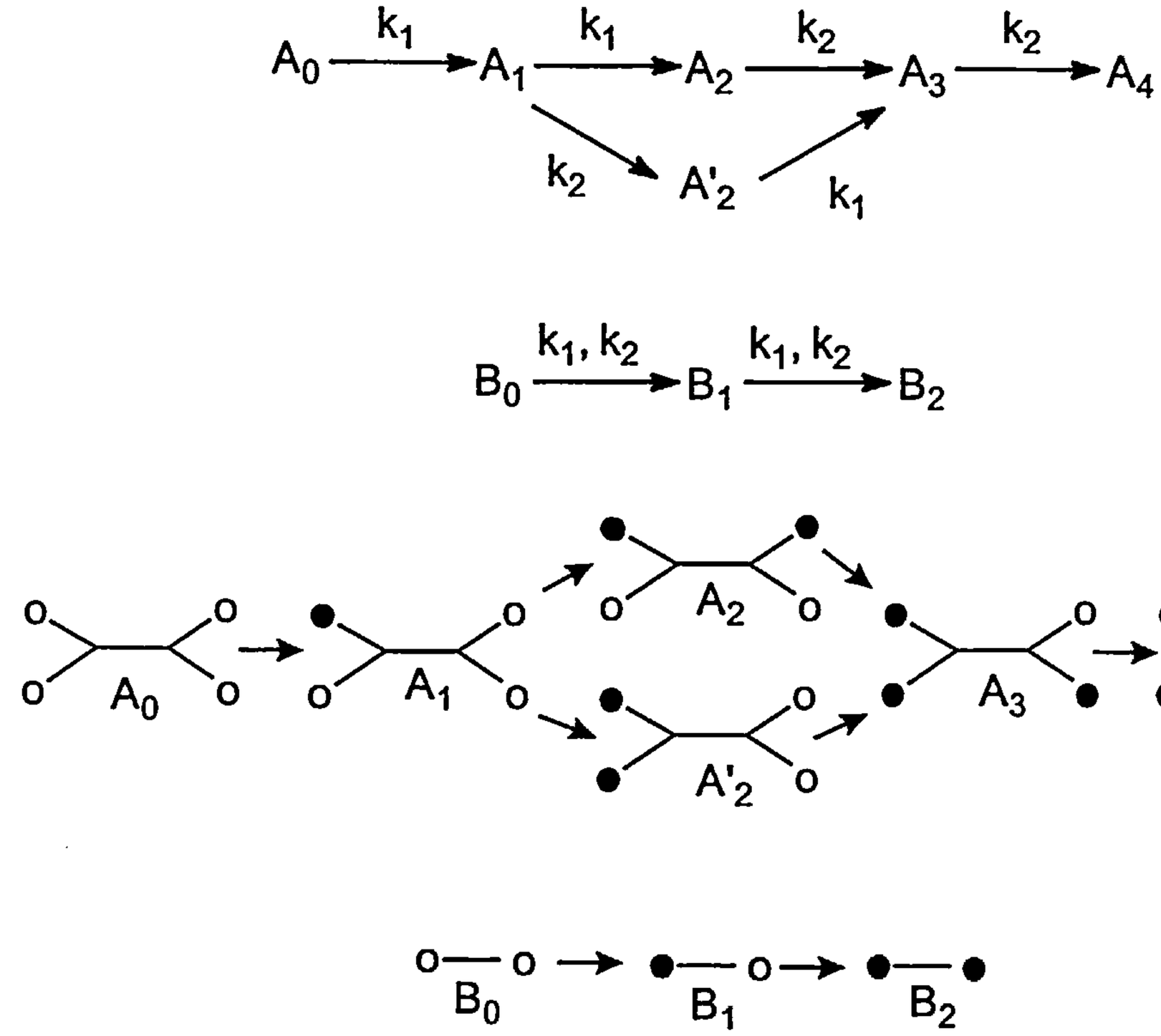

Figure 2.8 *Kinetic scheme of curing of diepoxide (B) with diamine (A) for monomer units with different number of reacted functionalities (from Ref. 38)*

In cases where there are no analytical experimental data available on the concentrations of the various reactive species during the cure, a more empirical way to determine reaction kinetics must be followed. The major assumption in this kind of investigation is the actual reaction mechanism that is followed during curing. A complicated reaction mechanism will result in a system of coupled differential equations that is unlikely to be resolved directly without any simplifications. The technique is based on a combination of a kinetic scheme accounting for the evolution of all possible fragments that may be generated from the network structure, together with a simple expectation theory[46, 47].

Dusek et al[38] have demonstrated the above kinetics modelling technique for a resin system consisting of a bifunctional epoxy and a bifunctional amine. The assumptions

that were made are:

- cyclisation and etherification reactions do not occur;
- reactivities of epoxy groups in diepoxide and amino groups in diamines are independent of each other;
- reaction between the amino and epoxy group is given in Figure 2.8;
- the rate constants k_1 and k_2 can depend on conversion but their ratio must not.

The kinetic differential equations that describe the kinetic mechanism of Figure 2.8 are:

- Amine consumption:

$$
\begin{aligned}
-\frac{dA_0}{dt} &= 4k_1A_0b \\
-\frac{dA_1}{dt} &= 2k_1A_1b+k_2A_1b-4k_1A_0b \\
-\frac{dA_2}{dt} &= 2k_2A_ab-2k_1A_1b \\
-\frac{dA_2'}{dt} &= 2k_1A_2'b-k_2A_1b \\
-\frac{dA_3}{dt} &= k_2A_3b-2k_1A_2'b-2k_2A_2b \\
-\frac{dA_4}{dt} &= -k_2A_3b
\end{aligned}
\qquad \text{(Eq. 2.12)}
$$

- Epoxy consumption:

$$
\begin{aligned}
-\frac{dB_0}{dt} &= 2B_0\left(k_1\alpha_p+k_2\alpha_s\right) \\
-\frac{dB_1}{dt} &= B_1\left(k_1\alpha_p+k_2\alpha_s\right)-2B_0\left(k_1\alpha_p+k_2\alpha_s\right) \\
-\frac{dB_2}{dt} &= -B_1\left(k_1\alpha_p+k_2\alpha_s\right)
\end{aligned}
\qquad \text{(Eq. 2.13)}
$$

In the above systems, b is the concentration of unreacted epoxy groups and α_p, α_s are the concentrations of the hydrogen atoms of the primary and secondary amino groups respectively.

By solving the system of Eq. 2.12 Dusek et al obtained:

$$\begin{aligned}
\alpha_1 &= 2p\left(\alpha_0^q - \alpha_0\right) \\
\alpha_2' &= p^2\left(-2\alpha_0^q + \alpha_0 + \alpha_0^{r/2}\right) \\
\alpha_2'' &= -2p\alpha_0^q + rp\alpha_0 + 2\alpha_0^{1/2} \\
\alpha_3 &= p^2\left[(r+2)\alpha_0^q - r\alpha_0 - (2-r)\alpha_0^{1/2} - 2\alpha_0^{r/2} + (2-r)\alpha_0^{r/4}\right] \\
\alpha_4 &= p^2\left[-r\alpha_0^q + \frac{r^2}{4}\alpha_0 + \frac{r}{p}\alpha_0^{1/2} + \alpha_0^{r/2} - (2-r)\alpha_0^{r/4}\right]
\end{aligned} \qquad \text{(Eq. 2.14)}$$

where $\alpha_i = \frac{A_i}{A^0}$, $r = \frac{k_2}{k_1}$, $p = \frac{1}{1-\frac{r}{2}}$, $q = \frac{1+\frac{r}{2}}{2}$ and A^0 is initial diamine concentration.

From the above solution, conversion of the amine hydrogens, ξ_α, can be calculated from the expression:

$$\xi_\alpha = 1 - \frac{1}{2-r}\left((1-r)\alpha_0^{1/2} + \alpha_0^{r/4}\right) \qquad \text{(Eq. 2.15)}$$

This equation is solved with respect to α_0 for a given ξ_α.

In the same way, solution of the system of Eq. 2.13 will give:

$$\begin{aligned}
\beta_0 &= (1-\xi_b)^2 \\
\beta_1 &= 2(1-\xi_b)\xi_b \\
\beta_2 &= \xi_b^2
\end{aligned} \qquad \text{(Eq. 2.16)}$$

where $\beta_i = \frac{B_i}{B^0}$, B^0 is the initial diepoxide concentration and ξ_b is the conversion of epoxy groups.

Since no etherification reaction occurs, if the ratio between epoxy groups and diamines is $e_b = \frac{b_0}{\alpha_0}$, we will have:

$$\xi_\alpha = e_b \xi_b \qquad \text{(Eq. 2.17)}$$

which is the expression that connects amine hydrogen conversion with epoxy groups conversion.

2.4.3 Statistical Kinetics

Statistical theories that can describe the structural changes in a polymer system as a function of time or functional conversion have been used extensively for several decades[38, 39, 48 - 50]. The pioneer work of Flory[26] and Stochmayer[40] in this field and their visualisation of the reaction process in the molecular forest as a system of "branching trees", has given the name of "branching theory" to this statistical treatment or otherwise "cascade theory", because it uses cascade substitution for generation of the trees. The initial composition of the system, functionality of the monomers, reactivity of the groups in terms of the rate constants or their ratios and the reaction mechanisms, which determine the sequence of formation of bonds of various types, are the input information.

In the tree - like model (see Figure 2.9), the building units (monomer) and molecules are represented by graphs. The node of the graph represents the building unit and the number of edges issuing from the node is equal to the number of functional groups capable of forming bonds. All the branched molecules, existing in the reacting system at a given conversion, are represented by a collection of molecular trees composed of units. This collection is then transformed into a collection of rooted trees by choosing

every node for the root with the same probability and placing it at a generation zero. All the other bounded roots of the same tree are placed in the first, second, etc. generations according to the place they are in the tree in respect to the root unit.

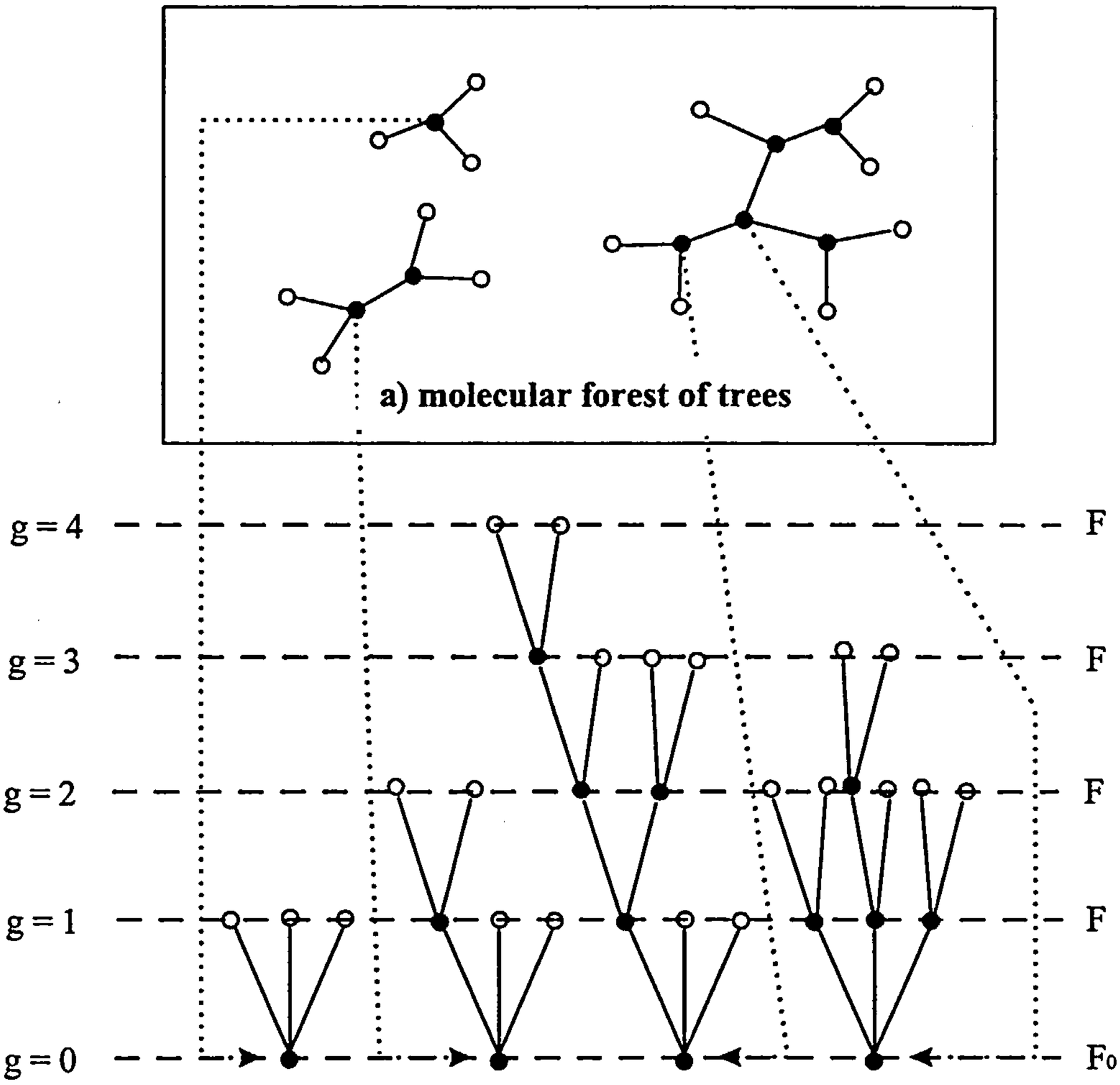

b) tree - like model of a trifunctional monomer up to the fourth generation

Figure 2.9 *A tree - like transformation of a trifunctional monomer to large molecules according to the branching theory. 1) a → b : transformation of the molecular forest of trees into a forest of rooted trees. 2) b → a : transformation of a trifunctional monomer to a molecular forest of trees (from Ref. 52)*

Node • represents a reacted functionality whereas node o represents an unreacted one

The transformation into the rooted trees is performed in order to be able to generate the trees using simple probabilistic considerations. The monomer units differ in the number of reacted functional groups they issue. The distribution of monomer units according to the number of bonds they issue is expressed through a "probability generating function" (*pgf*), which is used to generate the trees[51, 52]. For an *f*-functional monomer which is placed in the root of a tree, $F_0(z)$, the *pgf* for the number of issuing bonds is:

$$F_0(z) = \sum_{i=0}^{f} p_i z^i \qquad \text{(Eq. 2.18)}$$

In this expression, p_i is the probability of finding a monomer unit in the root issuing i bonds, which is equal to the fraction of units with i reacted functional groups, and z is a dummy variable which is used in the *pgf's* to perform the operations. For the statistical averages, z is set either to 1 or 0, which means:

$$F_0(z=1) = F_0(1) = \sum_{i=0}^{f} p_i = 1 \qquad \text{(Eq. 2.19)}$$

For the average number of bonds issuing from a monomer unit it stands:

$$\left(\frac{\partial F_0(z)}{\partial z}\right)_{z=1} = F_0'(1) = \sum_{i=0}^{f} i p_i \qquad \text{(Eq. 2.20)}$$

For the distribution of units in higher generations ($g > 0$), where monomers with no reacted groups (fraction p_0) cannot exist , the *pgf* is:

$$F(z) = \frac{\partial F_0(z)}{\partial z} \Bigg/ \left(\frac{\partial F_0(z)}{\partial z}\right)_{z=1} = \sum_{i}^{f} i p_i z^{i-1} \Bigg/ \sum_{i}^{f} i p_i \qquad \text{(Eq. 2.21)}$$

The coefficient $ip_i \Big/ \sum_i^f ip_i$ represents the probability of finding in generation $g > 0$ a unit with i reacted functional groups which issues $i-1$ bonds to the next generation.

If we consider the diepoxide - diamine system of section 2.4.2 (see Figure 2.8), then the application of branching theory will give:

- *pgf's* for the number of bonds issuing from diamine and diepoxide units respectively, in the root (application of Eq. 2.18):

$$\begin{aligned} F_{oA}(z_E) &= \sum_{i=0}^{4} a_i z_E^i = a_0 + a_1 z_E^1 + a_2 z_E^2 + a_3 z_E^3 + a_4 z_E^4 \\ F_{0E}(z_A) &= \sum_{i=0}^{2} e_i z_A^i = e_0 + e_1 z_A^1 + e_2 z_A^2 \end{aligned} \qquad \text{(Eq. 2.22)}$$

where the subscript E or A at the variable z means that the bond extends to the epoxide and amine unit, respectively.

If we set a_p, a_s and a_t as the fractions of monoamine units with zero (primary amine), one (secondary amine) and two (tertiary amine) reacted functionalities, and also as a_E the fraction of unreacted epoxy groups, then according to Figure 2.8 we will have:

$$\begin{gathered} a_0 = a_p^2, \quad a_1 = 2a_p a_s, \quad a_2' = a_s^2, \quad a_2'' = 2a_p a_t, \quad a_3 = 2a_s a_t, \quad a_4 = a_t^2 \\ e_0 = (1-a_E)^2, \quad e_1 = 2a_E(1-a_E), \quad e_2 = a_E^2 \\ a_p + a_s + a_t = 1 \\ a_s + 2a_t = 2a_A \end{gathered} \qquad \text{(Eq. 2.23)}$$

After substitution of Eq. 2.23 into Eq. 2.22 and some algebraic manipulation we have:

$$\begin{aligned} F_{0A}(z_E) &= \left(a_p + a_s z_E + a_t z_E^2\right)^2 \\ F_{0E}(z_A) &= \left(1 - a_E + a_E z_A\right)^2 \end{aligned} \qquad \text{(Eq. 2.24)}$$

which is simply the squared *pgf's* for amine and epoxy units $f_A(z)$ and $f_E(z)$ respectively.

- *pgf's* for the number of bonds issuing from units in generation $g > 0$ (application of Eq. 2.21):

$$F_A(z_E) = \frac{(a_p + a_s z_E + a_t z_E^2)(a_s + 2a_t z_E)}{a_s + 2a_t} \qquad \text{(Eq. 2.25)}$$
$$F_E(z_A) = 1 - a_E + a_E z_A$$

From Eq. 2.24 and Eq. 2.25 all structural characteristics of the system under consideration can be derived. For example, for the number average molecular weight we have:

1) (*number of molecules*) = (*number of units*) - (*number of connecting bonds*)

2) (*number of molecules*) / (*number of units*) =

= *1* - (*average number of connecting bonds*)

3) average number of bonds issuing from the respective monomer units (differentiation of Eq. 2.24 over z for $z = 1$):

$$F_{0a}^E = 2(a_s + 2a_t) = 4a_A \qquad \text{(Eq. 2.26)}$$
$$F_{oE}^A = 2a_E$$

4) average number of connecting bonds per unit:

$$\frac{n_A F_{0A}^E + n_E F_{0E}^A}{2} \qquad \text{(Eq. 2.27)}$$

where n_A and n_E are molar fractions of diepoxide and diamine respectively.

If r_A is the initial molar ratio of amine and epoxide functionalities, then $r_A = \frac{4n_A}{2n_E}$

5) Number average molecular weight, M_n:

$$M_n = \frac{\left(number\ of\ units\right)\cdot\left(n_A M_A + n_E M_E\right)}{\left(number\ of\ molecules\right)} \Rightarrow$$

$$M_n = \frac{\left(n_A M_A + n_E M_E\right)}{\dfrac{\left(number\ of\ molecules\right)}{\left(number\ of\ units\right)}} \overset{step\ 2}{\Rightarrow}$$

$$M_n = \frac{\left(n_A M_A + n_E M_E\right)}{1-\left(average\ number\ of\ connecting\ bonds\right)} \overset{step\ 4}{\Rightarrow} \qquad \text{(Eq. 2.28)}$$

$$M_n = \frac{n_A M_A + n_E M_E}{1-\dfrac{n_A F_{0A}^E + n_E F_{0E}^A}{2}} \overset{step\ 3}{=} \frac{n_A M_A + n_E M_E}{1-2n_E a_E}$$

where M_A and M_E are molecular weights of the diamine and the diepoxide respectively. The above analysis provides a theoretical tool to the explanation and prediction of the various phenomena occuring during a thermoset cure. Theoretical estimation of gelation, fractional weight ratios between sol and gel material within the curing resin are some of the areas that can be covered by this technique.

2.5 Flow Properties of Thermosetting Materials

Whether or not a particular thermoset resin is suitable for a given fiber-reinforced composite processing technique depends critically on its viscosity evolution during the processing cycle. For fabrication of composite parts from prepreg laminates, knowledge of the viscosity profile gives guidance on when the pressure should be applied during cure in order to achieve part consolidation without excessive resin flow. For resin transfer moulding (RTM), the viscosity of the resin at the early stages of cure is an additional concern. Viscosity requirements for successful mold filling are low viscosity for satisfactory impregnation of the preform and long pot-life. Thus understanding of the rheological properties of thermosets is essential for their successful processing.

For a thermoplastic material, the viscoelastic properties are fully determined by shear rate, processing temperatures and the flow geometry. For a thermosetting resin the rheology is influenced by one additional factor: the reaction kinetics of the resin system. Thus, it is essential to be able to obtain true chemorheology data as a function of reaction kinetics and temperature to have an overall view of the material characteristics.

It is well known that viscoelastic properties are influenced by the macromolecular chain length and branching. During the cure of thermosets, the structure of the resin undergoes a continuous transformation from a low molecular weight liquid to a high molecular weight 'melt' and eventually to a crosslinked network (see section 2.3). Therefore, the curves that define viscoelastic properties versus reaction time should reflect these transformations within the material. The study of viscoelastic properties of reacting systems can be separated into two categories: variations in viscosity due to chemical reaction and processing conditions (chemoviscosity) and characterisation of the growth of the infinite molecular network and immobilised glassy state (gelation and vitrification).

The chemoviscosity of thermosetting resins is affected by many variables. In general

the chemoviscosity (η) can be expressed as: [53]

$$\eta = \eta\left(T, P, \dot{\gamma}, t, F\right) \qquad \text{(Eq. 2.29)}$$

where T is the temperature, P is the pressure, $\dot{\gamma}$ is the shear rate, t is the time and F are the properties of any filler involved.

The effects of temperature and time on chemoviscosity can be described in terms of the extent of cure (α) by knowing the kinetics of the cure, $\alpha(T, t)$.

The general equation to express the effects of the cure on chemoviscosity is:

$$\eta_c = \eta_c\left(T, \alpha\right) \qquad \text{(Eq. 2.30)}$$

Extensive work has been done to determine the appropriate mathematical models that have the characteristics of Eq. 2.30. They range from empirical models[54, 55], probability based models[56, 57], gelation models[58, 59], to models based on free volume analysis[60] .

The most commonly used empirical model has the form:

Isothermal conditions:

$$\ell n\eta(t) = \ell n\eta_\infty + \frac{\Delta E_\eta}{RT} + tk_\infty \exp\left(\frac{\Delta E_k}{RT}\right) \qquad \text{(Eq. 2.31)}$$

Non – isothermal conditions:

$$\ell n\eta(t) = \ell n\eta_\infty + \frac{\Delta E_\eta}{RT} + \int_0^t k_\infty \exp\left(\frac{\Delta E_k}{RT}\right) dt$$

where: $\eta(t)$ = viscosity as a function of time at temperature T

η_∞ = calculated viscosity of the fully cured resin

ΔE_η = Arrhenius activation energy for viscosity

R = Universal gas constant

T = Absolute temperature

t = time

k_∞ = Kinetic analog of η_∞

ΔE_k = Kinetic analog of ΔE_η

This form of the relationship assumes no knowledge of the chemical conversion-time relationships.

A more comprehensive expression, that incorporates probabilistic considerations over the macromolecular network formed during the cure, is:

$$\ell n\eta = \ln A + \frac{D}{RT} + \left(S + \frac{C}{RT}\right)\ell n\frac{\overline{MW}}{MW_0} \qquad \text{(Eq. 2.32)}$$

where A, D, S, C are fitting parameters and $\overline{MW}, MW_0$ are the weight average molecular weight and the molecular weight at zero conversion respectively. Average molecular weight can be either a direct input from experimental measurements or values calculated from expressions like those extracted from the branching theory (see section 2.4.3).

Expressions that use information like the degree of cure at the gel point, α_{gel}, have also been used for viscosity modelling, as the one derived by Castro and Macosko[58] :

$$\eta = \eta_0\left(\frac{\alpha_{gel}}{\alpha_{gel}-\alpha}\right)^{A+B\alpha} \qquad \text{(Eq. 2.33)}$$

In this expression η_0 is the initial viscosity at temperature T, prior to the start of the cure.

Another expression that has been used extensively in viscosity modelling is the Williams - Landel - Ferry equation (WLF)[61] which has the form:

$$\ell n \frac{\eta(T)}{\eta(T_s)} = - \frac{C_1(T - T_s)}{C_2 + T - T_s} \qquad \text{(Eq. 2.34)}$$

where $\eta(T)$ and $\eta(T_s)$ are the viscosities at temperatures T and T_s respectively and C_1, C_2 are constants independent of temperature. Although this expression was derived in order to express the variation of the viscosity of amorphous thermoplastic polymers with temperature (between the glass transition and 100°K above the glass transition), subsequent studies have shown that the constants C_1 and C_2 are material-dependent and not universal constants. It was also pointed out that these constants are directly related to the fractional free volume at glass transition and the coefficient of thermal expansion of the fractional free volume[62].

If Eq. 2.34 is to be used for the prediction of the viscosity of thermosets during cure, one must account for the fact that: a) the glass transition temperature increases due to the network formation and hence must be evaluated as a function of the degree of cure and b) the parameters C_1 and C_2 may vary with cure temperature. The above considerations have been incorporated in the WLF equation resulting in a variety of expressions similar to the original one, such as the one used by Mijovic and Lee[63] :

$$\ell n \frac{n}{n_g} = - \frac{C_1(T)\left[T - T_g(T,t)\right]}{C_2(T) + T - T_g(T,t)} \qquad \text{(Eq. 2.35)}$$

Other more sophisticated expressions, which combine Arrhenius, probabilistic and

WLF terms, have also been used, for example an expression derived by Enns and Gillham[64], which has the form:

$$\ell n\eta = \ell n\eta_{\infty} + \ell n\overline{MW} + \frac{E_{\eta}}{RT_0} - \frac{C_1(T-T_0)}{C_2+T-T_0} \qquad \text{(Eq. 2.36)}$$

Other effects on the viscosity of thermosets, that are essential to the determination of the chemoviscosity, η, are shear rate and filler effects. The exact relationship that connects shear rate and filler type with viscosity will depend on the type of system used. Halley and Mackay[65], in their overview on the chemorheology of thermosets, have summarised the rheological models for shear rate and filler effects, which range from simple power law models to more complicated models incorporating WLF terms. In the present study, some of these expressions will be used in order to predict the viscosity profiles of the resins used, during the cure.

2.6 Cure Monitoring Techniques

The previous sections have indicated the complexity of thermoset cure and especially of epoxy - amine systems. The different reaction paths that can be followed during cure, the complicated reaction kinetics and the various transformations that occur, make necessary the application of sophisticated theories and methodologies to characterise these systems and extract the appropriate information on a macroscopic and microscopic scale. In this section, some of the methods will be reviewed briefly, concentrating on those aspects of instrumentation or methodology particularly pertinent to the study of curing thermosets.

2.6.1 Chemical and Physical Analysis

As mentioned in section 2.3, epoxy resins are converted by means of crosslinking reactions into a three-dimensional network with a finite gel time, depending on the epoxy resin - curing agent mixture. Prior to the gel point, the epoxy resin is soluble in suitable solvents whereas beyond that point, it is no longer entirely soluble. This property makes gel fraction determination a relatively accurate way of determining the gel point of an epoxy - amine system[64, 66]. The technique involves solution of a known-weight, partially cured resin, with known cure time and temperature, in a suitable solvent, extraction of the soluble part and comparison of the weight of the insoluble part with initial sample to calculate the gel fraction. By simply plotting a time-gel fraction curve and extrapolating back to zero gel fraction, direct estimation of gel time can be made.

Another technique that falls into this category of monitoring methods is size exclusion chromatography (SEC)[67]. Polymerisation kinetics can be followed by measuring partially reacted samples consisting of various molecular weight fragments. Gelation time can also be observed with the appearance of an insoluble fraction during the sample preparation prior to injection.

2.6.2 Thermal Analysis

Any technique that monitors the changes in thermal properties of a material undergoing a thermal cycle belongs to thermal analysis monitoring methods. For thermosetting resins, the most common techniques are: differential scanning calorimetry (DSC), differential thermal analysis (DTA), thermogravimetric analysis (TGA), thermomechanical analysis (TMA), dynamic mechanical thermal analysis (DMTA) and torsion braid analysis (TBA).

Differential Scanning Calorimetry (DSC)

The DSC technique has been used quite extensively in thermoset characterisation and remains one of the major techniques in the polymer research area. A major part of research by DSC involves evaluation of the chemical kinetics associated with the cure reaction during the heat cycle[68 - 79]. The sample is cured either isothermally or at a constant heating rate and a direct integration of the area enclosed under the resulting thermogram gives the degree of chemical conversion. Thus, by monitoring the cure at different temperatures and heating rates, the conversion profile of the system under investigation is obtained. It must be mentioned that care should be taken during the integration, as the baseline from which integration is made is rather arbitrary and false results may be obtained. The problem of the baseline has been investigated by many researchers[80], without any convincing conclusions so far.

The evolution of the glass transition temperature with cure temperature and time can also be obtained using DSC[81 - 86], thus giving a direct relationship between degree of reaction (conversion) and structure development (T_g). The endothermic shift in the enthalpy curve at the glass transition gives an estimation of the T_g.

Recent developments, involving the application of modulation on the temperature control, have broadened the horizons for new areas of implementation of DSC as a research tool. It is claimed that it is possible to monitor simultaneously both enthalpy and heat capacity changes from the same sample during the cure[87].

2.6.3 Spectroscopic Techniques

Infrared spectroscopy (IR) has long been recognised as a powerful tool for monitoring the curing process, and for characterising the cured epoxy composites[37, 44]. It is based on the absorption of radiation in the infrared frequency range due to the molecular vibrations of the functional groups contained in the polymer chain.

Prior to Fourier Transform Infrared Spectroscopy (FTIR), infrared spectroscopy was carried out using an instrumentation utilising prism or gratings to disperse the infrared radiation, a scanning mechanism to pass the radiation over to a slit system for frequency range isolation, and a detector[88 - 90]. Lack of sensitivity of this instrumentation, because of loss of energy through the slits, gave rise to the development of the FTIR. Quantitative IR methods are based on the Beer-Lambert law, $A = EC$, where A is the absorbance for unit path length, E is the extinction coefficient and C is the concentration. The above relationship shows a linear dependence of the absorption intensity on the concentration, an observation that makes it possible to extract quantitative information. For an epoxy system, where the epoxy groups show strong absorptions in the mid-infrared region, especially around 915cm^{-1}, after elimination of differences in specimen thickness and sample slippage by normalisation of the peak intensity by a reference band[91 - 93], the above law will give:

$$f_{915} = \frac{A_{915,t}}{A_{ref,t}} \cdot \frac{A_{ref,0}}{A_{915,0}} \qquad \text{(Eq. 2.37)}$$

where f_{915} is the fraction of unreacted epoxide at time t, $A_{915,t}$ is specimen absorbance at 915cm^{-1} due to epoxide at time t, $A_{ref,t}$ is specimen absorbance at reference band at time t, $A_{915,0}$ is specimen initial absorbance at 915cm^{-1} and $A_{ref,0}$ is specimen initial absorbance at reference band.

By monitoring other frequency bands and using Eq. 2.37, the appearance or disappearance of other functional groups can be followed, i.e. NH_2 or OH, that will give an overall view of the kinetics of the system under investigation.

In recent years, there has been a notable increase in research activity in the near-infrared region, which covers the wavenumber interval between approximately 14,000 and 4,000 cm^{-1} in contrast to the mid-infrared that covers the region from 4,000 to 400 cm^{-1}. This is particularly true in conjunction with the application of in-situ real time remote spectroscopy to "smart" processing [94]. The major advantage of the near-infrared frequency range is that it can be transmitted through silica type optical fibres, which are relatively inexpensive and readily available in a variety of types and forms. In the mid-infrared range, on the other hand, only special chalcogenide and metal halide fibres have the required transmission capabilities, and even then usually in a limited frequency range[95].

Another spectroscopic technique that has been used in cure monitoring is the evanescent wave monitoring[96]. By using fibre sensors, this technique permits the measurement at specific locations within the sample, and has the potential to monitor characteristics such as extent of cure and fibre wetting in several regions near the surface of the fibre[97].

2.6.4 Dielectric Cure Monitoring

Real time dielectric spectroscopy is becoming increasingly important as a potential means of feedback control in the area of polymer processing. The changes in the dielectric properties as a function of changing molecular weight or crosslinking density have been the subject of much research[98 - 101]. The more recent use of embedded microelectrodes in the composite structure has given the opportunity of in-situ, nondestructive monitoring of the cure process. Contributions to the overall polarisation from electrode blocking layers, migrating charge carriers and dipole relaxations are monitored in real-time during the cure, and are directly related to characteristic features of the polymeric material such as flow, molecular relaxation, thermal transition and degree of cure.

The method is based on the application of an AC voltage to the dielectric sensor and monitoring the electric response of the material from the outcome current and voltage over a multifrequency range. The response is translated to the respective dielectric

properties of the resin (dielectric constant and loss) and the changes in these properties are correlated to important process parameters - namely the point of maximum flow, onset of gelation and vitrification in the resin [98].

2.7 Theory of Dielectrics

2.7.1 Macroscopic Laws and Definitions

2.7.1.1 Dipole Moments and Polarisation

An electric dipole is a system formed from two point charges q with the same value but opposite signs separated by a distance d. The *dipole moment* can thus be defined as[102]:

$$p = qd \qquad \text{(Eq. 2.38)}$$

If we consider a volume V bounded by a closed surface A containing N dipoles, then the macroscopic dipole moment will be:

$$P_V = \sum_{i=1}^{N} p_i \qquad \text{(Eq. 2.39)}$$

In a volume dV, infinitesimal but large enough to contain a large number of dipoles, we can define a dipole moment density P, also called *polarisation*, as:

$$P = \frac{dp}{dV} \qquad \text{(Eq. 2.40)}$$

2.7.1.2 Electric Field and Displacement in a Dielectric

In the general case, a dielectric may contain a charge density corresponding to the presence of actual charges in addition to the dipoles. These actual charges are called *realised charges*[103].

Let D_m and E_m be the displacement field and electric field resulting from a dielectric. By convention, the displacement field is the result of only the realised charges. Thus, according to Gauss theorem, we can write:

$$\oint_A D dA = \sum q_{realised} + \oint_V P dV \quad \Rightarrow \quad D = D_m + P \qquad \text{(Eq. 2.41)}$$

Still, by convention, the electric field inside a dielectric results from both the polarisation and the realised charges, thus $E = E_m$. From electrostatic relationships in free space we have that the displacement field D_m, is connected to the electric field with the expression: $D_m = \varepsilon_0 E$, where ε_0 is the permittivity of the free space. From the above considerations and Eq. 2.41, we have:

$$D = \varepsilon_0 E + P \qquad \text{(Eq. 2.42)}$$

In dielectrics, the polarisation is produced by the electric field and disappears with it. It is therefore reasonable to set:

$$P = \chi_r \varepsilon_0 E \qquad \text{(Eq. 2.43)}$$

The quantity χ_r is called *relative dielectric susceptibility*. The above relation suggests that Eq. 2.42 can be written as:

$$D = \varepsilon_0 \varepsilon_r E \qquad \text{(Eq. 2.44)}$$

The term ε_r is called *relative permittivity* of the dielectric. The product $\varepsilon_0 \varepsilon_r$, often denoted as ε, is called the *absolute permittivity* of the dielectric.

The combination of Eq. 2.42 and Eq. 2.44, gives:

$$P = \varepsilon_0 (\varepsilon_r - 1) E \qquad \text{(Eq. 2.45)}$$

2.7.2 Microscopic Characteristics of Polarisation

2.7.2.1 Electric Field Acting on a Dipole

If we consider the plane capacitor shown in Figure 2.10, then the local field acting at the point *A* consists of two components:

$$E_L = E + E_{dip} \qquad \text{(Eq. 2.46)}$$

where E is the field imposed by the voltage source U. This field does not depend on the presence of a dielectric between the plates of the capacitor and is equal to U / d. E_{dip} is the field resulting from the presence of dipoles over the entire volume of the dielectric.

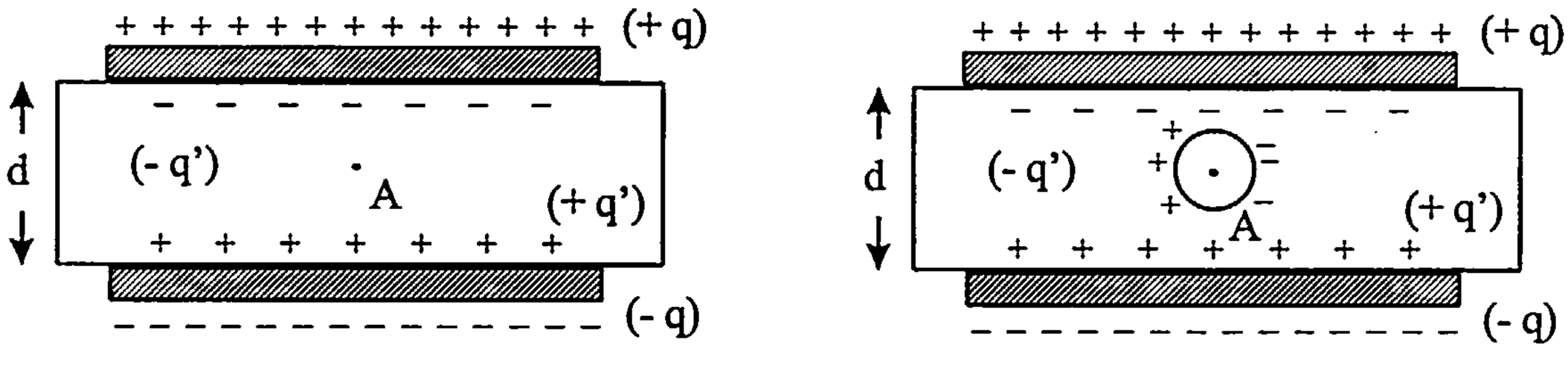

Figure 2.10 *The effect of polarisation represented by charges in a dielectric*

The calculation of the E_{dip} can be a difficult task and demands knowledge of the arrangement of the molecular structure of the dielectric in space. Although such knowledge most probably does not exist because of the complexity of the molecular network and the number of different polar groups that may exist, with a few assumptions in mind this calculation is feasible. For a dielectric that exhibits a cubic lattice structure the calculated local field, E_L, is[103, 104]:

$$E_L = E + \frac{P}{3\varepsilon_0} \qquad \text{(Eq. 2.47)}$$

2.7.2.2 Polarisation Mechanisms

Let an atom or molecule be subjected to a local field E_L, with a dipole moment p. The *polarisabillity*, α, is defined by the ratio[105]:

$$\alpha = \frac{p}{E_L} \quad \left(in\ F \cdot m^2\right) \qquad \text{(Eq. 2.48)}$$

Now, if we suppose that there is a number, N, of carriers of p per unit volume, then the polarisation due to the number of carriers is:

$$P = N\alpha E_L \qquad \text{(Eq. 2.49)}$$

The most important mechanisms of appearance of dipole moments, p, are the following:

- *Electronic polarisation* (α_e). Caused by the displacement of the electrons with respect to the nucleus of the atom.
- *Ionic polarisation* (α_a). Can only be found in ionic crystals and is caused by the displacement of ions of opposite signs in opposite directions.
- *Orientation polarisation* (α_o). A molecule formed from different atoms has a permanent dipole moment because of the displacement of the centres of the distributions of the total negative and positive charges. In the absence of a field, these moments are oriented in a random manner in space, thus showing no macroscopic polarisation. With the application of an external field, they tend to align with the field, showing a macroscopic polarisation.
- *Interfacial polarisation* (α_{in}). The charge carriers that exist in a dielectric, under the effect of an external field, have the tendency to concentrate around imperfections such as impurities, vacancies, grain boundaries, etc, producing a local displacement of the charge.

The mechanisms of appearance of dipole moments, p, are represented diagrammatically in Table 2.1.

Table 2.1 *Polarisation mechanisms.*

Type of polarisation	E = 0	→ E
Electronic	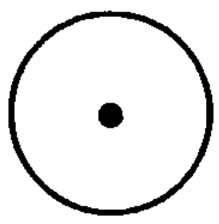	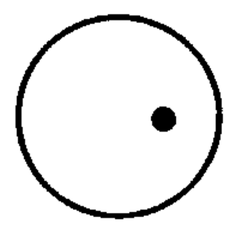
Ionic	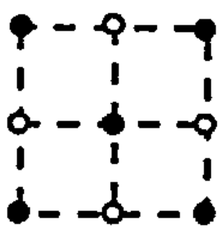	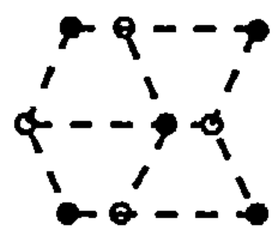
Orientation	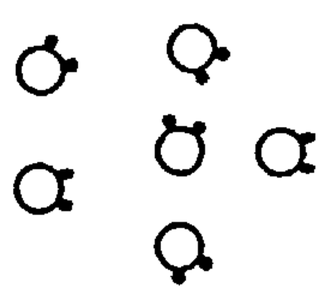	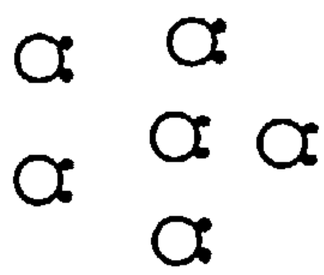
Interfacial	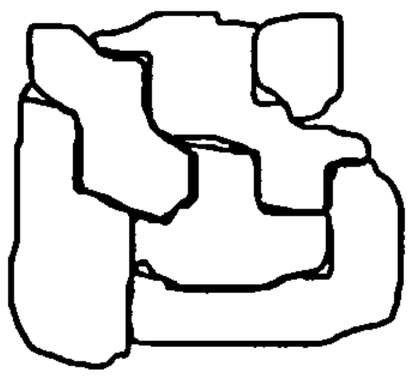	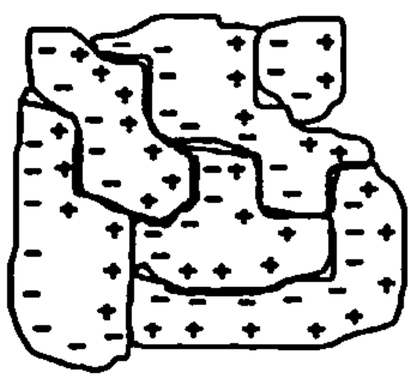

atomic nucleus

cation

anion

polar molecule

grain

From the above definitions, for the case where several different polarisation mechanisms exist at the same time, their effects are added together, so for the total polarisation, a generalised form of Eq. 2.49 can be written:

$$P = \sum N\alpha_i E_L \qquad \text{(Eq. 2.50)}$$

By substitution of Eq. 2.47, we get:

$$P = \left(E + \frac{1}{3\varepsilon_0} P\right) \sum N_i \alpha_i \qquad \text{(Eq. 2.51)}$$

or, if we also consider the expression for the polarisation given by Eq. 2.45:

$$\frac{\varepsilon_r - 1}{\varepsilon_r + 2} = \frac{1}{3\varepsilon_0} \sum N_i \alpha_i \qquad \text{(Eq. 2.52)}$$

This expression is known under the name Clausius - Mosotti equation[106] and connects the microscopic properties α_i to a macroscopic quantity, the permittivity, ε_r.

2.7.3 Permittivity under Sinusoidal Conditions

When a dielectric is subjected to a sinusoidal electric field of angular frequency ω, the polarisation factors must also be subjected to variations with the same angular frequency. The Clausius - Mosotti equation (Eq. 2.52) shows that permittivity should also vary with ω, thus making necessary the introduction of the complex permittivity:

$$\varepsilon_r(\omega) = \varepsilon_r' - j\varepsilon_r'' \qquad \text{(Eq. 2.53)}$$

In the case of the plane capacitor shown in Figure 2.10, with an electrode surface S and an inter-electrode spacing d, exhibiting an impedance:

$$Z(\omega) = \frac{1}{j\omega\varepsilon_0\varepsilon_r(\omega)\frac{S}{d}} \qquad \text{(Eq. 2.54)}$$

the resulting current flowing in the capacitor, subjected to a sinusoidally varying voltage:

$$U(\omega) = U_0 e^{i\omega t} \qquad \text{(Eq. 2.55)}$$

is equal to:

$$I(\omega - \phi) = I_0 e^{i\omega t - \phi} = \frac{U(\omega)}{Z(\omega)} = \varepsilon_0 \omega \frac{S}{d}\left(\varepsilon_r'' + j\varepsilon_r'\right) U_0 e^{i\omega t} \qquad \text{(Eq. 2.56)}$$

with a phase-shift, ϕ, with the applied voltage.

The in phase component of the resulting current with the applied voltage reflects the power dissipation in the dielectric and is associated to the *dielectric loss*. Separating real and imaginary parts, we obtain:

$$I_0 e^{j\omega t} e^{-j\phi} = \left(\varepsilon_0 \omega \frac{S}{d} \varepsilon_r' U_0 + \varepsilon_0 \omega \frac{S}{d} j\varepsilon_r' U_0\right) e^{j\omega t}$$

$$\Rightarrow \quad I_0 e^{-j\phi} = \varepsilon_0 \omega \frac{S}{d} \varepsilon_r' U_0 + j\varepsilon_0 \omega \frac{S}{d} \varepsilon_r' U_0$$

$$\Rightarrow \quad I_0 \sin\phi + jI_0 \cos\phi = \varepsilon_0 \omega \frac{S}{d} \varepsilon_r' U_0 + j\varepsilon_0 \omega \frac{S}{d} \varepsilon_r' U_0 \qquad \text{(Eq. 2.57)}$$

$$\Rightarrow \quad \sin\phi = \varepsilon_0 \omega \frac{S}{d} \varepsilon_r'' \frac{U_0}{I_0} \qquad \textit{and} \qquad \cos\phi = \varepsilon_0 \omega \frac{S}{d} \varepsilon_r' \frac{U_0}{I_0}$$

$$\Rightarrow \quad \tan\phi = \frac{\varepsilon_r''}{\varepsilon_r'}$$

The term $tan\phi$ is called the *loss angle* or *dissipation factor* and is the dielectric equivalent of $\tan\delta = \frac{E''}{E'}$ defined in the dynamic mechanical thermal analysis.

2.7.4 Frequency Dependence of Permittivity and Losses

The permanent moments of an assembly of dipolar molecules are distributed about an applied field in accordance with Boltzmann's law. Debye[107] calculated the polarisation due to dipole orientation in the absence of directional forces due to the structure of the material, as:

$$P_o = N_0 \frac{p^2 E}{3kT} \qquad \text{(Eq. 2.58)}$$

where N_0 is the number of dipoles per unit volume, k is the Boltzmann's constant and T is the temperature.

Generally, dipole orientation is affected by two factors: the local field E_L and the thermal motion in terms of collision of dipoles. Since the local field has the form:

$$E_L = \mathrm{Re}\left\{E_{L0} \exp(j\omega t)\right\} \qquad \text{(Eq. 2.59)}$$

the polarisation dP resulting from dn dipoles having collide for the first time in the time interval $(t_0, t_0 + dt)$ will be, according to Eq. 2.58:

$$dP = \mathrm{Re}\left\{\frac{p^2 dn}{3kT} E_{L0} \exp(j\omega t)\right\} \qquad \text{(Eq. 2.60)}$$

From considerations of electron collision times, the polarisation at time t from all the dipoles can be expressed as:

$$P = \mathrm{Re}\left\{\frac{N_0 p^2}{3kT} \frac{1}{1 + j\omega\tau} E_{L0} \exp(j\omega\tau)\right\} \qquad \text{(Eq. 2.61)}$$

Substitution of the above equation to Clausius - Mosotti equation will give:

$$\frac{\varepsilon_r - 1}{\varepsilon_r + 2} = \frac{1}{3\varepsilon_0}\left(\sum_i N_i \alpha_i + \frac{N_0}{1 + j\omega\tau}\frac{p^2}{3kT}\right) \qquad \text{(Eq. 2.62)}$$

where the sum over i includes all the polarisation mechanisms except for the orientation polarisation. The use of the boundary conditions:

$$\varepsilon_{rs} = \lim_{\omega \to 0} \varepsilon_r \qquad \textit{and} \qquad \varepsilon_{r\infty} = \lim_{\omega \to \infty} \varepsilon_r \qquad \text{(Eq. 2.63)}$$

will give for the dependence of permittivity on frequency:

$$\varepsilon_r = \varepsilon_{r\infty} + \frac{\varepsilon_{rs} - \varepsilon_{r\infty}}{1 + j\omega\beta} \qquad \textit{where} \qquad \beta = \frac{\varepsilon_{rs} + 2}{\varepsilon_{r\infty} + 2}\tau \qquad \text{(Eq. 2.64)}$$

or by separating real and imaginary parts:

$$\varepsilon_r' = \varepsilon_{r\infty} + \frac{\varepsilon_{rs} - \varepsilon_{r\infty}}{1 + \omega^2\beta^2} \qquad \textit{and} \qquad \varepsilon_r'' = \frac{\varepsilon_{rs} - \varepsilon_{r\infty}}{1 + \omega^2\beta^2}\omega\beta \qquad \text{(Eq. 2.65)}$$

These are known as the Debye equations for a single relaxation time τ. Their representation as a function of $\ell og\omega$ is shown in Figure 2.11 for a model with $\varepsilon_{rs} = 10$, $\varepsilon_{r\infty} = 2$ and $\beta = 10^{-4}$ sec.

2.7.5 Graphic Representation of Permittivity

Substitution of the complex form of relative permittivity, ε_r, into Eq. 2.64, will give:

$$\varepsilon_r' - \varepsilon_{r\infty} - j\varepsilon_r'' = \frac{\varepsilon_{rs} - \varepsilon_{r\infty}}{1 + j\omega\beta} \qquad \text{(Eq. 2.66)}$$

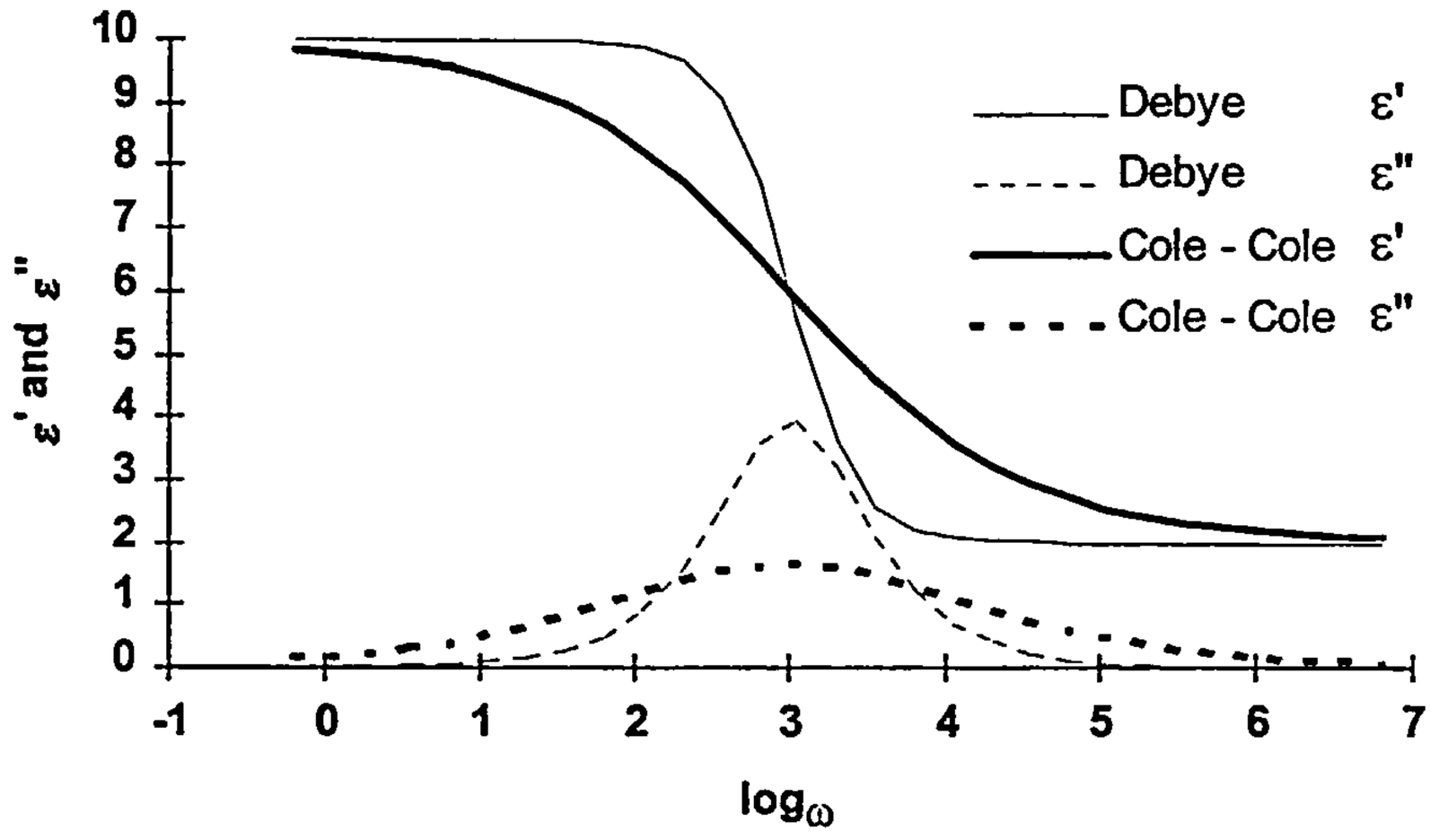

Figure 2.11 *ε'(ω), ε"(ω) plotted against ℓogω from Debye's single relaxation time model and Cole - Cole's relaxation time distribution model. The parameters used are:* $\varepsilon_{rs} = 10$, $\varepsilon_{r\infty} = 2$, $\beta = \beta_a = 10^{-4}$ *sec and* $\alpha = 0.5$

Further substitution of β (see Eq. 2.64) into the above equation, equation of real and imaginary parts of both sides and some algebraic manipulation will give:

$$\left(\varepsilon_r' - \varepsilon_{r\infty}\right)^2 + \varepsilon_r''^2 = \left(\varepsilon_r' - \varepsilon_{r\infty}\right)\left(\varepsilon_{rs} - \varepsilon_{r\infty}\right)$$

or (Eq. 2.67)

$$\left(\varepsilon_r' - \frac{\varepsilon_{r\infty} + \varepsilon_{rs}}{2}\right)^2 + \varepsilon''^2 = \left(\frac{\varepsilon_{rs} - \varepsilon_{r\infty}}{2}\right)^2$$

which, in a $\left(\varepsilon_r', \varepsilon_r''\right)$ coordinate system, is the equation of a circle with its centre on the ε_r' axis. The coordinates for the centre are $\left(\frac{\varepsilon_{r\infty} + \varepsilon_{rs}}{2}, 0\right)$ and the radius has a module $R = \frac{\varepsilon_{rs} - \varepsilon_{r\infty}}{2}$. The top half of this circle, which is the only part that has a physical

meaning, is called the Cole - Cole diagram[108] (see Figure 2.12).

For dielectrics that do not have a single relaxation time, τ, Cole and Cole suggest a generalised form of Eq. 2.64, that accounts for a distribution of relaxation times around the most probable value, τ_0, and has the form[109]:

$$\varepsilon_r = \varepsilon_{r\infty} + \frac{\varepsilon_{rs} - \varepsilon_{r\infty}}{1 + (j\omega\beta_a)^{1-\alpha}} \qquad \text{(Eq. 2.68)}$$

where α is a constant characterising the distribution of relaxation times, with $0 \le \alpha \le 1$.

Analysis of the above equation into real and imaginary parts will give:

$$\varepsilon_r' = \varepsilon_{r\infty} + (\varepsilon_{rs} - \varepsilon_{r\infty}) \frac{1 + (\omega\beta_a)^{1-\alpha} \cos\frac{(1-\alpha)\pi}{2}}{1 + 2(\omega\beta_a)^{1-\alpha} \cos\frac{(1-\alpha)\pi}{2} + (\omega\beta_a)^{2(1-\alpha)}} \qquad \text{(Eq. 2.69)}$$

$$\varepsilon_r'' = (\varepsilon_{rs} - \varepsilon_{r\infty}) \frac{(\omega\beta_a)^{1-\alpha} \sin\frac{(1-\alpha)\pi}{2}}{1 + 2(\omega\beta_a)^{1-\alpha} \cos\frac{(1-\alpha)\pi}{2} + (\omega\beta_a)^{2(1-\alpha)}}$$

with the distribution function, $\varphi_\varepsilon(\ell n\beta)$, of the relaxation times given by:

$$\varphi(\ell n\beta) = \frac{1}{2\pi} \frac{\sin(1-\alpha)\pi}{\cosh(1-\alpha)\ell n\frac{\beta}{\beta_a} + \cos(1-\alpha)\pi} \qquad \text{(Eq. 2.70)}$$

Their representation against $\ell og\omega$ is shown in Figure 2.11 for the same model system as Debye and with the constant $\alpha = 0.5$.

Representation of this model in a Cole - Cole diagram will also give a circle (Figure 2.12) with centre at:

$$\left(\frac{\varepsilon_{rs}+\varepsilon_{r\infty}}{2}, -\frac{\varepsilon_{rs}-\varepsilon_{r\infty}}{2}\tan\frac{\alpha\pi}{2}\right) \qquad \text{(Eq. 2.71)}$$

and radius:

$$R = \frac{\varepsilon_{rs}-\varepsilon_{r\infty}}{2}\sec\frac{\alpha\pi}{2} \qquad \text{(Eq. 2.72)}$$

The circle still passes through the points ε_{rs} *and* $\varepsilon_{r\infty}$ but its centre is below the ε_r' axis at a distance:

$$\Delta = \frac{\varepsilon_{rs}-\varepsilon_{r\infty}}{2}\tan\left(\alpha\frac{\pi}{2}\right) \qquad \text{(Eq. 2.73)}$$

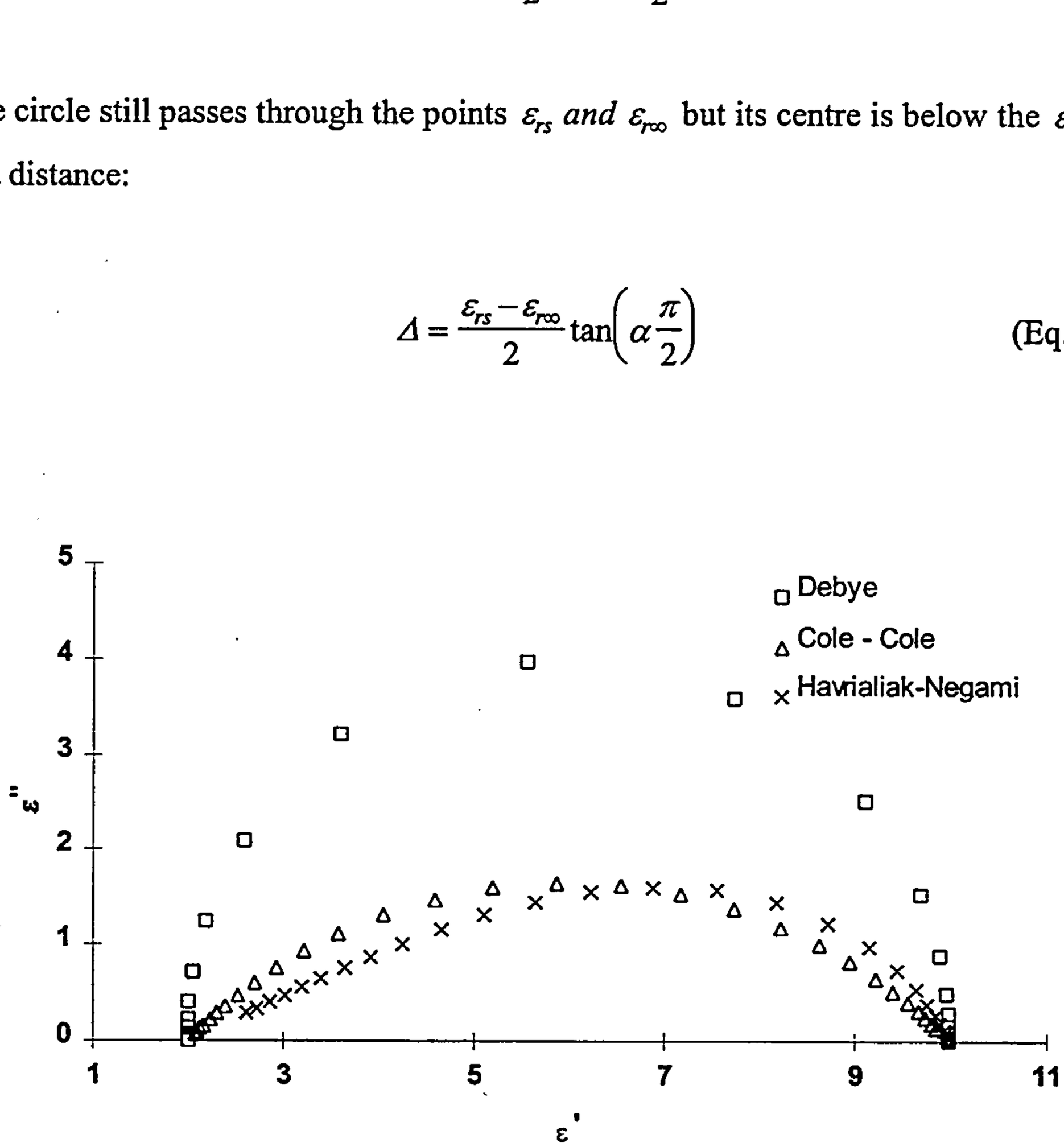

Figure 2.12 *Cole - Cole diagram for Debye's single relaxation time model and Cole - Cole, Havriliak - Negami (from Ref. 110) relaxation time distribution models. The parameters used are:* $\varepsilon_{rs} = 10$, $\varepsilon_{r\infty} = 2$, $\beta = \beta_a = 10^{-4}$ *sec,* $\alpha = 0.5$, $p = 0.7$ *and* $q = 0.4$

2.7.6 Dielectric response of Thermosets

Several microscopic and macroscopic phenomena cause a polymer to exhibit capacitive (relative permittivity) and conductive (loss) components. In general, the mechanisms that lead to this behaviour are[111 - 113]:

- *Induced dipoles*, the charge separation of non-polar bonds due to the presence of an electric field. The electron clouds may be slightly shifted inducing a slight polarisation that is aligned with the electric field. This acts to store energy and contributes to the capacitive nature of the material. The response times of the electronic shift are extremely fast so that at normal frequencies the effect is always present. These induced dipoles are responsible for non-polar or symmetrically polar polymers having permittivities of 2 or greater.
- *Static dipoles*, that require molecular motion to orient. Static dipoles consist of inherently polar moieties within the polymer such as carbonyl or alcohol groups. If sufficiently mobile, they may rotate in an electric field, thus also storing energy and contributing to the capacitive nature of the material. If a thermoset, such as an epoxy resin with many polar groups, is heated enough so that immobile dipoles become mobile, then an increase in permittivity is observed as the dipoles start to oscillate in an alternating electric field. Static dipoles also contribute to the loss factor. As the dipole rotates, the surrounding medium causes viscous drag to arise that can lead to significant phase lag between maximum applied field and maximum dipole deflection. The energy lost due to this phase lag reaches a peak as the angular frequency approaches the relaxation time of the material. At high frequencies, where the dipole can hardly move or at low frequencies, where the dipole can keep up with the changing field easily, little energy is lost. This explains the bell shaped curve of the loss factor in respect to the field frequency.
- *Ions*, that have a mobility limiting their speed which is independent of frequency. Ionic conduction is the result of current flow due to the motion of mobile ions within the material. Thermosets often contain free ions which may be formed either by weak dissociation of the cross-linking agent or be present as residual ionic impurity in both the resin and the cross-linking agent. As the viscosity and the

organic component consumption increases during the crosslinking reaction, the dc conductivity decreases as a result of the lower mobility and concentration of ions. Ionic conduction is reflected in the dielectric loss of the material. The energy that is absorbed or lost in moving ions within the thermoset will depend on the applied frequency. So, at low frequencies, where ions can easily follow the applied electric field, the loss factor is completely masked by ionic conduction, whereas at high frequencies, dipole relaxations are become visible.

- *Electrode polarisation*, as a result of the resin in combination with the electrodes used to introduce the electric field. When ionic conduction is high enough, ions are collected at the polymer/electrode interface during one-half cycle of the oscillating electric field cycle. This accumulation of ions at the electrodes forms a charge layer which is qualitatively similar to the layer of bound charge established by dipole orientation, but which can have a much greater charge per unit area. Thus, the measured capacitance, as viewed from the electrodes, can be much larger than would result from oriented dipoles. In the low frequency range, where ionic conduction is dominant, the effect of electrode polarisation would be maximum, causing an apparent permittivity which can be significant.

From the modelling point of view, the dielectric response of thermosets can be represented by an electrical circuit, that can represent the individual characteristics of each of the above described phenomena[114]. The induced dipoles, due to their frequency independence, are modelled with a capacitor C_1. The static dipoles, due to their frequency dependence, are modelled with a capacitor C_2 in series with a resistor R_2. At low frequencies, this capacitor becomes fully charged, due to the dipoles being fully oriented, whereas at high frequencies, the current limiting resistor prevents the charging of the capacitor. The conductive ions are modelled with a resistor R_3 with a conductance proportional to the concentration and mobility of the ions. The complete model, as described above, is shown in Figure 2.13. To compensate for the electrode polarisation effects, because they result in the build up of charge blocking layers at the electrode/polymer interfaces, they are modelled by the introduction of two extra capacitors, C_E, to the ends of the circuit of Figure 2.13.

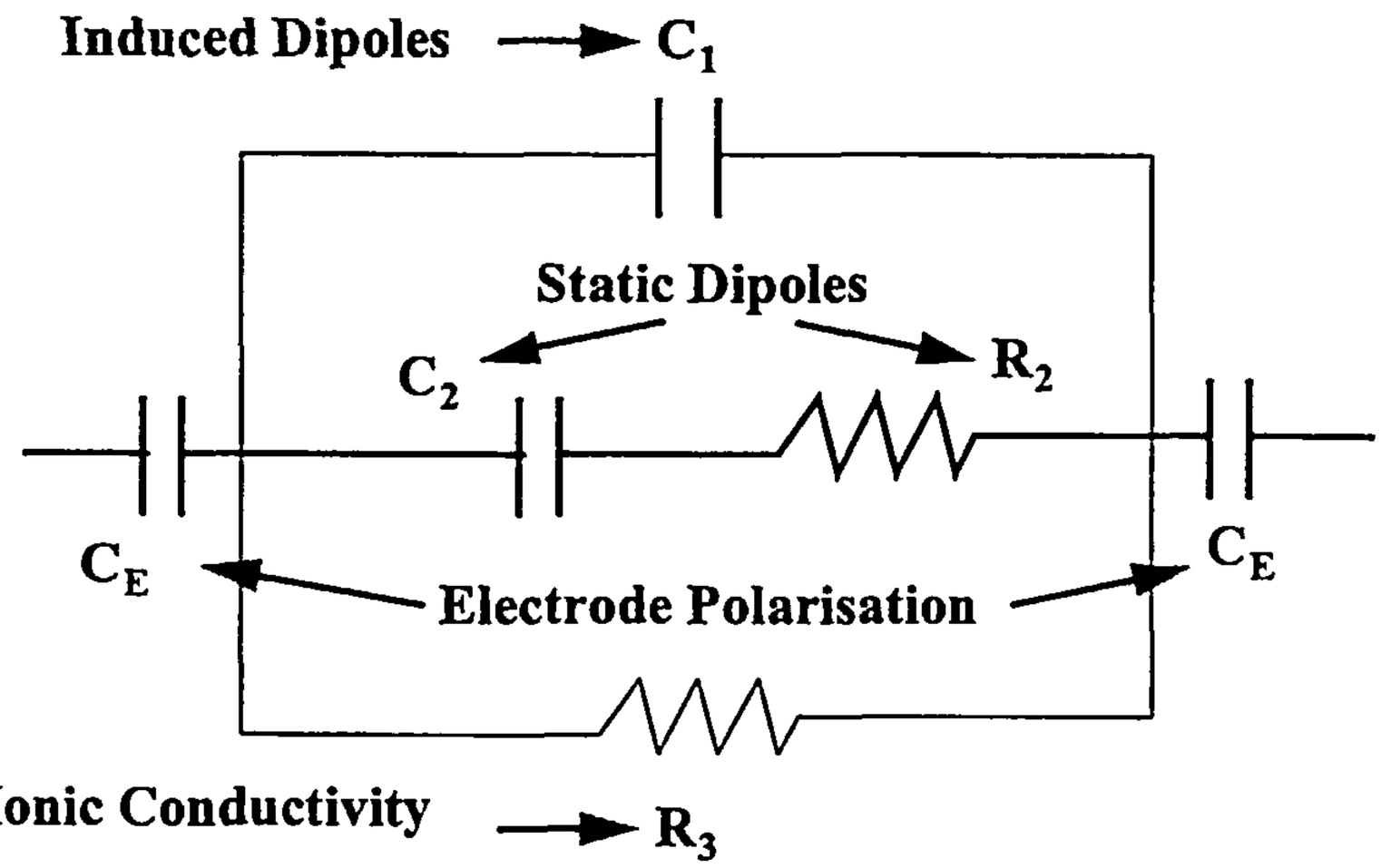

Figure 2.13 *Equivalent circuit of a polymeric material under testing (from Ref. 114)*

2.7.7 Dielectric Relaxation of Thermosets

In order to understand and predict the dielectric response of a thermoset, the lumped capacitive and conductive response of the circuit in Figure 2.13 has to be calculated. By adding the admittances of the individual components of this circuit, apart from the elements concerning electrode polarisation and ionic conductivity, and separating the capacitive and conductive components, the Debye equations for a single relaxation time are extracted, as these are expressed by Eq. 2.65. At high frequencies, only the induced dipoles C_1 contribute to the response, which also defines the unrelaxed permittivity $\varepsilon_{r\infty}$. At low frequencies both induced, C_1, and static, C_2, dipoles contribute to the response, thus defining the relaxed permittivity ε_{rs}. The ideal case of Debye behaviour for polymers exhibiting a single relaxation time was analytically discussed in section 2.7.4. Also in this section, the dielectric response of polymers exhibiting a normal distribution of relaxation times around an average relaxation time τ_0 was expressed by the Cole - Cole expression given in Eq. 2.68. There are thermosets that do not follow this kind of distribution of relaxation times. The molecular aspects of multiple dielectric relaxations in solid polymers, both amorphous and semi-crystalline, have been reviewed by Williams[115]. Several empirical equations have been put forward to account for the different existing relaxation distributions observed in

polymers. Some of them are listed in Table 2.2. In a Cole - Cole diagram, they are represented by squashed semicircles, slightly skewed (see Figure 2.12). In any case, the left semicircle intercept represents the unrelaxed permittivity and the right intercept represents the relaxed permittivity.

Table 2.2 Various expressions to describe the distribution of dielectric relaxation times. (α, γ, b, m, p, q in the expressions are constants)

Model expression (for complex permittivity ε^*)	**Model name**
$\varepsilon'' = (\varepsilon_{rs} - \varepsilon_{r\infty}) \frac{m}{2} \frac{(\omega\tau)^{m/2}}{1+(\omega\tau)^m}$	Fuoss-Kirkwood[116]
$\varepsilon^* = \varepsilon_{r\infty} + (\varepsilon_{rs} - \varepsilon_{r\infty}) \frac{1}{(1+i\omega\tau)^\gamma}$	Davidson-Cole[117]
$\varepsilon^* = \varepsilon_{r\infty} + (\varepsilon_{rs} - \varepsilon_{r\infty}) \frac{1}{\left(1+(i\omega\tau)^{1-\alpha}\right)^b}$	Scaife[118]
$\varepsilon^* = \varepsilon_{r\infty} + (\varepsilon_{rs} - \varepsilon_{r\infty}) \frac{1}{\left(1+(i\omega\tau)^p\right)^q}$	Havriliak-Negami[110]
$\varepsilon^* = \varepsilon_{r\infty} + (\varepsilon_{rs} - \varepsilon_{r\infty}) \left\{1 - i\omega \int_0^\infty \Gamma(t) \exp(-i\omega t) dt\right\}$ $\Gamma(t) = \exp\left(-t/\tau\right)^\beta$	Williams-Watts[119]

2.7.8 Ionic Conduction

Evaluation of the response of the circuit in Figure 2.13, this time including the ionic conduction term R_3, will give the mathematical representation of dielectric permittivity and dielectric loss as these are expressed in Eq. 2.74. The extra term in the loss representation (compared to Eq. 2.65) is the bulk ionic conductivity σ.

$$\varepsilon_r' = \varepsilon_{r\infty} + \frac{\varepsilon_{rs} - \varepsilon_{r\infty}}{1+\omega^2\beta^2} \qquad \textit{and} \qquad \varepsilon_r'' = \frac{\sigma}{\omega\varepsilon_0} + \frac{\varepsilon_{rs} - \varepsilon_{r\infty}}{1+\omega^2\beta^2}\omega\beta \qquad \text{(Eq. 2.74)}$$

The conductivity, σ, is equal to the product of the ion mobility, u, the concentration of mobile ions, $[C]$, and the charge of an ion, q, thus:

$$\sigma = u[C]q \qquad \text{(Eq. 2.75)}$$

This equation provides the characteristic relation between ionic conductivity and viscosity, since they depend on the mobility either of ions (conductivity) or of segments (viscosity).

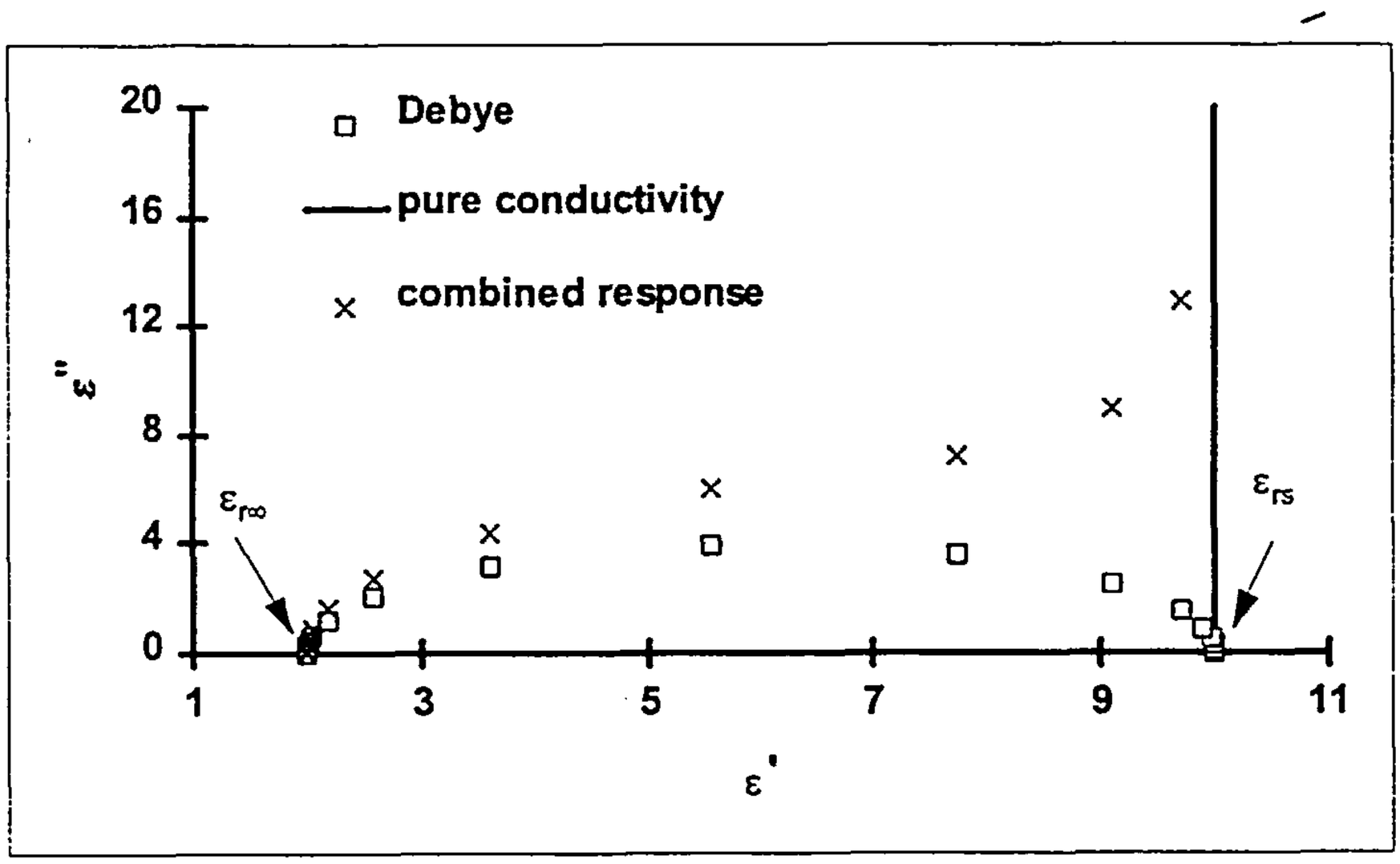

Figure 2.14 *The appearance of ionic conductivity and dipole terms in a Cole - Cole plot*

Day[114] has calculated the number of ions required to generate a loss factor of 1 at 100Hz. By assuming a typical mobility of 10^{-8} $cm^2/(volt \cdot sec)$, the calculated ionic concentration was found to be 1ppm or even 1ppb for elevated temperatures or at lower frequencies. This justifies the presence of an ionic conduction term in the dielectric response of a thermoset, especially in the liquid state and at low measured frequencies. Thus, when ion mobilities are small enough (at or below the T_g), ionic conduction does

not dominate the loss factor.

Figure 2.14 shows how ionic conduction appears in a Cole -Cole diagram. For purposes of comparison, the ideal case of a Debye behaviour has also been plotted.
As can be seen from this figure, as the conductivity level increases, it becomes increasingly difficult to discern the dipole loss peak. When the conductivity loss term $\sigma/\omega\varepsilon_0$ becomes two or three times greater than the relaxed permittivity of the material, the loss factor is completely dominated by conductivity and resembles a straight line, perpendicular to the permittivity axis at ε_{rs}.
Useful relations can be extracted between the mobility of ions and the properties of the resin. Senturia and Sheppard[111], by calculating the ion mobility with the aid of Stoke's law for the drift of a sphere in a viscous medium, suggest that ion mobility, and hence ionic conductivity, varies in inverse proportion to the viscosity, η. This oversimplified relation will fail completely as the curing resin reaches gelation. At gelation, the bulk viscosity becomes infinite because of the formation of a macroscopic molecular network, whereas resistivity, the inverse of conductivity, will remain finite, as polymer segments comparable in size to the ions are still mobile.

2.7.9 Electrode Polarisation

As was discussed in section 2.7.6, high levels of ionic conduction result in accumulation of ions at the interface between the electrode and the polymer. The resulting equivalent circuit (see Figure 2.13), is very complicated to analyse. Nevertheless, Day et al[120] carried out the analysis, with the following assumptions:

- The two charge layers that form at the electrodes have the same thickness, t_b.
- The permittivity within the blocking layer has the same value as that in the bulk.
- Ionic conductivity is the only contribution to the loss factor.

Following the above mentioned assumptions, they argued that there are two inequalities that must be satisfied if blocking layer effects are to be observed:

$$\tan\delta >> 1 \qquad \textit{and} \qquad \tan\delta >> \frac{L-2t_b}{2t_b} \qquad \text{(Eq. 2.76)}$$

where L is the inter-electrode spacing.

Using a subscript x to distinguish between the apparent measured permittivity and the actual bulk permittivity, the resulting expressions were:

$$\varepsilon'_x = \varepsilon' \frac{L}{2t_b}\left[\frac{(\tan\delta)^2 + \frac{L}{2t_b}}{(\tan\delta)^2 + \left(\frac{L}{2t_b}\right)^2}\right]$$

$$\varepsilon''_x = \varepsilon'' \frac{L}{2t_b}\left[\frac{\frac{L-2t_b}{2t_b}}{(\tan\delta)^2 + \left(\frac{L}{2t_b}\right)^2}\right] \qquad \text{(Eq. 2.77)}$$

In the ideal case of no blocking layer effects, where $L >> t_b$, the above equations become: $\varepsilon'_x = \varepsilon' \quad \textit{and} \quad \varepsilon''_x = \varepsilon''$.

The effects of the blocking layer thickness on the resulting dielectric properties are shown as a set of Cole - Cole plots in Figure 2.15. For an infinitesimally thin blocking layer compared to the inter-electrode spacing ($L/2t_b >> 1$), the Cole - Cole diagram approaches a vertical line which intersects the ε'_x axis at the bulk (dipolar) permittivity ε'. As the ratio $L/2t_b$ decreases, either due to a smaller inter-electrode spacing or a thicker layer, the Cole - Cole diagram becomes semicircular with the one ε'_x axis intercept at the bulk permittivity and the second intercept at the bulk permittivity multiplied by $L/2t_b$.

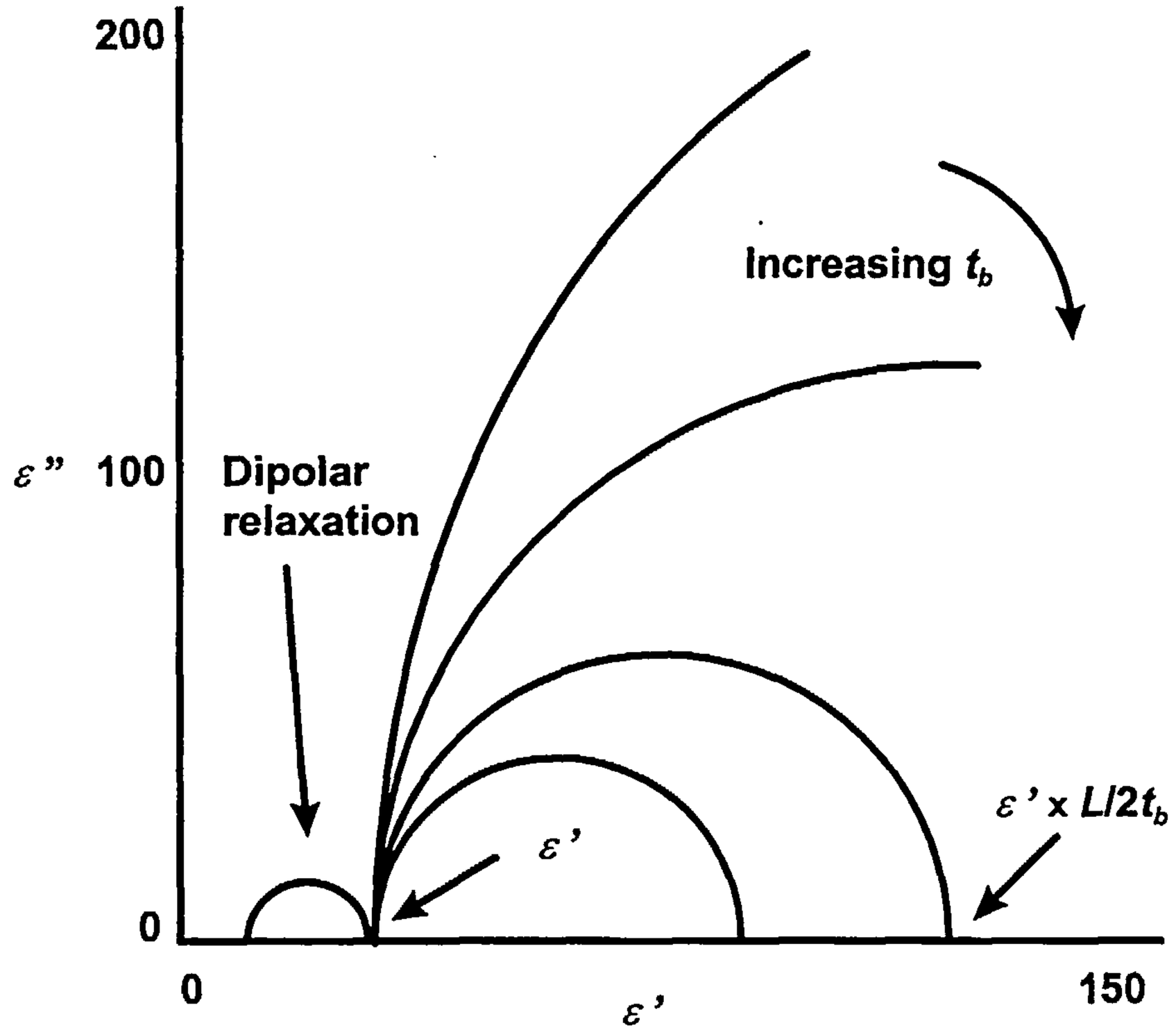

Figure 2.15 *Cole - Cole plots from Eq. 2.77 for various electrode blocking layer thickness (from Ref. 120)*

2.7.10 Dielectric Properties as an Index of the State of the Cure

In the previous sections it was demonstrated how the ionic conductivity is related to the viscosity before gelation. Conductivity can be extracted by determining which regions are dominated by a frequency dependence. When conductivity is dominant, then the loss factor of Eq. 2.74 will become:

$$\varepsilon'' = \frac{\sigma}{\omega \varepsilon_0} \quad \Rightarrow \quad \sigma = \varepsilon'' \varepsilon_0 \omega \qquad \text{(Eq. 2.78)}$$

By plotting $\varepsilon'' \varepsilon_0 \omega$ as a function of time at different frequencies, regions of superimposing data will appear. These regions will represent the ionic conductivity

term, since conductivity is frequency independent. Data that do not superimpose, have a dominant dipole term and can be thrown out, leaving the pure conductivity term. As it was discussed in section 2.7.8, conductivity is directly related to viscosity through a proportionality law. Thus conductivity can be used as an index for the viscosity profile of the resin. Several researchers have used conductivity data to extract information of the viscosity build up during cure of thermosets. The use of the WLF equation (see section 2.5) to model conductivity data is the most dominant. Since viscosity obeys WLF behavior, it is clear that conductivity will follow the same law if a proportionality relation exists between viscosity and conductivity. Tajima and Crozier[121] and Sheppard and Senturia[122] have demonstrated this very successfully. More recent work on the correlation between ionic conductivity and viscosity has demonstrated a number of ways of combining these two variables[123, 124].

The use of the WLF equation to model conductivity data reveals that conductivity can be used for a direct estimation of the T_g of the resin, since T_g is the main variable used in a WLF behaviour. Koike[125] demonstrated this for a DGEBA/aromatic amine system. Using a power law to correlate conductivity and viscosity and the WLF equation, he simulated the T_g advancement of the resin prior to gelation very successfully.

Although the proportionality law between conductivity and viscosity will start to collapse as the gel point is reached, correlation between conductivity and T_g indicates that the network build up during cure can be followed by monitoring conductivity variations in the resin. A number of papers exist in the literature dedicated in the exploitation of the relations governing structure development with the observed dielectric properties. Nass and Seferis[126], using a linear relationship between ionic conductivity and degree of cure, modelled the cure advancement of a TGDDM system with a good degree of accuracy. Day[127], introduces a cure index, defined by:

$$percent\ cure\ index = \frac{\ell og(current\ conductivity) - 0\%\ \ell og(conductivity)}{100\%\ \ell og(conductivity) - 0\%\ \ell og(conductivity)} \qquad \text{(Eq. 2.79)}$$

to follow the cure of an EPON 828/DDS system. The results, compared with DSC measurements, showed good correlation throughout the cure. It was also implied that conductivity measurements are more sensitive than DSC measurements, especially towards the end of the cure, where very little heat evolution is observed. Casalini et al[128], using a similar cure index with that of Day, also simulated the cure advancement of an EPON 828/EDA system. Instead of conductivity, the initial and final values of the real or the imaginary part of the dielectric constant were used in the cure index. All the above models rely on the initial and final properties of the material. For any of these models to be used in an industrial context, restrictions have to be applied to avoid having to take into account the final properties of the material, since these properties are not known a priori. Stephan et al[129], in a recent paper for in-process control of epoxy composites by microdielectrometry, suggest a normalisation of the conductivity data by the initial conductivities. They propose that using an Arrhenius type relationship between initial conductivity and temperature, a master curve between normalised conductivity and degree of conversion can be obtained, thus giving a more accurate description of the curing process.

2.7.11 Progress of Reactions by Complex Impedance Measurements

Another way of following the cure advancement of thermosets by dielectric measurements has been demonstrated by Mijovic and co-workers[130]. Their approach is based on the use of real and imaginary components of the complex impedance to monitor the progress of reactions. Their investigations have pointed out that the complex impedance varies in a systematic manner during the reaction. Again, the objective is to measure the variations in the contributions of migrating charges to the overall polarisation. The contribution of migrating charges to the overall polarisation varies during reaction as a consequence of physical and chemical changes in the reactive system. The equivalent circuit analysis is the heart of such investigations. In section 2.7.6, an equivalent circuit was constructed for the case of a polymeric system. Mijovic and co-workers, using the same interpretation, constructed a similar equivalent circuit, but now allowing for the presence of a distribution of relaxation times. The

model circuit is given in Figure 2.16 and the resolved real and imaginary parts of complex impedance for a single relaxation time system are given by Eq. 2.80.

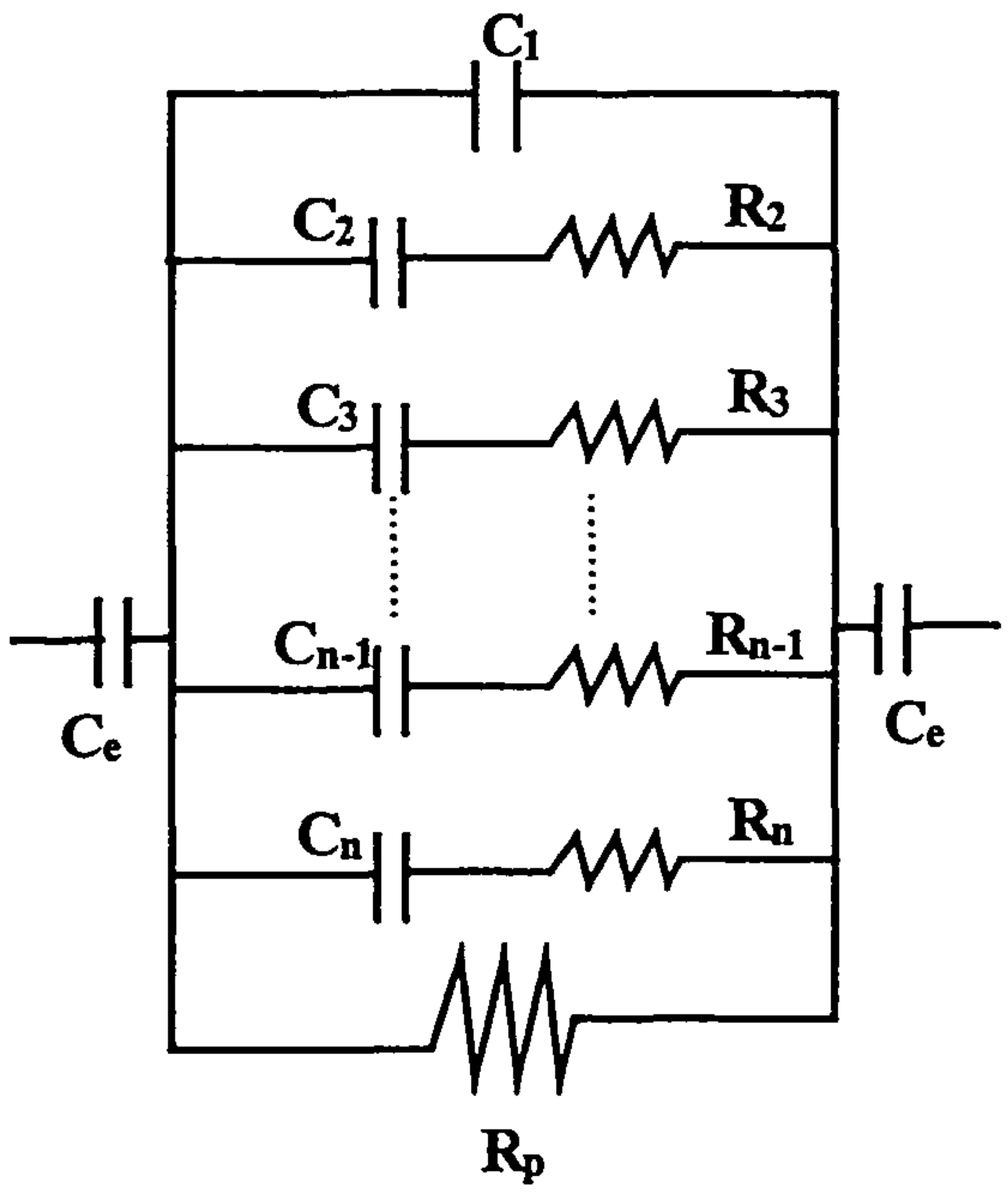

Figure 2.16 *Equivalent circuit of a thermoset exhibiting a distribution of relaxation times. The R_i-C_i elements in series represent this distribution. The elements C_l, C_e and R_p are similar with the ones shown in Figure 2.13 (from Ref. 130)*

$$Z' = \frac{R_p\left[1-R_p\tau C_1\omega^2+\tau\omega^2\left(R_pC_1+R_pC_2+\tau\right)\right]}{\left(1-R_p\tau\omega^2C_1\right)^2+\omega^2\left(R_pC_1+R_pC_2+\tau\right)^2} \qquad \text{(Eq. 2.80)}$$

$$Z'' = \frac{R_p\left[\omega\left(R_pC_1+R_pC_2+\tau\right)-\omega\tau\left(1-R_p\tau\omega^2C_1\right)\right]}{\left(1-R_p\tau\omega^2C_1\right)^2+\omega^2\left(R_pC_1+R_pC_2+\tau\right)^2}+\frac{2}{C_e\omega}$$

where: $C_1 = \varepsilon_{r\infty}C_0$, $C_2 = (\varepsilon_{rs} - \varepsilon_{r\infty})C_0$, $\tau = RC_2$ and R_p = ionic resistance

The graphical representation of the imaginary part of complex impedance, in a Bode diagram (impedance vs. frequency), can be seen in Figure 2.17. Three zones can be

identified in this figure: *Zone A*, where blocking electrode effects dominate the response, *Zone B*, where dissipative effects play the major role and *Zone C*, where relaxation contributions dominate. In Zone B, where the dielectric signal is not affected by electrode polarisation or relaxation phenomena, the equivalent circuit can be transformed to simple *R-C* parallel circuit with a total capacitance $C = C_1 + C_2$. The imaginary impedance of such a circuit is given by:

$$Z'' = \frac{\omega C R_p^2}{1+\omega^2 C^2 R_p^2} \qquad \text{(Eq. 2.81)}$$

The derivative of the imaginary impedance with respect to the angular frequency is:

$$\frac{dZ''}{d\omega} = \frac{CR_p^2\left(1-\omega^2 R_p^2 C^2\right)}{1+\omega^2 R_p^2 C^2} \qquad \text{(Eq. 2.82)}$$

which has a maximum at:

$$\omega = \frac{1}{R_p C} \qquad \text{(Eq. 2.83)}$$

Combination of Eq. 2.82 and Eq. 2.83 gives:

$$Z''_{\max} = \frac{R_p}{2} \qquad \text{(Eq. 2.84)}$$

Thus, the ionic resistance, R_p, can be directly determined from the maximum of the imaginary impedance observed in Zone B of Figure 2.17.

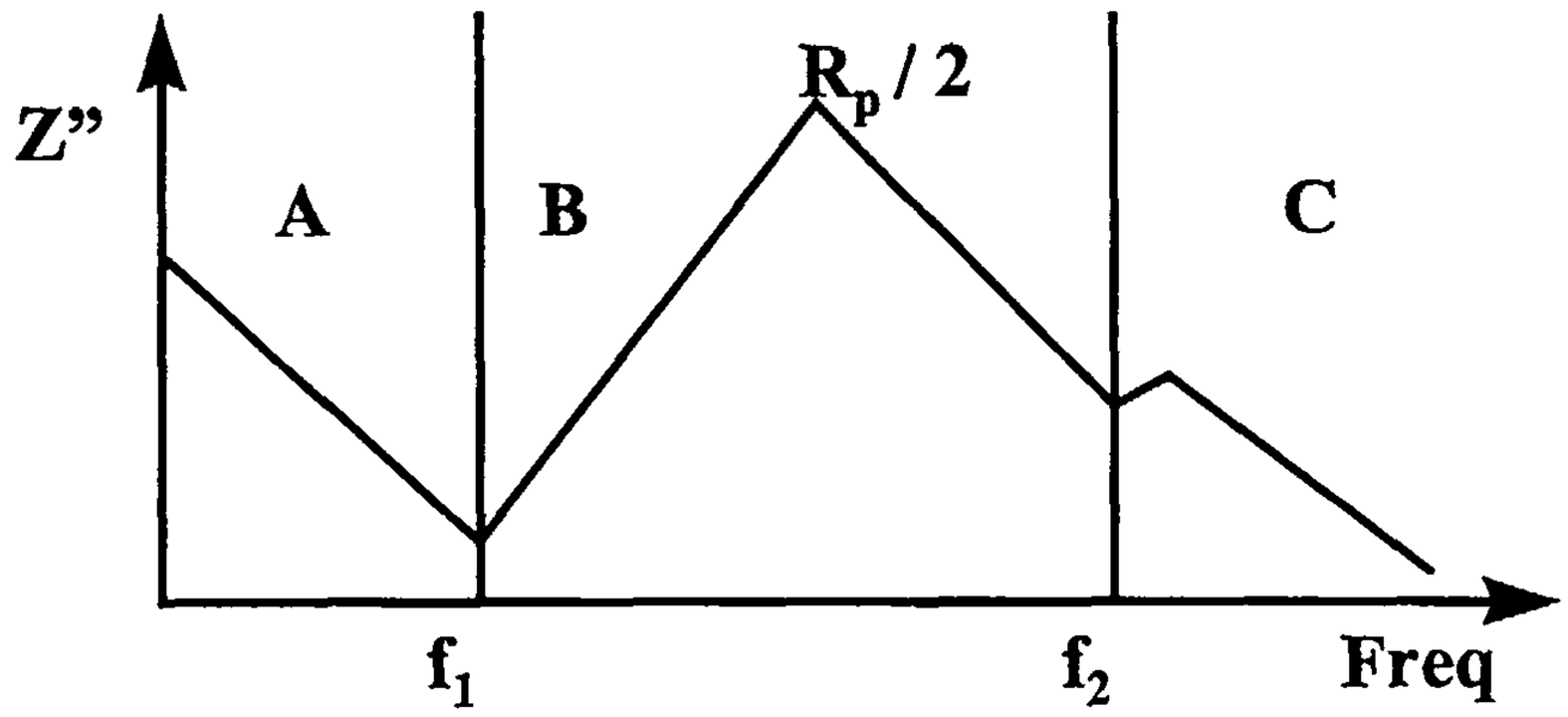

Figure 2.17 *Schematic plot of imaginary impedance as a function of frequency.* ***Zone A****: electrode polarisation.* ***Zone B****: migrating charges.* ***Zone C****: relaxation phenomena*

The straightforward determination of ionic resistance, and thus of the ionic resistivity, ρ, provides undoubtedly a great advantage over the trial and error search for the right frequency where the signal is dominated by conductivity (see section 2.7.10). Using the above method and empirical relations that correlate degree of cure with resistivity, Mijovic and co-workers established a good agreement between experimental results and model predictions for several epoxy/amine systems[131, 132]. The empirical relationship that connects the degree of cure with resistivity of the curing system, as used in the above mentioned studies, is given by:

$$\frac{\alpha}{\alpha_m} = \frac{\ell og\rho - \ell og\rho_0}{\ell og\rho_m - \ell og\rho_0}\left(\frac{\ell og\rho_m}{\ell og\rho}\right) \qquad \text{(Eq. 2.85)}$$

where ρ_0 is the initial resistivity of the resin and α_m, ρ_m are the maximum attained degree of cure and resistivity respectively.

2.7.12 Temperature Effects on the Dielectric Properties of Thermosets

Temperature is the key variable in determining the cure rate for a given chemical system and since all of the microscopic mechanisms depend directly on temperature, it is of interest to investigate how the dielectric response of a thermoset will change with

changing temperature. The temperature behaviour of epoxy resins *without any curing agents* can be readily investigated by a temperature scan through their T_g. The temperature dependence of the permittivity and loss factor of a DGEBA epoxy resin (Epon 828) in the vicinity of its glass transition is shown in Figure 2.18. At temperatures well below the monomer T_g, the permittivity at all frequencies has a value of 4.2 (unrelaxed permittivity). As the temperature approaches T_g, the dipoles are starting to contribute to the permittivity as their mobility increases. This is evident first at low frequencies, where the permittivity starts to rise rapidly with increasing temperature up to the relaxed permittivity. A drop in permittivity then occurs as the temperature increases further. The increase in thermal motion, that is induced by the increase in temperature, tends to randomly redistribute the orientation of the dipole moments p_m. The effect of the temperature to the orientation polarisation factor α_o is expressed by the function [105]:

$$\alpha_o = \frac{p_m^2}{3k_B T} \qquad \text{(Eq. 2.86)}$$

where k_B is the Boltzmann's constant. The negative effect of the increase of temperature to the orientation polarisation, and thus to the relaxed permittivity is evident from that expression. The drop of the relaxed permittivity is followed by a rapid increase due to electrode polarisation effects. Similar behaviour is observed in the loss factor, but now with a dipole peak appearing as the T_g of the uncrosslinked resin is reached. The increase in the loss factor at temperatures above the T_g is attributed to an increasing ionic conductivity. The above discussion indicates the ability of the dielectric properties to track the T_g of a resin. Several researchers have assigned the loss peak at low frequencies (around 1Hz) to be a measure of the T_g of the resin as that is measured by other independent techniques such as DSC measurements [113]. Sheppard and Senturia[122], investigating a series of DGEBA resins, have measured the temperature dependence of the frequency where the dipole loss peak appears. They have demonstrated the applicability of WLF behaviour to dipolar relaxations yielding values for the C_1, C_2 constants that are comparable to the universal values. The C_1

constant was attributed to the dipolar contribution of hydroxyether moieties.

The above results indicate that the temperature dependence of the dipole relaxation time at fixed conversion can be expected to follow WLF behaviour and that relaxation times of 1sec will track the T_g of a curing system[133]. Recent work in a series of epoxy/curing agent systems reveals that relaxation times around 1sec do track the vitrification point of the curing system to a good level of agreement[134 - 136].

In Chapter 8 the advancement of the cure reaction will be followed by monitoring the changes in the dielectric properties of the resin. The physical transformations (gelation and vitrification) will be investigated with respect to the characteristic changes in the dielectric signal. Mathematical formulae will also be constructed to represent the changes in the conductivity levels of the curing resin and any correlation between these changes and the advancement of the cure will be exploited.

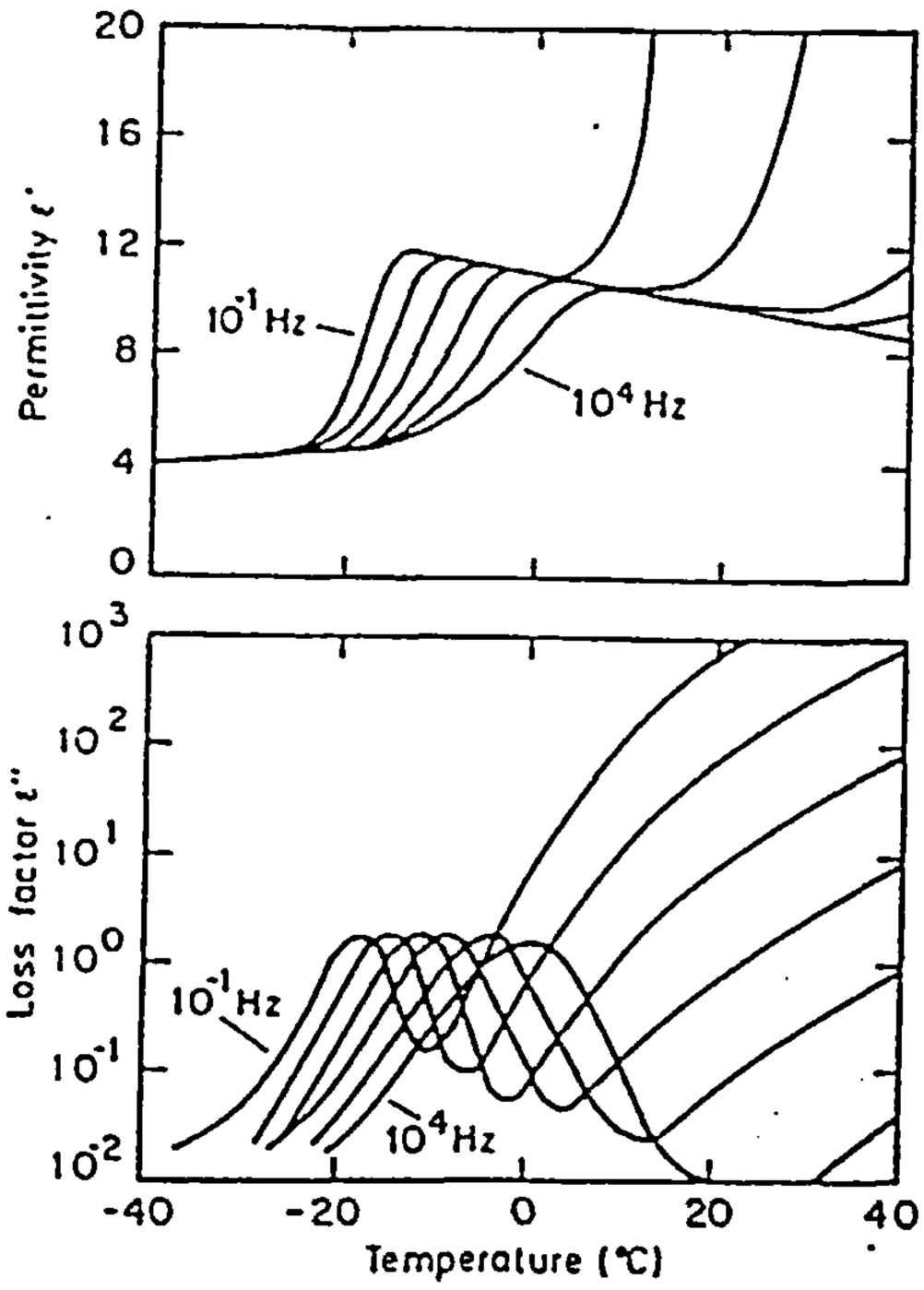

Figure 2.18 *Temperature dependence of dielectric permittivity and dielectric loss of Epon 828 resin in the vicinity of its glass transition temperature (from Ref. 110)*

Chapter Three

3. Materials and Methods

3.1 Materials

Four different epoxy-based resin systems were used in this study. Two of them were commercially available epoxy/amine systems, whereas the other two were specially prepared experimental systems based on one epoxy resin and two amine hardeners. A brief description of all the resin systems is given here.

3.1.1 Commercial Resin Systems

3.1.1.1 RTM6 Resin [137]

The first commercial resin system used has the trade name RTM6 and is supplied by Hexcel Composites. RTM6 is a premixed, monocomponent epoxy resin system, specially developed to fulfil the requirements of the aerospace and space industry in advanced resin transfer moulding (RTM) processes. The expected service temperatures of final products range from -60°C to 180°C. At room temperature, RTM6 is a translucent paste and its viscosity drops very quickly upon heating. The uncured resin has a density of 1.117 g/cm^3 and the fully cured resin 1.141 g/cm^3. When fully cured, it exhibits high glass transition temperatures, excellent hot/wet properties and low moisture absorption. According to the manufacturer, the shelf life of this resin at 23°C

is at least 15 days, whereas at -18°C it is approximately 9 months.

Manufacturer's process specification for the RTM process:

- Preheat resin at 80°C
- Degas for 10 min under 5 mbar residual pressure while stirring slowly
- Preheat the mould and the fibrous preform to 120°C
- Inject the resin (80°C) under vacuum/low pressure (1 to 3 bar)
- Cure in mould: 75 min at 160°C
- Free standing post-cure: 120 min at 180°C (ramp: 1 °C/min)

3.1.1.2 934 Resin

The other commercial resin system used has the trade name 934 and is supplied by Fiberite Inc [138]. The general use of this resin is as a matrix in composite materials and it is commercially available in a prepreg form. Primarily it consists of a TGDDM epoxy cured with DDS hardener but also contains boron trifluoride catalyst. The chemical constituents of the resin matrix in the carbon fibre 934 prepregs, as these are reported in the literature [76], are shown in Table 3.1.

Table 3.1 *Chemical Constituents of the resin matrix of C Fibre 934 Prepregs*

Constituent	pph
TGDDM	100
Diglycidyl orthophthalate epoxy (DGOP)	17.19
DDS	39.06
$BF_3:NH_2C_2H_5$	0.63

3.1.2 'Lab' Made Resin Systems

Along with the two commercial resin systems, two other systems were tested, that had been produced by mixing appropriate constituents in our laboratory equipment. Both of them were epoxy/amine resin systems. The pure materials used for the preparation of those resins were one polyfunctional epoxy resin and two amine hardeners, discussed below.

3.1.2.1 MY 721 Epoxy Resin

The epoxy resin used was supplied by Hexcel Composites with the trade name MY 721 [139]. This epoxy resin is based on the aromatic glycidyl amine resin TGDDM, whose molecular structure is shown in Figure 2.3. It was supplied as a high viscosity liquid with a density 1.19 - 1.22 g/cm^3 at 25°C.

3.1.2.2 Amine Hardeners

a) 4,4' - Methylenebis(2-isopropyl-6-methylaniline) (M-MIPA) [140]

One of the curing agents used in this study was 4,4' - Methylenebis(2 - isopropyl - 6 methylaniline) with a chemical formula $C_{21}H_{30}N_2$ and molecular weight 310.49. This is a diamine commercially supplied by LONZA Ltd under the trade name M-MIPA. The structural formula of this agent is shown in Figure 3.1. M-MIPA is a yellowish brown solidified melt with a solidification range 10 - 30 °C and density 0.99 g/ml (20 °C).

Typical applications of this hardener are:

- Chain extender for elastomeric polyurethanes;
- Curing agent for epoxides;
- Precursor for polyimides, polyesterimides and polyetherimides.

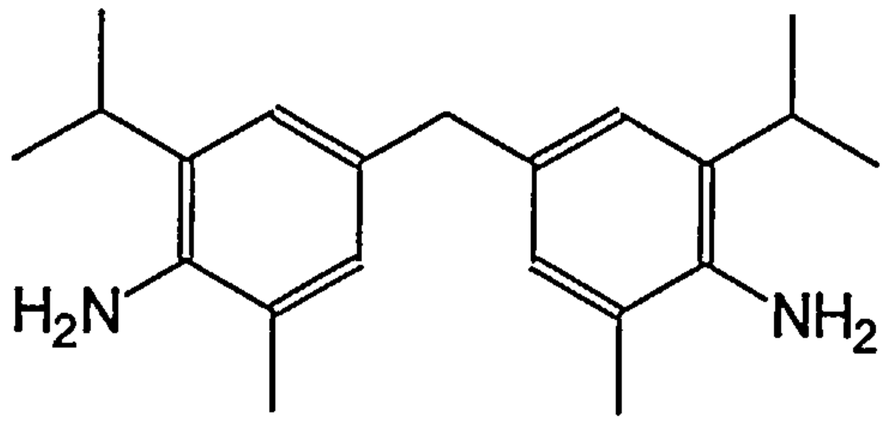

Figure 3.1 *Structural formula of M-MIPA amine hardener*

b) 4,4' - Methylenebis (2,6 - diethylaniline) (M-DEA) [141]

The other curing agent used was 4,4' - Methylenebis (2, 6 - diethylaniline) with the same chemical formula as M-MIPA but with a different structural formula (see Figure 3.2). This agent is also supplied by LONZA Ltd. under the trade name M-DEA. It is supplied as white to brown flakes with a bulk density of 0.5 kg/l and a melting point of 88°C. The same typical applications apply for this agent as for the M-MIPA agent.

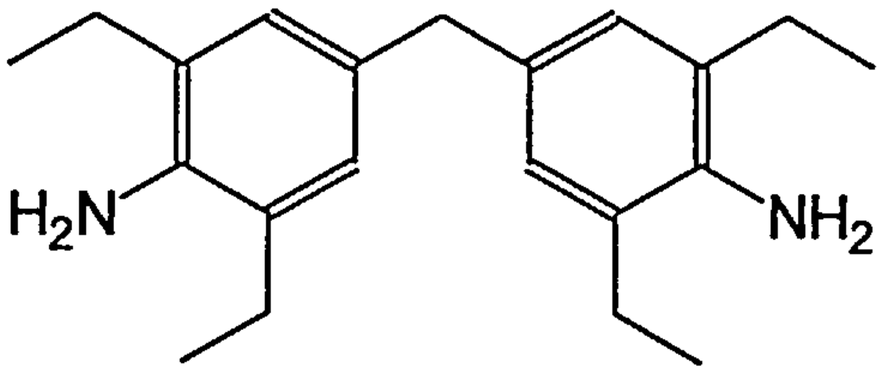

Figure 3.2 *Structural formula of M-DEA amine hardener*

3.1.2.3 Resin Preparation

Two different formulations were prepared in the laboratory from the above materials. The chemical constituents for each formulation are shown in Table 3.2. Stoichiometric mixing ratio 1:1 between epoxy groups and amino-hydrogens was adopted for Formulation B, whereas the epoxy groups and amino-hydrogens ratio of Formulation A was 0.85.

The epoxy resin was stored in a refrigerator, whereas the amine hardeners were stored

at room temperature. The epoxy resin was allowed to reach room temperature before opening to avoid moisture condensation on the surface of the material.

Table 3.2 *Chemical Constituents of 'lab' made resins*

Resin	pph		
	MY 721	*M-MIPA*	*M-DEA*
Formulation A (RMO)	100	43.7	26.7
Formulation B (RMO2)	100	70.4	-

In general, resin mixtures were prepared according to the following procedure: after the initial melting of the hardeners at 90°C, they were dissolved in the epoxy resin at 100°C. The mixing temperature was achieved using an oil bath. A magnetic stirrer was used throughout the mixing procedure, which lasted 30 minutes, for better mixing conditions. After the mixing, the resin was kept at 80°C under vacuum for 30 minutes to remove all air bubbles and then it was free cooled to room temperature. The mixtures were placed in glass containers and stored in a freezer at -18°C for further use.

3.1.2.4 Resin Formulations

As was mentioned in the above sections, the epoxy/amine hydrogen ratios in the resins prepared in the lab were kept between specific limits, based on the assumption that the pure materials do not contain any higher oligomers and homopolymer species. To verify this, HPLC experiments were made at Short Brothers [142] and the results were supplied to us for evaluation. These experiments showed that the neat materials were not as pure as expected. In particular the MY 721 epoxy resin had an equivalent molecular weight of 520, whereas the molecular weight of pure TGDDM resin is 422. The epoxy/amine hydrogen ratios, as determined by the HPLC experiments, are shown in Table 3.3 along with the data for the RTM6 resin. The HPLC experiments also

indicated that the RTM6 resin consists of two amine hardeners with an amine hydrogen ratio $r_\alpha = 0.62$.

Table 3.3 *Epoxy/amine hydrogen ratios for the resin systems RTM6, RMO and RMO2, as these were determined by HPLC experiments*

Resin	*RTM6*	*RMO*	*RMO2*
Epoxy/Amine hydrogen ratio (*r*)	0.85	0.95	0.83

3.2 Conventional Methods of Cure Monitoring

3.2.1 Differential Scanning Calorimetry (DSC)

This method was used in the cure reaction kinetics evaluation and in the glass transition temperature determinations. All experiments were conducted on a Perkin Elmer DSC-4 apparatus apart from the isothermal experiments on RTM6 resin which were made on a Mettler Toledo 8000 apparatus. The Perkin Elmer DSC-4 was fitted with a cooler unit to achieve measurements in sub-ambient temperatures. In both instruments, a nitrogen purge gas was used to avoid any oxidation of the samples during the experiments.

3.2.1.1 Dynamic DSC Experiments

Dynamic runs at constant heating rates were made in order to determine the conversion profile and the total heat of reaction released during dynamic curing of all resin systems. For that reason, 8-10 mg of the resin were encapsulated in an aluminum pan and placed in the instrument furnace at ambient temperature. After cooling to -50°C and 2 minutes equilibration, the heat evolution was monitored from -50°C to 320°C using the following heating rates: 2, 5, 7.5, 10, 15 and 20 °C/min. A typical thermogram of a dynamic cure is shown in Figure 3.3, translated into energy changes

per °C. The degree of cure, α, at any temperature T during the dynamic cure is given by:

$$\alpha = \frac{\int_{T_0}^{T_1} \frac{dH}{dT} dT}{\Delta H_T} \qquad \text{(Eq. 3.1)}$$

and represents the shaded proportion of the total area shown in the same figure. The lower bound of the integration, T_0, is the lowest temperature at which heat evolution begins. Integration of the total area enclosed under the thermogram will give the total heat of reaction released during the reaction, ΔH_T, since it is supposed that the curing reaction has proceeded to 100% of the extent of cure by the end of the run. Prior to each experiment the instrument background was collected by running the same experiment with an empty cell instead of a cell filled with resin. The instrument background was subsequently subtracted automatically from the response of the resin.

Integration of the above formula supposes an a priori knowledge of the baseline from which the integration has to be performed. The baseline is the sample background that has to be subtracted from the DSC curves to reveal the pure response of any endothermic or exothermic reactions. The problem of sample background correction arises from the fact that the specific heat of the system continuously changes during the thermal event (e.g. curing, melting) from the level of the initial substances to that of the final product. To obtain the net effect due to the thermal event, the course of the heat capacity changes should be subtracted from the data corrected for the instrument baseline. The standard method for sample background correction is the subtraction of a straight or a sigmoidal line connecting the initial and the final levels of the specific heats. In thermosets, straight or sigmoidal lines may not represent the real sample background, because the specific heat of the system during the thermal transition depends on both the current degree of cure and the temperature. Bandara[80], using the thermal response of the material before and after any thermal events, constructed an expression that incorporates changes in the specific heat due to the degree of cure. This expression is given by:

$$F(t) = \frac{\int_0^t \{G(t) - F(t)\}\, dt}{\int_0^{t_n} \{G(t) - F(t)\}\, dt} \{P_2(t) - P_1(t)\} + P_1(t) \qquad \text{(Eq. 3.2)}$$

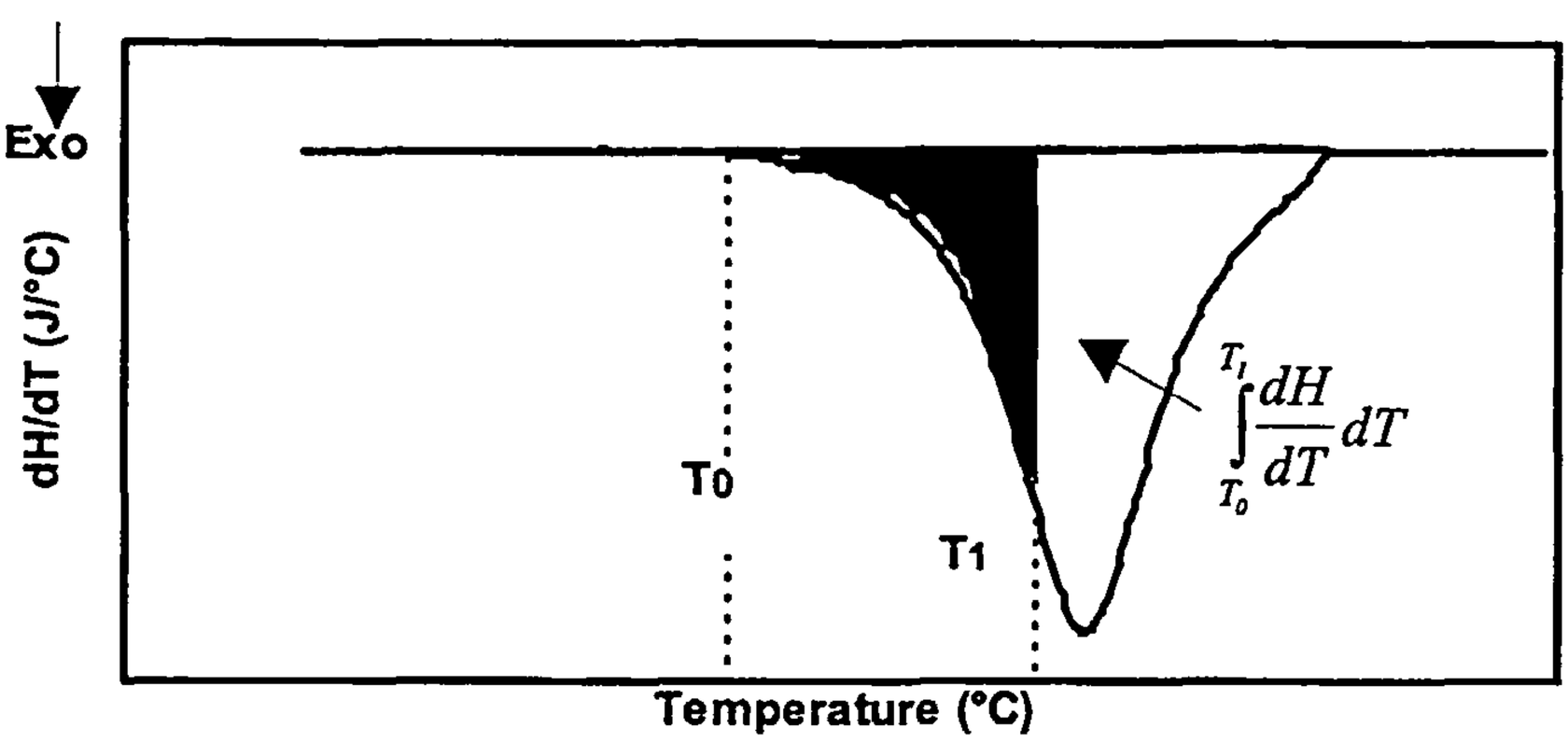

Figure 3.3 *Typical DSC thermogram of a curing resin under heating at constant heating rate. The shaded area is given by the integral shown*

In this expression, *F(t)* is the sample background, *G(t)* is the total signal corrected for the instrument background and t_n is the time of termination of the thermal event. $P_1(t)$ is the DSC signal for the initial substances in the absence of any events, which can be estimated through linear extrapolation of the portion of the total curve prior to the thermal event. $P_2(t)$ is the DSC signal from the product alone, which, for a thermoset, can be estimated by a rerun of the fully cured sample under the same experimental conditions. An iterative algorithm can be constructed to find a numerical solution for *F(t)*.

This form of baseline has been used in Chapter 4 for the calculation of the heats of reaction and the evaluation of the conversion profiles.

The overall reaction rate can be calculated directly from the rate of enthalpy change. Normalisation of the enthalpy rate by sample weight and division by the total heat of reaction will give the reaction rate.

3.2.1.2 Isothermal DSC Experiments

Isothermal experiments were carried out only for the RTM6 resin. Isothermal experiments were also tried for 934 resin, but the produced thermograms did not show a clear baseline for the integration. Therefore, the isothermal experiments on 934 resin were aborted. For the isothermal experiments on RTM6 resin, 2 - 3 mg of the resin were encapsulated in an aluminum pan and the pan was placed in the pre-heated furnace of the instrument at the isothermal temperature of the experiment. After 2 minutes thermal equilibrium was achieved, the isothermal cure monitoring started. The temperatures used were: 140, 160, 170 and 180 °C.

The measurement of the heat released during the curing reaction is used for the determination of the cure kinetics. A typical isothermal curve is shown in Figure 3.4. The degree of cure, α, at any time t during the isothermal reaction can be obtained from:

$$\alpha = \frac{\int_0^t \frac{dH}{dt} dt}{\Delta H_T} \qquad \text{(Eq. 3.3)}$$

The numerator is the heat released until time t and is equivalent to the shaded area shown in the same figure. The baseline for the integration was estimated by drawing a horizontal line, extrapolating the baseline reached on the completion of the cure peak to the start of the peak. ΔH_T is the total heat of reaction for a 100% cured sample. For the determination of the total heat of reaction, dynamic DSC experiments were conducted, as described in Section 3.2.1.1. Numerical methods were used to calculate the integral of the above equation at various time intervals in order to obtain the conversion profile at each experiment.

The overall reaction rates were calculated using the same method as in the dynamic case.

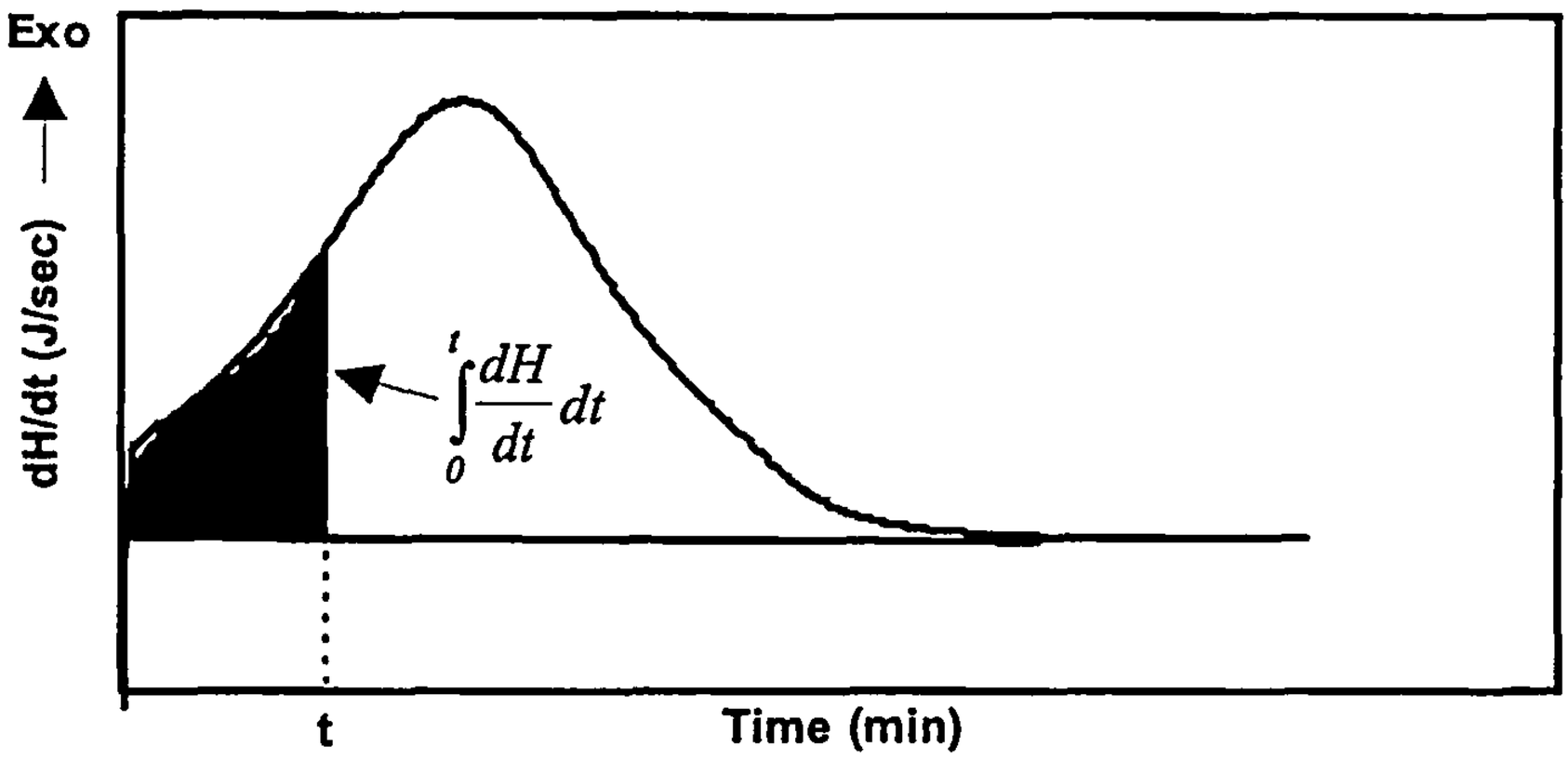

Figure 3.4 *Typical DSC thermogram of a curing resin under isothermal conditions. The shaded area is given by the integral shown*

3.2.1.3 Residual Heat of Reaction DSC Experiments

The conversion profile of all the resin systems, under isothermal conditions, was also constructed by measuring the residual heat of reaction after partial cure of the resin at different time intervals and cure temperatures. For these experiments 8-10 mg of the resin were encapsulated in an aluminum pan and placed in the pre-heated furnace of the instrument at the isothermal temperature of the experiment. After 2 minutes of equilibration, the time elapsed during the cure started to be measured. When the predetermined time interval had elapsed, the sample was quenched to -50°C and subsequently scanned at 10 °C/min until fully cured in order to determine the residual heat of reaction, ΔH_{res}.

The respective degree of conversion was calculated by:

$$\alpha = \frac{\Delta H_T - \Delta H_{res}}{\Delta H_T} \qquad \text{(Eq. 3.4)}$$

The above procedure was repeated, using different samples, for a range of time intervals and temperatures, until enough points had been determined to enable the construction of the conversion profiles.

Some samples showed a characteristic spike in the thermogram just before the exotherm started, which was attributed to the physical aging of the resin. When the resin has passed the vitrification point, a subsequent dynamic scan of that resin usually shows an endothermic spike in the vicinity of the T_g, as can be seen clearly in the thermogram of Figure 3.5. To eliminate this sub-T_g physical annealing, the specimens were quickly quenched from temperatures just above the endothermic peak to the temperature of -50°C. The subsequent re-heating of the specimens using the same experimental conditions was free of the endothermic peak as can be seen in the same figure. This method, also used by Gillham and co-workers [77], results in an error introduced by the cooling and the subsequent re-heating of the specimens of not more than 1 - 2 °C of the final T_g value of the cured resin.

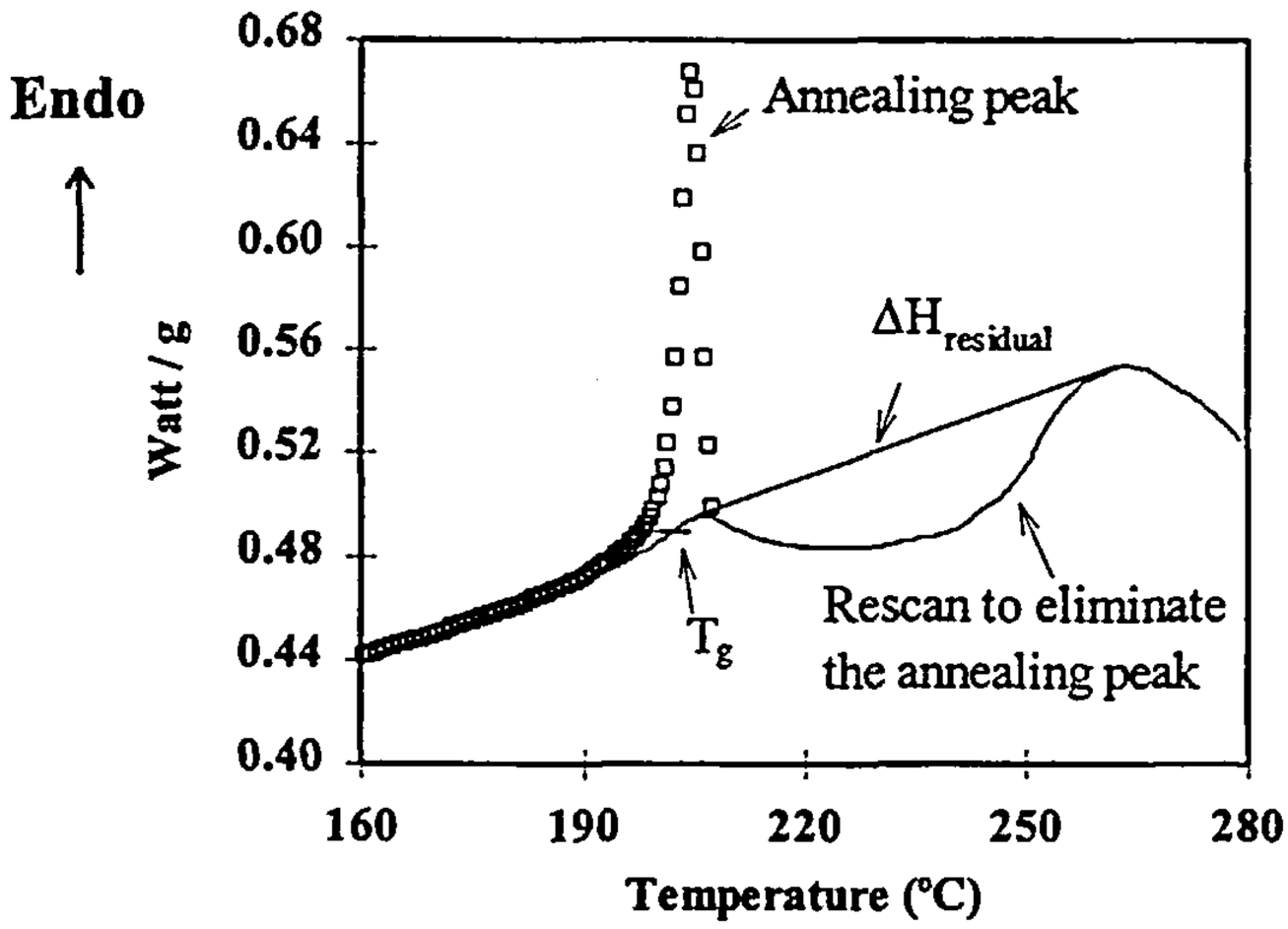

Figure 3.5 *Endothermic physical aging peak for samples that had vitrified during cure. a)* ***symbols****: aging peak. b)* ***solid line****: rescan to eliminate the physical aging peak. The T_g of the partially cured resin is also shown in this picture as the midpoint of the endothermic shift in the thermogram*

3.2.1.4 T_g Measurements

Estimation of the T_g of the partially or fully cured resin was made from the experimental results of the residual heat of reaction experiments. The glass transition temperature was determined as the midpoint of the endothermic shifts observed during the rescans of the partially cured resin. An example of T_g determination is shown in Figure 3.5.

At the later stages of the cure, when the resin has reached vitrification, the residual reaction exotherm starts in the immediate vicinity of the T_g region. This made the determination of the glass transition and subsequently of the residual heat of reaction difficult, since no experimental method exists to separate these two phenomena. Because of the above difficulty, the T_g results will be presented in the following sections as approximate values of the actual T_g values.

3.2.2 Fourier Transform Infrared Spectroscopy (FTIR)

Alongside the DSC experiments, kinetic studies of the resin systems were also conducted by FTIR. All experiments were made on a Perkin Elmer System 2000 FT-IR spectrometer with a cell controlled by a SPECAC temperature controller. The cure of the resin was investigated under isothermal conditions at temperatures of 130, 140, 150 and 160 °C.

Disposable window samples had to be used because following the completion of the cure, the window sample system would be firmly bonded and irrecoverable. For that purpose, freshly prepared KBr disks were made following a standard method and were kept in a moisture free environment. Absorption of moisture from the KBr disks could cause interference both with the measured spectrum and with the actual kinetics of the curing resin. As discussed in the theoretical part, OH groups accelerate the reaction between the epoxy and the amino groups. Thus, the presence of moisture could cause acceleration of the overall reaction rate during the cure.

The specimens consisted of two KBr disks with a couple of drops of resin placed in between. The sample system was placed in the pre-heated cell attached on the spectrometer window, and after allowing two minutes for equilibration, the spectra

started to be recorded at regular time intervals. Thirty to forty readings were collected for each sample allowing an average of sixteen spectra for each reading. The collection of the spectrum was concentrated in the mid-infrared region (wavenumbers 4000cm^{-1} - 400cm^{-1}) using a resolution of 1cm^{-1}. Prior to each run, the background spectrum was collected and automatically subtracted from the resin spectrum. A typical absorption spectrum of a curing resin is shown in Figure 3.6. Identification of the peaks according to the chemical groups involved, along with the quantitative analysis performed to extract the conversion profiles will be discussed during the presentation of the experimental results, in Section 4.2.

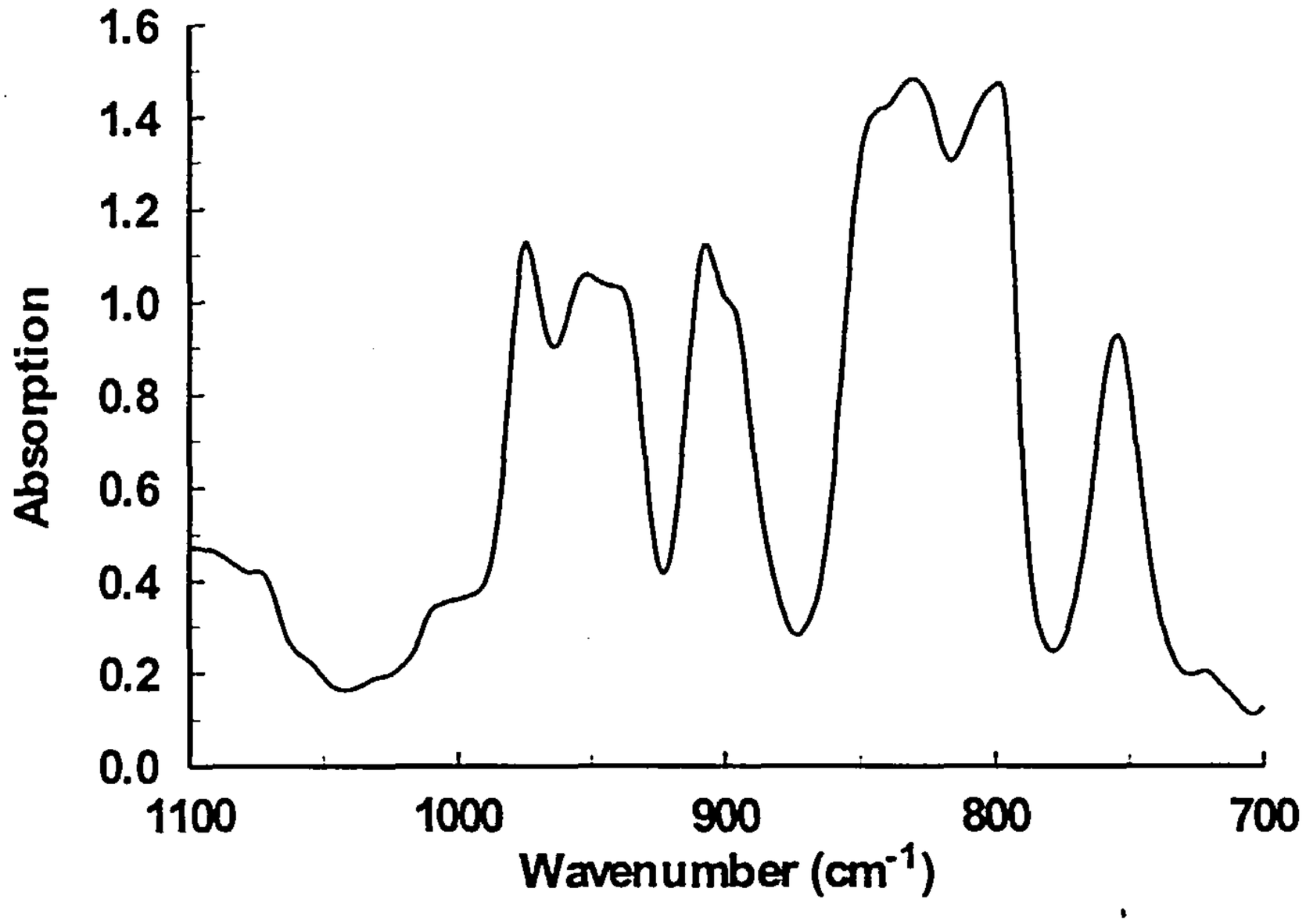

Figure 3.6 *Typical absorption spectrum of a curing resin in the wavenumber range between 1100cm^{-1} and 700cm^{-1}*

3.2.3 Rheometry

The viscosity of all the resin systems was measured during the course of cure using a Bohlin Instruments CVO-10 rheometer. The measuring geometry used was a 40mm parallel plate system with the bottom plate fixed and the top plate oscillating at a fixed frequency. The measurements were made by controlling the applied stress so that the

corresponding strain never exceeded predetermined limits. Prior to each experiment, frequency and stress sweeps were made, in order to determine the appropriate frequency and stress ranges within which the curing resin behaved as a linearly viscoelastic material.

All experiments were conducted under isothermal conditions at temperatures of 130, 140, 150 and 160 °C. After pre-heating the plates to the experimental temperature, the resin was placed on the bottom plate and the upper plate was lowered down until a fixed gap of 0.5mm between the plates had been reached. After allowing 2 - 3 min for temperature equilibrium to establish, the measurement was started collecting the viscosity response at fixed time intervals. When the measured viscosity had exceeded the value of 20 kPas, the measurement was stopped and the data were stored for subsequent analysis.

Control of the temperature was made by an electrical heater with two individual heating elements, one for each plate. To prevent any heat losses, a specially designed insulating system was used, enclosing the measuring unit. Because the measuring parallel plates would be firmly bonded and irrecoverable at the end of the experiments, disposable plates were used. These plates withstand high temperatures, so after each experiment, the cured resin was burned off at 500°C in order to recover the plates for another use.

3.3 Dielectric Measurements

Dielectric measurements were performed using a Solartron SI 1260 Frequency Response Analyser (FRA) controlled by a PC using 'in-house' produced software. Communication between the computer and the FRA was accomplished via an IEEE interface which enabled both the conditions of the measurements to be pre-programmed and automated and also the data to be collected and stored for subsequent analysis. All measurements were performed in the frequency range between 0.1Hz and 1MHz. In this frequency range, 29 spot frequencies were swept in a logarithmic scale at specific time intervals during the cure. The AC voltage supplied by the FRA was set to 0.3V.

Commercial sensors, which are Dek-Dyne interdigitated electrodes, were used in this study. The sensors consist of an electrode assembly placed on a Kapton layer. The size of the Kapton layer was 25 x 13 mm, of which 19 x 10.5 mm comprise the actual electrode assembly. The interelectrode spacing was 15μm, thus allowing for a localised measurement of the dielectric properties to be achieved. A schematic representation of the sensor along with the produced electric field is shown in Figure 3.7.

Towards the end of the cure, the resin exhibits high impedance values in the range of MOhms , thus the currents that have to be measured fall in the range of nA. In order to increase the sensitivity of the measurement and enable a more accurate measurement of the current, an Electrochemical Interface (Solartron SI 1287) was used as a potentiostat, in series with the FRA. Using this configuration, the dielectric properties that could be monitored were the real and the imaginary parts of the impedance of the system.

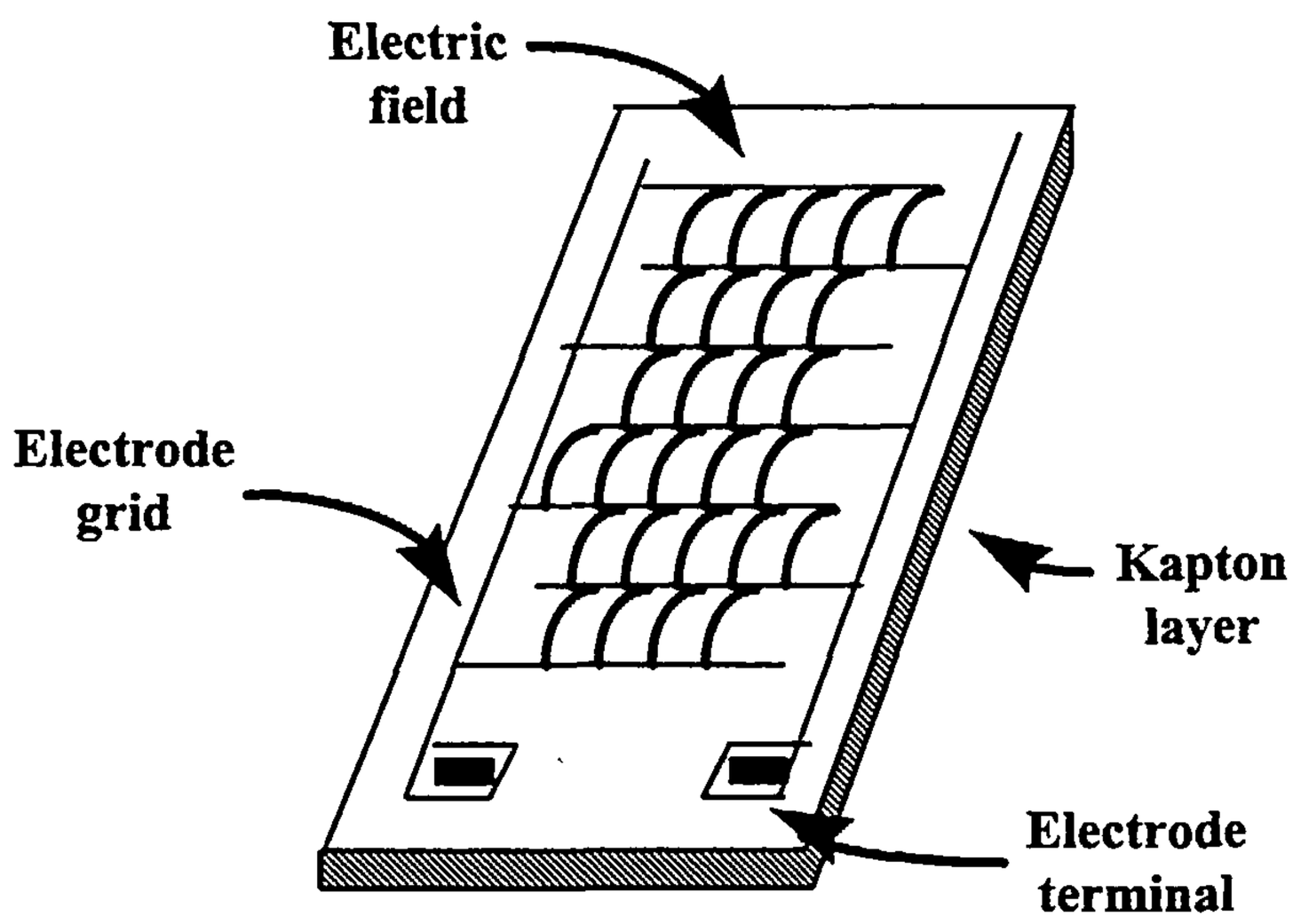

Figure 3.7 *Schematic representation of the Dek-Dyne interdigitated electrode*

All experiments were made under isothermal conditions at temperatures of 130, 140, 150 and 160 °C. A specially designed furnace consisting of a hollow copper tube was used, controlled by a EUROTHERM temperature controller. The heating elements were placed around the copper tube to enable better heat transfer conditions. A control thermocouple was placed in a hole on the side walls of the copper tube. The final temperature control achieved by this configuration was excellent with the applied temperature varying about ± 1 °C in the isothermal stage.

The comb electrodes were connected to the dielectric apparatus via shielded cables. At one end, the connecting cables were soldered onto the electrode terminals, whereas at the other end, they were plugged in the potentiostat through the appropriate co-axial fittings.

The complete experimental procedure, from the beginning to the end of each experiment was as follows:

- Setup of the experimental parameters that had to be transmitted to the FRA and to the potentiostat via the 'in-house' produced software;
- Setup of the temperature controller to the experimental temperature;
- Pre-heating of the measuring cell (test tube) at the experimental temperature;
- Pouring of the resin into the pre-heated test tube;
- Immersion of the sensor into the resin with the sensing side facing the inner side of the test tube;
- Immersion of the test tube into the hollow copper tube and shielding of the furnace to prevent heat losses;
- Equilibrium at the experimental temperature for 2 - 3 minutes;
- Start of the experiment via the software and collection of the dielectric response at predetermined time intervals throughout the cure;
- Stop of the experiment and storage of the data when no further change in the dielectric response observed.

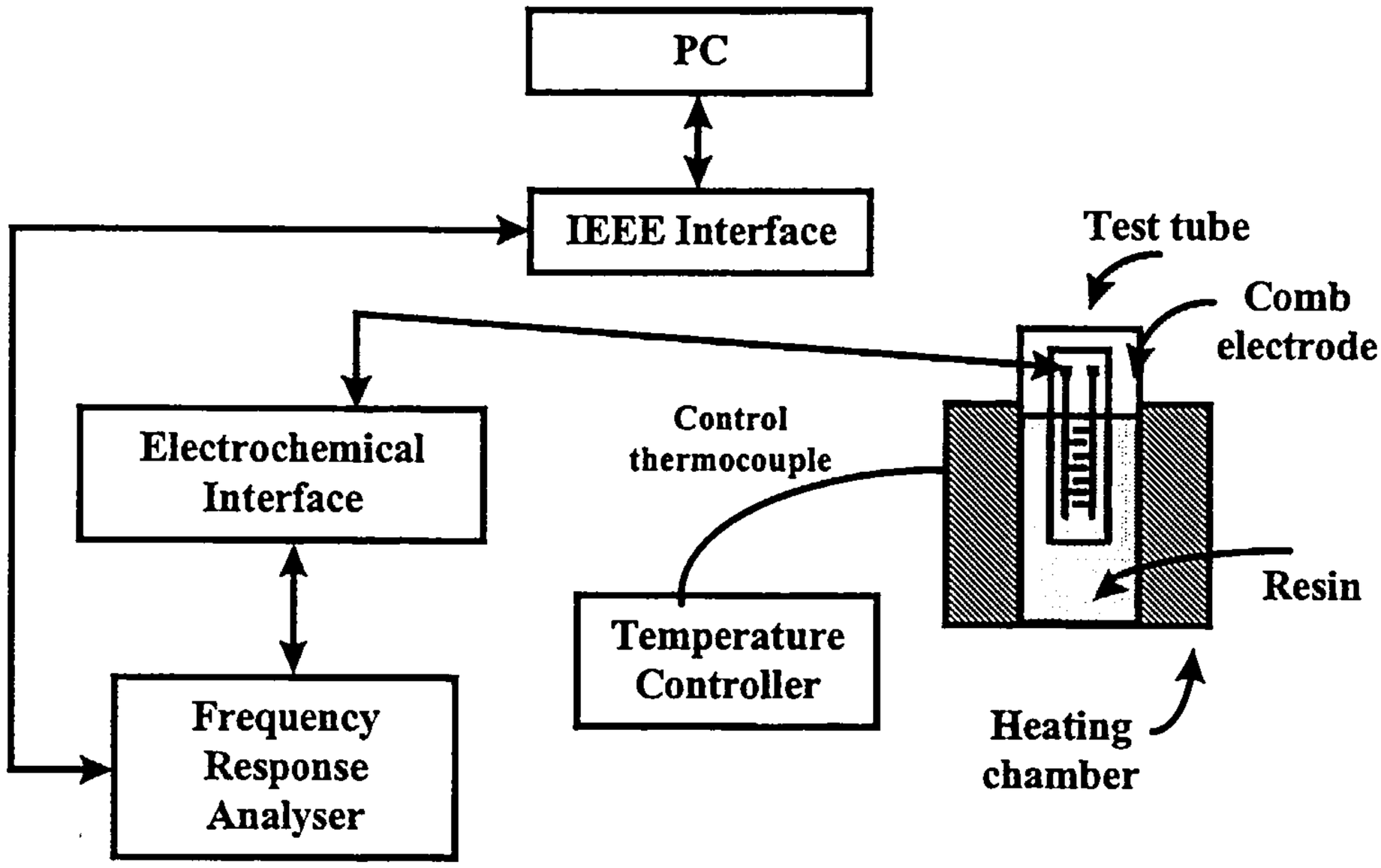

Figure 3.8 *Schematic representation of the experimental setup used for the dielectric measurements*

A schematic representation of the complete experimental setup is shown in Figure 3.8. The design of the Dek-Dyne sensor has the disadvantage that the electric field is not well defined. The two-terminal configuration of the sensor does not allow for correction of the electric field as it is usually achieved by the use of a three-terminal cell, where the third terminal (guard ring) fixes the geometry of the produced field. This necessitates the use of calibration for determining the permittivity and the dielectric loss of the material. The following empirical formulae were given by the manufacturer of the sensors for the calibration and allowed for the end effects due to the two-terminal nature of the cell:

$$\varepsilon' = 3.93\frac{C_s}{C_0} - 2.93$$

$$\varepsilon'' = 3.93\frac{G_s}{2\pi f C_0} \qquad \text{(Eq. 3.5)}$$

In the above expressions, C_s and G_s are the sample capacitance in F and the sample conductance in S respectively, C_0 is the free air capacitance in F and f is the test frequency in Hz.

Prior to each experiment, measurement of the free air capacitance was made, in order to be used in the calculation of the permittivity and the dielectric loss of the material. For this reason, the same experimental parameters used for the curing of the resins were also used in the air capacitance measurements.

All the experimental results along with an analytical discussion will be presented in the Chapter 8.

Chapter Four

4. Cure Kinetics Modelling

4.1 Introduction

In this chapter results of measurements obtained from DSC and Infra-red spectroscopy are presented. The formation of the three-dimensional network during the cure of the epoxy-amine system and the transformations that occur (liquid-to-rubber-to-glass transitions) are phenomena that are controlled and influenced by the reaction kinetics of the curing system. In the following sections the results from the above two monitoring techniques are compared to each other and are used to construct mathematical models that follow the reaction kinetics throughout the cure cycle. Subsequently, gelation and vitrification points will be evaluated and their dependence upon the reaction kinetics of the epoxy-amine systems used will be investigated.

4.2 Preliminary Remarks on the Experimental Results

At first, the total heat of reaction, ΔH_T, was evaluated for all the epoxy-amine systems used in this study. Dynamic DSC runs were conducted at constant heating rates and ΔH_T was evaluated as discussed in Section 3.2.1.1. To check if the reaction mechanism changes with the heating rate used, the dynamic runs were repeated at six different heating rates for each resin system used. The results for all the resins at heating rates 2, 5, 7.5, 10, 15 and 20 °C/min are shown in Table 4.1.

It is evident from these results that the total heat of reaction remains constant for all resin systems in the range of heating rates used. This observation might suggest that the reaction mechanism remains constant at constant heating rates in the range between 2 and 20 °C/min. In the following sections, an average value of the total heat of reaction will be used for each resin system. These average values are given in Table 4.1.

Table 4.1 *Total heats of reaction of all resin systems at different heating rates.*

Resin System	**Heating Rate (°C/min)**						**Average ΔH_T (J/g)**
	2	*5*	*7.5*	*10*	*15*	*20*	
	Total Heat of Reaction ΔH_T (J/g)						
RTM6	432	437	440	431	437	438	436
RMO	478	473	480	477	495	476	*480*
RMO2	443	451	452	446	456	454	*450*
F934	450	447	449	452	449	452	*450*

The evolution of the fractional degree of cure, α, of all resin systems with temperature under dynamic cure at constant heating rates was calculated using the method described in Section 3.2.1.1, with the assumption that the material is fully cured after the end of the dynamic run. The calculated results are shown in Figure 4.1 - Figure 4.4 for all resin systems. As can be seen from these figures, curing of the resin at low heating rates has as a result a drop of the onset of the reaction to lower temperatures. A similar effect is observed throughout the cure for all the resin systems; at a specific temperature, the degree of cure is higher at lower heating rates. A simple explanation can be given for this trend. Two phenomena take place during dynamic cure: a) appearance of increasing temperature lags between the temperature of the material and the instrument temperature with increasing heating rates and b) higher heat evolution for higher heating rates.

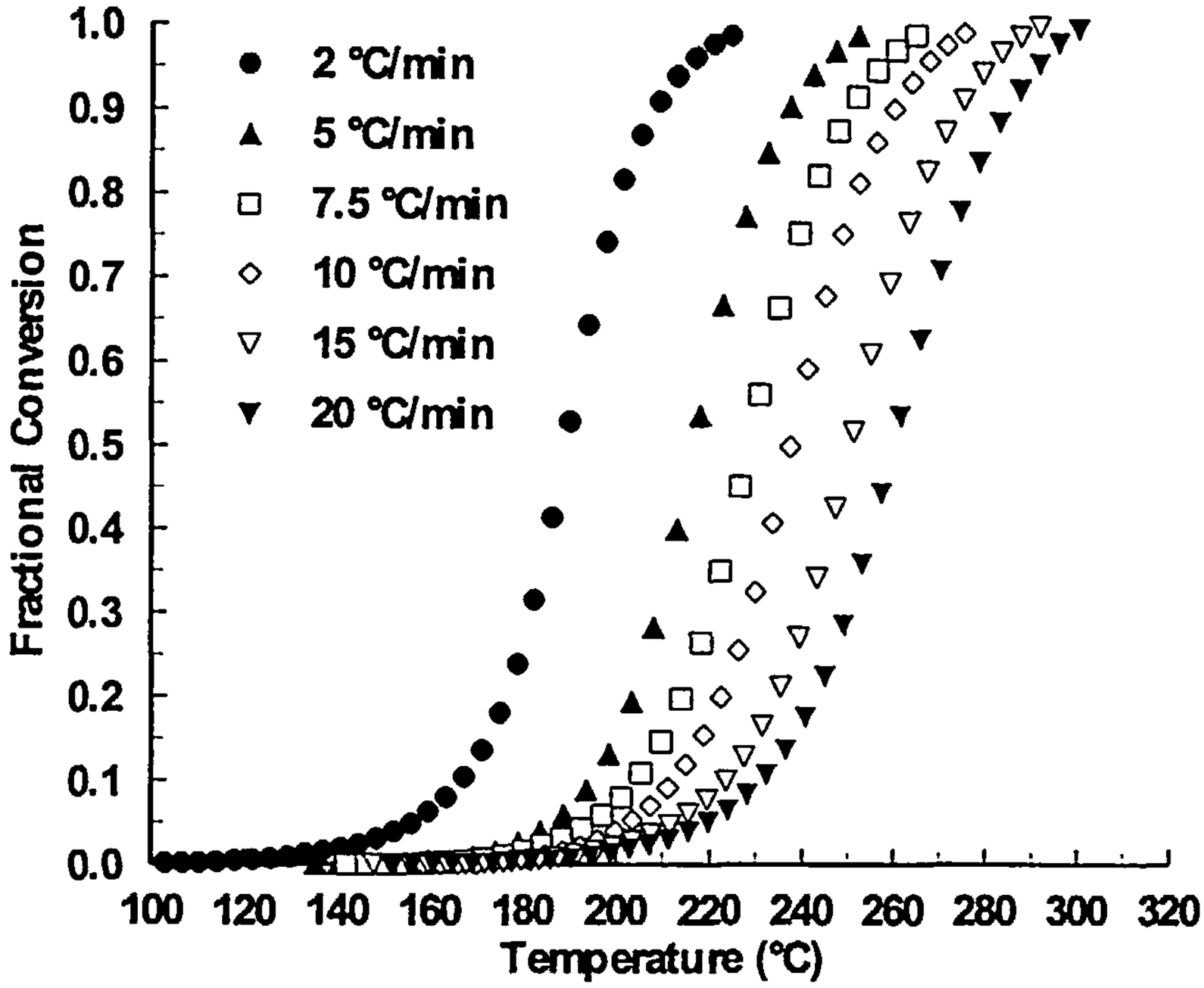

Figure 4.1 *Evolution of fractional conversion with temperature during dynamic cure of RTM6 resin at constant heating rates. Experimental results from DSC scans*

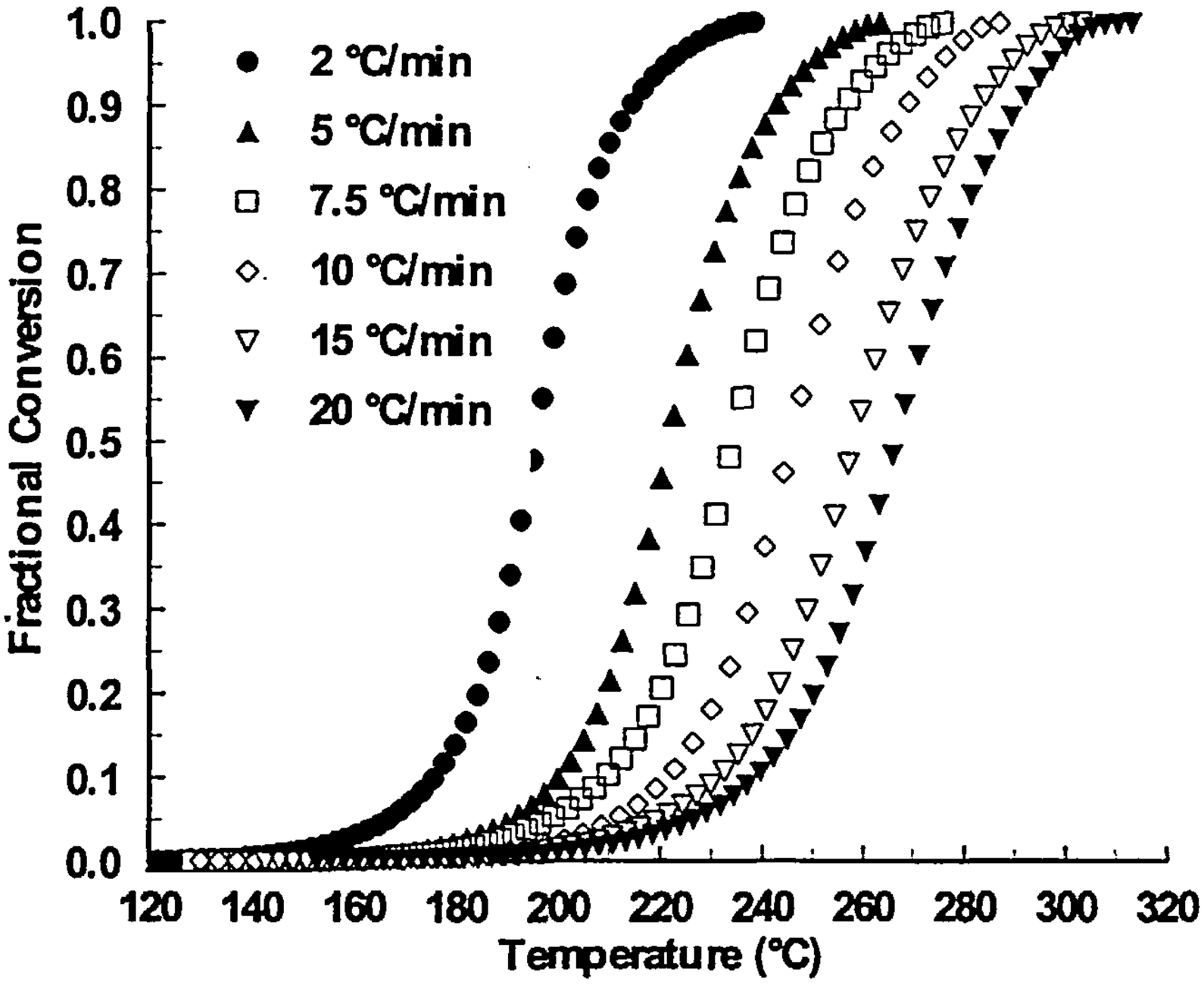

Figure 4.2 *Evolution of fractional conversion with temperature during dynamic cure of RMO resin at constant heating rates. Experimental results from DSC scans*

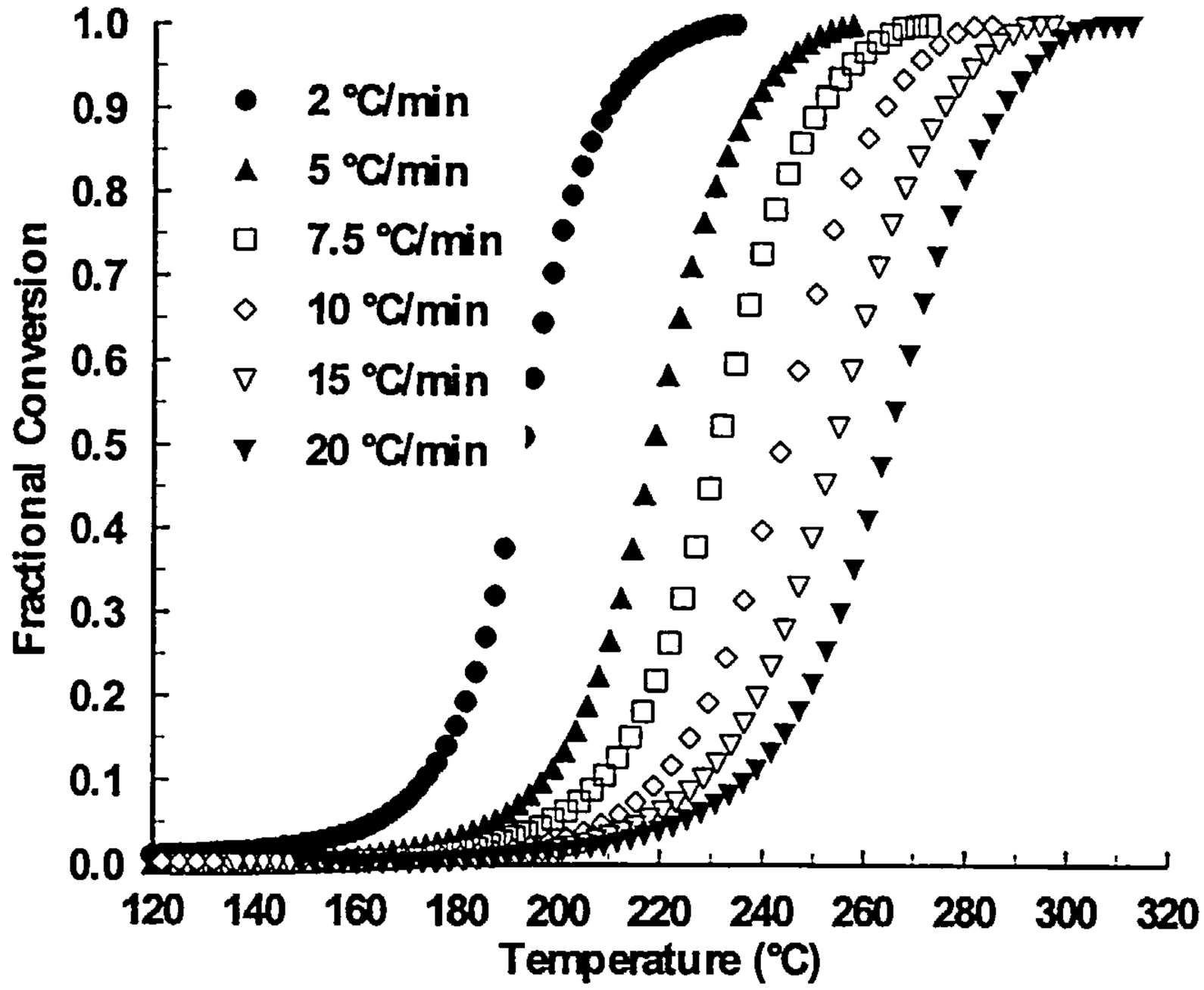

Figure 4.3 *Evolution of fractional conversion with temperature during dynamic cure of RMO2 resin at constant heating rates. Experimental results from DSC scans*

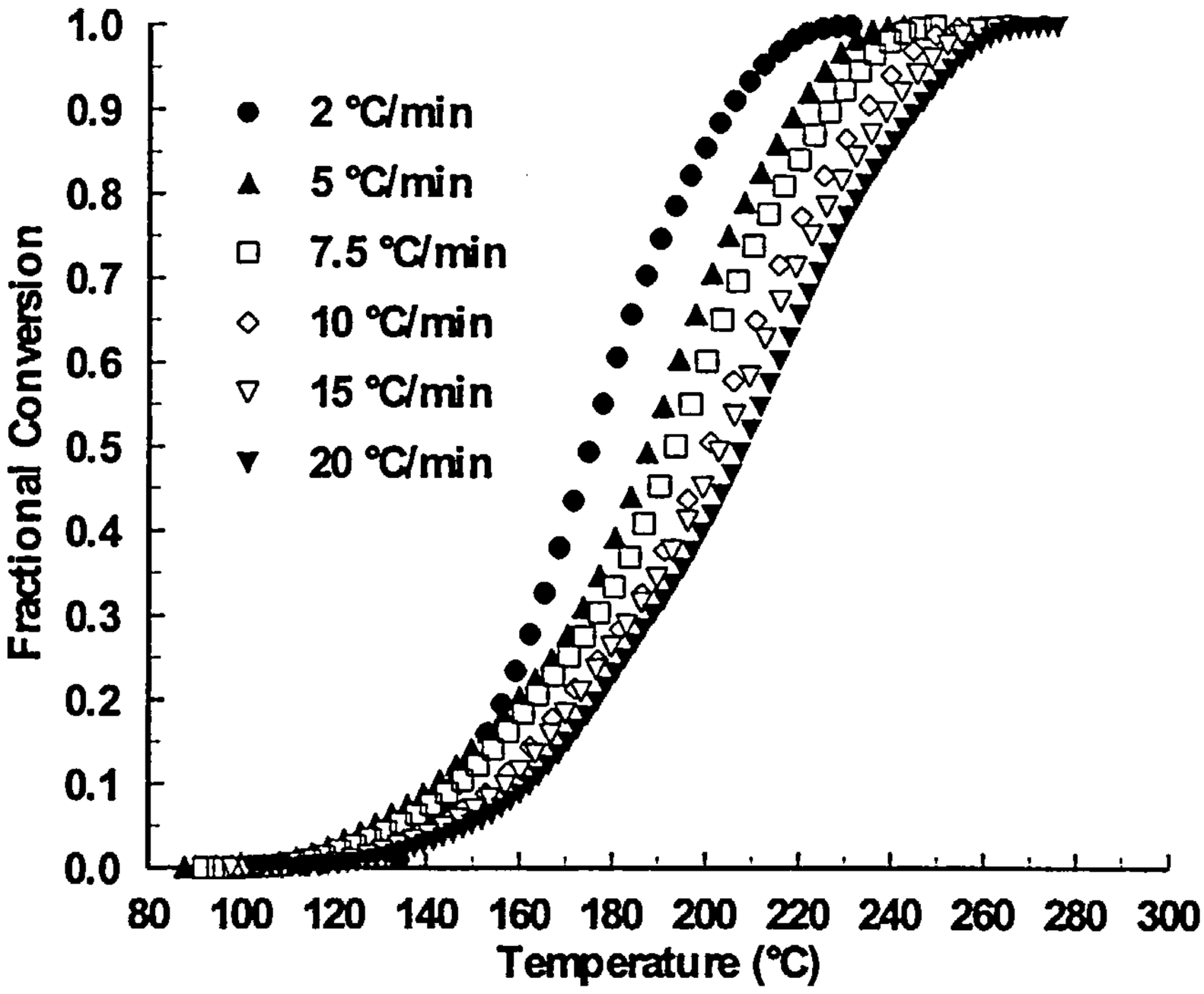

Figure 4.4 *Evolution of fractional conversion with temperature during dynamic cure of 934 resin at constant heating rates. Experimental results from DSC scans*

The first phenomenon is a consequence of heat transfer limitations within the test material and indicates that at slow heating rates the material can respond almost instantaneously to any temperature variations, reaches temperature equilibrium faster and as a result starts to react at apparently lower temperatures.

The second phenomenon is a result of the amount of external energy that is supplied to the reacting system. Fast heating rates impose high energy level inputs to the material, that are translated into large heat evolution from the curing resin. This phenomenon can be observed in Figure 4.5. In this figure, heat evolution normalised by the sample weight is plotted against temperature for RMO resin cured at two constant heating rates, 5 and 20 °C/min. It is evident that curing at 20 °C/min results in the release of larger amounts of heat than the 5 °C/min cure.

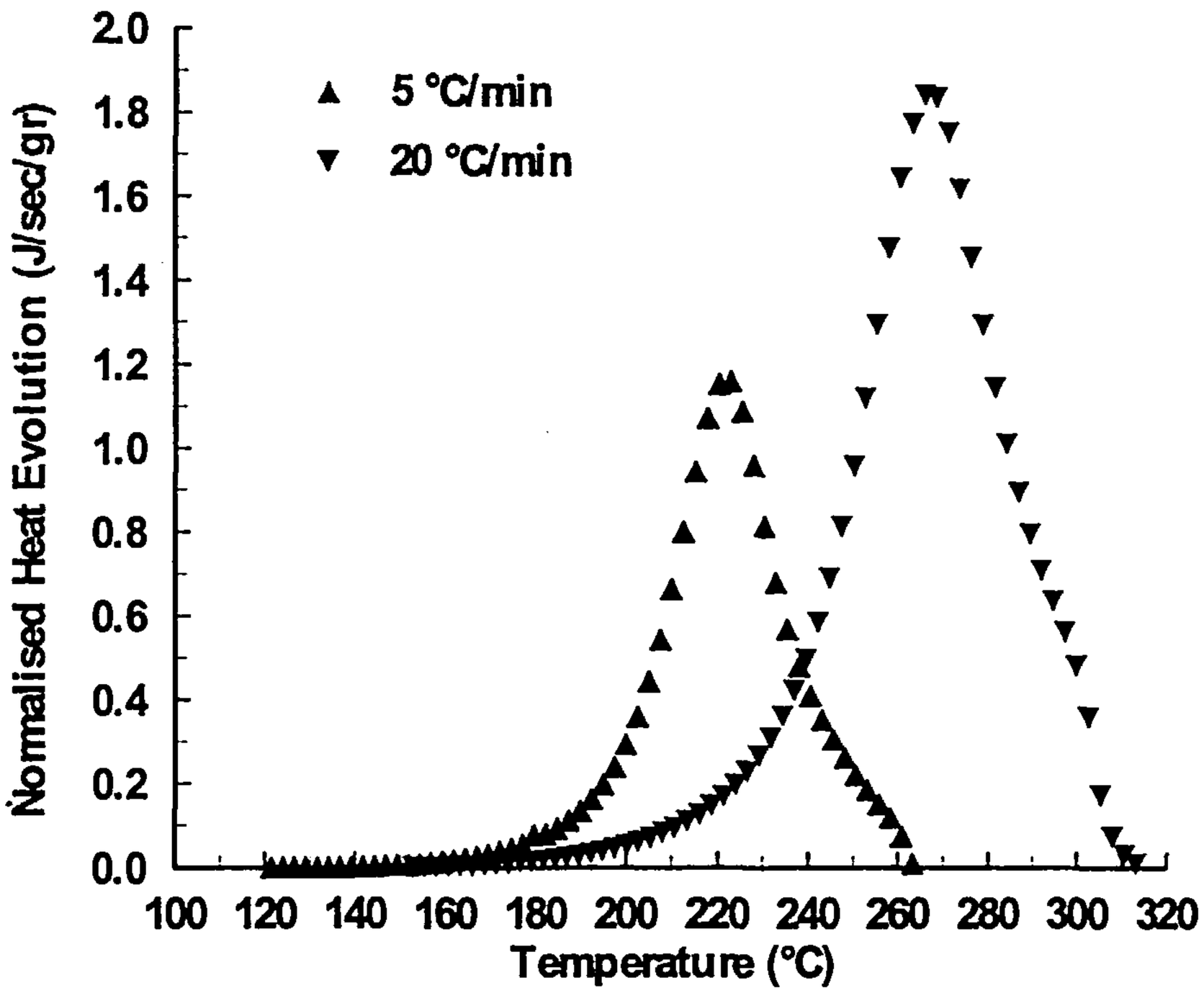

Figure 4.5 *Normalised heat evolution of RMO resin as a function of temperature for dynamic cure at constant heating rates. Experimental results from DSC scans*

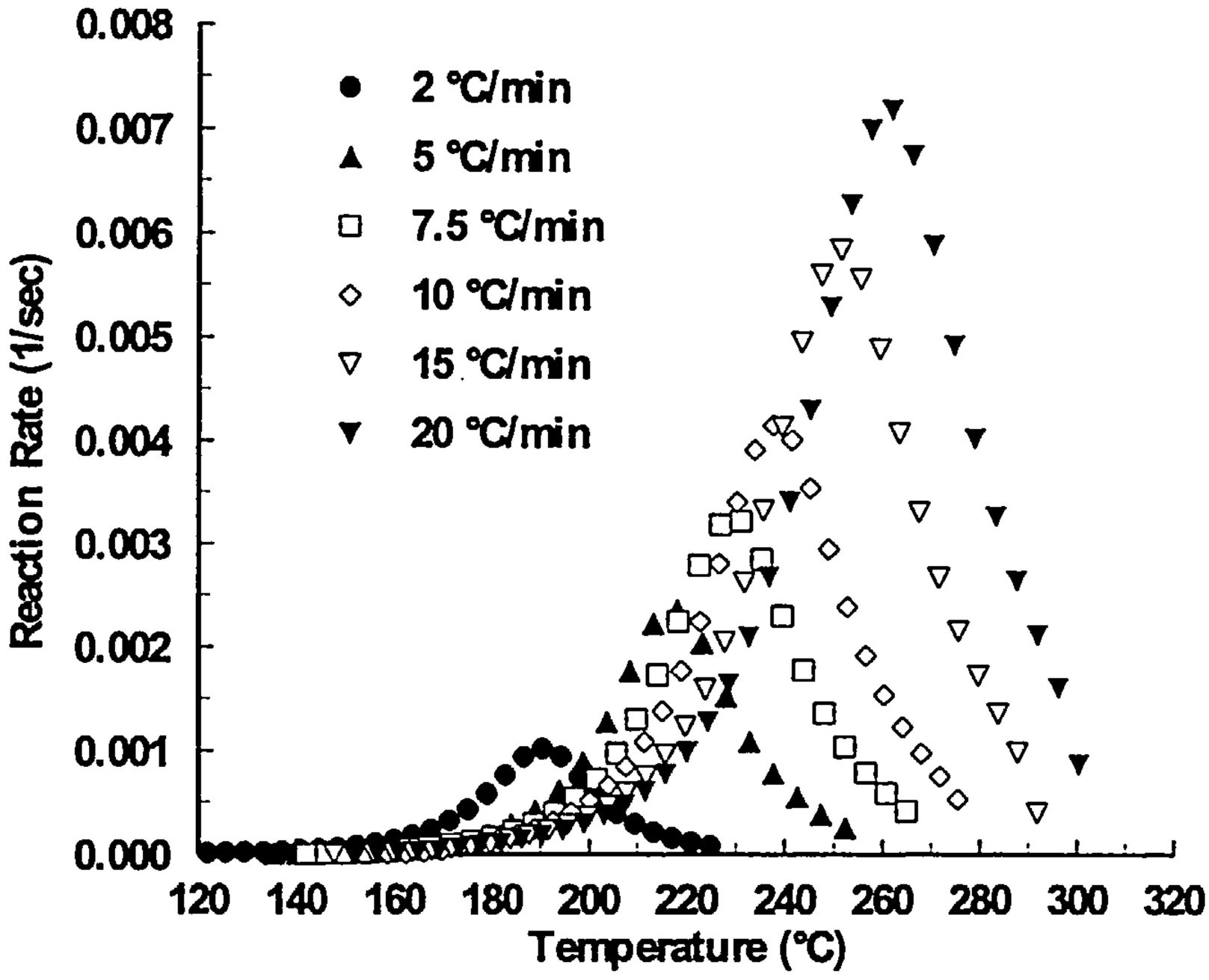

Figure 4.6 *Evolution of reaction rate with temperature during dynamic cure of RTM6 resin at constant heating rates. Experimental results from DSC scans*

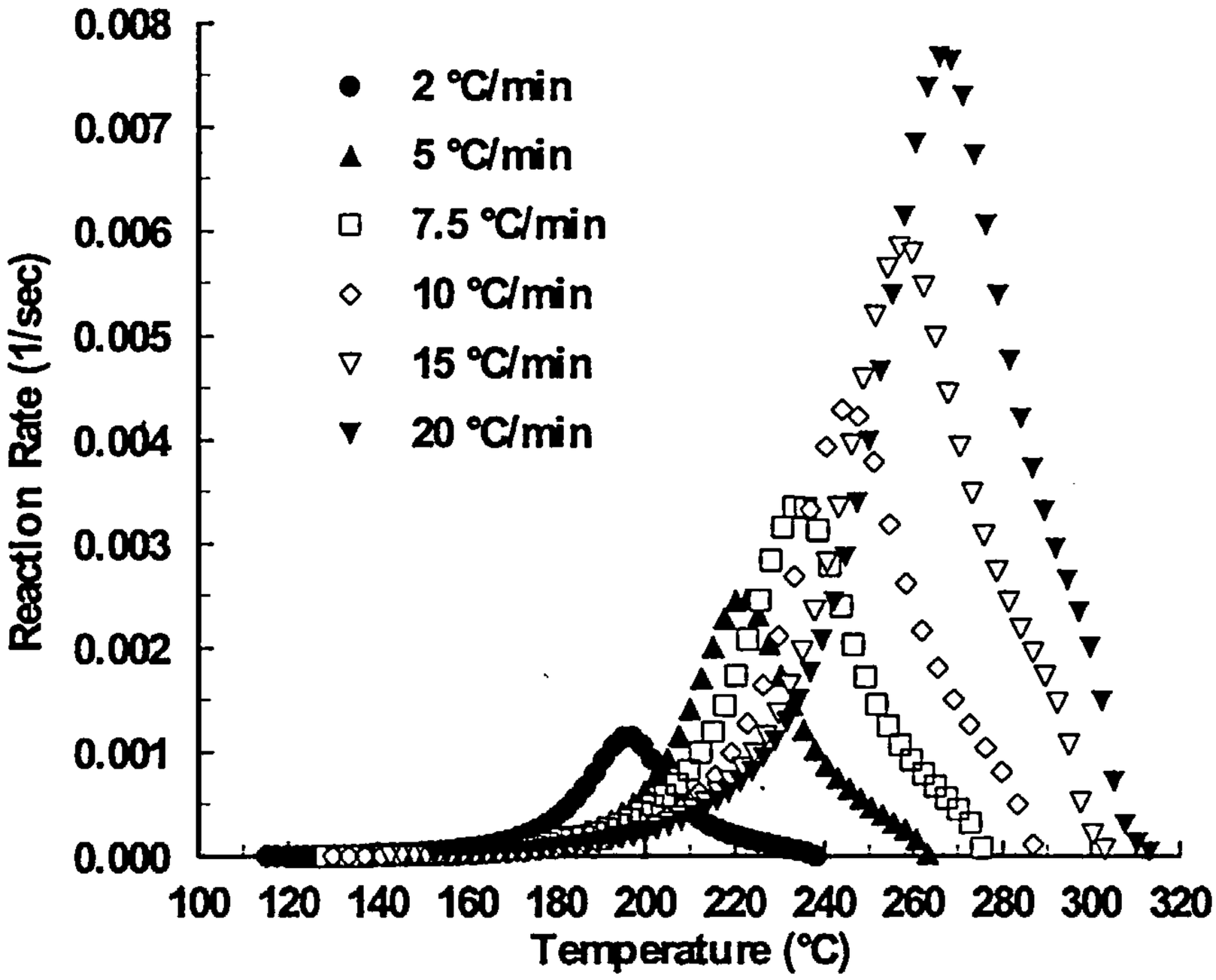

Figure 4.7 *Evolution of reaction rate with temperature during dynamic cure of RMO resin at constant heating rates. Experimental results from DSC scans*

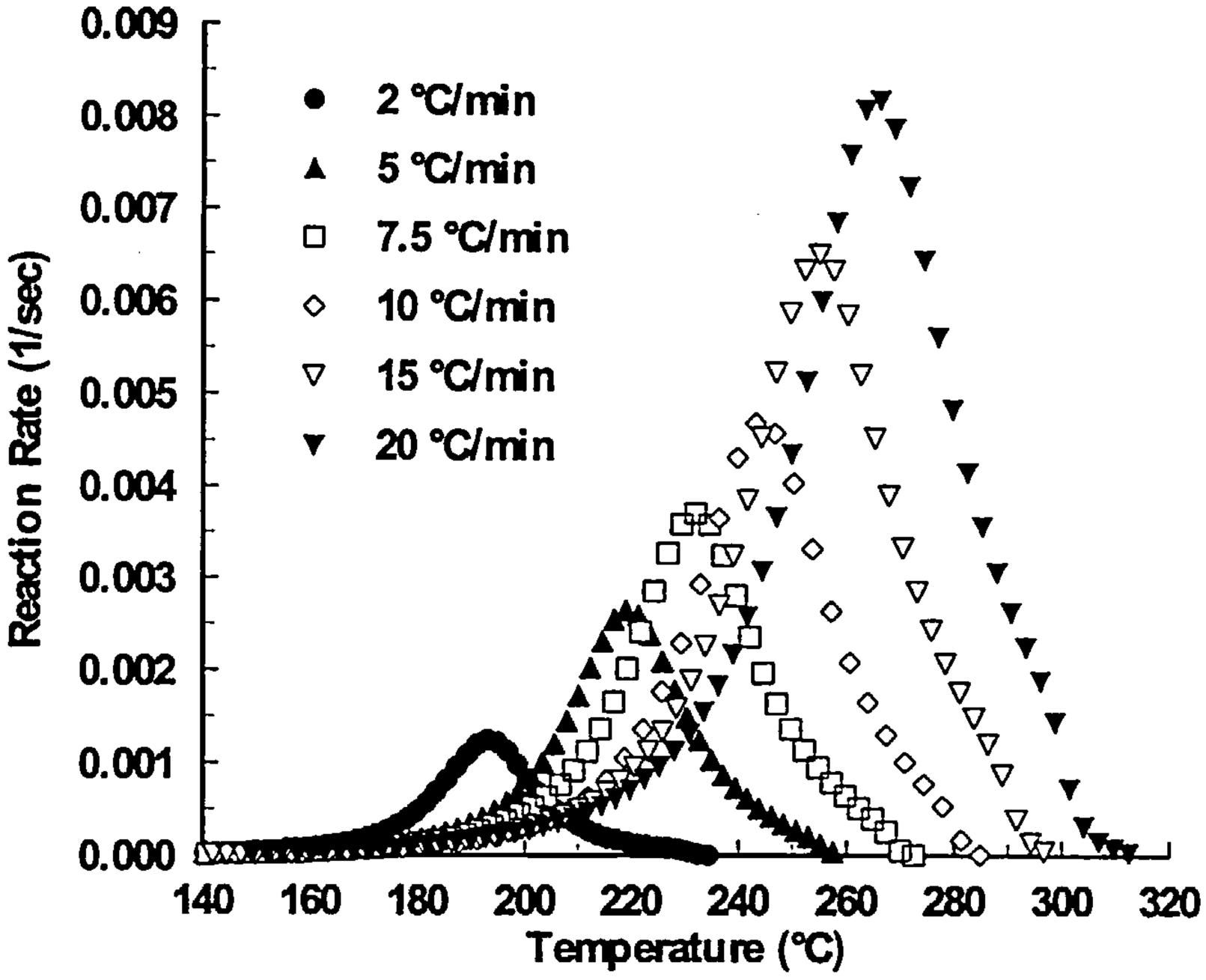

Figure 4.8 *Evolution of reaction rate with temperature during dynamic cure of RMO2 resin at constant heating rates. Experimental results from DSC scans*

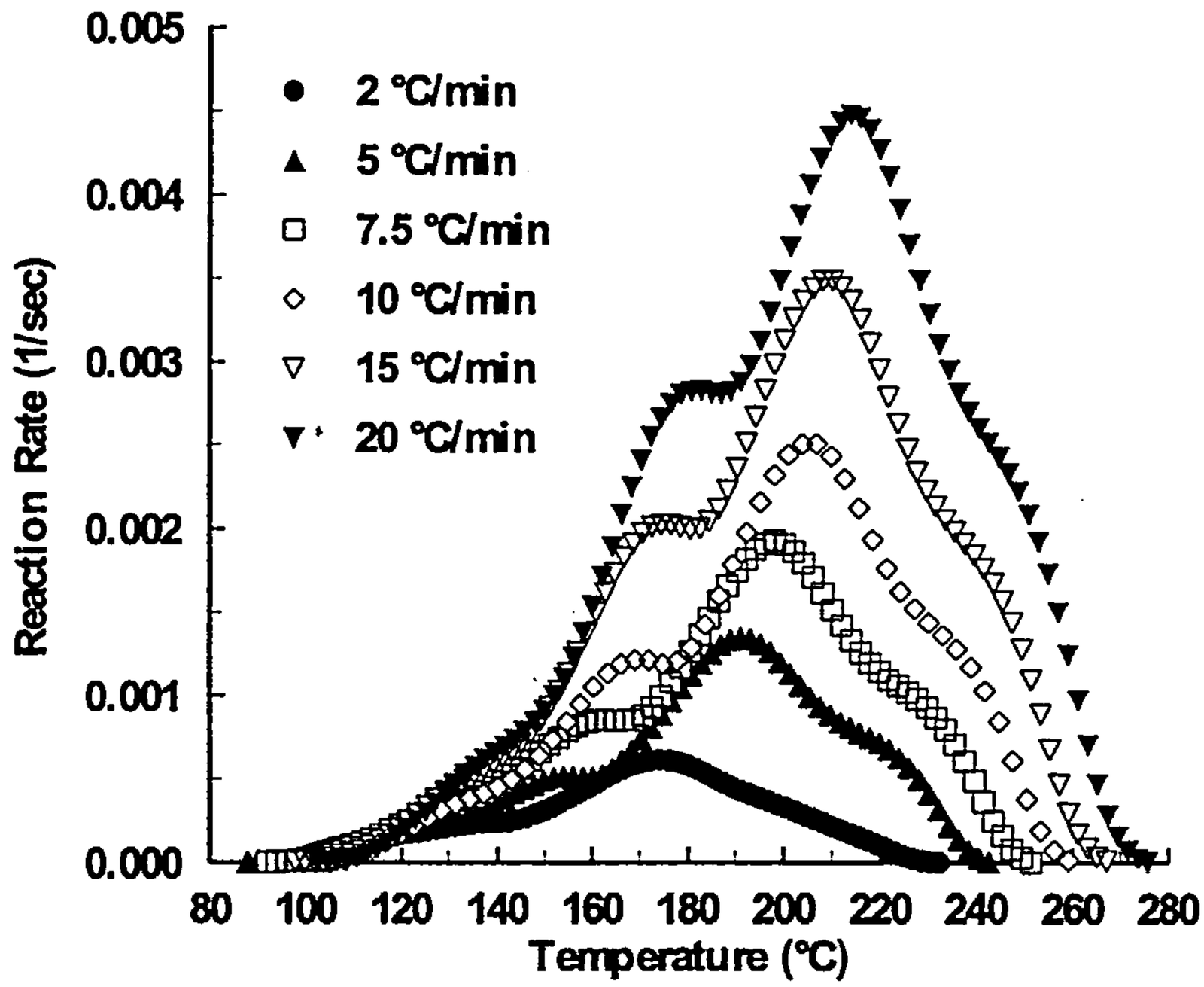

Figure 4.9 *Evolution of reaction rate with temperature during dynamic cure of 934 resin at constant heating rates. Experimental results from DSC scans*

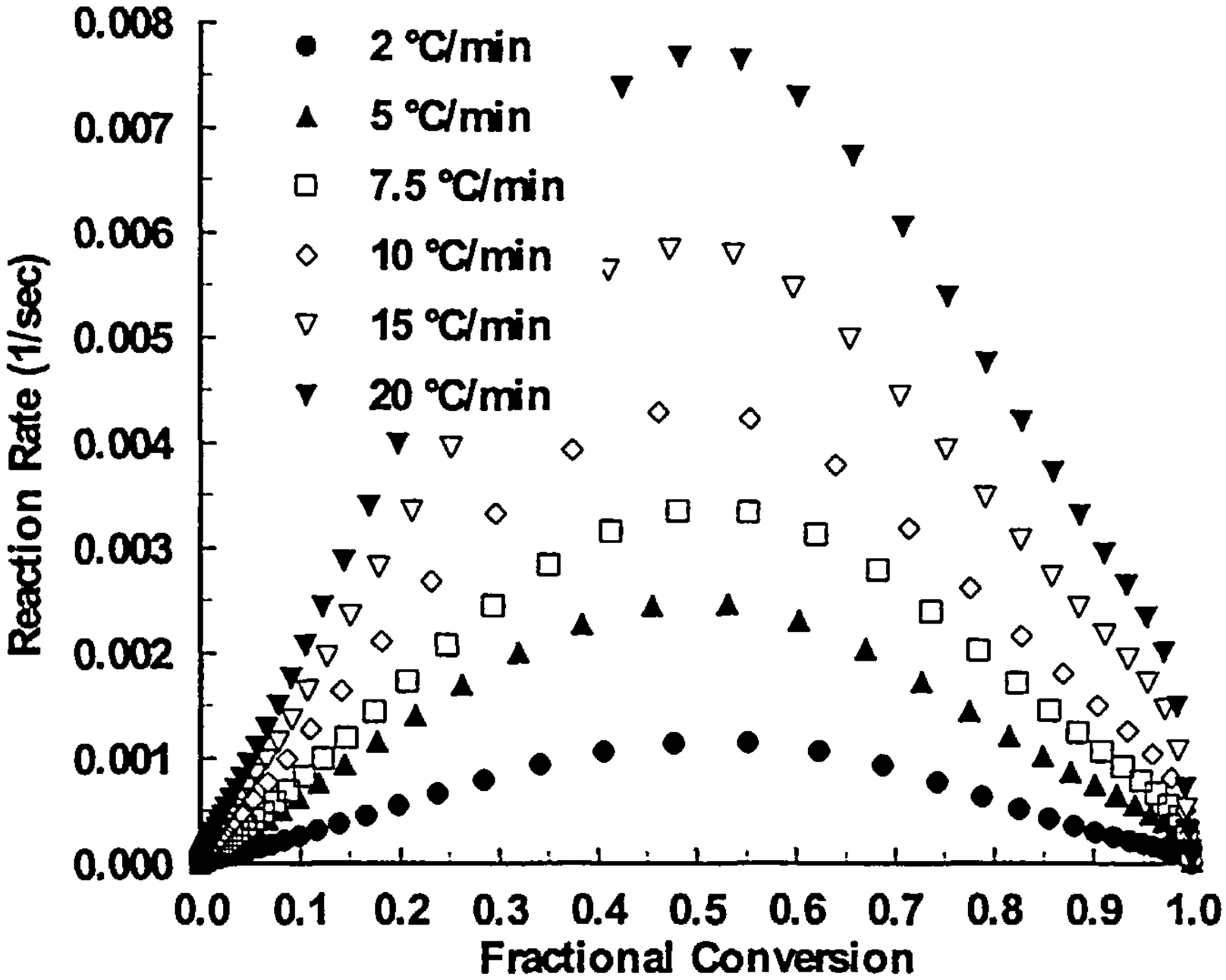

Figure 4.10 *Reaction rate as a function of fractional conversion for dynamic cure of RMO resin system at different heating rates. Experimental results from DSC scans*

Figure 4.6 - Figure 4.9, show the reaction rates versus cure temperature for all the resin systems, cured at constant heating rates. Calculation of reaction rates was done according to the method given in Section 3.2.1.1 for the dynamic case. The higher reaction rates achieved with the fast heating rates are evident, implying that the reaction progresses faster at quick heat up.

More information can be extracted if we consider the reaction rate as a function of the degree of cure. In Figure 4.10 the reaction rate is plotted as a function of the degree of cure for the RMO resin system for all the heating rates used. At a specific conversion the reaction rate is higher for higher heating rates and reaches a maximum value at a fixed conversion for all heating rates. This last observation indicates that the reaction mechanism remains the same for all heating rates. In order to check the validity of this statement, the reaction rates, normalised by the maximum reaction rate attained at each heating rate, are plotted as a function of the degree of cure for the same resin system.

The plots are shown in Figure 4.11. It is evident from this figure that all plots fall into a master curve up to around 60% conversion where higher heating rates start to deviate upwards slightly, showing higher reaction rates. This master curve provides strong evidence that the reaction mechanism does not change significantly with different heating rates.

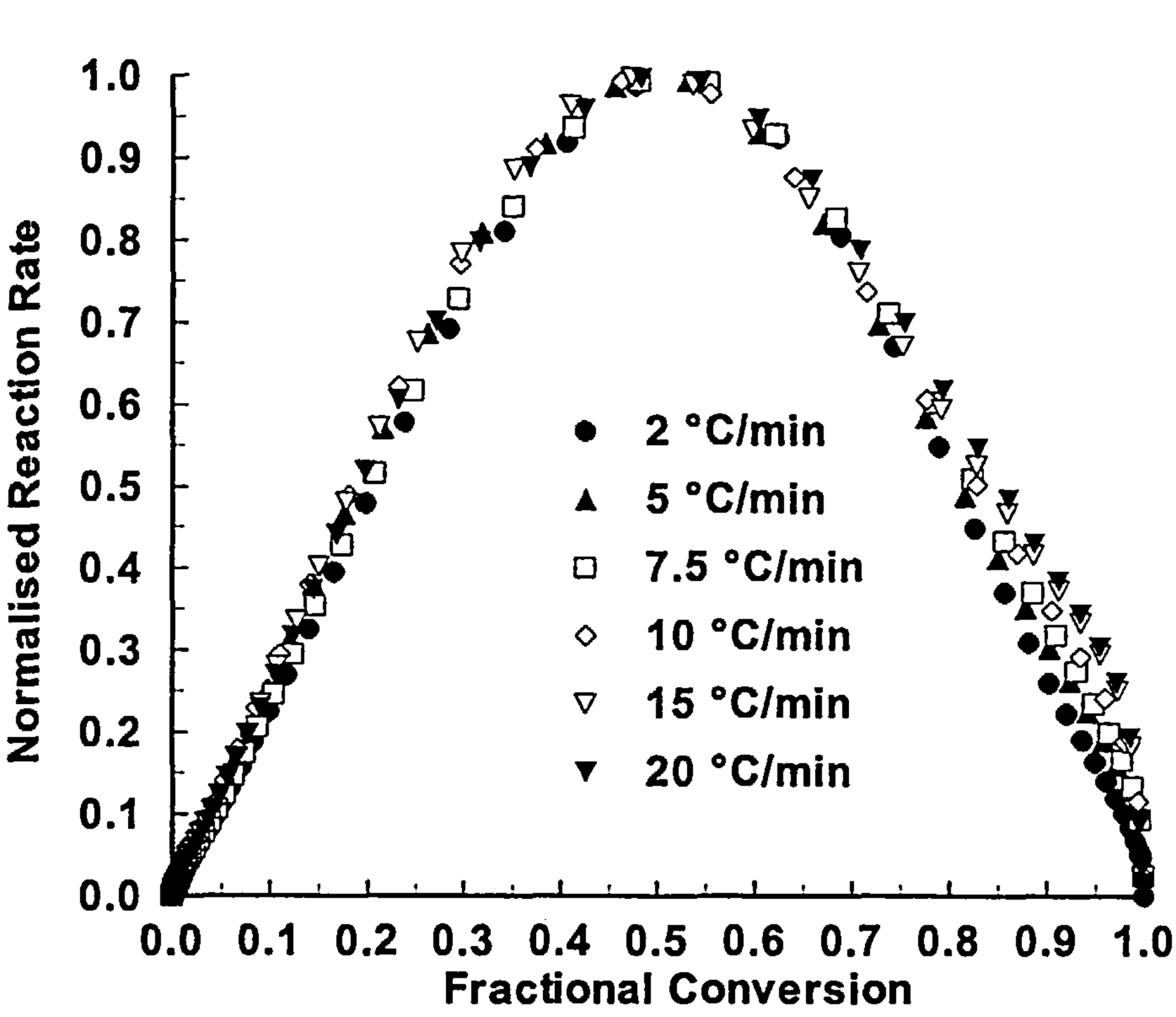

Figure 4.11 *Reaction rate normalised by the maximum reaction rate as a function of fractional conversion for the RMO resin system, for dynamic cure at different heating rates. Experimental results from DSC scans*

The same trend is followed for all the resin systems apart from the 934 resin. In Figure 4.12 the reaction rates are plotted as a function of temperature for this system. A constant reaction rate is observed for all heating rates in a conversion window of about 10% in the low conversion area. The conversion range for which this plateau is observed falls down to lower conversions for slower heating rates, an indication that the heating rate does affect the reaction mechanism for this particular resin system. A more detailed analysis for the reaction mechanism during the cure of this resin system

will be given in Section 4.4.4.

Apart from the experiments for the dynamic cure of all the resin systems, the same resins were also cured isothermally over a range of temperatures in order to obtain the cure profile under isothermal conditions. Currently, there are two methods to follow the advancement of the reaction isothermally by a DSC: a) direct isothermal experiments and integration of the thermogram to calculate conversions throughout the cure and b) experiments to obtain the residual heat of reaction at specific time intervals at each temperature. The experimentation and the way the results are obtained were described in Sections 3.2.1.2 and 3.2.1.3.

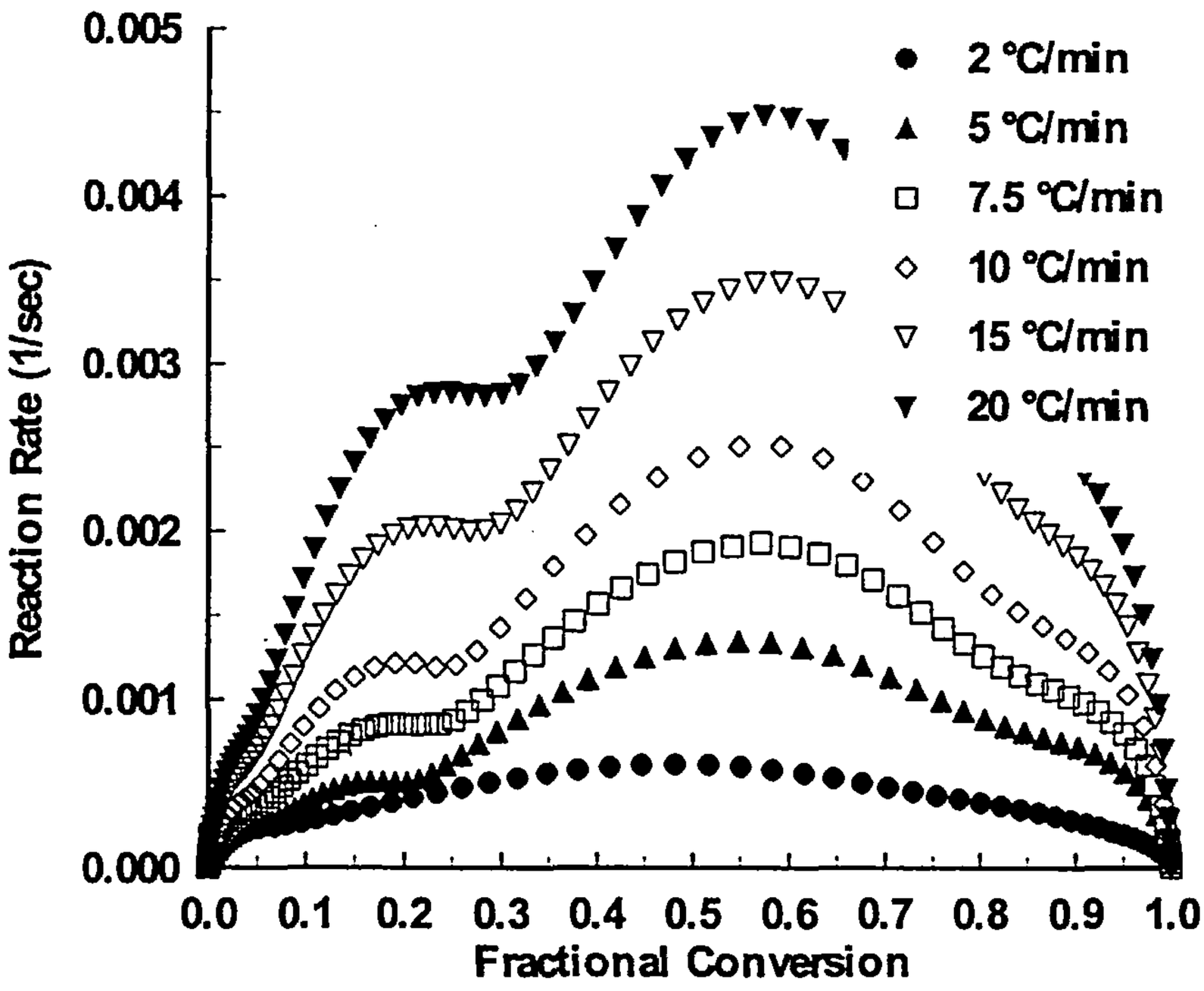

Figure 4.12 *Reaction rate as a function of fractional conversion for dynamic cure of 934 resin system at different heating rates. Experimental results from DSC scans*

Before any results are presented, a comparison between these two methods will be made in order to identify the advantages and disadvantages of each method. For this purpose, results from both methods obtained on the RTM6 resin system will be presented.

The reaction rates for the isothermal cure of RTM6 resin at 140°C and 160°C as a function of time are shown in Figure 4.13.

Reaction rates were calculated according to the method described in Section 3.2.1.2 for the isothermal case. Apart from the expected faster cure of the resin at the higher temperature of 160°C in respect to the cure at 140°C, another interesting aspect of the isothermal cure of this resin is the autocatalytic behaviour that it shows (increasing reaction rate as cure progresses). Since this resin is an epoxy - amine system, the cure reaction is expected to be autocatalytic, catalysed by the hydroxyl groups produced from the epoxy - amine addition reaction, especially early in the cure. Details of this mechanism can be found in Section 2.2.2. In order to verify if the curing reaction had fully progressed for both temperatures, the degree of cure was calculated according to the method described in Section 3.2.1.2. The results are shown in Figure 4.14 as plots of fractional conversion against cure time.

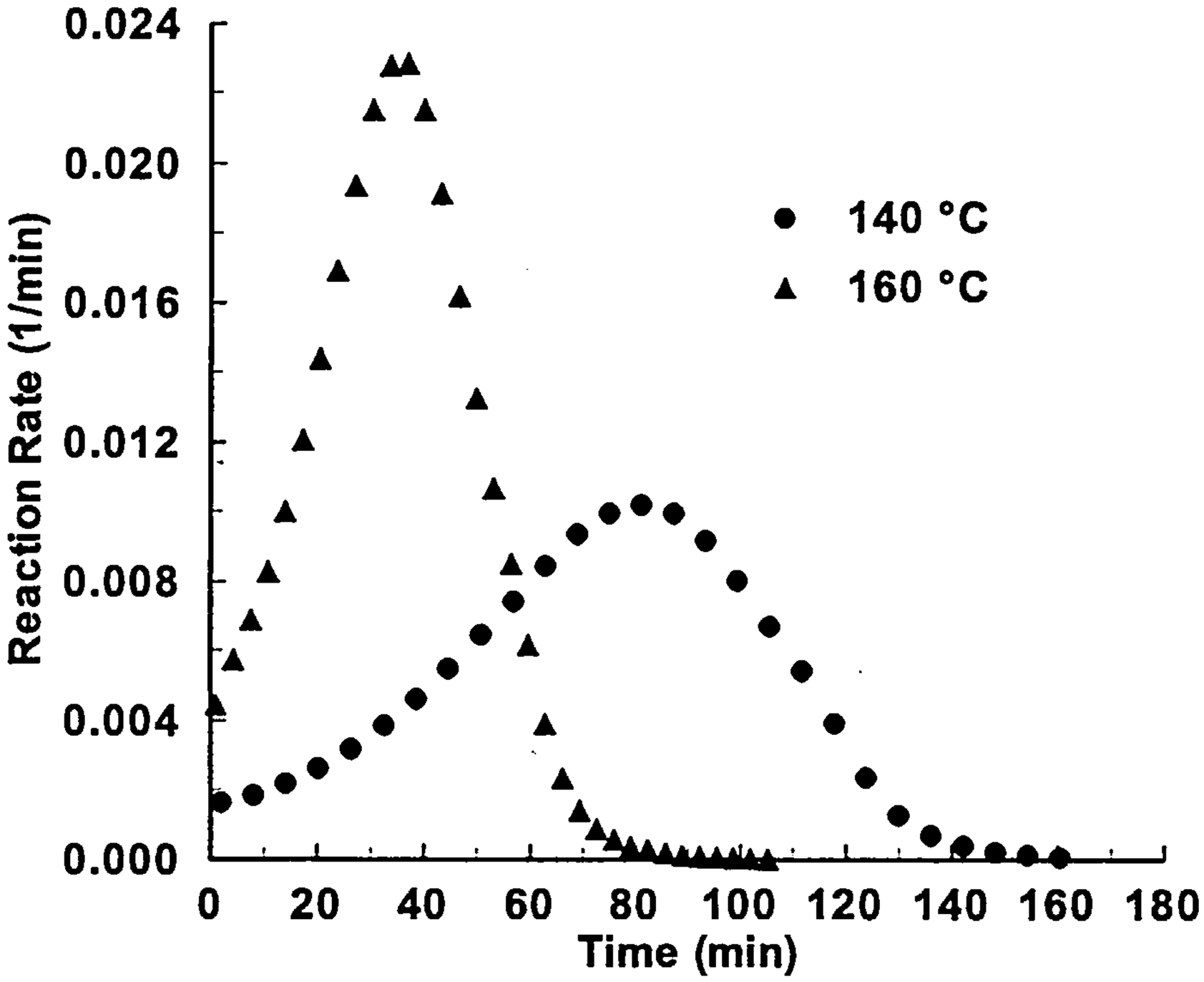

Figure 4.13 *Reaction rate as a function of time for an isothermal cure of RTM6 resin at 140 °C and 160°C. Experimental results from isothermal DSC scans*

As can be seen from these plots, the reaction stops before full conversion has been achieved, (around 90% for the 160°C cure and 80% for the 140°C), probably hindered because of structural limitations. As was discussed in Section 2.3, isothermal cure of thermosets leads to incomplete reaction as diffusion processes take control during the construction of the three dimensional network. At this point no further explanation will be given on the issue of whether and when diffusion starts. A detailed analysis will be given in the following sections in which the kinetic models are constructed (see Sections 4.4.1, 4.4.3 and 4.4.4).

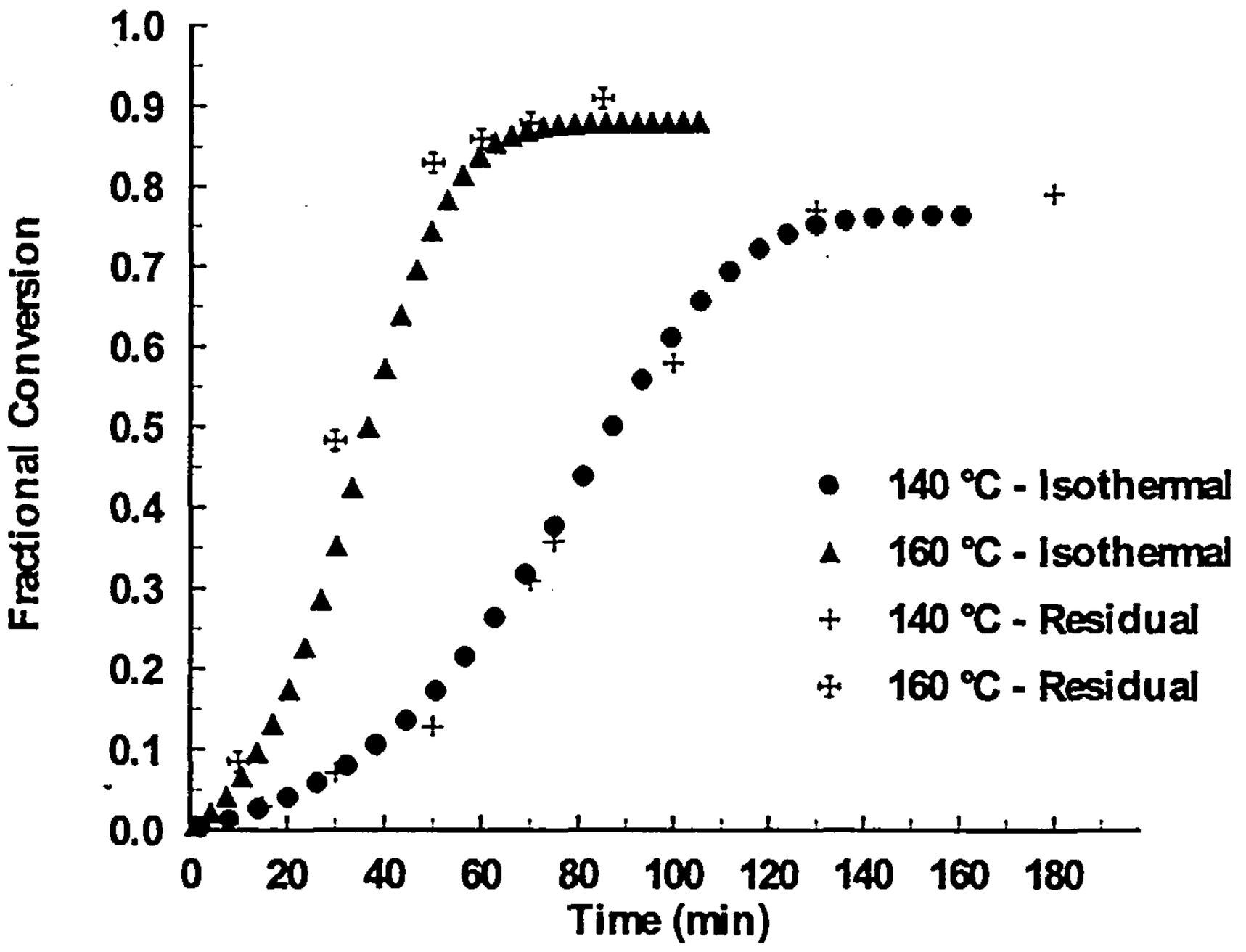

Figure 4.14 *Fractional conversion as a function of time for an isothermal cure of RTM6 resin at 140 °C and 160°C. Experimental results from isothermal and residual heat of reaction DSC scans*

As was mentioned earlier, the degree of cure was also calculated by the method of residual heat of reaction of partially isothermally cured samples. The results for the RTM6 resin system for temperatures 140°C and 160°C are shown in Figure 4.14 as plots of fractional conversion against cure time. Results from isothermal experiments

for the same resin system and temperatures are also plotted in the same figure for comparison.

As can be seen from this figure, the correlation is very good for the cure at 140°C but there is a small deviation for the 160°C cure. In order to determine which of these two methods gives the more accurate results, another technique had to be used, that could give the degree of cure independently of the DSC experiments. The technique that was chosen for this correlation was Infra-red spectroscopy.

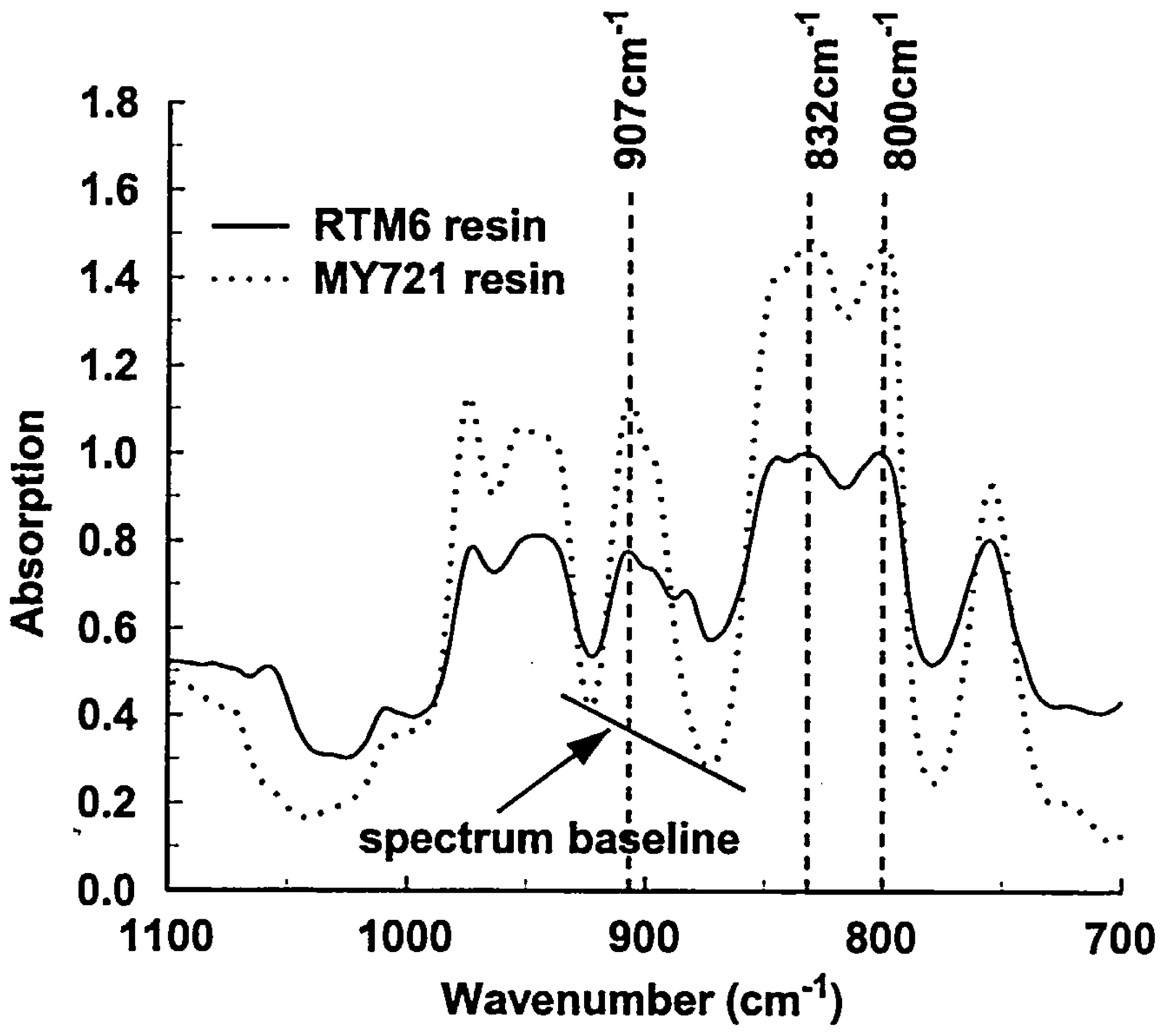

Figure 4.15 *Absorption spectra for RTM6 and MY721 resin*

As indicated in Section 2.6.3, Infra-red spectroscopy provides a very good insight into the curing reaction since it can follow the concentrations of all the reactive species throughout the cure. For the purpose of correlating the degree of cure by DSC and Infra-red experiments the reactive groups that had to be monitored were the epoxy groups. In the mid-infrared region, the epoxy groups absorb radiation at more than one

wavelength. In cases were quantitative measurements have to be performed, like our case, one should choose a wavelength that gives a distinctive absorption peak with an easily measured height.

In Figure 4.15, the absorption spectrum of RTM6 resin is given for wavenumbers from 1100cm^{-1} to 700cm^{-1} at room temperature. For reasons of comparison the spectrum of the pure tetrafunctional epoxy resin MY721 can be seen in the same figure at the same wavenumbers. The literature contains several reports assigning characteristic absorption peaks to the epoxide group in small molecules. The most common absorption peaks in the wavenumber range of Figure 4.15 are those appearing at 907cm^{-1} and 832cm^{-1} [143]. As can be seen from this figure, the epoxy ring absorption at these wavenumbers gives well resolved peaks in both the pure epoxy resin MY721 and the RTM6 resin, that can be used for quantitative analysis. To eliminate baseline changes between the spectra, the epoxy ring absorption peaks have to be normalised in respect to a reference peak that is in the vicinity of them and does not change in intensity. The absorption peak at 800cm^{-1}, that refers to the aromatic C-H bend, was chosen for that purpose.

For quantitative analysis of these peaks, the formula given by Eq. 4.1 was used. In this expression, E_i and R_i are the peak heights of the epoxy ring absorption either at 907cm^{-1} or at 832cm^{-1} and the reference peak height at 800cm^{-1} at time t = i respectively. The subscripts, 0 and f, refer to the initial and final height at time t = 0 and t = t_{max} respectively. A typical baseline from which heights were measured is shown in Figure 4.15.

$$\textit{relative fractional conversion} = \frac{\frac{E_0}{R_0} - \frac{E_i}{R_i}}{\frac{E_0}{R_0} - \frac{E_f}{R_f}} \qquad \text{(Eq. 4.1)}$$

To establish the reproducibility of the results, both peaks were analysed and compared with the DSC results. As the *true* baseline from which the heights have to be measured is unknown, the *relative changes* of the peaks were monitored as those were varying

between the minimum and the maximum values. The outcome of the analysis can be seen in Figure 4.16 for the cure of RTM6 resin at 140°C and 160°C. The conversion data from DSC experiments have also been translated to relative conversion in order for the comparison to be possible. A close look at this figure shows that the peak at 907cm^{-1} follows the cure in a similar way the DSC does and gives almost identical results with the experiments on the residual heat of reaction.

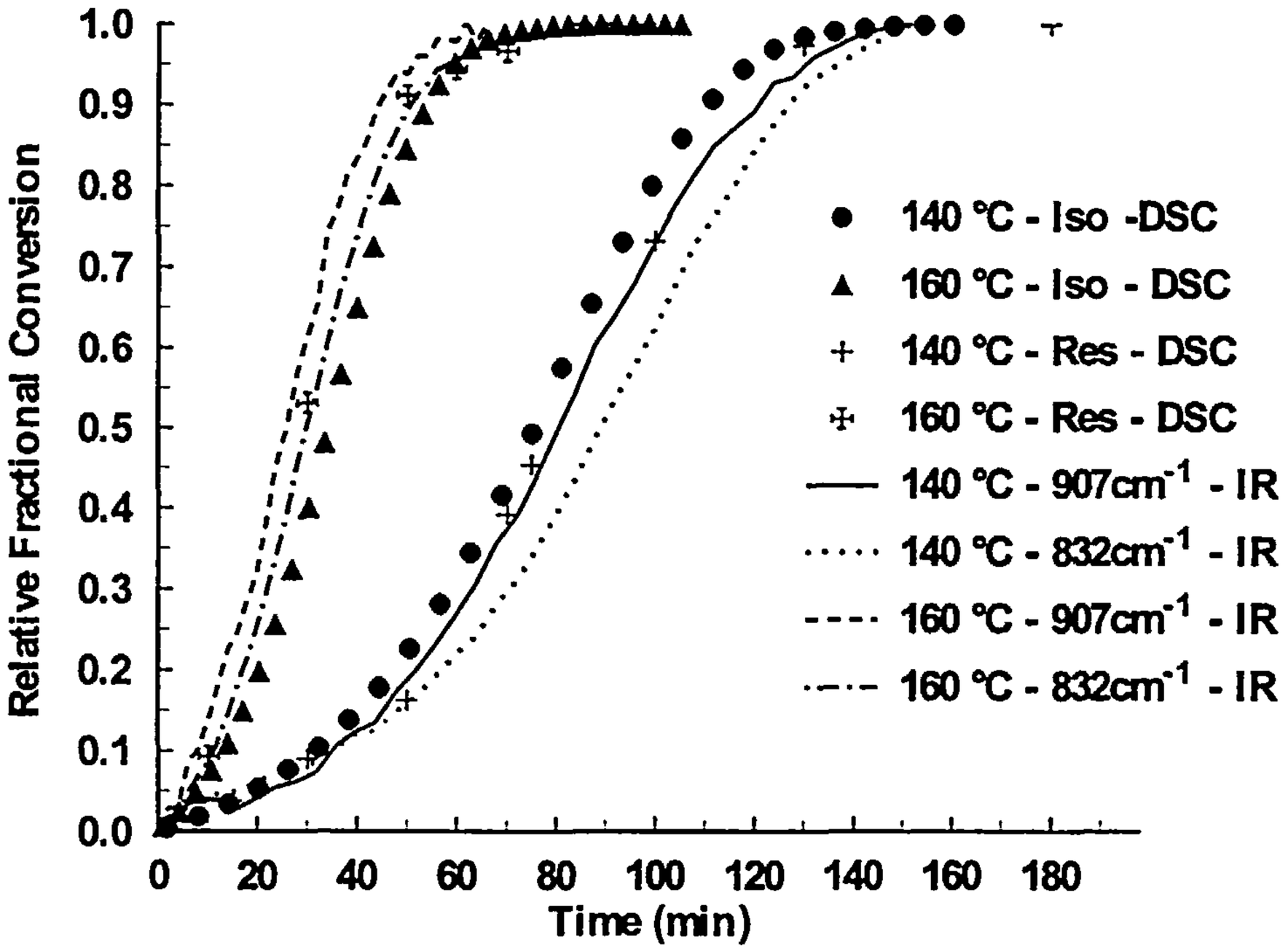

Figure 4.16 *Relative fractional conversion of RTM6 resin at 140°C and 160°C against cure time. Comparison between DSC experiments (isothermal and residual heat of reaction) and infrared absorption experiments.*

Further analysis on the isothermal cure of all the resin systems will be therefore based on experimental data from these two methods. The infrared technique will be the basic method providing experimental data for analysis, whereas the DSC experiments on the residual heat of reaction will be used for cross checking. The reason for choosing the infrared spectroscopy as the main method is because the experimental database arising from each experiment is greater than that obtained from the DSC experiments.

4.3 A Model - Free Cure Kinetics Prediction

In general, the overall reaction rate during the cure of a thermosetting resin can be written as [144] :

$$\frac{d\alpha}{dt} = K(T) \cdot f(\alpha) \qquad \text{(Eq. 4.2)}$$

where α is the overall epoxide conversion and K, f are functions of temperature and conversion respectively. Assuming that the function K has an Arrhenius dependence on temperature, and taking the natural logarithm of both sides of Eq. 4.2, we get:

$$\ell n\frac{d\alpha}{dt} = \ell nA - \frac{E}{R}\cdot\frac{1}{T} + \ell nf(\alpha) \qquad \text{(Eq. 4.3)}$$

where A and E are the Arrhenius parameters, R, is the universal gas constant and T, is the absolute temperature. Since the function f depends only on the overall conversion and not on the temperature, if we assume a specific conversion, α_{iso}, the function f will have a constant value, $f(\alpha_{iso})$, for any cure temperature, with the constraint that the reaction mechanism does not change with temperature, that is the function f is uniquely defined in respect to α.

Based on the above analysis, the construction of the "isoconversion" plots [145, 146], that is the plots of the natural logarithm of the reaction rate at a specific conversion against the inverse of the absolute cure temperature, will give straight lines with slope, $-\frac{E}{R}$ and an intercept, $\ell nA + \ell nf(\alpha_{iso})$.

The isoconversion plots for the dynamic cure of RTM6 resin can be seen in Figure 4.17. The temperatures to reach the predetermined conversions along with the corresponding reaction rates at each heating rate were calculated by polynomial interpolation of the raw DSC data. The isoconversions used along with the fitted straight lines are given in Table 4.2.

An interesting aspect of the above isoconversion analysis of the cure is the quick estimation of the activation energy of the reacting system. Since the slope of the isoconversion lines actually represents the activation energy, which is given by:

$$Activation\ Energy\ E = -slope \cdot R \qquad \text{(Eq. 4.4)}$$

the activation energy and the way it varies with the advancement of the cure are easy to calculated. In Figure 4.18 the activation energy of RTM6 resin, is plotted as a function of the fractional conversion during the dynamic cure at constant heating rates.

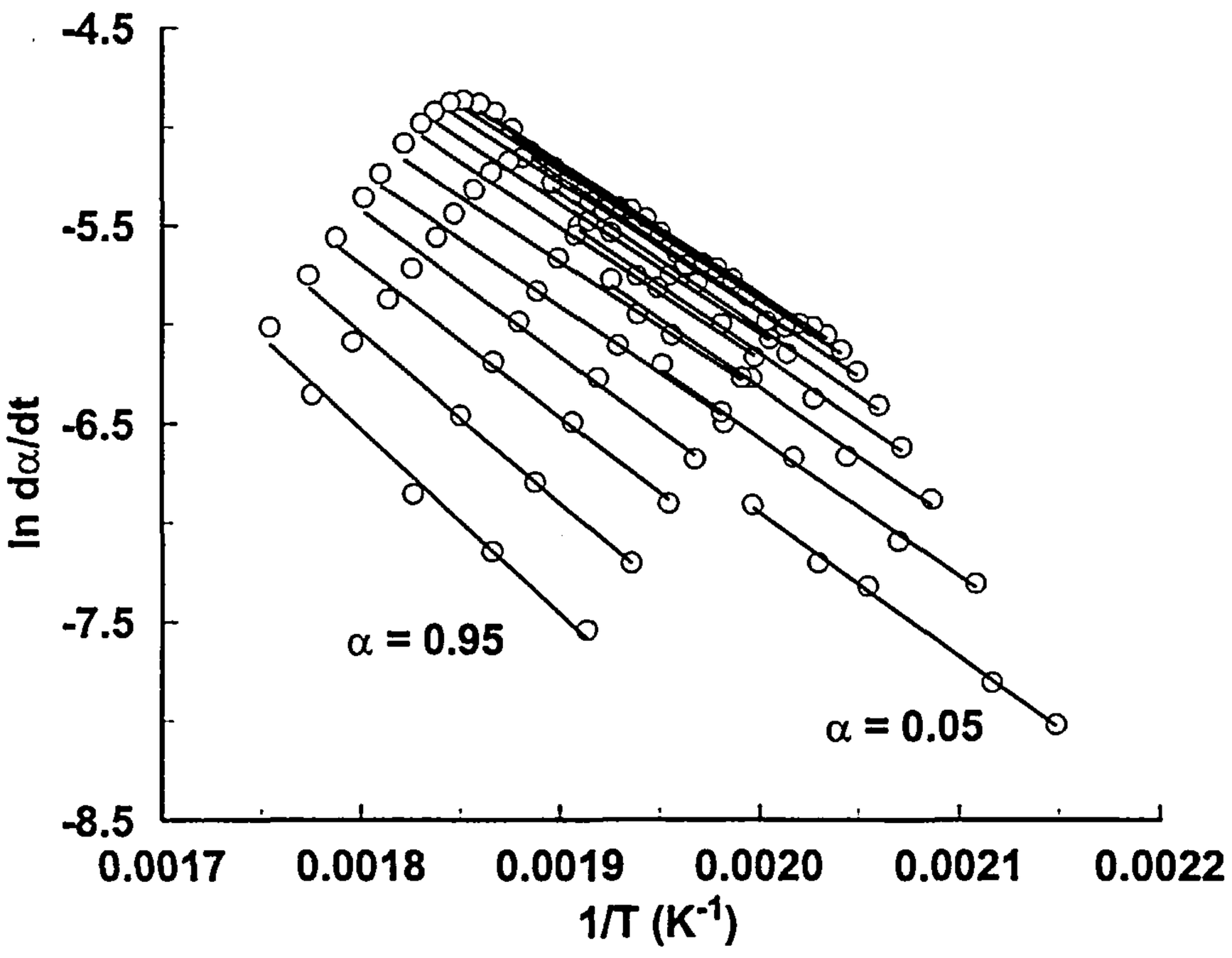

Figure 4.17 *Isoconversion plots of RTM6 resin for dynamic cure at 5, 7.5, 10, 15 and 20 °C/min.* ***Symbols*** *represent the raw data of DSC experiments and* ***solid lines*** *the regression lines at each conversion level*

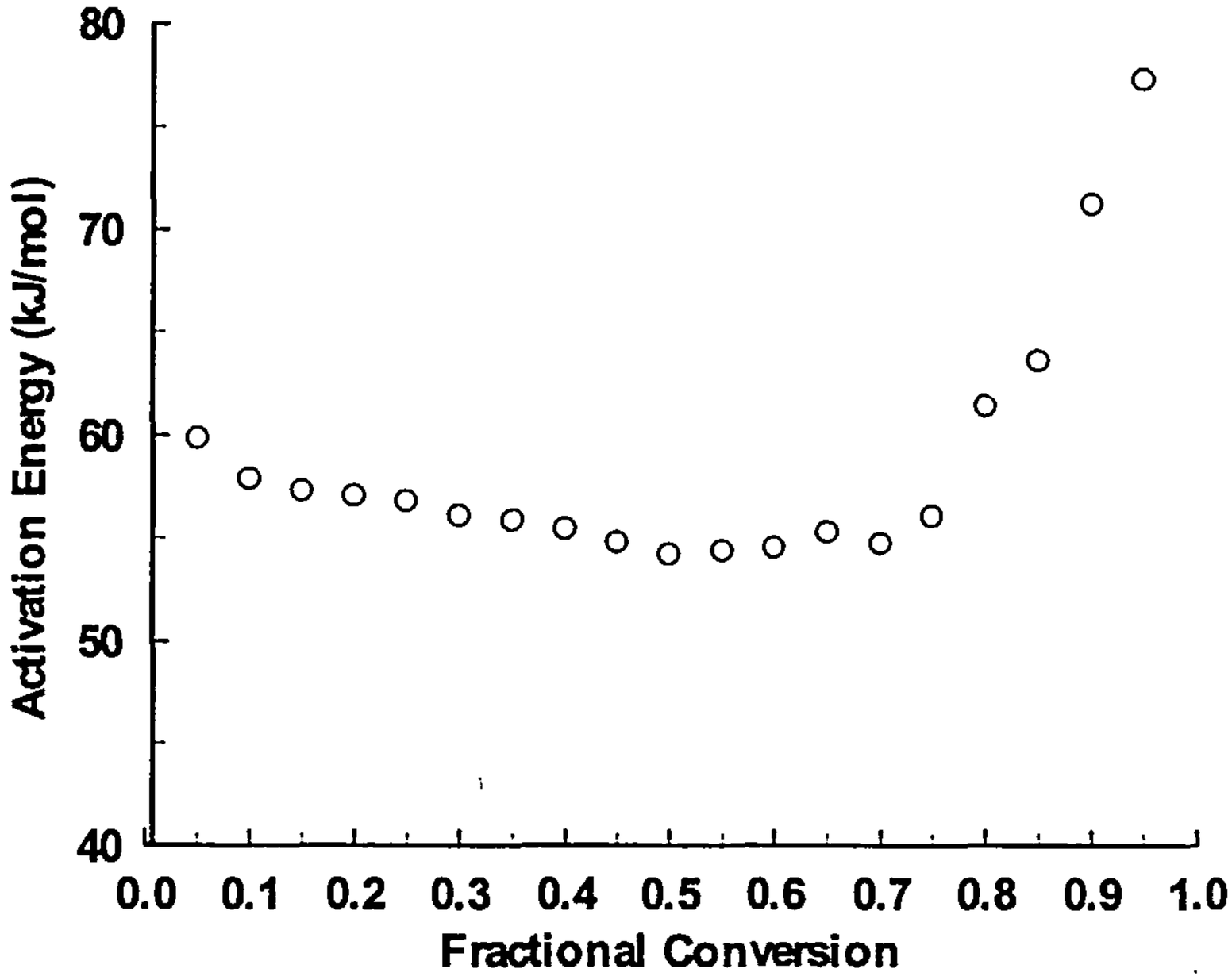

Figure 4.18 *Variation of activation energy with conversion for the dynamic cure of RTM6 resin. Activation energy was calculated from the slopes of the isoconversion lines of Figure 4.17*

As can be seen in this figure, the activation energy of the curing system changes throughout the cure. The initial decrease of E for low conversions follows a plateau at intermediate conversions, whereas at conversions of around 60% and above the activation energy starts to increase.

The initial small values of the activation energies can be attributed to the autocatalytic nature of the reaction. Since the reaction is catalysed by the hydroxyl groups formed during the epoxy - amine addition reaction, it is evident that the reaction will proceed with greater ease in the initial stages. As the reaction advances, the autocatalysis diminishes giving way to the non catalytic epoxy - amine addition reaction, with a consequent increase in the activation energy of the reacting system.

For the dynamic cure it holds:

$$\frac{d\alpha}{dT} = \frac{1}{\beta}\frac{d\alpha}{dt} \qquad \text{(Eq. 4.5)}$$

where β is the heating rate. Substitution of the above equation into Eq. 4.3 and some rearrangement will give:

$$\int_0^{\alpha} \frac{d\alpha}{Af(\alpha)} = \frac{1}{\beta}\int_{T_0}^{T} \exp\left(-\frac{E}{RT}\right) dT \qquad \text{(Eq. 4.6)}$$

Since $E / RT >> 1$, the integral of the right hand side of the above equation can be approximated by [147]:

$$\int_{T_0}^{T} \exp\left(-\frac{E}{RT}\right) dT \approx \frac{RT^2}{E}\exp\left(-\frac{E}{RT}\right) \qquad \text{(Eq. 4.7)}$$

which, if substituted in the original expression, will give:

$$\int_0^{\alpha} \frac{d\alpha}{Af(\alpha)} = \frac{RT^2}{\beta E}\exp\left(-\frac{E}{RT}\right) \qquad \text{(Eq. 4.8)}$$

The terms $Af(\alpha)$ and E/R in the above equation are known from the intercept and the slope of the isoconversion plots respectively. Thus, by numerical integration of the left hand side of Eq. 4.8 and a numerical solution in respect to T, the temperatures to reach the specific conversions can be determined for a specified heating rate β. Back-substitution of the calculated temperatures to the initially determined regression lines of the isoconversion plots will give the respective reaction rates, thus allowing for a simulation of the cure at any heating rate.

The same analysis can be applied for the isothermal cure, but now the reaction rates

can be directly estimated from the regression lines giving the reaction rate / conversion profile at different cure temperatures. Direct integration of Eq. 4.2 will give the times to reach specific conversions at each cure temperature.

Although the above analysis can give with a relatively small amount of effort, a prediction of the cure state for any cure cycle, it is lacking of a scientific explanation of the way the data are treated.

Table 4.2 *Isoconversion data for the dynamic cure of RTM6 resin*

Isoconversion	Slope	Intercept	Activation Energy (kJ/mol)
0.05	-7200	7.45	59.86
0.10	-6962	7.35	57.88
0.15	-6893	7.47	57.31
0.20	-6865	7.58	57.08
0.25	-6833	7.65	56.81
0.30	-6750	7.57	56.13
0.35	-6720	7.57	55.87
0.40	-6674	7.50	55.49
0.45	-6597	7.35	54.85
0.50	-6527	7.18	54.27
0.55	-6548	7.16	54.44
0.60	-6564	7.08	54.57
0.65	-6654	7.13	55.33
0.70	-6589	6.84	54.78
0.75	-6750	6.92	56.13
0.80	-7390	7.88	61.44
0.85	-7655	8.08	63.65
0.90	-8575	9.39	71.29
0.95	-9311	10.23	77.42

In order to describe the reaction rate as the product of two independent phenomena, one incorporating the temperature influence in the form of Arrhenius dependent reaction rate constants and the other the cure advancement as in Eq. 4.2, it is necessary that all the reactions involved be equally activated. This is true for an one-step reaction, but in the case of an epoxy - amine reaction, since catalysed and non-catalysed reactions do have different activation energies, the validity of this analysis is questionable. However, from the industrial point of view, the interest falls on how to predict the cure state and not whether the method used is always necessarily scientifically rigorous. Thus, this kind of analysis is of great interest and can be relatively easily applied in an industrial context.

4.4 Semi-Empirical Cure Kinetics Modelling

4.4.1 Isothermal Curing

In the previous section, a cure kinetics prediction was made based on a direct analysis of the experimental results through the iso-conversion plots. As was indicated, this kind of analysis is lacking of a rigorous scientific background, as it does not relate the intermediate reaction steps that occur during an amine cure of epoxy resins. In Section 2.4.1, the epoxy - amine reactions were thoroughly analysed and an expression was established that relates the reaction rate to the cure advancement (see Eq. 2.8). If the proposed mechanism also stands for the resin systems studied here, a plot of the left hand side of that expression, normalised by the factor $(1 - x_E)^2$, against x_E should give a straight line up to the point where the factor H_C starts to become significant. This kind of plot is shown in Figure 4.19 for the isothermal cure of RTM6 resin at 140°C.

As can be seen in this figure, there is a deviation from linearity throughout the cure. The slope continuously increases up to the point where a maximum occurs and a sudden drop appears. The drop for conversions above 60% occurs because the factor H_C becomes significant as the reaction enters the diffusion stage. It is evident from the above analysis that the proposed reaction mechanism does not stand for this resin

system, thus, a more analytical cure mechanism has to be adopted.

The generalised form of Eq. 2.8, which is given by Eq. 4.9, can compensate for the non-linearity of the plot in Figure 4.19.

$$\frac{d\alpha}{dt} = \left(k_1 + k_2\alpha^m\right)\cdot\left(1-\alpha\right)^n \qquad \text{(Eq. 4.9)}$$

The reaction orders that appear in that expression can be varied in a manner that will definitely give a straight line up to the diffusion controlled region. Although this kind of adjustment of the parameters has no direct explanation in terms of the true reactions that take place, nevertheless, the fits obtained can be very good.

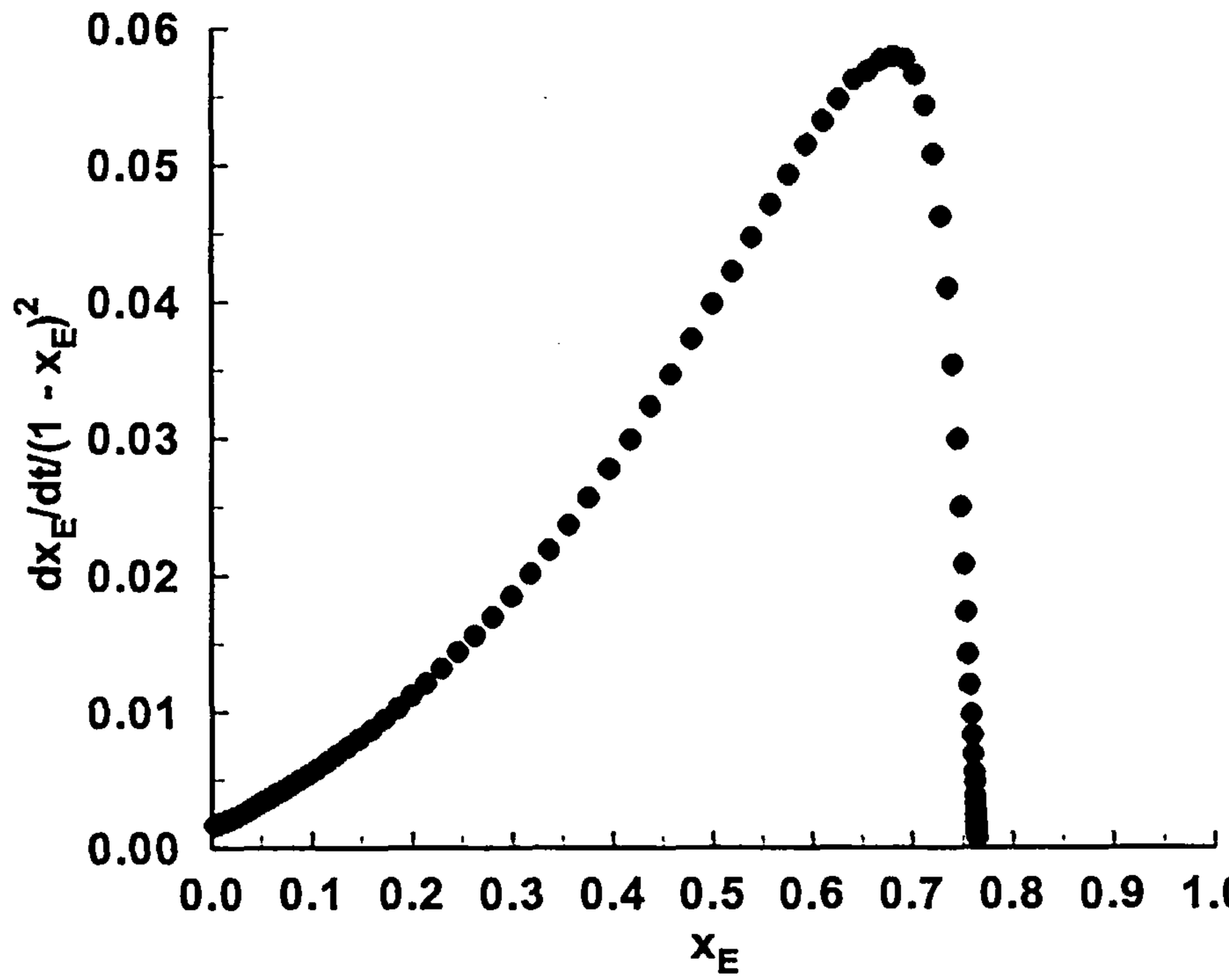

Figure 4.19 *Plot of* $\frac{1}{\left(1-x_E\right)^2}\frac{dx_E}{dt}$ *against* x_E *for a cure of RTM6 resin at 140°C (see Eq. 2.8)*

In order to construct a curve similar to the one given in Figure 4.19 for the new model, the kinetic parameters k_1, k_2, m and n have to be estimated. Since the expression in Eq. 4.9 has four parameters to be estimated, three more conditions are required to obtain a unique solution. The first one arises from the total order of the reaction, r, which in our case can be represented by the sum of the partial orders, m and n, thus:

$$r = m+n \qquad \text{(Eq. 4.10)}$$

Total orders, r, between second and third order kinetics will be tried in this study. According to the technique introduced by Ryan and Dutta [71], the other two conditions can be met by selecting two specific points in the cure. The first one is the beginning of the cure (t = 0) and the second one is the point at the maximum reaction rate.

Initially, when the reaction starts, the conversion, α, is zero, thus $\alpha = 0$. From this condition, the initial reaction rate according to Eq. 4.9 becomes:

$$\left.\frac{d\alpha}{dt}\right|_{t=0} = k_1 \qquad \text{(Eq. 4.11)}$$

From the second condition, at the maximum reaction rate, the differential of the reaction rate has to be zero, thus $\frac{d^2\alpha}{dt^2} = 0$. Differentiation of the expression that gives the reaction rate (Eq. 4.9) gives after some algebraic manipulation:

$$n \cdot k_1 \cdot \alpha_p^{1-m} + k_2 \cdot r \cdot \alpha_p - m \cdot k_2 = 0 \qquad \text{(Eq. 4.12)}$$

where the subscript, p, refers to the value at the maximum reaction rate.

The system of the above three equations along with the expression that gives the reaction rate can now be solved for a given value of the total order, r, to give a unique solution for the estimated kinetic parameters (see Appendix A).

The solution of this system will be first tried for the isothermal cure of RTM6 resin,

using the isothermal DSC data at 140, 160, 170 and 180°C.

The first reaction rate constant, k_1, can be directly estimated from the initial reaction rates according to Eq. 4.11. The values of the calculated reaction rate constant k_1 at the temperature range used are shown in Table 4.3. For this rate constant to have a direct correlation to any chemical phenomena occurring during the cure, it must follow an Arrhenius type dependence on temperature. The plot of the natural logarithm of k_1 with respect to the inverse of the absolute temperature is shown in Figure 4.20. As can be seen in this figure, there exist a linear dependence of ℓnk_1 with $1/T$. The resulting correlation coefficient is $R^2 = 0.999$, indicating that Arrhenius behaviour is followed by the reaction rate constant k_1. The estimated activation energy and pre-exponential factor of k_1, as they were calculated from the slope and the intercept of the Arrhenius straight line, are: 74.69kJ/mol and $4.5 \cdot 10^6$ min^{-1} respectively.

For the calculation of the rest of the kinetic parameters, a routine was written in the EXCEL spreadsheet format that solves the system of Eqs. 4.9 - 4.12 simultaneously for all the temperatures used. The routine takes as an input a fixed total reaction order, r, and a "guess" value for the reaction order , m. Using an iterative procedure, the best results were evaluated by minimising the differences between the input and estimated values of m for all the temperatures. The estimated kinetic parameters along with the raw DSC data used are shown in Table 4.3.

An Arrhenius plot was also constructed for the reaction rate constant k_2, to check the dependence of that parameter on temperature. The plot is shown in Figure 4.20, demonstrating a linear dependence of ℓnk_2 with the inverse of temperature, with a correlation coefficient: $R^2 = 0.999$. The estimated activation energy and pre-exponential factor, as calculated from the slope and intercept of the Arrhenius straight line are: 58.37 kJ/mol and $1.3 \cdot 10^6$ min^{-1} respectively.

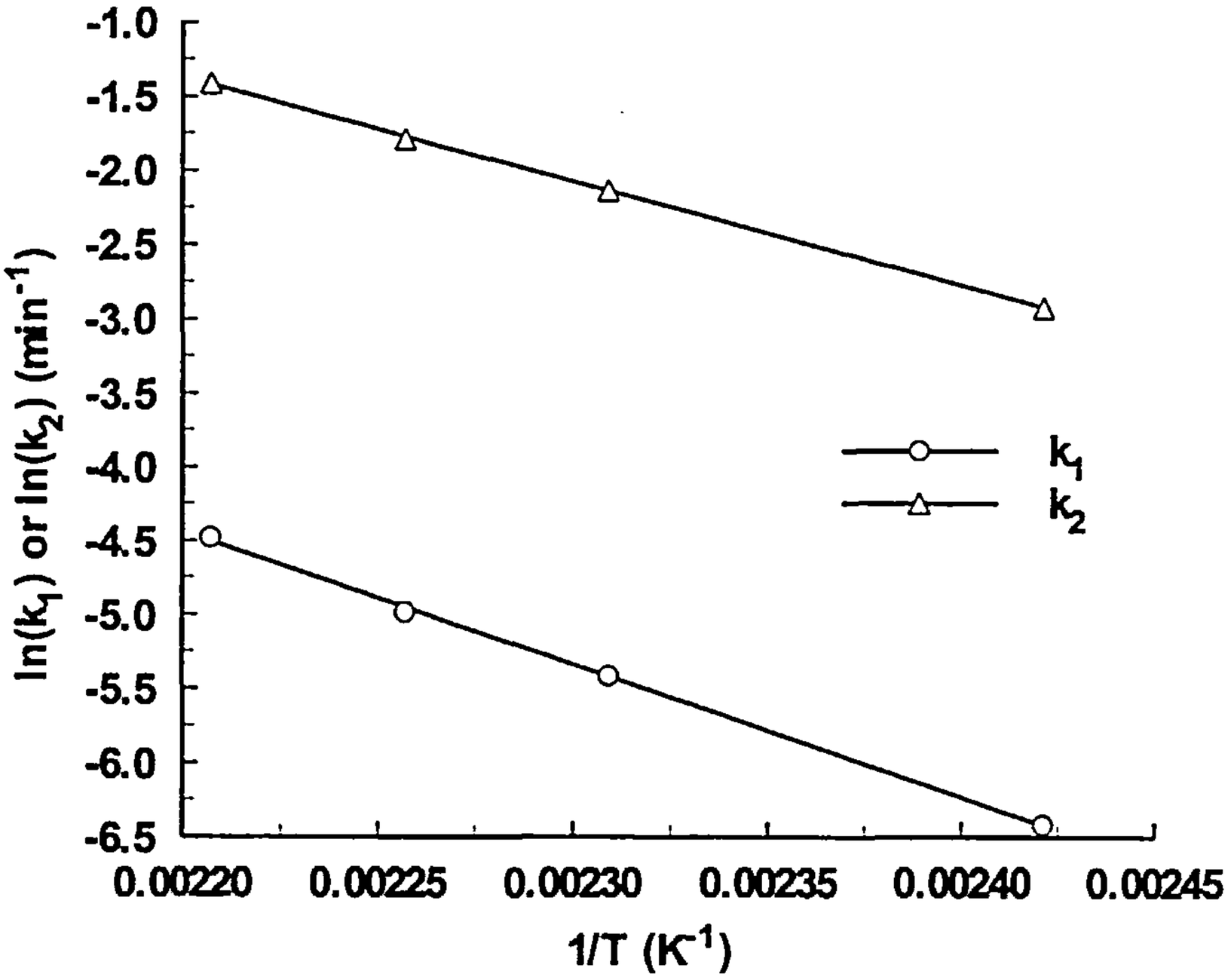

Figure 4.20 *Arrhenius diagram of the kinetic rate constants k_1 and k_2 of the kinetic model given by Eq. 4.9 for the isothermal cure of RTM6 resin. Analysis was done according to the Ryan - Dutta method*

Some useful results can be extracted from the values of the reaction rate constants. Firstly, k_2 is higher than k_1 throughout the temperature range used, indicating that the autocatalytic epoxy - amine addition reaction proceeds faster than the non-autocatalytic epoxy - amine reaction. This is also indicated by the comparison of the activation energies of the two reactions.

The lower activation energy of the autocatalytic reaction means that the energy barrier for that reaction to happen can be easily overcome by the high energy potential that is supplied to the system by the use of high cure temperatures. On the other hand, the pre-exponential factors of the two rate constants follow the opposite trend. The pre-exponential factor of k_2 is lower than the pre-exponential factor of k_1. That means that the autocatalytic reaction has a lower probability to occur than the non-autocatalytic reaction.

Table 4.3 *Kinetic results from DSC experiments of the isothermal cure of RTM6 resin. Kinetic analysis by the Ryan - Dutta method on Eq. 4.9.*

Temperature (°C)	k_1 (min^{-1})	Maximum rate (min^{-1})	Time at max t_p (min)	Conversion at max α_p	k_2 (min^{-1})
140	0.0016	0.0102	81.29	0.439	0.0538
160	0.0044	0.0229	35.84	0.474	0.1189
170	0.0068	0.0328	23.94	0.461	0.1682
180	0.0113	0.0479	16.28	0.477	0.2431

Reaction Orders

r	*m*	*n*
2.5	1.216	1.284

Arrhenius Straight Lines

Rate Constant	Slope	Intercept
k_1	-8983	15.327
k_2	-7020	14.076

Although this effect is easily overcome at the beginning of the cure, when the resin is liquid, by the lower activation energy, this might not be the case when the resin starts to solidify. At high cure temperatures, where the two rate constants start to become comparable (see Figure 4.20), the effect of the lower probability of the autocatalytic reaction may result in the inverse of the reaction mechanism, with the non-autocatalytic reaction being the dominant reaction. The result of such an inverse in the reaction mechanism might be more visible in the dynamic cure of the resin. In a cure cycle where the resin is heated at a continuously increasing temperature, the energy barrier for the two reactions (autocatalytic and non-autocatalytic) could be easily overcome for both of them. That means that the pre-exponential factor will play the major role, which in our case is in favour of the non-autocatalytic reaction. The fact that the reaction mechanism may change between isothermal and dynamic cure of

thermosetting resins has been the centre of a lot of discussion in the past few years and has drawn the interest and comments of many researchers [148, 149]. A further analysis on the subject of the dynamic cure will be made in the following paragraphs.

To have an indication of the goodness of the fit of the above constructed model with the experimental results, plots of the reaction rates have been made against cure time for the four temperatures used in the analysis. The plots are shown in Figure 4.21.

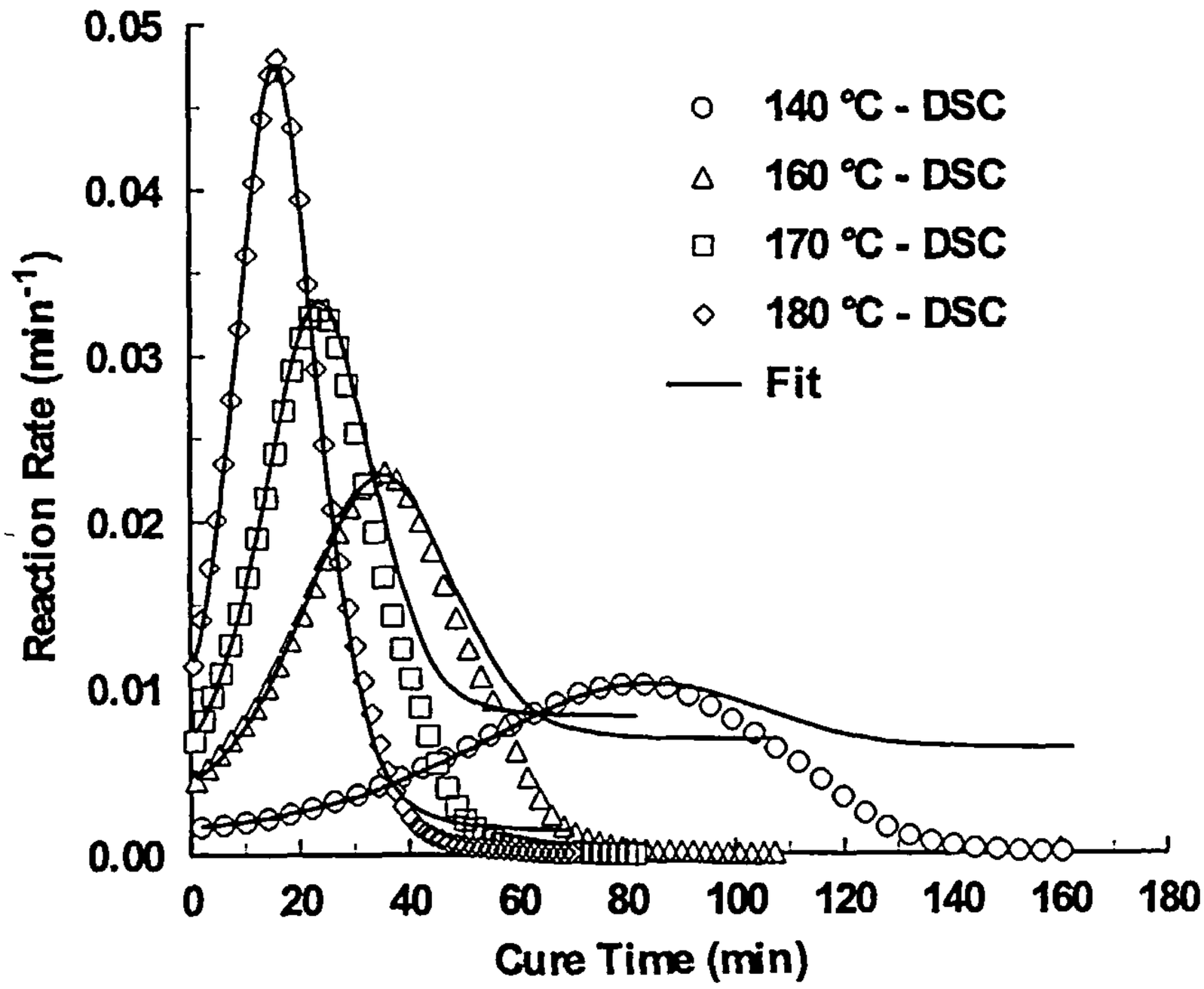

Figure 4.21 *Comparison between experimental data and kinetic model for the isothermal cure of RTM6 resin. Kinetic analysis made according to the Ryan -Dutta method. The kinetic model used is given by Eq. 4.9 without the incorporation of diffusion control*

Since the above model does not compensate for the diffusion phenomena that are expected to occur as the resin passes from the rubbery to the glassy state, the fit starts to deviate from the experimental data for conversions approximately above 50%. In the range of conversions between 50 - 60 %, the resin is expected to gel, (theoretical gelation at 58% for a bifunctional epoxy - amine system), which means that the

rubbery state is reached at these conversions. Thus, the diffusion phenomena start to take control of the curing process, causing the diversion of the fit. In Chapter 6, diffusion will be incorporated in the model to compensate for this diversion.

The evaluation of the parameters of this kinetic model (Eq. 4.9), was also made by another technique, which from this point forward will be referred to as the "Present" method (see Appendix B), in order to estimate the errors imposed by the evaluation method. The model given in Eq. 4.9, after some algebraic manipulation can be expressed according to the following expression:

$$\ell n\left(\frac{\frac{d\alpha}{dt}}{(1-\alpha)^{r-m}}-k_1\right)=\ell nk_2+m\cdot\ell n\alpha \qquad \text{(Eq. 4.13)}$$

where, r, is again the total reaction order. For an isothermal situation, a plot of the left hand side of the above equation in respect to $\ell n\alpha$ will give a straight line with slope, m, and intercept, ℓnk_2. The reaction rate constant k_1, can be similarly calculated by the values of the initial reaction rate, as in the method of Ryan and Dutta. A similar routine was written in the EXCEL spreadsheet format, as in the previous case, to evaluate the kinetic parameters k_2, m, n, simultaneously for all the isothermal experiments. Since diffusion control is expected to occur for conversions above gelation, the evaluation of the parameters was made for conversion up until 55%. The results of the above evaluation procedure are shown in Table 4.4. The plot of the left hand side of Eq. 4.13 against $\ell n\alpha$, for a cure at 160°C, is shown in Figure 4.22 for the computed parameters given in Table 4.4. The effect of the diffusion processes is evident from the sudden drop of the curve for conversions above 60% ($\ell n\alpha \approx$ -0.5).

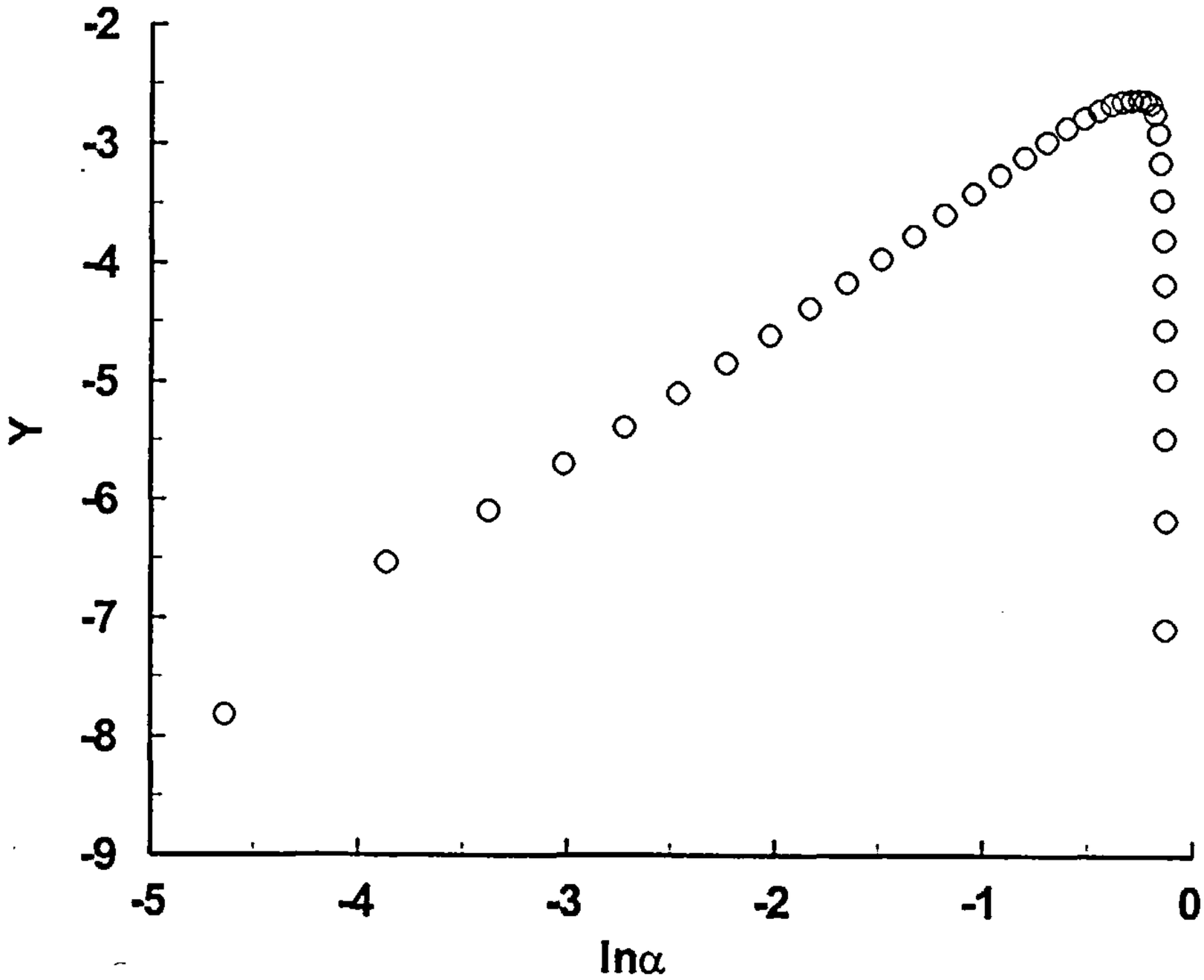

Figure 4.22 *Plot of the left hand side of Eq. 4.13, (Y =)* $\ell n\left(\frac{d\alpha/dt}{(1-\alpha)^{r-m}}-k_1\right)$*, as a function of* $\ell n\alpha$ *for the cure of RTM6 resin at 160°C*

An Arrhenius plot was constructed for the reaction rate constant k_2, to check the dependence of that parameter on temperature. The plot is shown in Figure 4.20. As it can be seen in this figure, there exist a linear dependence of k_2 on temperature. The correlation coefficient is $R^2 = 0.996$. The estimated activation energy and pre-exponential factor, as they were calculated by the slope and intercept of the Arrhenius straight line are: 59.18 kJ/mol and $1.6 \cdot 10^6$ min^{-1} respectively. The results from the two methods are summarised in Table 4.5. Apart from the first reaction rate constant, which was calculated with the same method for both techniques, the other parameters show a very small deviation between each other.

Table 4.4 *Kinetic results from DSC experiments of the isothermal cure of RTM6 resin. Kinetic analysis using Eq. 4.13.*

Temperature (°C)	Rate Constant k_1 (min^{-1})	Rate Constant k_2 (min^{-1})
140	0.0016	0.0531
160	0.0044	0.1159
170	0.0068	0.1587
180	0.0113	0.2509
Reaction Orders		
r	***m***	***n***
2.5	1.202	1.298
Arrhenius Straight Lines		
Rate Constant	**Slope**	**Intercept**
k_1	-8983	15.327
k_2	-7117	14.284

Table 4.5 *Comparison of Ryan - Dutta and Present methods for the computation of the parameters of the model given by Eq. 4.9. Results for the cure of RTM6 resin under DSC isothermal conditions.*

Method	*r*	*m*	*n*	E_1 (kJ/mol)	A_1 (min^{-1})	E_2 (kJ/mol)	A_2 (min^{-1})
Ryan - Dutta	2.5	1.216	1.284	74.69	$4.5 \cdot 10^6$	58.37	$1.3 \cdot 10^6$
Present	2.5	1.202	1.298	74.69	$4.5 \cdot 10^6$	59.18	$1.6 \cdot 10^6$

Although the results for both methods indicate that the use either of them should give essentially the same prediction, the computation effort that is needed to reach those results is different. Care has to be taken during the construction of the straight lines for the second method, since the initial points from the DSC data tend to destabilize the

results. The same problem was observed by Kenny who also implemented this technique for the evaluation of the kinetic parameters [150] . For that reason, it is better to construct the lines for conversions well into the cure. The accuracy of the second method seams to be better since it takes into account all the experimental data, whereas the Ryan - Dutta method uses only the initial and maximum points, disregarding what happens in between.

Both these methods were applied to the other resin systems, in order to establish the appropriate parameter set for each resin system that best describes the cure kinetics.

Since results from direct isothermal DSC experiments were not available, data either from infrared spectroscopy or residual heat of reaction DSC experiments had to be used. These experiments do not give the reaction rate during the cure, but only the degree of conversion. Thus the conversion data had to be differentiated with respect to cure time in order to get the reaction rates. Finite differences were used along with polynomial interpolation for the numerical differentiation of the raw conversion data.

The conversion data for the RMO and RMO2 resin systems are shown in Figure 4.23 and Figure 4.24 respectively, for the cure temperatures 130°C, 140°C, 150°C and 160°C. The calculated reaction rates for the RMO and RMO2 resin systems along with the fits from the Ryan - Dutta method are shown in Figure 4.25 and Figure 4.26 respectively, for the cure temperatures of 140°C and 160°C. The calculated parameters from both evaluating methods are shown in Table 4.6 for both resin systems. The evaluation of the kinetic parameters was done for conversions up to 55% in order to avoid interference from diffusion processes that are expected to occur at higher conversions.

Table 4.6 *Comparison of Ryan - Dutta and Present methods for the computation of the parameters of the model given by Eq. 4.9. Results for the cure of RMO and RMO2 resins under DSC isothermal conditions.*

Method	*r*	*m*	*n*	E_1 (kJ/mol)	A_1 (min^{-1})	E_2 (kJ/mol)	A_2 (min^{-1})
RMO Resin							
Ryan - Dutta	2.5	1.192	1.308	78.44	$1.3 \cdot 10^7$	57.88	$9.1 \cdot 10^5$
Present	2.5	1.278	1.222	78.44	$1.3 \cdot 10^7$	56.14	$5.6 \cdot 10^5$
RMO2 Resin							
Ryan - Dutta	2.5	1.300	1.200	75.54	$6.1 \cdot 10^6$	53.08	$2.7 \cdot 10^5$
Present	2.5	1.313	1.187	75.54	$6.1 \cdot 10^6$	54.68	$4.3 \cdot 10^5$

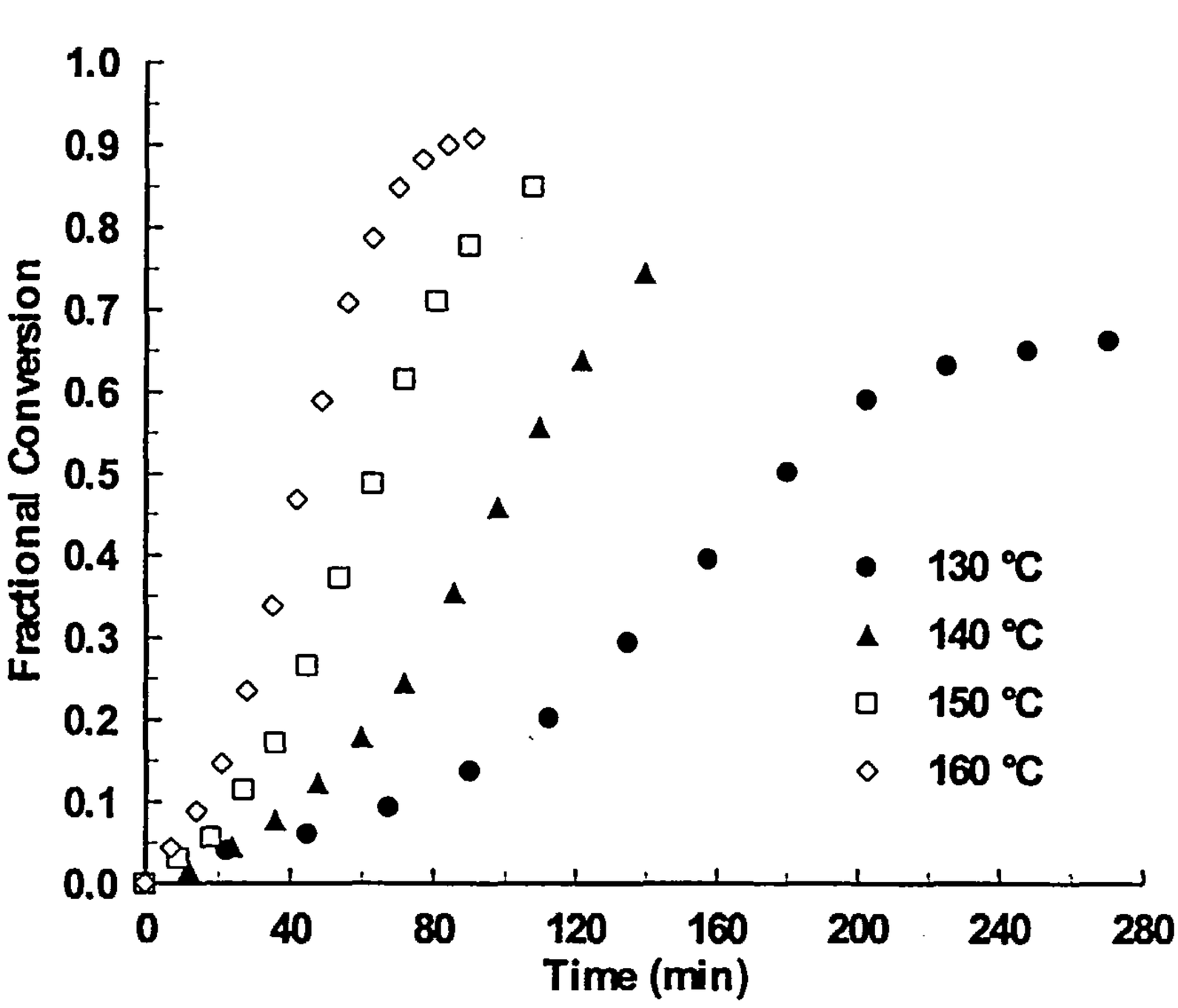

Figure 4.23 *Fractional conversion versus cure time of RMO resin under isothermal cure*

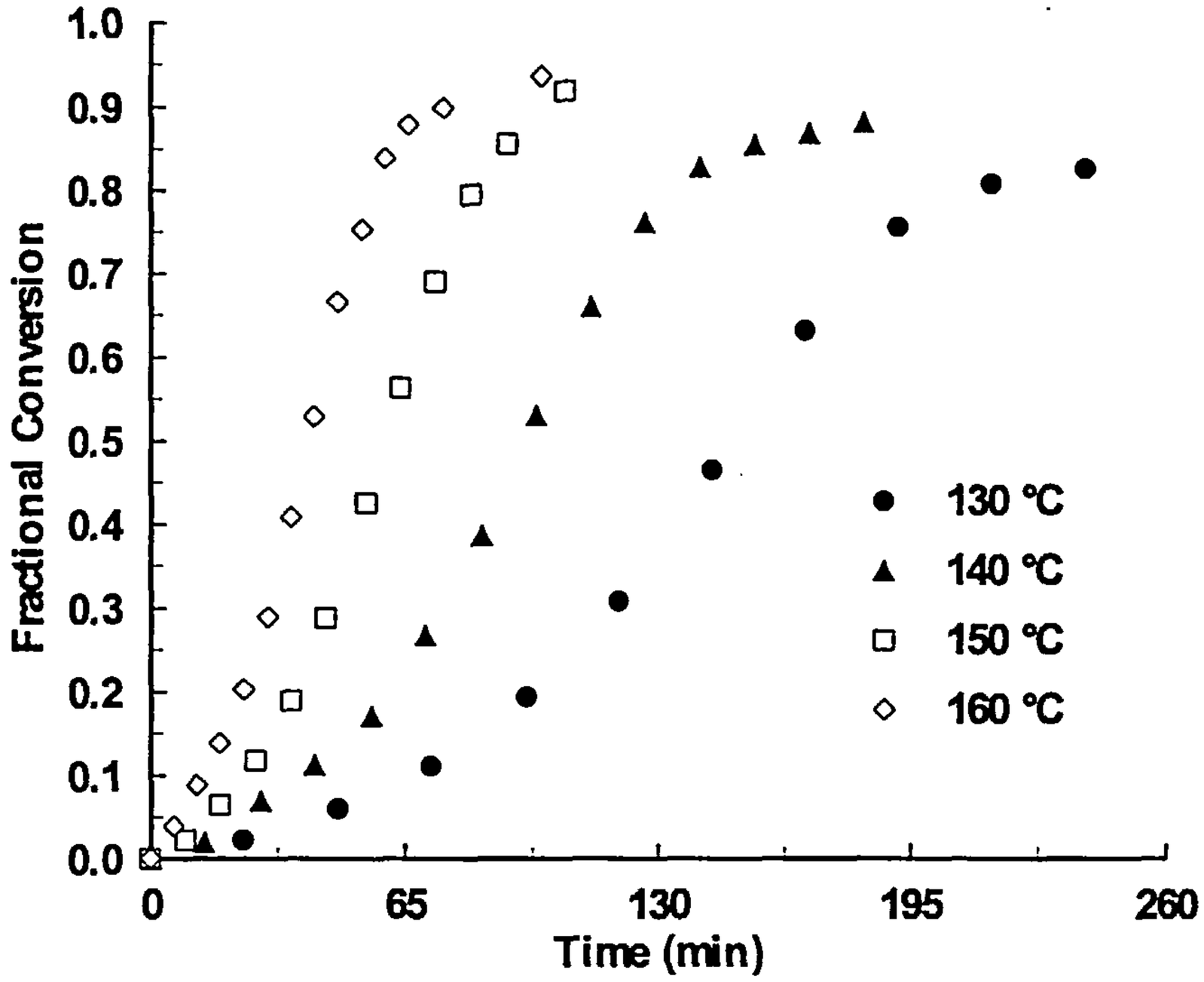

Figure 4.24 *Fractional conversion versus cure time of RMO2 resin under isothermal cure*

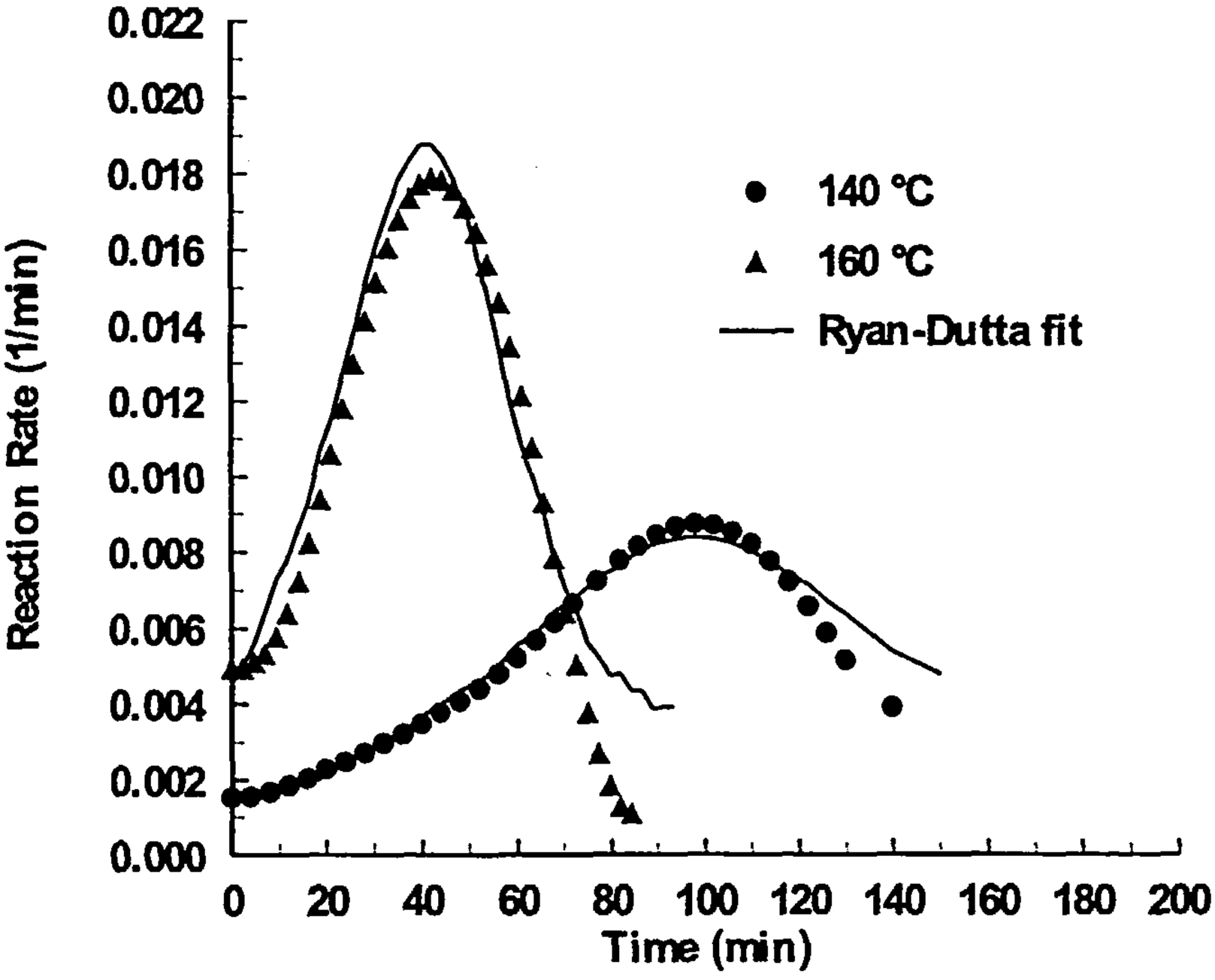

Figure 4.25 *Reaction rate versus cure time of RMO resin under isothermal cure. Symbols indicate experimental data, whereas solid lines indicate fits of Eq. 4.9 with parameters evaluated by the Ryan - Dutta method*

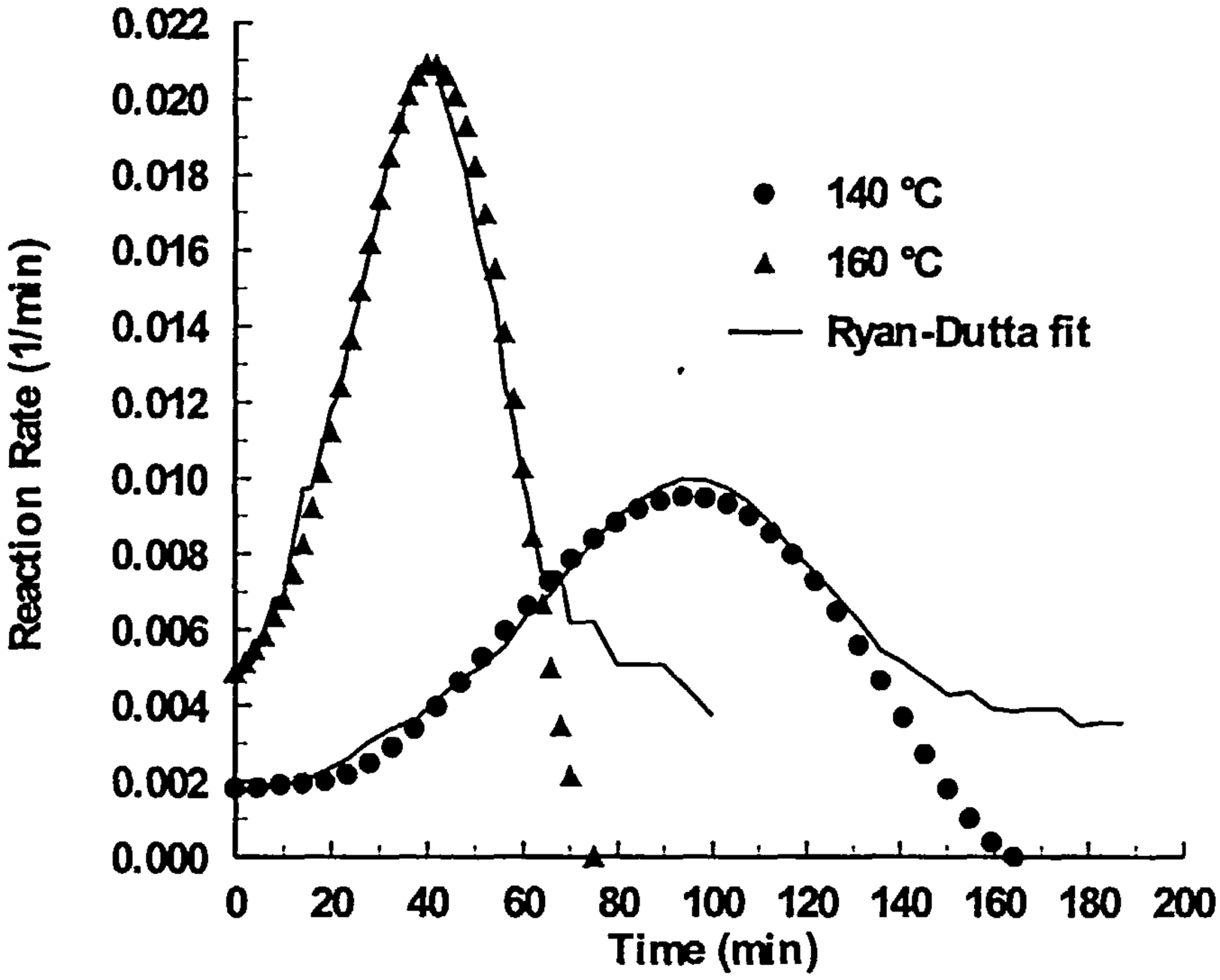

Figure 4.26 *Reaction rate versus cure time of RMO2 resin under isothermal cure. Symbols indicate experimental data, whereas solid lines indicate fits of Eq. 4.9 with parameters evaluated by the Ryan - Dutta method*

A close look in Table 4.5 and Table 4.6 shows the similarity of the cure kinetics for all three resin systems. Comparable values have been evaluated for all the kinetic parameters. The activation energies fall in the same range of values deviating only 2-3 kJ/mol from the average values of about 76 kJ/mol for the non-catalytic reaction and 56 kJ/mol for the catalytic reaction. The same trend is observed for the reaction orders. All resin systems follow the same total order of 2.5 with the partial reaction orders being about the half of the total order. The similarity of the activation energies is indicative of the similarity of the reaction mechanism. All three resins are epoxy/amine systems, thus the main reactions during the cure should be the same for all of them. Deviation of the conversion profiles of these resin systems between each other is reflected in the different pre-exponential factors obtained during the evaluation procedure. The relative weight of each reaction to the total reaction is different for each

resin system, is proportional to the pre-exponential factor and depends on the individual chemical constituents used. Thus, although the epoxy resin used is the same (TGDDM), the use of different amine hardeners in various concentrations, is likely to favour some reactions more than others.

4.4.2 Dynamic Curing at Constant Heating Rates

In the previous section the kinetics models for the resin systems RTM6, RMO and RMO2 were established for curing under isothermal conditions. Application of the same models to the dynamic cure of these resins is guaranteed to fail a priori because of the following reasons:

- narrow temperature range for which the kinetic parameters have been evaluated
- empirical nature of the kinetic model
- possible change in the reaction mechanism

The failure of the model can be seen in Figure 4.27, where the cure of RMO resin under dynamic conditions at 5 and 20 °C/min has been simulated with the kinetic parameters evaluated by the Ryan - Dutta method, as these are given in Table 4.6. Although the fit of the model is reasonably good for the low heating rate of 5 °C/min, probably because of the low temperature window that is followed for this cure, the fit is well deviated for the 20 °C/min cure, especially in the area of the maximum reaction rate.

A reevaluation of the kinetic parameters of the model of Eq. 4.9 is needed to achieve a better fit. The two methods described in the previous section for the isothermal cure are not applicable in this case, since we are under dynamic conditions (continuous changing temperature). Both these methods treat the reaction rate constants as unchanged throughout the cure, which is true under isothermal conditions, as these are functions only of temperature. Under dynamic cure, at each point into the cure, the rate constants will have a different value, since the temperature is changing. For this reason some other technique has to be used for the kinetic parameters evaluation.

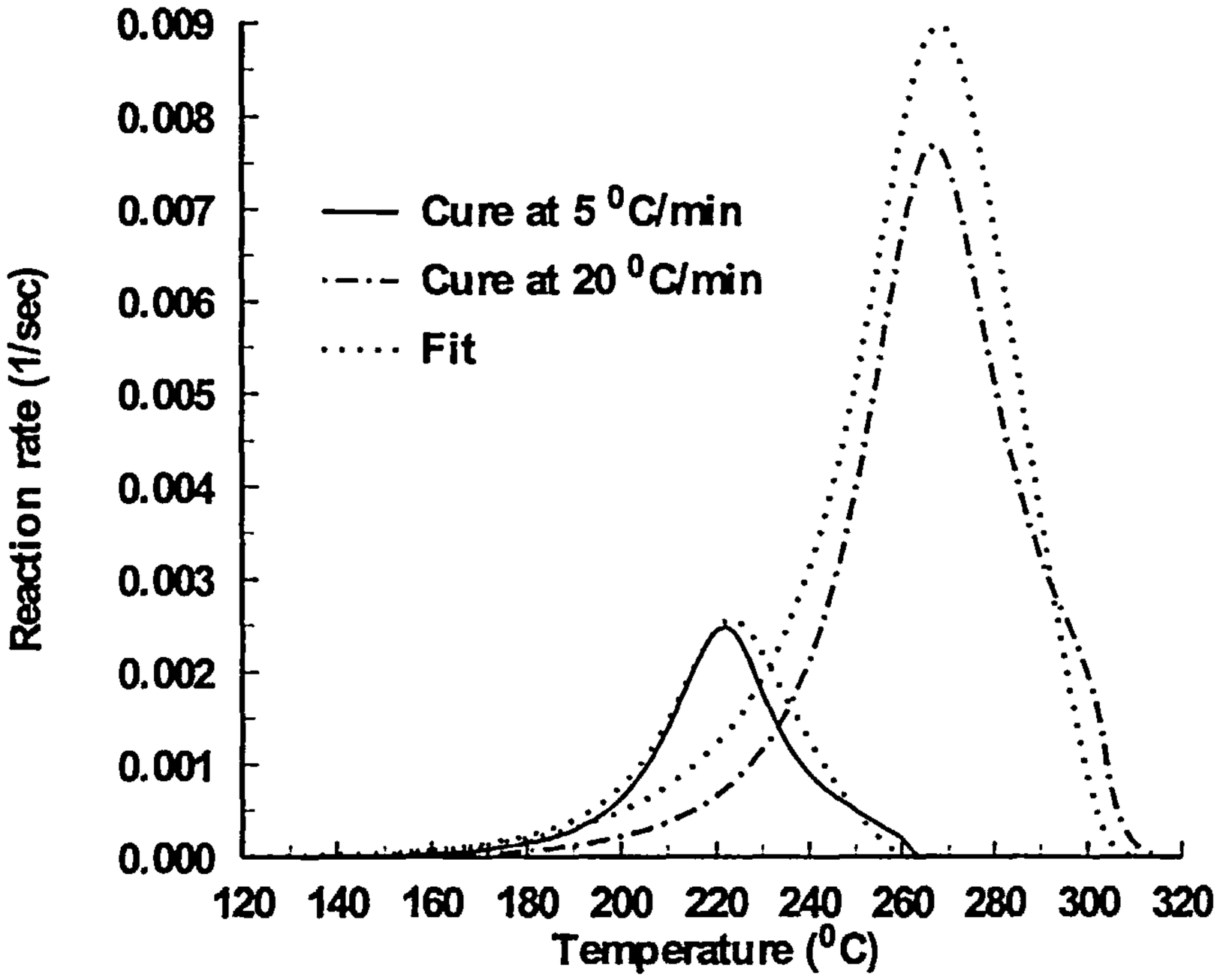

Figure 4.27 *Dynamic cure of RMO resin at various heating rates. Fit was made using Eq. 4.9 and the parameters calculated by the Ryan - Dutta method (Table 4.5)*

As a first approximation, simple nth order kinetics given by Eq. 4.14 will be tried, as it is most probable that the autocatalytic nature of the curing reaction will not be significant under dynamic conditions.

$$\frac{d\alpha}{dt} = k(1-\alpha)^n \qquad \text{(Eq. 4.14)}$$

Eq. 4.14 after some algebraic manipulation leads to:

$$\ell n\left(\frac{d\alpha/dt}{(1-\alpha)^n}\right) = \ell nA - \frac{E}{R}\frac{1}{T} \qquad \text{(Eq. 4.15)}$$

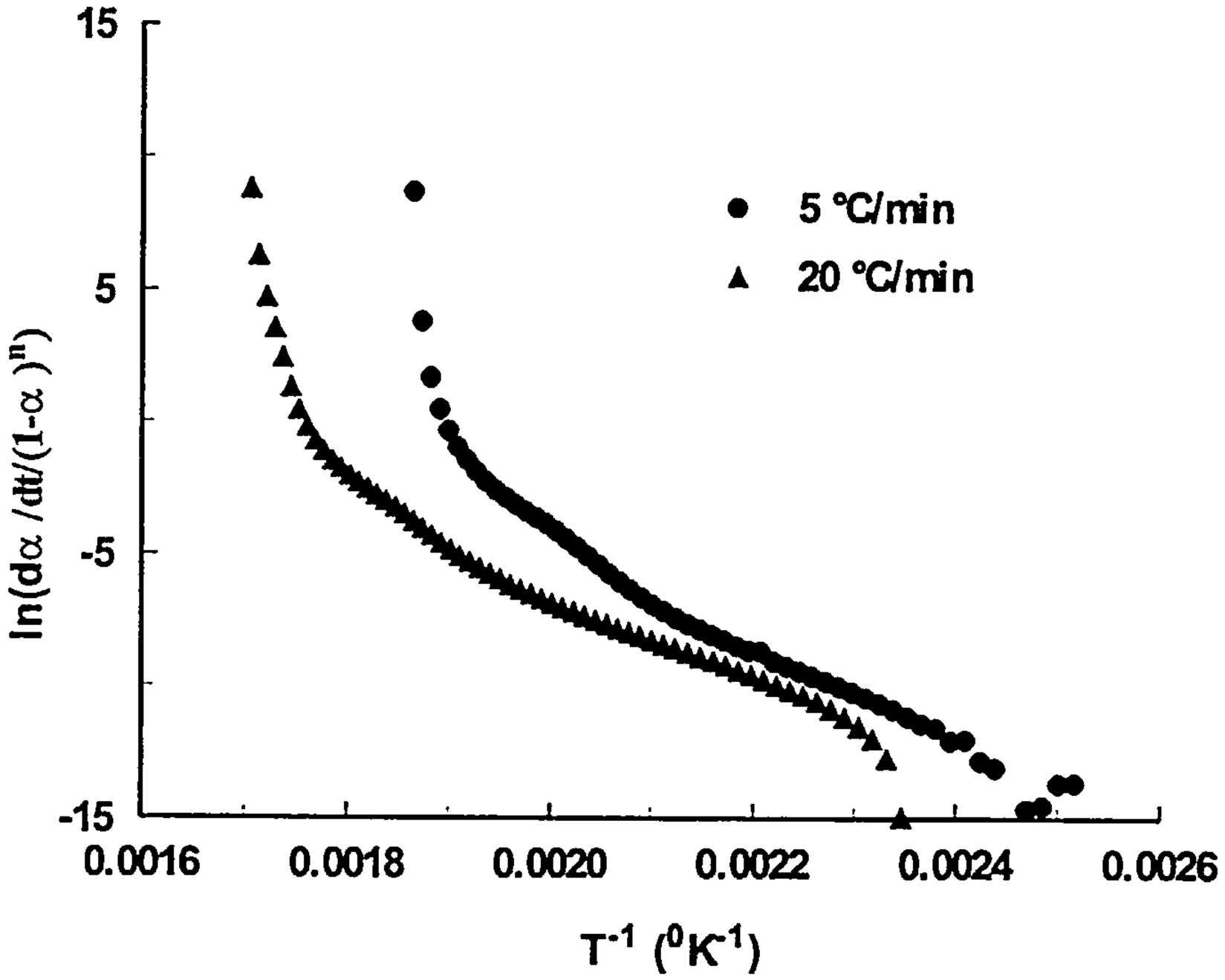

Figure 4.28 *Plots of the left hand side of Eq. 4.15 against the inverse of temperature for the dynamic cure of RMO resin*

A plot of the left hand side of the above equation against the inverse of temperature will give a straight line with slope $-E/R$ and intercept ℓnA. Since the right hand side of this equation is independent of the heating rate, it is evident that plots like this will form a master curve if repeated at different heating rates. A plot like this is shown in Figure 4.28 for the dynamic cure of RMO resin at 5 and 20 °C/min. Apart from the non-linearity that is observed in this plots, there is an absence of a master curve, indicating that nth order kinetics is not followed from this resin system. However, for reasons of investigating the goodness of the fit that would have resulted from such a model, the data of the dynamic cure of RMO resin at the above heating rates were modelled. Linear regression was performed for the intermediate temperature range, where there exists some linearity for both heating rates. The results are shown in Table 4.7 and the corresponding fits in Figure 4.29.

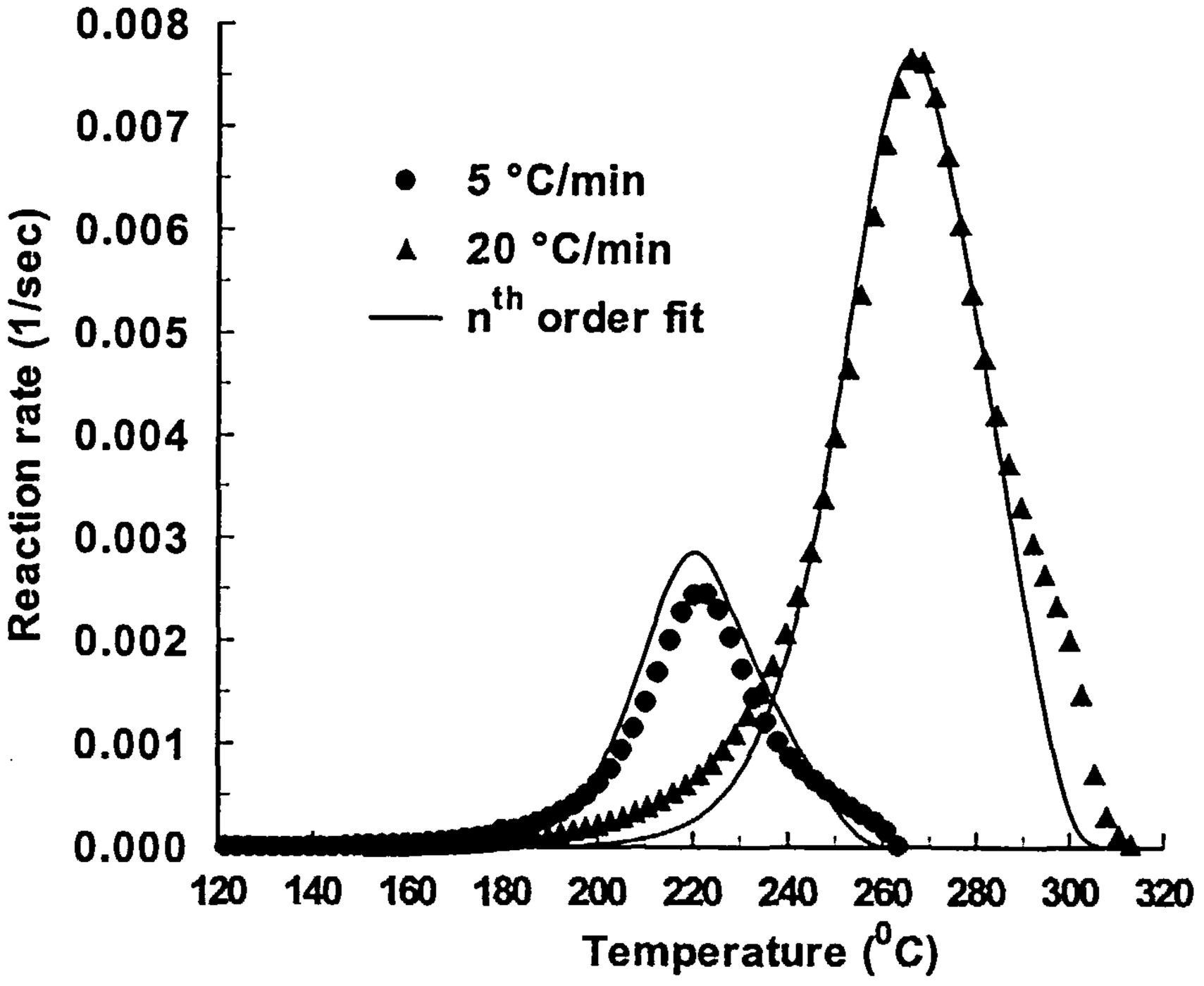

Figure 4.29 *Fit of nth order kinetics of the form of Eq. 4.14 for the dynamic cure of RMO resin. The fitting parameters are shown in Table 4.7*

Table 4.7 *Kinetic parameters for nth order kinetics (Eq. 4.14) fitting of RMO resin dynamic cure*

Fitting model	n	A (sec^{-1})	E (kJ/mol)
$\frac{d\alpha}{dt} = k(1-\alpha)^n$	2.12	$8.3 \cdot 10^{22}$	236

The fit obtained from nth order kinetics, although not strictly appropriate as indicated in the previous paragraphs, gives reasonable agreement with the experimental data. However, it has to be mentioned that the parameters obtained seem rather unreasonable, since the activation energy of 236 kJ/mol is way out of the normal

activation energies obtained for the epoxy/amine reactions (in the range of 50-80 kJ/mol). To clarify this observation the multiple heating rate method of Kissinger [69] and Ozawa [70] was applied. According to this method, for reactions following nth order kinetics, the expression that connects the applied heating rate with the temperature at the maximum reaction rate is:

$$\ell n\left(\frac{\beta}{T_m^2}\right) = \ell n\left(\frac{AR}{E}\right) - \ell og\left(\frac{ART_m^2}{\beta E}\exp\left(-\frac{E}{RT_m}\right)\right) - \frac{E}{R}\frac{1}{T_m} \qquad \text{(Eq. 4.16)}$$

where β is the heating rate, T_m is the temperature at the maximum reaction rate and A, E are the Arrhenius parameters.

A plot of the left hand side of the above equation with respect to the inverse of the temperature at the maximum reaction rate will give a straight line with slope -E/R. This is shown in Figure 4.30 for the resin systems RTM6, RMO and RMO2. The calculated Arrhenius parameters in Table 4.8 are almost identical indicating the similarity in the cure kinetics for all three of the resin systems. The range of activation energies falls in the same value range of the activation energies obtained by the isothermal method for these resin systems and more close to the activation energy of the autocatalytic reaction (see Table 4.5 and Table 4.6).

Application of *n*th order kinetics with the Arrhenius parameters previously obtained gives the fit shown in Figure 4.31 for the RMO resin system cured at 5 °C/min with reaction order $n = 0.61$. It is obvious that although the activation parameters are in the right range, nth order kinetics is not followed by this system.

Table 4.8 *Arrhenius parameters for RTM6, RMO and RMO2 resins by the Ozawa method (Eq. 4.16).*

Resin System	A (min^{-1})	E (kJ/mol)
RTM6	$3.04 \cdot 10^5$	59.14
RMO	$3.08 \cdot 10^5$	59.98
RMO2	$2.28 \cdot 10^5$	58.51

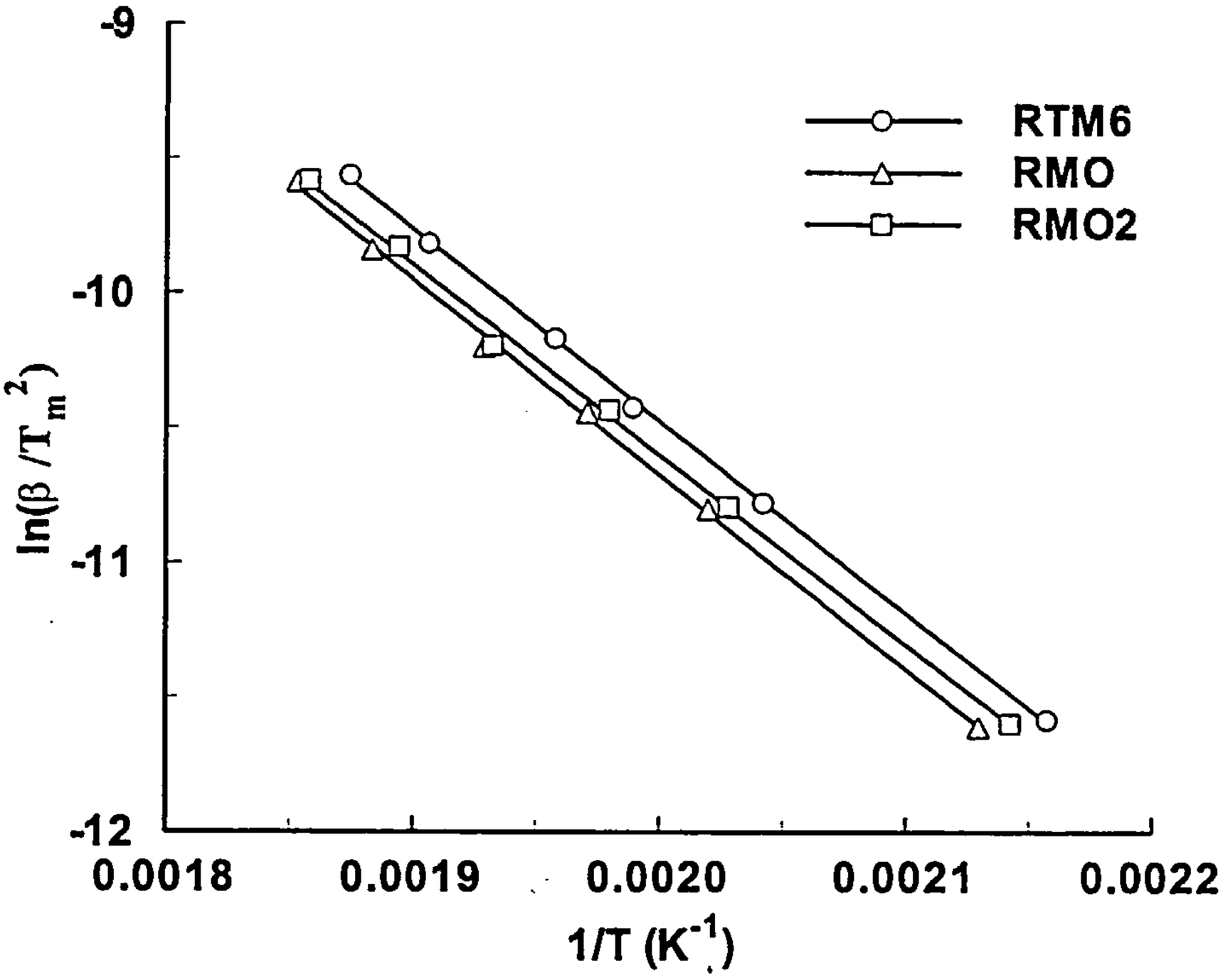

Figure 4.30 *Ozawa plots from Eq. 4.16 for the resin systems RTM6, RMO and RMO2*

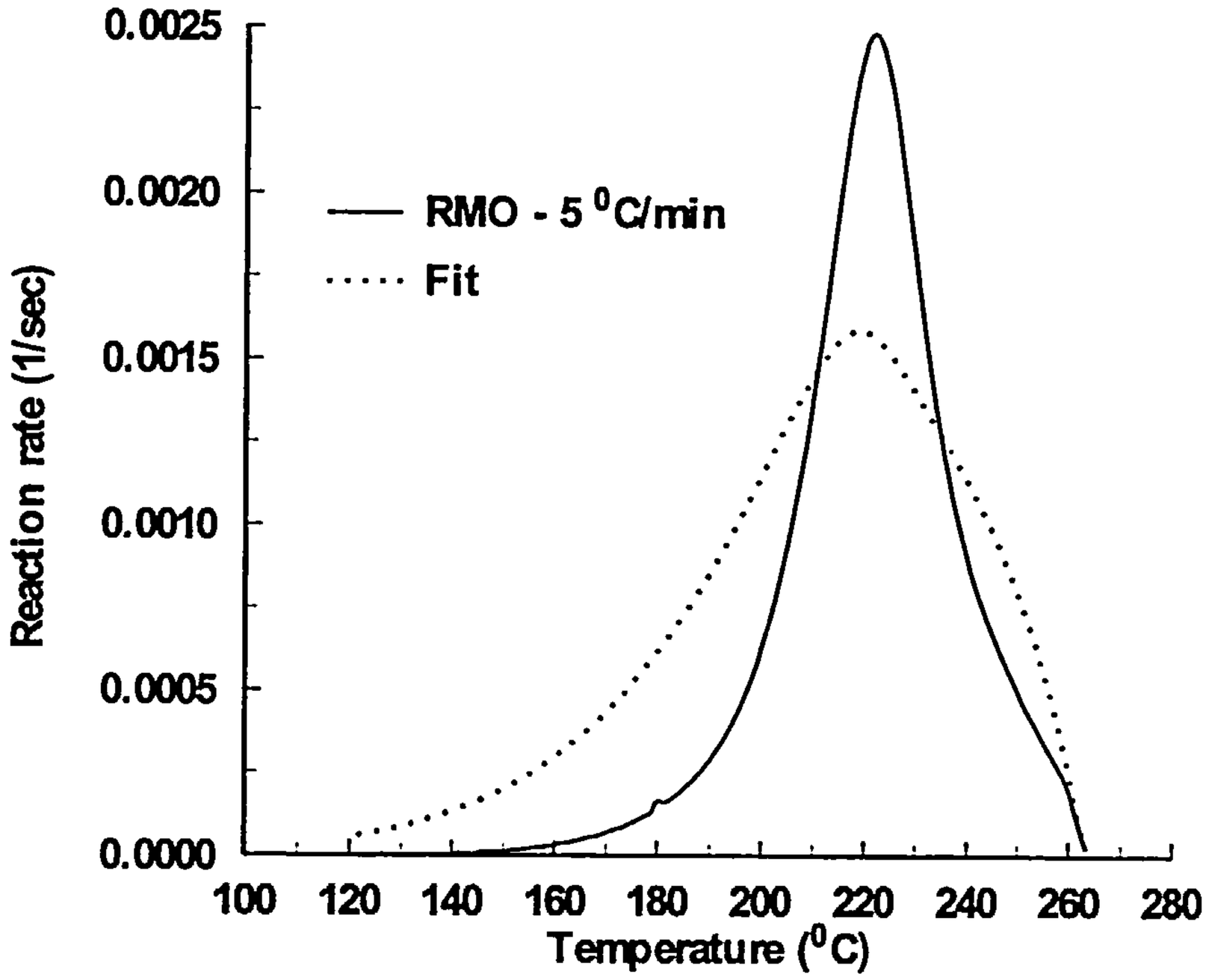

Figure 4.31 *Application of nth order kinetics on RMO resin cured at 5°C/min. Arrhenius parameters from Ozawa method (Table 4.8) and reaction order n = 0.61*

Table 4.9 *Kinetic parameters evaluated by non-linear regression analysis for the dynamic cure of RTM6, RMO and RMO2 resins. The kinetic model given by Eq. 4.9 was used.*

Resin	A_1 (sec^{-1})	E_1 (kJ/mol)	A_2 (sec^{-1})	E_2 (kJ/mol)	m	n
RTM6	$1.68 \cdot 10^4$	74.69	$2.15 \cdot 10^4$	58.37	0.869	1.390
RMO	$2.51 \cdot 10^5$	78.44	$1.42 \cdot 10^5$	57.88	1.204	1.656
RMO2	$8.57 \cdot 10^3$	75.54	$6.77 \cdot 10^4$	53.08	1.268	1.521

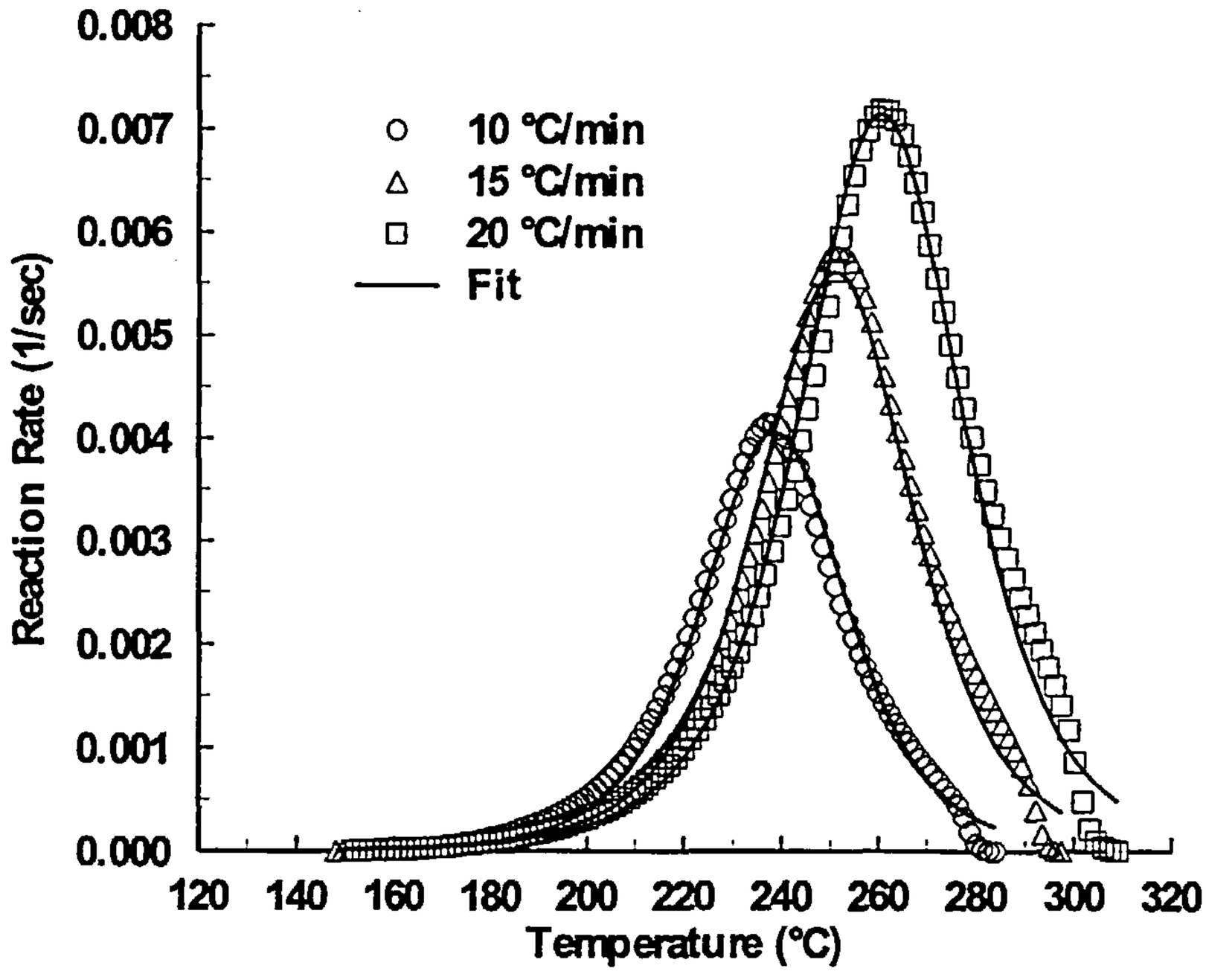

Figure 4.32 *Cure kinetics simulation of RTM6 resin under dynamic conditions. Eq. 4.9 was used for the fit with the parameters given in Table 4.9*

The above discussion on the failure of *n*th order kinetics to describe the cure kinetics of the investigated resin systems suggests that a multiple activated kinetic scheme has to be adopted.

In the beginning of this section, the application of the kinetic model evaluated for the isothermal cure of the resin systems did not give satisfactory results. Reevaluation of the kinetic parameters of the model of Eq. 4.9, this time with the experimental data of the dynamic cure results in a better fit for all heating rates. The goodness of the fit can be seen in Figure 4.32 for the dynamic cure of RTM6 resin at various heating rates. The kinetic parameters were evaluated using non-linear regression analysis on the combined experimental data of all the heating rates used (see Appendix C). The activation energies computed for the isothermal curing were kept unchanged, whereas the rest of the parameters were varied accordingly until the best fit had been achieved.

The set of the parameters that minimised the sum of the squared differences between experimental reaction data and predicted reaction rates was taken as the model-estimated set of parameters. The evaluated parameters are given in Table 4.9 for all resin systems. Comparison between the experimental data and the model prediction shows very good agreement over almost the whole range of the cure, apart from the end of the cure where some deviation is observed. This observation suggests that a different model should be used to accurately fit the experimental data throughout the cure.

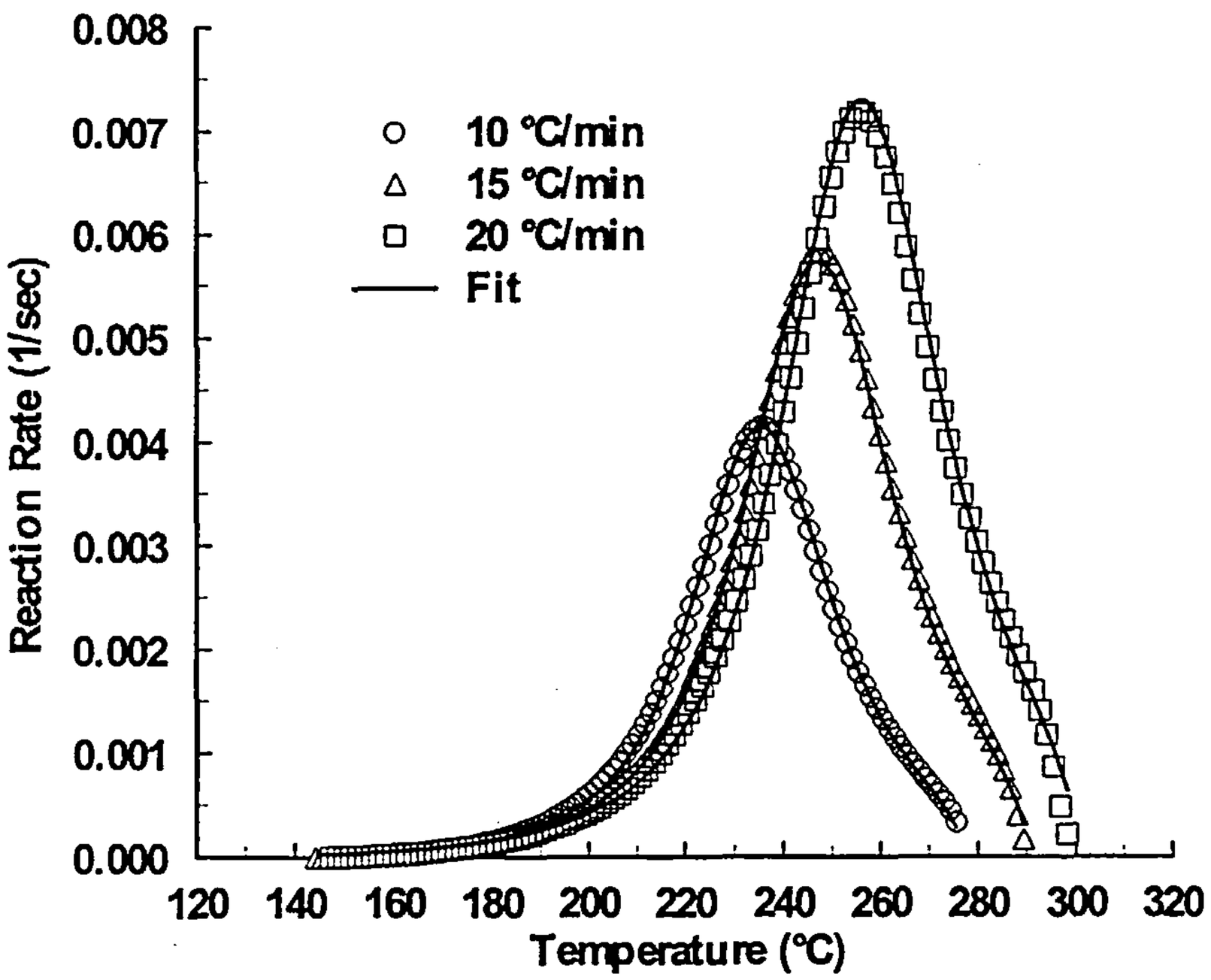

Figure 4.33 *Cure kinetics simulation of RTM6 resin under dynamic conditions. Eq. 4.17 was used for the fit with the parameters given in Table 4.10*

4.4.3 Modified Kinetic Model

The unsuitability of the model given by Eq. 4.9 to fit the experimental data for the entire dynamic cure of the investigated resin systems led to a modification of that model, in order to compensate for the observed deviation towards the end of the cure. The new expression is given by:

$$\frac{d\alpha}{dt} = k_1(1-\alpha)^{n_1} + k_2\alpha^m(1-\alpha)^{n_2} \qquad \text{(Eq. 4.17)}$$

Application of the above model, following the same evaluation procedure of non-linear regression (see Appendix C), resulted in the fit shown in Figure 4.33 - Figure 4.35 for the RTM6, RMO and RMO2 resin systems respectively. The kinetic parameters used for the fits are given in Table 4.10. The fits that were obtained by the modified model show a very good agreement with the experimental results throughout the cure and at all heating rates, justifying the use of Eq. 4.17 as the most appropriate cure kinetics model for these resin systems.

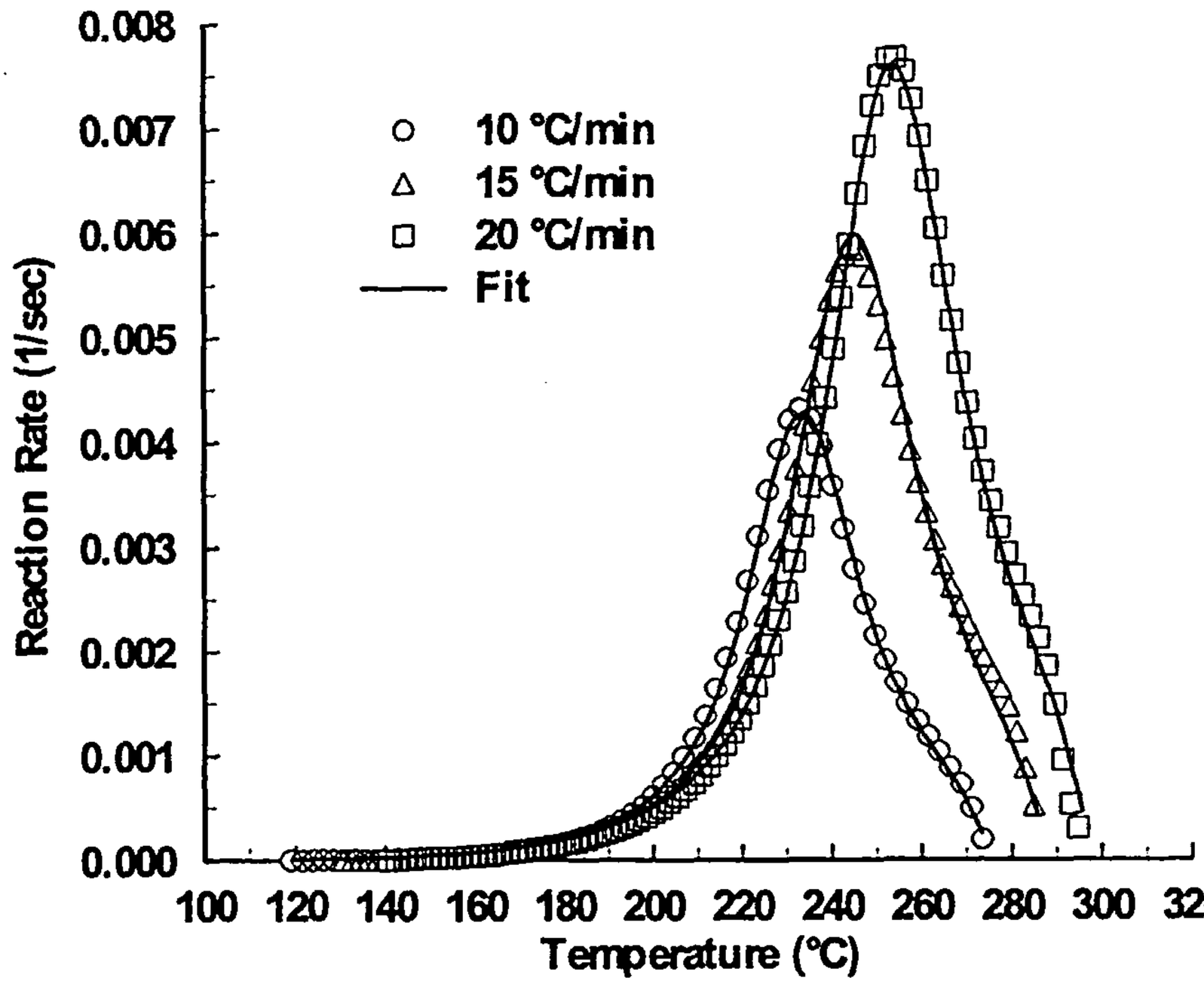

Figure 4.34 *Cure kinetics simulation of RMO resin under dynamic conditions. Eq. 4.17 was used for the fit with the parameters given in Table 4.10*

Table 4.10 *Kinetic parameters evaluated by non-linear regression analysis for the dynamic cure of RTM6, RMO and RMO2 resins. The kinetic model given by Eq. 4.17 was used.*

Resin	A_1 (sec^{-1})	E_1 (kJ/mol)	A_2 (sec^{-1})	E_2 (kJ/mol)	m	n_1	n_2
RTM6	$2.60 \cdot 10^4$	74.69	$5.78 \cdot 10^4$	58.37	1.217	0.449	1.786
RMO	$4.24 \cdot 10^4$	78.44	$2.13 \cdot 10^5$	57.88	1.668	0.519	2.221
RMO2	$1.13 \cdot 10^4$	75.54	$9.04 \cdot 10^4$	53.08	1.495	0.449	1.845

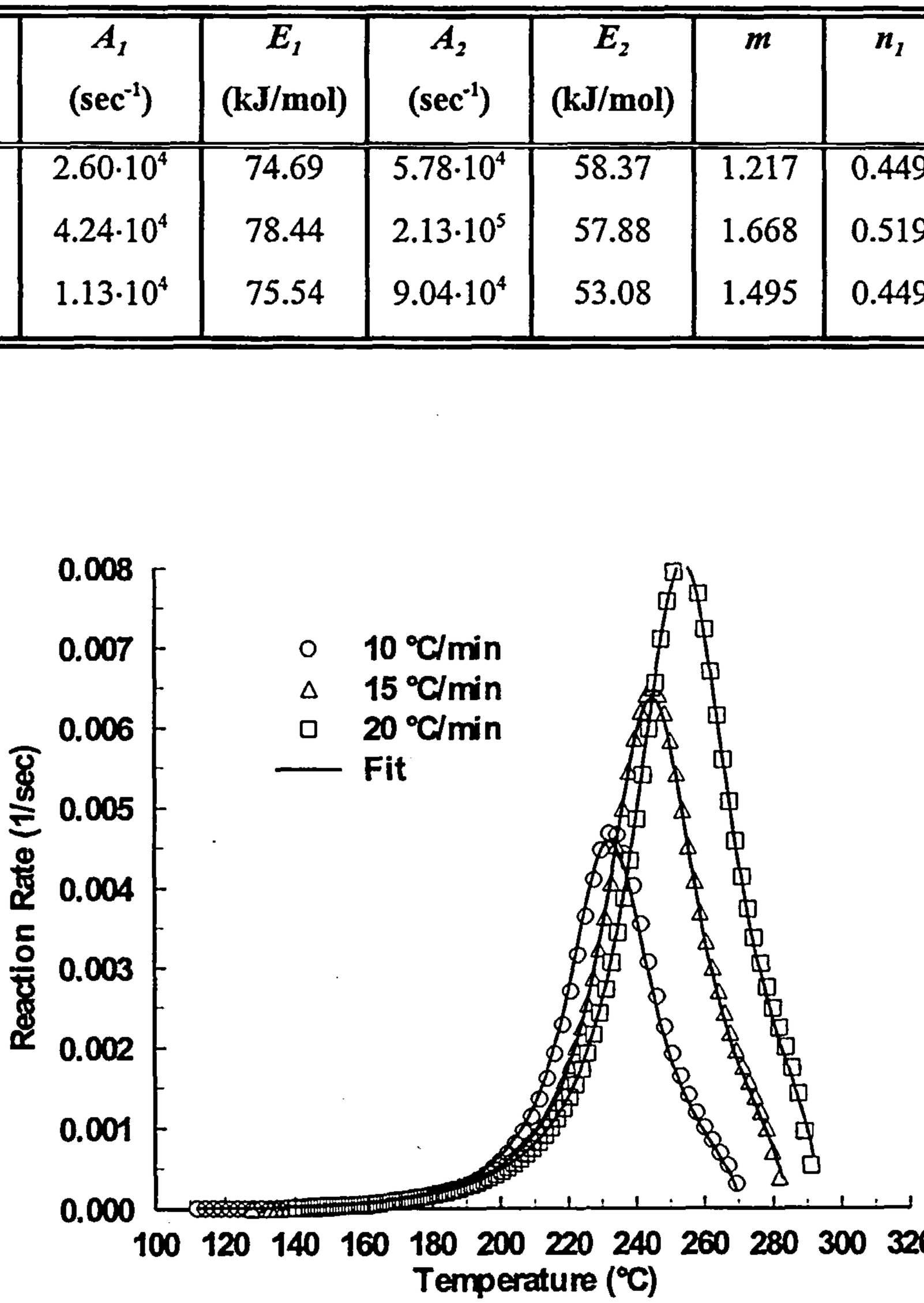

Figure 4.35 *Cure kinetics simulation of RMO2 resin under dynamic conditions. Eq. 4.17 was used for the fit with the parameters given in Table 4.10*

4.4.4 Cure Kinetics Modelling of 934 Resin

In the previous sections, the cure kinetics of the resin systems RTM6, RMO and RMO2 were investigated as a whole, since all three systems exhibit the same overall reaction mechanism. In this section the reaction kinetics of the last system, 934 resin, will be investigated. This system should follow a different reaction mechanism since it contains various catalysts which accelerate the amine-epoxy and epoxy-epoxy reactions in various ways. The catalysts contained in the commercial 934 resin are in the form of BF_3 salts. In Section 2.2.2 a complete description of the way these catalysts interact with the reacting system was given. The catalytic nature of the reaction should in principle give rise to the non-OH-catalysed reactions. For that reason, a simple *n*th order reaction scheme was first applied to the isothermal experimental data of 934 resin. The conversion profile of 934 resin cured under isothermal conditions at 130, 140, 150 and 160 °C is shown in Figure 4.36.

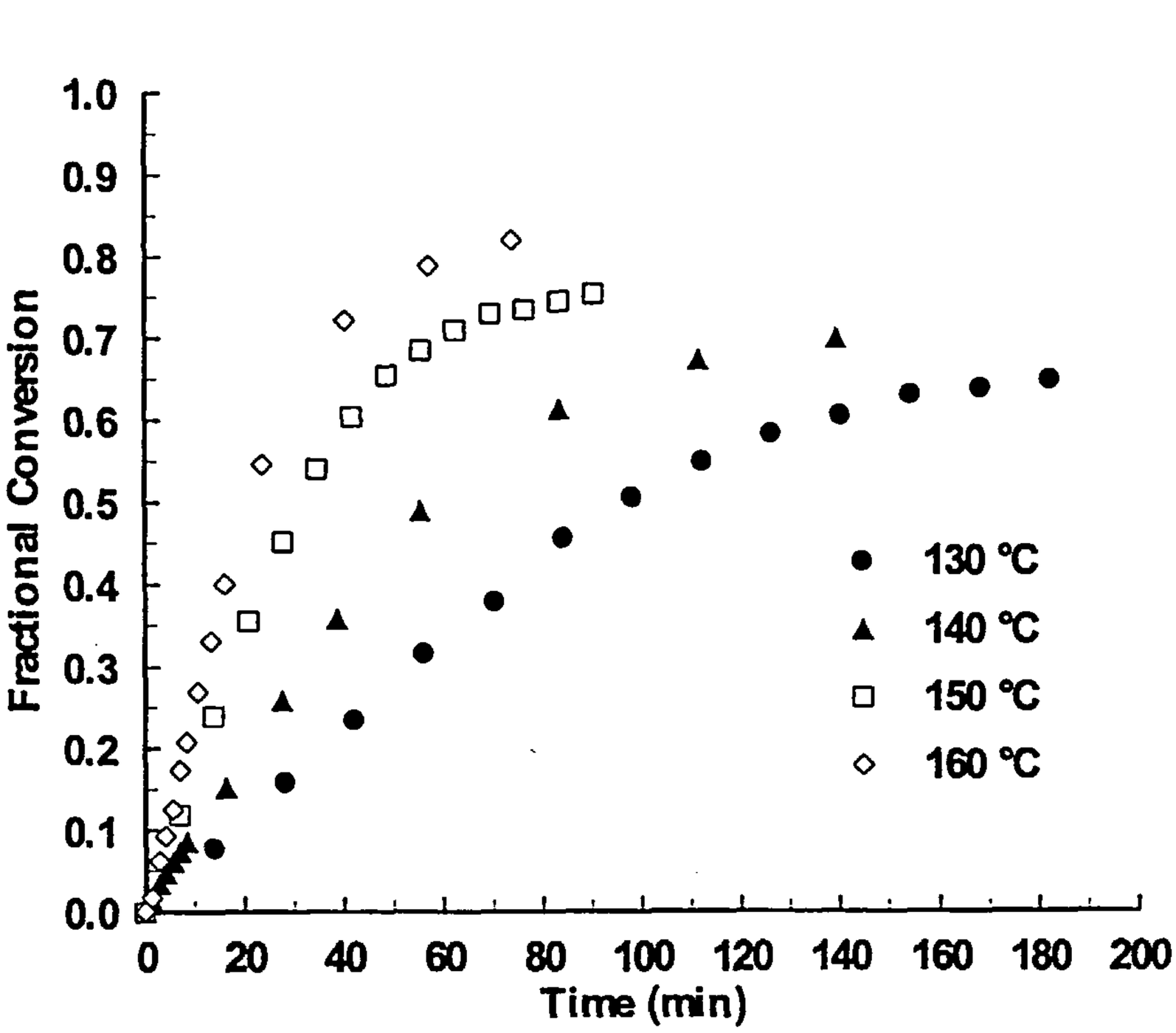

Figure 4.36 *Conversion profile of 934 resin under isothermal conditions*

For a reaction that follows *n*th order kinetics (see Eq. 4.14), integration of the reaction rate under isothermal conditions will give:

$$\frac{(1-\alpha)^{n-1}-1}{n-1} = kt \qquad \text{(Eq. 4.18)}$$

A plot of the left hand side of Eq. 4.18 against the cure time t will give a straight line with slope k. These plots were constructed for the four temperatures used in this investigation. The reaction order n was varied accordingly until a straight line with the highest correlation coefficient R^2 had been achieved. Combined results from all the isothermal experimental data were used in order to calculate a unique reaction order for all the cure temperatures. Data manipulation was made for levels of conversions up to 50% in order to avoid interference with diffusion at the later stages of the cure.

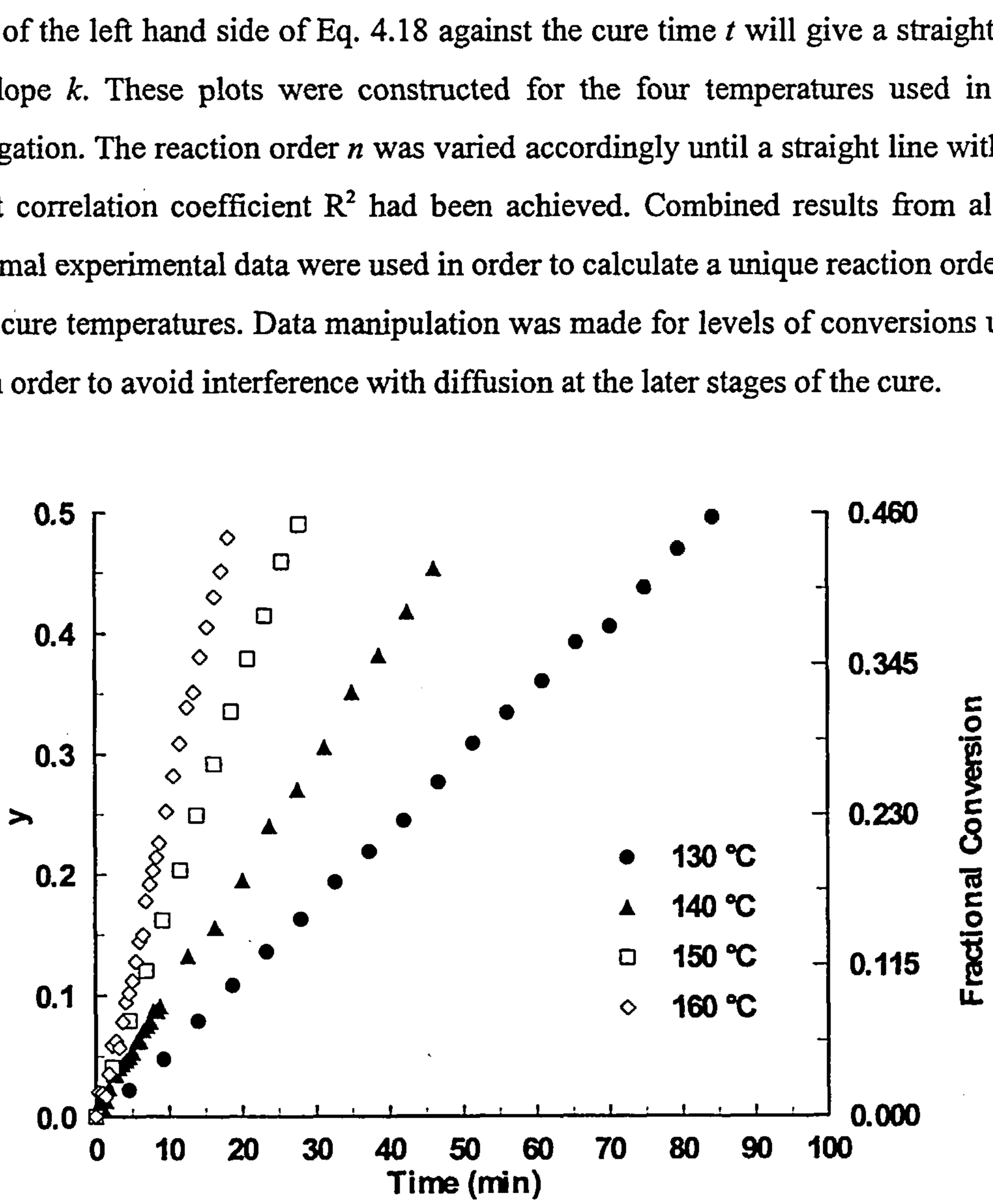

Figure 4.37 *Plots of the left hand side of Eq. 4.18 (= y) as a function of cure time at various temperatures for the isothermal cure of 934 resin. The right hand side axis indicates the level of conversion*

The plots from Eq. 4.18 are shown in Figure 4.37 and the computed parameters in Table 4.11. The Arrhenius dependence of the reaction rate constant was investigated by plotting ℓnk as a function of the inverse of the cure temperature. This plot is shown in Figure 4.38 and the calculated Arrhenius parameters in Table 4.11.

Comparison of the evaluated parameters with the ones obtained for the cure of the other three resin systems (see Table 4.5 and Table 4.6), shows that there is a very good agreement between the activation energy of the cure reaction of 934 resin and the activation energy of the non-catalysed epoxy/amine addition reaction of RTM6, RMO and RMO2 resin systems. This observation suggests that the catalyst in 934 resin favours the non-OH-catalysed reactions. This catalysis is reflected in the conversion profiles of 934 resin (see Figure 4.36). Differentiation of these profiles will produce the reaction rate profiles, which are shown in Figure 4.39. As can be seen in this figure, a continuous decrease in the reaction rate at all cure temperatures is observed. This suggests that there is an absence of autocatalytic behaviour during the isothermal cure of 934 resin. The fit of the *n*th order kinetics model can also be seen in the same figure. The agreement between experimental data and model prediction is very good up to conversion of 50%, where deviation starts to appear because of diffusion limitations of the curing reaction.

Table 4.11 *Kinetic parameters for nth order kinetics (Eq. 4.14) of 934 resin cure under isothermal conditions.*

Temperature (°C)	T^{-1} **(°K^{-1})**	k **(sec^{-1})**	ℓnk
130	0.002481	0.006035	-5.1102
140	0.002421	0.009719	-4.63367
150	0.002364	0.01747	-4.04725
160	0.002309	0.027192	-3.60484

Kinetic Parameters

n	A **(sec^{-1})**	E **(kJ/mol)**
0.298	$2.34 \cdot 10^{7}$	74.03

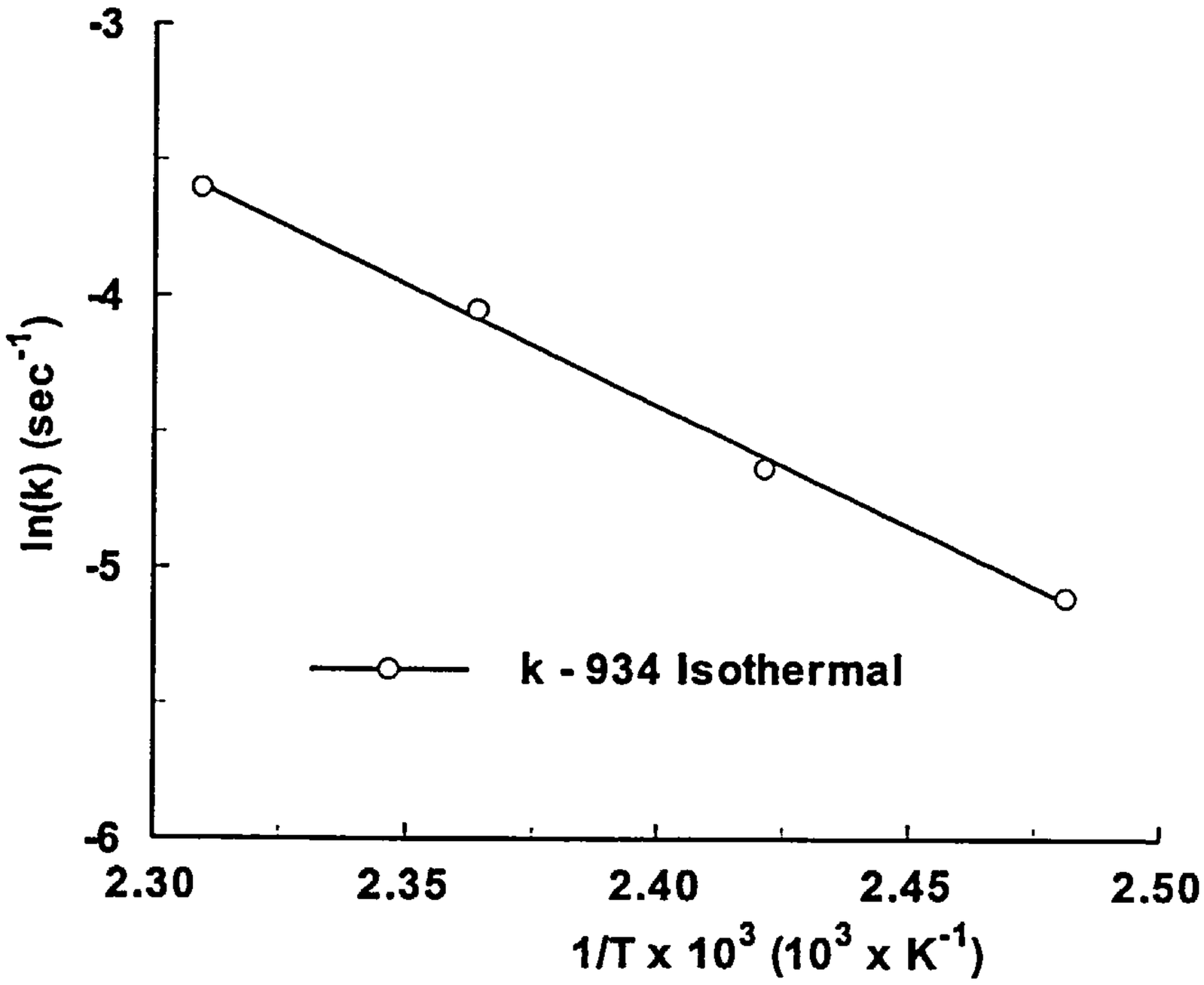

Figure 4.38 *Arrhenius plot of rate constant k of nth order kinetics of isothermal cure of 934 resin*

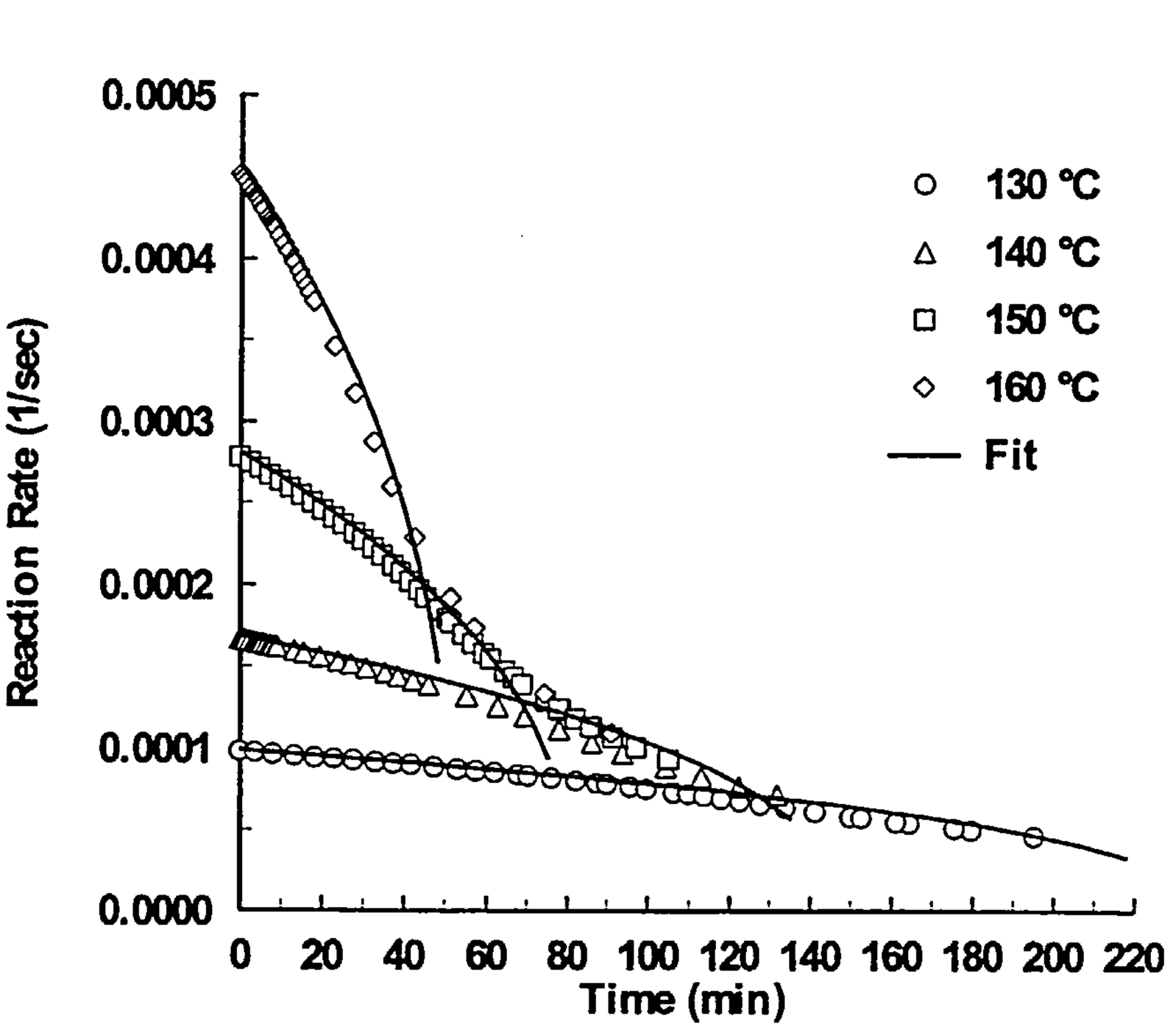

Figure 4.39 *Reaction rate during isothermal cure of 934 resin at various cure temperatures*

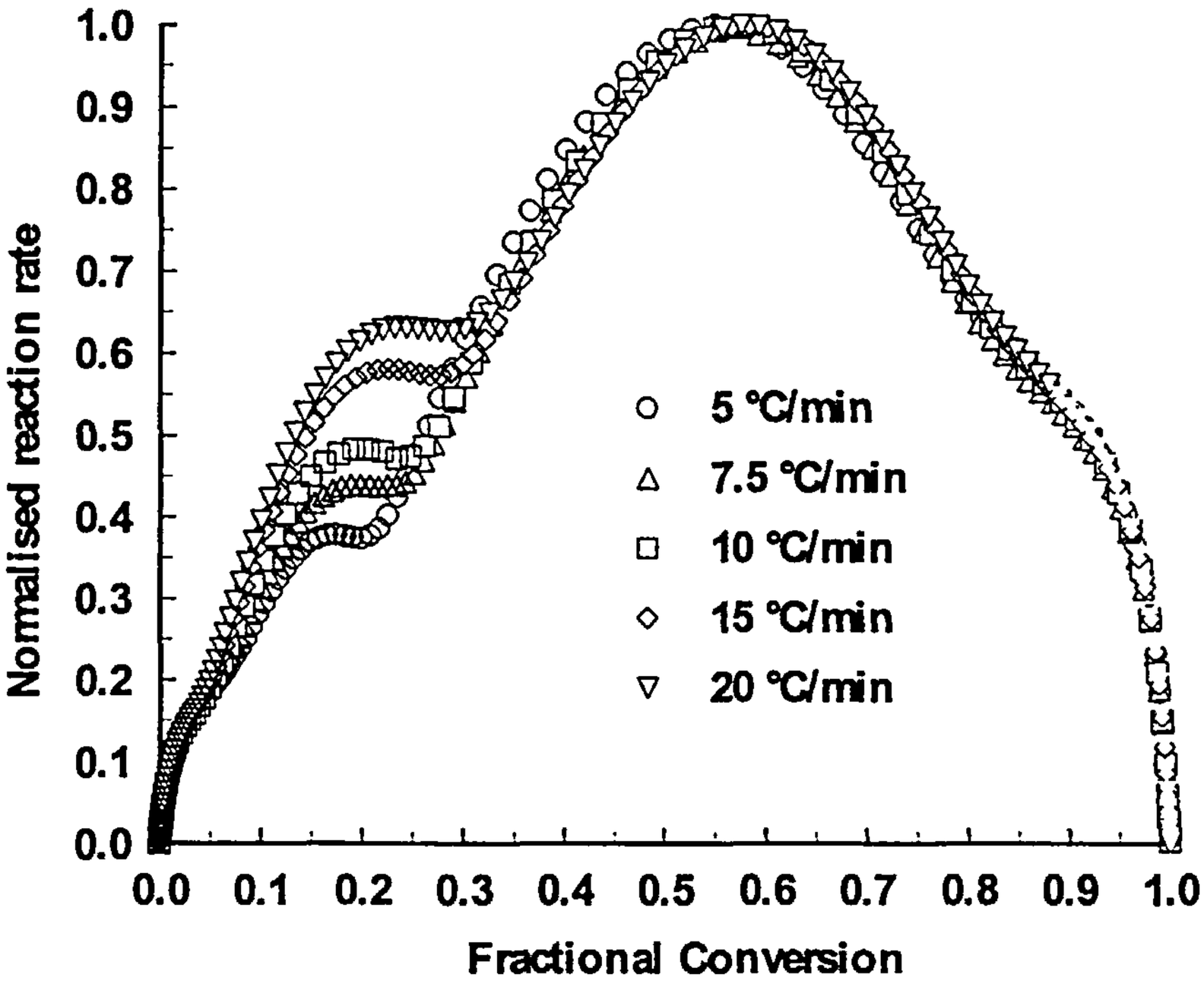

Figure 4.40 *Normalised reaction rate over the maximum reaction rate as a function of the degree of conversion of the dynamic cure of 934 resin at various heating rates*

In the previous sections, the experimental results of the dynamic cure of 934 resin were presented and some preliminary remarks were made (see Section 4.2). The plots of the reaction rate during dynamic cure, as presented in Figure 4.9, show the appearance of multiple peaks. This suggests that a multiple activated reaction mechanism is followed during curing, thus simple *n*th order reaction kinetics is not applicable for this resin under dynamic cure conditions. In Section 4.2 it was suggested that the reaction mechanism might also change as the heating rate changes. To check this, the normalised reaction rates over the maximum reaction rate attained at each heating rate were plotted as a function of the fractional conversion and can be seen in Figure 4.40.

As can be seen in this figure, there exists a master curve that describes the change of the reaction rate with the conversion except from the low conversion area, where this correlation breaks down.

The appearance of multiple peaks in the dynamic thermograms indicates a multiple reaction mechanism during the cure. In order to have an indication of the relative weight of each reaction to the overall reaction rate and to identify which reaction is responsible for the break down of the master curve, peak separation was applied to the experimental data of the dynamic cure of 934 resin. A Gaussian distribution was applied for the peak separation and the number of peaks was limited to four (see Appendix D). The result of the peak analysis for the heating rate of 5°C/min can be seen in Figure 4.41 and the evaluated parameters of the Gaussian distribution for each peak at all heating rates are given in Table 4.12.

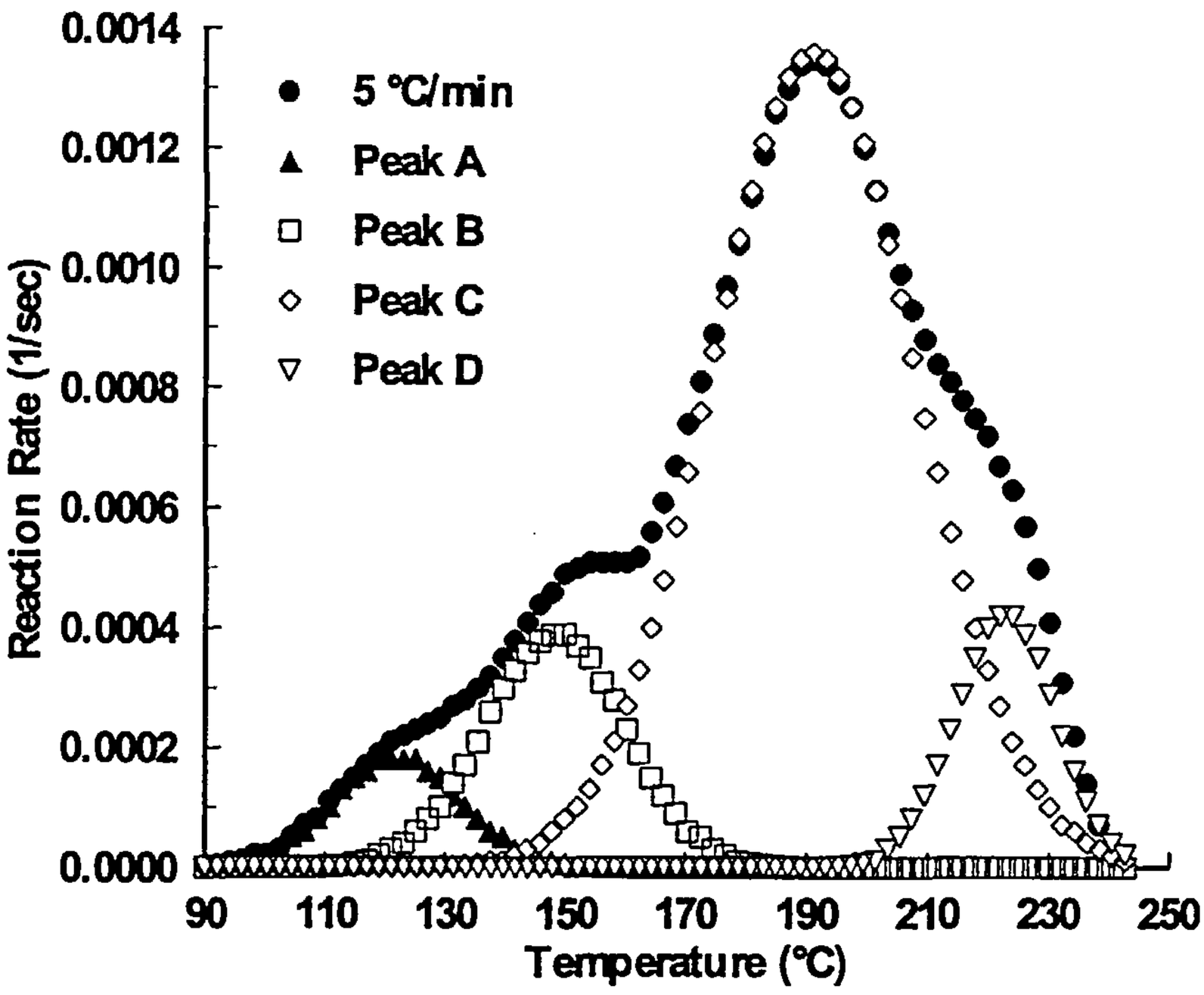

Figure 4.41 *Peak separation of the reaction rate profile of 934 resin under dynamic cure at 5°C/min. Four peaks were identified using Gaussian distribution*

Table 4.12 *Peak separation results of reaction rate of 934 resin cured under dynamic conditions at various heating rates.*

Heating Rate (°C/min)	Peak No	Peak Temperature (°C)	Height (sec^{-1})	Normalised Height over Peak C
5.0	A	124.58	2.08E-04	1.55E-01
	B	149.80	3.80E-04	2.83E-01
	C	191.27	1.34E-03	1.00E+00
	D	223.14	4.10E-04	3.06E-01
7.5	A	129.29	2.95E-04	1.54E-01
	B	156.62	6.67E-04	3.48E-01
	C	197.99	1.92E-03	1.00E+00
	D	230.99	5.92E-04	3.09E-01
10	A	136.49	3.63E-04	1.44E-01
	B	164.31	9.46E-04	3.77E-01
	C	205.39	2.51E-03	1.00E+00
	D	238.52	7.75E-04	3.09E-01
15	A	140.12	5.33E-04	1.53E-01
	B	169.22	1.55E-03	4.45E-01
	C	209.44	3.48E-03	1.00E+00
	D	244.03	1.11E-03	3.19E-01
20	A	143.85	6.43E-04	1.44E-01
	B	174.81	2.19E-03	4.91E-01
	C	214.73	4.46E-03	1.00E+00
	D	249.96	1.49E-03	3.35E-01

In order to examine the relative weights of each peak the peak heights were normalised over the peak height of Peak C. The normalised results can also be seen in the same table. Close examination of these results shows that the peaks A, C, D have the same

contribution to the overall reaction rate at all heating rates, whereas Peak B has variable contribution. The weight of Peak B increases as the reaction rate increases, indicating that the reaction mechanism that is hidden under that peak depends on the heating rate. This observation matches the previous observation of the break down of the master curve in Figure 4.40. The conversion range where the break down was observed is in the temperature range of Peak B.

The results obtained from the peak separation were further used to obtain the cure kinetics of 934 resin. The temperature dependence of each peak at all heating rates was investigated. The method used was the Ozawa method (see Eq. 4.16). The application of Eq. 4.16 to the peak temperatures gave the activation energies and the pre-exponential factors for each peak, thus the Arrhenius parameters of the reaction rate constants for each reaction mechanism responsible for each peak were evaluated.

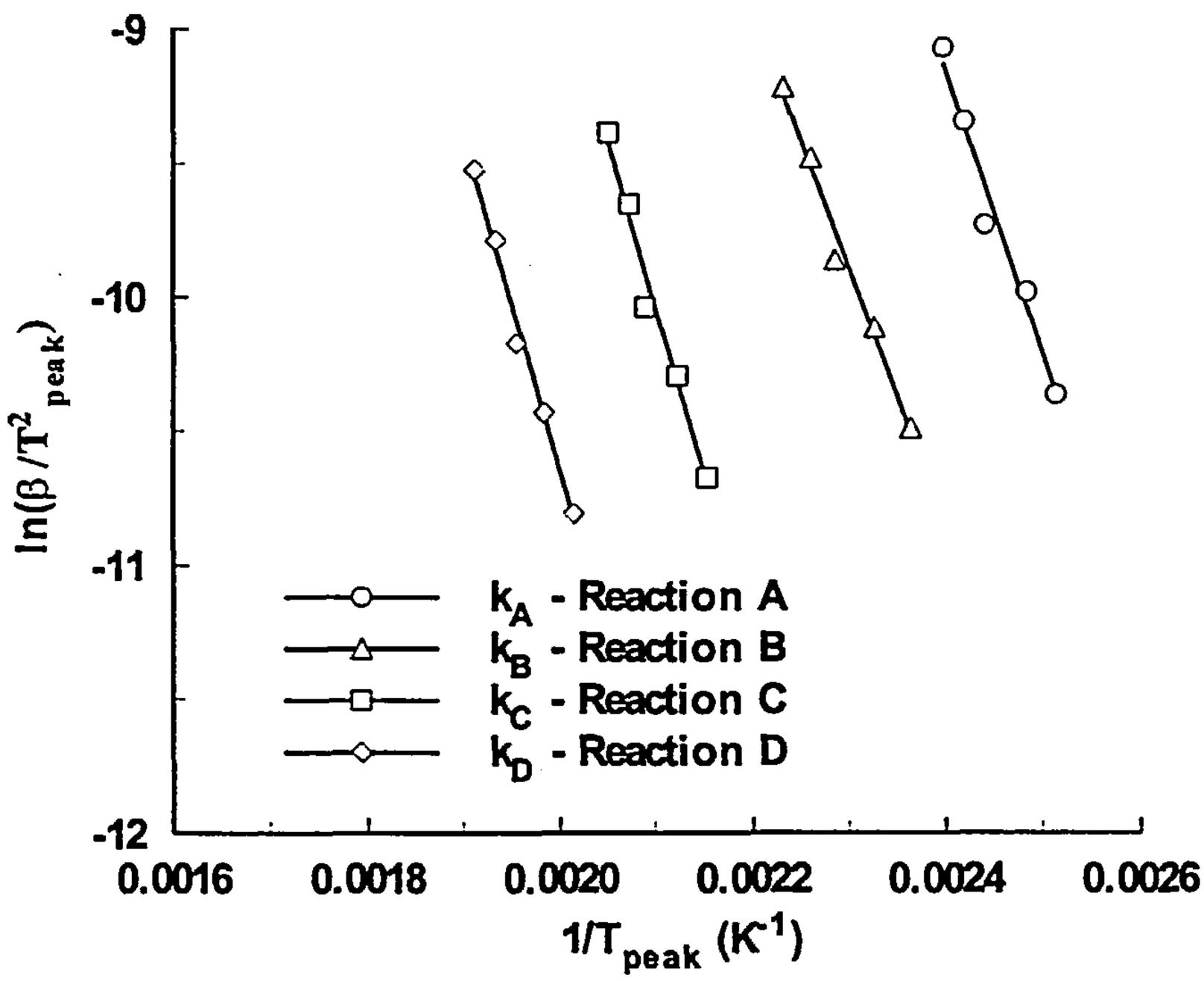

Figure 4.42 *Ozawa plots from Eq. 4.16 for 934 resin. Individual peaks were de-convoluted and the results are shown in Table 4.12*

The Arrhenius plots for each reaction are shown in Figure 4.42 and the respective parameters in Table 4.13. From the above analysis it follows that the overall reaction rate for the dynamic cure of 934 resin can be written as a sum of four individual reaction rates, one for each peak previously identified. Using a simple *n*th order reaction scheme for each individual reaction, the overall reaction rate can be expressed as:

$$\left.\frac{d\alpha}{dt}\right|_{Total} = \sum_{i=1}^{4} W_i k_i (1-\alpha_i)^{n_i} \qquad \text{(Eq. 4.19)}$$

where W_i is the relative weight of each reaction rate to the total. In order to evaluate the parameters of this model, the same non-linear regression technique was used as with the other models. The Arrhenius parameters in Table 4.13 were used in this model in order to evaluate the rest of the parameters (reaction orders n_i and relative weights W_i).

The results were evaluated from the combined experimental reaction rates at all heating rates. Variation of the relative weight of Reaction B was allowed, as this was changing with heating rate (see previous discussion). The evaluated parameters are given in Table 4.13. The relative weight W_2 was found to change linearly with the natural logarithm of the heating rate. The expression derived is shown in the same table.

The fit of the model given by Eq. 4.19 with the kinetic parameters of the above table is shown in Figure 4.43 for the dynamic cure of 934 resin at 5°C/min. The individual reaction rates of the constituent reactions can also be seen in the same figure as separate plots.

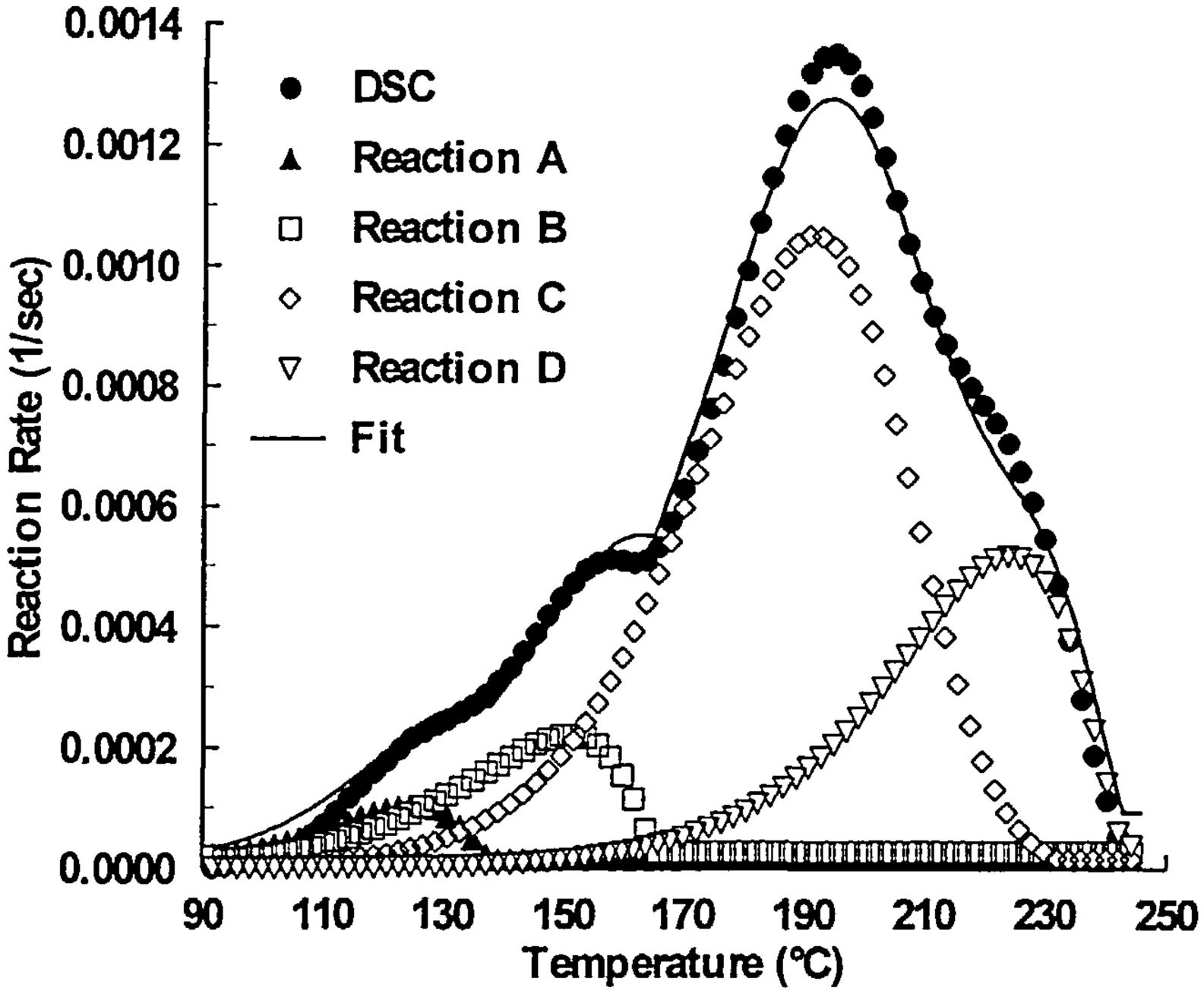

Figure 4.43 *Kinetic modelling of 934 resin cured under dynamic conditions at 5°C/min. Eq. 4.19 was used for the fit with the kinetic parameters shown in Table 4.13*

Table 4.13 *Kinetic parameters evaluated by non-linear regression analysis for the dynamic cure of 934 resin.*

Arrhenius Parameters	**Reaction A**	**Reaction B**	**Reaction C**	**Reaction D**
E_i *(kJ/mol)*	88.11	79.16	102.42	102.93
A_i (sec^{-1})	$2.15 \cdot 10^9$	$2.64 \cdot 10^7$	$1.55 \cdot 10^9$	$2.81 \cdot 10^8$
n_i	0.617	0.560	1.094	0.644
W_i	0.035	-	0.586	0.255
Relative weight factor W_2				
$W_2 = 0.0302 + 0.04 \cdot \ell n(\beta)$				

4.5 Mechanistic Cure Kinetics Modelling

In the previous sections the cure kinetics of all the resin systems were investigated using phenomenological models. Although the results of the modelling were in very good agreement with the experimental data, it was not possible to relate any of the kinetic parameters obtained to specific chemical reactions taking place during the cure. Apart from the activation energies, which fall in the same value range with the activation energies found in the literature for the autocatalytic and the non-catalytic reactions, the rest of the kinetic parameters were just fitting parameters. In order to understand the reaction mechanism that is followed during the cure, a mechanistic model was constructed based on the available information on the different reactions that might take place during the cure. The model was specifically constructed to describe the reaction kinetics of the RTM6 resin from information on the chemical formulation of this resin and on the relative concentrations of the various constituents. This information was given in the description of this resin system in Section 3.1.2.4.

This system is assumed to consist of a tetrafunctional epoxy resin (e.g. TGDDM) and a mixture of two diamine hardeners, A and B respectively. The proposed reaction mechanism for the cure of this epoxy/amine system is:

- Non-catalysed reaction between primary amines and epoxides (primary amine addition reaction)
- Non-catalysed reaction between secondary amines and epoxides (secondary amine addition reaction)
- Non-catalysed reaction between epoxides and hydroxyls (etherification)
- Hydroxyl-catalysed reaction between primary amines and epoxides (primary amine addition reaction)
- Hydroxyl-catalysed reaction between secondary amines and epoxides (secondary amine addition reaction)
- Hydroxyl-catalysed reaction between epoxides and hydroxyls (etherification)

The following symbols will be used to differentiate between the various reactive groups involved in the cure reactions:

- E_1 = diepoxides with both epoxide groups unreacted (e_1)
- E_2 = diepoxides with one reacted epoxide group (e_2)
- A_1 = primary amine groups of hardener A (a_1)
- A_2 = secondary amine groups of hardener A (a_2)
- B_1 = primary amine groups of hardener B (b_1)
- B_2 = secondary amine groups of hardener B (b_2)
- OH = hydroxyl group (h)

The symbols in brackets indicate the normalised concentrations over the initial concentration A_1^0 of the primary amines A_1

The symbol K_{ijk}^z will be used to express the various reaction rate constants. The superscript z and the subscripts i, j, k take the following values:

Superscript z

$\Rightarrow$ 0 for the non-catalysed reactions

$\Rightarrow$ 1 for OH - catalysed reactions

Subscript i

$\Rightarrow$ 1 for reaction of E_1 with other reactive groups

$\Rightarrow$ 2 for reaction of E_2 with other reactive groups

Subscript j

$\Rightarrow$ 1 for reaction of A_1 or A_2 groups of amine hardener A with other reactive groups

$\Rightarrow$ 2 for reaction of B_1 or B_2 groups of amine hardener B with other reactive groups

Subscript k

$\Rightarrow$ 1 for reaction of A_1 or B_1 groups with E_1 or E_2 groups

$\Rightarrow$ 2 for reaction of A_2 or B_2 groups with E_1 or E_2 groups

$\Rightarrow$ 3 for reaction of E_1 or E_2 groups with OH groups

According to the above proposed reaction mechanism and using the nomenclature previously described, the rate equation for the consumption of the primary amine A_1 is:

$$-\frac{dA_1}{dt} = K^0_{111}A_1E_1 + K^0_{211}A_1E_2 + K^1_{111}A_1E_1OH + K^1_{211}A_1E_2OH \qquad \text{(Eq. 4.20)}$$

If we suppose that the rate constants of the reaction between A_1 and E_1 or E_2 can depend on conversion but their ratio must not, that is:

$$\frac{K^1_{211}}{K^1_{111}} = \frac{K^0_{211}}{K^0_{111}} = \beta \qquad \text{(Eq. 4.21)}$$

then Eq. 4.20 becomes, after some algebraic manipulation:

$$-\frac{dA_1}{dt} = A_1\left(E_1 + \beta E_2\right)\left(K^0_{111} + K^1_{111}OH\right) \qquad \text{(Eq. 4.22)}$$

In a similar way, the production rate of the secondary amines A_2 can be written:

$$\begin{aligned}\frac{dA_2}{dt} = {} & K^0_{111}A_1E_1 + K^0_{211}A_1E_2 + K^1_{111}A_1E_1OH + K^1_{211}A_1E_2O \\ & - K^0_{112}A_2E_1 - K^0_{212}A_2E_2 - K^1_{112}A_2E_1OH - K^1_{212}A_2E_2OH\end{aligned} \qquad \text{(Eq. 4.23)}$$

Assuming that the amino groups are independent of each other and that the reaction rate constants in the reaction between primary amine with epoxide and secondary amine with epoxide can depend on conversion but their ratio must not, that is:

$$\frac{K_{112}^{1}}{K_{111}^{1}} = \frac{K_{112}^{0}}{K_{111}^{0}} = \frac{K_{212}^{1}}{K_{211}^{1}} = \frac{K_{212}^{0}}{K_{211}^{0}} = \gamma \qquad \text{(Eq. 4.24)}$$

then, the incorporation of Eqs 4.21 and 4.22 into Eq. 4.23 will give:

$$a_2 = \frac{a_1 - a_1^{\gamma}}{\gamma - 1} \qquad \text{(Eq. 4.25)}$$

By using a similar set of equations to describe the kinetics of the second amine hardener, B, and if we assume that the reactivity of the amine hardener B is δ times that of the amine hardener A and that the initial primary amine ratio between the two amine hardeners is:

$$\frac{B_1^0}{A_1^0} = r_a \qquad \text{(Eq. 4.26)}$$

then, the normalised concentrations of primary and secondary amine groups of hardener B will be given by:

$$b_1 = r_a a_1^{\delta} \quad and \quad b_2 = \frac{r_a\left(a_1^{\delta} - a_1^{\gamma\delta}\right)}{\gamma - 1} \qquad \text{(Eq. 4.27)}$$

The rate equation for the hydroxyl groups is:

$$\begin{aligned}\frac{dOH}{dt} = {} & K_{111}^{0}A_1E_1 + K_{211}^{0}A_1E_2 + K_{111}^{1}A_1E_1OH + K_{211}^{1}A_1E_2OH \\ & + K_{112}^{0}A_2E_1 + K_{212}^{0}A_2E_2 + K_{112}^{1}A_2E_1OH + K_{212}^{1}A_2E_2OH \\ & + K_{121}^{0}B_1E_1 + K_{221}^{0}B_1E_2 + K_{121}^{1}B_1E_1OH + K_{221}^{1}B_1E_2OH \\ & + K_{122}^{0}B_2E_1 + K_{222}^{0}B_2E_2 + K_{122}^{1}B_2E_1OH + K_{222}^{1}B_2E_2OH\end{aligned} \qquad \text{(Eq. 4.28)}$$

By using the above equations and integration, the expression for the normalised hydroxyl concentration becomes:

$$h = h_0 + 2(1+r_a) - \frac{1}{\gamma - 1}\left[(2\gamma - 1)a_1 - a_1^{\gamma} + r_a(2\gamma - 1)a_1^{\delta} - r_a a_1^{\gamma\delta}\right] \quad \text{(Eq. 4.29)}$$

where h_0 is the initial concentration of OH groups normilised over A_1^0.

In the same way, if we suppose that the ratio of the rate constants between the etherification reaction and the primary amine addition is constant, that is:

$$\frac{K_{103}^1}{K_{111}^1} = \frac{K_{103}^0}{K_{111}^0} = \frac{K_{203}^1}{K_{211}^1} = \frac{K_{203}^0}{K_{211}^0} = \varepsilon \quad \text{(Eq. 4.30)}$$

integration of the rate equation for the consumption of epoxide groups, will give:

$$x = \frac{1}{e_0}\left(C_0 - C_1 a_1 - C_2 a_1^{\gamma} - C_3 a_1^{\delta} - C_4 a_1^{\gamma\delta} - C_5 \ell n a_1\right) \quad \text{(Eq. 4.31)}$$

where: x = epoxide fractional conversion given by $x = \frac{E_0 - E}{E_0}$ where E_0 is the initial epoxide concentration and E is the concentration of epoxide groups at time t

e_0 = initial epoxide concentration E_0, normalised over A_1^0

$C_0 = C_1 + C_2 + C_3 + C_4$

$$C_1 = \frac{(2\gamma - 1)(1 - \varepsilon)}{\gamma - 1}$$

$$C_2 = \frac{\varepsilon - \gamma}{\gamma(\gamma - 1)}$$

$$C_3 = r_a + \frac{\gamma\, r_a}{\gamma - 1} - \frac{\varepsilon\, r_a(2\gamma - 1)}{\delta(\gamma - 1)}$$

$$C_4 = -\frac{r_a(\gamma\ \delta - \varepsilon)}{\gamma\ \delta(\gamma - 1)}$$

$$C_5 = \varepsilon\left[h_0 + 2(1 + r_a)\right]$$

The expression that connects the concentrations of the individual epoxide groups E_1 and E_2 is given by:

$$e_2 = \frac{1}{\beta - 1}\left[e_1 - \left(\frac{e_0}{2}\right)^{1-\beta} e_1^{\beta}\right] \qquad \text{(Eq. 4.32)}$$

Since: $E = 2E_1 + E_2$, the fractional conversion of epoxide groups can also be written as:

$$x = 1 - \frac{1}{e_0}\left\{2e_1 + \frac{1}{\beta - 1}\left[e_1 - \left(\frac{e_0}{2}\right)^{1-\beta} e_1^{\beta}\right]\right\} \qquad \text{(Eq. 4.33)}$$

Eqs. 4.31 and 4.33 can be numerically solved in respect to a_1 and e_1, for a given conversion x. These values can then be used to obtain the concentrations for the other reactive groups as given by the above described expressions.

Using the above equations for the concentrations of the various reactive groups, the rate expression for the epoxide consumption can be written as:

$$\frac{dx}{dt} = \left(a_1 + \gamma\ a_2 + \delta\ b_1 + \gamma\ \delta\ b_2 + \varepsilon\ h\right)\left(e_1 + \beta\ e_2\right)\left(L + L'h\right) \qquad \text{(Eq. 4.34)}$$

where: $L = \frac{A_1^0}{e_0} K_{111}^0$ *and* $L' = \frac{\left(A_1^0\right)^2}{e_0} K_{111}^1$

The main expressions that describe the kinetics of RTM6 are Eqs. 4.25, 4.27, 4.29, 4.31 - 4.34 . These equations contain seven parameters that constitute the input of the kinetic model. These parameters are:

- Parameter h_0: initial hydroxyl concentration
- Parameter r_a: initial primary amine B / primary amine A ratio
- Parameter e_0: initial epoxy groups / primary amine A ratio
- Parameter β: reactivity ratio of mono-reacted diepoxide to unreacted diepoxide
- Parameter γ: reactivity ratio of secondary amine to primary amine
- Parameter δ: overall reactivity difference between amine A and amine B
- Parameter ε: reactivity ratio between etherification reaction and primary amine addition reaction

Parameter h_0 was set equal to zero since the initial concentration of hydroxyls in a resin is usually very low. Parameter r_a was given in Section 3.2.1.4 and is equal to 0.62. From the overall epoxy groups / amino-hydrogens ratio r ($r = 0.85$, see Table 3.3) and r_a, parameter e_0 can be calculated and is equal to 2.74. The rest of the parameters were evaluated using non-linear regression analysis and simultaneous solution of the system of the kinetic equations.

The evaluation procedure was as follows:

1) Initial guesses of the parameters β, γ, δ, ε
2) Solution of Eqs. 4.31 and 4.33 for a given conversion x in respect to α_1 and e_1 respectively
3) Substitution in the rest of the kinetic equations to obtain α_2, b_1, b_2, e_2, h
4) Repetition of steps 2-3 for all conversions at all temperatures
5) Rearrangement of Eq. 4.34 into the form:

$$\frac{dx}{dt} \Big/ \left(a_1 + \gamma\, a_2 + \delta\, b_1 + \gamma\, \delta\, b_2 + \varepsilon\, h\right)\left(e_1 + \beta\, e_2\right) = L + L'h \qquad \text{(Eq. 4.35)}$$

and determination of L, L' by linear regression of the left hand side of the above expression over h

6) Determination of expected reaction rate
7) Calculation of the sum of squared differences between experimental reaction rate and calculated reaction rate at all times and temperatures
8) Non-linear regression to give new estimates of parameters β, γ, δ, ε
9) Repetition of steps 2 - 8 for the new estimates and termination when the sum of squared differences between experimental reaction rate and calculated reaction rate at all times and temperatures became minimum

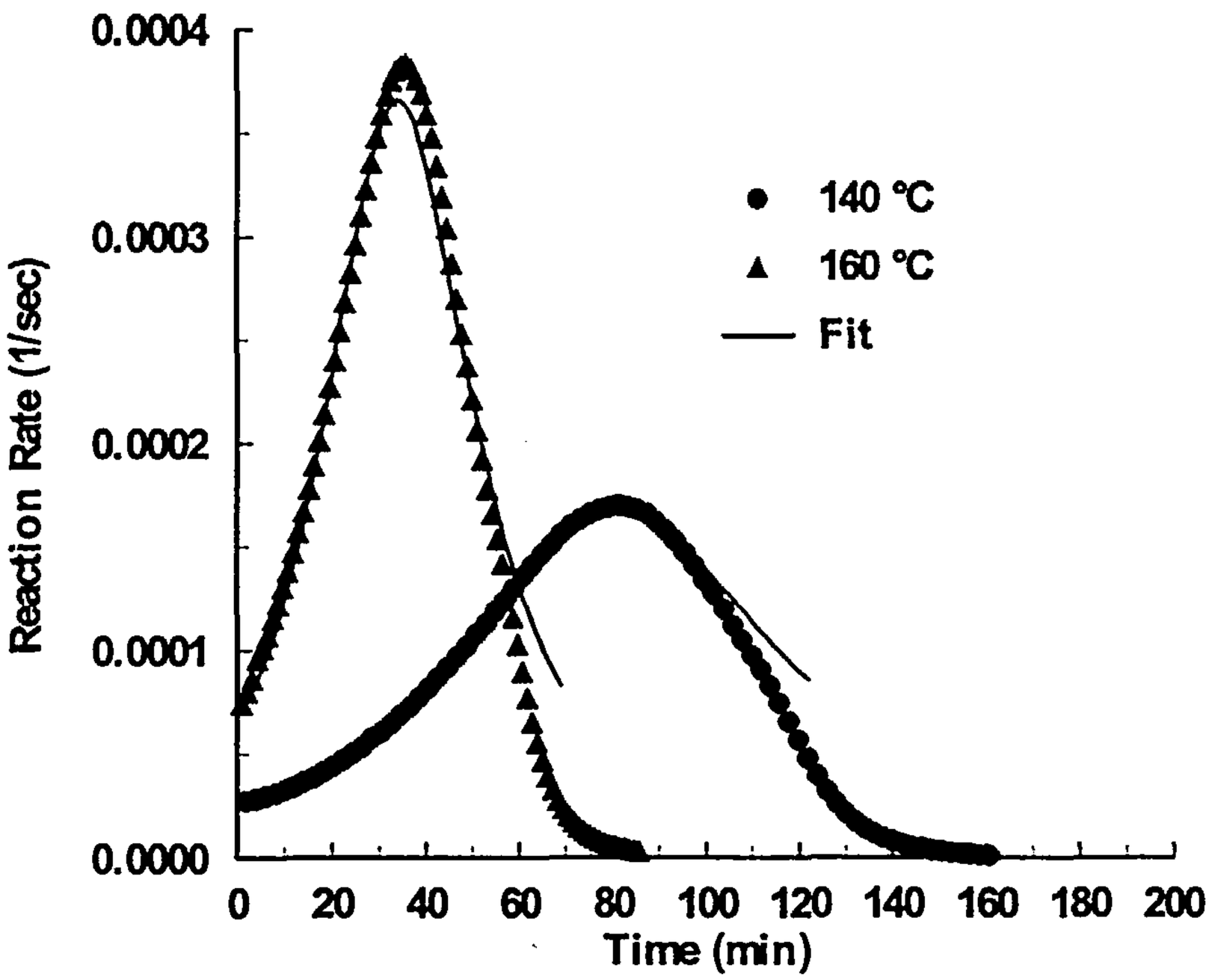

Figure 4.44 *Fit of mechanistic kinetic model to experimental data from isothermal DSC runs of RTM6 resin at 140 and 160°C. Kinetic parameters are given in Table 4.14 in the free estimation section*

The experimental data from the isothermal DSC runs at 140, 160, 170 and 180 °C were used in the above evaluation. The estimated parameters are given in Table 4.14 and the fit of the model for the isothermal cures at 140 and 160 °C is given in Figure 4.44 as plots of the overall epoxide consumption rate against cure time. The fit is very good up to the maximum reaction rate, where deviations start to appear because of diffusion limitations. This was expected since no diffusion control was introduced in the model.

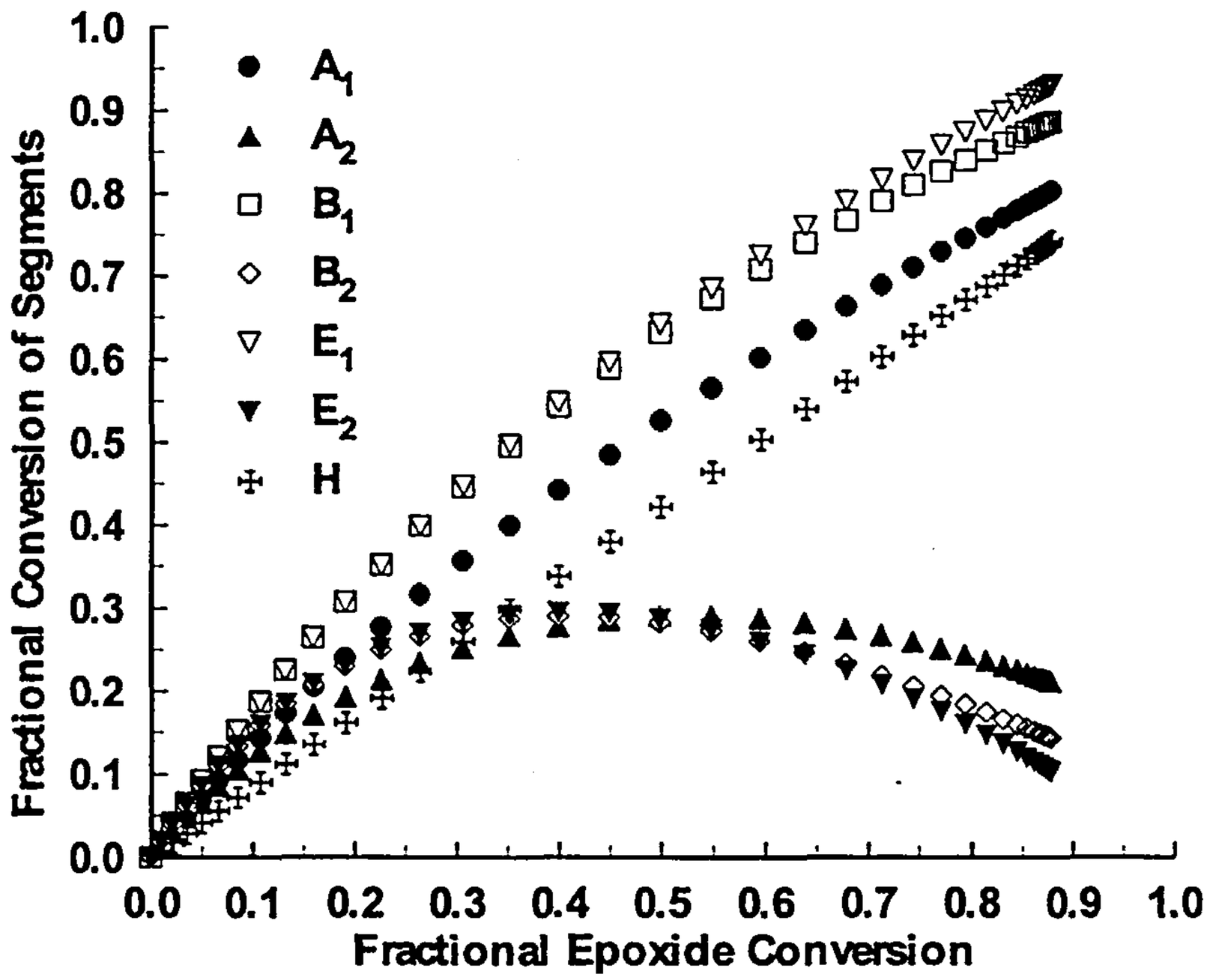

Figure 4.45 *Fractional consumption or production of reactive species against the overall epoxide conversion during the isothermal cure of RTM6 resin at 160°C. Results from the application of the mechanistic kinetic model with the kinetic parameters given in Table 4.14 in the free estimation section*

The concentration profiles of the individual reactive species are given in Figure 4.45 for the cure at 160°C as plots of consumption or production of the individual species against fractional conversion of epoxide groups. These were calculated as follows:

- Primary amine A_1 consumption: Fractional consumption over the maximum number of A_1 which is A_1^0
- Secondary amine A_2 production: Fractional production over the maximum number of A_2 that could be produced, which is A_1^0
- Primary amine B_1 consumption: Fractional consumption over the maximum number of B_1, which is B_1^0
- Secondary amine B_2 production: Fractional production over the maximum number of B_2 that could be produced, which is B_1^0
- Unreacted diepoxide E_1 consumption: Fractional consumption over the maximum number of unreacted diepoxides, which is $E_0/2$
- Mono-reacted diepoxide E_2 production: Fractional production over the maximum number of E_2 that could be produced, which is $E_0/2$
- Hydroxyl OH production: Fractional production over the maximum number of OH that could be produced, which is $2(A_1^0+B_1^0)$

Some preliminary remarks can be made by studying the plots in the last figure. Both primary (A_1, B_1) and secondary (A_2, B_2) amine consumption is incomplete and so is the epoxide (E_1, E_2) consumption. This is expected, since the reaction is hindered due to diffusion limitation that stop the reaction before completion. The amine consumption is also in lower overall levels because of the higher initial amounts of these species in the reactive system. The secondary amines increase in concentration in the initial stages of the cure because of the faster reaction between primary amines and epoxides in respect to the secondary amine/ epoxide reaction. At a level of about 40 to 50% epoxide conversion, the secondary amines start to disappear faster than they are produced, showing an overall reduction in concentration. This reduction starts at about 60% consumption of both the primary amines. The absence of the etherification reaction, which was depicted by the very low value of the parameter ε, can also be seen in this figure. The hydroxyl production (H) follows a linear dependence on the epoxide conversion. If the etherification reaction was present, then the epoxide would have been consumed without any change in the net concentration of the hydroxyls; during etherification, one hydroxyl group is consumed and immediately another one is

produced. The absence of etherification was expected, firstly because the amines are in excess and secondly because of the low cure temperatures.

Table 4.14 *Kinetic parameters of mechanistic kinetic model for the isothermal cure of RTM6 resin.*

Free Estimation

h_0	e_0	r_a	β	γ	δ	ε
0	2.74	0.62	1.75	1.64	1.37	$6 \cdot 10^{-3}$

Activation Energies (kJ/mol)

Autocatalytic Reaction	Non-Catalytic Reaction
54.62	74.57

Bounded Estimation ($\gamma \leq 0.5$)

h_0	e_0	r_a	β	γ	δ	ε
0	2.74	0.62	2.29	0.5	0.98	$8 \cdot 10^{-3}$

Activation Energies (kJ/mol)

Autocatalytic Reaction	Non-Catalytic Reaction
55.53	79.88

Another interesting aspect of the above analysis is the high value of the parameter γ, which refers to the different reactivities between the amino hydrogens in the primary and the secondary amines. If the reactivities were equal then this parameter should have been equal to 0.5 since there are two hydrogens in the primary amine compared to the secondary amine where only one exists. In the literature there is evidence that a negative substitution effect is operative between primary and secondary amines [151], that means that this parameter should be lower than 0.5. This is true for a reaction between a bifunctional epoxy with amines. In our case the epoxy resin is tetrafunctional. That means that cyclisation reactions are very likely to take place (see Section 2.2.2). These kinds of reactions were not included in the above analysis

because the analytical solution of the differential system would have been very difficult if not impossible. Despite that, it is certain that the secondary amines would have a higher reactivity than usual because of the ease of the cyclisation reaction.

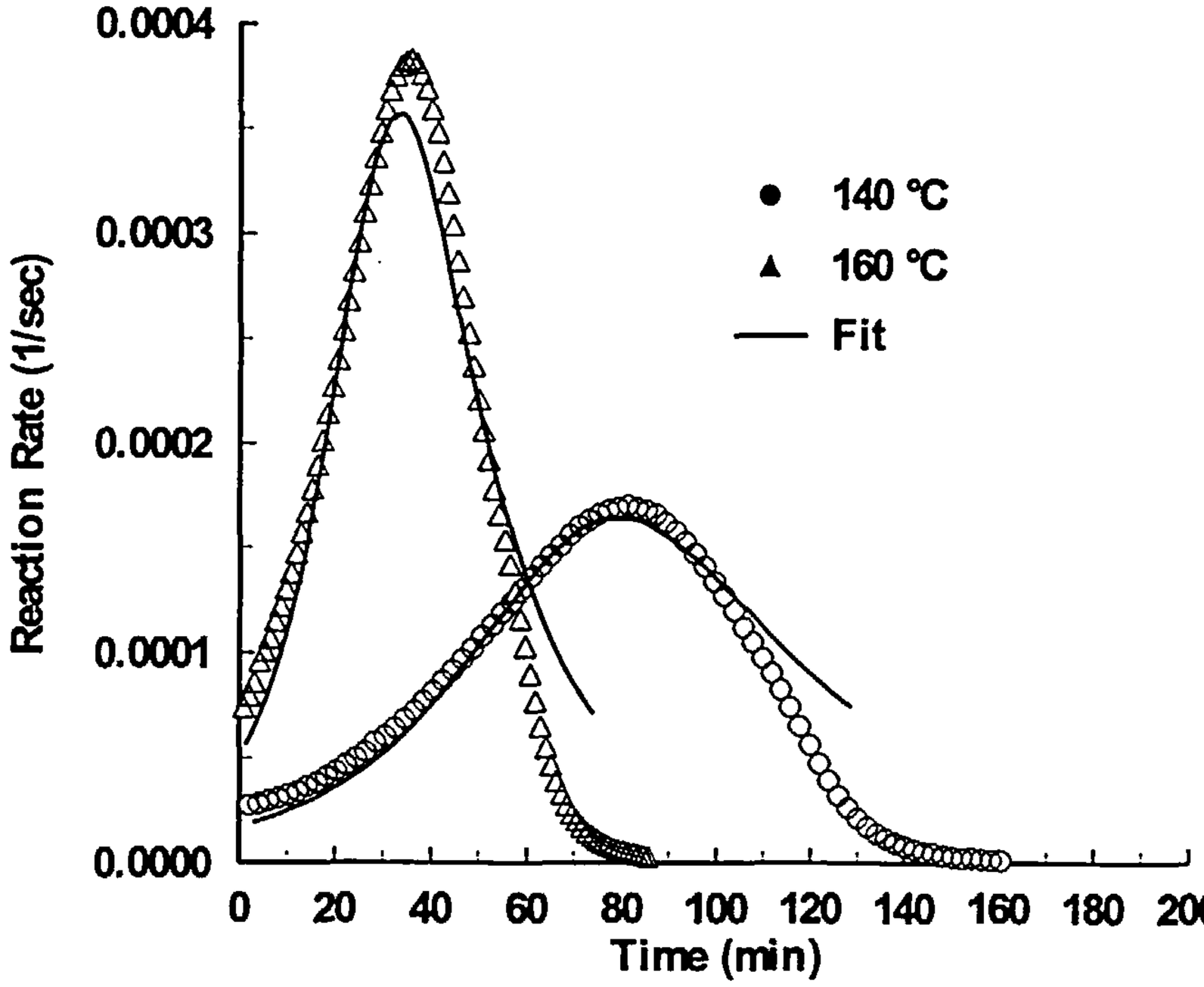

Figure 4.46 *Fit of the mechanistic model on the isothermal data of RTM6 resin at 140 and 160 °C. The kinetics parameters used are given in Table 4.14 in the bounded estimation section*

To take into account the cyclisation without disturbing the differential system, the parameter γ was allowed to take higher values, that is to exhibit a positive substitution effect ($\gamma > 0.5$). To verify this, the evaluation of the model was repeated, this time keeping the parameter γ below 0.5. The results are given in Table 4.14 and the produced fit in Figure 4.46. As can be seen in this figure, the fit is not very good even at low conversions, implying that this parameter has to take higher values. Although the incorporation of cyclisation in parameter γ is not mathematically correct, it was the only way to compensate for it.

The mechanistic model, as presented in the above paragraphs, is described by two different activation mechanisms, one for the non-catalytic reactions and one for the hydroxyl-catalysed reactions. These two different activated mechanisms are represented by the factors L and L' respectively (see Eq. 4.34).

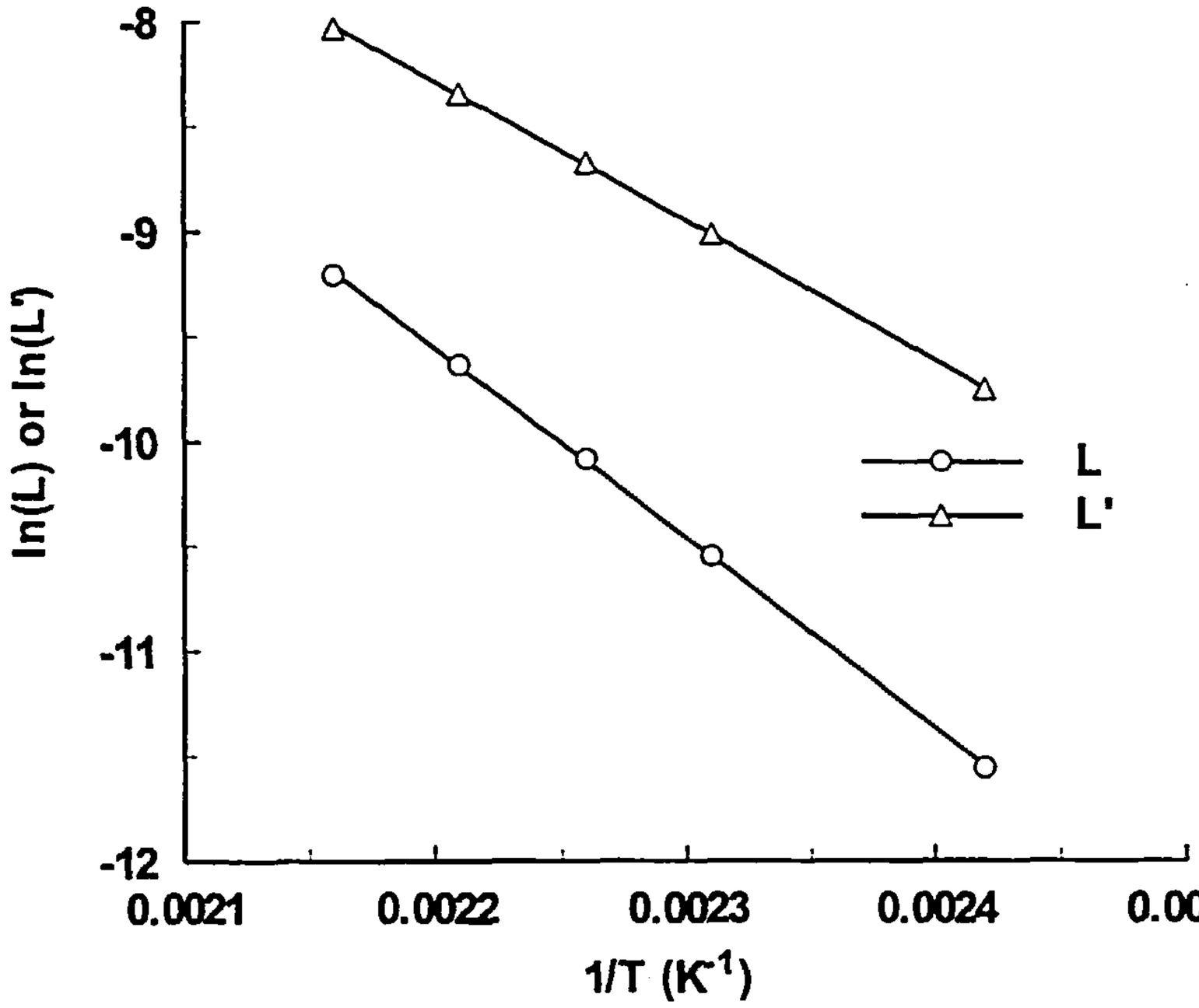

Figure 4.47 *Arrhenius plots of L, L' parameters of Eq. 4.34 for the isothermal cure of RTM6 resin*

The Arrhenius dependence of these parameters is shown in Figure 4.47 and the activation energies in Table 4.14. The values obtained are comparable with values from the literature for epoxy/amine cure and are also comparable with the previously calculated values for these kinds of resin systems (see Table 4.5, Table 4.6 and Table 4.10). Calculation of the true pre-exponential factors was not possible because both the parameters L and L' contain the absolute value of the initial concentration of the primary amines A_1^0, which is unknown.

Chapter Five

5. Glass Transition Advancement During Cure

In the previous chapter the chemical kinetics during the cure of all the resin systems were investigated and adequate models were constructed in order to predict the chemical changes during the cure. In a thermoset cure, the advancement of the reaction affects the structure of the developing three dimensional network in a unique way for each reactive system. This network is highly correlated to the chemical constituents of the resin system and the reaction path that is followed during the cure. The conditions that are applied during the curing of the resin, usually different temperatures, affect the development of the network in a unique way. The most sensitive property of the material that reflects the structure development during the cure is the glass transition temperature (T_g). This chapter, describes the development of expressions, that will allow us to predict the changes in the T_g of the resin during the cure. Correlation of the T_g changes with the chemical composition of the resin and the degree of conversion will be used as a tool for the model development.

5.1 Experimental Results of T_g Measurements

The T_g advancement during the cure of all the resin systems studied was investigated according to the method described in Section 3.2.1.4. The profile of this advancement at different cure temperatures for all resin systems is shown in Figure 5.1 - Figure 5.4 as plots of T_g against cure time. The arrows drawn in the figures indicate the

vitrification points at each cure temperature as these are defined by $T_g = T_{cure}$. As can be seen in these figures the final T_g is different at each cure temperature. This is a result of the diffusion control, which becomes significant after the vitrification point has been reached. The reaction is hindered because of structural limitations, which become more pronounced at low cure temperatures, where the energy supplied to the curing system is lower. The shape of the plots follows a similar trend with the conversion profiles (see Section 4.4.1), indicating the high correlation between these two properties. Any changes in the cure advancement have a direct impact on the T_g of the resin. An observation that was made during the evaluation of the T_g and the conversion at the later stages of the cure was the accuracy of the measurement. The endothermic shift at the T_g region is easily depicted by the DSC, whereas the residual heat of reaction is not. This makes the determination of the T_g more accurate than the calculation of the conversion at these stages of the cure.

The interrelation between T_g and cure advancement can be seen in Figure 5.5 - Figure 5.8, where the cure advancement has been plotted against the glass transition temperature. The one to one relationship that exists is evident by the master curve that is formed. For all resin systems, there exists a unique master curve, independent of the cure temperature, that is followed throughout the cure. The significant scatter in the data at the later stages of the cure is attributed to the lower sensitivity of the DSC to measure the level of conversion compared to the sensitivity of the T_g measurement.

The relationship between T_g and conversion has the form (see Section 2.3):

$$T_g = T_{g0} + \frac{\left(\frac{E_x}{E_m} - \frac{F_x}{F_m}\right) T_{g0} \alpha}{1 - \left(1 - \frac{F_x}{F_m}\right) \alpha} \qquad \text{(Eq. 5.1)}$$

where α is the conversion at the glass transition temperature T_g, T_{g0} is the glass transition temperature of the uncrosslinked prepolymer, E_x/E_m is the ratio of lattice energies for the crosslinked and uncrosslinked polymer and F_x/F_m is the corresponding ratio of segmental mobilities.

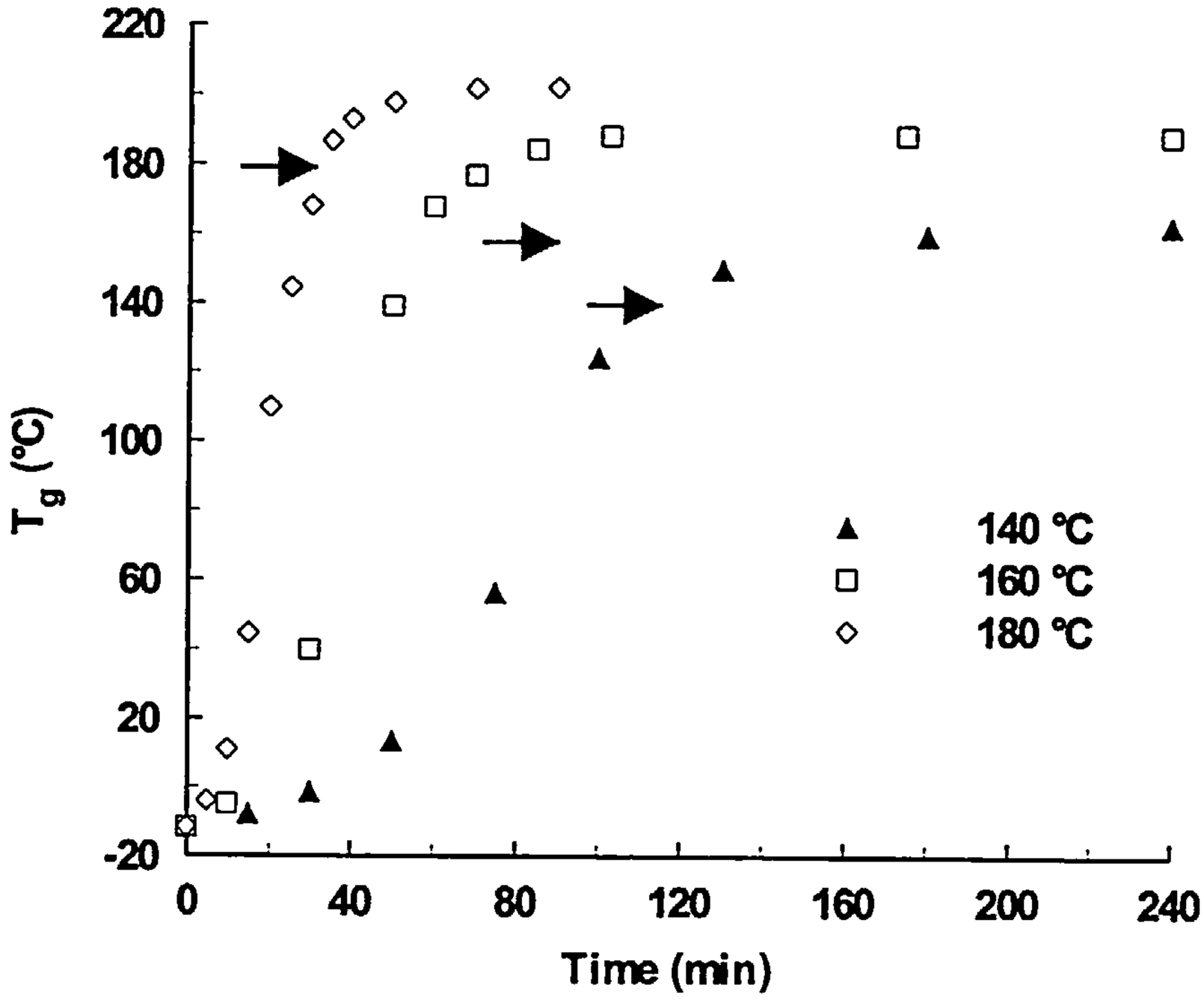

Figure 5.1 *Glass transition temperature profile of RTM6 resin at different cure temperatures*

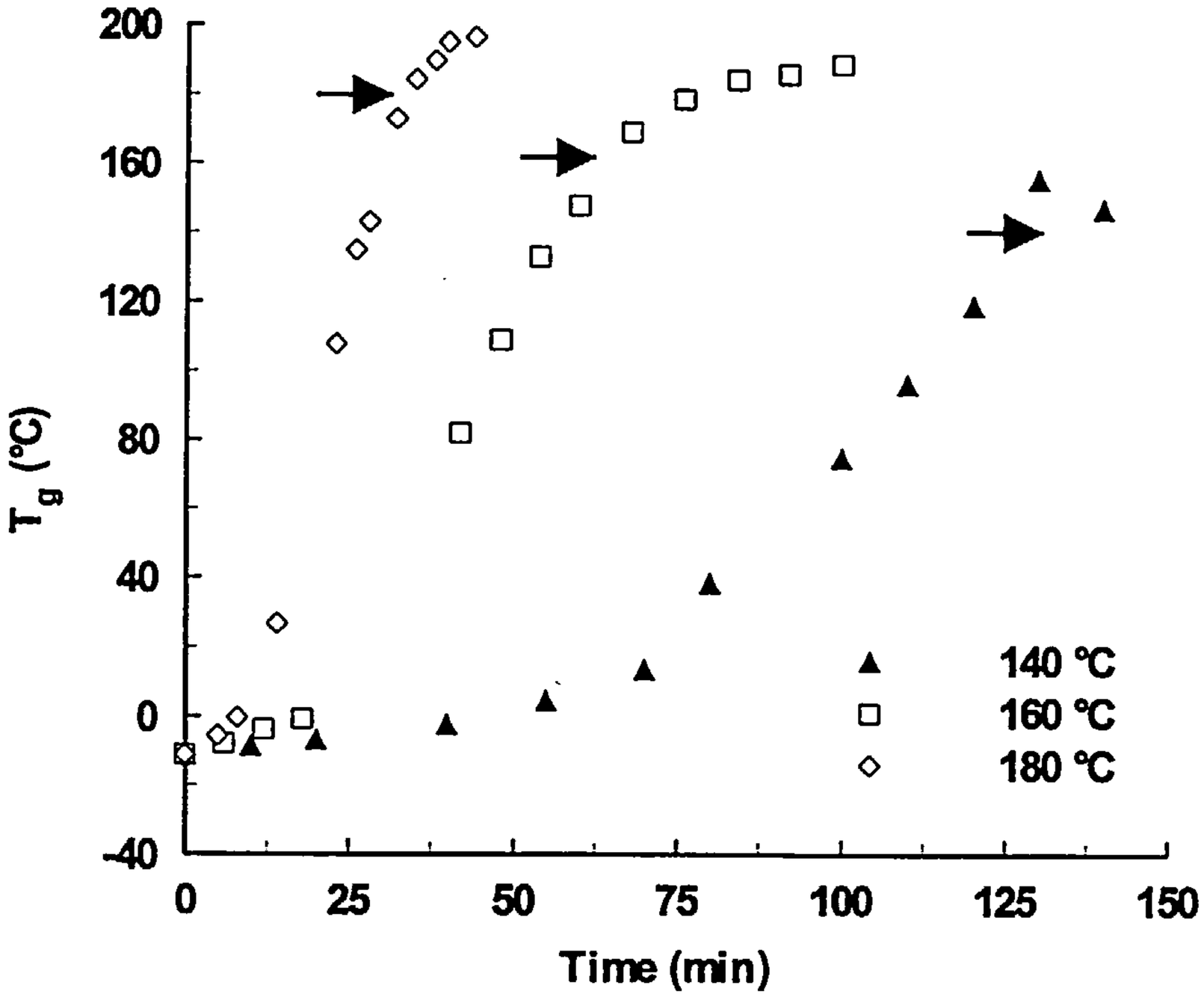

Figure 5.2 *Glass transition temperature profile of RMO resin at different cure temperatures*

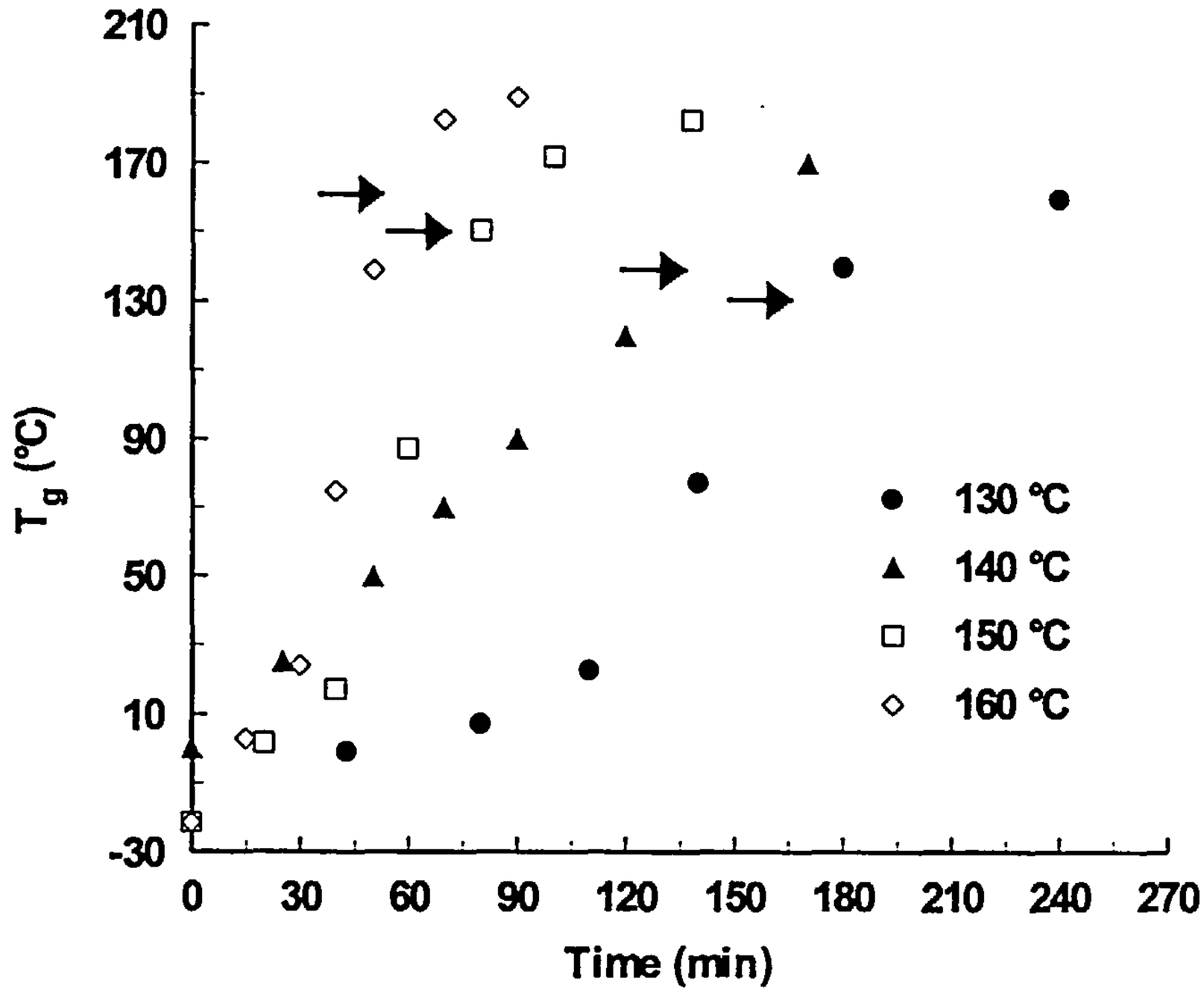

Figure 5.3 *Glass transition temperature profile of RMO2 resin at different cure temperatures*

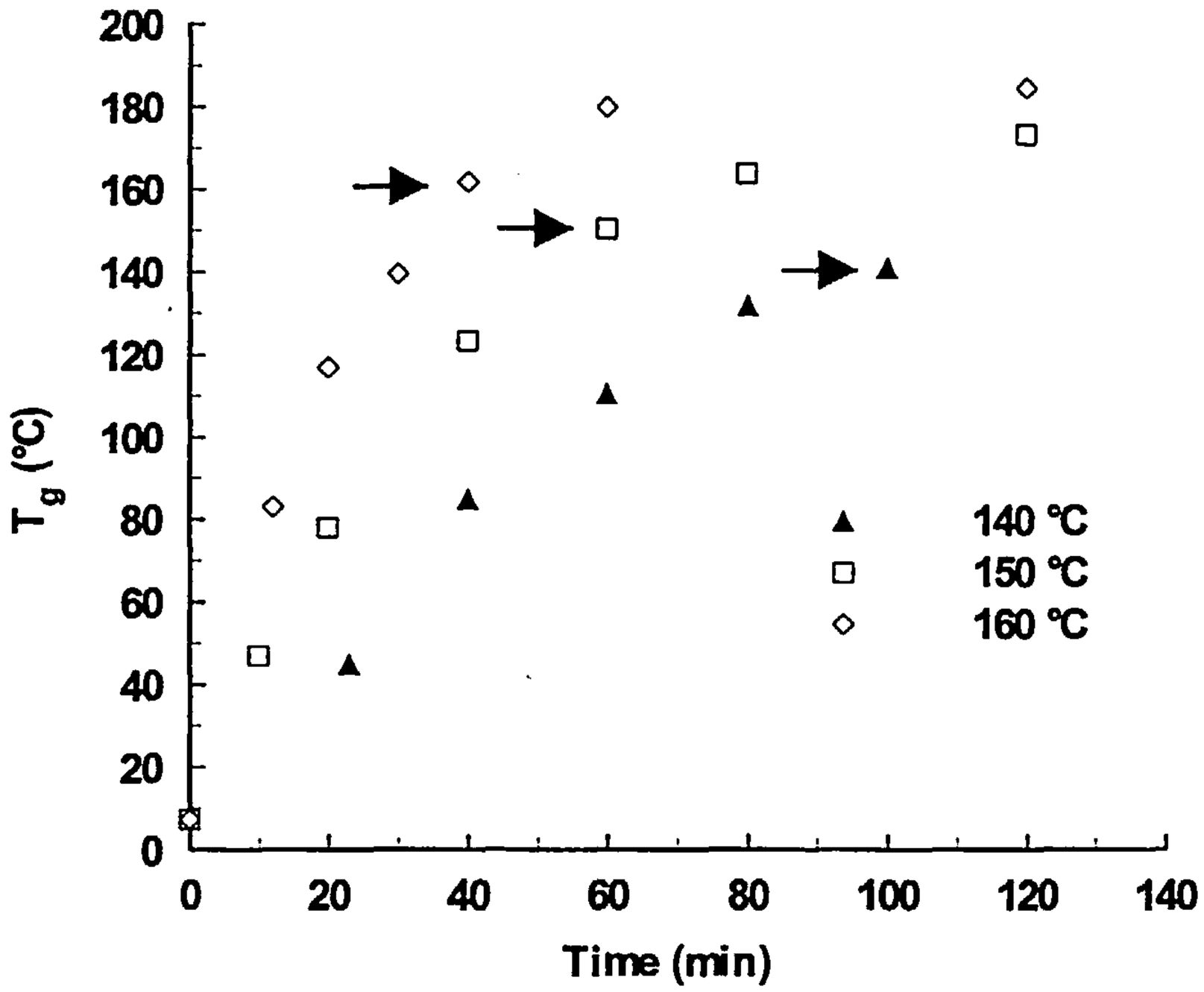

Figure 5.4 *Glass transition temperature profile of 934 resin at different cure temperatures*

It has been found that the ratio $(E_x/E_m)/(F_x/F_m)$ can be determined from the following equation [152] :

$$\frac{E_x/E_m}{F_x/F_m} = \frac{T_{g\infty}}{T_{g0}} \qquad \text{(Eq. 5.2)}$$

where $T_{g\infty}$ is the maximum attainable glass transition temperature of the fully cured resin. Incorporation of this equation into Eq. 5.1 will give:

$$T_g = T_{g0} + \frac{(T_{g\infty} - T_{g0})\lambda\alpha}{1-(1-\lambda)\alpha} \qquad where \qquad \lambda = \frac{F_x}{F_m} \qquad \text{(Eq. 5.3)}$$

The above equation can be used to model the T_g-conversion relationship by treating λ as an adjustable parameter. The results from the application of Eq. 5.3 to the experimental data for all resin systems are given in Table 5.1 and the corresponding fitting results in Figure 5.5 - Figure 5.8.

Table 5.1 *Results from the application of Eq. 5.3 to model the T_g-conversion relationship for all resin systems.*

Resin	T_{g0} (°C)	$T_{g\infty}$ (°C)	λ
RTM6	-11	206	0.435
RMO	-11	208	0.677
RMO2	-21	193	0.847
934	7	208	1.000

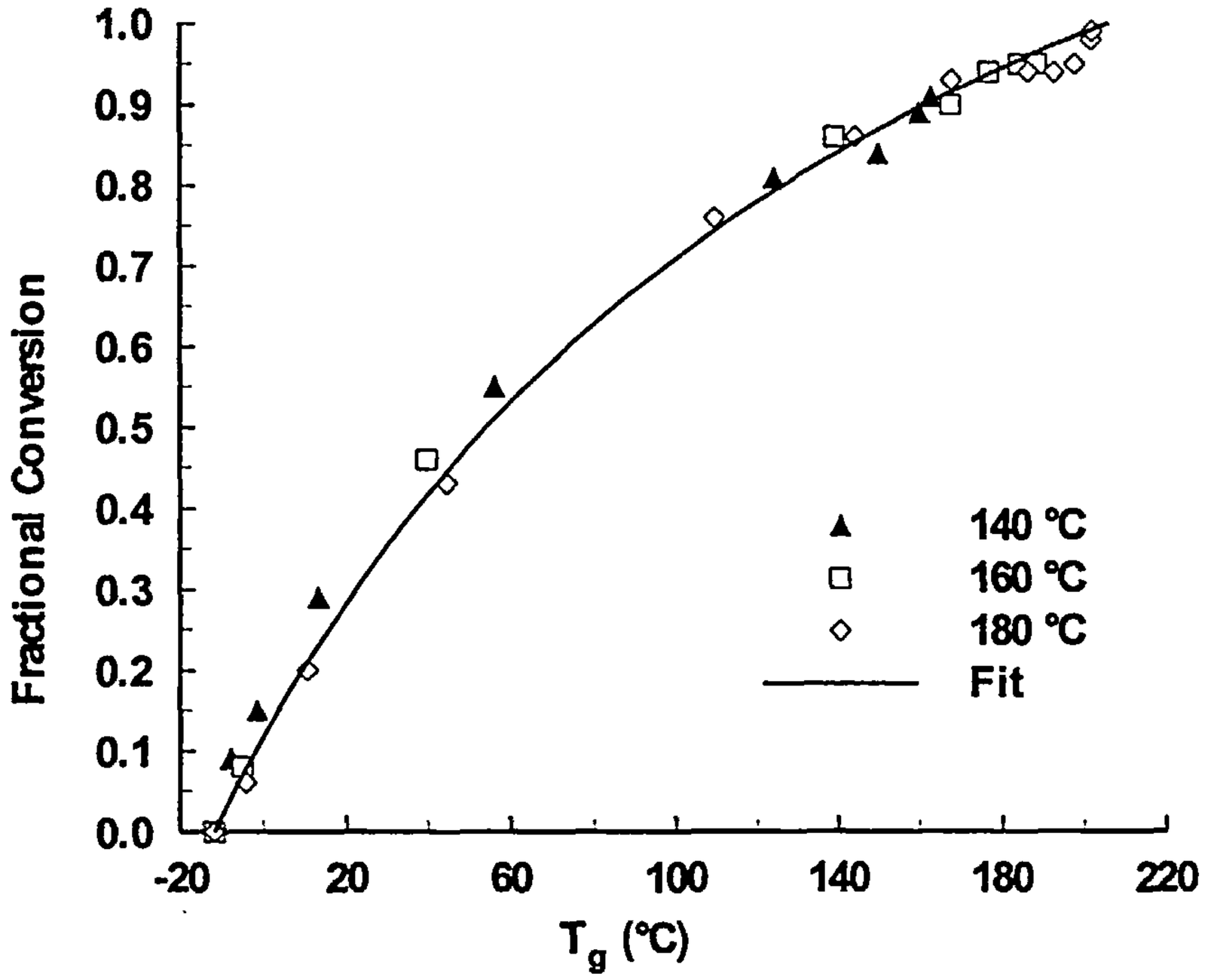

Figure 5.5 *Plots of fractional conversion versus T_g for the cure of RTM6 resin. The fit was produced by Eq. 5.3*

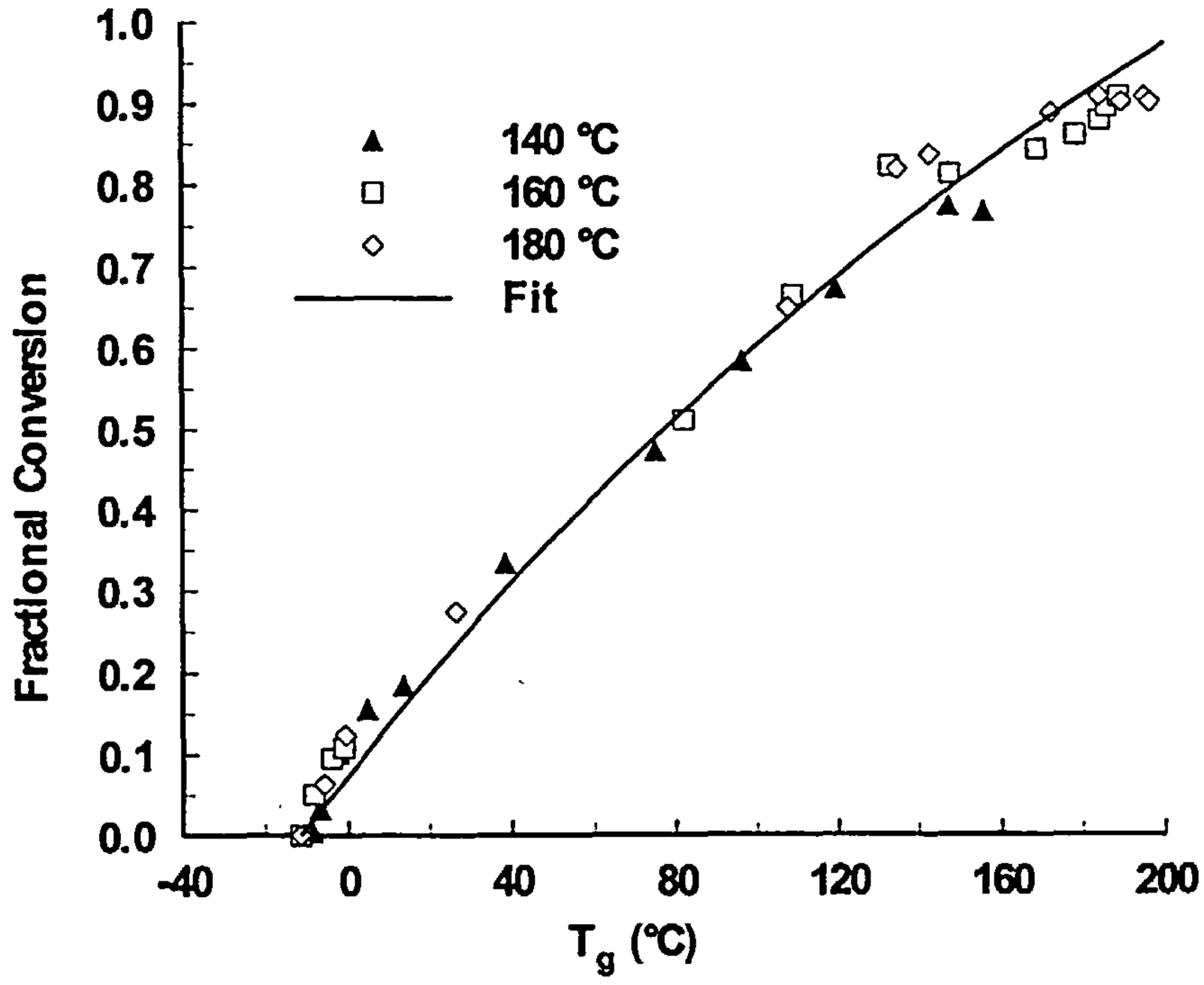

Figure 5.6 *Plots of fractional conversion versus T_g for the cure of RMO resin. The fit was produced by Eq. 5.3*

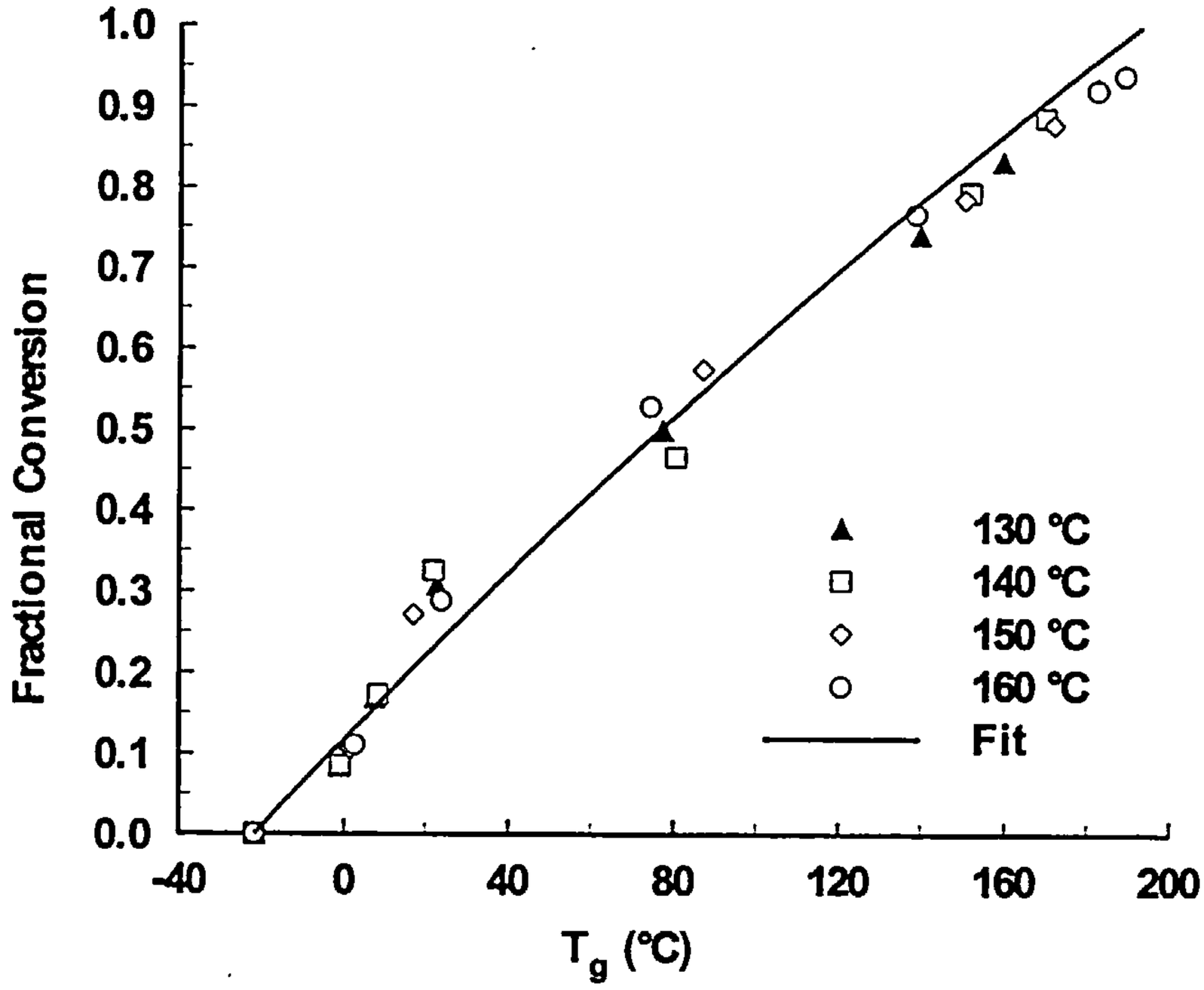

Figure 5.7 *Plots of fractional conversion versus T_g for the cure of RMO2 resin. The fit was produced by Eq. 5.3*

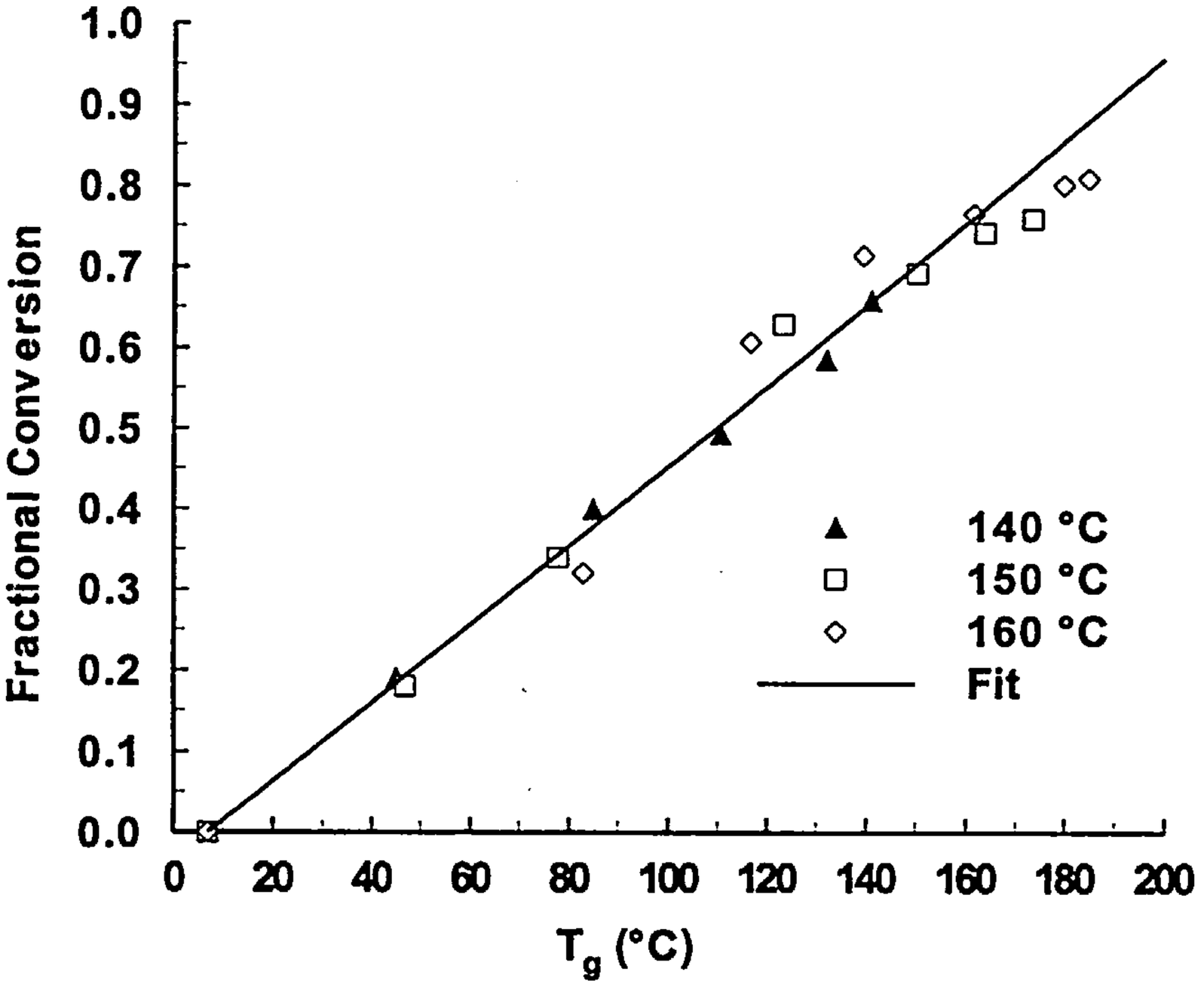

Figure 5.8 *Plots of fractional conversion versus T_g for the cure of 934 resin. The fit was produced by Eq. 5.3*

If the curing reaction was chemically controlled, that is if there are no contributions from diffusion control, the reaction rate can be expressed as:

$$\frac{d\alpha}{dt} = k(T) \cdot f(\alpha) \qquad \text{(Eq. 5.4)}$$

where $k(T)$ is the reaction rate constant, which is a function of temperature and $f(\alpha)$ is some function of conversion. Integration of the above expression at constant temperature and taking the natural logarithm will give:

$$\ell n\left(\int_0^{\alpha} \frac{d\alpha}{f(\alpha)}\right) = \ell n k(T) + \ell n t \qquad \text{(Eq. 5.5)}$$

The left-hand side of this expression is a function only of conversion, or if we consider the one-to-one relationship between conversion and T_g, a function only of T_g. Thus:

$$F\left(T_g\right) = \ell n k(T) + \ell n t \qquad \text{(Eq. 5.6)}$$

Since the function F depends only on T_g, for the cure at two different temperatures, T_1 and T_2, it follows that:

$$F\left(T_g\right) = \ell n k\left(T_1\right) + \ell n t_1 = \ell n k\left(T_2\right) + \ell n t_2$$

$$\Rightarrow \ell n A - \frac{E}{R}\frac{1}{T_1} + \ell n t_1 = \ell n A - \frac{E}{R}\frac{1}{T_2} + \ell n t_2 \qquad \text{(Eq. 5.7)}$$

$$\Rightarrow \frac{E}{R}\left(\frac{1}{T_2} - \frac{1}{T_1}\right) = \ell n t_2 - \ell n t_1$$

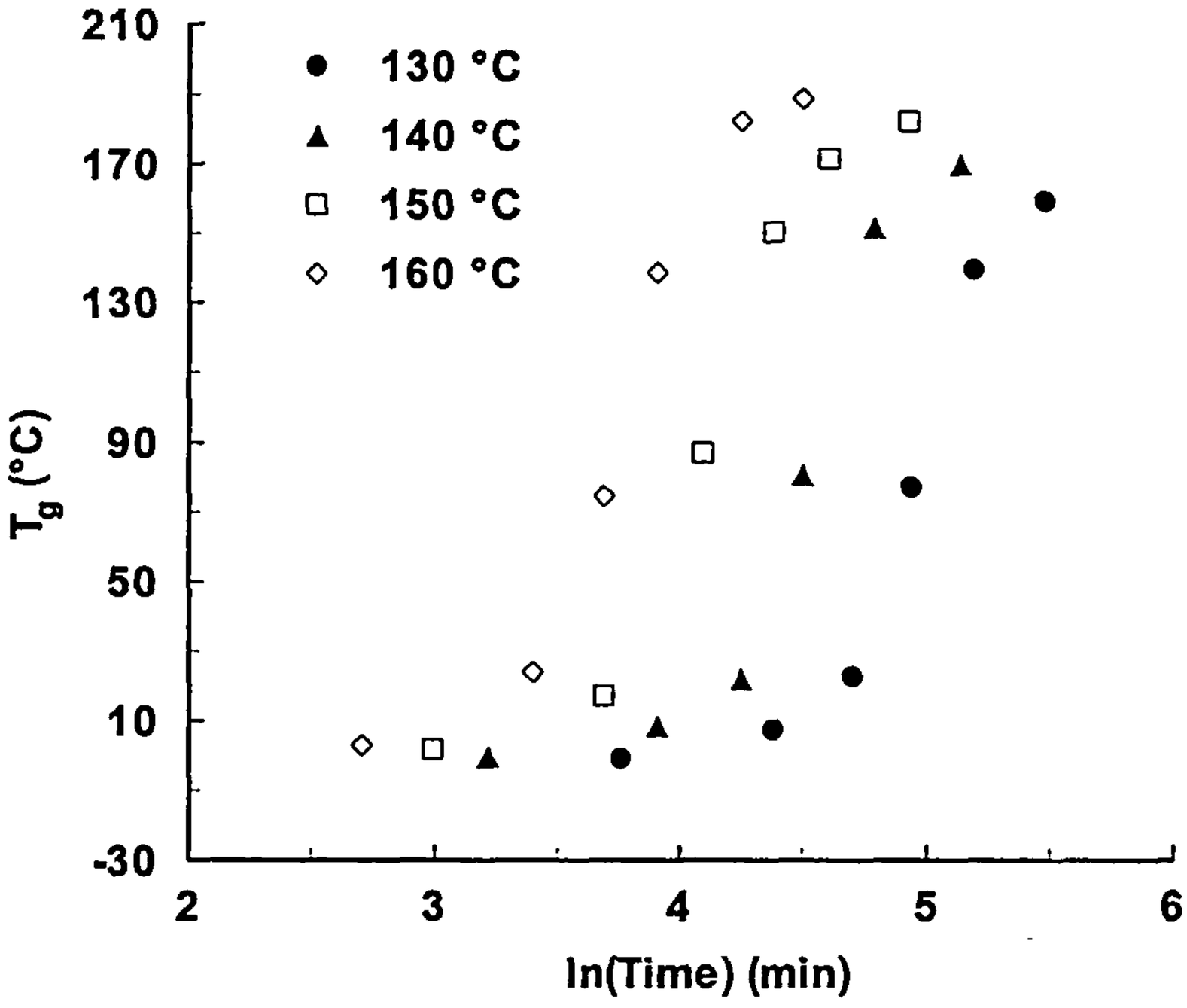

Figure 5.9 *Plots of T_g against the natural logarithm of cure time for the isothermal cure of RMO2 resin at different cure temperatures*

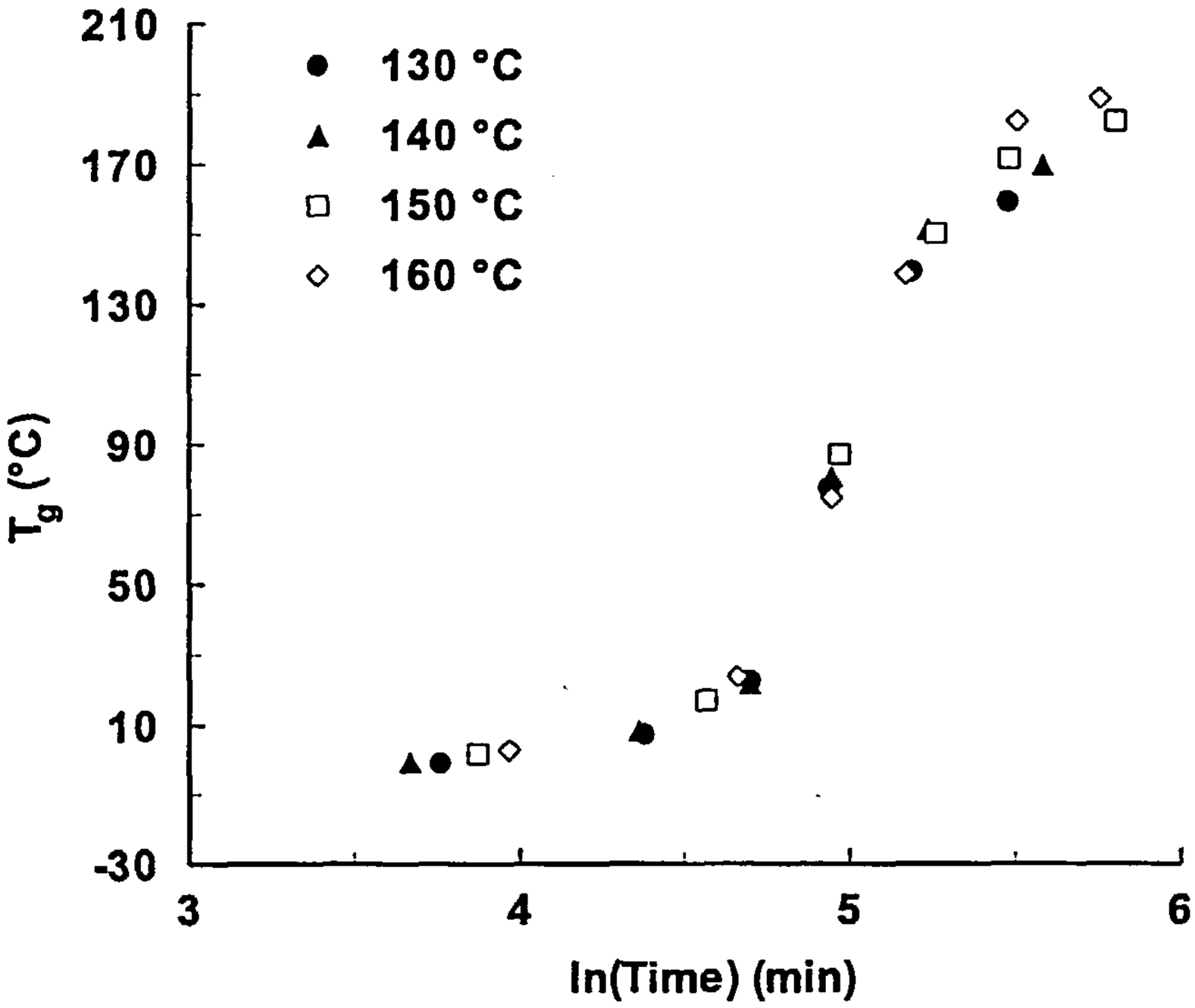

Figure 5.10 *Superposition of the T_g vs. ln(time) RMO2 resin data by horizontal shifting of the original curves to form a master curve*

What the above means is that the cure times to reach a specific T_g during the cure at two different temperatures differ by a constant amount, $S(T)$, on a logarithmic scale, which is equal to:

$$S(T) = \frac{E}{R}\left(\frac{1}{T_2} - \frac{1}{T_1}\right) \qquad \text{(Eq. 5.8)}$$

To demonstrate this, the experimental data on T_g of RMO2 resin have been plotted as a function of cure time on a logarithmic scale. The plots are shown in Figure 5.9. It is obvious from these plots that a horizontal shift of the curves relative to a reference cure temperature (e.g. 130°C) will make them superimpose to a master curve up to the vitrification point, since above that point the cure is not chemically controlled. The master curve produced by the horizontal shift of the curves relative to the 130°C data is shown in Figure 5.10. The shift factors used have been plotted in Figure 5.11 as a function of the differences between the inverse of the cure temperature and the inverse of the reference temperature. According to Eq. 5.8, this plot should give a straight line with a slope equal to E/R.

The activation energy for the curing reaction, as calculated from the slope of the Arrhenius plot in Figure 5.11, is 60kJ/mol. The existence of a master curve for the T_g development and the Arrhenius dependence of the shift factors on temperature suggest that this resin system follows one overall reaction mechanism with a single apparent activation energy [153] . This contradicts the results obtained from the reaction kinetics in the previous chapter, where two activated reaction mechanisms were obtained. The explanation for this discrepancy lies in the form of the expression used to describe the correlation between T_g and conversion (see Eq. 5.3). Although there exists a one-to-one relationship between these two properties, that does not mean that this relationship is linear. These two properties are related by a proportionality function only, and only when the parameter λ in Eq. 5.3 is equal to 1. Then, this expression can be written as:

$$T_g = T_{g0} + \left(T_{g\infty} - T_{g0}\right)\alpha \qquad \text{(Eq. 5.9)}$$

which expresses a linear dependence of T_g on conversion. Thus, any change in conversion has a similar effect on *Tg*. For the RMO2 resin, this is not the case. The parameter λ is equal to 0.847 (see Table 5.1), thus the proportionality law does not hold. The above can be demonstrated easily by plotting conversion as a function of the natural logarithm of cure time. These plots are shown in Figure 5.12 for the isothermal cure of the above resin at different cure temperatures, horizontally shifted to produce a master curve. It is evident that these curves cannot be superimposed accurately at low conversions. At these conversions, the autocatalytic reaction mechanism is in control. If the curves were shifted to superimpose at these low conversions, then the high conversion data would had deviated from the master curve. At these high conversions, the non-catalytic reaction mechanism is in control.

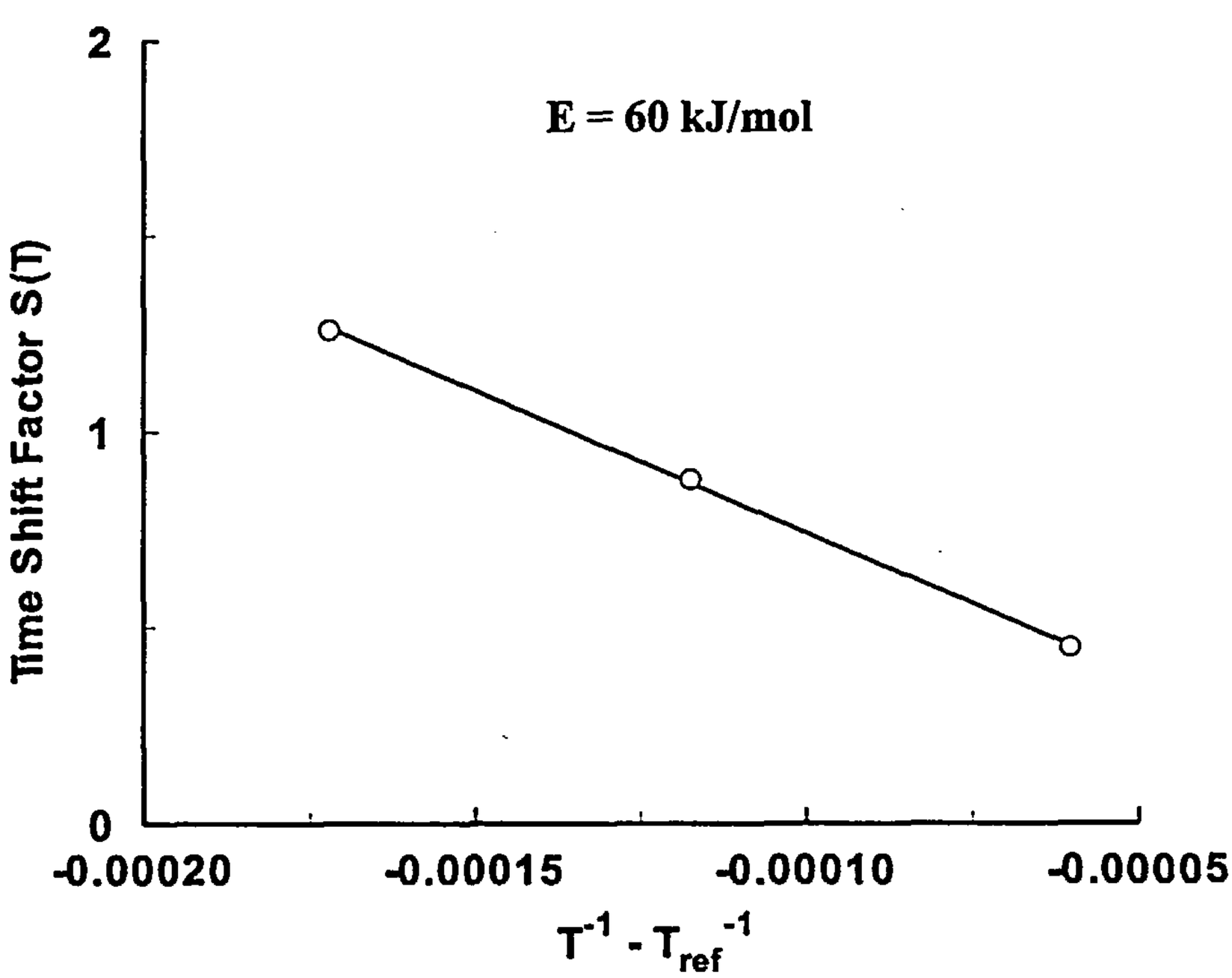

Figure 5.11 *Arrhenius plot of the shift factors, S(T), used to construct the master curve in Figure 5.10. The reference temperature was 130°C*

However, this is not the case for 934 resin. As demonstrated in the previous chapter, this resin follows a single activated reaction mechanism (nth order kinetics) under isothermal conditions. This means that there should be a proportionality law describing the relation between T_g and conversion for this resin.

Indeed, the results of the fit of Eq. 5.3 on the experimental *Tg* data support this. The parameter λ was calculated to be equal to 1 (see Table 5.1), thus plotting conversion against the natural logarithm of cure time should produce a master curve. This is shown in Figure 5.13. A master curve is followed for all cure temperatures. Deviations start to appear above the vitrification point, where the reaction is not chemically controlled but diffusion controlled.

From the above discussion it follows that Eq. 5.4 does not hold for all resin systems. What it does hold however is that:

$$\frac{dT_g}{dt} = k(T) f\left(T_g\right) \qquad \text{(Eq. 5.10)}$$

since the T_g advancement follows a single activated mechanism for all resin systems. The above expression suggests that the T_g development should be treated in a completely different way than the reaction kinetics. Reaction kinetics are influenced by the chemical constituents of the reactive system, the possible interactions that can be established between them and the relative distances between the various reactive species as these are determined by the positions that they hold in space during the development of the three dimensional network. From the other hand, T_g seems to be influenced only by the structural configuration of the forming network itself and not by the possible reactions that can lead to this network.

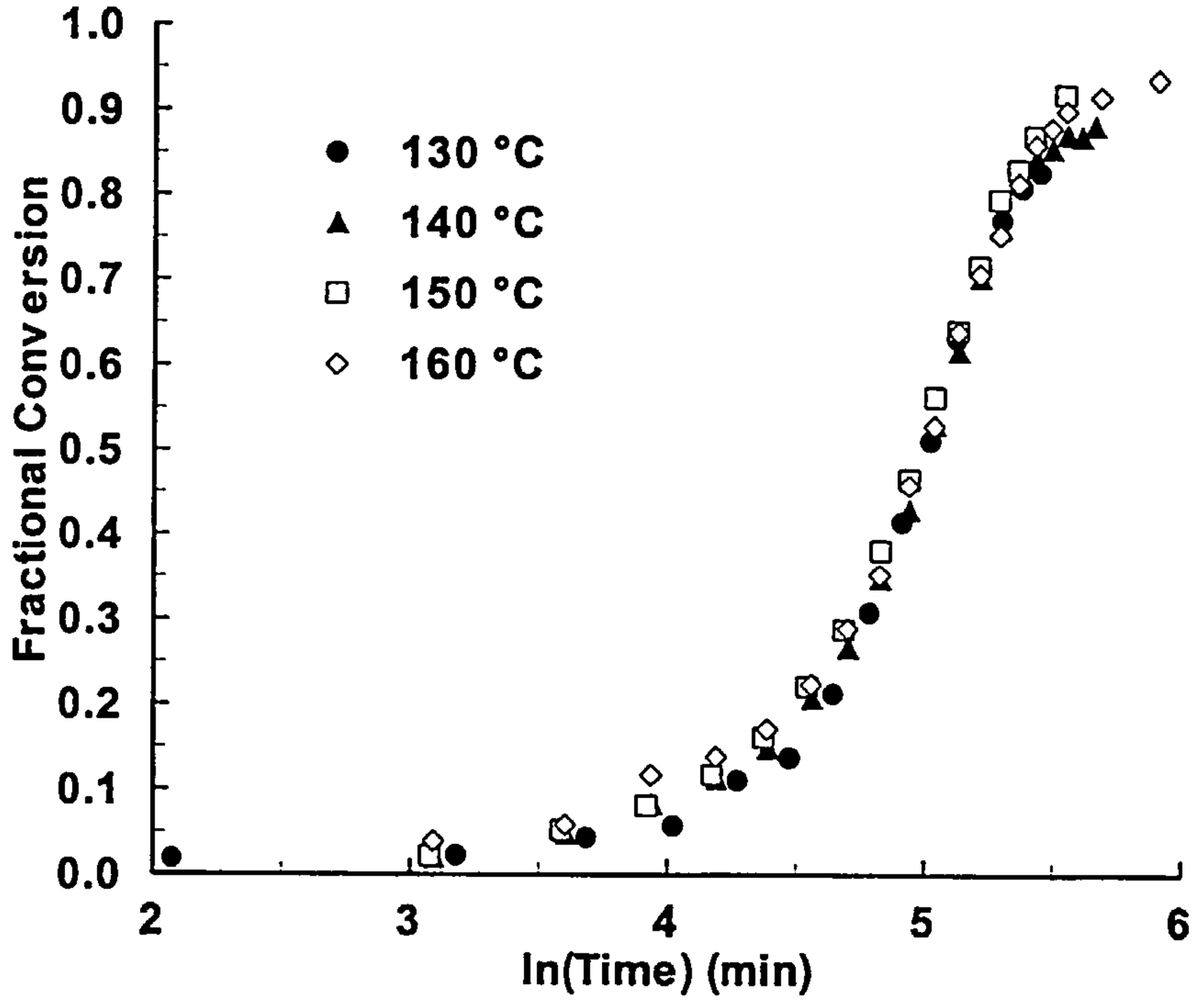

Figure 5.12 *Superposition of the conversion vs. ℓn(time) data for the isothermal cure of RMO2 resin*

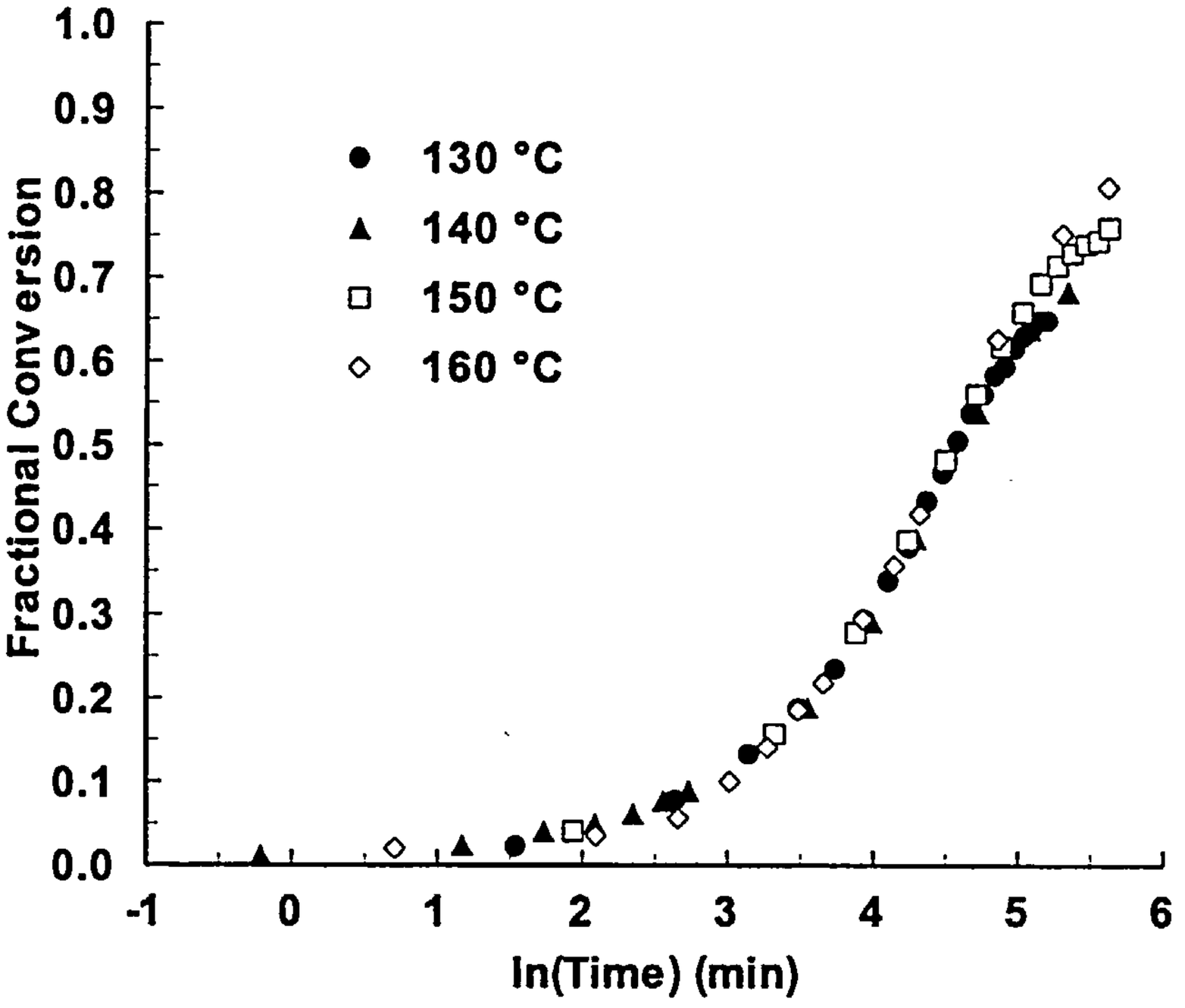

Figure 5.13 *Superposition of the conversion vs. ℓn(time) data for the isothermal cure of 934 resin*

Chapter Six

6. Diffusion Limitations of Cure Kinetics

In the previous chapters the reaction kinetics were investigated for all resin systems in the chemically controlled region. The reactions were treated as being influenced only by the applied temperature and the chemical formulation of the reactive system. This is true only in the early stages of the curing reaction, where there is not any three dimensional network formed. As the cure progresses, this network starts to form, limiting the probabilities of the various reaction to happen and eventually freezing them as the vitrification point is reached. From the above, it seems reasonable to assume that a structural parameter has to be introduced in the expressions describing the reaction kinetics to account for the limiting factor of structure development in them. In the previous chapter, T_g was found to be a very sensitive parameter of the changes in the developing network. For that reason, T_g will be used as the limiting factor in the reaction kinetics and mathematical expressions will be developed to express the influence of T_g on the cure kinetics.

6.1 Mathematical Representation of Diffusion Control

The curing reaction, as discussed above, involves two different mechanisms: pure chemical reactions and reactions controlled by the diffusion of the reactive species through the reactive mixture. Thus, the reaction can be visualised as the product of two parallel mechanisms: chemical reaction and diffusion controlled reaction. The

parameter that controls the rate of reaction is the reaction rate constant, k_i, which, if we use the nomenclature of two parallel mechanisms occurring simultaneously, can be expressed as [154] :

$$\frac{1}{k_{overall}} = \frac{1}{k_{chemical}} + \frac{1}{k_{diffusion}} \qquad \text{(Eq. 6.1)}$$

In the above expression, $k_{overall}$ is the apparent rate constant, $k_{chemical}$ is the rate constant of the chemically controlled reaction and $k_{diffusion}$ is the rate constant of the same reaction this time controlled by diffusion. Whilst the chemical rate constant follows an Arrhenius temperature dependence, this is not the case for the diffusion rate constant. Since diffusion is a measure of the structure development, it must follow the changes both in T_g and in cure temperature. Two general expressions have been suggested for the mathematical representation of $k_{diffusion}$, which from now on will be represented by k_d. These expressions are:

Representation A [154]:

$$k_d = k_{d0} \exp\left(-\frac{b}{f}\right) \qquad \text{(Eq. 6.2)}$$

Parameter k_{d0} follows an Arrhenius dependence of the form:

$$k_{d0} = A_d \exp\left(-\frac{E_d}{RT_c}\right) \qquad \text{(Eq. 6.3)}$$

where E_d is the activation energy for diffusion and T_c is the cure temperature.

Parameter b in Eq. 6.2 is treated as an adjustable parameter. Parameter f in the same equation represents the equilibrium free volume given by the expression:

$$f = 0.00048\left(T_c - T_g\right) + 0.025 \qquad \text{(Eq. 6.4)}$$

By taking the natural logarithm of both sides of Eq. 6.2, we get:

$$\ell n\left(k_d\right) = \ell n\left(k_{d0}\right) - b\frac{1}{f} \qquad \text{(Eq. 6.5)}$$

A plot of the left hand side of the above equation against $1/f$ will give a straight line with slope $-b$ and intercept $\ell n(k_{d0})$. Repetition of this procedure at different temperatures will give the Arrhenius parameters of K_{d0} from the intercepts previously obtained.

Representation B [77] :

An alternative expression for the diffusion rate constant is a modification of the Williams-Landel-Ferry equation (see Section 2.5):

$$\ell n\left(k_d\right) = \ell n\left(k_{d0}\right) + \frac{C_1\left(T_c - T_g\right)}{C_2 + \left(T_c - T_g\right)} \qquad \text{(Eq. 6.6)}$$

where C_1 and C_2 are adjustable parameters.

Both of the above representations have T_g as parameter in order to adjust the reaction kinetics accordingly to the structure developed up to that point.

These expressions will be used in the following sections to describe the reaction kinetics of all the resin systems in the diffusion controlled region.

6.2 Development of Kinetic Models for the Diffusion Controlled Region

The first attempt of diffusion modelling was made for the isothermal cure of 934 resin, since this resin follows a simple nth order reaction mechanism.

Table 6.1 *Diffusion parameters for the isothermal cure of 934 resin*

Cure Temperature (T_c / °C)	$\ell n(k_{d0})$	b	b Average
130	0.7872	0.1115	
140	1.1106	0.1152	0.1134
150	1.6153	0.1136	
160	0.1618	0.0721	

Arrhenius parameters of k_{d0}

A_d (sec^{-1})	E_d (kJ/mol)
$8.29 \cdot 10^7$	58.57

The values of k_d were obtained by substituting the rate constant with the expression given in Eq. 6.1. The best values of k_d that fitted the experimental data for conversions above 50% were taken as the estimated diffusion rate constants at each conversion level. The results for all temperatures are shown in Figure 6.1 as plots of the natural logarithm of k_d as a function of $1/f$. The f values were calculated according to Eq. 6.4 with T_g values obtained from the T_g - Conversion relationship obtained in the previous chapter (see Eq. 5.3 and Table 5.1). The parameters of the best fitted straight lines, calculated using Eq. 6.5, are given in Table 6.1. As can be seen from the values given in this table, the results obtained at the first three cure temperatures follow the same trend. The parameter b is apparently constant for curing between 130 to 150 °C, whereas at 160 °C parameter b has a different value. For that reason, the Arrhenius parameters, calculated by Eq. 6.3, were based on the results obtained for the first three

temperatures. The value of b was also taken as the average value for these three temperatures. The results are shown in Table 6.1. The fitting of the complete model (incorporating diffusion control) is shown in Figure 6.2 as plots of the fractional conversion against cure time for various temperatures. As can be seen, the fitting is very good throughout the cure, even for the 160°C cure, the results of which were not incorporated in the calculation of the diffusion parameters.

The above method was also applied to estimate the diffusion rate constants for the cure of the other resin systems. Since diffusion depends on the three dimensional network that is formed during the cure, the rate constant k_d was taken as the same for all the reaction mechanisms that occur during the cure of a resin. Thus, for the cure of the resins, RTM6, RMO and RMO2 the overall reaction rate constants can be written as:

$$\frac{1}{k_{i,overall}} = \frac{1}{k_{i,chemical}} + \frac{1}{k_d} \qquad \text{(Eq. 6.7)}$$

with the subscript i indicating the kind of reaction; in our case either autocatalytic or non-catalytic. What became apparent during the calculation of the k_d values of the above resin systems was that the results were not following a trend similar to the one obtained for 934 resin. Apart from RMO2 resin, which gave straight lines for the dependence of $\ell n k_d$ on $1/f$, the other two resins were following a more complicated dependence of $\ell n k_d$ on $1/f$ than a simple linear dependence. The results are shown in Figure 6.3 and Figure 6.4 for the resins RTM6 and RMO2 respectively.

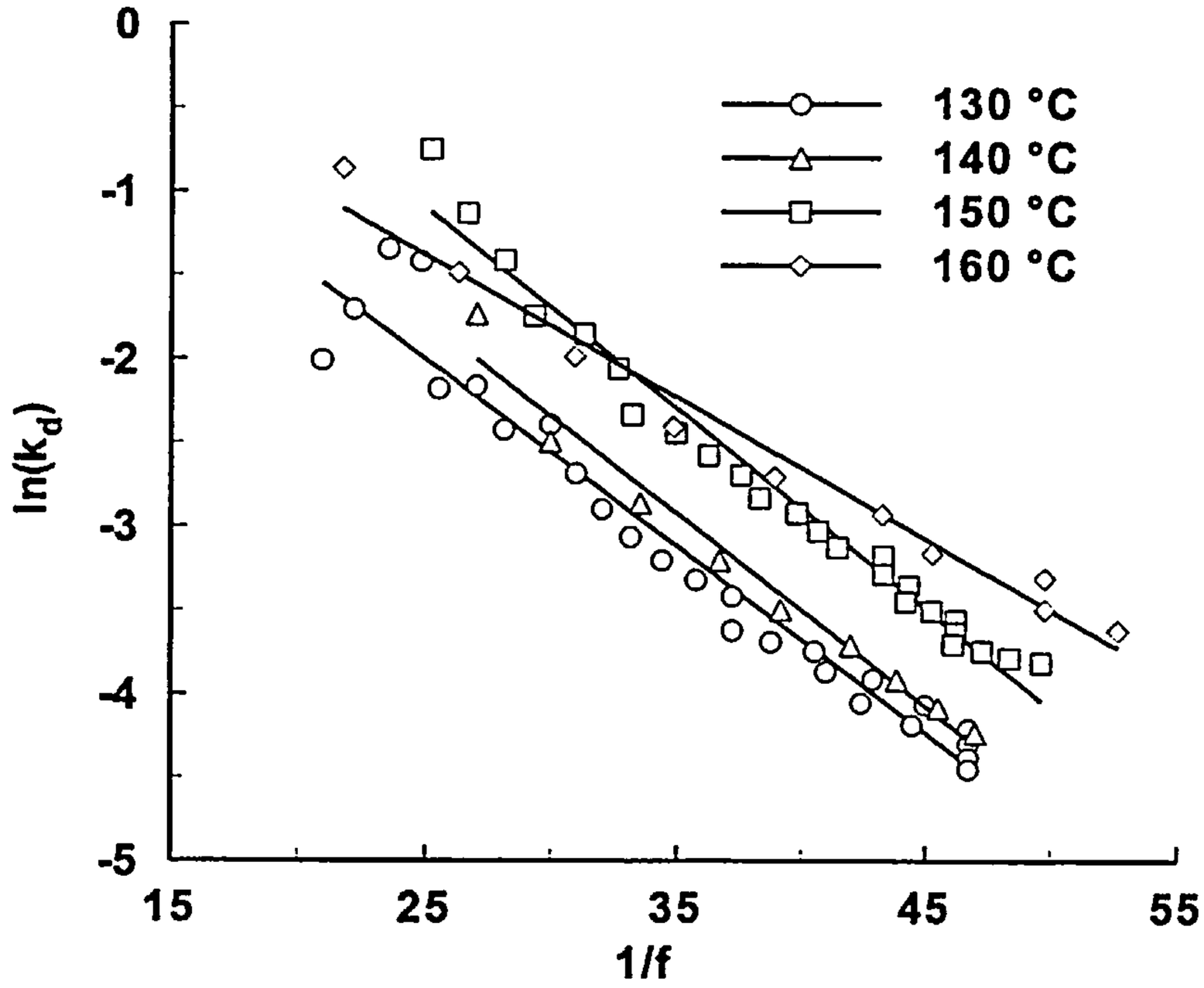

Figure 6.1 *Plots of ln(k_d) vs. 1/f for the isothermal cure of 934 resin*

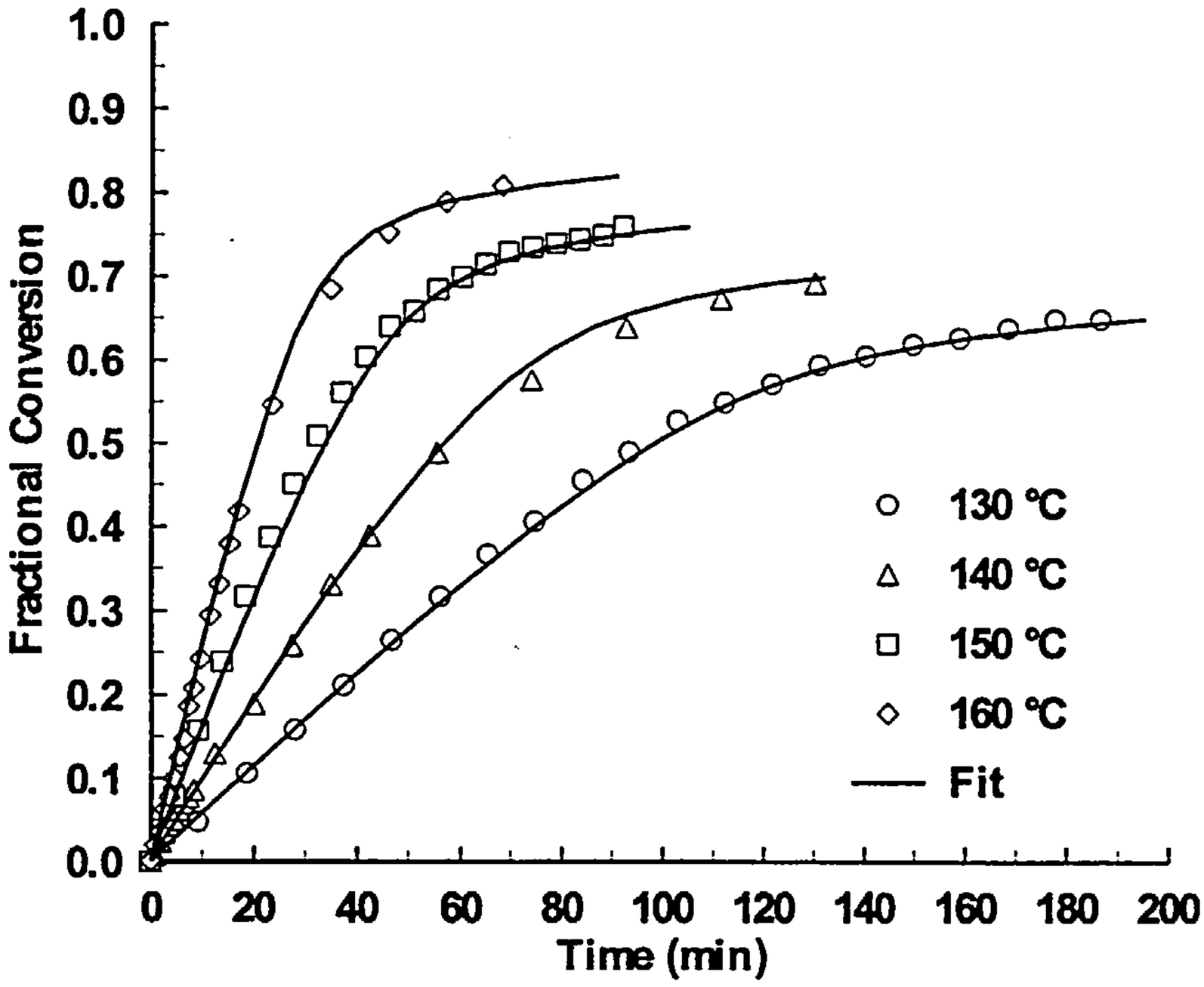

Figure 6.2 *Fit of kinetic model (Eq. 4.14) incorporating diffusion control for the isothermal cure of 934 resin*

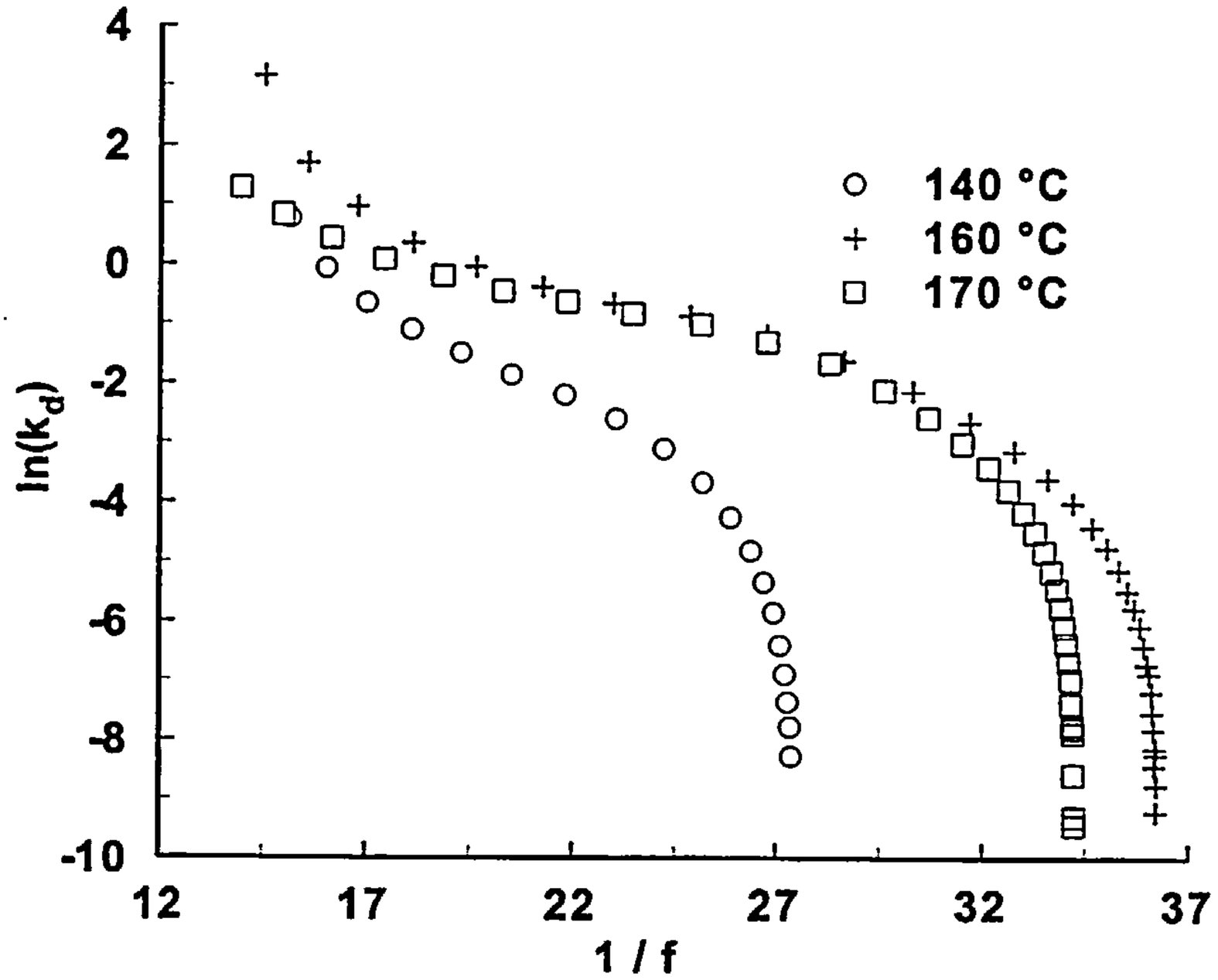

Figure 6.3 *Plots of ℓn(k_d) vs. 1/f for the isothermal cure of RTM6 resin*

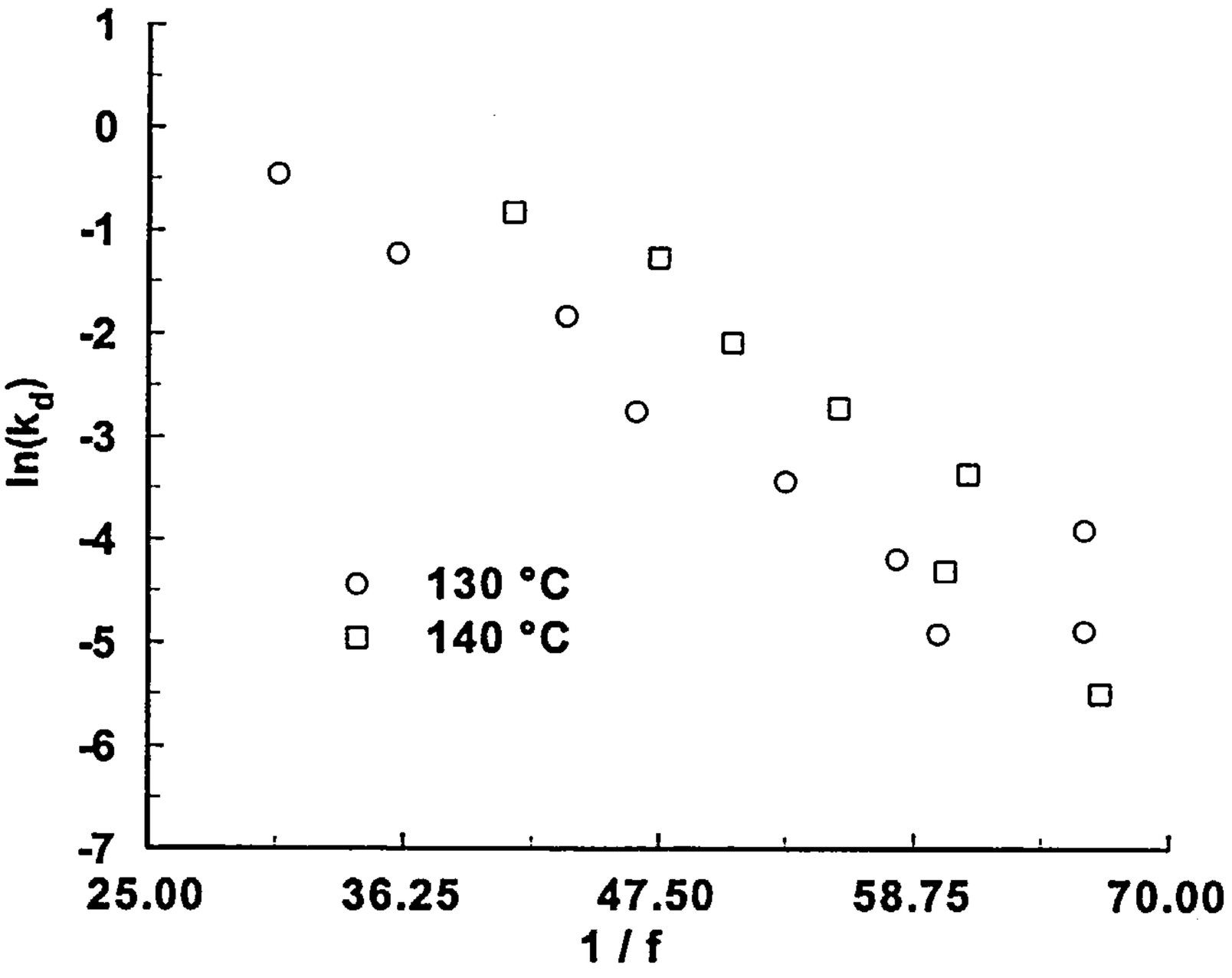

Figure 6.4 *Plots of ℓn(k_d) vs. 1/f for the isothermal cure of RMO2 resin*

This finding made the use of Eq. 6.5 impossible. For that reason, the diffusion parameters for these resins were calculated as the best fit values from the application of non-linear regression to the experimental results (see Appendix C). The estimated parameters, as calculated by that method, are given in Table 6.2 for all the resin systems and the produced fits in Figure 6.5 - Figure 6.7 as plots of the fractional conversion against the cure time. The activation energies obtained by this method do not show any particular correlation to each other, something which was expected as these are best fit values and are not based to any particular equation.

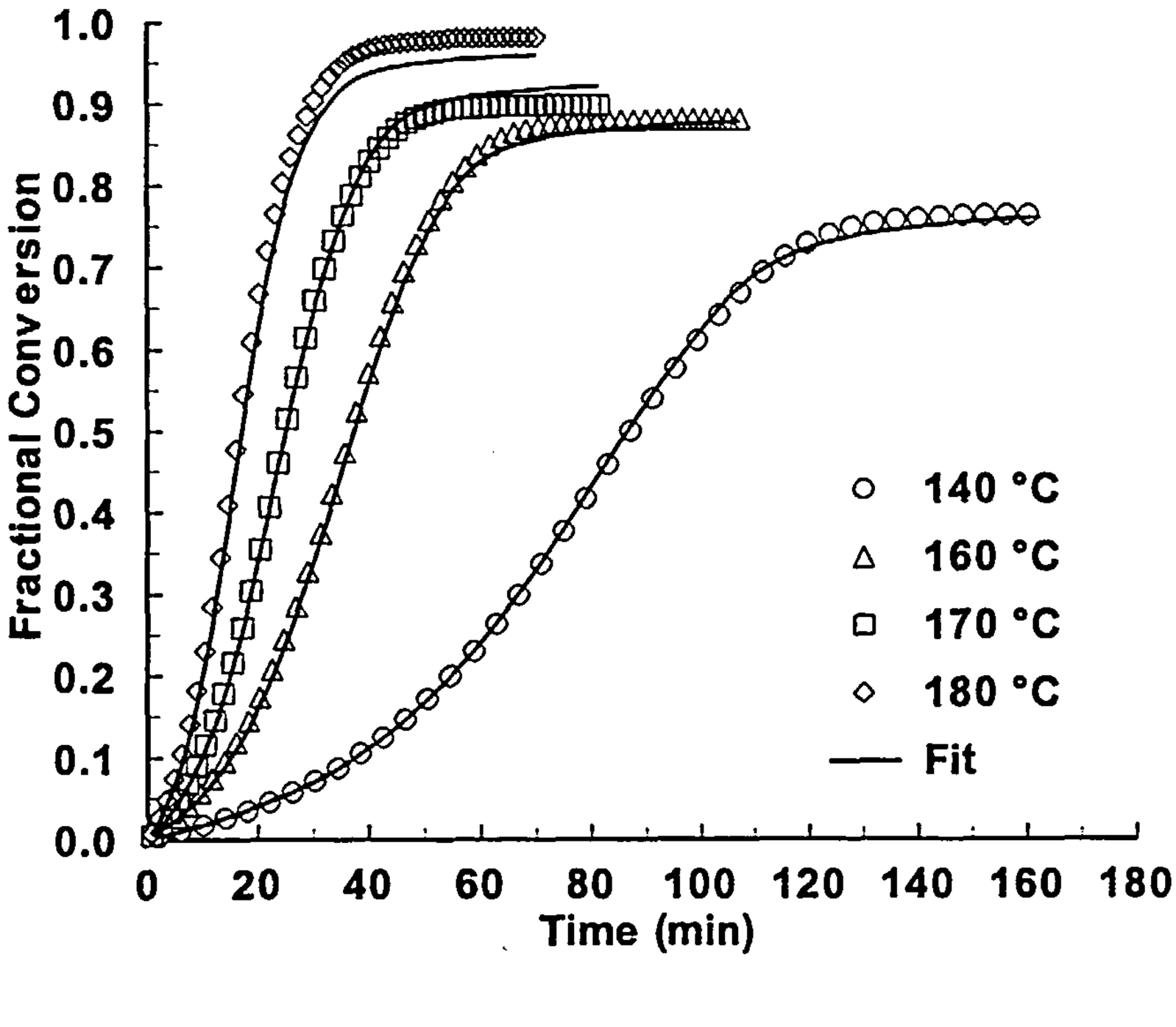

Figure 6.5 *Fit of kinetic model (Eq. 4.9) incorporating diffusion control for the isothermal cure of RTM6 resin*

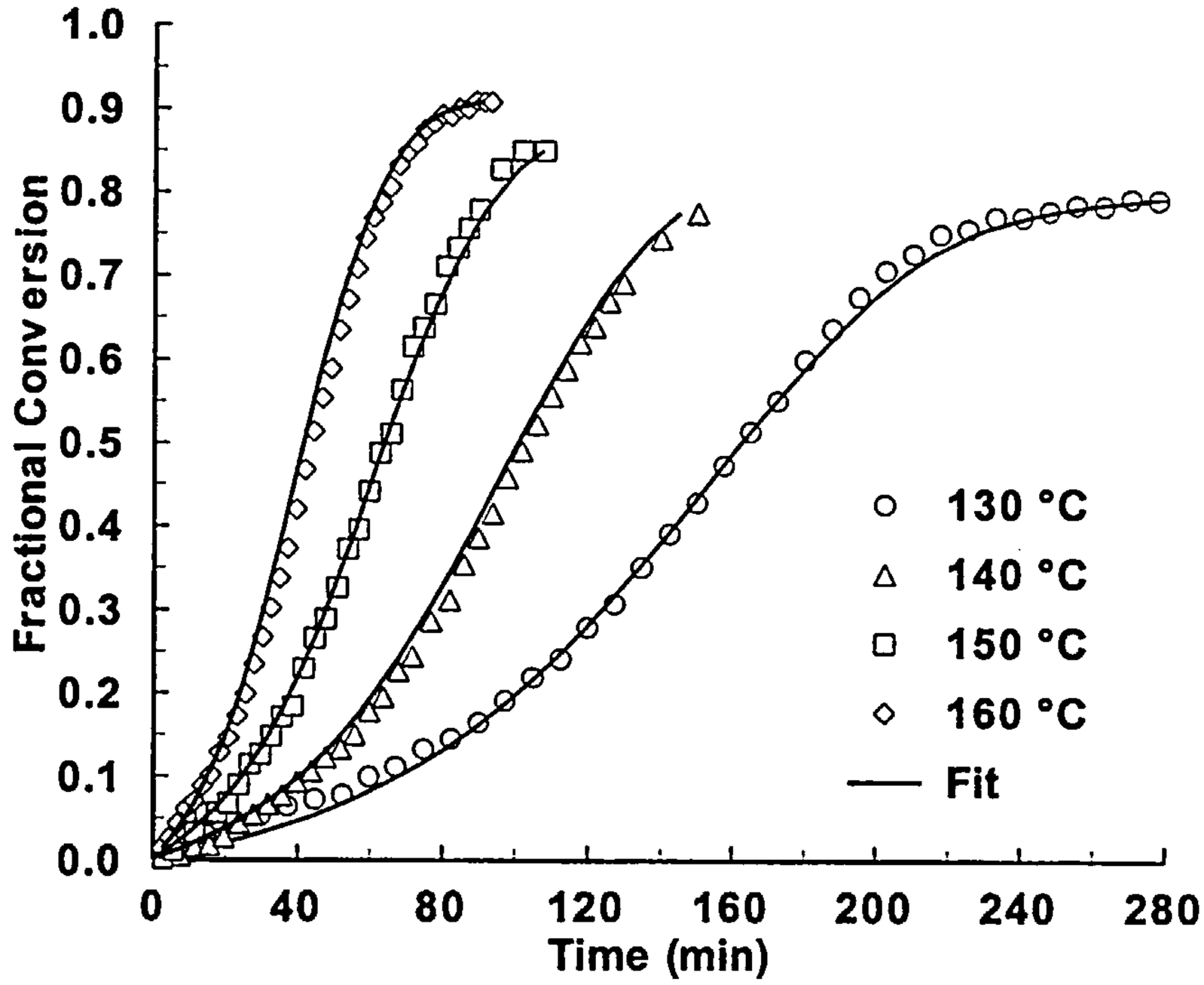

Figure 6.6 *Fit of kinetic model (Eq. 4.9) incorporating diffusion control for the isothermal cure of RMO resin*

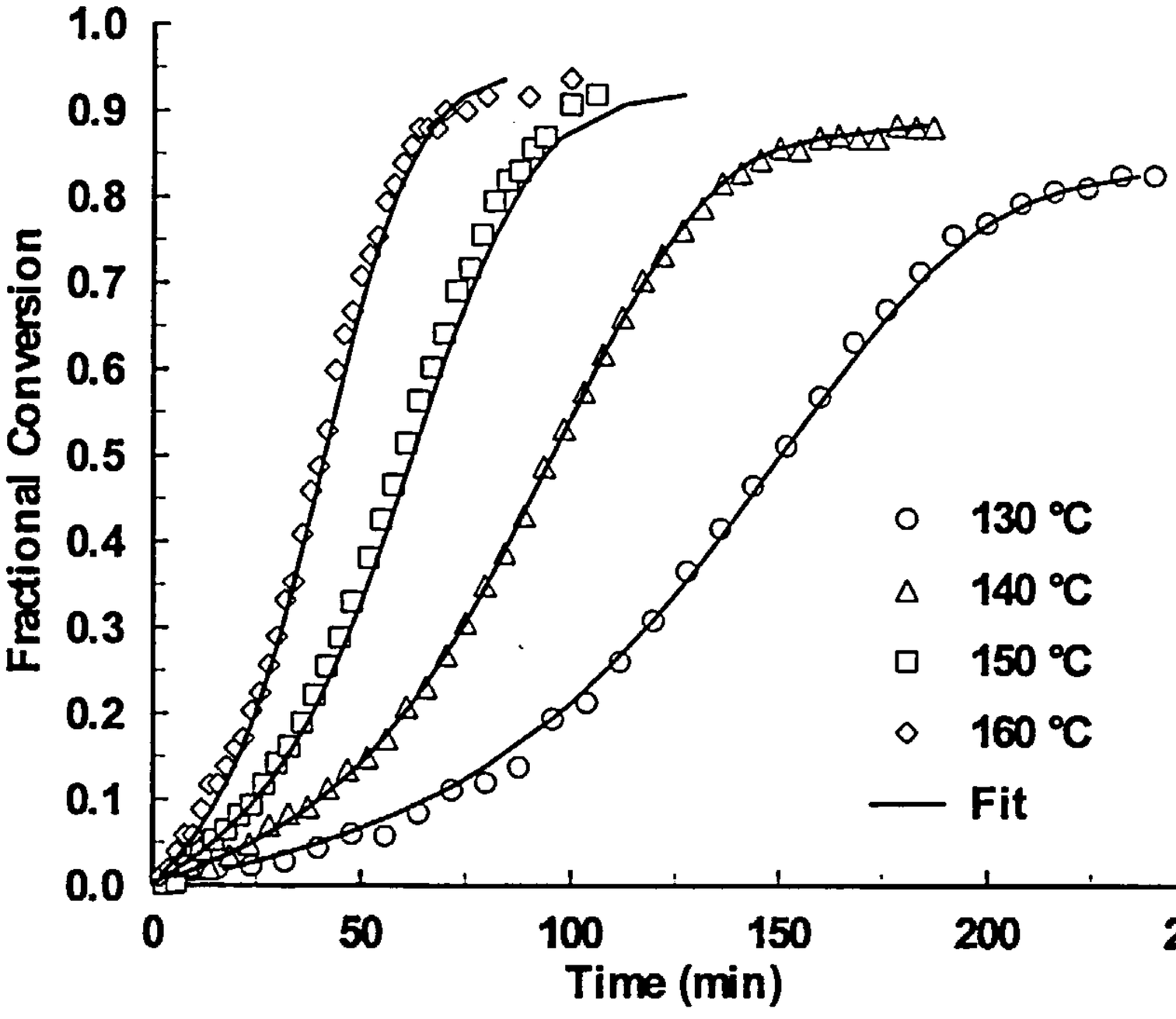

Figure 6.7 *Fit of kinetic model (Eq. 4.9) incorporating diffusion control for the isothermal cure of RMO2 resin.*

In the implementation of diffusion in the cure kinetics models that were developed in Chapter 4, the focus was concentrated in the structural development during the cure. The expressions that were used in the above analysis are based on the free volume changes during the cure progress, since that property is the key factor influencing the diffusivity of the reactive species through the reactive resin matrix. The derived diffusion expressions, compensate for the free volume changes through the incorporation of the glass transition temperature of the resin. Changes of the structure of the resin during the cure, thus of T_g, have a direct effect on the free space available between the produced molecular chains. That free space will regulate the ability of the reactive species to diffuse through the resin matrix and subsequently react with each other and will also determine the mobility with which the reactive species will diffuse. Therefore, knowledge of the diffusion parameters of the curing reactions and especially of the activation energy for diffusion, are critical issues for an accurate determination of the cure kinetics of thermosetting resins.

Table 6.2 *Diffusion parameters for the isothermal cure of RTM6, RMO and RMO2 resin systems.*

Cure Temperature (°C)	**Resin System**		
	RTM6	**RMO**	**RMO2**
Parameter b			
130	0.23	0.14	0.12
140	0.25	0.17	0.13
150	0.26	0.17	0.25
160	0.29	0.18	0.45
Arrhenius parameters of diffusion			
A_d *(sec^{-1})*	$6.5 \cdot 10^{18}$	$1 \cdot 10^{32}$	$3.5 \cdot 10^{27}$
E_d *(kJ/mol)*	136	236	200

Chapter Seven

7. Viscosity Advancement During Cure

In this chapter the viscosity profiles of the resin systems will be investigated. The transformation of a resin system from the initial liquid state to the crosslinked structure of the end product, has as a result a continuous change in the viscosity of the curing resin. Because of instrumentation limitations, the viscosity of the curing resins was followed up to gelation, the characteristic point in the cure where the resin transforms from the liquid to the rubbery state. The influence of the cure process (cure temperature) and the continuous change in the structure of the resin will be used to produce appropriate mathematical models that can simulate the development of the viscosity profiles of all resin systems during cure.

7.1 Mathematical Representation of Viscosity Model

In Section 2.5 a number of mathematical expressions were given, mostly phenomenological in nature, that have been used extensively to simulate the viscosity changes during the cure of thermosetting resins. During an isothermal cure, the viscosity of a thermoset will increase continuously as a result of the extension of the molecular chains and the crosslinks that develop between them. As the point of gelation is reached, the increase in viscosity becomes very high because of the formation of joint macromolecules extending throughout the resin mass. Thus, in a viscosity vs cure time plot, the sudden increase in viscosity will mark the onset of

gelation with the actual gelation usually occurring a few minutes after the onset has been reached. The viscosity profile given in Figure 7.1 is the profile obtained from an isothermal cure of RTM6 resin at 140°C and represents a common viscosity profile obtained from an isothermal cure of an epoxy resin system. As seen in this figure, the actual gelation region represents only a very small time period in the overall curing procedure. Thus any time in this region will represent the actual gelation time to a very good degree of accuracy. For reasons of reproducibility of the results on gelation times and for comparison between different cure temperatures and resin systems, the time needed to reach a viscosity value of 10kPas will be taken here as the gelation time.

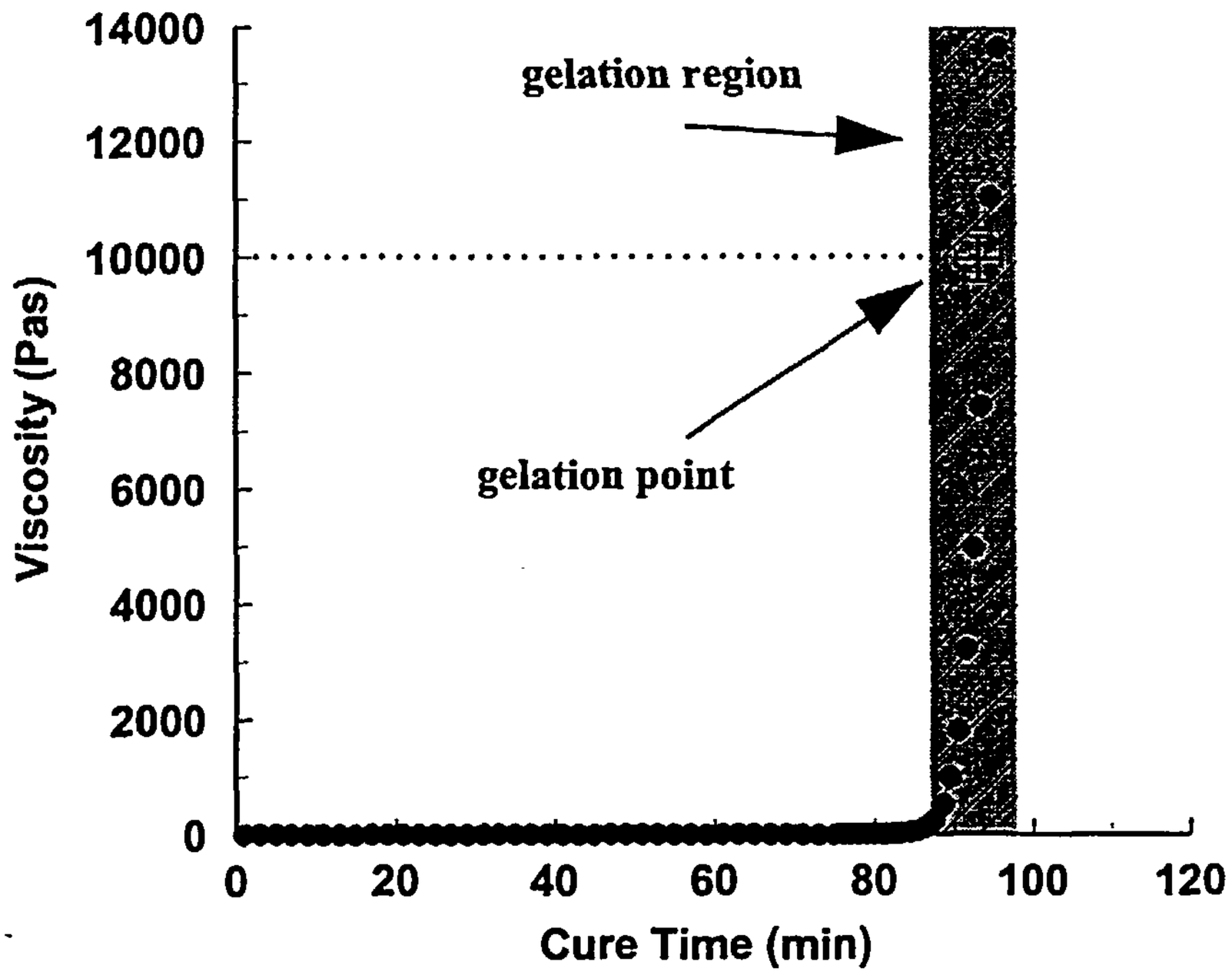

Figure 7.1 *Viscosity profile of RTM6 resin cured isothermally at 140°C.*

The most commonly used mathematical expression to model viscosity data as appears in the literature is the Williams-Landel-Ferry (WLF) equation, and especially for thermoset cure, a modified WLF equation, given by [56] :

$$\ell n\frac{\eta}{\eta_g} = -\frac{C_1\left(T_{cure}-T_g\right)}{C_2+T_{cure}-T_g} \qquad \text{(Eq. 7.1)}$$

In the above expression η is the apparent viscosity at time t, η_g is the viscosity of the fully cured resin, T_{cure} is the cure temperature and T_g is the glass transition temperature at time t. The parameters C_1 and C_2 are usually treated as adjustable parameters depending on the resin system under investigation.

The form of Eq. 7.1 has been found to be very adequate to model the viscosity advancement during cure. Apart from the exponential nature of this expression, that makes it appropriate to follow the exponential growth of viscosity, the parameters C_1 and C_2 can be varied in such a manner to always give values which produce a very good fitting to the experimental viscosity data. In the following sections, this expression will be used to model the viscosity data obtained from the rheology experiments for our resin systems.

7.2 Viscosity Modelling of RTM6, RMO and RMO2 Resins

The viscosity profiles of the isothermal cure of the resin systems RTM6, RMO and RMO2 at various cure temperatures, as obtained by the rheological technique described in Section 3.2.3, are shown in Figure 7.2 - Figure 7.4. All profiles exhibit the usual shape of a thermosetting resin isothermal cure (see Figure 7.1). Thus, the use of Eq. 7.1 to model the viscosity advancement during the cure should be appropriate for all resin systems.

The parameters that have to be evaluated are the constants C_1 and C_2. In order for the evaluation procedure to be more effective, the expression given by Eq. 7.1 had to be transformed to the form:

$$1 = -C_1\frac{1}{\ell n\eta-\ell n\eta_g}-C_2\frac{1}{T_{cure}-T_g} \qquad \text{(Eq. 7.2)}$$

or, by substituting:

$$X_1 = -\frac{1}{\ell n\eta - \ell n\eta_g} \quad and \quad X_2 = -\frac{1}{T_{cure} - T_g} \qquad \text{(Eq. 7.3)}$$

to the form:

$$1 = C_1 X_1 + C_2 X_2 \qquad \text{(Eq. 7.4)}$$

The expression given by Eq. 7.4 makes possible the use of multiple linear regression analysis to obtain the parameters C_1 and C_2 by treating the variables X_1 and X_2 as the independent variables.

The values of the independent variables X_1 and X_2 can be easily obtained from Eq. 7.3, since all the variables involved are known; η is the experimentally obtained viscosity, T_{cure} is the temperature of the experiment and T_g is the glass transition temperature, which can be easily obtained using the models developed in Chapter 4 to describe the T_g advancement for all the resin systems (see Eq. 5.3). The value of η_g was taken from values obtained from the literature [63]. The value chosen for η_g was 10^{12} Pas.

The application of Eq. 7.3 and Eq. 7.4 to model the experimental data of the isothermal cure of RTM6 resin at 160°C produced the fit shown in Figure 7.5. The calculated parameters C_1 and C_2 had the values 45.46 and 68.72 respectively. The observed deviation of the fitting from the experimental data suggests that some modifications need to be made to the model. The modified model that was used has the form:

$$\ell n\frac{\eta}{\eta_g} = -\frac{C_1\left(T_{cure} - T_r - T_g\right)}{C_2 + T_{cure} - T_r - T_g} \qquad \text{(Eq. 7.5)}$$

where T_r is a reference temperature, which can be treated as an adjustable parameter. This form of viscosity model has been used successfully by Gillham and co-workers[64].

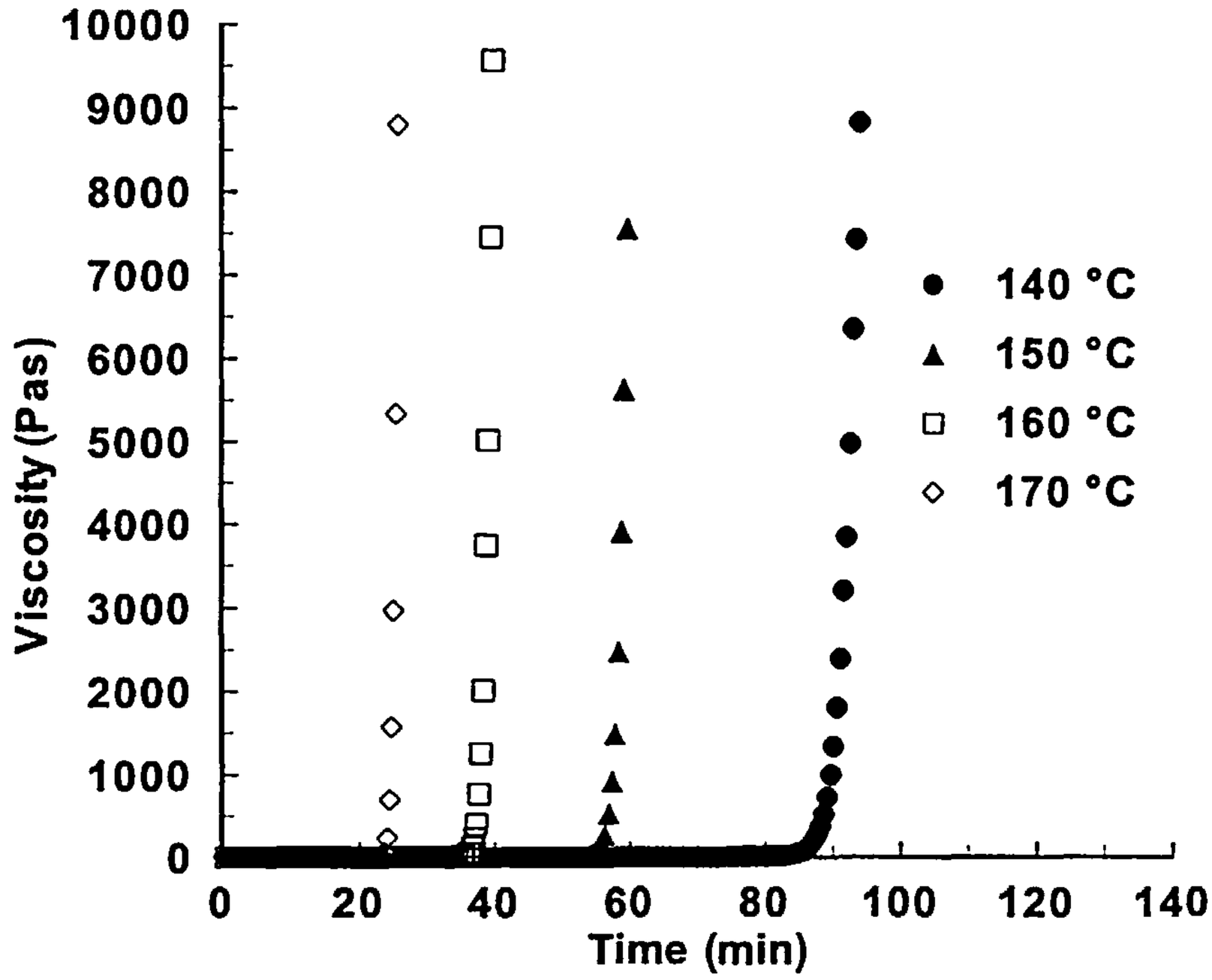

Figure 7.2 *Viscosity profile of RTM6 resin cured isothermally at various temperatures*

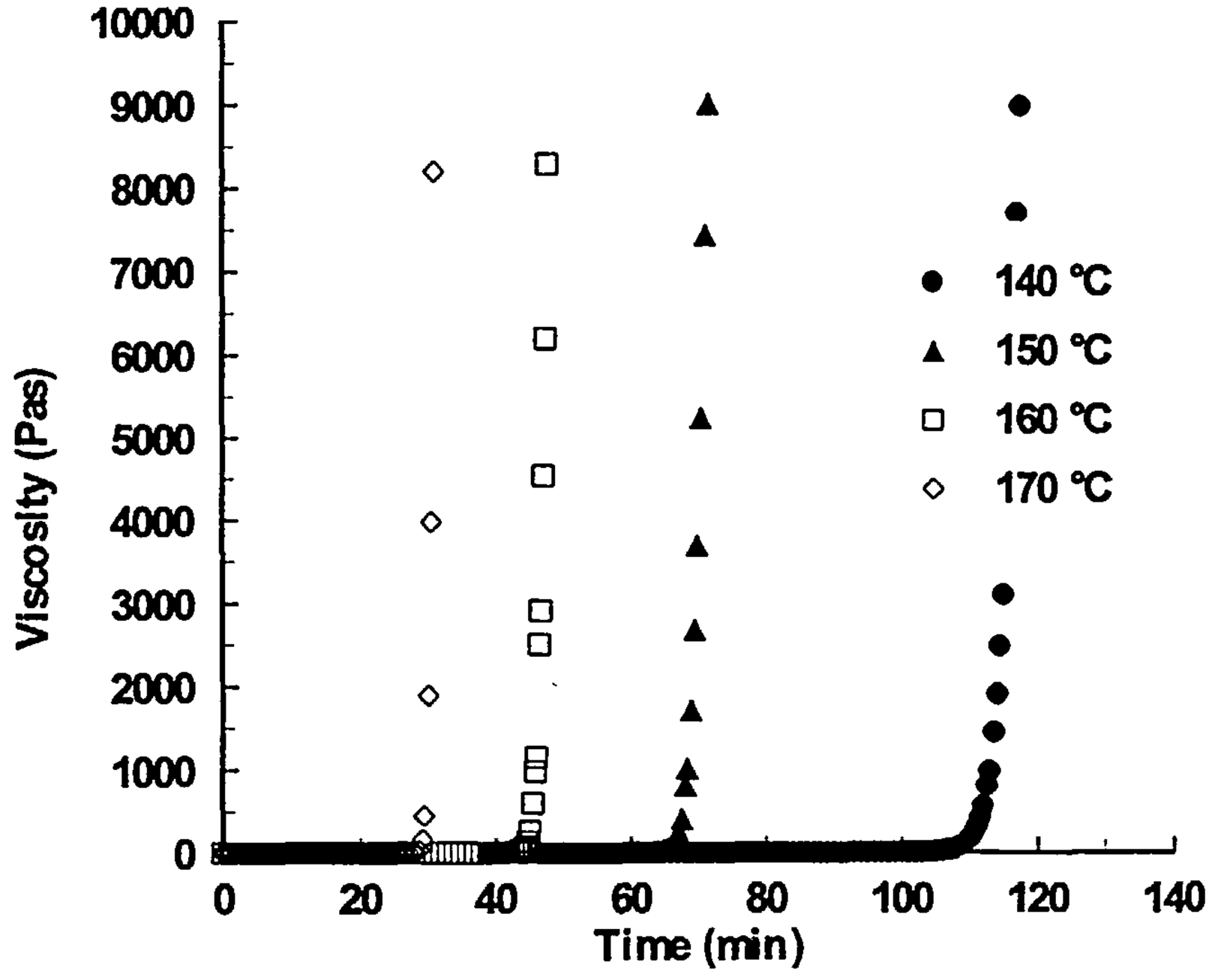

Figure 7.3 *Viscosity profile of RMO resin cured isothermally at various temperatures*

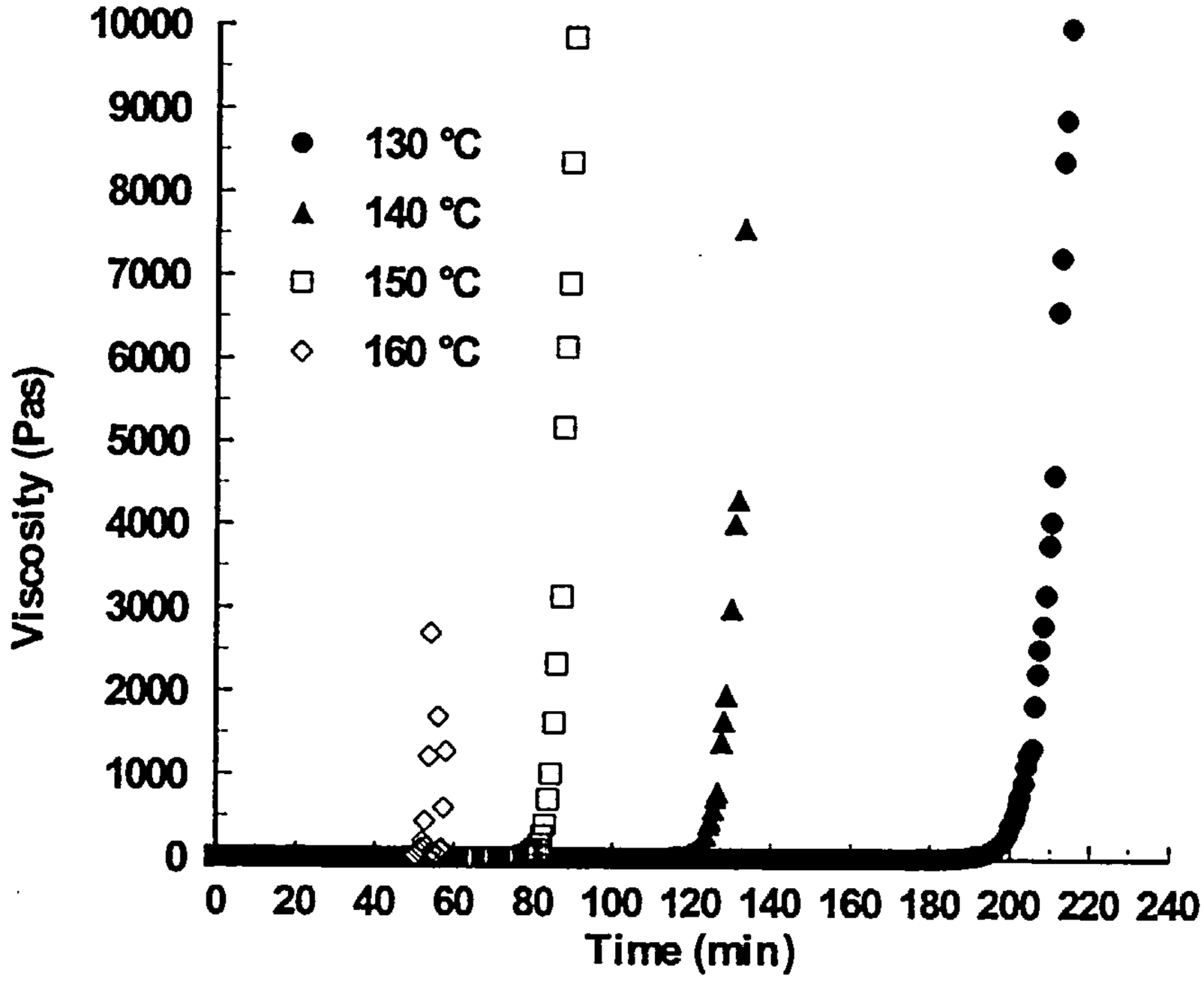

Figure 7.4 *Viscosity profile of RMO2 resin cured isothermally at various temperatures*

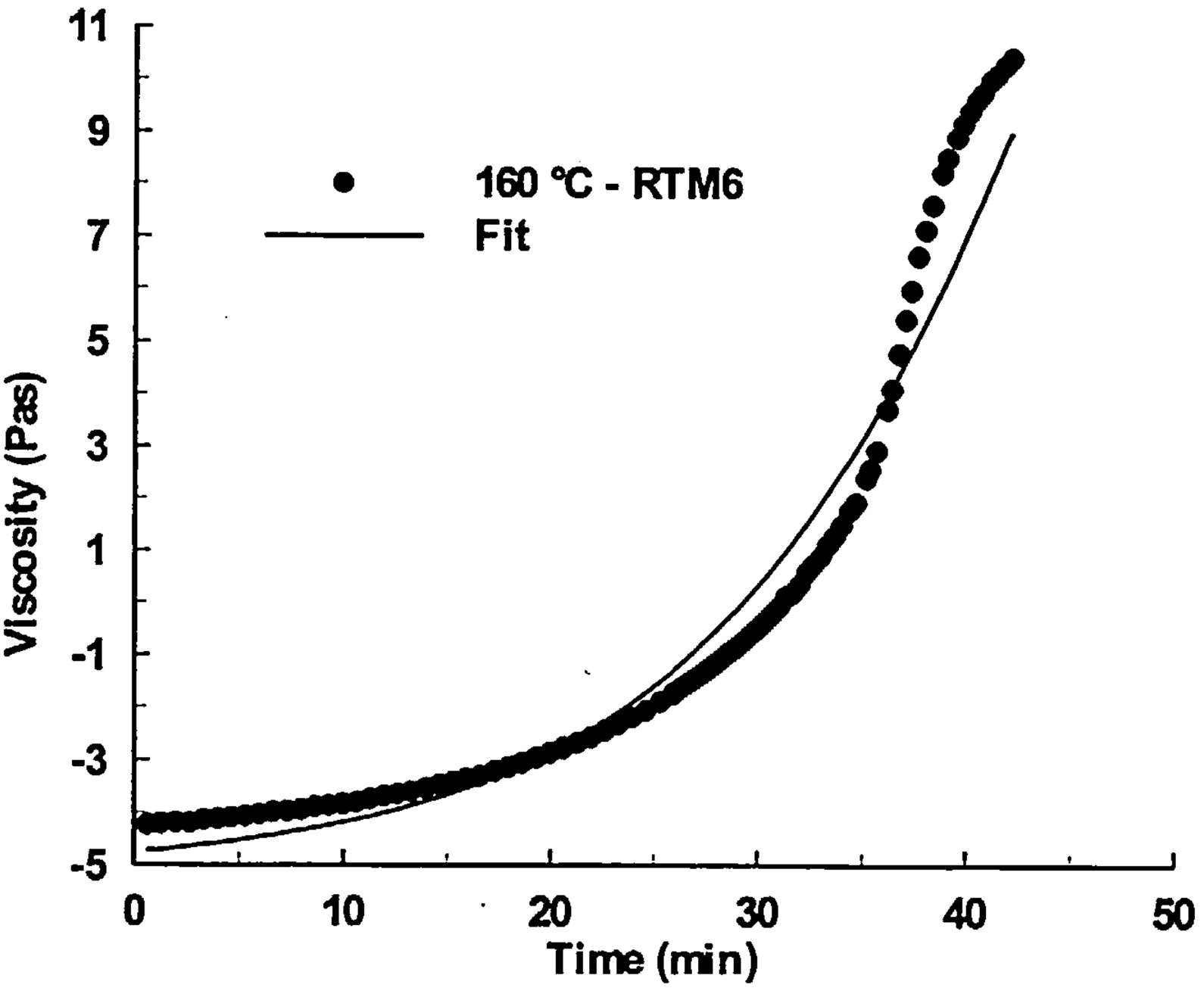

Figure 7.5 *Application of Eq. 7.3 and Eq. 7.4 to model the experimental viscosity data of the isothermal cure of RTM6 resin at 160°C*

In a similar manner with the expressions given by Eq. 7.3 and Eq. 7.4, the transformation of the new model can be written as:

$$X_1' = -\frac{1}{\ell n\eta - \ell n\eta_g} \quad and \quad X_2' = -\frac{1}{T_{cure} - T_r - T_g} \qquad \text{(Eq. 7.6)}$$

or:

$$1 = C_1 X_1' + C_2 X_2' \qquad \text{(Eq. 7.7)}$$

The application of Eq. 7.6 and Eq. 7.7 to the experimental data of RTM6, RMO and RMO2 resin systems resulted in the fittings shown in Figure 7.6 - Figure 7.8. The improvement of the fitting is evident from these figures. The simulation of the viscosity advancement is very successful up to gelation.

The calculated values of the parameters C_1, C_2 and T_r were found to depend on the cure temperature. The plots of the reference temperature T_r against the cure temperature and the plots of the natural logarithm of the parameters C_1 and C_2 against the inverse of the absolute cure temperature are shown in Figure 7.9 - Figure 7.11 respectively. These plots indicate a linear dependence of T_r on cure temperature and that of ℓnC_1, ℓnC_2 on the inverse of the absolute temperature. The best fitted lines for all the parameters and for all our resin systems are given in Table 7.1.

Table 7.1 *Best fit values of parameters T_r, C_1 and C_2 of Eq. 7.6 and Eq. 7.7 for viscosity modelling of RTM6, RMO and RMO2 resin systems*

Resin	**Best fit lines**		
	T_r (°C)	ℓnC_1	ℓnC_2
RTM6	$-145 + 1.239 \cdot T_{cure}$	$2.908 + 291.8 \cdot T^{-1}$	$-5.485 + 3562 \cdot T^{-1}$
RMO	$-162 + 1.289 \cdot T_{cure}$	$3.120 + 185.0 \cdot T^{-1}$	$-5.964 + 3617 \cdot T^{-1}$
RMO2	$-196 + 1.243 \cdot T_{cure}$	$3.502 + 9.644 \cdot T^{-1}$	$-1.120 + 1602 \cdot T^{-1}$

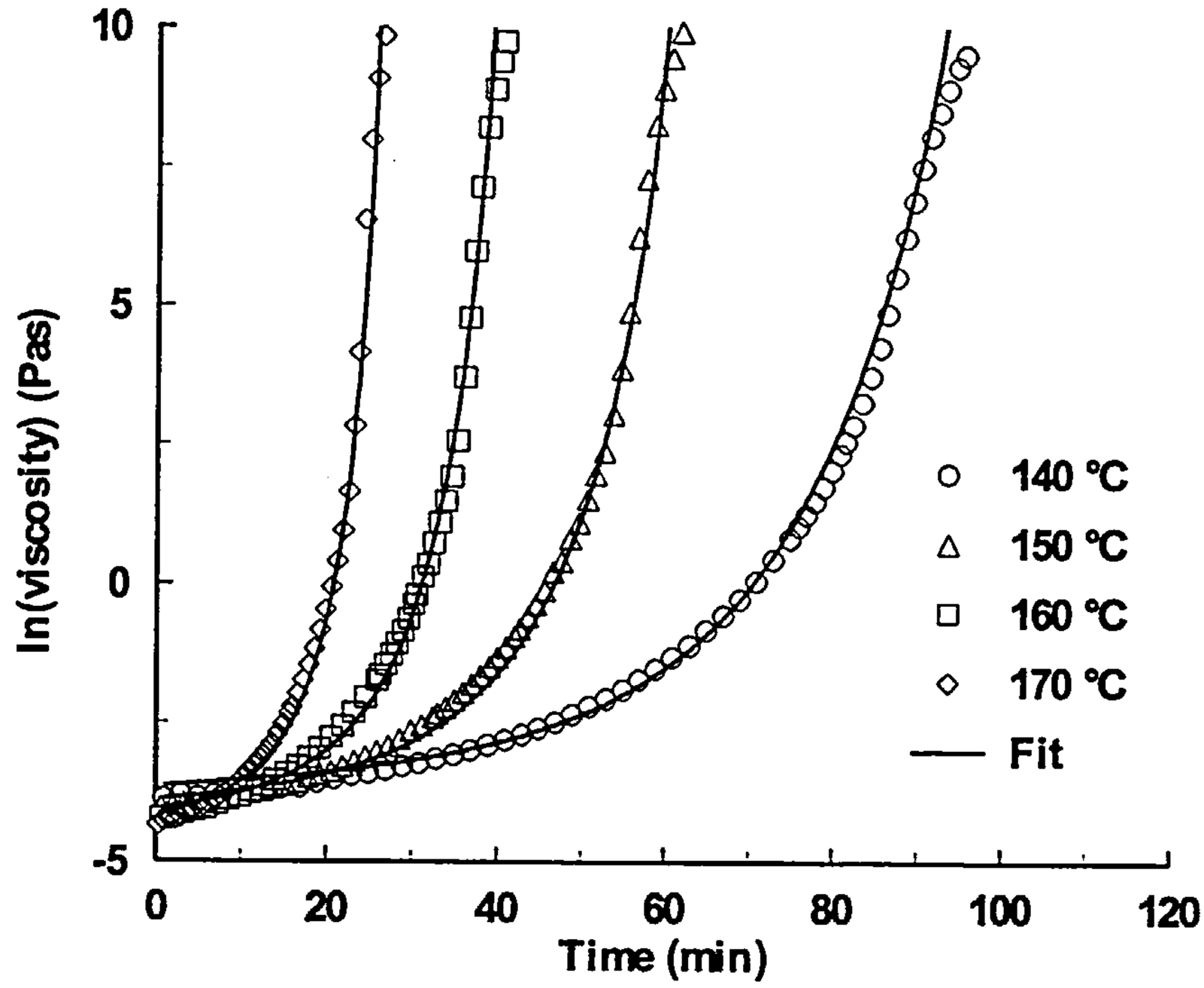

Figure 7.6 *Application of Eq. 7.6 and Eq. 7.7 to model the experimental viscosity data of the isothermal cure of RTM6 resin at various cure temperatures*

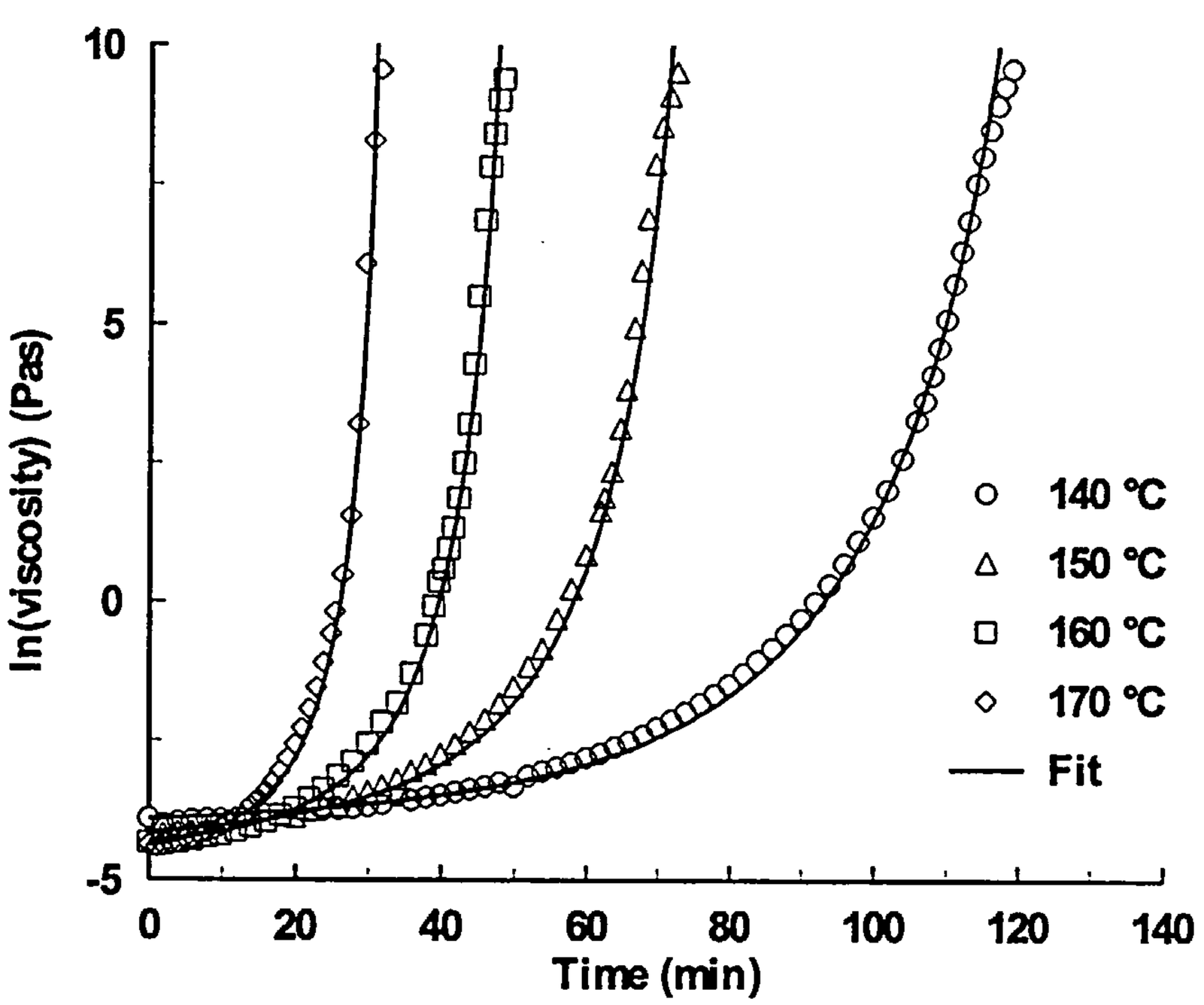

Figure 7.7 *Application of Eq. 7.6 and Eq. 7.7 to model the experimental viscosity data of the isothermal cure of RMO resin at various cure temperatures*

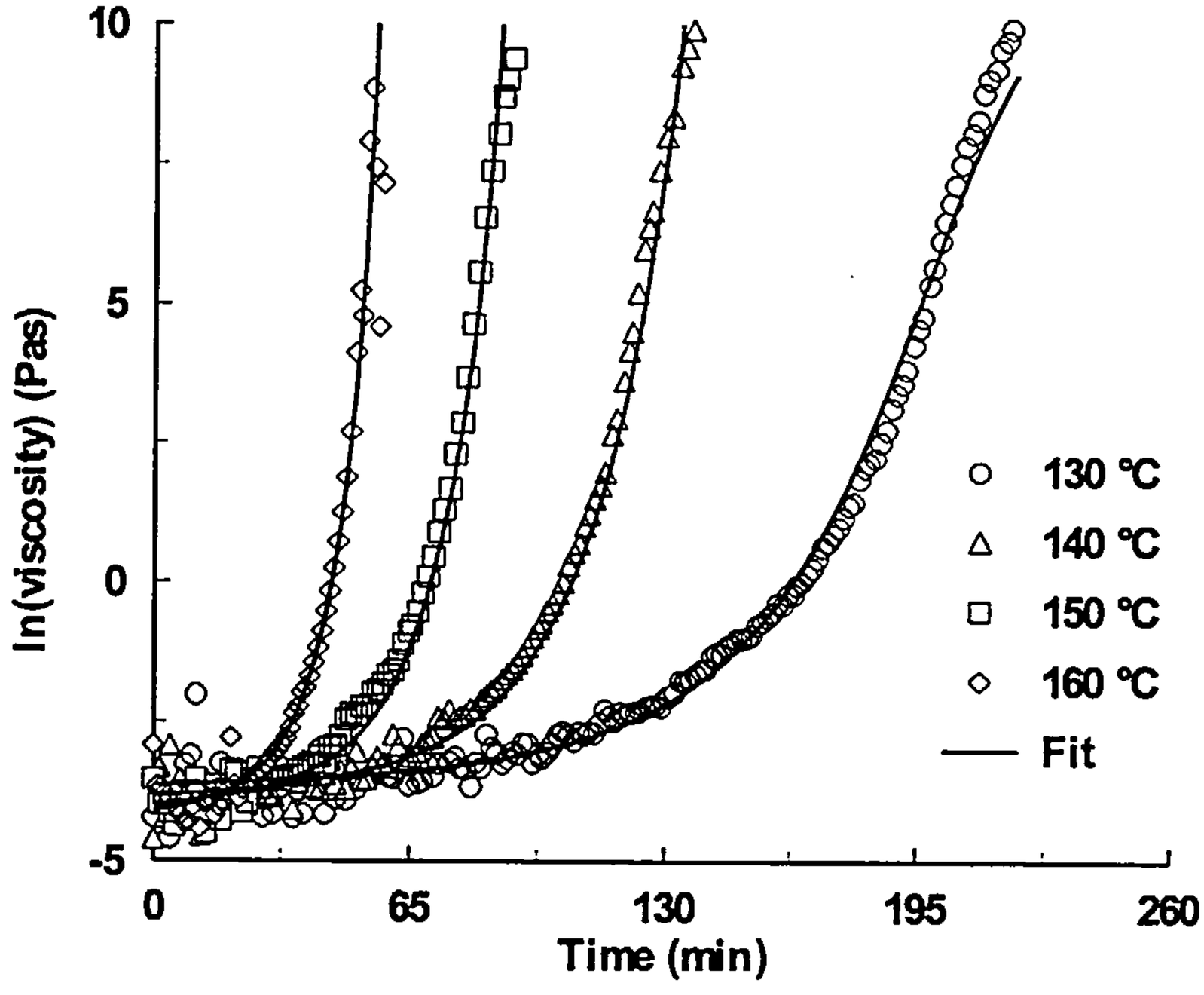

Figure 7.8 *Application of Eq. 7.6 and Eq. 7.7 to model the experimental viscosity data of the isothermal cure of RMO2 resin at various cure temperatures*

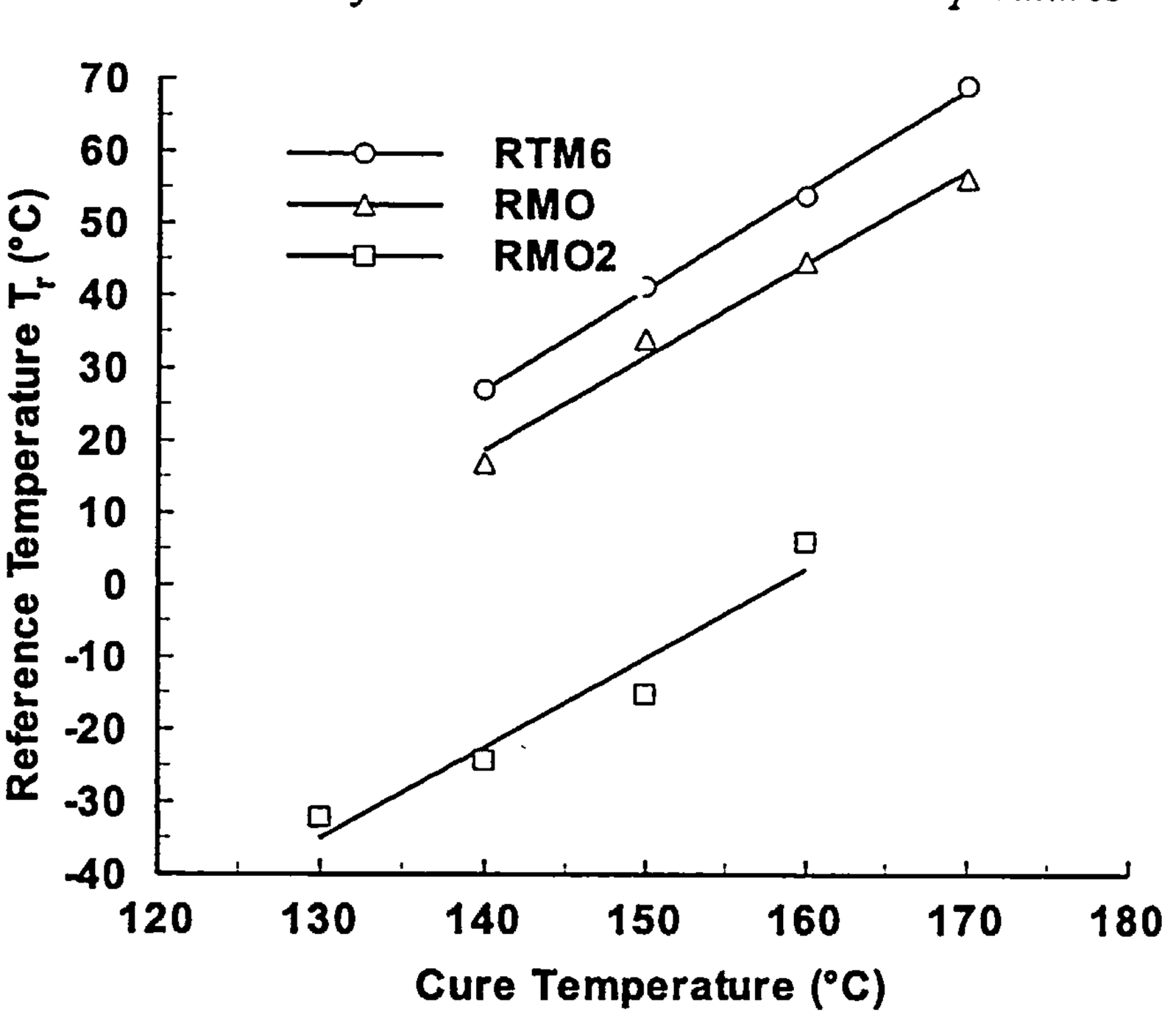

Figure 7.9 *Plot of parameter T_r of Eq. 7.5 against cure temperature for the isothermal cure of RTM6, RMO and RMO2 resins at various cure temperatures*

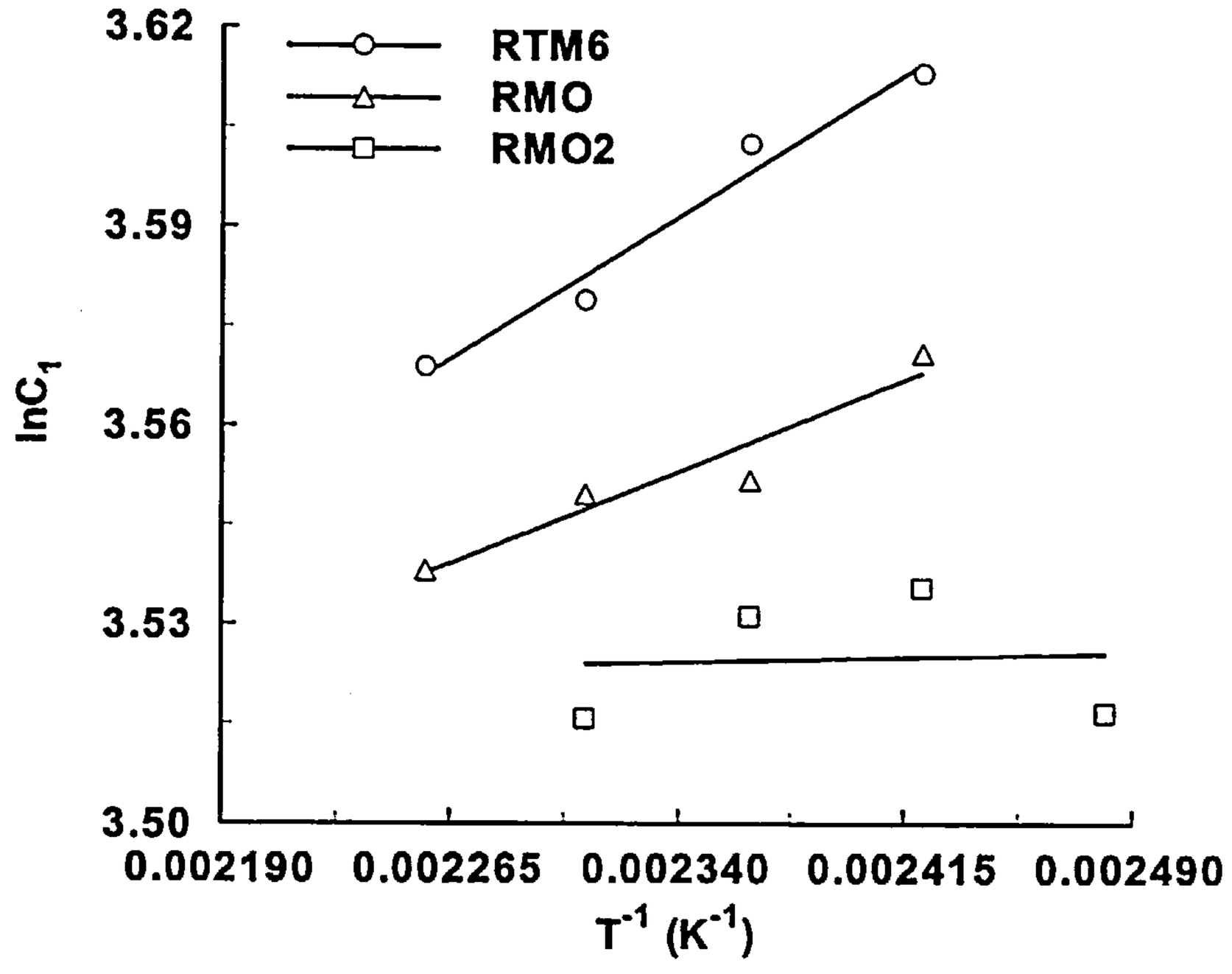

Figure 7.10 *Plot of parameter C_1 of Eq. 7.5 against cure temperature for the isothermal cure of RTM6, RMO and RMO2 resins at various cure temperatures*

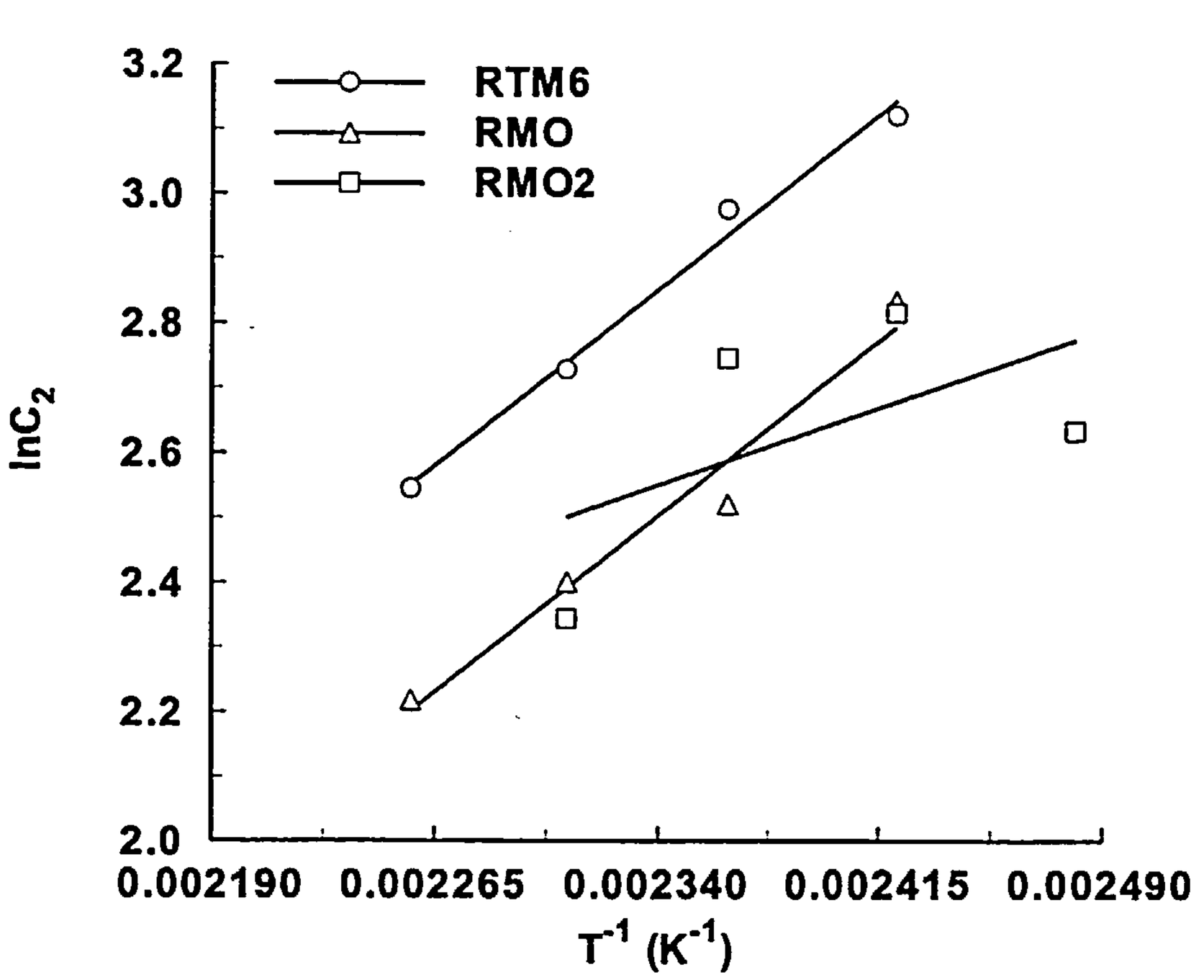

Figure 7.11 *Plot of parameter C_2 of Eq. 7.5 against cure temperature for the isothermal cure of RTM6, RMO and RMO2 resins at various cure temperatures*

Some deviation from linearity exists for the cure of RMO2 resin. To have a better insight into the way the evaluated parameters reflect the differences in structure between the different resin systems, viscosity was plotted against T_g advancement for all resins. These plots are shown in Figure 7.12 - Figure 7.14.

It is evident from these plots that viscosity converges to a unique T_g value at gelation point. At a specific T_g, the viscosity is higher at lower cure temperatures. As the cure progresses, the differences in viscosity between different cure temperatures at specific T_g values become smaller and the curves slowly converge to a unique T_g value at gelation. The approximate T_g values at gelation and the corresponding conversions for all resins are given in Table 7.2 along with the cure times to reach gelation at each cure temperature.

A close inspection of these values reveals that for the RMO2 resin system gelation occurs at a conversion level of about 80%, which corresponds to a T_g of about 144°C. This value of T_g indicates that the cure has already reached the vitrification point for the two low cure temperatures (130 and 140 °C). Thus the cure has become diffusion controlled prior to gelation. This could explain the diversion from linearity that was observed for the estimated parameters of the viscosity model for that particular resin system.

Table 7.2 *Characteristic points at gelation for the isothermal cure of RTM6, RMO and RMO2 resins*

Resin	Gelation Time (t_{gel} / min)					$_{gel}T_g$ (°C)	α_{gel}
	130°C	140°C	150°C	160°C	170°C		
RTM6	-	95	61	40	26	94	0.59
RMO	-	117	72	48	32	105	0.62
RMO2	215	132	87	56	-	144	0.80

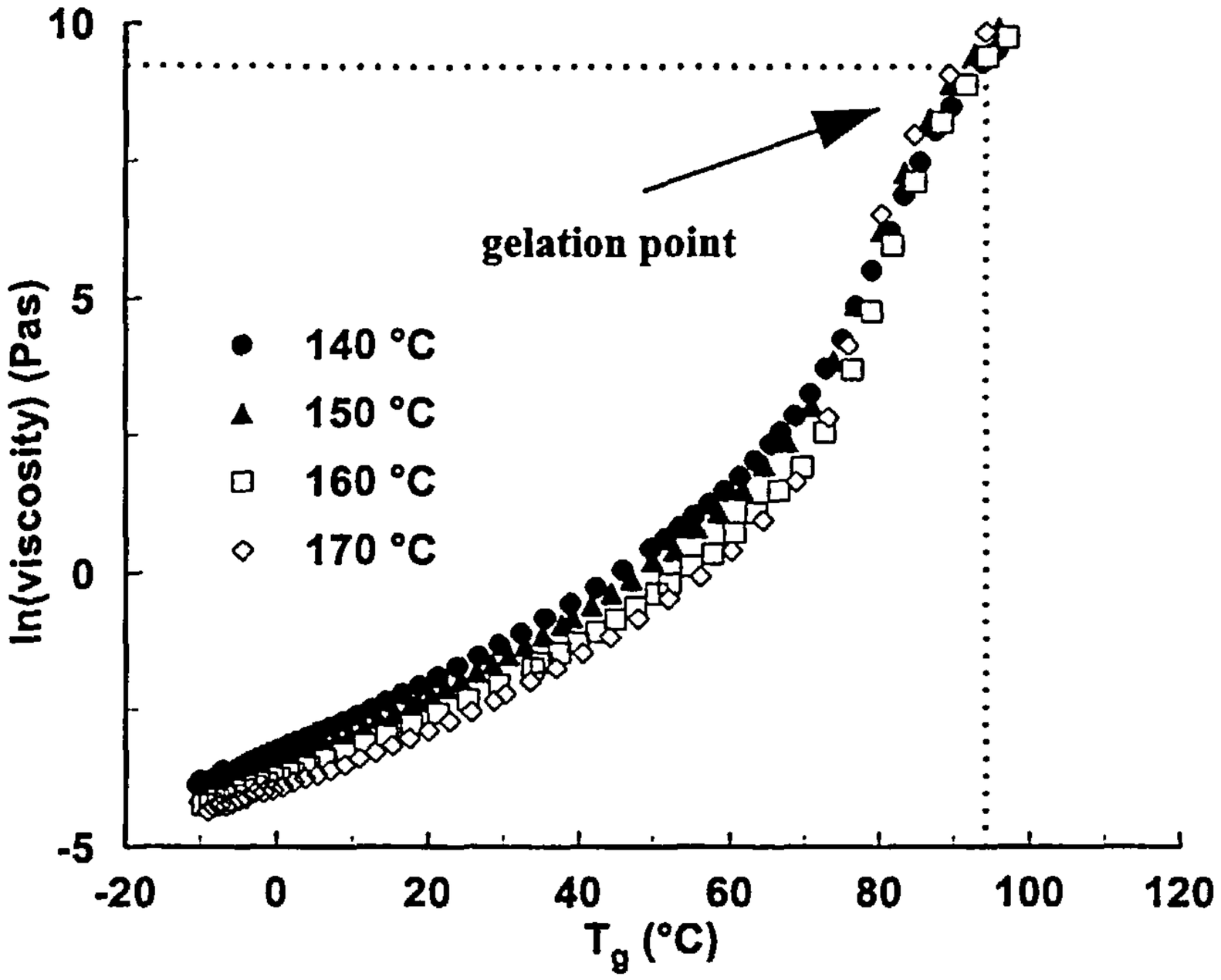

Figure 7.12 *Viscosity vs Tg for the isothermal cure of RTM6 resin at various cure temperatures. Gelation point is also shown in the picture*

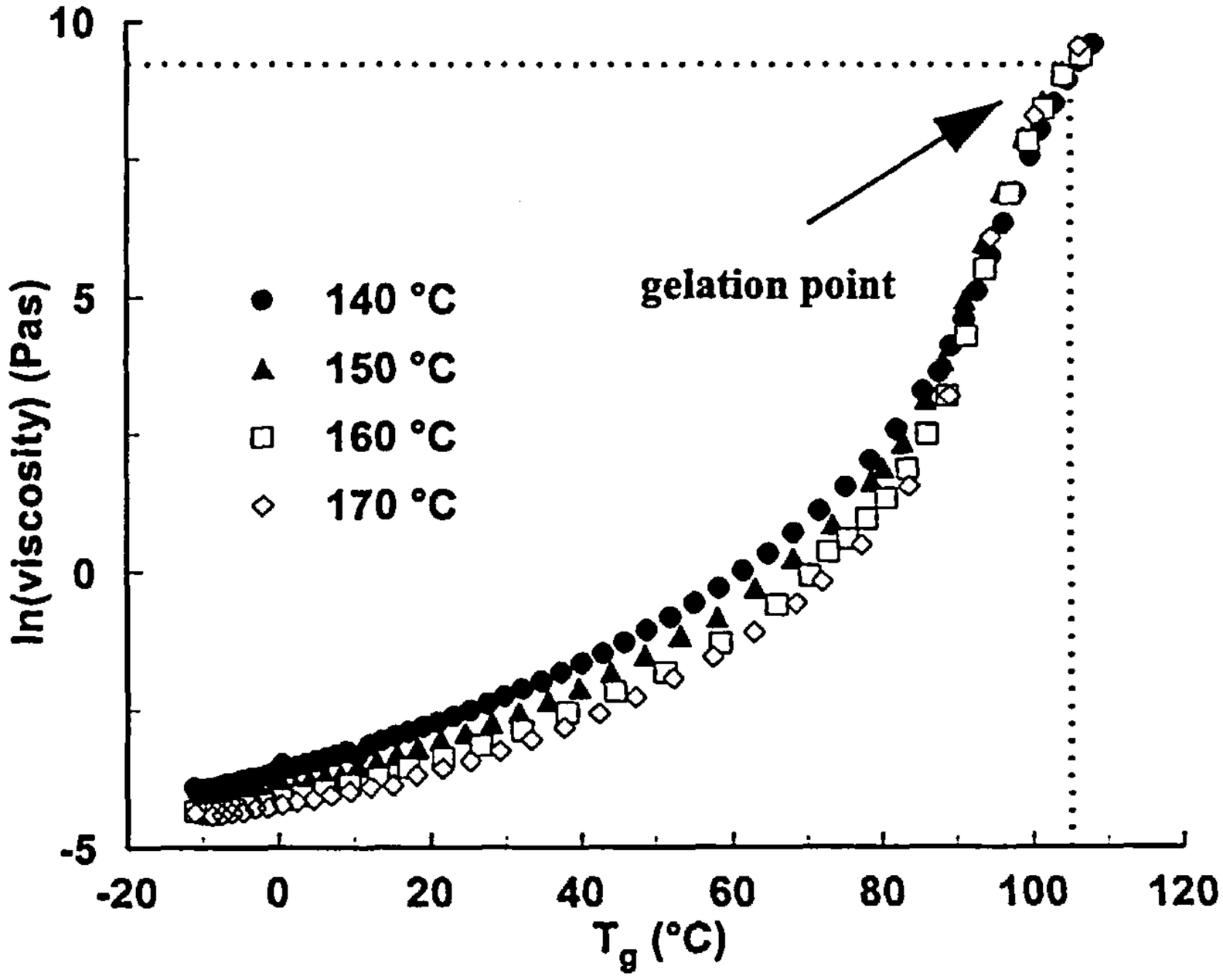

Figure 7.13 *Viscosity vs Tg for the isothermal cure of RMO resin at various cure temperatures. Gelation point is also shown in the picture*

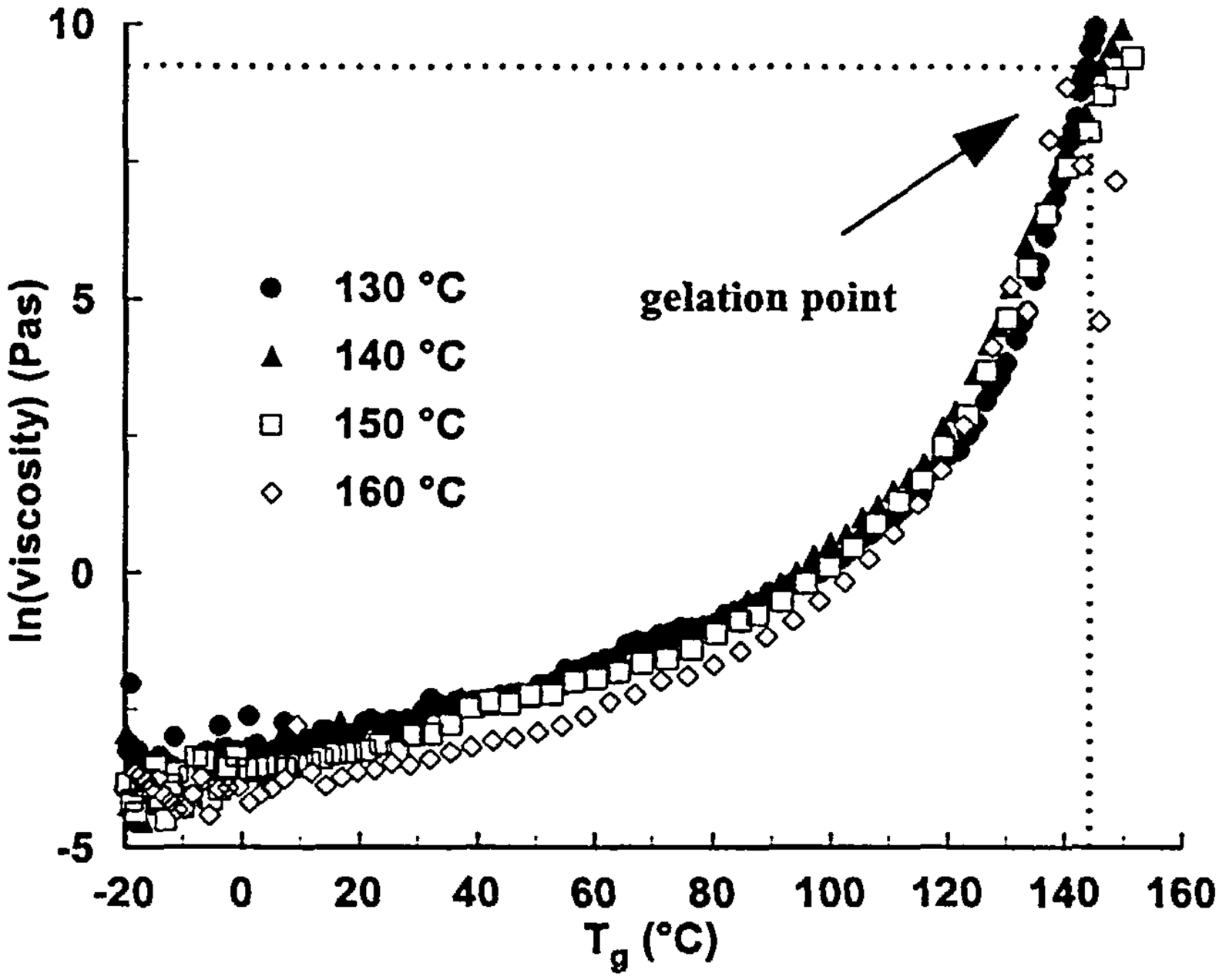

Figure 7.14 *Viscosity vs Tg for the isothermal cure of RMO2 resin at various cure temperatures. Gelation point is also shown in the picture*

7.3 Viscosity Modelling of 934 Resin

The viscosity profile of the 934 resin at various cure temperatures is shown in Figure 7.15 as plots of the natural logarithm of viscosity against the cure time. Comparison of these plots with the viscosity profiles of the other resin systems (see Figure 7.6 - Figure 7.8) reveals some differences between them. Apart from the slow increase in viscosity at the later stages of the cure and especially towards gelation, there is a different trend in the viscosity increase at the beginning of the cure. At low conversion levels, viscosity follows a logarithmic growth rate up to approximately 5 - 10 % conversion. Above that point, viscosity increases following the normal exponential growth rate.

As mentioned in Section 3.2.1.2, isothermal DSC experiments were also made for 934 resin, but since it was impossible to draw a proper baseline for the integration of the isothermal DSC thermogram, these isothermal runs were not used in the development of the kinetic models in Chapter 4. Instead, the conversion profiles and the subsequent

kinetic analysis were based on experimental results from FTIR and residual heat of reaction experiments. Despite the fact that the isothermal DSC runs were not used in the kinetic analysis, they exhibited a characteristic phenomenon in the thermogram; a sudden drop in the heat evolution approximately at 5-10% level of conversion. The sudden drop in the reaction rate observed in the isothermal DSC experiments was not depicted from the FTIR and the residual heat of reaction DSC experiments. A comparison between viscosity and heat evolution calculated from the isothermal DSC experiments can be seen in Figure 7.16 for the isothermal cure at 150°C. This figure shows that at the point where the heat evolution rate exhibits a sudden change, viscosity shows an inflection point. This observation suggests that at this point of the cure there should be a change in the reaction mechanism. Although this was not considered in the previous discussion on the reaction kinetics of this particular resin system (see Section 4.4.4), the combined results of viscosity and isothermal DSC experiments imply that a more careful analysis need to be made.

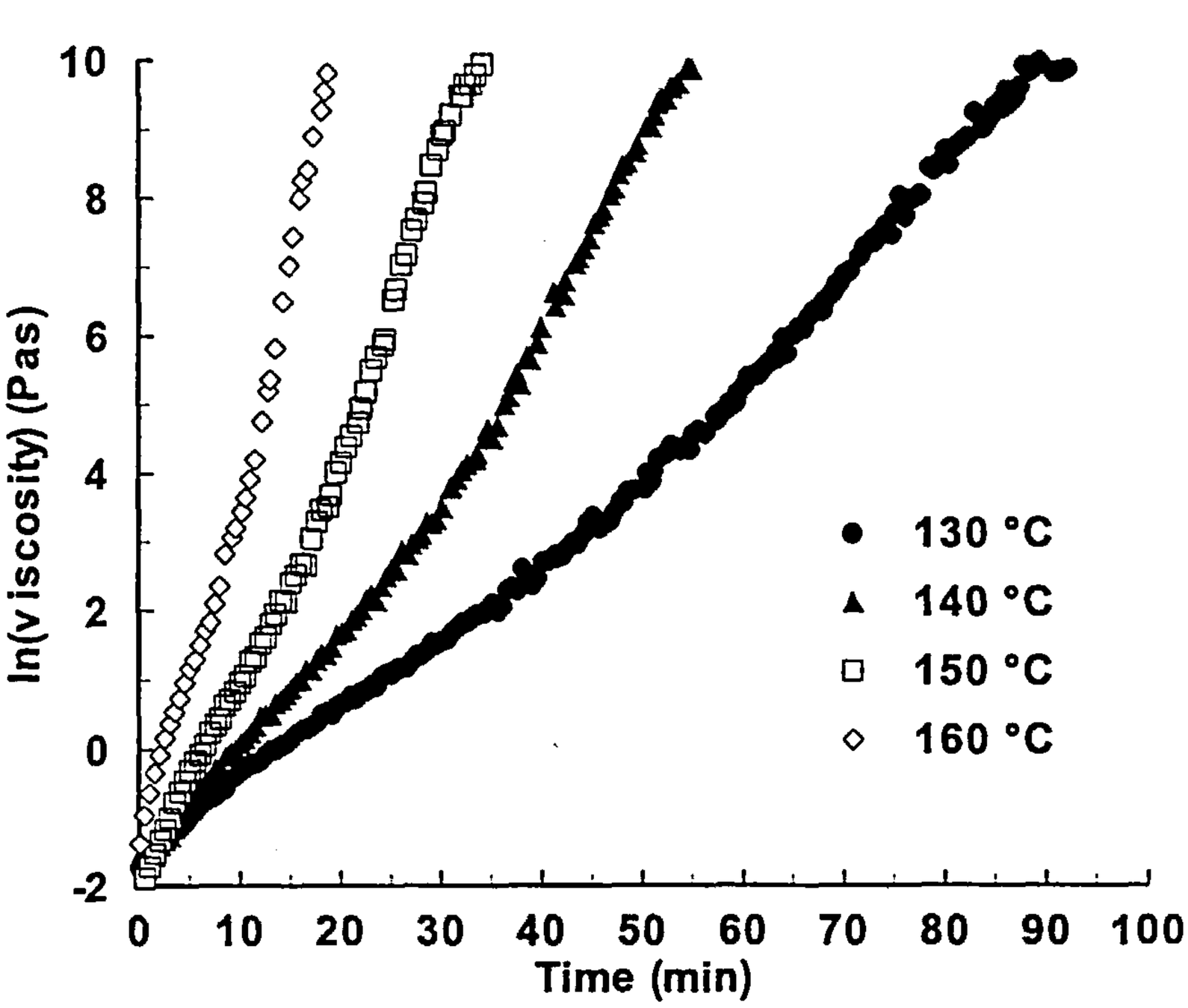

Figure 7.15 *Plot of the natural logarithm of viscosity against cure time for the isothermal cure of 934 resin at various cure temperatures*

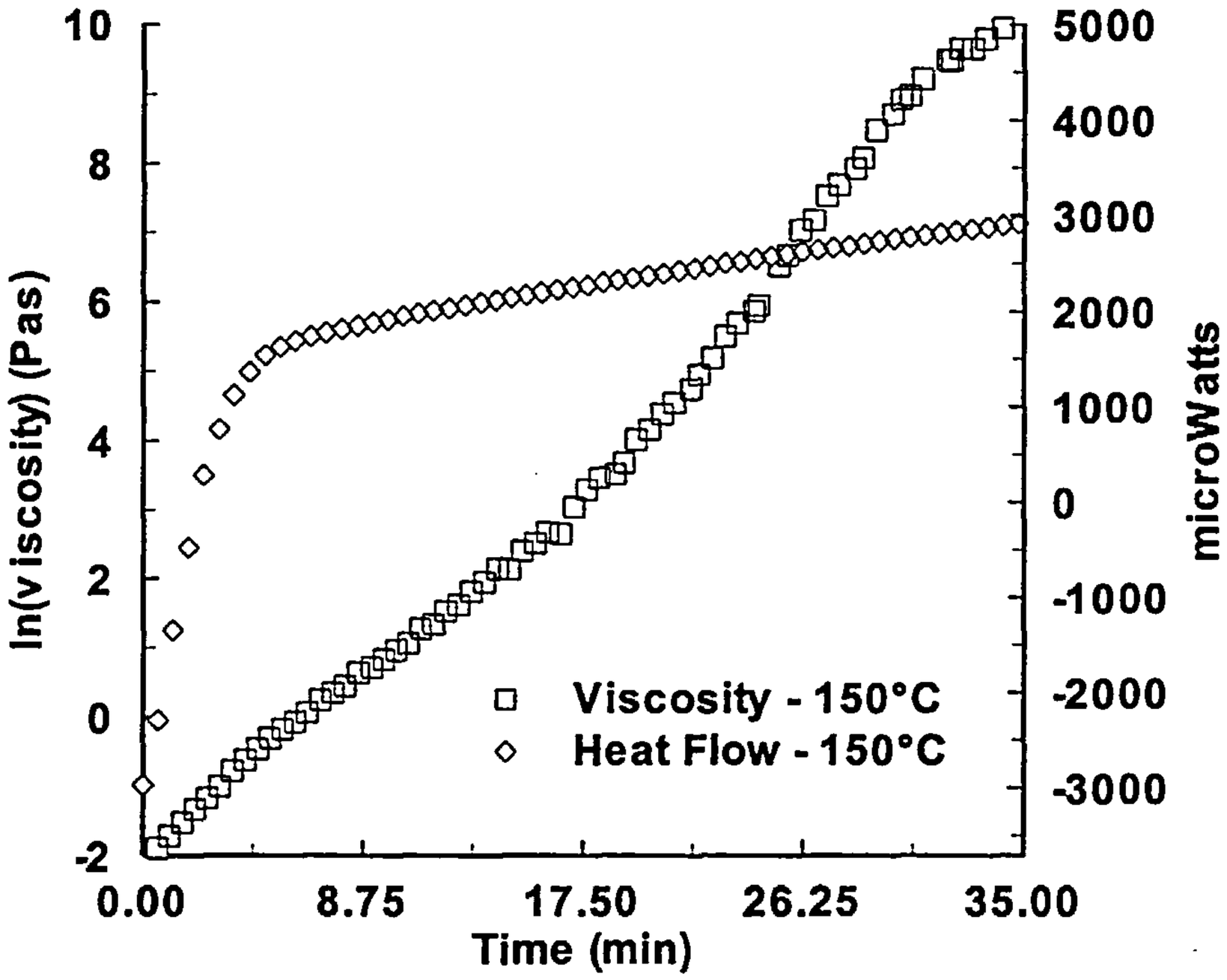

Figure 7.16 *Comparison between viscosity and heat flow during the isothermal cure of 934 resin at 150°C*

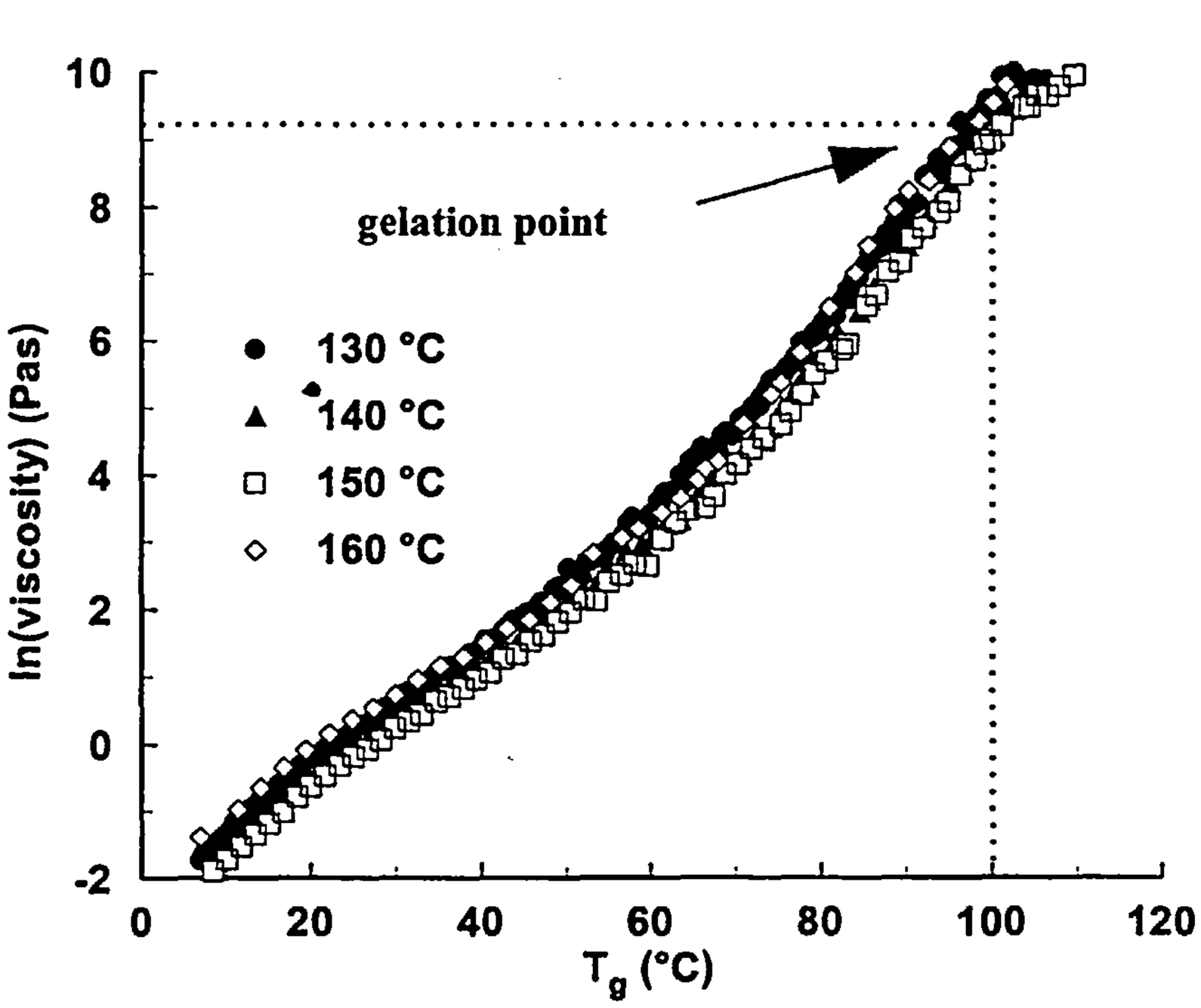

Figure 7.17 *Viscosity vs Tg for the isothermal cure of 934 resin at various cure temperatures. Gelation point is also shown in the picture*

The different viscosity profile that was obtained for the isothermal cure of 934 resin can be seen more clearly in Figure 7.17. In this figure the natural logarithm of viscosity has been drawn as a function of the T_g at various cure temperatures. It can be seen that the approach to gelation does not follow a sudden increase in viscosity as was the case with the other resin systems. Instead, there is an almost linear increase in viscosity with Tg, which makes the determination of gelation a rather difficult task. However, for reasons of comparison, gelation was also determined as the point where viscosity reaches a value of 10kPas (see Table 7.3).

Table 7.3 *Characteristic points at gelation for the isothermal cure of 934 resin at various cure temperatures*

Gelation Time (t_{gel} / min)				T_g (°C)	α_{gel}
130°C	140°C	150°C	160°C		
87	51	30	18	100	0.47

For comparison purposes, Eq. 7.6 and Eq. 7.7 were applied to model the viscosity profile of 934 resin. The resulting fittings are shown in Figure 7.18 and the calculated parameters T_r, C_1 and C_2 in Figure 7.19 and Figure 7.20 as plots against cure temperature for T_r and inverse of absolute cure temperature for C_1 and C_2. These parameters were also found to follow a linear dependence on temperature, with the best fitted lines given in Table 7.4.

Table 7.4 *Best fit values of parameters T_r, C_1 and C_2 of Eq. 7.6 and Eq. 7.7 for viscosity modelling of 934 resin system*

T_r (°C)	ℓnC_1	ℓnC_2
$-137 + 1.096 \cdot T_{cure}$	$3.240 + 251.5 \cdot T^{-1}$	$2.785 + 724.1 \cdot T^{-1}$

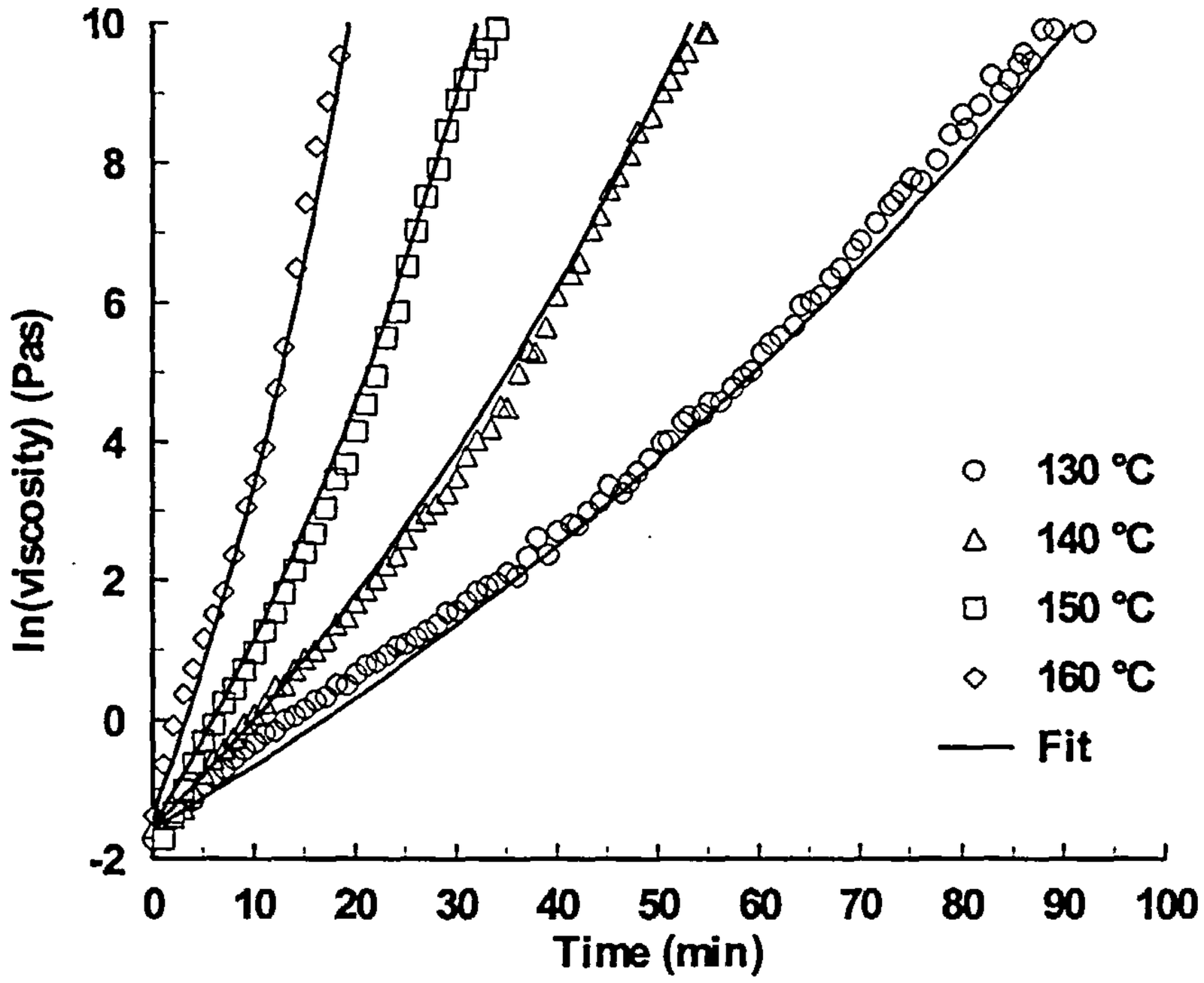

Figure 7.18 *Application of Eq. 7.6 and Eq. 7.7 to model the experimental viscosity data of the isothermal cure of 934 resin at various cure temperatures*

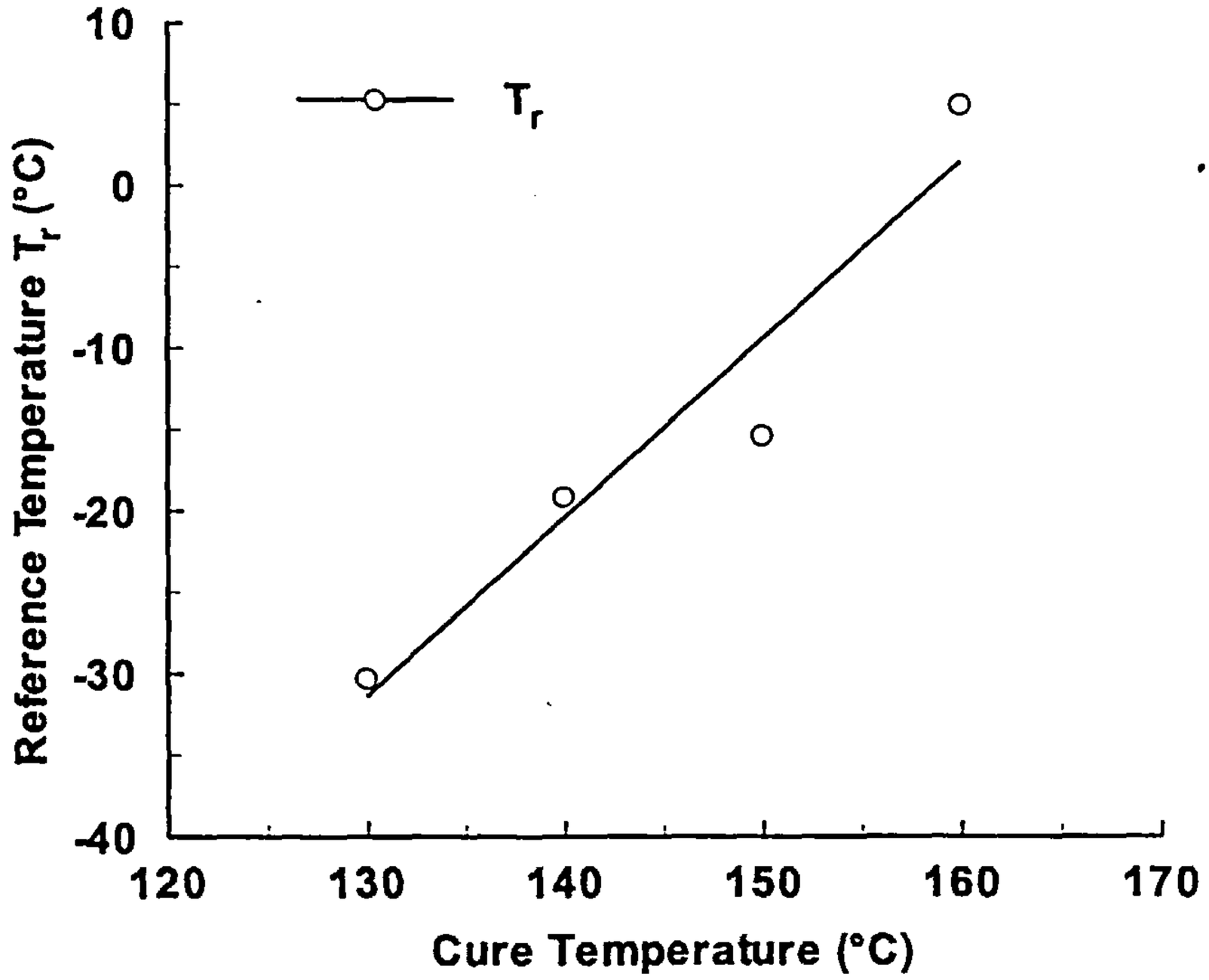

Figure 7.19 *Plot of parameter T_r of Eq. 7.5 against cure temperature for the isothermal cure of 934 resin at various cure temperatures*

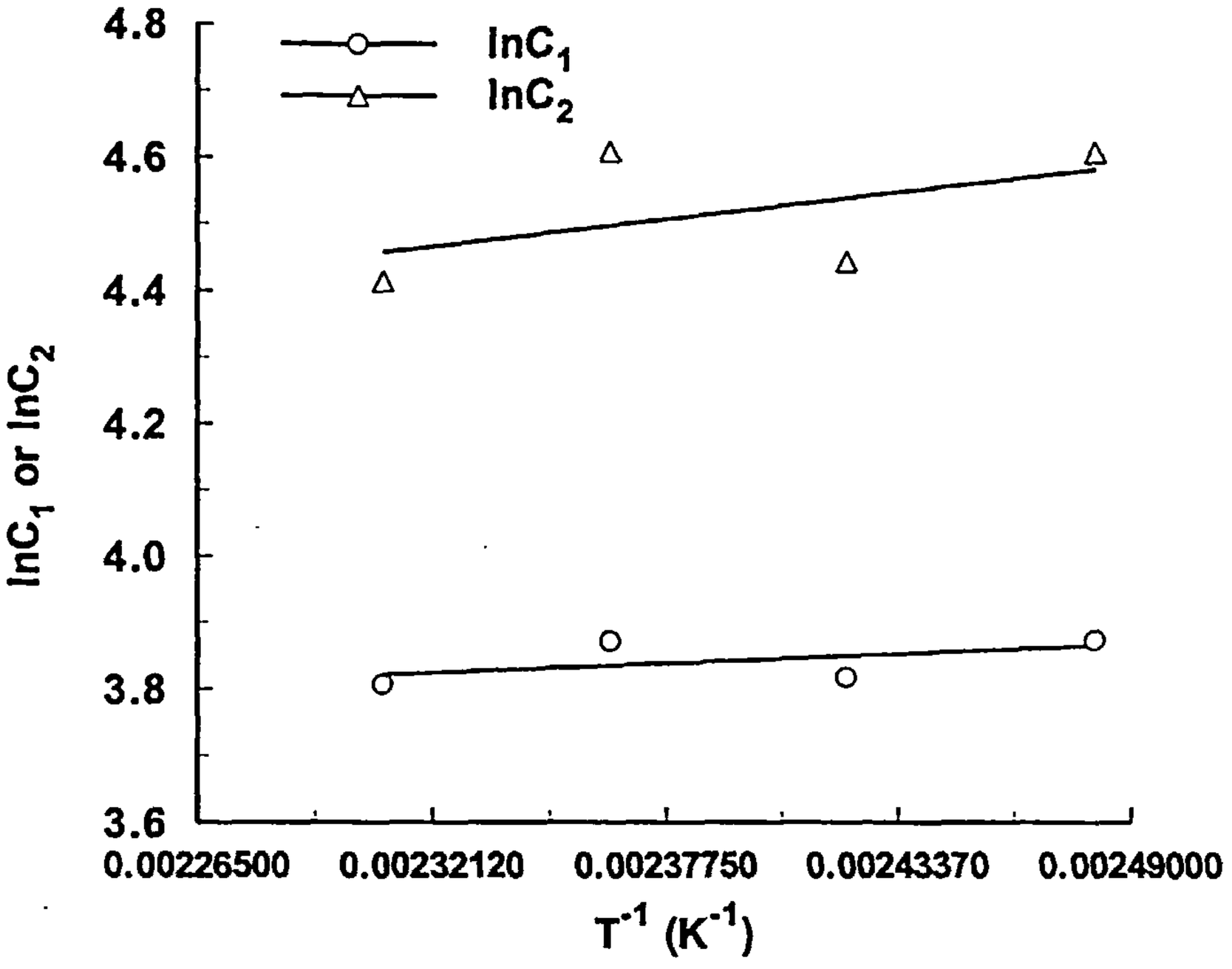

Figure 7.20 *Plot of parameters C_1 and C_2 of Eq. 7.5 against cure temperature for the isothermal cure of 934 resin at various cure temperatures*

The majority of results obtained here suggests that the rheological technique used in this study was very sensitive in the changes that occur during the cure of the epoxy resins investigated. It enable us to identify the gelation region during the isothermal cure and predict, via the use of a modified WLF equation, the viscosity advancement as the resin transforms from the viscous liquid state to the rubbery state. The viscosity profiles and gelation times evaluated here will be used in Chapter 8 as a comparison to the results on gelation and viscosity by the dielectric cure monitoring technique.

Chapter Eight

8. Dielectric Cure Monitoring

In this chapter, the results from the dielectric experiments will be presented. The changes in the dielectric response, that occur during the cure of the resin under isothermal conditions will be investigated. The structural changes and the phase transitions will be correlated to distinctive changes in the dielectric signal and mathematical expressions will be constructed to describe them quantitatively.

8.1 Dielectric Signal Interpretation

The experimental set-up used for the dielectric measurements permitted the direct measurement of the real and imaginary part of the complex impedance of the resin (See Section 3.3). In order to apply the theory described in Section 2.7.11 for direct evaluation of the state of the cure, the evaluation procedure of the dielectric response has to concentrate on the contribution of the migrating charges to the overall signal. Since the dielectric response of the migrating charges can be represented by an equivalent parallel R-C circuit, the characteristic maximum of the imaginary part of the complex impedance in the frequency domain, can be directly attributed to the resistivity of the curing resin (see Section 2.7.11, Eq. 2.84).

A representative output of the dielectric response is shown in Figure 8.1, which accounts for the isothermal cure of RTM6 resin at 140°C and 22 minutes into the cure. The characteristic peak appearing in this plot is the one which should be attributable to

the migrations of any charged quantities within the resin. To verify the above assumption, an appropriate reconstruction of the dielectric response has to be made, that accurately simulates the true signal of the curing resin. Some of the mathematical expressions given in Section 2.7.11 will be retrieved for that purpose.

The imaginary impedance of a parallel R-C circuit can be expressed as:

$$Z'' = \frac{\omega C R^2}{1+\omega^2 C^2 R^2} \qquad \text{(Eq. 8.1)}$$

By taking the logarithms of both sides of the above expression and using the expression:

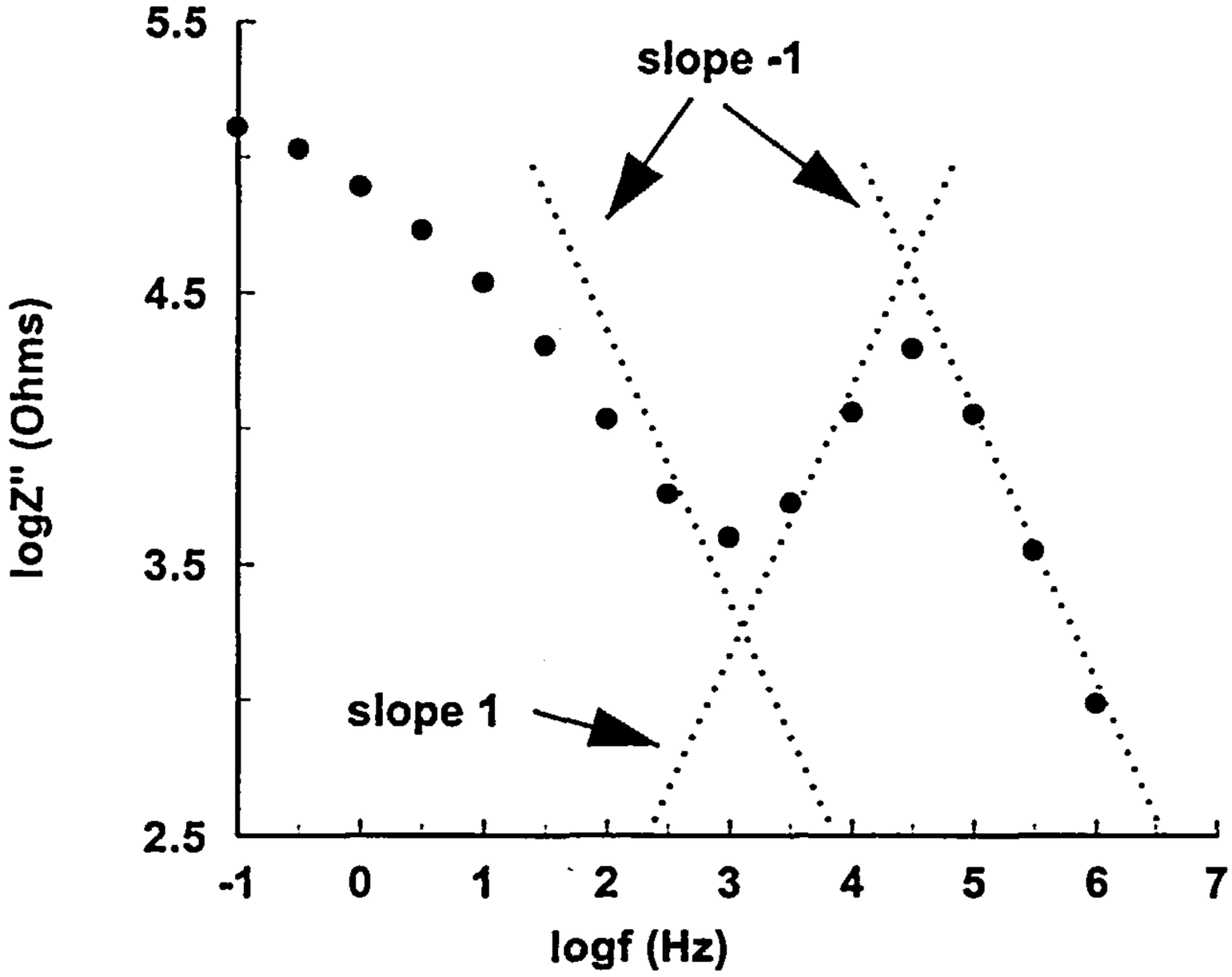

Figure 8.1 *Imaginary impedance vs frequency for the isothermal cure of RTM6 resin at 140°C for 22 min. Dotted lines represent the schematic representation of straight lines that intersect the logf axis at 45°.*

$$\omega = 2\pi f \qquad \text{(Eq. 8.2)}$$

the following equation can be obtained:

$$\ell ogZ'' = \ell og\left(2\pi CR^2\right) + \ell ogf - \ell og\left(1+4\pi^2 f^2 C^2 R^2\right) \qquad \text{(Eq. 8.3)}$$

The first derivative of this expression with respect to ℓogf is:

$$\frac{d\ell ogZ''}{d\ell ogf} = 1-2\frac{4\pi^2 f^2 C^2 R^2}{1+4\pi^2 f^2 C^2 R^2} \qquad \text{(Eq. 8.4)}$$

As discussed in Section 2.7.11, for a parallel R-C circuit, the imaginary impedance has a maximum at a characteristic angular frequency ω:

$$\omega_c = \frac{1}{RC} \quad or \quad f_c = \frac{1}{2\pi RC} \qquad \text{(Eq. 8.5)}$$

Substitution of the characteristic frequency into Eq. 8.4 yields:

$$\frac{d\ell ogZ''}{d\ell ogf} = 1-2\frac{\left(\frac{f}{f_c}\right)^2}{1+\left(\frac{f}{f_c}\right)^2} \qquad \text{(Eq. 8.6)}$$

So, the plot of $\ell ogZ''$ against ℓogf will have a slope that will be given by Eq. 8.6. The visualisation of the slope changes in the frequency domain can be easily exploited if we consider frequencies well above and well below the characteristic frequency. At that range of frequencies we get:

$$slope \approx -1 \quad for \quad f >> f_c$$
$$slope \approx 1 \quad for \quad f << f_c \qquad \text{(Eq. 8.7)}$$

Thus, in the frequency domain and on a logarithmic scale, ℓogZ'' can be represented by a peak, that intersects the ℓog$f$ axis at an angle of 45° from either side.

The above are demonstrated graphically in Figure 8.1. In this figure, the imaginary impedance of the isothermal cure of RTM6 resin at 140°C has been plotted on a logarithmic scale as a function of the logarithm of frequency. The dotted lines drawn on the same figure represent linear extrapolation of the data at frequencies well above and well below the peak frequency. These have a slope of -1 and 1 respectively.

The above discussion supports the idea that the peak observed in the ℓogZ'' vs ℓog$f$ plot can be related to an equivalent parallel R-C circuit, which in turn represents contributions from migrating charges within the resin. One more thing that has to be cleared in order to attribute the observed peak to migrating charges, is the sudden increase in the signal at frequencies well below the peak frequency. As discussed in Section 2.7.8, the dielectric signal is strongly affected by conductivity contributions, especially at low frequencies. This effect can lead to a strong electrode polarisation, which will increase the measured values by a high order of magnitude (10^3 x or 10^4 x). The equivalent circuit that was given in Section 2.7.6 (see Figure 2.13) compensates for electrode polarisation effects by the two extra capacitors placed in series at both sides of the circuit. The impedance of a pure capacitor can be written as:

$$Z_C'' = \frac{1}{\omega C} \quad or \quad \ell og Z_C'' = -\ell og 2\pi C - \ell og f \qquad \text{(Eq. 8.8)}$$

The plot of ℓogZ'' against ℓog$f$ will give a straight line with slope -1. A schematic representation of such a plot is shown in Figure 8.1 , appropriately shifted in order to coincide with the data of the RTM6 cure shown in the same figure.

It is evident from all the above, that the responses of the parallel R-C circuit (migrating charges) and pure capacitor (electrode polarisation), if combined appropriately, will

give a very good approximation of the true dielectric signal obtained for the cure of any resin system, at least in the range of frequencies where the distinctive peak appears.

Thus, the observed peak in the $\ell ogZ''$ vs ℓogf plot can actually be attributed to the contribution of the migrating charges within the resin.

8.2 Cure State Prediction by Dielectric Measurements

In Figure 8.2, the imaginary impedance, obtained for the isothermal cure of RTM6 resin at 140°C, is plotted as a function of frequency at various time intervals into the cure. The characteristic peak observed in all these plots changes its position throughout the cure. In the initial stages of the cure, the peak appears at high frequencies and exhibits low impedance values. As the cure progresses, that peak moves to lower frequencies with a continuous increase in magnitude. If we consider the analysis given in section 8.1, the peak magnitude is directly related to the resistivity of the curing resin. In the initial stages of the cure, where the resin is still in the liquid phase, the resistivity is low, thus the imaginary impedance has to be small in magnitude. Also in this liquid state, the migrating charges are easier to move and follow the changes in the polarity of the alternating electric field at high frequencies. That explains why the peak appears at high frequencies at the beginning of the cure. As the cure progresses and the material starts to solidify, the resistivity of the resin rises and the migrating charges become hindered. The difficulty in the movement of these charges is reflected in the appearance of the peak at lower frequencies, where the polarity of the field changes slowly, giving time to the migrating charges to align with it.

The reflection of the changes that occur during the cure in the intensity of the peak can be visualised more easily by plotting the logarithm of the imaginary impedance at the peak as a function of the cure time. Such a plot is shown in Figure 8.3 along with the plot of conversion at the same cure temperature, in order to have a better view of any correlation that might exist between changes in the imaginary impedance and changes in the conversion level.

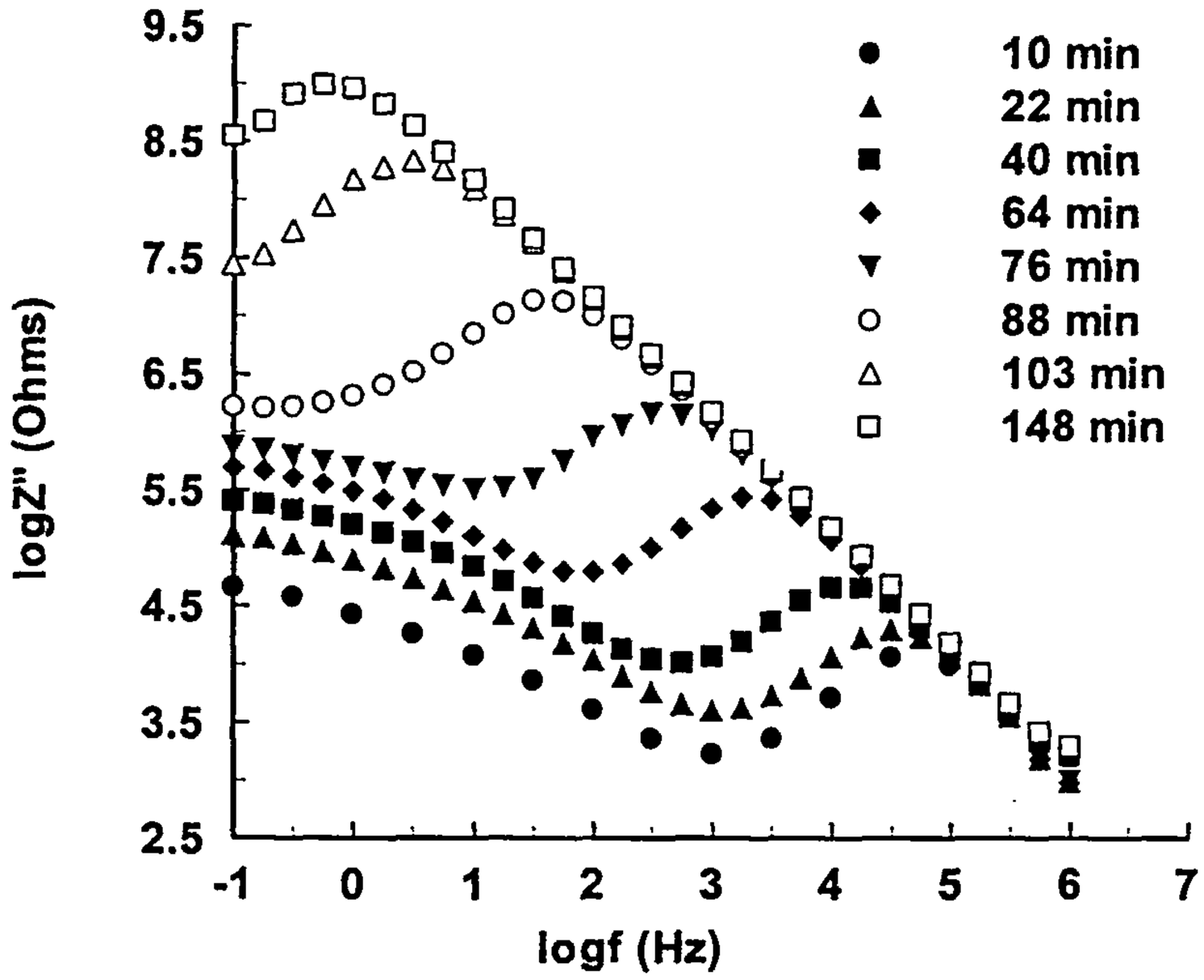

Figure 8.2 *Plot of the logarithm of imaginary impedance as a function of frequency at different time intervals into the cure for the isothermal cure of RTM6 resin at 140°C.*

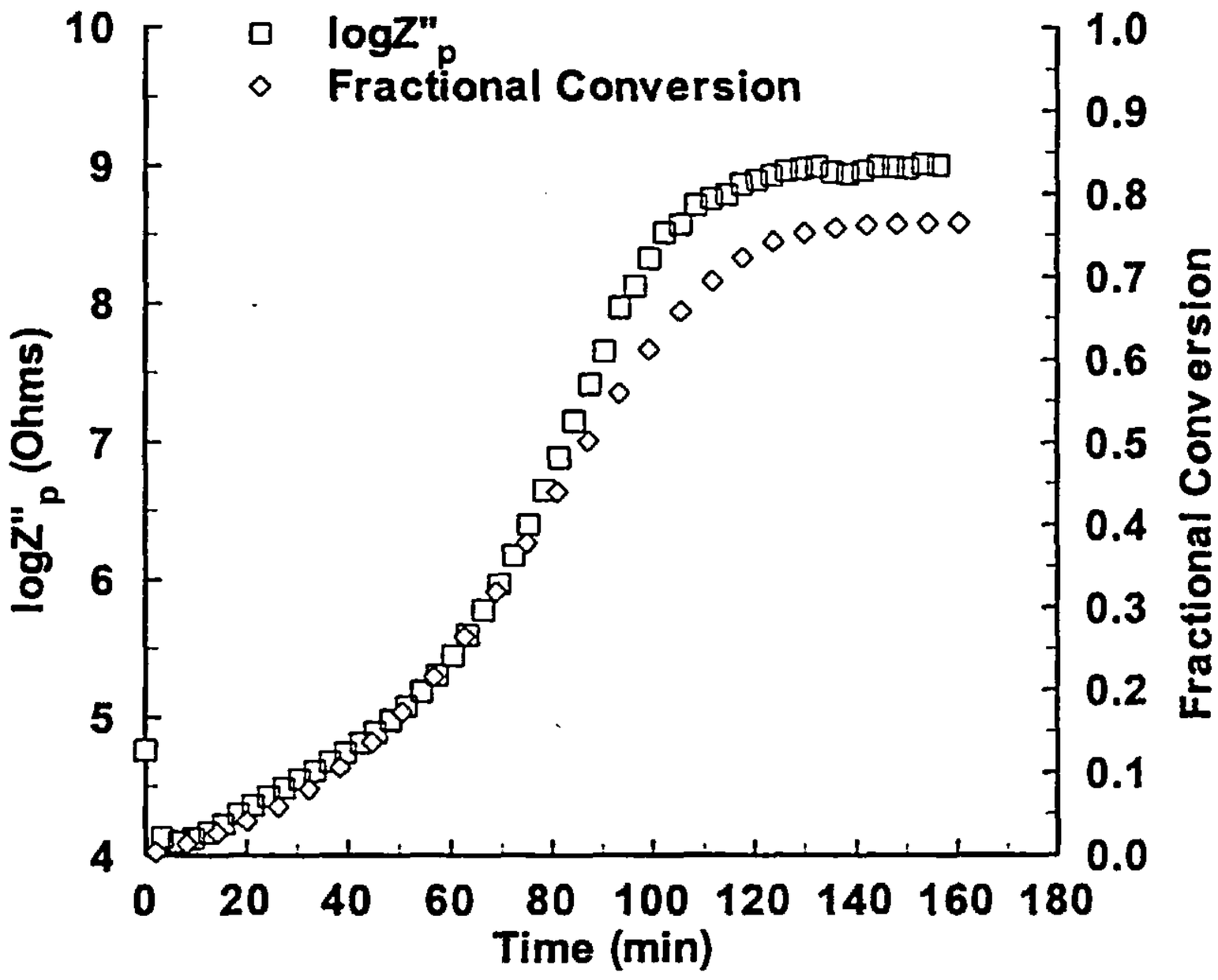

Figure 8.3 *Plot of logarithm of imaginary impedance values at the peak against cure time for the isothermal cure of RTM6 at 140°C. Fractional conversion is also plotted for comparison.*

The comparison of these two curves suggests that there should be a direct correlation between the changes in the imaginary impedance and the changes in the level of conversion. The trend of the two curves is similar throughout the cure and if using an appropriate scaling factor for *ℓogZ"* the two curves should superimpose. The simplest way to demonstrate this is to plot both *ℓogZ"* and conversion as relative changes between the minimum and the maximum values attained for this particular cure cycle. Such plots are shown in Figure 8.4 for RTM6 resin cured at 140 and 160°C.

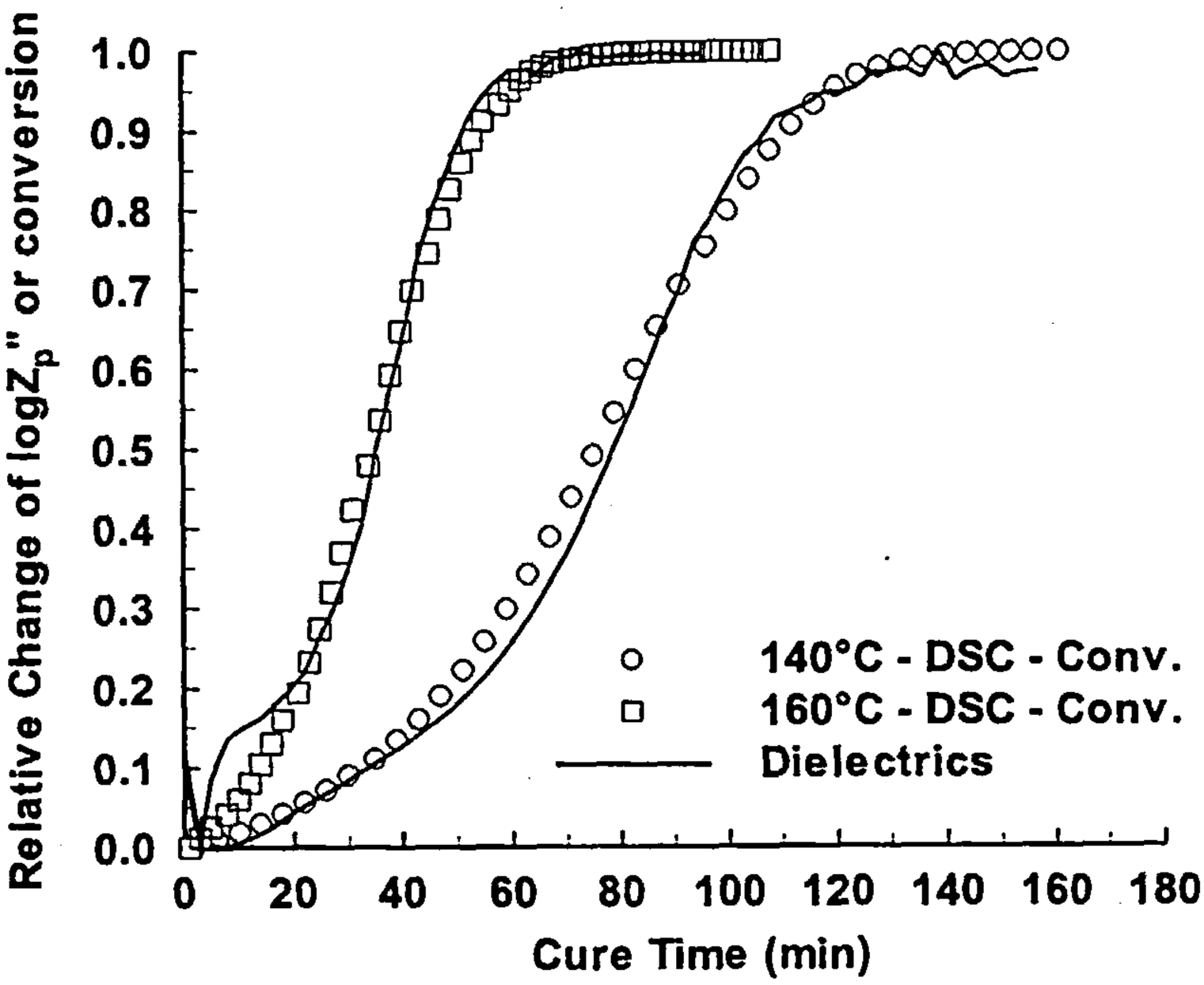

Figure 8.4 *Plots of the relative changes of ℓogZ$_p$" and conversion between the minimum and maximum values attained during the isothermal cure of RTM6 resin at 140 and 160°C, as functions of cure time.*

This figure shows that by monitoring the relative changes in the peak intensity of the imaginary impedance versus frequency plots, the changes in the conversion level during the cure can be approximated to a very good degree of accuracy. The application of the above procedure for conversion determination by impedance measurements to the other resin systems produced the curves shown in Figure 8.5 -

Figure 8.7 for isothermal cures of RMO, RMO2 and 934 resins respectively. The maximum level of conversion reached at each dielectric experiment was determined by the maximum degree of conversion obtained by the other thermoanalytical techniques for the same cure temperatures. The resulted curves show very good agreement with the conversion results obtained with the other thermoanalytical techniques (DSC and FTIR). Some deviations occur, especially at low cure temperatures, in all the experiments, which can be attributed to a slow heat up as the temperature of the resin was approaching the cure temperature. The estimated elapsed time to reach equilibrium was 10 to 12 minutes. Temperature variations during the dielectric experiments can also be responsible for the observed deviations. In particular, the exotherm produced during the dielectric experiments was about 10 - 20 °C higher than the applied cure temperature, which of course accelerated the cure reaction. These exotherms, which were minimum for the uncatalysed resin systems (RTM6, RMO and RMO2), are more likely to have produced the observed deviations between the cure level obtained by dielectric experiments and the cure level obtained by DSC and FTIR experiments.

Despite the difficulty of a direct correlation between the cure levels obtained by dielectric and FTIR experiments, mostly because of the above mentioned temperature control problems, the shapes of the curves are similar. The dielectric response of the curing resin can actually follow the different kinetics of the different resins investigated. In Chapter 3, the resin systems investigated in this study were separated into two categories; those following autocatalysis (RTM6, RMO and RMO2 resins) and those not following autocatalysis (934 resin). The autocatalysis effect can be identified by the appearance of an inflection point in the conversion profile. A close inspection of the conversion profiles given in Figure 8.5 - Figure 8.7 reveals that RMO and RMO2 resins do give an inflection point in the conversion profile, whereas 934 resin does not. The inflection point is evident in the conversion profiles obtained by both techniques (FTIR and Dielectrics).

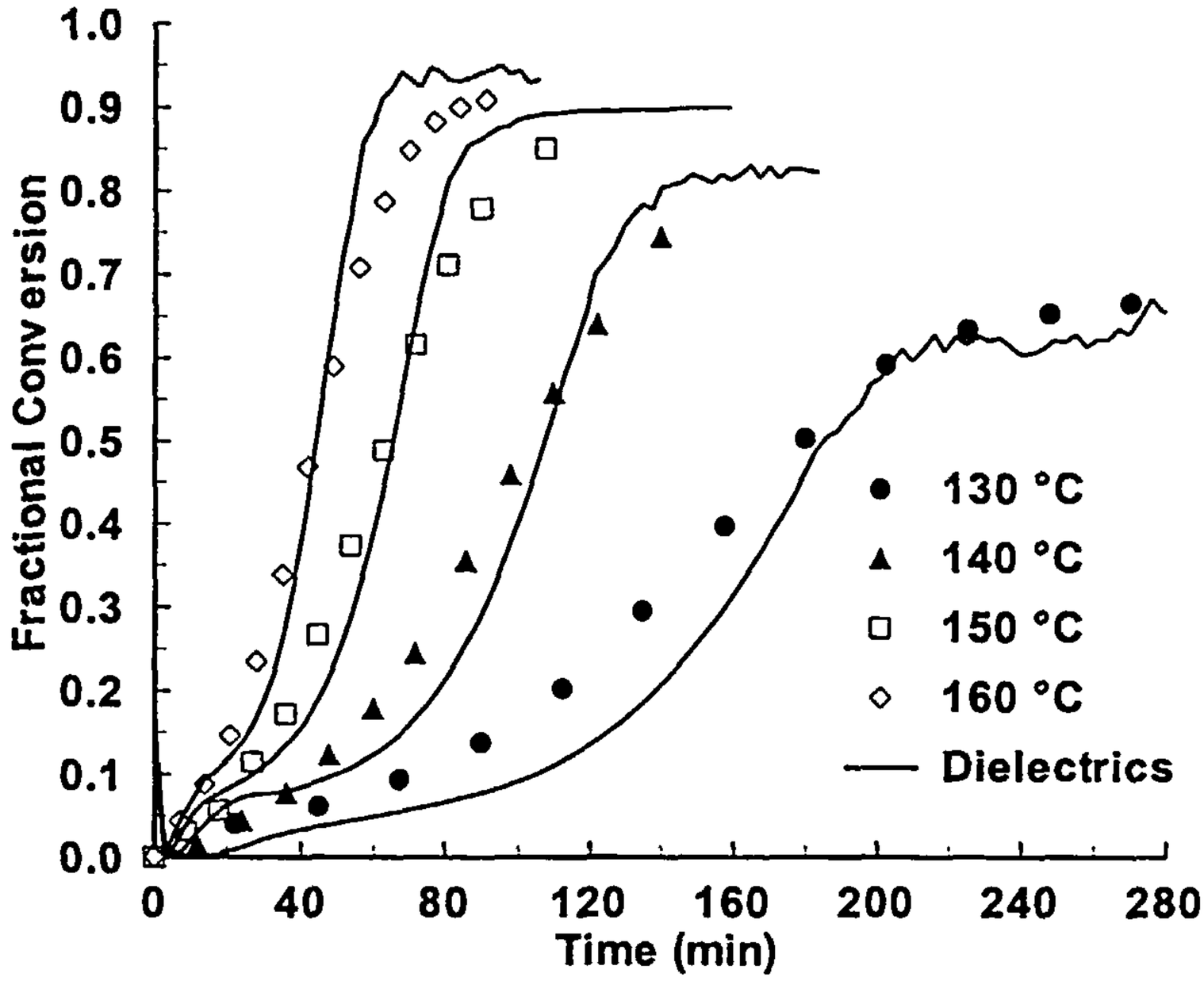

Figure 8.5 *Plots of fractional conversion during the isothermal cure of RMO resin at various temperatures, as a function of cure time. Symbols represent experimental results from FTIR experiments and solid lines results from dielectric experiments.*

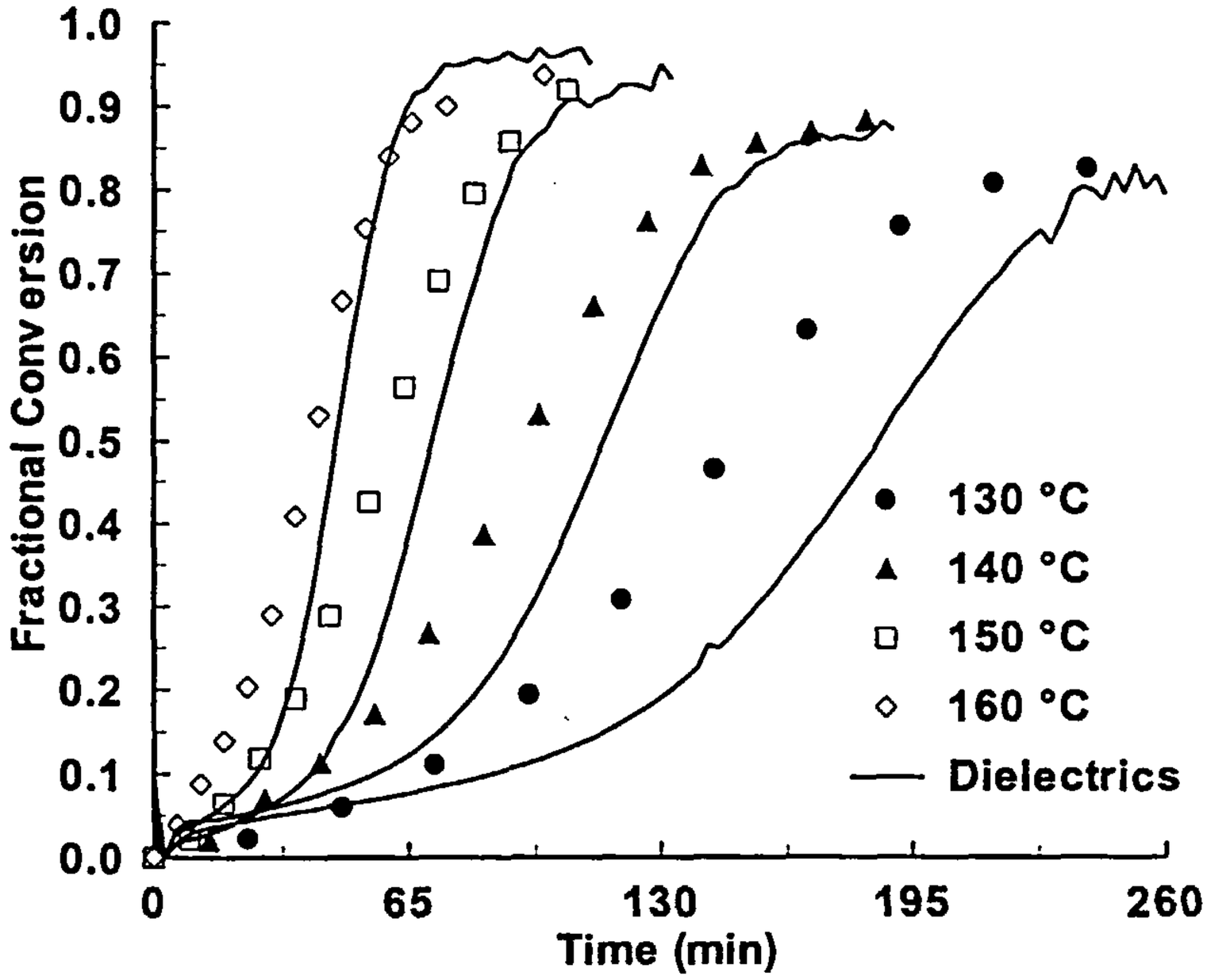

Figure 8.6 *Plots of fractional conversion during the isothermal cure of RMO2 resin at various temperatures, as a function of cure time. Symbols represent experimental results from FTIR experiments and solid lines results from dielectric experiments.*

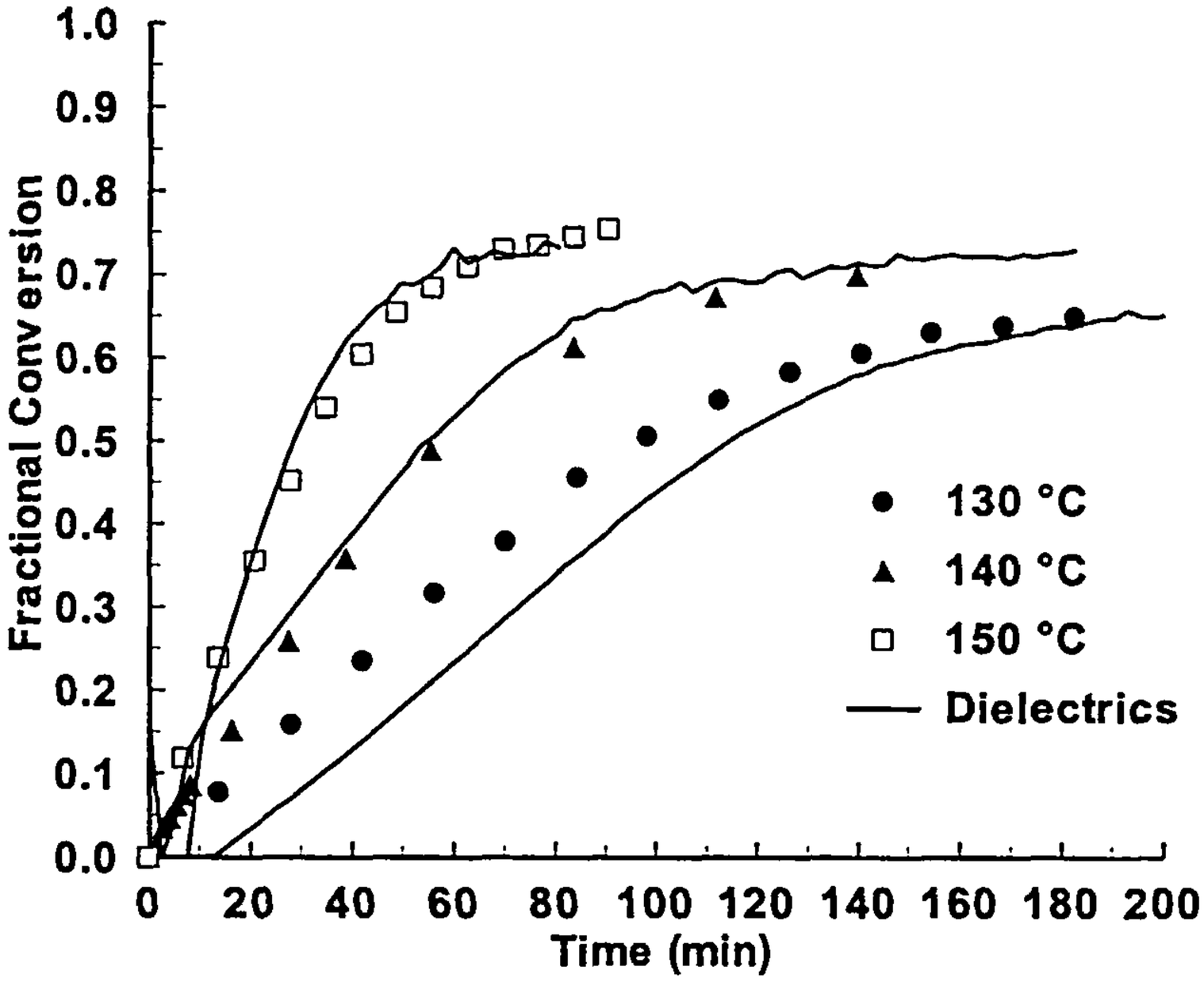

Figure 8.7 *Plots of fractional conversion during the isothermal cure of 934 resin at various temperatures, as a function of cure time. Symbols represent experimental results from FTIR experiments and solid lines results from dielectric experiments.*

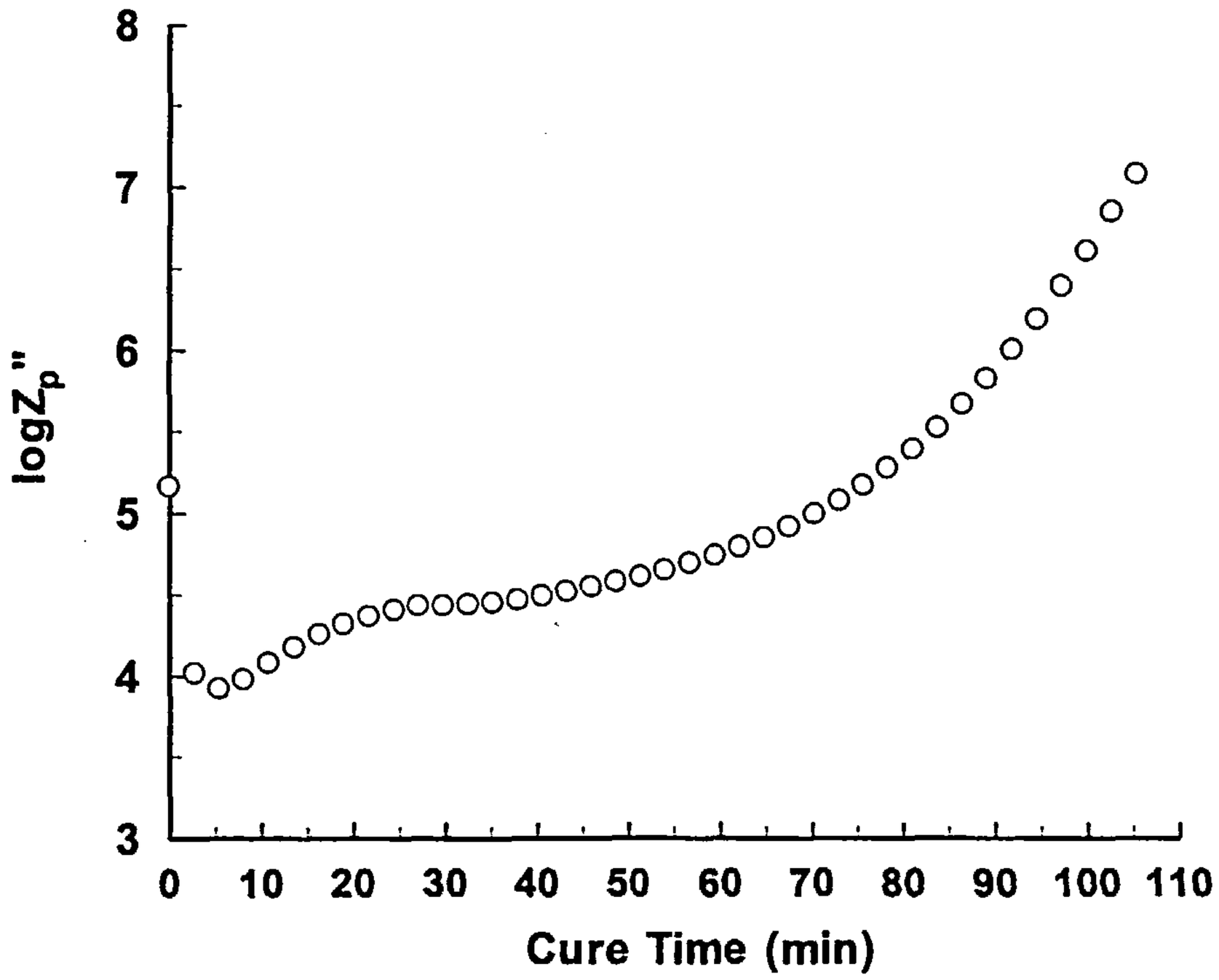

Figure 8.8 *Plot of $\log Z_p''$ as a function of cure time for the isothermal cure of RMO resin at 140°C.*

Another interesting point in the conversion profiles obtained by the impedance measurements is the appearance of a 'hump' in the early stages of the cure. For a better visualisation of that characteristic effect, the imaginary impedance values at the characteristic peak of the isothermal cure of RMO resin at 140°C have been plotted in Figure 8.8 as a function of cure time in the early stages of the cure. The change in the rate of increase of the imaginary impedance up to about 25 minutes into the cure in a continuous fashion marks that characteristic area and is observed in all the impedance measurements for all the resin systems studied.

At that stage of the cure, the dielectric signal is affected by two distinctive phenomena. The first one is the increase in the resin temperature and the second one is the wetting of the dielectric sensor. Since all the experiments were started after the resin had reached an equilibrium at 75°C, the quick heat up of the resin to the cure temperature will produce a drop in the resin viscosity and as a consequence a drop in the resistivity of the resin. That will affect the imaginary impedance values in a similar way; the value at the characteristic peak will drop. The effect of the temperature increase can be seen in Figure 8.8. The first three points in that plot are indicative of a temperature increase. Although the resin temperature is expected to increase even after that point (temperature equilibrium after 10 - 12 minutes), the drop in the impedance values is masked by the second effect, the wetting of the sensor. The viscosity of the resin is affecting the wetting of the sensor; lower viscosity produces better wetting of the sensor. Since the inter-electrode spacing of the particular sensor is about 15μm, better wetting will produce an evenly shaped resin film on top of the sensor, free of any empty or partly resin occupied spaces. That will produce an increase in the imaginary impedance as a consequence of the increase of the amount of resin in contact with the sensor. Another effect of the increase of the resin temperature or similarly the decrease in the resin viscosity, is the increase in the blocking layer thickness. As mentioned in Section 2.7.9, lower viscosity or higher temperature have as an effect the accumulation of an increasing amount of charged moieties at the resin/electrode interfaces, which are responsible for the blocking layer effect. As the resin approaches temperature equilibrium, the thickness of that layer will increase with a decreasing rate until the

point of equilibrium where it will stabilise. The thickness of that layer affects the dielectric signal; the thicker the blocking layer the higher the impedance values.

Although there are not any experimental results that would help us to separate the two phenomena, as a general rule we could say that:

- At the beginning of the experiment a decrease in the imaginary impedance should be expected, because of the increase in temperature;
- As the temperature increases, a point is reached where the wetting of the sensor and the blocking layer effect become more significant and an overall increase in the signal is observed;
- The increase in the imaginary impedance values continues with a decreasing rate until temperature equilibrium is reached;
- In the region of thermal equilibrium, the effect of the curing reaction becomes operative and a further increase in the imaginary impedance will occur, reflecting the kinetic characteristics of the resin.

8.3 Cell Constant Calculation

If we consider that a resin can be expressed as a simple R-C parallel circuit, then the application of a sinusoidal voltage of the form:

$$V(t) = V_0 \exp(j\omega t) \qquad \text{(Eq. 8.9)}$$

will result in a time-dependent current which can be expressed as:

$$I(t) = YV(t) \qquad \text{(Eq. 8.10)}$$

where Y is the admittance of the system.

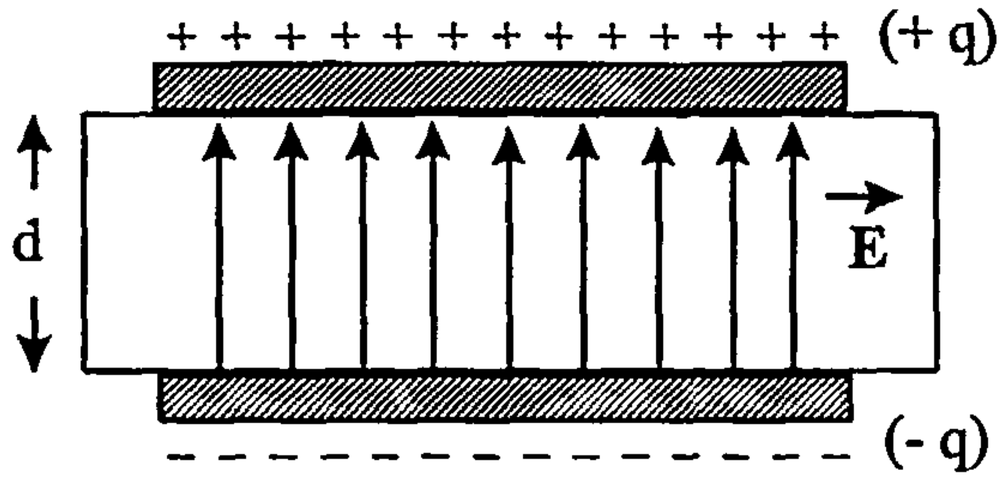

Figure 8.9 *Electric field produced from a plane capacitor. The lines of flux are represented by the arrows.*

For a R-C parallel circuit, the total admittance is:

$$Y = \frac{1}{R} + j\omega C \qquad \text{(Eq. 8.11)}$$

If we also assume that the applied electric field is perpendicular to the resin, as that produced from a parallel plate capacitor (see Figure 8.9), then the complex dielectric constant of the resin can be expressed as:

$$\varepsilon^* = \frac{Y}{j\omega C_0} = \frac{1}{j\omega RC_0} + \frac{C}{C_0} = \frac{C}{C_0} - j\frac{1}{\omega RC_0} \qquad \text{(Eq. 8.12)}$$

or, by separating real and imaginary parts:

$$\varepsilon' = \frac{C}{C_0} \quad and \quad \varepsilon'' = \frac{1}{\omega RC_0} \qquad \text{(Eq. 8.13)}$$

In the above expressions, C_0 is the air capacitance given by:

$$C_0 = \varepsilon_0 K \qquad \text{(Eq. 8.14)}$$

where ε_0 is the permittivity of the free space. K is the cell constant, which can be expressed as:

$$K = \frac{S}{L} \qquad \text{(Eq. 8.15)}$$

where S is the effective surface onto which the field is applied and L is the length of the lines of flux. In the case of the plane capacitor, S will be the surface of one of the electrodes and L the distance separating them.

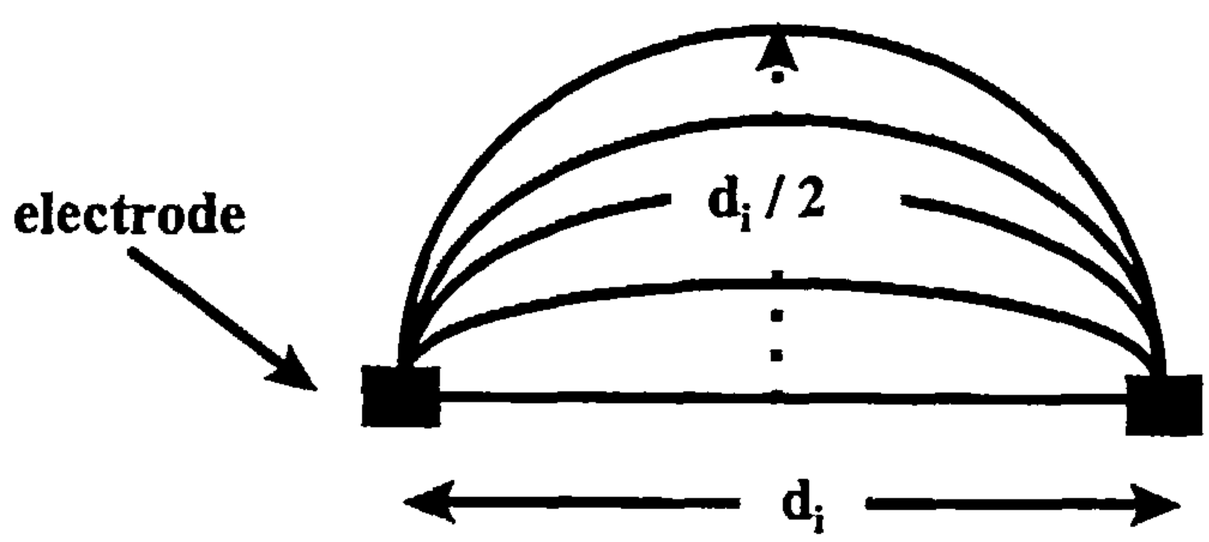

Figure 8.10 *Electric field produced by two consecutive electrodes of the Dek-Dyne sensor, separated by a distance* d_i

This however is not the case for the dielectric sensors used in this study. The fringing field that is produced (see Figure 8.10) will affect the measurement. The manufacturer of the sensors, in order to compensate for the curvature of the electric field, has produced some calibration formulae that correct the measurement in an appropriate manner (see Eq. 3.5).

The dielectric sensor is an assembly of electrodes printed on a Kapton film (see Figure 3.7). If we consider each pair of consecutive electrodes as a micro-capacitor in an overall assembly of n micro-capacitors, then the overall measured capacitance will be:

$$C_T = C_1 + C_2 + \ldots + C_n \qquad \text{(Eq. 8.16)}$$

If we also assume that the geometry if each pair of electrodes is the same, then the cell constant for each micro-capacitor will be the same. Thus, from Eqs. 8.14 and 8.16 we will get for the overall C_0:

$$C_{0,T} = \varepsilon_0 n K_i = \varepsilon_0 n \frac{S_i}{L_i} \qquad \text{(Eq. 8.17)}$$

If d_i is the distance between two consecutive electrodes and if we assume that the electric field produced by these electrodes cannot extend beyond the semicircular path connecting them (see Figure 8.10), then the length L_i will be limited between:

$$d_i \leq L_i \leq \pi \frac{d_i}{2} \qquad \text{(Eq. 8.18)}$$

If the overall surface area comprised by the electrode assembly is S and the distance separating the first and the last electrode is L, then by combining Eqs. 8.17 and 8.18 we will get:

$$\varepsilon_0 n \frac{S_i}{d_i} \geq \varepsilon_0 n K_i \geq \varepsilon_0 n \frac{2S_i}{\pi d_i} \quad \Rightarrow \quad \varepsilon_0 n \frac{nS_i}{nd_i} \geq \varepsilon_0 n K_i \geq \varepsilon_0 n \frac{2nS_i}{\pi n d_i}$$

$$\Rightarrow \quad \frac{S}{L} \geq K_i \geq \frac{2}{\pi}\frac{S}{L} \qquad \text{(Eq. 8.19)}$$

For the sensors used in this study:

$$S = 19x10.5\ mm^2 \quad and \quad L = 19\ mm$$

So, the cell constant will be limited between the values:

$$6.69\ mm \leq K_i \leq 10.5 mm \qquad \text{(Eq. 8.20)}$$

Since the inter-electrode spacing is approximately 15μm (= d_i), the approximate number of electrodes and hence the number of micro-capacitors will be:

$$n = \frac{L}{d_i} = \frac{19 \cdot 10^3}{15} \approx 1{,}270 \qquad \text{(Eq. 8.21)}$$

which leads to an approximate overall cell constant:

$$8.49m \leq K \leq 13.33m \qquad \text{(Eq. 8.22)}$$

8.4 Dielectric Sensor Calibration for ε' and ε'' Evaluation

The dielectric sensors used in this study were comprised of an electrode assembly printed on a Kapton substrate (see Figure 3.7). The measurement of the dielectric properties of the resins, involved two kinds of measurements; one measurement of the response of the sensor in a free air environment and one with the sensor immersed in the resin. These two measurements are represented schematically in Figure 8.11. If we represent the Kapton substrate by an admittance Y_s, the air by an admittance Y_a and the resin by an admittance Y_r, then the overall measured systems can be represented by the equivalent electrical circuits shown in the same figure. They both represent an in parallel connection of two admittances; one connection for the measurement in the free air environment and one connection for the measurement of the resin.

The total real and imaginary admittance, Y_t' and Y_t'', of these circuits is:

$$Y'_{t,air} = Y'_s + Y'_a \quad , \quad Y''_{t,air} = Y''_s + Y''_a$$

$$Y'_{t,resin} = Y'_s + Y'_r \quad , \quad Y''_{t,resin} = Y''_s + Y''_r \qquad \text{(Eq. 8.23)}$$

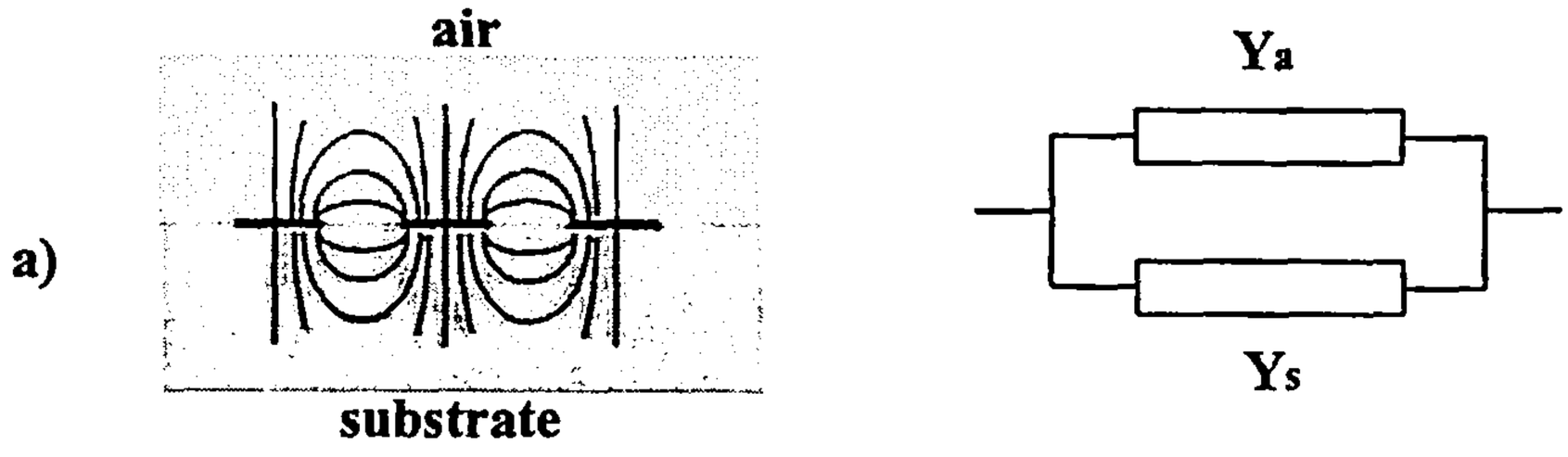

Figure 8.11 *Electrical field lines surrounding the electrodes of the dielectric sensor. a) Schematic representation of the measuring system in the free air environment with the resulting equivalent circuit. b) Schematic representation of the measuring system in the resin with the resulting equivalent circuit. Subscripts a, s, r stand for air, substrate and resin respectively.*

In the case of a single admittance, Y, the application of a voltage $V(t) = V_0 \exp(i\omega t)$ will result in a current $I(t)$ which is:

$$I(t) = \frac{dq}{dt} = \frac{d[CV(t)]}{dt} = CV_0 i\omega \exp(i\omega t) = iC\omega V(t) = i\varepsilon^* C_0 \omega V(t) = \quad \text{(Eq. 8.24)}$$

$$= i(\varepsilon' - i\varepsilon'')C_0\omega V(t) = (\omega C_0\varepsilon'' + i\omega C_0\varepsilon')V(t)$$

Since the current $I(t)$ is:

$$I(t) = YV(t) = (Y' + iY'')V(t) \quad \text{(Eq. 8.25)}$$

the real and imaginary parts of the admittance can be written according to Eq. 8.24:

$$Y' = \omega C_0 \varepsilon'' \qquad and \qquad Y'' = \omega C_0 \varepsilon' \tag{Eq. 8.26}$$

Combination of Eqs 8.23 and 8.26 yields:

$$\varepsilon_r' = \frac{Y''_{t,resin}}{Y''_{t,air}}\left(1+\varepsilon_s'\right)-\varepsilon_s' \quad and \quad \varepsilon_r'' = \frac{Y'_{t,resin}}{Y''_{t,air}}\left(1+\varepsilon_s'\right) \tag{Eq. 8.27}$$

These are the expressions that have to be used in order to calculate the dielectric permittivity and dielectric loss of the cured resin. By measuring the real and imaginary parts of the total admittance in free air and in the resin and by knowing the permittivity of the substrate, the dielectric properties of the resin itself can be evaluated.

Since all the measurements were made by assuming an R-C parallel circuit, for which:

$$Y' = \frac{1}{R} \quad and \quad Y'' = \omega C \tag{Eq. 8.28}$$

then the expressions given by Eq. 8.27 transform into the calibration equations given by Eq. 3.5 for a permittivity of the substrate equal to 2.93. That permittivity is used as a constant for all frequencies and temperatures.

8.5 Dielectric Sensor Calibration for Conductivity Evaluation

The cell constant is an important parameter that has to be known in order to calculate the conductivity levels in the resin and the way they change during the cure. In section 8.1 a method for measuring the ion resistance, R_p, was given. The distinctive peak of the imaginary impedance in the frequency domain was related to R_p with the following expression:

$$R_p = 2Z''_{r,peak} \tag{Eq. 8.29}$$

The ionic resistance is related to the ionic resistivity, ρ, of the resin according to the relation:

$$\rho = R_p \frac{S}{L} = KR_p \qquad \text{(Eq. 8.30)}$$

Since the ionic conductivity, σ, is the inverse of the ionic resistivity, it follows that:

$$\sigma = \frac{1}{KR_p} \qquad \text{(Eq. 8.31)}$$

or, by using Eqs. 8.14 and 8.29:

$$\sigma = \frac{\varepsilon_0}{2C_0 Z''_{r,peak}} \qquad \text{(Eq. 8.32)}$$

From Eqs. 8.26 and 8.27 it follows that the pure response of the resin, in terms of admittance, can be expressed as:

$$Y'_r = Y'_{t,resin} \quad and \quad Y''_r = Y''_{t,resin} - Y''_{t,air} \frac{\varepsilon'_s}{1+\varepsilon'_s} \qquad \text{(Eq. 8.33)}$$

which can be easily transformed to impedance by:

$$Z'_r = \frac{Y'_r}{|Y_r|^2} \quad and \quad Z''_r = \frac{Y''_r}{|Y_r|^2} \qquad \text{(Eq. 8.34)}$$

From that expression, the "true" peak of the imaginary impedance, $Z''_{r,peak}$ can be calculated and form the input in Eq. 8.32 for the calculation of the conductivity level.

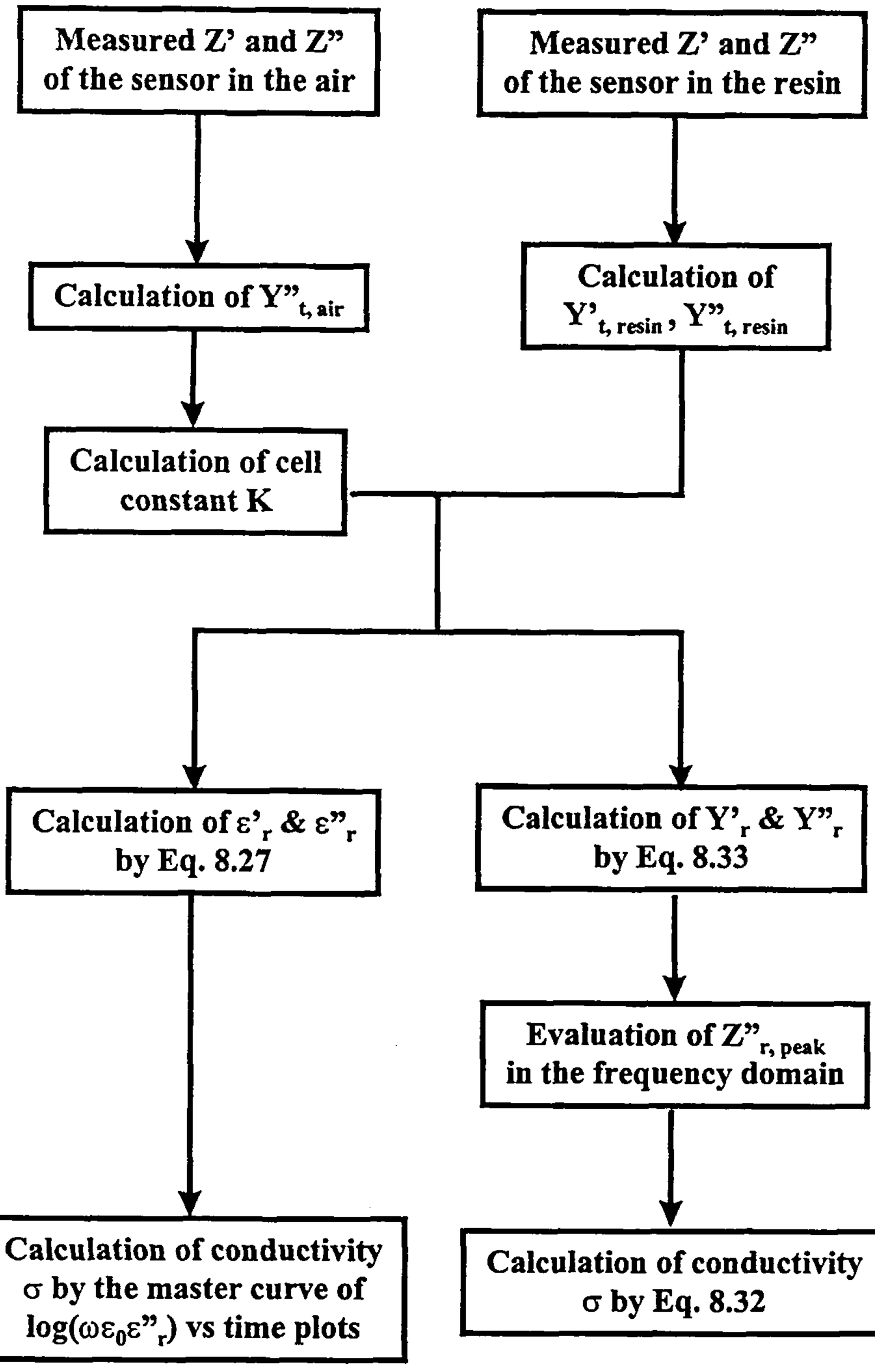

Figure 8.12 *Flow diagram for the evaluation of the dielectric properties and the conductivity levels of the curing resins.*

The complete procedures for the calculation of the conductivity levels along with the calculation of the dielectric properties of the resin (permittivity and loss) are given in Figure 8.12.

8.6 Conductivity Changes During Cure

The procedure established in the previous section to evaluate the conductivity changes during the cure of the resin (see Eq. 8.32), was used to determine the conductivity levels in the various resins.

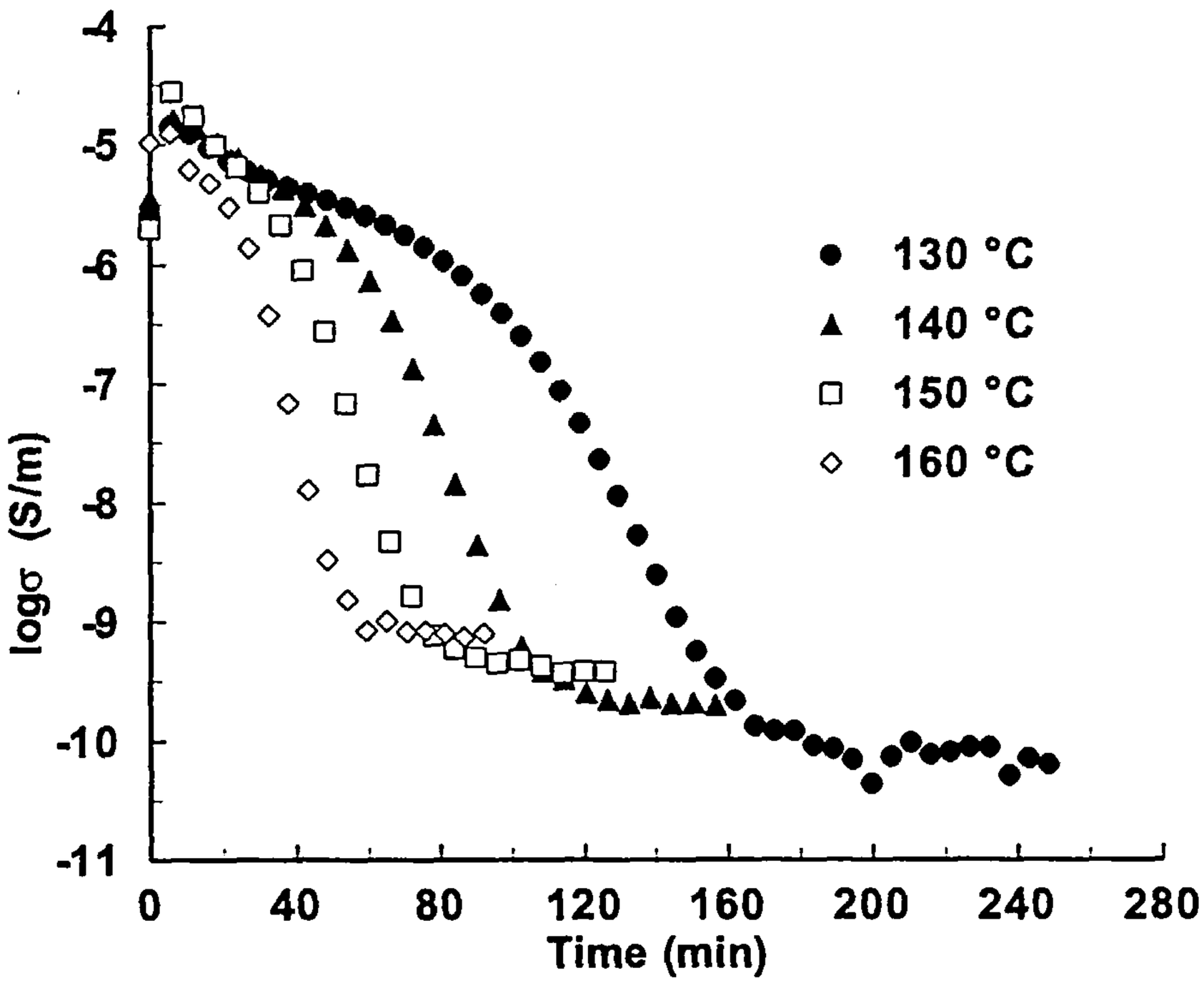

Figure 8.13 *Conductivity changes during isothermal cure of RTM6 resin at various cure temperatures*

The resulting conductivity profiles for the isothermal cure of RTM6 resin at various cure temperatures are shown in Figure 8.13. Conductivity follows the same trend with Z''_{peak} but inverse (see Figure 8.4), thus the same phenomena will also affect the variation in the conductivity signal. The lack of stability in the temperature control and

the variation in the electrode blocking layer thickness, as identified in section 8.2 ,are the most likely reasons for the fluctuation of the conductivity values in the early stages of the cure. One interesting aspect of the conductivity profiles shown in Figure 8.13 is the higher final conductivity that is observed for the higher cure temperatures. Although the cure advancement is higher at higher cure temperatures, which would have resulted in lower conductivity levels, the higher temperature increases conductivity and actually masks the effect of the final cure level.

The cell constants that were used in the calculation of conductivity were evaluated by using Eq. 8.14. The values of the measured air capacitance were used in that evaluation and the permittivity of the free space was taken as $\varepsilon_0 = 8.85$ pF/m. The calculated cell constants are given in Table 8.1 for all the experiments along with the measured air capacitance.

Table 8.1 *Air Capacitance and Cell Constants for all the dielectric experiments*

Resin	**Air Capacitance (pF)**			
	130°C	**140°C**	**150°C**	**160°C**
RTM6	74.39	74.76	69.37	60.74
RMO	77.34	83.64	72.26	72.29
RMO2	58.19	66.81	64.06	65.15
934	67.62	67.72	58.67	
Resin	**Cell Constant *K* (m)**			
RTM6	9.72	9.76	9.07	7.95
RMO	8.74	9.45	8.17	8.17
RMO2	7.60	8.74	7.79	8.59
934	7.64	7.65	6.63	

The calculated cell constants do fall in the range of values that were estimated in the previous section (see Eq. 8.22) with an average value, which is about the same with the estimated lower-bound value cell constant. The above suggests that the effective

electric field produced by the sensors should be conformed by arc-shaped lines of flux with a length approximately equal to the inter-electrode spacing. The observed deviation between the sensors should be attributed to the geometry of each individual sensor and actually of each individual micro-capacitor produced by two consecutive electrodes. Any damaged electrodes will reduce the effective cell constants to values even lower than the lower predicted value.

The validity of the conductivity profiles obtained by the above method was checked using the method described in Section 2.7.10. The conductivity contribution to the dielectric loss ε'' can be expressed as:

$$\varepsilon''_{cond} = \frac{\sigma}{\omega \varepsilon_0} \quad \Rightarrow \quad \sigma = \omega \varepsilon_0 \varepsilon''_{cond} \qquad \text{(Eq. 8.35)}$$

Early in the cure, where the dielectric signal is completely masked by conductivity, the measured dielectric loss should be attributed only to conductivity. Thus, by plotting $\ell og(\omega \varepsilon_0 \varepsilon'')$ as a function of time at various frequencies would produce a master curve, at least up to the point where conductivity is the major contribution to the loss. The plots of $\ell og(\omega \varepsilon_0 \varepsilon'')$ as a function of time at various frequencies are given in Figure 8.14 for the isothermal cure of RTM6 resin at 140°C.

The master curve that is formed from the superposition of the $\ell og(\omega \varepsilon_0 \varepsilon'')$ plots is not followed for all frequencies throughout the cure. Early in the cure, superposition occurs only for frequencies above approximately 100Hz. As the cure progresses, lower frequencies start to superimpose, whereas the higher frequencies start to deviate. The deviation of the high frequencies at the later stages of the cure can be attributed to the contribution of the dipolar relaxations to the overall signal.

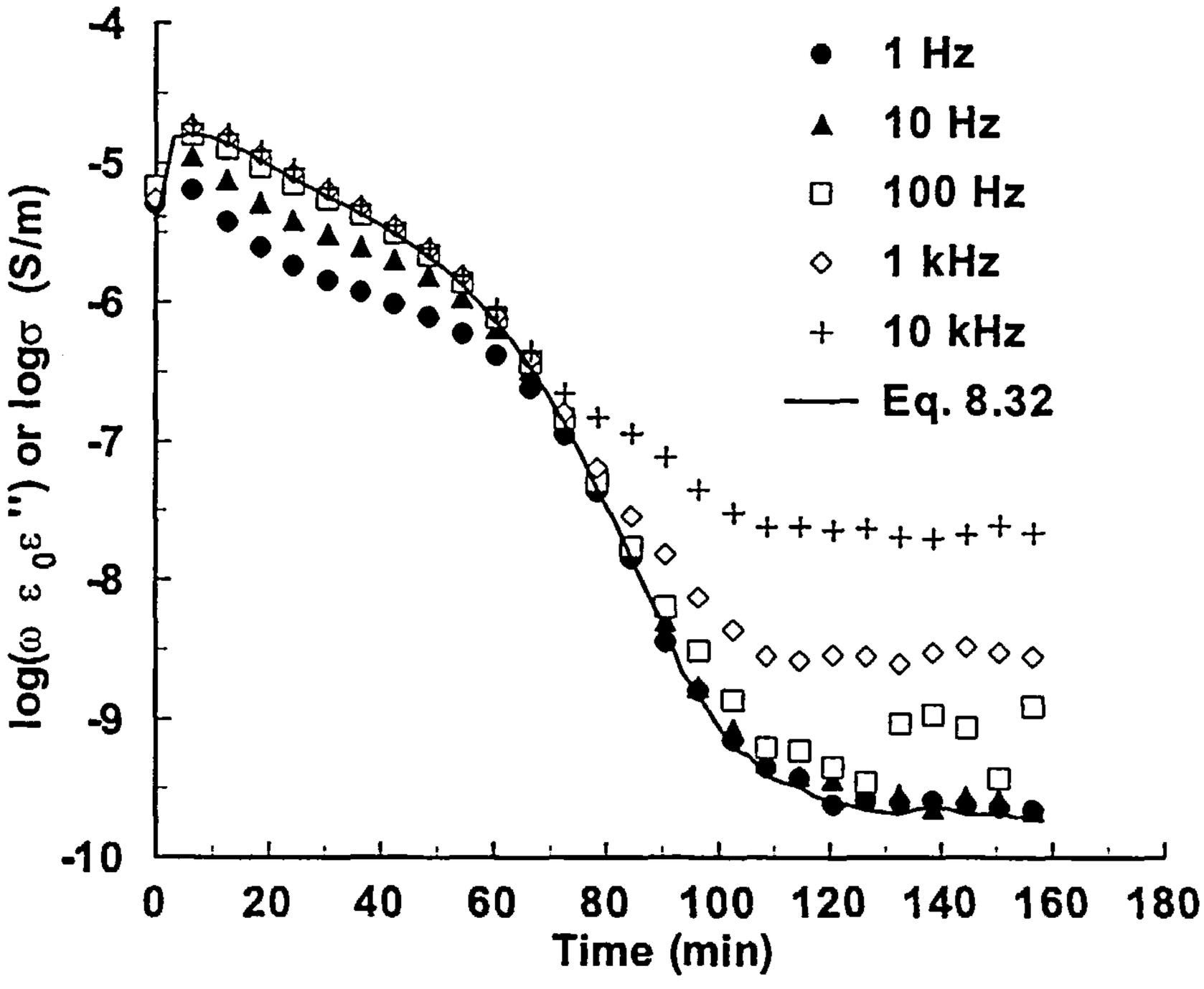

Figure 8.14 *Symbols: Plots of $\ell og(\omega\varepsilon_0\varepsilon'')$ as a function of time at various frequencies. Solid line: Plot of $\ell og\sigma$ vs time using Eq. 8.32. Isothermal cure of RTM6 resin at 140°C.*

In the early stages of the cure, the dipolar relaxations are masked by the high levels of conductivity of the liquid resin. As the resin starts to solidify, conductivity drops and the dipolar relaxations start to become visible, especially at high frequencies.

The deviation of the low frequencies from the master curve that is observed in the early stages of the cure is a consequence of the electrode polarisation effects. In the liquid state, the resin exhibits high conductivity levels, which promote the build up of charged layers at the interfaces between the electrodes and the resin. The effect of the blocking layer is more visible at the low frequencies. The effect of the blocking layer on the dielectric signal can be identified more easily by plotting the real impedance, Z' and the imaginary impedance, Z'', in a Cole - Cole plot. The Cole - Cole plots of the isothermal cure of RTM6 resin at 140°C at various time intervals into the cure are shown in Figure 8.15.

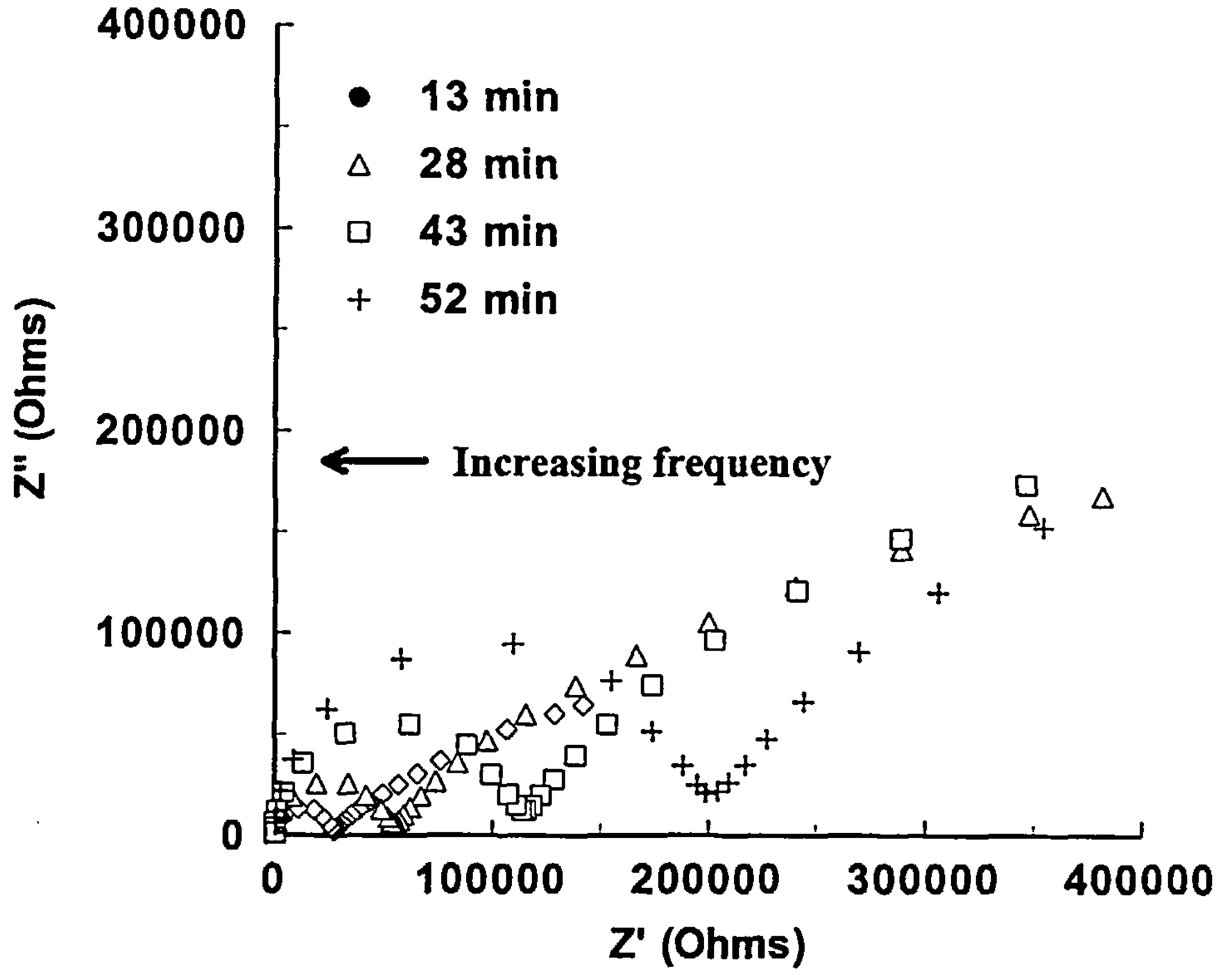

Figure 8.15 *Cole - Cole plots of the real and imaginary parts of complex impedance of isothermal cure of RTM6 resin at 140°C at various time intervals*

The semicircle that is formed in the high frequency range, which is attributed to the ionic relaxations, is followed by an arc shaped curve in the low frequency range, that is attributed to the electrode polarisation. If we consider the theoretical plot of the electrode polarisation that was given in Section 2.7.9 (see Figure 2.15), the effect of the cure advancement is reflected in the decrease of the polarisation effects (the polarisation arc in Figure 8.15 tends to form a perpendicular line to the *Z'*-axis). The reduction in the curvature of the polarisation arc is a direct indication of a reduction of the electrode blocking layer thickness. This is reasonable, since the solidification of the resin hinders the mobility of the charged species and thus reduces the amount of charge carriers that can accumulate on the electrode/resin interfaces. This reduction has a direct effect on the blocking layer thickness; fewer charge carriers produce a thinner layer.

The $\ell og\sigma$ vs time plot of the same resin (RTM6) at 140°C is also shown in Figure 8.14, as a solid line, with conductivity values calculated by Eq. 8.32. This plot actually falls on the master curve and follows it throughout the cure. The advantages of the determination of conductivity from the peak of the imaginary impedance in the frequency domain are unequivocally predominant. While the conductivity profile, as calculated from the traditional method (plot of $\ell og\left(\omega\varepsilon_0\varepsilon''\right)$ to construct a master curve), is usually a "trial and error" procedure to detect the right frequencies that fall onto the master curve, the evaluation of conductivity from impedance is straightforward. Thus, the incorporation of this method of conductivity evaluation into a general dielectric monitoring method would give a direct determination of the conductivity levels, which, as will be shown in the next sections, can provide information on the viscosity, the gelation event and the vitrification point of the curing resin.

8.7 Gelation Determination

In the previous section, the ability of the dielectric signal to reflect the changes in the curing resin was investigated. The trend of the imaginary impedance was shown to follow that of the cure advancement with good degree of accuracy, considering the variations in the temperature of the curing resin during the dielectric experiments. Another aspect of the dielectric measurements that has to be investigated is whether they can detect the characteristic events of the cure (gelation and vitrification) and how accurate that determination might be with respect to the same events as measured by other techniques.

The changes in the conductivity level of the resin reflect the changing mobilities of the charged groups within the resin system. Any phase transitions that might occur during the cure should have a reflection in the conductivity of the resin. This can be more easily understood if we consider the variations in the conductivity levels as a function of the changes in the resin viscosity. The conductivity profiles of the isothermal cure of RTM6 resin at different temperatures are shown in Figure 8.16. In the same figure, the viscosity profiles of the same resin and at the same cure temperatures have also been plotted. The vertical dotted lines appearing in that figure represent the times where an

inflection point appears in the conductivity curves. That inflection point has been attributed to the liquid to rubber transformation (gelation) [155 - 157], at least for simple epoxy - amine systems. The horizontal dotted line that appears in the same figure represents the arbitrary level of viscosity at gelation (10 kPas), as that was defined in Section 7.1.

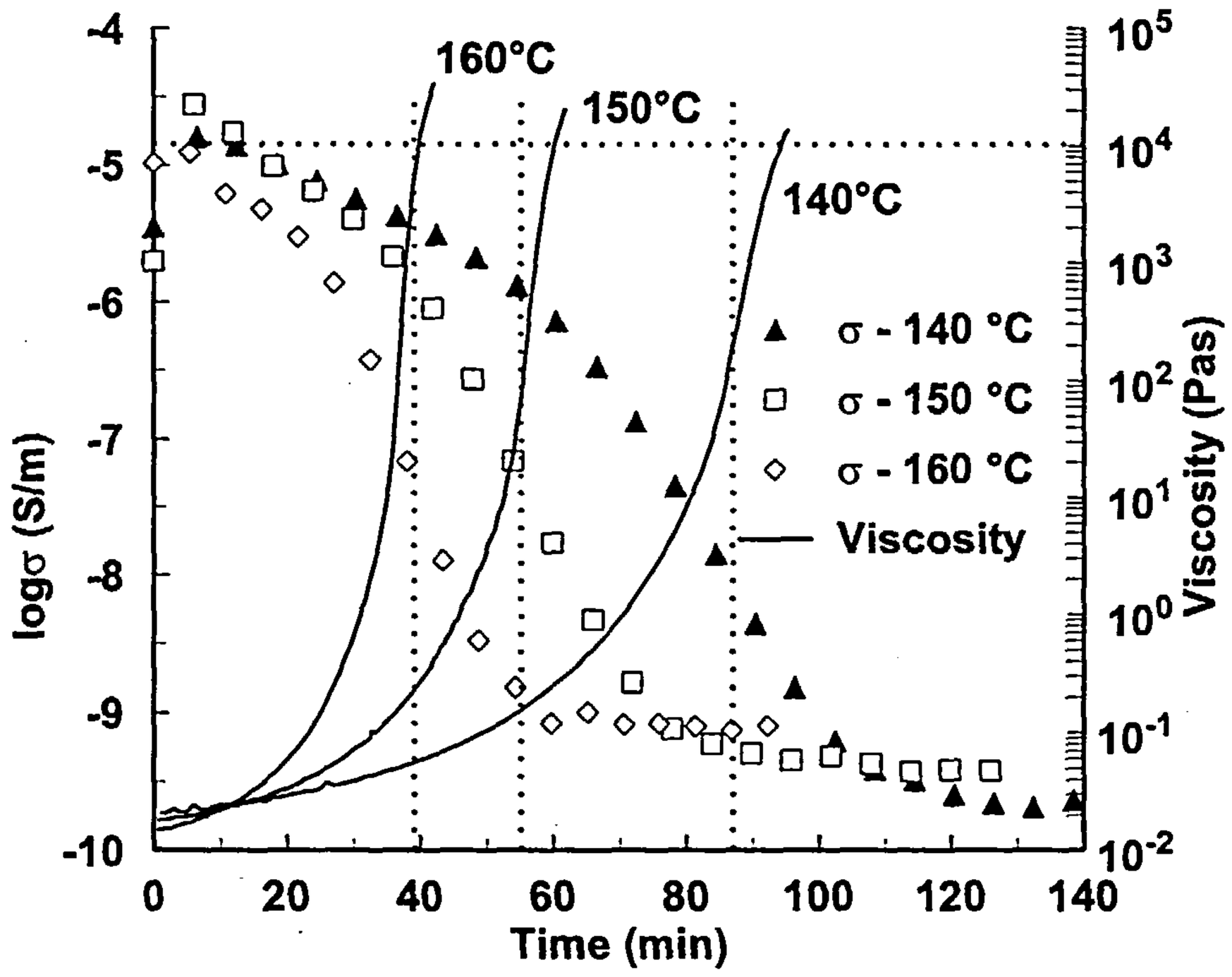

Figure 8.16 *Combined conductivity and viscosity profiles of the isothermal cure of RTM6 resin at various temperatures. Symbols: Conductivity profiles. Solid lines: Viscosity profiles. Vertical dotted lines: Inflection points of conductivity curves. Horizontal dotted line: Level of viscosity at gelation (10 kPas).*

As can be seen in that figure, the inflection point in the conductivity curves coincides in time to a very good agreement with the gelation, as established by the viscosity curves. The small deviations observed are probably due to temperature differences between the dielectric experiments and the viscosity experiments.

The equivalent plots were produced for the isothermal cure of 934 resin (see Figure 8.17).

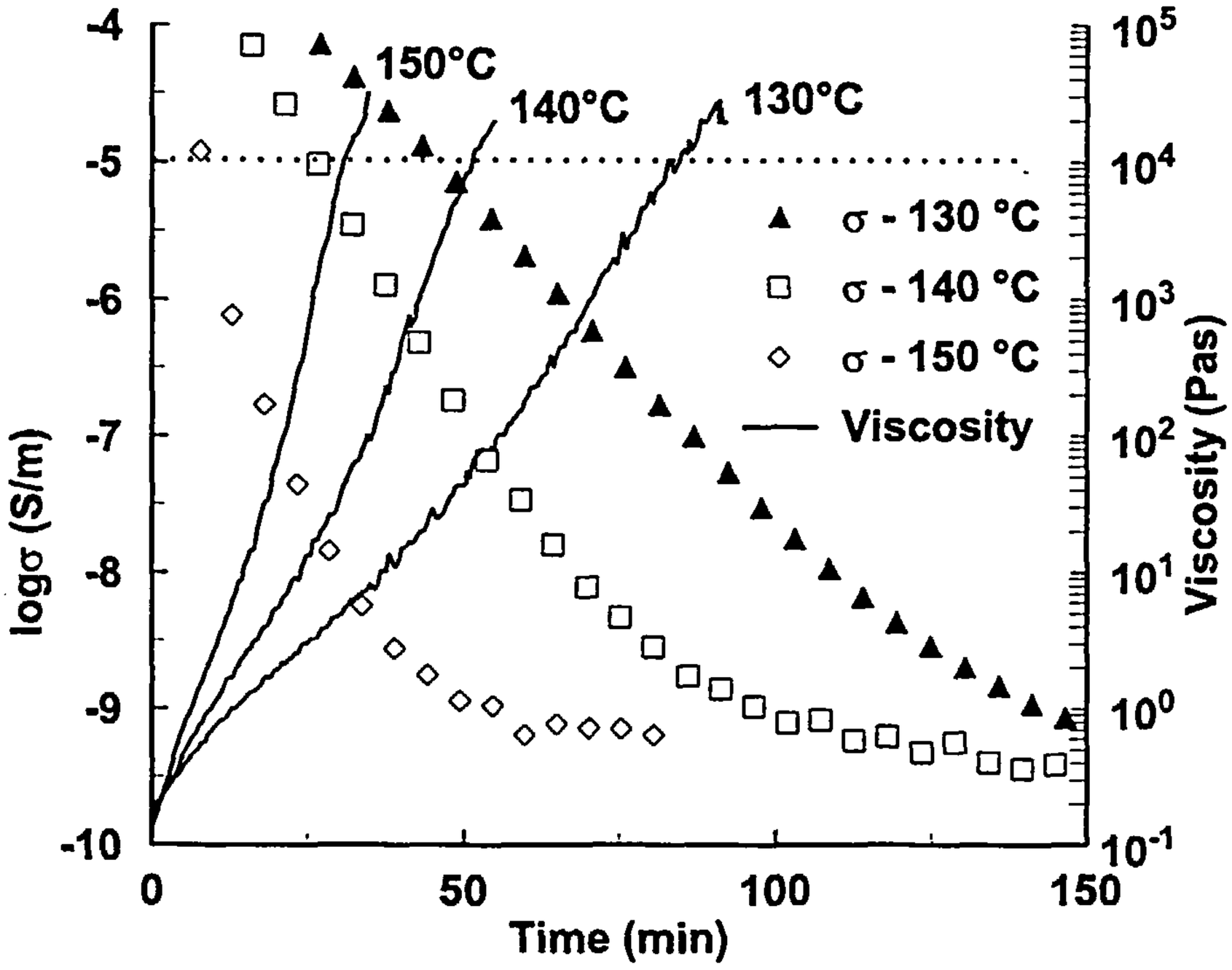

Figure 8.17 *Combined conductivity and viscosity profiles of the isothermal cure of 934 resin at various temperatures. Symbols: Conductivity profiles. Solid lines: Viscosity profiles. Horizontal dotted line: Level of viscosity at gelation (10 kPas).*

As can be seen in this figure, the conductivity curves do not show any inflection points, which means that the principle of determining gelation from the inflection point in the conductivity curves is not valid for some resins. Clearly, this has some implications on the ability of dielectric cure monitoring to pinpoint some events in the cure of some resins.

In Section 8.2 a correlation was established between the variation in the peak of the imaginary impedance in the frequency domain and the changes in the conversion level

of the curing resin. The curves that describe these changes were shown to follow a similar trend for both resin groups, autocatalytic resin systems (RTM6, RMO and RMO2) and catalyst activated resins (934). It was shown, through the similarity in the curve trends, that the inflection point in the conversion profiles of the autocatalysed resin systems does appear in the curve that describes the imaginary impedance peak changes, whereas the catalytic 934 resin was found not to show inflection point in either the conversion profiles or the imaginary impedance profiles. Since any inflection points appearing in conversion translate to maximum in the reaction rate and since a maximum was observed in the reaction rate of the autocatalysed systems and not in the reaction rate of the catalytic systems, it is reasonable to assume that the inflection point that was observed in the imaginary impedance will reflect the maximum reaction rate.

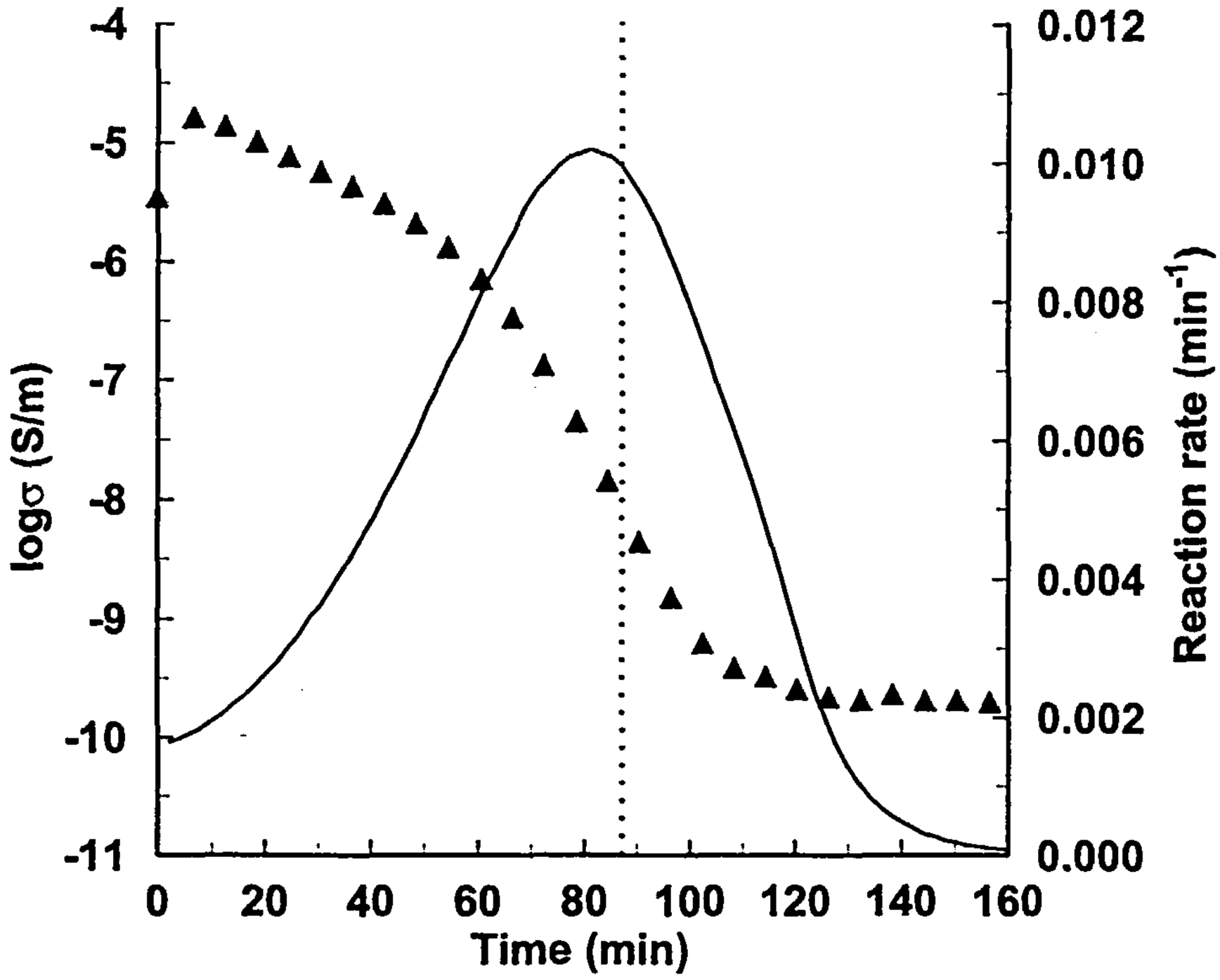

Figure 8.18 *Isothermal cure of RTM6 resin at 140°C. Symbols: Conductivity profile. Solid line: Reaction rate. Vertical dotted line: Inflection point of the conductivity curve.*

Consequently, if we consider Eq. 8.32, the inflection point in the conductivity curve should reflect the time of maximum reaction rate.

To demonstrate the above, a combined plot of conductivity and of the reaction rate was produced and is shown in Figure 8.18. The correlation between maximum in reaction rate and inflection in conductivity is very good, suggesting that the observed inflection point in the conductivity curve is more likely to be attributed to reaction kinetic changes rather than to physical transformations, like gelation.

8.8 Vitrification Determination

The well established relationship between the changes in the dielectric response of the curing resin and the physical transformation of the resin from the rubbery to the glassy state has been presented in Section 2.7.12. The experimental evidence suggests that the dipolar peak in the dielectric loss can track the T_g of the resin quite accurately, particularly the peak at 1Hz [158, 159]. One of the difficulties that arises from this kind of approach is the necessity for a "clear" dielectric signal. What that means is that the pure response of the resin system has to be monitored without the interference of the measuring dielectric sensor. During a dielectric measurement, the free ionic species that are present at all resin systems tend to form a blocking layer at the interface between the electrodes and the resin, which produces a large increase in the apparent measured dielectric loss (see Section 2.7.9). This artefact masks the dipolar peak and thus makes it very difficult to follow the changes in the dipolar peak and therefore track the vitrification time.

The almost entire absence of any dipolar peaks in the dielectric response can be seen in Figure 8.19. At this figure, $\ell og\varepsilon''$ has been plotted in a three-dimensional diagram against the test frequency and the cure time for the isothermal cure of RTM6 resin at 140°C. A close examination of the figure reveals the following:

- In the early stages of the cure, $\ell og\varepsilon''$ follows a linear dependence with $\ell og f$, indicating that the signal is dominated by conductivity. At this point it has to be recalled that the contribution of ionic conduction to the overall dielectric loss is

given by the relationship: $\varepsilon''_{ionic} = \frac{\sigma}{\varepsilon_0 \omega}$, which in $\ell og\varepsilon''$ vs. $\ell og f$ plot is a straight line with slope -1 (see Section 8.1 for Z'' interpretation).

- As the cure progresses the overall loss decreases and the linear dependence of $\ell og\varepsilon''$ with $\ell og f$ starts to collapse as the ionic conduction reduces in magnitude because of the stiffening of the curing resin.
- Further into the cure dipolar contributions start to become visible, especially at high frequencies where the signal is not affected significantly by conductivity (α relaxation).
- Towards the end of the cure the loss reaches a minimum value, still depending on the test frequency though, indicating that the resin has reached a final point for that specific cure cycle.

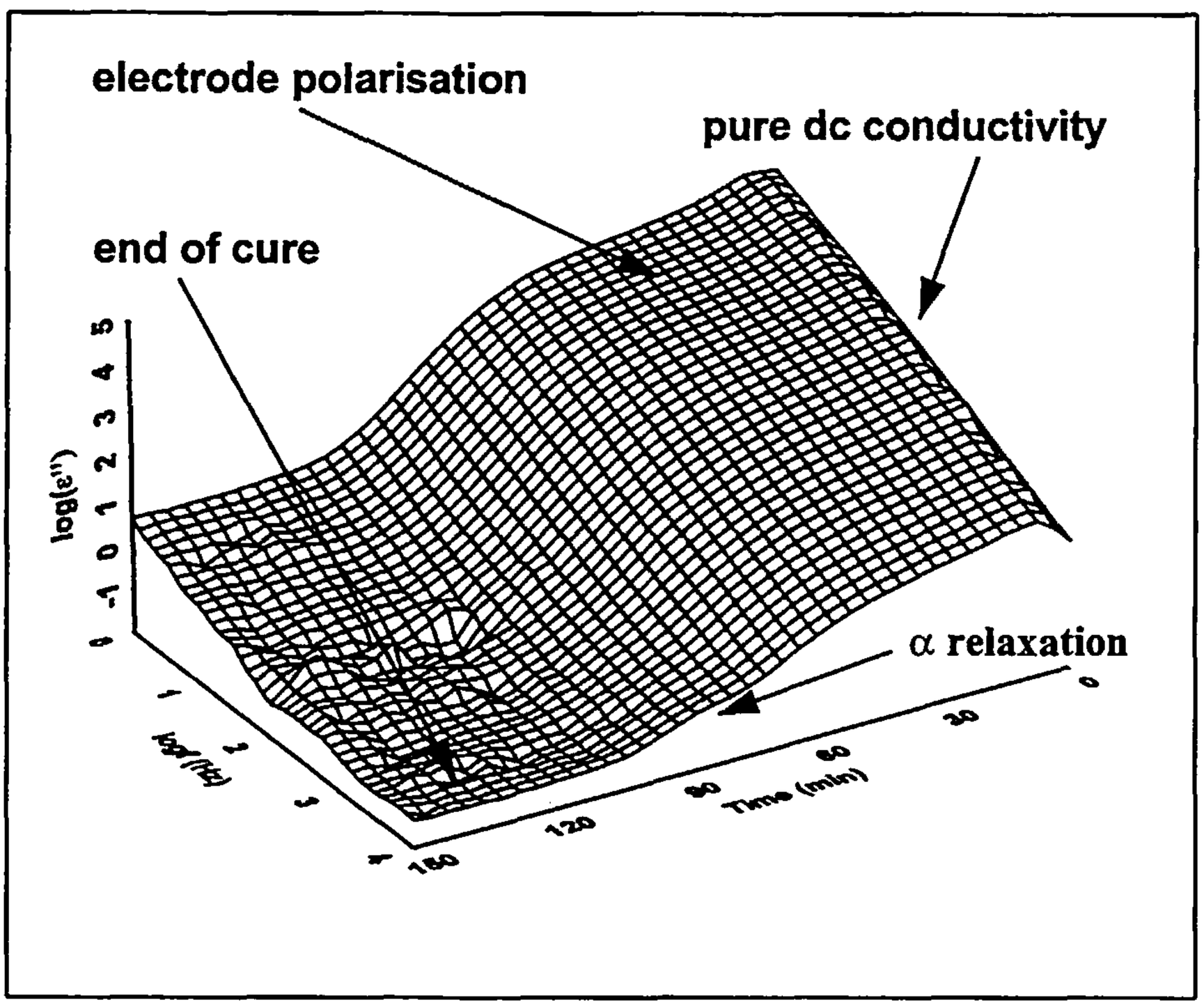

Figure 8.19 *Three-dimensional plot of dielectric loss against test frequency and cure time for the isothermal cure of RTM6 resin at 140°C.*

All the above observations are indicated in Figure 8.19 by the arrows, which have been drawn for demonstration purposes.

Even though the dielectric loss, at least for the resin systems investigated, does not show clearly the dipolar contributions, which could lead to the evaluation of the vitrification point, this is not the case for the dielectric permittivity. The ionic conductivity does not affect the permittivity of the resin system but only the dielectric loss (see Sections 2.7.6 and 2.7.8). Although the artefact of electrode polarisation can still be observed in the signal, it is more likely that later in the cure, the contribution from electrode polarisation will be reduced, since the cured resin will not allow any ion migration, which lead to the build up of the electrode blocking layer. The permittivity of RTM6 resin, cured isothermally at 140°C, can be seen in Figure 8.20.

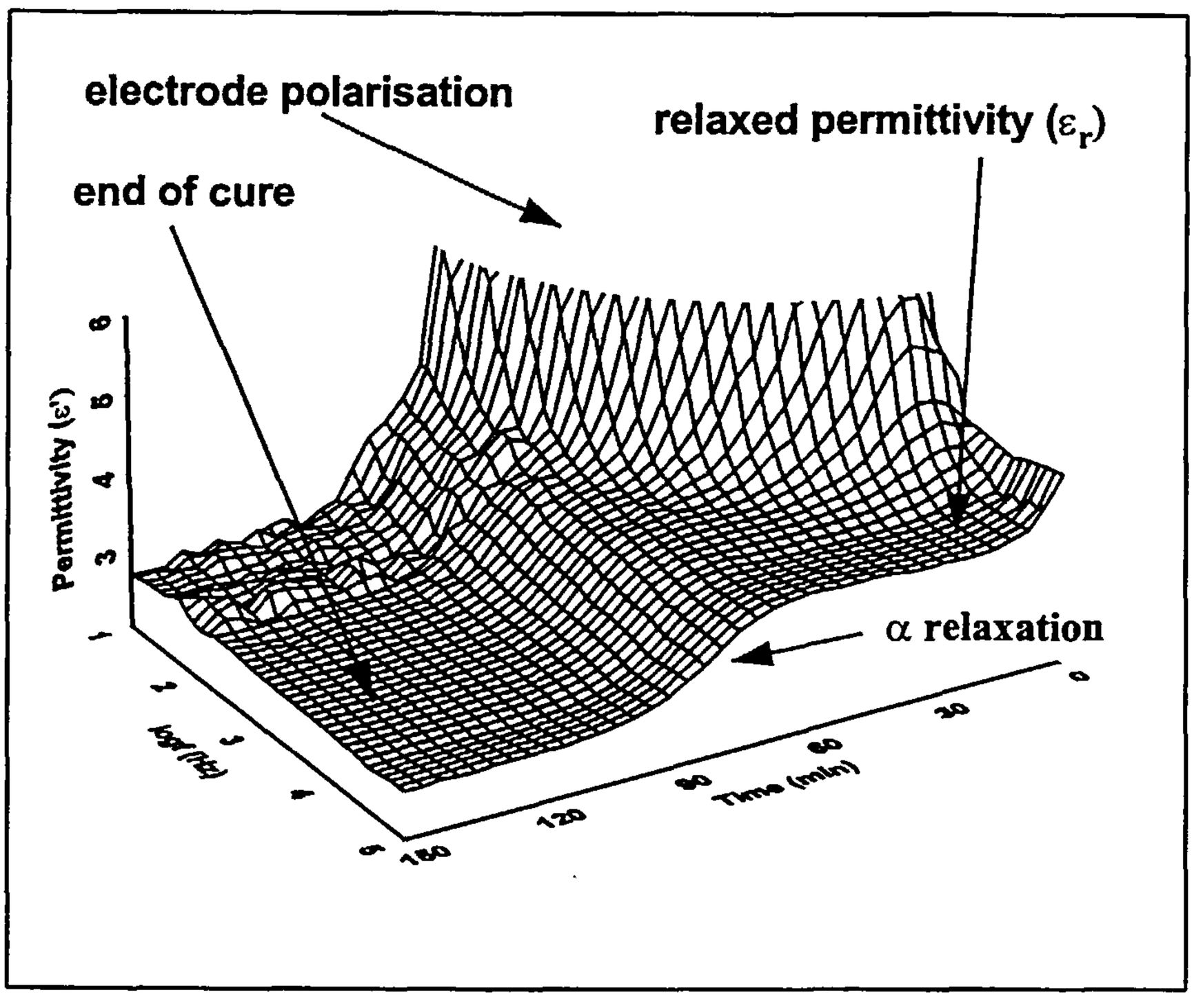

Figure 8.20 *Three-dimensional plot of permittivity against test frequency and cure time for the isothermal cure of RTM6 resin at 140°C.*

The effect of electrode polarisation is evidenced by the high values of permittivity obtained early in the cure and especially at low frequencies. At these frequencies, the electric field changes polarity slowly compared to the ability of the ionic species to reorient, thus allowing for the accumulation of these species at the electrode/resin interface. In the high frequency region however, the ions cannot follow the changes in the polarity, which means that at that region the dielectric response is free of any electrode polarisation contributions. This is evidenced by the plateau observed in that region. We can confidently suppose then that the permittivity values, as measured at the high frequency range, reflect the changes in the relaxed permittivity of the resin (ε_r). If we follow the changes of permittivity throughout the cure we can observe a significant step drop in its magnitude, an indication of approaching the α relaxation of the resin (the physical transformation from the rubbery to the glassy state).

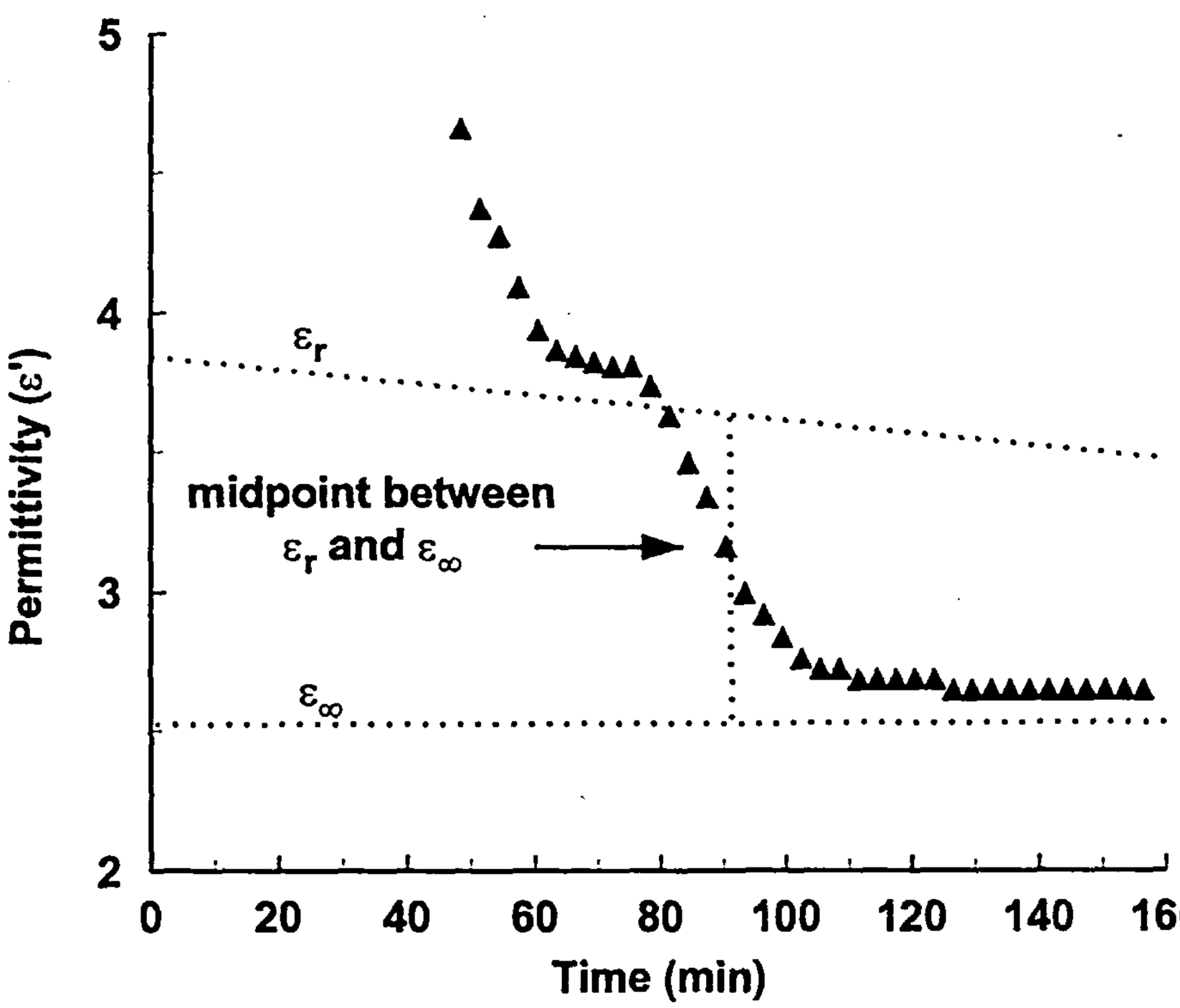

Figure 8.21 *Schematic representation of the determination of the relaxation time τ from the permittivity data.*

This can be more easily understood if we compare Figure 8.20 with the permittivity of the pure DGEBA resin shown in Figure 2.18. The step in permittivity at the α relaxation is evident in both cases. The pioneer work of Debye [107] has demonstrated that the point where the dipolar peak in the dielectric loss is observed, is the point where permittivity is mid-way between the relaxed permittivity ε_r and the unrelaxed permittivity ε_∞. If we consider that the unrelaxed permittivity is the permittivity of the fully cured resin (see Section 2.7.12), then the way of estimating the relaxation time τ (cure time at the dipolar peak) can be schematically represented by Figure 8.21. At each frequency, the permittivity is monitored throughout the cure and the point in time where it reaches the mid-point between ε_r and ε_∞ coincides with the relaxation time. Since electrode polarisation is always present at low frequencies, this procedure cannot be followed to frequencies as low as 1Hz, which is the frequency that tracks the vitrification point. Thus, the above procedure is usually repeated for three or four orders of magnitude of frequency in the high frequency range and back extrapolation of the relaxation times down to 1Hz is made to give the relaxation time at that frequency, which identifies the vitrification point [155].

Before any calculations of the relaxation times can be made, the relaxed permittivities need to be evaluated. The permittivity data at the frequency of 178kHz will be used for this purpose. This frequency falls in the plateau region previously assigned to the relaxed permittivity of the resin (see Figure 8.20). These data are shown in Figure 8.22 for the isothermal cure of RTM6 resin at various temperatures. An apparent conclusion that can be drawn from the figure is the specific trend that is followed by permittivity at a specific frequency at various cure temperatures. The higher the cure temperature the lower the apparent permittivity and the lower the cure time required to reach the α relaxation. The above observation is in a good agreement with the general case of the relaxed permittivity reducing as the temperature increases. From the generalised form of the Clausius - Mossoti equation (see Eq. 2.62), it follows that as the temperature increases the relaxed permittivity drops to lower values. The lower cure times to reach the α relaxation at elevated cure temperatures are the direct outcome of the higher reaction rates that are achieved at higher temperatures.

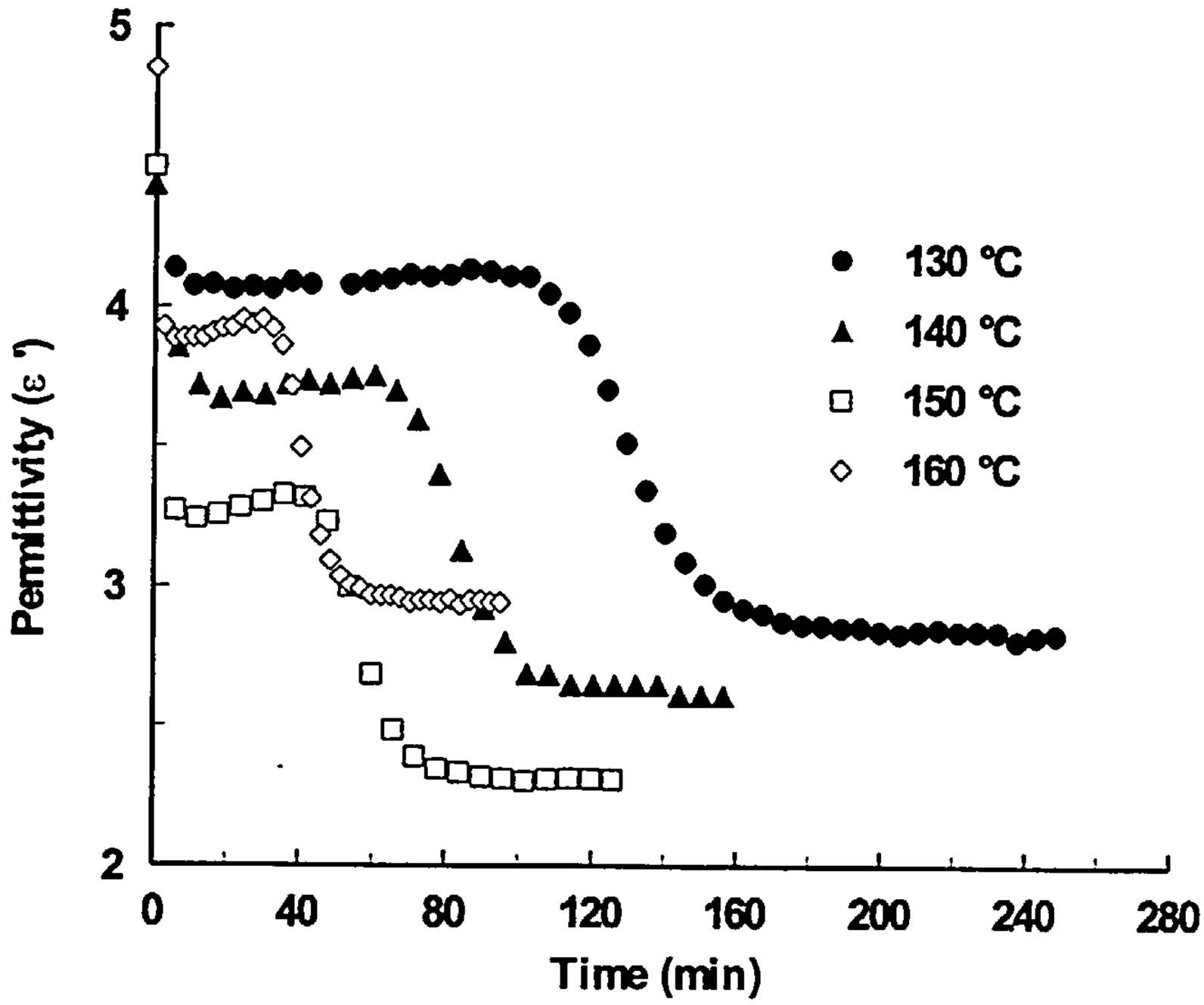

Figure 8.22 *Permittivity plots at 178kHz of the isothermal cure of RTM6 resin at various temperatures.*

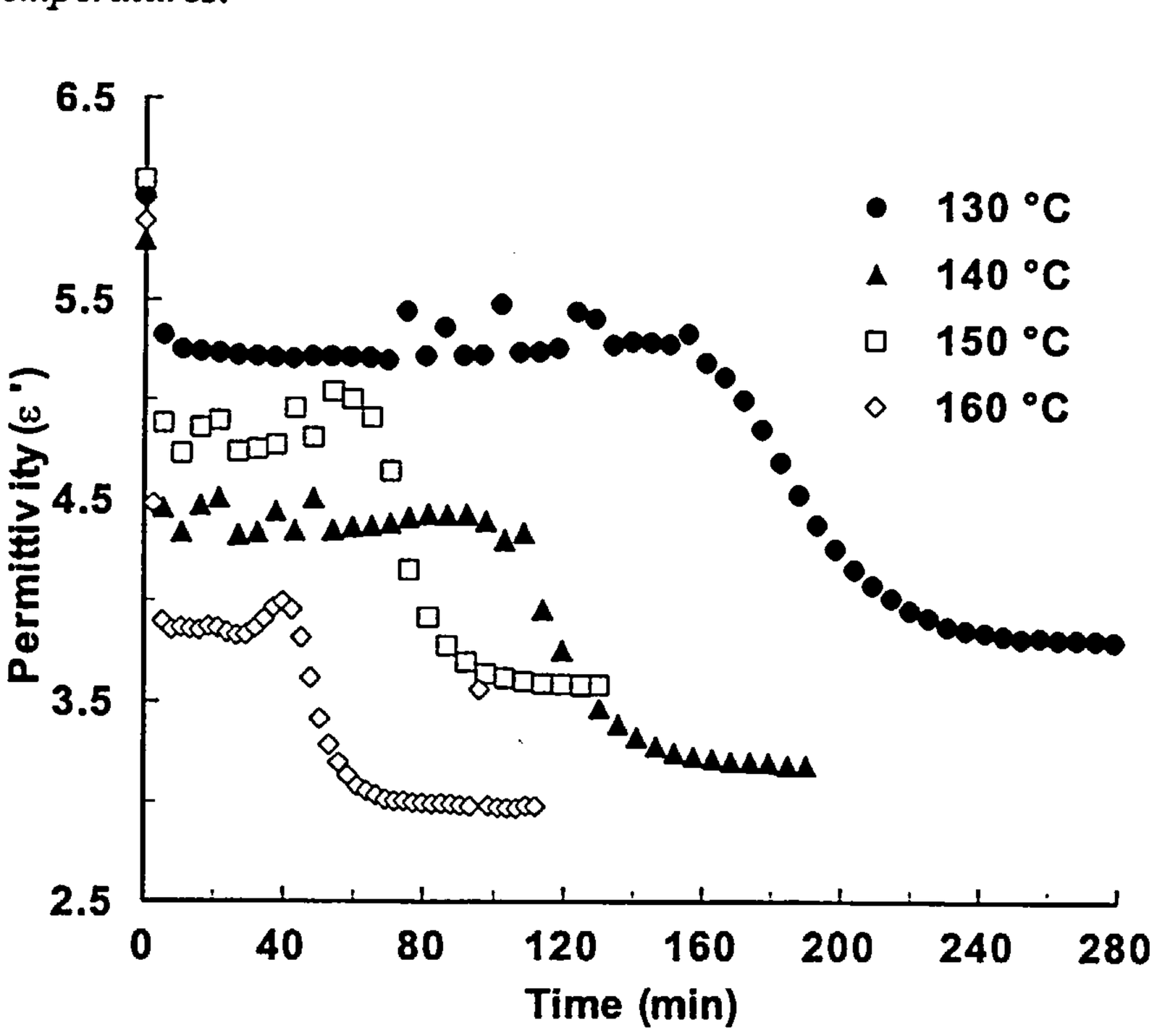

Figure 8.23 *Permittivity plots at 178kHz of the isothermal cure of RMO2 resin at various temperatures.*

The only exception from the general trend in permittivity is obtained by the cure at 160°C, which is completely out of the trend. The same effect was also observed for the isothermal cure of RMO2 resin. The permittivity profiles at 178kHz for that resin are shown in Figure 8.23. They follow the same trend with the profiles of RTM6 resin apart from the cure at 150°C. For both resin systems the permittivity profile that is not following the trend seems to overestimate the permittivity. While the α relaxation follows the trend, the overall values of permittivity are higher than they should be. If we consider the effective air capacitance measured by the sensors used in the measurement of RMO2 resin (see Table 8.1) we can conclude that they are sensing approximately the same effective volume (the air capacitance is approximately constant). What that means is that the same should be expected if they were sensing the same resin at the same cure temperature. However, this is not the case. The cure at 150°C shows higher permittivity values than the 140°C cure, thus higher overall capacitance. This effect should suggest that the sensor for the 150°C senses more effective volume than the sensor for the 140°C or vice versa. No further explanation can be given at the moment for the observed controversy in the experimental results.

Another phenomenon that is also observed is the increase of permittivity during a cure cycle in the region prior to the step drop at the α relaxation (see Figure 8.22 and Figure 8.23). A better insight can be achieved if we overlay the actual temperature profiles that were followed by the resins during the experiments. The permittivity profile at 178kHz for the isothermal cure of RTM6 resin at 150°C is shown in Figure 8.24 along with the actual temperature profile for this cure cycle.

The first remark that can be made is that the actual temperature of the resin is a few degrees above the programmed cure temperature, which means that the resin was cured faster than it should be. The temperature profile also reveals that as the cure progresses the temperature of the resin increases as a result of the exotherm produced by the curing reaction. The permittivity profile also follows the same trend as the temperature profile. After the initial drop in permittivity because of the heat up of the resin to the isothermal temperature, permittivity increases as the temperature of the resin increases during the curing. This is contrary to the expected drop of permittivity with increasing temperature.

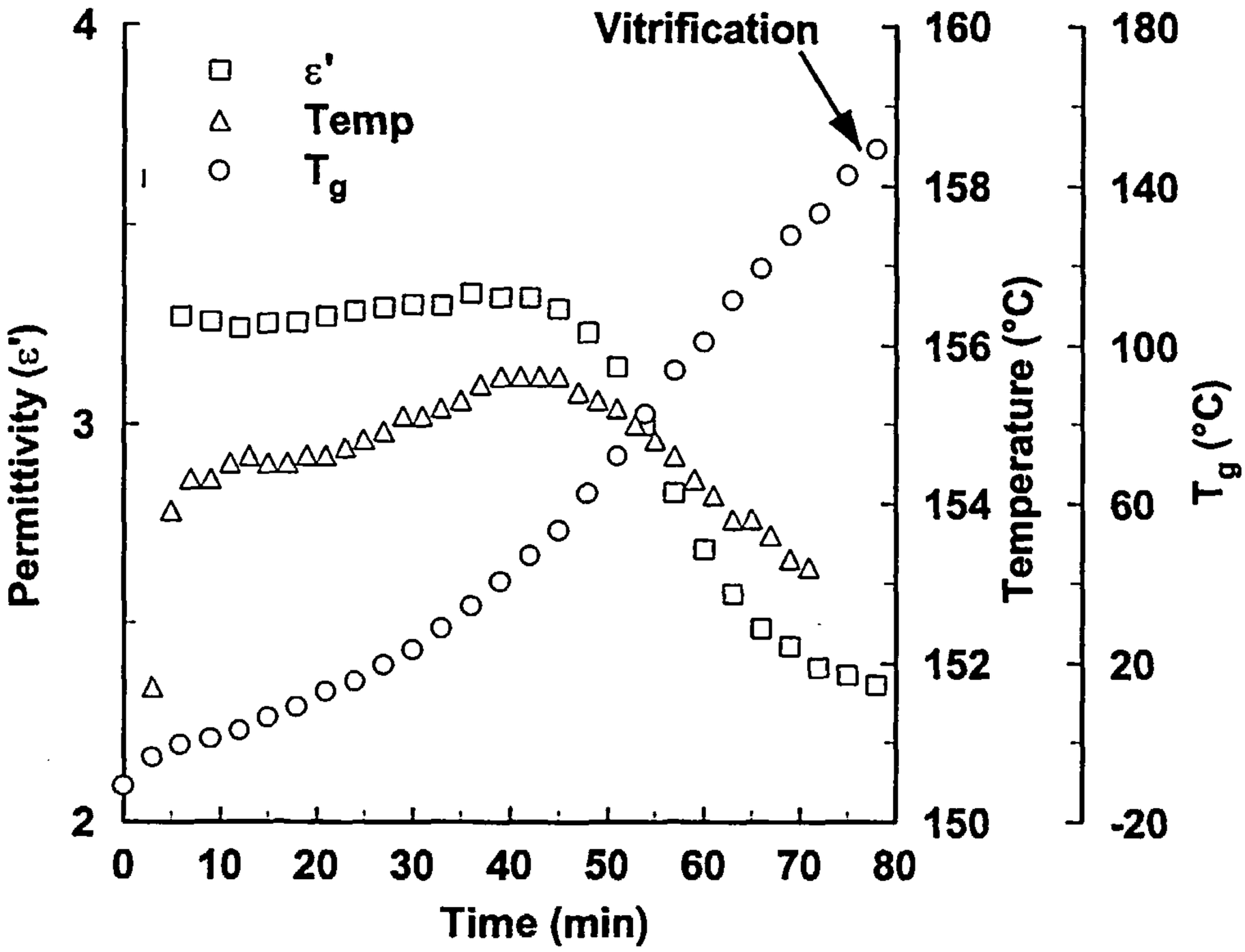

Figure 8.24 *Overlaying of permittivity at 178kHz and temperature profiles of the isothermal cure of RTM6 resin at 150°C. The glass transition temperature profile is also plotted for comparison of the vitrification points.*

The resin, before it reaches vitrification, has a T_g which is always below the cure temperature (see Figure 8.24). Thus, according to Eq. 1.62 and Figure 2.18, the relaxed permittivity should keep dropping as the temperature of the resin increases. The apparent controversy of the experimental results with what was expected can be resolved if we consider the geometry of the applied electric field. Because of the two terminal nature of the sensor used, the electric field that is produced is a fringing field. That means that the curvature of electric field lines will depend upon the permittivity of the medium that the field is applied to. For the measurement in free air, the permittivity of the medium is constant ($\varepsilon_r = 1$). But in the case of the resin, permittivity is not constant. It drops as the resin cures. At the beginning of the cure, where the resin is in the liquid state, the resin permittivity is high. That will cause reduction in the

curvature of the field lines (the radius of the elliptic field lines will be smaller than that of the field lines in free air). As the cure progresses, the curvature will increase as a result of the lower permittivity of the curing resin and it will approximately resemble the field lines in the free air towards the end of the cure. What that means is that the effective area that is measured is smaller at the beginning of the cure compared to the effective area measured in free air. Thus, at least until the vitrification point has been reached (the step drop in permittivity), the admittance of the sensor in free air should be adjusted to smaller values than actually used in the calculation of permittivity by Eq. 8.27. This adjustment would increase the permittivity values and might result in non-appearance of the controversy in the permittivity results presented in Figure 8.24 (increase in permittivity while the temperature increases).

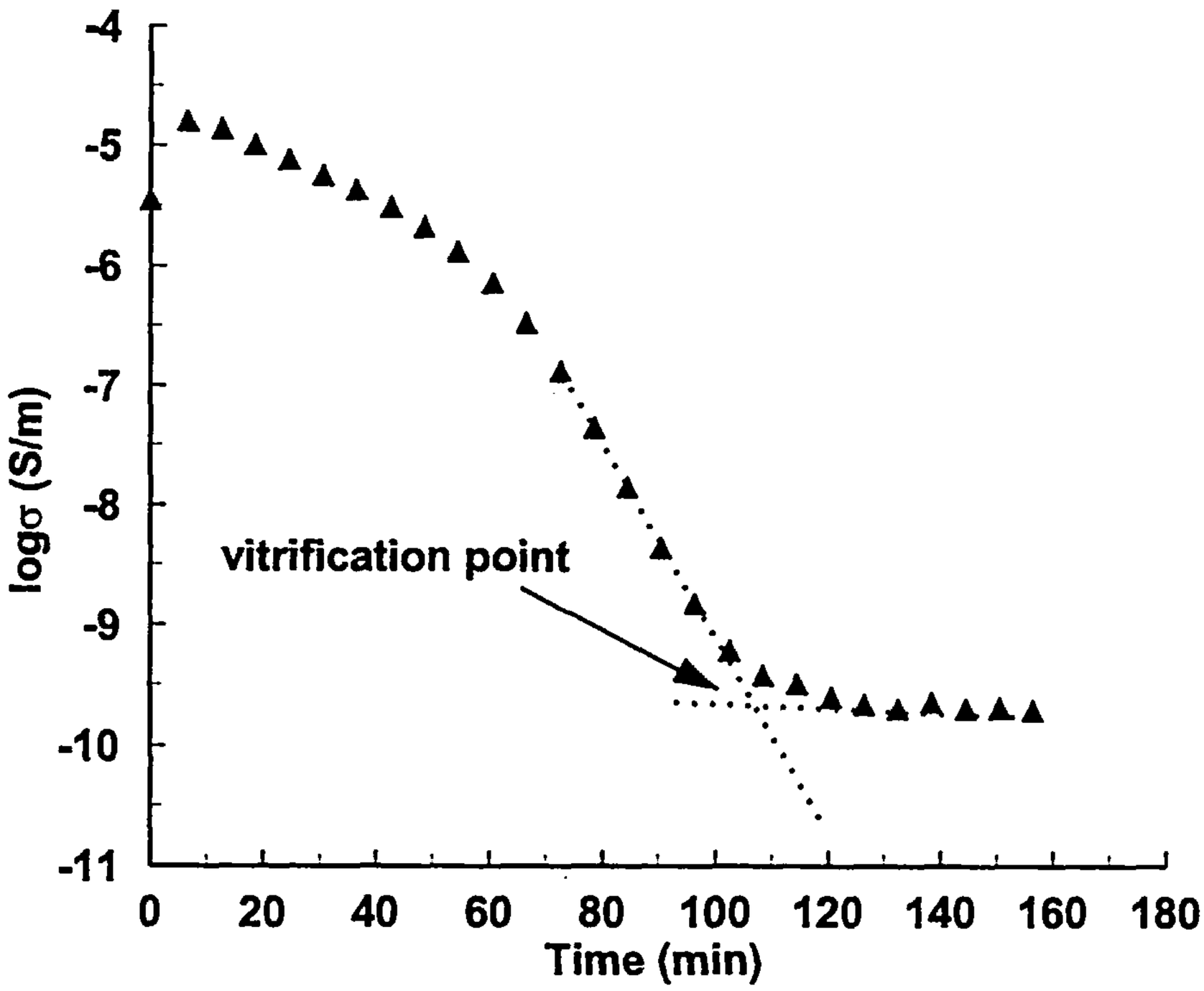

Figure 8.25 *Determination of vitrification point by conductivity measurements. The intersection point between the linear extrapolation of conductivity before and after the end step in conductivity at the end of the cure defines vitrification.*

The above discussion would suggest that the experimental data, at least as they were presented, are not really suitable for any further treatment. The application of the method presented in Figure 8.21 for the calculation of the relaxation times would probably produce untrustworthy results. Thus, at least for the evaluation of the vitrification points, the most suitable method would seem to be to find the endset of the conductivity profiles, determined by the intersection of the extrapolated conductivities before and after the final step in conductivity at the end of the cure (see Figure 8.25). The vitrification times thus determined for some of the resin systems and for some cure temperatures are given in Table 8.2 along with the vitrification times determined by DSC T_g measurements (see Chapter 5).

Table 8.2 *Vitrification times as determined by the intersection of the extrapolated conductivities before and after the final step in conductivity at the end of the cure, for all resin systems. Values in brackets indicate vitrification times as determined by DSC measurements.*

Resin	Vitrification Time (min)			
	130°C	140°C	150°C	160°C
RTM6	165 (191)	106 (130)	75 (88)	52 (60)
RMO	240 (180)	148 (118)	88 (78)	64 (51)
RMO2	200 (191)	136 (130)	82 (88)	60 (66)

The comparison between the two techniques does not show any particular correlation, as expected from the key points discussed in this section.

8.9 General Comments on the Dielectric Monitoring Results

The results presented in this chapter have demonstrated the complex fashion by which the dielectric response of the resin reflects any chemical or physical changes during the cure. The initial aim of the implementation of the dielectric cure monitoring in the present study was to investigate the feasibility of detecting the cure advancement and

the major physical transformations that occur during the cure of epoxy resins, by monitoring the changes in the dielectric properties of the curing resin. Detection and quantification of cure advancement was accomplished with a reasonably good degree of accuracy. The changes in the imaginary impedance and in the conductivity levels of the resin were shown to follow a trend similar to that exhibited by the degree of cure. The characteristics of the reaction mechanism, such as the autocatalytic behaviour of some of the resin systems investigated and the maximum in the reaction rate, were successfully detected and showed a very good correlation with the same characteristics detected by the more traditional cure monitoring techniques (DSC and FTIR).

The next step was to investigate the possibility of detecting gelation and vitrification by monitoring the changes in the dielectric signal and in particular the changes in the conductivity levels and the relaxed permittivity of the curing resin. Such studies have been undertaken by several research groups in the past and have shown very promising results. However, equivalent attempts in this study gave unexpected results. Some of the reasons for this have already been given in the previous sections of this chapter. In particular, the suggested reasons for this discrepancy are:

- Temperature instability during the dielectric experiments;
- Higher overall cure temperatures than those achieved during the DSC and FTIR experiments;
- Variations in the effective measured volumes between different dielectric sensors;
- Intrinsic deficiencies in the design of the dielectric sensors. The two terminal design of the sensors leads to a permittivity dependent applied electric field;

The above mentioned key points, that affected the dielectric measurements, did not allow for direct evaluation of gelation and vitrification from the changes in the dielectric signal. However, this is a consequence of the attempt to correlate the absolute values of the dielectric response of the resin to the observed physical transformations during the cure. This was demonstrated in Figure 8.22 and Figure 8.23, which show the relaxed permittivity profiles of the RTM6 and the RMO2 resin systems at various cure temperatures. In these figures, two of the experiments fall out

of the general trend that is followed by the rest of the experiments. Despite the fact that this observation means that the absolute values cannot be trusted, completely different results will be obtained if we plot the relative changes of the relaxed permittivity. This is demonstrated in Figure 8.26, where the same data shown in Figure 8.22 have been plotted, but this time normalised by the minimum permittivity attained at each cure temperature.

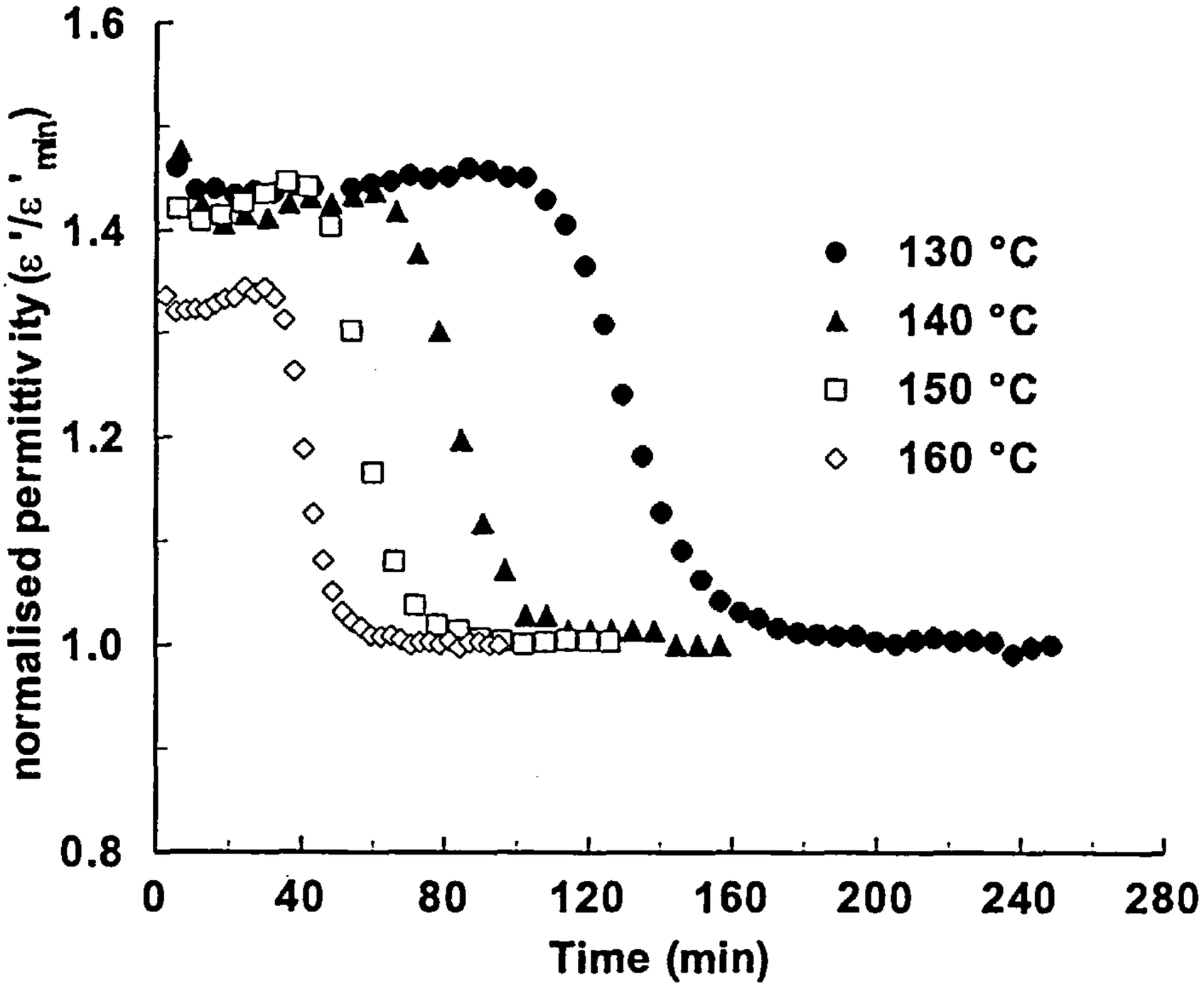

Figure 8.26 *Permittivity plots at 178kHz of the isothermal cure of RTM6 resin at various temperatures. Data have been normalised by the minimum permittivity attained at each cure temperature.*

The difference in the trends of the curves between Figure 8.22 and Figure 8.26 is evident. The normalised permittivities follow the expected trend. At low cure temperatures the relaxed permittivities in the beginning of the cure are higher than at high cure temperatures. As the cure progresses all the profiles show a step drop at the α relaxation and then level off to the unrelaxed permittivity. At this point, it has to be

recalled that the unrelaxed permittivity is independent of temperature and test frequency, at least in the frequency range of the present experiments. The unrelaxed permittivity is the "background" permittivity of the resin and is attributed to the electronic and the atomic polarisation. These kinds of polarisation are expected to exhibit a relaxation at very high frequencies (probably ten orders of magnitude or more above the maximum frequency measured in the present experiments). For more details in these kinds of polarisation, the reader can refer to Section 2.7.2.2 in Chapter 2 of the present thesis.

The above described normalisation of the relaxed permittivities could make it possible to use the method described in Section 8.8 for the estimation of the relaxation times of the α relaxation process (see Figure 8.21) and consequently for the estimation of the vitrification times. In an industrial context, an estimation of the vitrification times would be invaluable as it would allow the use of a feedback-loop control system for the cure process, based on the estimation.

However, for the purposes of this study the absolute values of the dielectric response are more valuable and able to reflect the changes in the curing resin system. Therefore, the effort was focused on the extraction of the "real" dielectric response of the resin and on the correlation of the "real" relaxations to the characteristic points of the cure.

Chapter Nine

9. Overall Discussion

The cure profiles of several commercial and laboratory made epoxy resins were investigated in this study by several thermoanalytical techniques. The investigation was concentrated not only on gathering the appropriate information of the characteristic elements of each individual cure (degree of conversion, glass transition temperature, viscosity), but also in the development and application of mathematical models that could simulate any cure profile under isothermal or dynamic conditions. Effort was also applied to utilise a monitoring technique potentially able to characterise the cure of these materials by in-situ and in real time.

The techniques employed for the thermoanalytical characterisation of the epoxy resins investigated were Differential Scanning Calorimetry (DSC), Fourier Transform Infrared Spectroscopy (FTIR) and Rheometry. The key issues that were identified from the results of a range of experiments on those resins, concerning their cure mechanism, were (see Chapter 4 for more details):

- Complex reaction mechanisms for all resins;
- Constant cure mechanism for all resins apart from the cure of the catalyst containing resin 934, which showed indications of changes in the reaction mechanism in cures at different heating rates;

- Autocatalytic phenomena for the resin systems not containing catalysts;
- Diffusion phenomena for all isothermal cure cycles, leading to incomplete curing.

The experimental data on the reaction rate and the degree of conversion obtained by DSC and FTIR were further analysed in order to construct kinetic models that could accurately predict the cure advancement for all resin systems. Various techniques were applied, based on information on the reaction mechanism of each individual resin and on the characteristic points that they show. These models varied from pure phenomenological models derived for a simple epoxy/amine cure to complex mechanistic models, that could describe the concentration evolution of all the reactive species involved in the cure reactions (see Sections 4.4 and 4.5). Irrespective of the nature of the kinetic model, the activation energies that were estimated revealed that three of the four resin systems investigated (RTM6, RMO and RMO2) were following the same reaction mechanism (see Tables 4.5 and 4.6). Some variability was observed in the values of the calculated kinetic parameters such as the pre-exponential factors of the reaction rate constants. This is more likely to be a direct effect of the stoichiometry differences, leading to different contributions from individual reaction types, rather than any intrinsic differences in the overall reactions mechanisms.

Assumptions of simple reactions of the epoxide groups with the amines were found to be adequate to mathematically describe the cure kinetics of all the resins. The use of both autocatalytic and non-autocatalytic reaction schemes in the models was able to describe the two activation mechanisms that are followed during the cure reaction for the resins not containing any catalysts (see Eq. 4.9 and Section 4.5). The autocatalysis was attributed to the hydroxyl groups produced during the epoxy/amine reaction. For the 934 resin, which contained BF_3 catalysts, a simple *n*th order reaction mechanism was found sufficient to describe the cure kinetics under isothermal conditions (see Eq. 4.14).

The cure kinetics under dynamic conditions was found to be more complex to model. A modified model was used to fit the experimental data on the cure kinetics under dynamic conditions (see Eq. 4.17). In the case of the 934 resin, peak separation was needed to identify the individual reaction steps that were observed in the DSC

thermograms. Further modelling of each individual reaction step was implemented by the use of a simple *n*th order reaction mechanism (see Eq. 4.19).

The fitting on the models was very good for all the resins suggesting, apart from the success of the evaluation procedures, that the models implemented were adequate to describe the kinetics of those resins.

The kinetic data were then combined with T_g data in order to describe the structural development during the cure and also to identify and analyse the diffusion regions in the cure cycles. The analysis of the glass transition temperature profiles revealed that a single activation mechanism is followed during the build up of the three dimensional network, in contrast to the reaction kinetics, which follow several activation mechanisms depending on the nature of the individual cure reaction (see Section 5.1). The combined results on cure kinetics and *Tg* were further analysed to describe the diffusion processes during the cure reaction. Although the experimental data were not adequate enough to analyse in all cases, for some of the cure cycles, where the analysis was possible, it was indicated that diffusion is a single activated mechanism correlating to the structure development characteristics of each resin (see Chapter 5).

Viscosity changes were also monitored during the cure of each resin system. The rheometric results on viscosity showed the typical behaviour of an epoxy amine cure. An exponential growth of viscosity was followed for all resin systems apart from the 934 resin. Application of a modified version of the WLF equation (see Eq. 7.5) was very successful in the modelling of the viscosity data. All the parameters of that equation were found to depend on the cure temperature in a systematic manner. The physical transformation from the liquid to the rubbery state (gelation) was detected from the viscosity profiles. Further combination of the viscosity results with the kinetic and the T_g results revealed that gelation is occurring at a specific T_g, which is unique for each resin system (see Figures 7.12 - 7.14 and Figure 7.17).

The sensitivity of all the mathematical models constructed in this study was also evaluated by incorporating a fixed 5% error on the estimated model parameters. A template for this kind of error analysis is given in Appendix E.

While the thermoanalytical techniques and the chemorheological modelling provided all the information needed to characterise the curing behaviour of the resin systems studied, the monitoring technique that was utilised (Dielectric Analysis), provided the tool for the on-line detection of the curing characteristics of these resins. Because of the non-destructive nature of that technique and the sensing devices that were used (see Figure 3.7), the dielectric properties of the curing resins were collected and analysed in order to investigate the feasibility of actually correlating these properties with the cure characteristics of the resins. The sensing devices were simulated by the use of suitable equivalent electrical circuits and the resin response was separated from the bulk measured signal (see Section 8.4). The characteristic peaks that were observed in the impedance response of the resin were attributed to the dc conductivity of the curing resin. That enabled a simulation of the cure advancement during the cure to be made. Although the correlation with the kinetic results from the DSC measurements was not very good, because of temperature variations and intrinsic disadvantages of the sensors (see Section 8.8), the trends were similar, suggesting that the dielectric technique is capable of detecting the cure advancement (see Figures 8.4 - 8.7). An attempt was also made to correlate the dielectric signal to the physical transformations that occur during the cure of the resin. Despite the fact that the gelation times that were estimated from the inflection points in the conductivity curves were shown very good agreement with the gelation times estimated by the viscosity profiles for all the RTM6 related resins, the failure of the method in the case of the 934 resin suggests that further considerations have to be made in the interpretation of the results and in the experimental setup.

From the above summary it can be concluded that:

- The aim for a universal cure kinetics model remains an unachieved target;

- The effort needed to produce models that can accurately describe the cure processes in thermosets is significant;
- Elegant mathematical techniques have to be implemented for the application of more complex models;
- On-line monitoring is achievable, although some further considerations have to be given to the experimental dielectric setup. The interpretation of the results also needs some reevaluation.

Chapter Ten

10. Conclusions

Thermoanalytical techniques and dielectric analysis were used to describe and characterise the cure processes during the isothermal and dynamic cure of various epoxy/amine resin systems.

The kinetic analysis of the experimental data by DSC and FTIR measurements revealed that:

a) Reaction mechanism:

The reaction path that is followed is reactions between:

- Epoxy groups with primary amines (primary amine addition reaction);
- Epoxy groups with secondary amines (secondary amine addition reaction);
- Epoxy groups with primary amines catalysed by the produced hydroxyl groups;
- Epoxy groups with secondary amines catalysed by the produced hydroxyl groups;
- Epoxy groups with the produced hydroxyl groups (etherification reaction);
- There was no experimental evidence to support any reaction between epoxy groups (homopolymerisation reaction) although it is believed that these reaction should occur during the dynamic cure of these resins.

b) Activated mechanisms:

- Two overall activated mechanisms were identified for the cure of the non-catalytic resins (RTM6, RMO and RMO2). The activation energies obtained were approximately 72-75 kJ/mol for the non-autocatalysed reactions and 53-56 kJ/mol for the autocatalysed reactions;
- One overall activation mechanism was identified for the isothermal cure of the catalytic resin system (934). The activation energy obtained was 74 kJ/mol, a value that falls in the range of the previously estimated activation energies for the non-autocatalysed reactions of the other resin systems. Thus, it is suggested that the reactions occurring have the same overall identity for all resin systems.

The combined results of the T_g measurements and the reaction kinetics data suggest that:

a) Three dimensional network development:

- The glass transition temperature advancement during the cure follows the same trend with the reaction advancement;
- A one-to-one relationship exists between T_g and conversion, suggesting that the formed network is independent of the conditions under which the cure reactions occur;
- All the resin systems vitrify under isothermal conditions without reaching 100% conversion.

b) Activation mechanism of structure advancement:

- A single activation mechanism is followed for all resin systems as the T_g advances, indicating that the development of the three-dimensional network does not depend on the various reactions that may or may not occur during the cure;
- The occurrence of diffusion depends on the structure development (T_g) and it is an activated mechanism.

The viscosity data collected by the rheometric technique revealed that:

- The viscosity profile of the curing resin follows the usual exponential growth under isothermal conditions;
- At the gelation region the viscosity increases very rapidly in a very narrow time window compared to the overall time scale of the curing, making the above technique adequate to measure the gelation times with a very good degree of accuracy;
- The combined results of viscosity and T_g suggest that gelation occurs at a specific T_g which is unique for each resin system.

The chemoviscosity modelling that was applied to describe the cure kinetics, the T_g advancement and the viscosity increase during the cure process of all resins indicated that:

a) Cure kinetics:

- Various mathematical models, either phenomenological or mechanistic, had to be applied to describe accurately the cure advancement in respect to the degree of cure;
- Elegant mathematical techniques had to be applied in order to evaluate the kinetic parameters of the above models;
- The evaluated kinetic parameters were in the range of the parameters obtained from the literature for similar epoxy/amine systems;
- The simulation of the cure advancement made by these models was very successful under all circumstances and for the cure temperatures that were studied experimentally.

b) T_g development:

- Di-Benedetto's equation was an adequate expression to describe mathematically the one-to-one relationship between T_g and degree of conversion;
- The fitting achieved was very good for all resin systems.

Viscosity modelling:

- A modified version of the well known WLF equation had to be implemented in order to simulate accurately the viscosity profiles of all the resin systems under isothermal conditions;
- The parameters of the WLF equation depend on the cure temperature.

The dielectric monitoring technique that was implemented to investigate the feasibility of following the cure under isothermal conditions showed that:

- The characteristic peak that appears in the imaginary impedance of the curing resin in the frequency domain reveals the characteristics of the cure mechanism (autocatalysis, freezing of the reaction prior to fully cure under isothermal conditions);
- The advancement of the peak in the imaginary impedance with cure time shows the same overall trend with the degree of conversion obtained by DSC and FTIR experiments;
- The conductivity profile obtained by analysing the imaginary impedance peak is the same as the conductivity profiles obtained by conventional methods (superposition of dielectric loss profiles at different frequencies), but superior in the way that it is not a "trial and error" method in picking up the right frequency for which the dielectric loss data represent the conductivity of the resin;
- There exists a definite drop in permittivity toward the α relaxation (physical transformation from the rubbery to the glassy state), visible in the high frequency range but masked by the high conductivity levels in the low frequency range;
- The major physical transformations during the cure (gelation and vitrification) do show up in the dielectric signal, but temperature variations and intrinsic experimental difficulties currently prevent a more detailed quantitative analysis of the results.

Chapter Eleven

11. Suggestions for Further Work

The detailed investigation of the cure kinetics of the resin systems utilised in the present study has resulted in the following two overall conclusions:

- Simple autocatalytic cure kinetics models or modified versions of them can be easily adapted to describe the cure of almost every epoxy/amine resin system cured under isothermal conditions;
- The transition from the isothermal cure to the non-isothermal cure results in more complex reaction kinetics and, thus, in more complex kinetic models and a need for sophisticated mathematical methods for the kinetic parameters evaluation.

The reason for the failure of the models, at the transition from the isothermal to the non-isothermal case, is that these models are mostly phenomenological and unable to describe accurately the true reaction mechanisms that take place during the cure. Therefore, it would seem advisable to utilise appropriate experimental methods that could give the concentration profiles of all the reactive species involved in the cure reactions and to model each individual concentration profile for any kind of cure, isothermal or non-isothermal. These methods will yield the kinetic parameters for each individual reaction and thus provide a better insight into the overall reaction mechanism. Infrared spectroscopy and especially near-infrared spectroscopy is

probably the best method for such an investigation since it has been shown to give information in areas where mid-infrared spectroscopy has failed.

The new concept of the Modulated-DSC is also attractive in the investigation of the cure kinetics of thermosetting resins. If the separation of the heat capacity signal from the exothermic signal of the cure reaction is achievable, as it is claimed, then a completely new area is open for investigation. Thermograms that are free of any changes in the physical state of the resin reflect only the "true" chemical reactions that occur during the cure, thus allowing calculation of the degree of cure with a better degree of accuracy and consequently evaluation of kinetic parameters of the actual reaction mechanism. The concept of the isolated heat capacity profile suggests new areas of investigation. Heat capacity is a property that reflects the structural development of the curing resin and therefore should reflect the physical transformations that occur during the cure. Detection of gelation or/and vitrification from the heat capacity changes, therefore from direct DSC measurements, will produce the extra link that is needed in the interpretation of the signal obtained from an online, real time monitoring technique, such as dielectric cure monitoring.

Another point that was picked up in this study is the interpretation of the dielectric signal and how it is affected by the experimental setup and in particular by the design of the dielectric sensors. It is suggested that an investigation of the characterisation of the electric field produced by these sensors should be performed. The potential of applying the dielectric technique in an industrial context, as a means of real-time monitoring of thermoset cure processes, suggests a need for an improvement of the "robustness" of the dielectric signal. Such an approach would require the filtration of any "artefacts" that could interfere with the detection of the critical points in the cure, in particular gelation and vitrification.

The good degree of accuracy that was obtained from the correlation between the changes in the dielectric signal and the changes in the degree of cure indicates that this particular cure monitoring technique would be attractive in an industrial context. For

that reason, it would be of interest to further investigate the existence of any correlation between cure reaction mechanisms, cure kinetics and viscosity, as determined by conventional cure monitoring methods (DSC, FTIR and Rheometry), and dielectric behaviour, as determined by the individual elements that constitute the dielectric response of the resin, such as ionic conductivity and dipolar relaxations. The use of equivalent electrical circuits, as demonstrated in the present study, can be the means to establish this correlation. An investigation of the feasibility of relating the responses of individual circuit elements, or combinations thereof, to changes in resin temperature, resin viscosity, reaction mechanism or degree of cure and the development of mathematical models representing any such connections would seem to be the next step in the design of a potential feedback loop control system for the manufacture of thermoset composites parts.

REFERENCES

1) H. Lee and K. Neville, "Handbook of Epoxy Resins", McGraw-Hill, New York, (1967).

2) J. M. Barton, D. C. L. Greenfield and K. A. Hodd, "Some Effects of Structure on the Cure of Glycidylether Epoxy Resins", *Polymer*, **33**, 1177, (1992).

3) A. Agrawal and D. R. Uhlmann, "Modelling of Condensation Reactions in an Amine-Cured Epoxy System with Groups of Unequal Reactivity", *Polymer*, **32**, 290, (1991).

4) K. C. Cole, "A New Approach to Modeling the Cure Kinetics of Epoxy Amine Thermosetting Resins. 1. Mathematical Development", *Macromolecules*, **24**, 3093, (1991).

5) A. Apicella, L. Nicolais, M. Iannone and P. Passerini, "Thermokinetics and Chemorheology of the Cure Reactions of the Tetraglycidyl Diamino Diphenyl Methane - Diamino Diphenyl Sulfone Epoxy Systems", *J. Appl. Polym. Sci.*, **29**, 2083, (1984).

6) H. H. Winter and F. Chambon, "Analysis of Linear Viscoelasticity of a Crosslinked Polymer at the Gel Point", *J. Rheol.*, **30**, 367, (1986).

7) C.-Y. M. Tung and P. J. Dynes, "Relationship Between Viscoelastic Properties and Gelation in Thermosetting Systems", *J. Appl. Polym. Sci.*, **27**, 569, (1982).

8) W. M. Sanford and R. L. McCullough, "A Free-Volume Approach to Modeling Thermoset Cure Behavior", *J. Polym. Sci.: Part B: Polym. Phys.*, **28**, 973, (1990).

9) D. Hunston, W. McDonough, B. Fanconi, F. Mopsik, F. Wang, F. Phelan and M. Chiang, "Assessment of the State-of-the-Art for Process Monitoring Sensors for Polymer Composites", *NISTIR 4514*, US, Department of Commerce, June 1, (1991).

10) D. E. Kranbuehl, P. Kingsley, S. Hart, G. Hasko, B. Dexter and A. C. Loos, "In Situ Sensor Monitoring and Intelligent Control of the Resin Transfer Molding Process", *Polym. Comp.*, **15**, 299, (1994).

11) S. S. J. Roberts and R. Davidson, "Cure and Fabrication Monitoring of Composite Materials with Fibre-Optic Sensors", *Comp. Sci. Tech.*, **49**, 265, (1993).

12) G. M. Maistros and C. B. Bucknall, "Modelling the Dielectric Behavior of Epoxy Resin Blends During Cure", *Polym. Eng. Sci.*, **34**, 1517, (1994).

13) J. Mijovic, F. Bellucci and L. Nicolais, "Impedance Spectroscopy of Reactive Polymers. Correlations with Chemorheology During Network Formation", *J. Electrochem. Soc.*, **142**, 1176, (1995).

14) B. Ellis, "Chemistry and Technology of Epoxy Resins", Blackie Academic & Professional, Glasgow, (1993).

15) J. M. Barton, "The Application of Differential Scanning Calorimetry (DSC) to the Study of Epoxy Resin Curing Reactions", *Adv. Pol. Sci.*, **72**, 111, (1985).

16) I. T. Smith, "The Mechanism of the Crosslinking of Epoxide Resins by Amines", *Polymer*, **2**, 95, (1961).

17) P. Johncock, G. F. Tudgey, A. V. Cunliffe and R. K. Morell, "Structural Features in Epoxy Networks from N-diglycidyl Epoxies and Amines: 1. Dominant Intramolecular Cyclization Reaction in the Reactions of N, N-diglycidylaniline with Aniline and Substituted Anilines", *Polymer*, **32**, 323, (1991).

18) J. E. Baldwin, "Rules for Ring Closure", *J. Chem. Soc.: Chem. Commun.*, 734, (1976).

19) L. Matejka, M. Tkaczyk, S. Pokorny and K. Dusek, "Cyclization in the Reaction Between Diglycidylaniline and Amine", *Polym. Bull.*, **15**, 389, (1986).

20) L. Matejka, P. Spacek and K. Dusek, "Cyclization in Amine-Cured N, N - diglycidylaniline Epoxy Resins", *Polymer*, **32**, 3190, (1991).

21) W. W. Wright, "Tetraglycidyldiaminodiphenylmethane-Based Epoxy Resin Systems for Aerospace Applications. A Review - Part I", *Composite Polym.*, **No 4**, 275, (1989).

22) J. A. Happe, R. J. Morgan and C. M. Walkup, "^{1}H, ^{19}F and ^{11}B Nuclear Magnetic Resonance Characterization of BF3: Amine Catalysts Used in the Cure of C Fibre-Epoxy Prepregs", *Polymer*, **26**, 827, (1985).

23) A. C. Grillet, J. Galy, J. P. Pascault and I. Bardin, "Effects of the Structure of the Aromatic Curing Agent on the Cure Kinetics of Epoxy Networks", *Polymer*, **30**, 2094, (1989).

24) M.-F. Grenier-Loustalot and P. Grenier, "The Mechanism of Epoxy-Resin Curing in the Presence of Glass and Carbon Fibres", *Polymer*, **33**, 1187, (1992).

25) S. Wang and A. Garton, "Chemical Interactions at the Interface Between a Carbon Fiber and a Boron Trifluoride-Catalyzed Epoxy Matrix", *J. Appl. Polym. Sci.*, **45**, 1743, (1992).

26) P. J. Flory, "Principles of Polymer Chemistry", Cornell University Press, Ithaca, New York, (1953).

27) M. Gordon and G. R. Scantlebury, "The Theory of Branching Processes and Kinetically Controlled Ring-Chain Competition Processes", *J. Polym. Sci.: Part C*, **16**, 3933, (1968).

28) M. Pollard and J. L. Kardos, "Analysis of Epoxy Resin Curing Kinetics Using the Avrami Theory of Phase Change", *Polym. Eng. Sci.*, **27**, 829, (1987).

29) S. L. Simon and J. K. Gillham, "Thermosetting Cure Diagrams: Calculation and Application, *J. Appl. Polym. Sci.*, **53**, 709, (1994).

30) G. Wisanrakkit and J. K. Gillham, "Continuous Heating Transformation (CHT) Cure Diagram of an Aromatic Amine / Epoxy System at Constant Heating Rates", *J. of Appl. Polym. Sci.*, **42**, 2453, (1991).

31) X. Wang and J. K. Gillham, "T_g - Temperature - Property (TgTP) Diagram for Thermosetting Systems: Anomalous Behavior of Physical Properties vs. Extent of Cure", *J. Appl. Polym. Sci.*, **47**, 425, (1993).

32) A. Eisenberg, "The Glassy State and the Glass Transition", in *Physical Properties of Polymers* by J. E. Mark et al, 2nd edition, Chap. 2, 61-96, ACS Professional Reference Book, American Chemical Society, Washington, DC, (1993).

33) J. O. Simpson and S. A. Bidstrup, "Correlation Between Chain Segment and Ion Mobility in an Epoxy Resin System. A Free Volume Analysis", *J. Polym. Sci.: Part B: Polym. Phys.*, **31**, 609, (1993).

34) E. Adabbo and R. J. J. Williams, "The Evolution of Thermosetting Polymers in a Conversion-Temperature Phase Diagram", *J. Appl. Polym. Sci.*, **27**, 1327, (1982).

35) L. E. Nielsen, "Cross-Linking - Effects on Physical Properties of Polymers", *J. Macromol. Sci. - Revs Macromol. Chem.*, **C3**, 69, (1969).

36) K. Horie, H. Hiura, M. Sawada, I. Mita and H. Kambe, "Calorimetric Investigation of Polymerization Reactions. III. Curing Reaction of Epoxides with Amines", *J. Polym. Sci.: Part A-1*, **8**, 1357, (1970).

37) N. A. St. John and G. A. George, "Cure Kinetics and Mechanisms of a Tetraglycidyl - 4,4' - diaminodiphenylmethane / diaminodiphenylsulphone Epoxy Resin Using Near I.R. Spectroscopy", *Polymer*, **33**, 2679, (1992).

38) K. Dusek, M. Ilavsky and S. Lunak, "Curing of Epoxy Resins: I. Statistics of Curing of Diepoxides with Diamines", *J. Polym. Sci.: Poly. Symp.*, **53**, 29, (1975).

39) M. Gordon, G. N. Malcolm and D. S. Butler, "Configurational Statistics of Copolymer Systems" *Proc. Roy. Soc. : A*, **295**, 29, (1966).

40) W. H. Stochmayer, "Theory of Molecular Size Distribution and Gel Formation in Branched-Chain Polymers", *J. Chem. Phys.*, **11**, 45, (1943).

41) R. B. Prime, "Differential Scanning Calorimetry of the Epoxy Cure Reaction" *Polym. Eng. Sci.*, **13**, 365, (1973).

42) M. R. Keenan, "Autocatalytic Cure Kinetics from DSC Measurements: Zero Initial Cure Rate", *J. Appl. Polym. Sci.*, **33**, 1725, (1987).

43) M. R. Kamal and S. Sourour, "Kinetics and Thermal Characterisation of Thermoset Cure", *Polym. Eng. Sci.*, **13**, 59, (1973).

44) C. J. de Bakker, N. A. St john and G. A. George, "Simultaneous Differential Scanning Calorimetry and Near-infra-red Analysis of the Curing of Tetraglycidyldiaminodiphenylmethane with Diaminodiphenylsulphone", *Polymer*, **34**, 716, (1993).

45) K. A. Kozielski, G. A. George, N. A. St John and N. C. Billingham, "Kinetic Studies by FT-NIR of the Curing Reaction of Two Glycidyl Ether Epoxy Resins Mixed with Stoichiometric Quantities of 4,4'-DDS", *High Perform. Polym.*, **6**, 263, (1994).

46) C. C. Riccardi and R. J. J. Williams, "Statistical Structural Model for the Build-up of Epoxy-Amine Networks with Simultaneous Etherification", *Polymer*, **27**, 913, (1986).

47) A. M. Gupta and C. W. Macosko, "Modeling Strategy for Systems with Both Stepwise and Chainwise Chemistry: Amine-Epoxy Networks with Etherification" *J. Polym. Sci.: Part B: Polym. Phys.*, **28**, 2585, (1990).

48) I. J. Good, "Cascade Theory and the Molecular Weight Averages of the Sol Fraction" *Proc. Roy. Soc.: A*, **272**, 54, (1963).

49) D. R. Miller, E. M. Valles and C. W. Macosko, "Calculation of Molecular Parameters for Stepwise Polyfunctional Polymerization", *Polym. Eng. Sci.*, **19**, 72, (1979).

50) D. Stauffer, A. Coniglio and M. Adam, "Gelation and Critical Phenomena", *Adv. Polym. Sci.*, **44**, 103, (1982).

51) T. E. Harris, "The Theory of Branching Processes", Springer-Verlag, Germany, (1963).

52) K. Dusek, "Network Formation in Curing of Epoxy Resins", *Adv. Polym. Sci.*, **78**, 1, (1986).

53) M. E. Ryan, "Rheological and Heat-Transfer Considerations for the Processing of Reactive Systems", *Polym. Eng. Sci.*, **24**, 698, (1984).

54) M. B. Roller, "Rheology of Curing Thermosets: A Review" *Polym. Eng. Sci.*, **26**, 432, (1986).

55) K. C. Cheng, W. Y. Chiu, K. H. Hsieh and C. C. M. Ma, "Chemorheology of Epoxy Resin. Part I: Epoxy Resin Cured with Tertiary Amine", *J. Mat. Sci.*, **29**, 721, (1994).

56) J. Mijovic and C. Hung Lee, "A Comparison of Chemorheological Models for Thermoset Cure", *J. Appl. Polym. Sci.*, **38**, 2155, (1989).

57) S. D. Lipshitz and C. W. Macosko, "Rheological Changes During a Urethane Network Polymerization", *Polym. Eng. Sci.*, **16**, 803, (1976).

58) J. M. Castro and C. W. Macosko, "Kinetics and Rheology of Typical Polyurethane Reaction Injection Molding Systems", *Soc. Plast. Eng. Tech. Papers*, **26**, 434, (1980).

59) M. J. Perry, T. James Wang, Y. Ma, and L. James Lee, "Resin Transfer Molding of Epoxy/Graphite Composites", *24th Int. SAMPE Tech. Conf.*, **24**, 421, (1992).

60) S. A. Bidstrup and C. W. Macosko, "Chemorheology Relations for Epoxy/Amine Crosslinking", *J. Polym. Sci.: Part B: Polym. Phys.*, **28**, 691, (1990).

61) M. L. Williams, R. F. Landel and J. D. Ferry, "The Temperature Dependence of Relaxation Mechanisms in Amorphous Polymers and Other Glass-Forming Liquids", *J. Am. Chem. Soc.*, **77**, 3701, (1955).

62) J. D. Ferry, "Viscoelastic Properties of Polymers", 3rd ed., J. Wiley and Sons, New York, (1980).

63) J. Mijovic and C. Hung Lee, "Modeling of Chemorheology of Thermoset Cure by Modified WLF Equation", *J. Appl. Polym. Sci.*, **37**, 889, (1989).

64) J. B. Enns and J. K. Gillham, "Time-Temperature-Transformation (TTT) Cure Diagram: Modeling the Cure Behavior of Thermosets", *J. Appl. Polym. Sci.*, **28**, 2567, (1983).

65) P. J. Halley and M. E. Mackay, "Chemorheology of Thermosets - An Overview", *Polym. Eng. Sci.*, **36**, 593, (1996).

66) L. Matejka and K. Dusek, "Influence of the Reaction Mechanism on Network Formation in Amine-Cured N,N-diglycidylamine Epoxy Resins", *Polymer*, **32**, 3195, (1991).

67) K. Dusek, M. Bleha and S. Lunak, "Curing of Epoxide Resins: Model Reactions of Curing with Amines", *J. Polym. Sci.: Polym. Chem.*, **15**, 2393, (1977).

68) R. A. Fava, "Differential Scanning Calorimetry of Epoxy Resins", *Polymer*, **9**, 137, (1968).

69) H. E. Kissinger, "Reaction Kinetics in Differential Thermal Analysis", *Anal. Chem.*, **29**, 1702, (1957).

70) T. Ozawa, "Kinetic Analysis of Derivative Curves in Thermal Analysis", *J. Therm. Anal.*, **2**, 301, (1970).

71) M. E. Ryan and A. Dutta, "Kinetics of Epoxy Cure: A Rapid Technique for Kinetic Parameter Estimation", *Polymer*, **20**, 203, (1979).

72) A. A. Duswalt, "The Practice of Obtaining Kinetic Data by Differential Scanning Calorimetry", *Thermochim. Acta*, **8**, 57, (1974).

73) J. M. Barton, "Kinetics of Cure of Epoxy Resin Systems Bisphenol-A diglycidylehter-di(4-aminophenyl)sulphone", *Polymer*, **21**, 603, (1980).

74) A. Sabra, J. P. Pascault and G. Seytre, "Epoxy Thermosetting Systems Based on Cycloaliphatic Diamines", *J. Appl. Polym. Sci.*, **32**, 5147, (1986).

75) A. Moroni, J. Mijovic, E. M. Pearce and C. Ching Foun, "Cure Kinetics of Epoxy Resins and Aromatic Diamines", *J. Appl. Polym. Sci.*, **32**, 3761, (1986).

76) R. J. Morgan and E. T. Mones, "The Cure Reactions, Network Structure and Mechanical Response of Diaminodiphenyl Sulfone - Cured Tetraglycidyl 4,4'-Diaminodiphenyl Methane Epoxies", *J. Appl. Polym. Sci.*, **33**, 999, (1987).

77) G. Wisanrakkit and J. K. Gillham, "The Glass Transition Temperature (T_g) as an Index of Chemical Conversion for a High-T_g Amine/Epoxy System: Chemical and Diffusion-Controlled Reaction Kinetics", *J. Appl. Polym. Sci.*, **41**, 2885, (1990).

78) J. M. Kenny and A. Trivisano, "Isothermal and Dynamic Reaction Kinetics of High Performance Epoxy Matrices" *Polym. Eng. Sci.*, **31**, 1426, (1991).

79) J.-D. Nam and J. C. Seferis, "Application of the Kinetic Composite Methodology to Autocatalytic-Type Thermoset Prepreg Cures", *J. Appl. Polym. Sci.*, **50**, 1555, (1993).

80) U. Bandara, "A Systematic Solution to the Problem of Sample Background Correction in DSC Curves", *J. Therm. Anal.*, **31**, 1063, (1986).

81) V. Bellenger, W. Dhaoui, J. Verdu, J. Galy, Y. G. Won and J. P. Pascault, "Glass Transition Temperature Predictions for Non-Stoichiometric Epoxide-Amine Networks", *Polymer*, **30**, 2013, (1989).

82) A. Hale, C. W. Macosko and H. E. Bair, "Glass Transition Temperature as a Function of Conversion in Thermosetting Polymers", *Macromolecules*, **24**, 2610, (1991).

83) M. J. Richardson, "Characterization of the Cure of Resins by Differential Scanning Calorimetry", *Pure & Appl. Chem.*, **64**, 1789, (1992).

84) B.-G. Min, Z. H. Strachurski and J. H. Hodgkin, "Cure Kinetics of Elementary Reactions of a DGEBA/DDS Epoxy Resin: 1. Glass Transition Temperature Versus Conversion", *Polymer*, **34**, 4908, (1993).

85) S. Wasserman and G. P. Johari, "Relaxations in Thermosets. XXIX. Calorimetric Studies of the Curing Kinetics of Nonstoichiometric Diamine-Epoxy Mixtures", *J. Appl. Polym. Sci.*, **53**, 331, (1994).

86) R. A. Venditti and J. K. Gillham, "A Relationship Between the Glass Transition Temperature (T_g) and Fractional Conversion for Thermosetting Systems", *J. Appl. Polym. Sci.*, **64**, 3, (1997).

87) M. Reading, "Modulated Differential Scanning Calorimetry - A New Way Forward in Materials Characterisation", *TRIP*, **1**, 248, (1993).

88) J. L. Koenig, "Spectroscopy of polymers", ACS Professional Reference Book, American Chemical Society, Washington, DC, (1992).

89) D. O. Hummel, "Infrared Spectra of Polymer in the Medium and Long Wavelength Regions", Intersience Publishers, J. Wiley and Sons, London, (1966).

90) J. L. Koening, "Spectroscopic Characterisation of Polymers", in *Physical Properties of Polymers* by J. E. Mark et al, 2nd edition, Chap. 6, 263-312, ACS Professional Reference Book, American Chemical Society, Washington, DC, (1993).

91) A. Sabra, T. M. Lam, J. P. Pascault, M. F. Grenier-Loustalot and P. Grenier, " Characterization and Behaviour of Epoxy - Based Diamino-diphenyl-sulphone Networks", *Polymer*, **28**, 1030, (1987).

92) D. W. Schiering, J. E. Katon, L. T. Drzal and V. B. Gupta, "An Infrared Spectroscopic Investigation of the Curing Reactions of the EPON 828 / Meta - Phenylenediamine System", *J. Appl. Polym. Sci.*, **34**, 2367, (1987).

93) J. Mijovic and S. Andjelic, "Monitoring of Reactive Processing by Remote Mid Infra-Red Spectroscopy", *Polymer*, **37**, 1295, (1996).

94) D. L. Woerdeman, J. K. Spoerre, K. M. Flynn and R. S. Parnas, "Cure Monitoring of the Liquid Composites Molding Process Using Fiber Optic Sensors", *Poly. Comp.*, **18**, 133, (1997).

95) M. Tackie and G. C. Martin, "The Polymerization Mechanism and Kinetics of DGEBA with BF_3-MEA", *J. Appl. Polym. Sci.*, **48**, 793, (1993).

96) G. A. George, P. Cole-Clarke, N. St. John and G. Friend, "Real-Time Monitoring of the Cure Reaction of a TGDDM/DDS Epoxy Resin Using Fiber Optic FT-IR", *J. Appl. Polym. Sci.*, **42**, 643, (1991).

97) D. L. Woerdeman and R. S. Parnas, "Cure Monitoring in RTM Using Fluorescence", *Plast. Eng.*, **51**, Oct. '95, 25, (1995).

98) M. L. Bromberg, D. R. Day, H. L. Lee and K. A. Russell, "New Applications for Dielectric Cure Control", 42nd Annual Conference, Composites Institute, The Society of the Plastics Industry, Inc. February 2-6, 1/Session22-E, (1987).

99) P. R. Giriscioli and G. S. Springer, "Dielectric Cure Monitoring - A Critical Review", *34th Int. SAMPE Symp.*, May 8-11, 312, (1989).

100) M. Sanford and R. L. McCullough, "Modelling the Viscosity and Dielectric Behavior During the Cure of Epoxy Matrix Composites", *Proc. Amer. Soc. Comp., 2nd Int. Conf.*, September 23-25, University of Delaware, 21, (1987).

101) J. W. Lane, J. C. Seferis and M. A. Bachmann, "Dielectric Modeling of the Curing Process", *Polym. Eng. Sci.*, **26**, 346, (1986).

102) H. Frohlich, "Theory of Dielectrics", Oxford Press, (1949).

103) P. Robert, "Electrical and Magnetic Properties of Materials", Artech House, Norwood, USA, (1988).

104) A. Hinchliffe and R. W. Munn, "Molecular Electromagnetism", J. Wiley and Sons, Chichester, UK, (1985).

105) F. J. Bottcher, "Theory of Electric Polarisation: Dielectrics in Static Field", Vol. I, 2nd ed., Elsevier, Amsterdam, (1973).

106) N. E. Hill, W. E. Vaughan, A. H. Price and M. Davies, "Dielectric Properties and Molecular Behavior", Van Nostrand Reinhold Company, London, (1969).

107) P. Debye, "Polar Molecules", Dover Publications, New York, (1945).

108) F. J. Bottcher and P. Bardewijk, "Theory of Dielectric Polarisation: Dielectrics in Time-Dependent Fields", Vol. II, 2nd ed., Elsevier, Amsterdam, (1978).

109) G. McGrum, B. E. Read and G. Williams, "Anelastic and Dielectric Effects in Polymer Solids", J. Wiley and Sons, London, (1967).

110) S. Havriliak and S. Negami, "A Complex Plane Representation of Dielectric and Mechanical Relaxation Processes in Some Polymers", *Polymer*, **8**, 161, (1967).

111) S. D. Senturia and N. F. Sheppard Jr., "Dielectric Analysis of Thermoset Cure", *Adv. Polym. Sci.*, **80**, 1, (1986).

112) J. Mijovic, J. M. Kenny, A. Maffezzoli, A. Trivisano, F. Bellucci and L. Nicolais, "The Principles of Dielectric Measurements for In Situ Monitoring of Composite Processing", *Comp. Sci. Tech.*, **49**, 277, (1993).

113) S. A. Bidstrup and D. R. Day, "Assignment of the Glass Transition Temperature Using Dielectric Analysis: A Review", *Assignment of the Glass Transition ASTM STP 1249*, R. J. Seyler, Ed., American Society for Testing and Materials, Philadelphia, 108, (1994).

114) A. Wall, "Dielectric Properties of Polymeric Materials", Published by Micromet Instruments Inc., 2nd ed., (1988).

115) G. Williams, *Adv. Polym. Sci.*, **33**, 59, (1979).

116) M. Fuoss and J. G. Kirkwood, *J. Am. Chem. Soc.*, **63**, 385, (1941).

117) W. Davidson and R. H. Cole, *J. Chem. Phys.*, **18**, 1417, (1950).

118) K. Scaife, *Proc. Phys. Soc. London*, **81**, 124, (1963).

119) G. Williams and D. C. Watts, "Non-Symmetrical Dielectric Relaxation Behaviour Arising from a Simple Empirical Decay Function", *Trans. Faraday Soc.*, **66**, 80, (1970).

120) D. R. Day, T. J. Lewis, H. L. Lee and S. D. Senturia, "The Role of Boundary Layer Capacitance at Blocking Electrodes in the Interpretation of Dielectric Cure Data in Adhesives", *J. Adhesion*, **18**, 73, (1985).

121) Y. A. Tajima and D. Crozier, "Thermokinetic Modelling of an Epoxy Resin I. Chemoviscosity", *Polym. Eng. Sci.*, **23**, 186, (1983).

122) F. Sheppard Jr. And S. D. Senturia, "Dielectric Properties of Bisphenol-A Epoxy Resins", *J. Polym Sci: Polym. Phys.*, **27**, 753, (1989).

123) W. L. Bruckman and M. P. de Goeje, "Dielectric Method for Monitoring the Curing of Polyester-Melamine Coatings", *Prog. Org. Coat.*, **20**, 501, (1992).

124) J. O. Simpson and S. A. Bidstrup, "Rheological and Dielectric Changes During Isothermal Epoxy-Amine Cure", *J. Polym. Sci.: Part B: Polym. Phys.*, **33**, 55, (1995).

125) T. Koike, "Determination of Glass Transition Temperature from Viscosity and Conductivity Measurements for an Epoxy-Amine System During Curing", *J. Appl. Polym. Sci.*, **50**, 1943, (1993).

126) K. A. Nass and J. C. Seferis, "Analysis of the Dielectric Response of Thermosets During Isothermal and Nonisothermal Cure", *Polym. Eng. Sci.*, **29**, 315, (1989).

127) D. R. Day, "Dielectric Determination of Cure State During Non-Isothermal Cure", *Polym. Eng. Sci.*, **29**, 334, (1989).

128) R. Casalini, S. Corezzi, A. Livi, G. Levita and P. A. Rolla, "Dielectric Parameters to Monitor the Crosslink of Epoxy Resins", *J. Appl. Polym. Sci.*, **65**, 17, (1997).

129) F. Stephan, A. Fit and X. Duteurtre, "In-Process Control of Epoxy Composite by Microdielectrometric Analysis", *Polym. Eng. Sci.*, **37**, 436, (1997).

130) F. Bellucci, M. Valentino, T. Monetta, L. Nicodemo, J. Kenny, L. Nicolais and J. Mijovic, "Impedance Spectroscopy of Reactive Polymers. 1", *J. Polym. Sci.: Part B: Polym. Phys.*, **32**, 2519, (1994).

131) J. Mijovic and C. F. Winnie Yee, "Use of Complex Impedance to Monitor the Progress of Reactions in Epoxy/Amine Model systems", *Macromolecules*, **27**, 7287, (1994).

132) F. Bellucci, M. Valentino, T. Monetta, L. Nicodemo, J. Kenny, L. Nicolais and J. Mijovic, "Impedance Spectroscopy of Reactive Polymers. 2. Multifunctional Epoxy/Amine Formulations", *J. Polym. Sci.: Part B: Polym. Phys.*, **33**, 433, (1995).

133) M. Olyphant Jr., "Effect of Cure and Aging on Dielectric Properties of Plastics - Part I", *Proc. 6th IEEE Electrical Insulation Conf.*, 12, (1965).

134) W. X. Zukas and S. E. Wentworth, "Microdielectric Monitoring of Prepreg Cure", *Polym. Comp.*, **8**, 232, (1987).

135) J. Gotro and M. Yandrasits, "Simultaneous Dielectric and Dynamic Mechanical Analysis of Thermosetting Polymers", *Polym. Eng. Sci.*, **29**, 278, (1989).

136) G. M. Maistros, "Dielectric Monitoring During the Cure of Epoxy Blends", PhD Thesis, School of Industrial and Manufacturing Science, Cranfield University, Cranfield, Beds, UK, (1991).

137) RTM6 material data sheet, Hexcel Composites.

138) 934 material data sheet, Fiberite Inc.

139) MY 721 material data sheet, Hexcel Composites.

140) M-MIPA material data sheet, LONZA Ltd.

141) M-DEA material data sheet, LONZA Ltd.

142) G. Cracknell and A. Milburn, Short Brothers's plc, Belfast, Northern Ireland, unpublished data.

143) L. J. Bellamy, "The Infra-red Spectra of Complex Molecules", 2nd ed., Methuen and Co Ltd., London, (1964).

144) T. Ozawa, T. Sunose and T. Kaneko, "Historical Review On Research Of Kinetics In Thermal-Analysis And Thermal Endurance Of Electrical Insulating Materials. 1. Thermal Endurance Test And Isoconversion Methods", *J. Therm. Anal.*, **44**, 205, (1995).

145) R. E. Lyon, "An Integral Method of Nonisothermal Kinetic Analysis", *Thermochim. Acta*, **297**, 117, (1997).

146) J. M. Salla and X. Ramis, "Comparative Study of the Cure Kinetics of an Unsaturated Polyester Resin Using Different Procedures", *Polym. Eng. Sci.*, **36**, 835, (1996).

147) P. Murray and J. White, *Trans. Brit. Ceram. Soc.*, **54**, 204, (1955).

148) C. C. Riccardi, H. E. Adabbo and R. J. J. Williams, "Curing Reaction of Epoxy Resins with Diamines", *J. Appl. Polym. Sci.*, **29**, 2481, (1984).

149) P.-L. Chiou and A. Letton, "Modelling the Chemorheology of an Epoxy Resin System Exhibiting Complex Curing Behaviour", *Polymer*, **33**, 3925, (1992).

150) J. M. Kenny, "Determination of Autocatalytic Kinetic Model Parameters Describing Thermoset Cure", *J. Appl. Polym. Sci.*, **51**, 761, (1994).

151) B.-G. Min, Z. H. Stachurski and J. H. Hodgkin, "Cure Kinetics of Elementary Reactions of a Diglycidyl Ether of Bisphenol A / Diaminodiphenylsulfone Epoxy Resin: 2. Conversion Versus Time", *Polymer*, **34**, 4488, (1993).

152) S. Carrozzino, G. Levita, P. Rolla and E. Tombari, "Calorimetric and Microwave Dielectric Monitoring of Epoxy Resin Cure", *Polym. Eng. Sci.*, **30**, 366, (1990).

153) M. T. DeMeuse, J. K. Gillham and F. Parodi, "Evolution of Properties of an Isocyanate/Epoxy Thermosetting System During Cure: Continuous Heating (CHT) and Isothermal Time-Temperature-Transformation (TTT) Cure Diagram", *J. Appl. Polym. Sci.*, **64**, 15, (1997).

154) S. L. Simon and G. K. Gillham, "Cure Kinetics of a Thermosetting Liquid Dicyanate Ester Monomer / High-T_g Polycyanurate Material", *J. Appl. Polym. Sci.*, **47**, 461, (1993).

155) G. M. Maistros and I. K. Partridge, "Dielectric Monitoring of Cure in a Commercial Carbon-Fibre Composite", *Comp. Sci. Tech.*, **53**, 355, (1995).

156) R. D. Hoffman, J. J. Godfrey R. J. Ehrig, D. E. Kranbuehl, L. Weller and M. Hoff, "Dynamic Dielectric Analysis: Development of Techniques for following the Curing Process of Laminating Polyester Resins", *J. Polym. Sci.: Polym. Symp.*, **74**, 71, (1986).

157) J. Mijovic, S. Andjelic, B. Fitz, W. Zurawsky, I. Mondragon, F. Bellucci and L. Nicolais, "Impedance Spectroscopy of Reactive Polymers. 3. Correlations Between Dielectric, Spectroscopic and Rheological Properties During Cure of a Trifunctional Epoxy Resin", *J. Polym. Sci.: Part B: Polym. Phys.*, **34**, 379, (1996).

158) J. Fournier, G. Williams, C. Duch and G. A. Aldridge, "Changes in Molecular Dynamics During Bulk Polymerisation of an Epoxide-Amine System as Studied by Dielectric Relaxation Spectroscopy", *Macromolecules*, **29**, 7097, (1996).

159) D. Kranbuehl, S. Delos, M. Hoff, P. Haverty, W. Freeman, R. Hoffman and J. Godfrey, "Use of the Frequency Dependence of the Impedance to Monitor Viscosity During Cure", *Polym. Eng. Sci.*, **29**, 285, (1989).

APPENDIX A

Ryan - Dutta Method

The Ryan - Dutta method is based on the solution of the system of Eqs. 4.9 - 4.12, which are:

$$a)\quad \frac{d\alpha}{dt} = \left(k_1 + k_2\alpha^m\right)\cdot\left(1-\alpha\right)^n$$

$$b)\quad r = m+n \qquad \text{(Eq. A.1)}$$

$$c)\quad \left.\frac{d\alpha}{dt}\right|_{t=0} = k_1$$

$$d)\quad nk_1\alpha_p^{1-m} + k_2 r\alpha_p - mk_2 = 0$$

where the subscript p refers to the point at the maximum reaction rate.

The solution of the above equations was made according to the following method:

1) Determination of initial reaction rates $\left.\frac{d\alpha}{dt}\right|_{t=0}$, maximum reaction rates $\left.\frac{d\alpha}{dt}\right|_{t=t_p}$ and corresponding conversions at maximum reaction rates α_p.
2) Substitution of initial reaction rates to Eq. A.1c to calculate k_1.
3) Guess of total reaction order r and partial reaction order m.
4) Substitution to Eq. A.1.b to calculate n.
5) Substitution to Eq. A.1a and solution with respect to k_2.
6) Substitution to Eq. A.1d and solution with respect to m.
7) Loop between steps 4 - 6 until the difference between guessed m and calculated m was less than 10^{-4}.

The flow diagram of the above estimation procedure is given in Figure A.1.

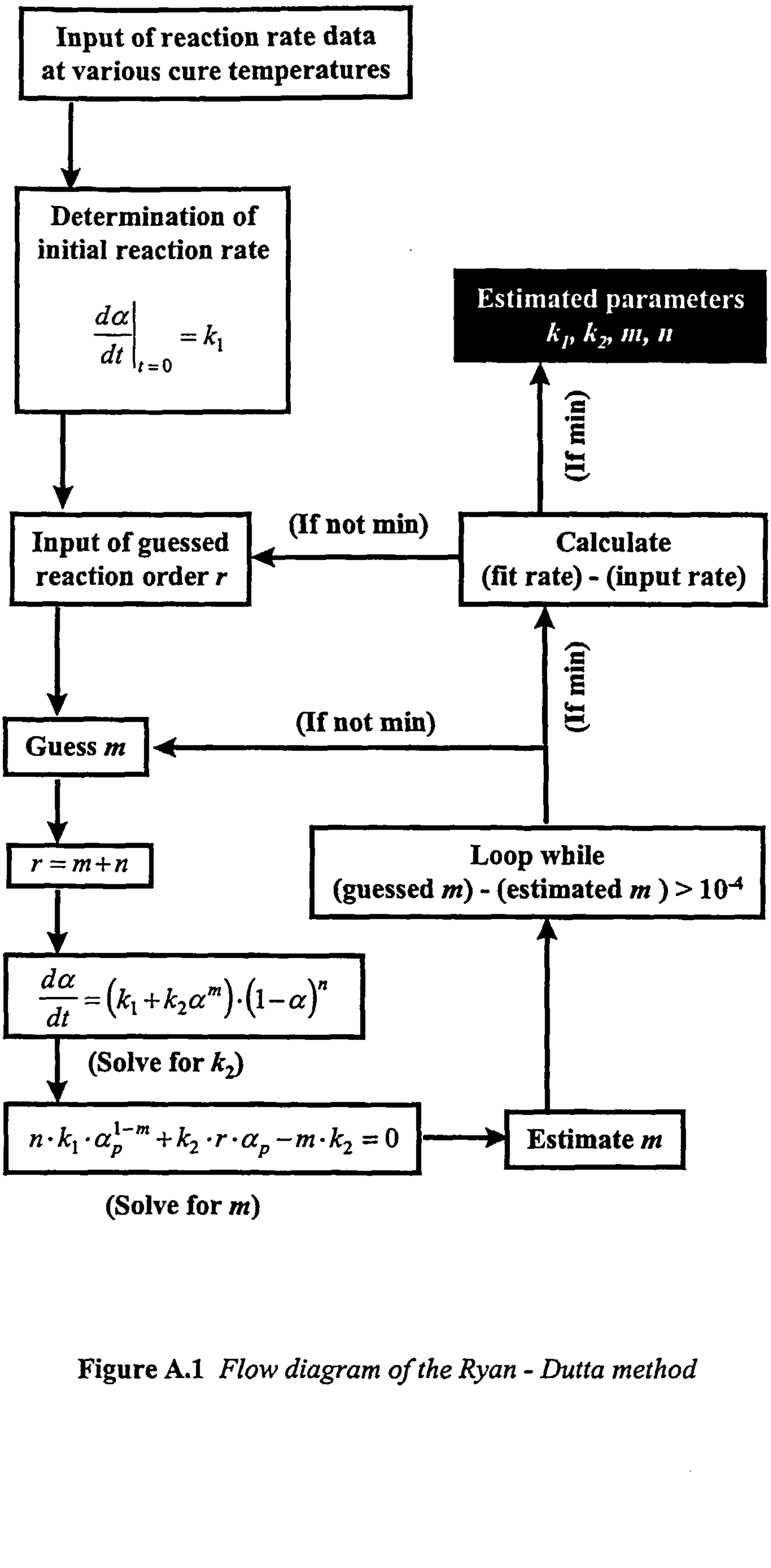

Figure A.1 *Flow diagram of the Ryan - Dutta method*

APPENDIX B

Present Method

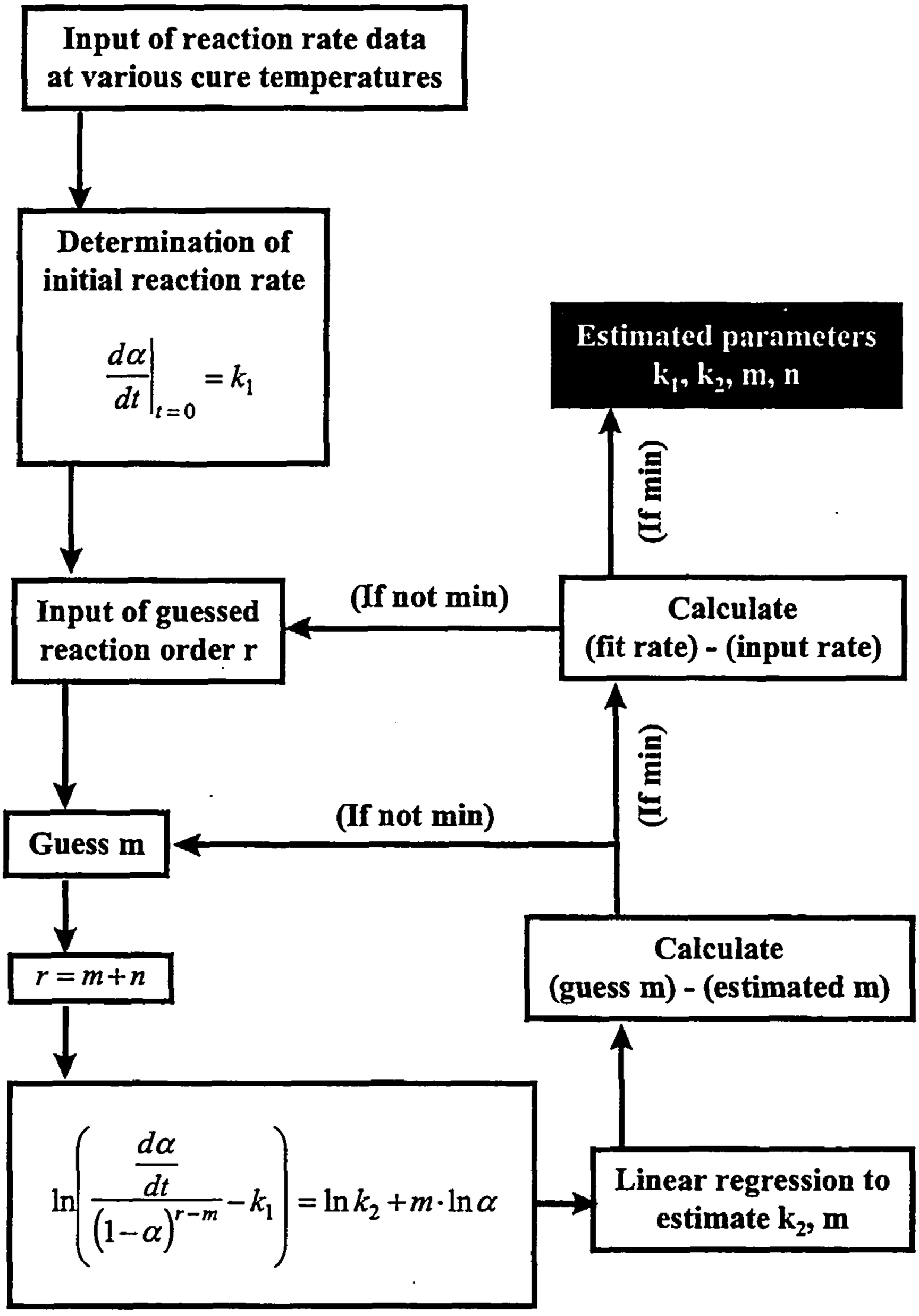

APPENDIX C

Levenberg - Marquardt Method of non-linear regression analysis (*)

If we consider the fitting of the model:

$$y = y(x, \mathbf{a}) \qquad \text{(Eq. C.1)}$$

to N observations (x_i, y_i), then if that model depends nonlinearly on the set of M unknown parameters α_k, the best-fit parameters can be evaluated by the minimisation of a χ^2 merit function of the form:

$$\chi^2(\mathbf{a}) = \sum_{i=1}^{N} \left[\frac{y_i - y(x_i, \mathbf{a})}{\sigma_i} \right]^2 \qquad \text{(Eq. C.2)}$$

The procedure for solving a nonlinear estimation problem is iterative. Sufficiently close to the minimum, the merit function χ^2 is expected to be well approximated by a quadratic form, which can be written as:

$$\chi^2(\mathbf{a}) \approx \gamma - \mathbf{d} \cdot \mathbf{a} + \frac{1}{2} \mathbf{a} \cdot \mathbf{D} \cdot \mathbf{a} \qquad \text{(Eq. C.3)}$$

where **d** is an M-vector and **D** an M × M matrix. If the approximation is good, the jump from the current trial parameters $\mathbf{a}_{cur}$ to the minimising ones $\mathbf{a}_{min}$, in a single step is:

(*) D. W. Marquardt, "An Algorithm for Least-Squares Estimation of Nonlinear Parameters", *J. Soc. Indust. Appl. Math.*, 11, 431, (1963).

$$\mathbf{a}_{\min} = \mathbf{a}_{cur} + \mathbf{D}^{-1} \cdot \left[-\nabla \chi^2 \left(\mathbf{a}_{cur} \right) \right] \qquad \text{(Eq. C.4)}$$

or, if we get a poor local approximation to the shape of the function that we are minimising, a step down the gradient according to the steepest descent method:

$$\mathbf{a}_{\min} = \mathbf{a}_{cur} - cons\tan t \times \nabla \chi^2 \left(\mathbf{a}_{cur} \right) \qquad \text{(Eq. C.5)}$$

The gradient of χ^2 with respect to the parameters **a**, if we disregard terms involving the second derivatives of the function $y = y(x, \mathbf{a})$, has components:

$$\frac{\partial \chi^2}{\partial a_k} = -2 \sum_{i=1}^{N} \frac{y_i - y(x_i, \mathbf{a})}{\sigma_i^2} \frac{\partial y(x_i, \mathbf{a})}{\partial a_k} \qquad k = 1, 2, \ldots, M \qquad \text{(Eq. C.6)}$$

$$\frac{\partial^2 \chi^2}{\partial a_k \partial a_l} = 2 \sum_{i=1} \frac{1}{\sigma_i^2} \left[\frac{\partial y(x_i, \mathbf{a})}{\partial a_k} \frac{\partial y(x_i, \mathbf{a})}{\partial a_l} \right] \qquad \text{(Eq. C.7)}$$

By defining:

$$\beta_k \equiv -\frac{1}{2} \frac{\partial \chi^2}{\partial a_k} \qquad a_{kl} = \frac{1}{2} \frac{\partial^2 \chi^2}{\partial a_k \partial a_l} \qquad \text{(Eq. C.8)}$$

then, Eq. C.4 can be rewritten as the set of linear equations:

$$\sum_{i=1}^{M} a_{kl} \delta a_l = \beta_k \qquad \text{(Eq. C.9)}$$

This set is solved for the increments $\delta \alpha_l$, that are added to the current approximation to give the next approximation.

In the case of the steepest descent method (Eq. C.5), the set of equations is:

$$\delta a_l = constant \times \beta_l \qquad \text{(Eq. C.10)}$$

Marquardt argued, that in order to scale the problem, Eq. C.10 needs to be rewritten as:

$$\delta a_l = \frac{1}{\lambda a_{ll}} \beta_l \qquad \text{(Eq. C.11)}$$

where the parameter λ is a fudge factor correcting the scaling factor $\frac{1}{a_{ll}}$

Marquardt's second insight was that Eqs. C.9 and C.11 can be combined by defining a new matrix **a'** as:

$$a'_{jj} \equiv a_{jj}(1+\lambda)$$
$$a'_{jk} \equiv a_{jk} \qquad (j \neq k) \qquad \text{(Eq. C.12)}$$

Then, Eqs. C.9 and C.11 can be replaced by:

$$\sum_{i=1}^{M} a'_{kl} \delta a_l = \beta_k \qquad \text{(Eq. C.13)}$$

Given an initial guess for the set of fitted parameters **a**, the recommended Marquardt recipe is as follows:

1) Compute $\chi^2(\mathbf{a})$;
2) Pick a modest value for λ (say λ =0.001)
3) Solve the linear equations (Eq. C.13) for $\delta\mathbf{a}$ and evaluate $\chi^2(\mathbf{a} + \delta\mathbf{a})$;

4) If $\chi^2(\mathbf{a} + \delta\mathbf{a}) \geq \chi^2(\mathbf{a})$, increase λ by a factor of 10 (or any other substantial factor) and return to step 3;

5) If $\chi^2(\mathbf{a} + \delta\mathbf{a}) < \chi^2(\mathbf{a})$, decrease λ by a factor of 10, update the trial solution $\mathbf{a} \leftarrow \mathbf{a} + \delta\mathbf{a}$, and go back to step 3;

6) Stop the iterative procedure when the minimum in χ^2 has been reached.

The complete evaluation procedure is given in Figure C.1.

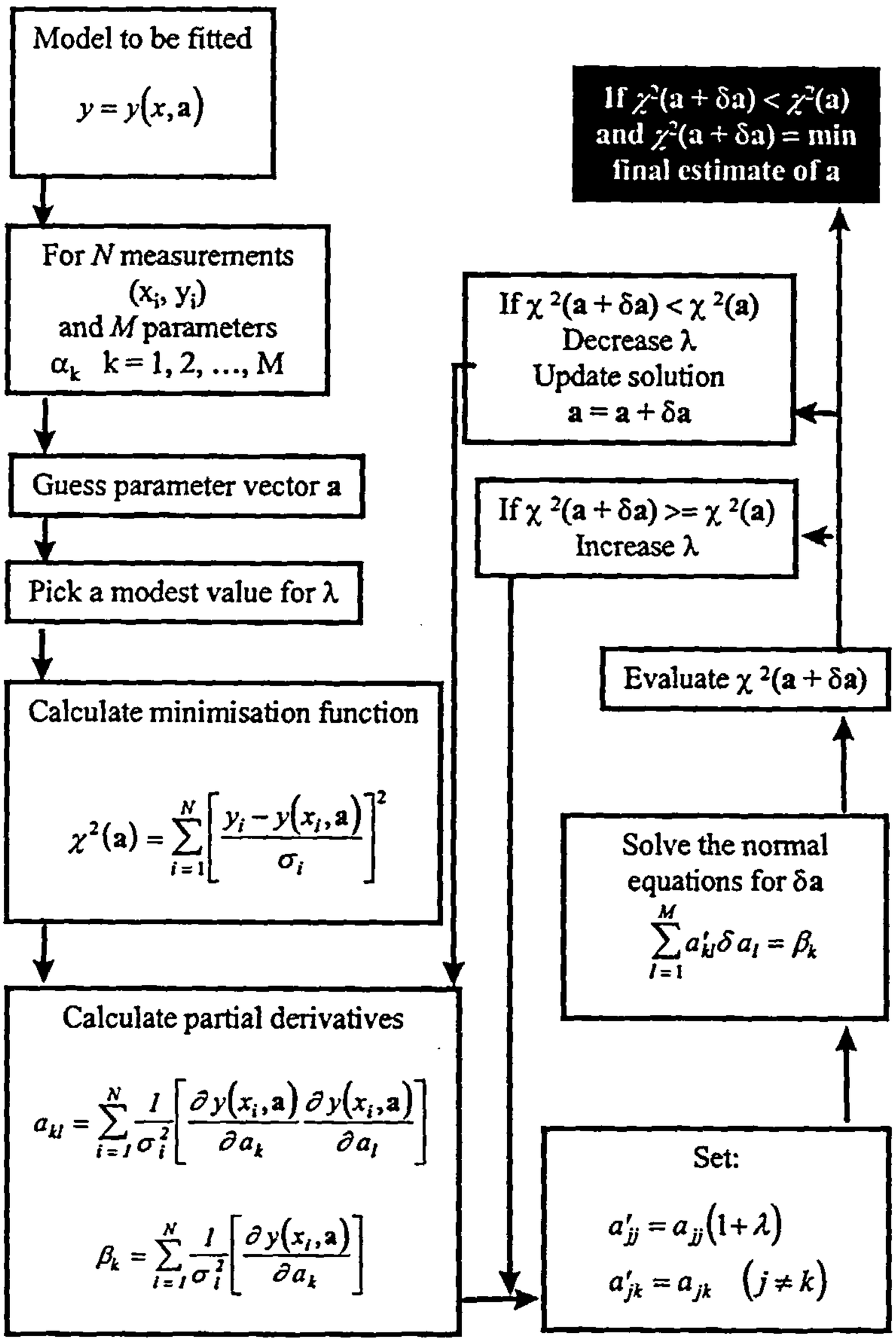

Figure C.1 *Flow diagram of the application of Levenberg - Marquardt method of non-linear regression.*

APPENDIX D

Gaussian Distribution

For a peak of the form $y = y(x)$ that follows a Gaussian distribution it holds:

$$y(x) = \frac{A}{w \cdot \sqrt{\frac{\pi}{2}}} \cdot \exp\left(-2\frac{\left(x - x_C\right)^2}{w^2}\right) + y_0$$

where: x_C = centre of the peak

w = approximately the width of the peak at half height

A = area under the peak

y_0 = baseline offset

APPENDIX E

Model Sensitivity Analysis

The sensitivity of all the mathematical models constructed in this study was evaluated by incorporating a fixed % error on the estimated model parameters. For demonstration purposes, the kinetic model of the isothermal cure of RTM6 resin was selected, as given in Section 4.4.1. The model is given by Eq. 4.9 and the estimated parameters in Table 4.5 for the Ryan - Dutta estimation procedure.

A fixed error of 5% was incorporated in the model for each parameter in turn and the kinetic simulation was repeated for the isothermal cure of RTM6 resin at 140°C. The initially estimated values of the kinetic parameters, as these were given in Table 4.5, are shown in Table E.1 along with the parameters in the model sensitivity analysis. The simulated kinetics results of the effect of each kinetic parameter individually are shown in Figure E.1 - Figure E.6 as plots of reaction rate against cure time.

Table E.1 *Kinetic parameters used in the model sensitivity analysis of the kinetic model of the isothermal cure of RTM6 resin.*

	Model Parameter					
	m	n	E_1	A_1	E_2	A_2
from Table 4.5	1.216	1.284	74.69	$4.500 \cdot 10^6$	58.37	$1.300 \cdot 10^6$
-5%	1.155	1.220	70.96	$4.275 \cdot 10^6$	55.45	$1.235 \cdot 10^6$
+5%	1.277	1.348	78.42	$4.725 \cdot 10^6$	61.29	$1.365 \cdot 10^6$

Combinations of two parameters changed simultaneously were also tested in order to check the effect upon the accuracy of the fitting. The results of the effects of the pairs m / n and m / E_1 on the simulation are shown in Figure E.7 and Figure E.8 respectively.

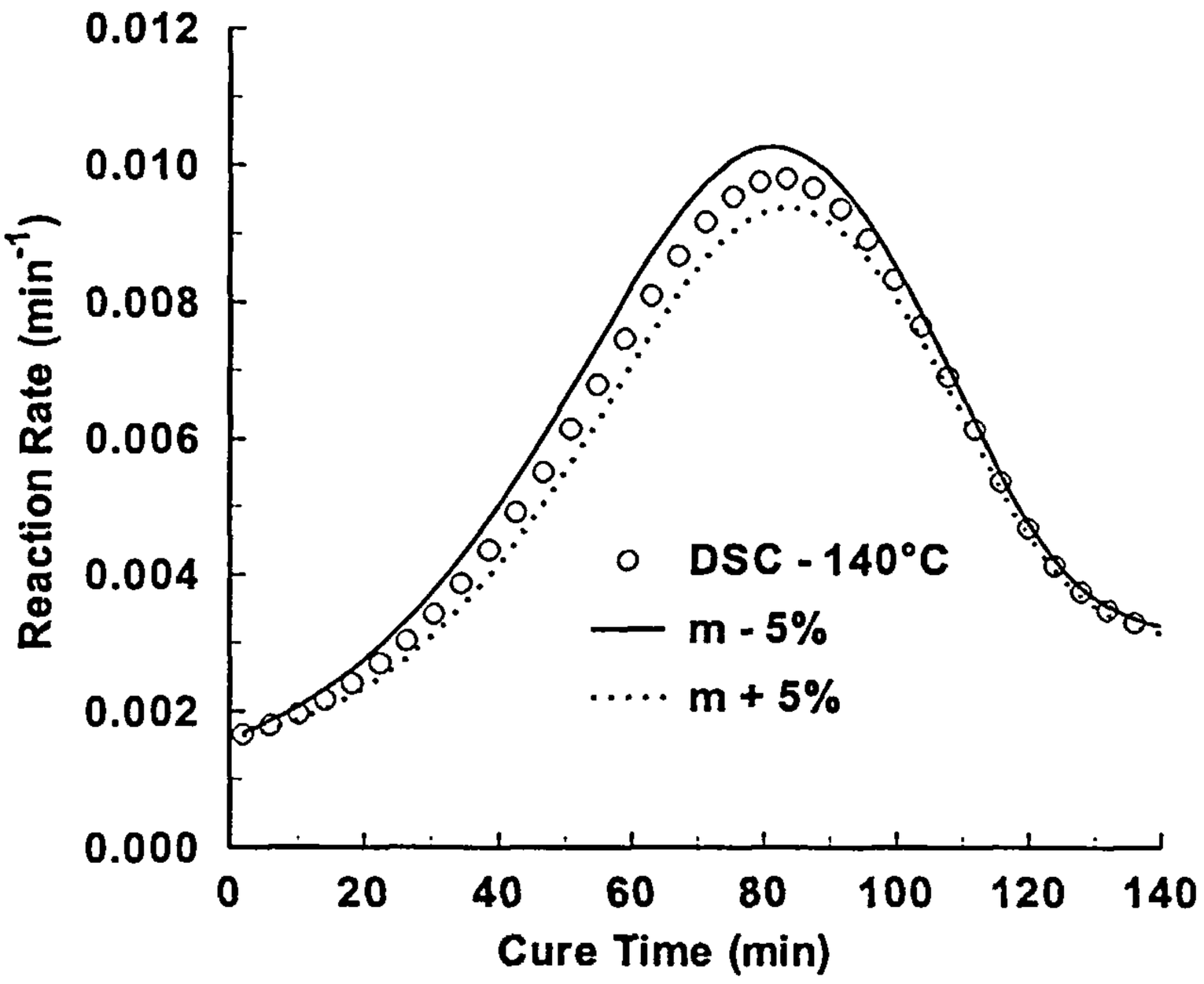

Figure E.1 *Reaction rate of an isothermal cure of RTM6 resin at 140°C. a)* ***Symbols:*** *raw data from DSC experiments. B)* ***Lines:*** *simulation using Eq. 4.9 and the parameters given in Table E.1*

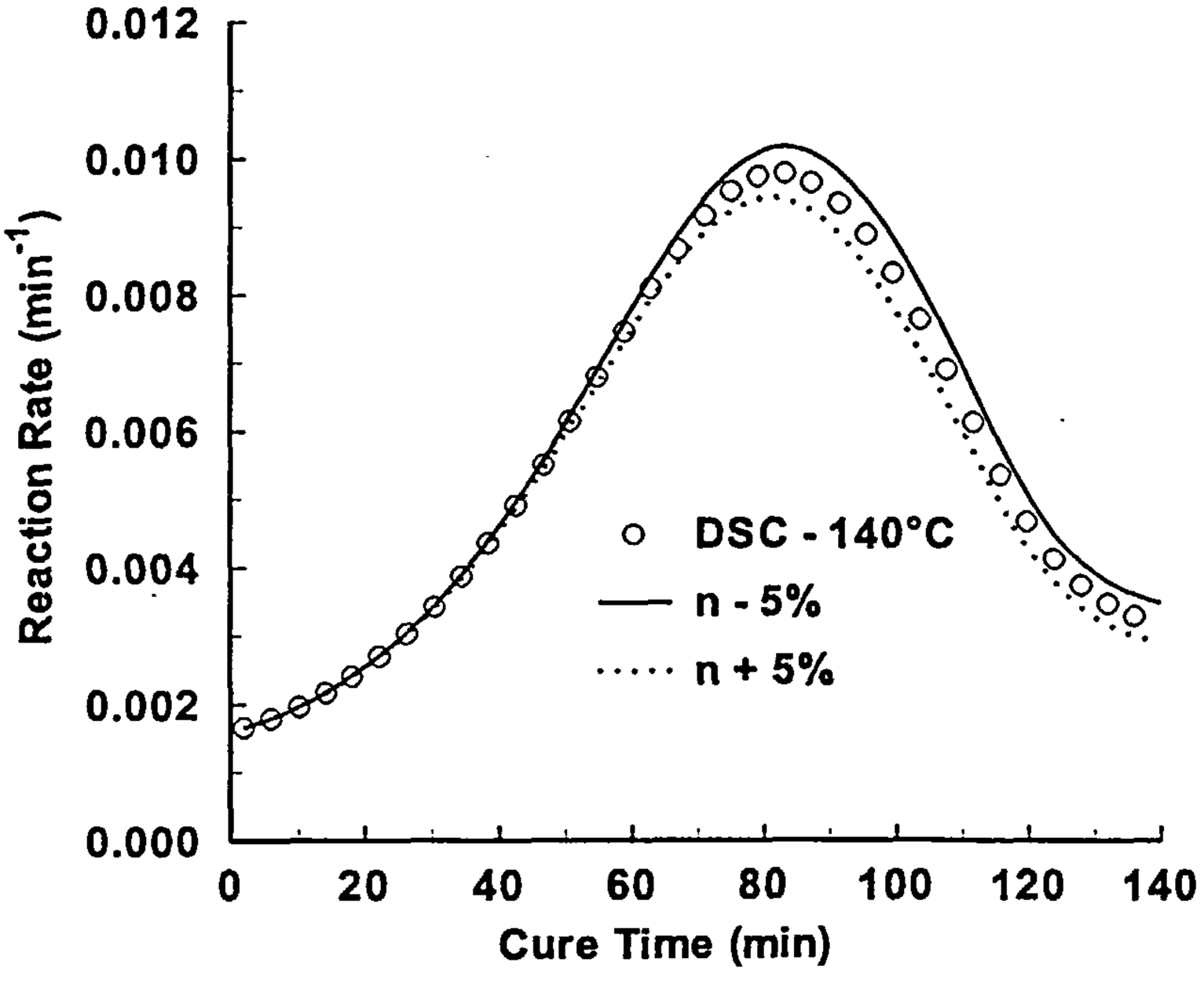

Figure E.2 *Reaction rate of an isothermal cure of RTM6 resin at 140°C. a)* ***Symbols:*** *raw data from DSC experiments. B)* ***Lines:*** *simulation using Eq. 4.9 and the parameters given in Table E.1*

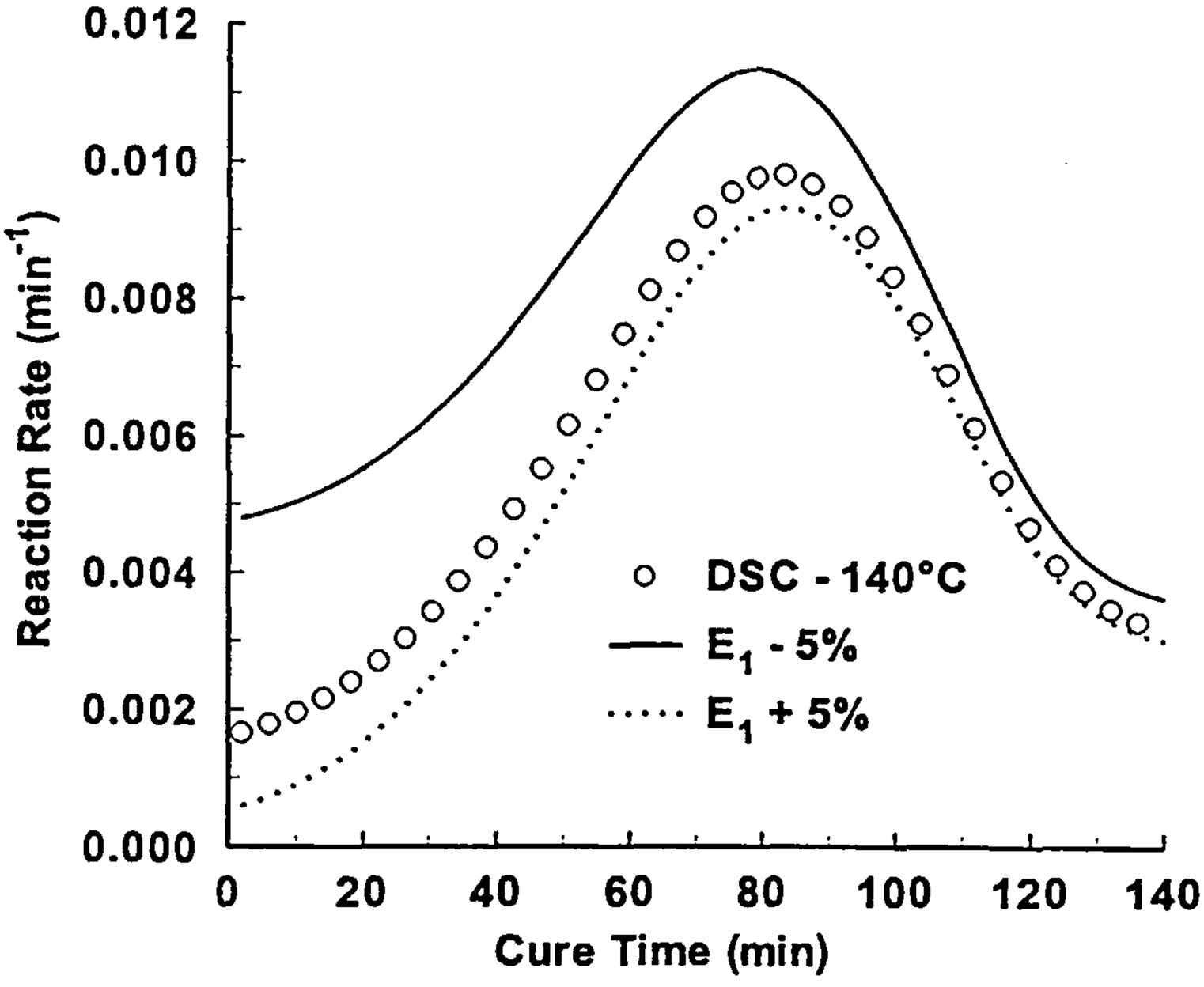

Figure E.3 *Reaction rate of an isothermal cure of RTM6 resin at 140°C. a)* ***Symbols:*** *raw data from DSC experiments. B)* ***Lines:*** *simulation using Eq. 4.9 and the parameters given in Table E.1*

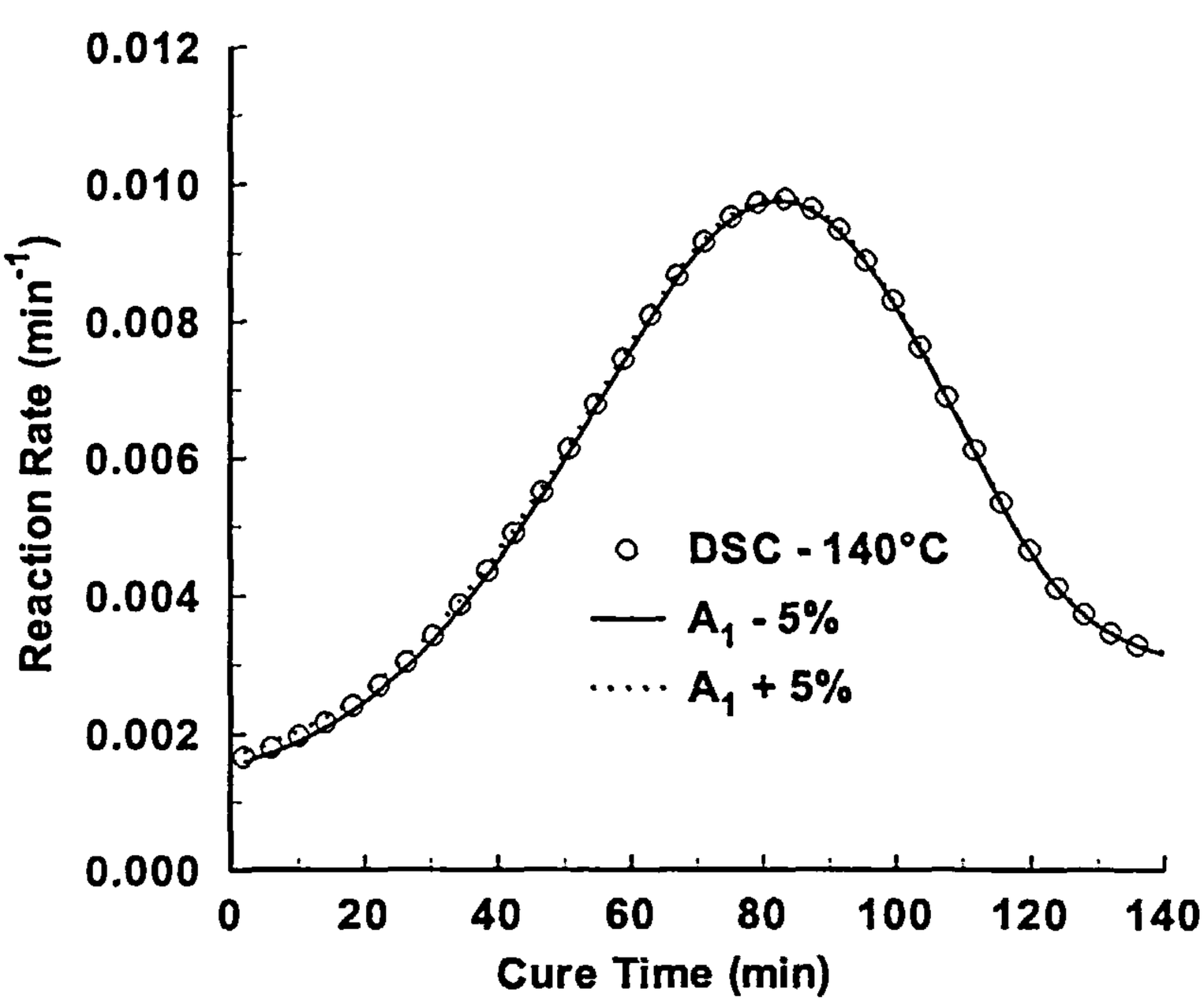

Figure E.4 *Reaction rate of an isothermal cure of RTM6 resin at 140°C. a)* ***Symbols:*** *raw data from DSC experiments. B)* ***Lines:*** *simulation using Eq. 4.9 and the parameters given in Table E.1*

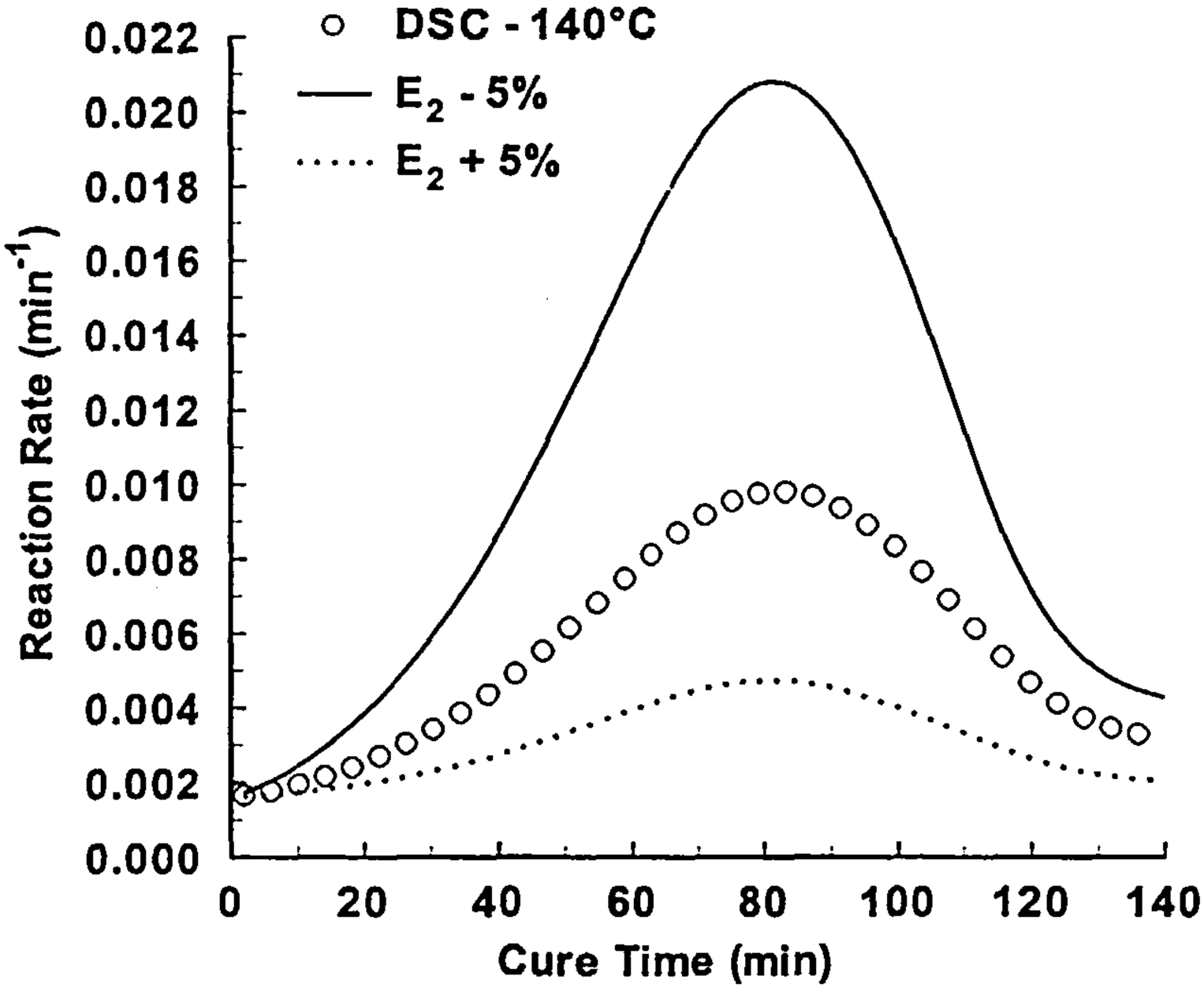

Figure E.5 *Reaction rate of an isothermal cure of RTM6 resin at 140°C. a)* ***Symbols:*** *raw data from DSC experiments. B)* ***Lines:*** *simulation using Eq. 4.9 and the parameters given in Table E.1*

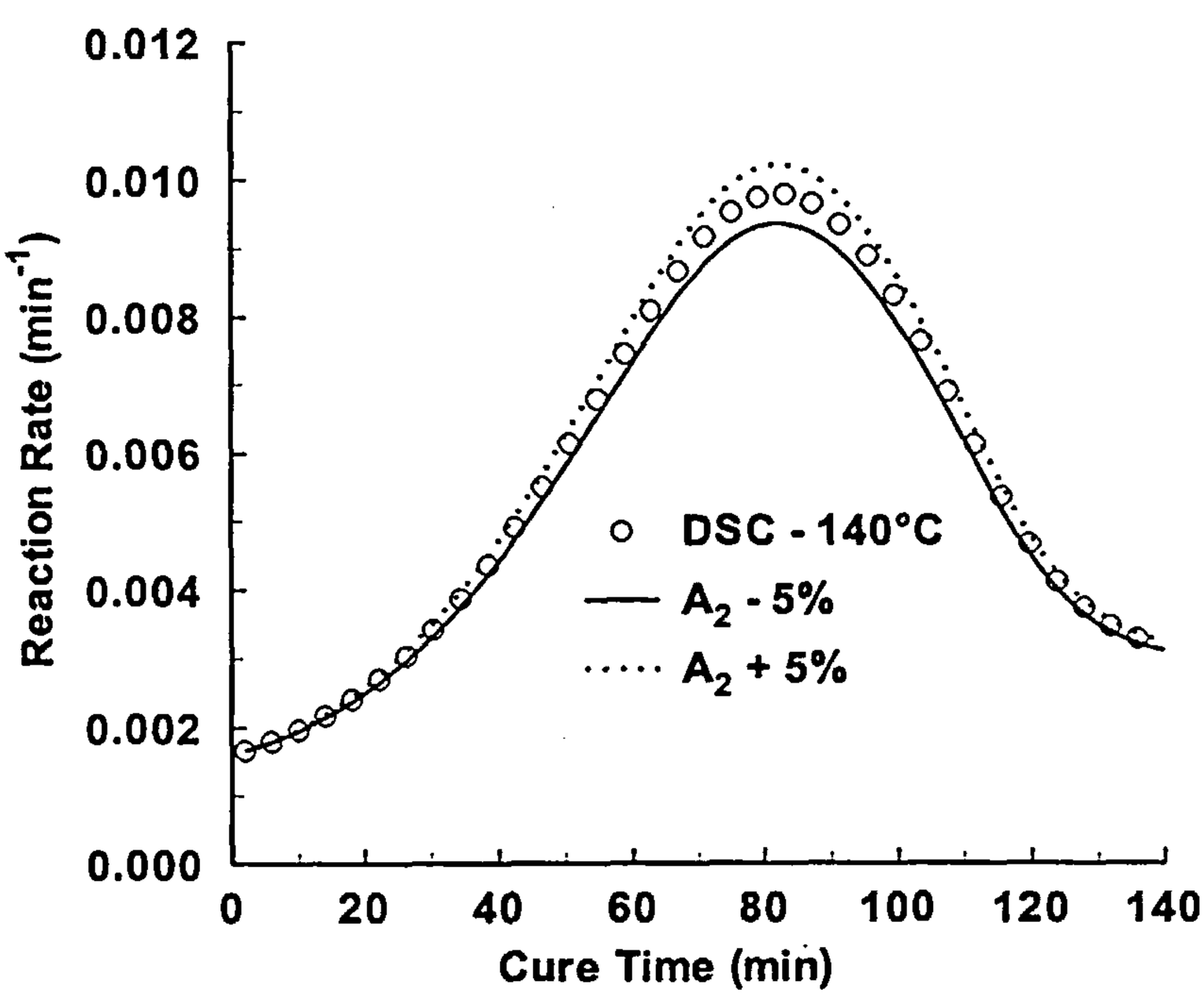

Figure E.6 *Reaction rate of an isothermal cure of RTM6 resin at 140°C. a)* ***Symbols:*** *raw data from DSC experiments. B)* ***Lines:*** *simulation using Eq. 4.9 and the parameters given in Table E.1*

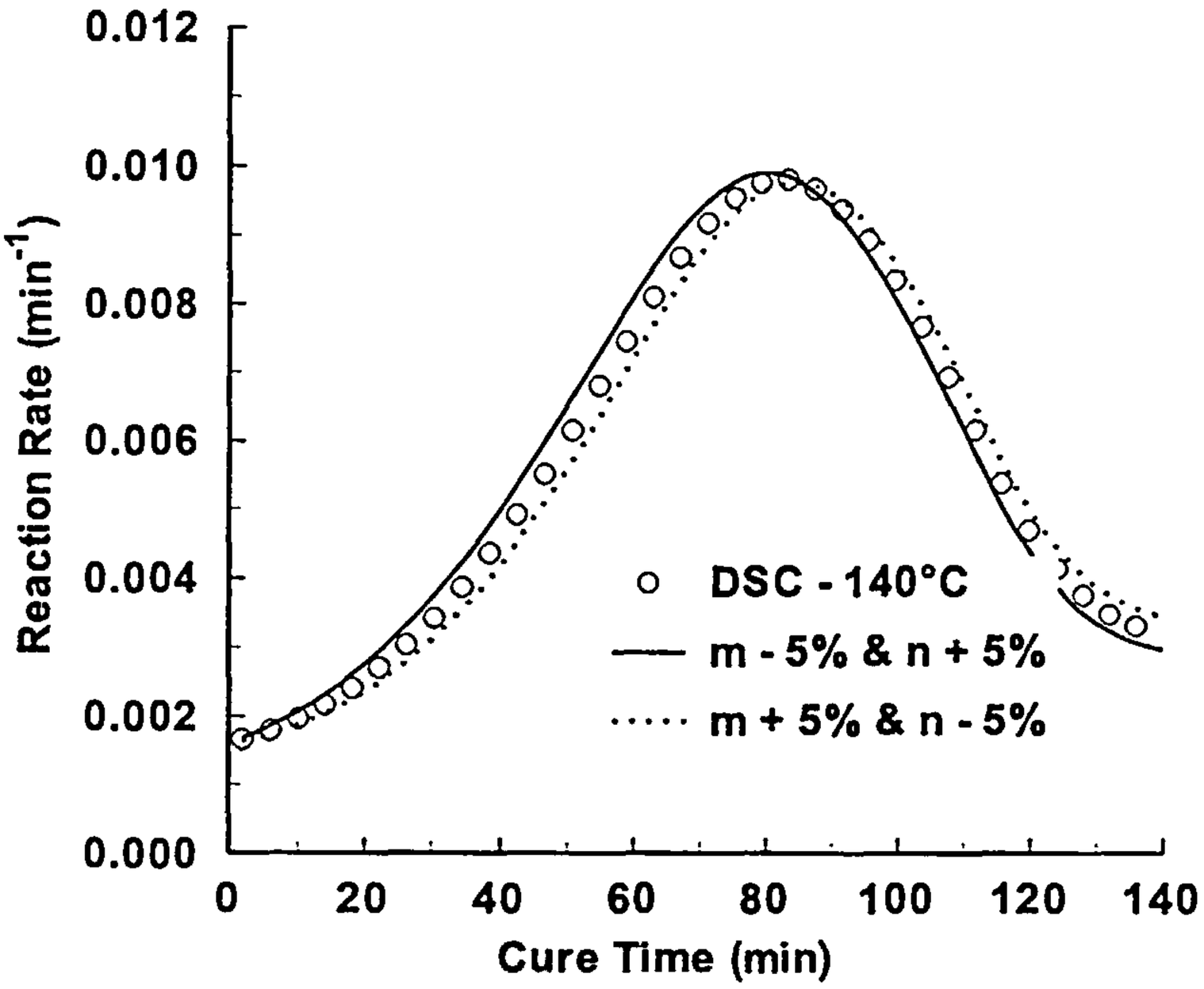

Figure E.7 *Reaction rate of an isothermal cure of RTM6 resin at 140°C. a)* ***Symbols:*** *raw data from DSC experiments. B)* ***Lines:*** *simulation using Eq. 4.9 and the parameters given in Table E.1*

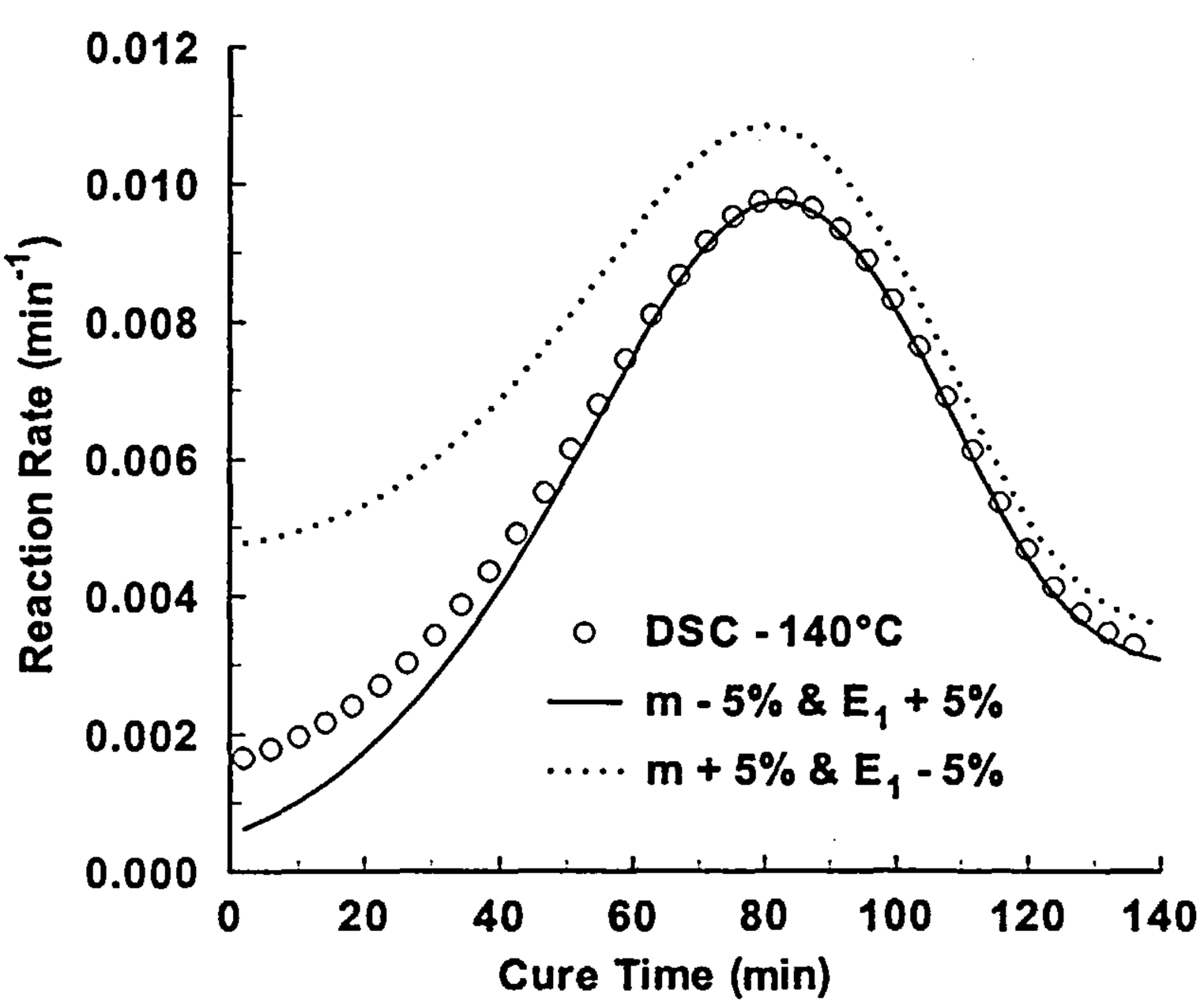

Figure E.8 *Reaction rate of an isothermal cure of RTM6 resin at 140°C. a)* ***Symbols:*** *raw data from DSC experiments. B)* ***Lines:*** *simulation using Eq. 4.9 and the parameters given in Table E.1*

As can be concluded from the above figures, the kinetic model is rather insensitive to the reaction orders m and n (Figure E.1 and Figure E.2) and to the pre-exponential factors A_1 and A_2 (Figure E.4 and Figure E.6). The fitting of the kinetic model is still adequate despite the fact that the parameters have been changed by 5%. On the other hand, the effect of the activation energies values on the simulation is very significant. A 5% change in the values of the activation energies has a dramatic effect on the fitting. The activation energy E_1 (Figure E.3), which represents the non-autocatalytic reactions, produces a large divergence at the initial stages of the cure. This is expected since the reaction rate constant k_1 represents the intercept of the plots given in Figure E.1 - Figure E.8. The effect of the activation energy of the autocatalytic reactions E_2 (Figure E.5) has a greater effect on the fitting than E_1. This behaviour is a direct outcome of the exponential nature of the reaction rate constants (Arrhenius type). The lower the activation energy the higher the value of the exponent $\exp\left(-\frac{E_i}{RT}\right)$. Since the pre-exponential factors for both the autocatalytic and non-autocatalytic reactions, A_i, are similar (see Table E.1), the relative weighting of each reaction on the total reaction rate will depend upon the activation energy. The lower the activation energy of a particular reaction, the greater the effect of that reaction on the overall reaction rate will be. Thus, a 5% decrease in the activation energy for autocatalysis will increase to the relative weighting of autocatalysis and will produce higher overall reaction rates. On the other hand, a 5% increase will reduce the significance of autocatalysis and will produce lower overall reaction rates.

The high sensitivity of the kinetic models to the activation energies restricts the use of activation energies taken from the literature in any attempts of simulating the reaction kinetics behaviour of any epoxy/amine resin systems. As mentioned in Section 2.4.2, the values of the recorded activation energies for autocatalytic and non-autocatalytic reactions are within a range of 4-5 kJ/mol of the estimated activation energies given in this study. The 5% error introduced here is within that range and as explained in the previous paragraphs produces a big divergence during the simulation.

Another interesting point that become apparent from the simulations given in the above figures is that a reduction in the estimated kinetic parameters produces an increase in the overall reaction rates, apart from the case of the pre-exponential factors, which produces the opposite effect.

The combined effect of two kinetic parameters changed simultaneously can be seen in Figure E.7 and Figure E.8. The first figure shows the response of the kinetic model by decreasing the reaction order m and increasing the reaction order n and vice versa. Both simulations give a very good fitting to the experimental data suggesting that the increase of one of the reaction orders and the decrease of the other produces a zero net effect. The combined effect of the changes in the reaction order m and the activation energy of the non-autocatalysed reactions E_1, is shown in Figure E.8. The bigger effect of the activation energy in the simulations is still predominant. However, the response of the kinetic model shows higher reaction rates for higher activation energies, which is the opposite from the simulations with only the parameter E_1changed (see Figure E.3).

Equivalent effects are expected to occur for all other kinetic models introduced in this study, because of the similar nature of the models themselves. This sample error analysis therefore represents a template for any similar specific error analysis.